DESIGN AND DOSIMETRY OF EPITHERMAL NEUTRON BEAMS FOR CLINICAL TRIALS OF BORON NEUTRON CAPTURE THERAPY AT THE MITR-II REACTOR

by

RONALD DANIEL ROGUS

B.S., PENNSYLVANIA STATE UNIVERSITY (1982)
M.S., MASSACHUSETTS INSTITUTE OF TECHNOLOGY (1990)

SUBMITTED TO THE DEPARTMENT OF
NUCLEAR ENGINEERING IN PARTIAL FULFILLMENT OF
THE REQUIREMENTS FOR THE DEGREE OF

DOCTOR OF PHILOSOPHY

at the

MASSACHUSETTS INSTITUTE OF TECHNOLOGY

January, 1994

Signature of Author _____
Department of Nuclear Engineering
January 14, 1994

Certified by _____
Otto K. Harling, Thesis Supervisor
Professor of Nuclear Engineering

Certified by _____
Jacquelyn C. Yanch, Thesis Supervisor
Professor of Nuclear Engineering

Accepted by _____
Prof. Allan F. Henry, Chairman
Departmental Graduate Committee

vol. 1

DESIGN AND DOSIMETRY OF EPITHERMAL NEUTRON BEAMS FOR CLINICAL TRIALS OF BORON NEUTRON CAPTURE THERAPY AT THE MITR-II REACTOR

by

RONALD DANIEL ROGUS

Submitted to the Department of Nuclear Engineering on January 14, 1994 in partial fulfillment of the requirements for the Degree of Doctor of Philosophy.

ABSTRACT

Over 20 different epithermal neutron beams for Boron Neutron Capture Therapy (BNCT) have been designed and dosimetrically characterized in realistic phantoms at the MITR-II Research reactor. Photon and fast neutron doses were measured with ionization chambers using the dual chamber technique. Thermal neutron and B-10 doses were determined by measuring the thermal neutron flux using the cadmium difference technique, and then multiplying the flux by the thermal neutron and B-10 kerma factors. A clinical protocol for mixed field dosimetry of epithermal neutron beams was developed. Procedures for the clinical dosimetry, including quality control, were written and performed. The filtering configuration and the measured dose-versus-depth profiles for each beam are provided.

One of these beams (M67) was selected for use in phase I clinical trials of patients with subcutaneous peripheral melanoma. The M67 beam is moderated with D_2O, filtered with cadmium, aluminum, and sulfur, and has a final photon shield of bismuth. It has a lithiated paraffin delimiter and a borated polyethylene whole body shield to minimize the patient's dose outside the treatment area. Assuming a bilateral irradiation of a standard size, ellipsoidal head phantom, reasonable B-10 concentrations for the B-10 delivery agent L-p-boronophenylalanine, BPA, (30 ppm in tumor, 7.5 ppm in healthy tissue), and reasonable RBE's (B-10, 4.0; thermal and fast neutrons, 2.3; photons, 0.5 for a fractionated therapy), the beam provides an average tumor-to-healthy tissue dose ratio of 2.0. The experimentally determined dose components have been used to normalize a companion set of dose components generated by the Monte Carlo based transport code MCNP; the normalization factors are used in the treatment planning software. A 250 minute unilateral irradiation would deliver 2000 RBE cGy peak dose to healthy tissue in the treatment zone, and a whole body dose of 57 RBE cGy. Judicious positioning of the patient, and use of additional shielding, can reduce the patient's whole body dose by a factor of 2 or more.

The medical room was prepared for clinical trials. Neutron absorbing materials were added to reduce activation and a radiation shield was designed that would reduce doses to personnel working inside the medical room.

Finally, as part of an interinstitutional biodistribution and pharmacokinetic study of BPA in humans, the B-10 concentrations of blood and urine samples from two glioblastoma and four melanoma patients were analyzed by prompt gamma neutron activation analysis.

The technical elements and the federal and institutional approvals are all now in place to initiate a phase-I clinical trial of boron neutron capture therapy for the treatment of subcutaneous peripheral melanoma.

Thesis Supervisor: Otto K. Harling
Title: Professor of Nuclear Engineering

Thesis Supervisor: Jacquelyn C. Yanch
Title: Associate Professor of Nuclear Engineering

DEDICATION

TO MY PARENTS

ACKNOWLEDGMENTS

During my years at MIT I have met many wonderful people. First, I would like to acknowledge my thesis advisors, Professors Otto Harling and Jacquelyn Yanch. Both are extraordinary persons and superb scientists; it was an honor working and learning with them. A great experience is was. My thanks also to Professor Robert Zamenhof for all his help, especially with the dosimetry. And thanks to Frank Masse and Professors Yip, Henry, and Rasmussen. Also, I would like to thank Dr. John Bernard for all his help, humor, and encouragement. And thanks to Dr. Olmez for his help with the Ge(Li)'s.

I would also like to acknowledge my fellow students - Guido, Sam, Jean-Michel, Damien, Richard, Gopika, and Everett on the BNCT project, and Jeff, Tony, Toni, Scott, Rena, Ernesto, Sinan, Wen, Kevin and Jianmei. I especially want to thank and acknowledge Guido for teaching and helping me so much with work, computers, and with life.

I would also like to thank the people in Reactor Operations - Kwan, Eddy, Tom, Ed, Jay, John, Bill, Paul, Mark, Ara, Lenny, Susan, John, Frank, and Don. And in Radiation Protection - Fred, Bruce, Marcia, Todd, and Kitty. And Carolyn, Georgia, Henry, and, especially, Dorothy. And thanks to John and Ron in the Machine Shop and to Pete. And thank you, Guillermo. Thanks, too, to Sarah and Drs. DiPetrillo and Wazer. And thanks to Clare, Marsha, and Anne.

This research was generously supported through the United States Department of Energy under Grant No. DE-FG02-87ER-6060

TABLE OF CONTENTS

Chapter 3 PROTOCOL FOR MIXED FIELD DOSIMETRY OF THE EPITHERMAL NEUTRON BEAMS

Chapter 4 EPITHERMAL NEUTRON BEAM DESIGN, INSTALLATION, AND DOSIMETRY

Chapter 5 DESCRIPTION AND DOSIMETRY OF THE BEAM SELECTED FOR CLINICAL TRIALS

Chapter 6 MODIFICATIONS MADE TO THE MEDICAL ROOM FOR CLINICAL TRIALS

LIST OF FIGURES

Chapter 1 INTRODUCTION

Chapter 2 OVERVIEW OF THE MITR-II REACTOR, BEAM DESIGN, AND DOSIMETRY

Chapter 3 PROTOCOL FOR MIXED FIELD DOSIMETRY OF THE EPITHERMAL NEUTRON BEAMS

Chapter 4 EPITHERMAL NEUTRON BEAM DESIGN, INSTALLATION, AND DOSIMETRY

Chapter 5 DESCRIPTION AND DOSIMETRY OF THE BEAM SELECTED FOR CLINICAL TRIALS

Chapter 6 MODIFICATIONS MADE TO THE MEDICAL ROOM FOR CLINICAL TRIALS

Chapter 7 BIODISTRIBUTION AND PHARMACOKINETICS OF BPA IN HUMANS

LIST OF TABLES

Chapter 1 INTRODUCTION

Chapter 2 OVERVIEW OF THE MITR-II REACTOR, BEAM DESIGN, AND DOSIMETRY

Chapter 3 PROTOCOL FOR MIXED FIELD DOSIMETRY OF THE EPITHERMAL NEUTRON BEAMS

Chapter 4 EPITHERMAL NEUTRON BEAM DESIGN, INSTALLATION, AND DOSIMETRY

Chapter 5 DESCRIPTION AND DOSIMETRY OF THE BEAM SELECTED FOR CLINICAL TRIALS

Chapter 6 MODIFICATIONS MADE TO THE MEDICAL ROOM FOR CLINICAL TRIALS

Chapter 7 BIODISTRIBUTION AND PHARMACOKINETICS OF BPA IN HUMANS

Chapter 8 CONCLUSIONS AND RECOMMENDATIONS FOR FUTURE WORK

CHAPTER 1 INTRODUCTION

Boron neutron capture therapy (BNCT) is a binary form of radiation therapy that has the potential ability to kill tumor cells or cell clusters embedded within normal tissue.[1-3] A tumor seeking drug is tagged with the stable isotope boron-10 (B-10). After tumor cells have been loaded with sufficient B-10, on the order of 20 ppm or higher [4,5], the region of the body containing tumor is irradiated with neutrons from a nuclear reactor or, in the future, possibly from other neutron sources such as accelerators. Absorption of a neutron by B-10 results in an excited B-11 nucleus, which instantly decays into an energetic alpha particle and Li-7 nucleus that travel in opposite directions. The reaction is: [6,7]

$$\text{B-10} + \text{n} \rightarrow \alpha + \text{Li-7} + \gamma \qquad Q = 2.79 \text{ MeV}$$

$$\sigma_{th} = 3837 \text{ barns}$$

In 94% of the reactions, the recoiling Li-7 is produced in an excited state; the excited Li-7 nuclei decay by emission of 478 keV prompt gammas. The other 6% of the reactions lead directly to the ground state of Li-7. The α and Li-7 lose energy as shown in figure 1.1. [8] They are densely ionizing and have a range of 9 and 5 μm, respectively, in tissue.[8] The diameter of many cells is of the order 10 μm; therefore, the radiation dose deposited by the reaction products is localized to tumor cells that have taken up the B-10 loaded drug, or their nearest neighbors; adjacent healthy tissue cells are spared if they have not taken up B-10.

The thermal neutron cross section for the B-10(n,α)Li-7 reaction is large, 3837 barns.[6] Because of the high thermal neutron cross section and the (n,α) type of reaction,

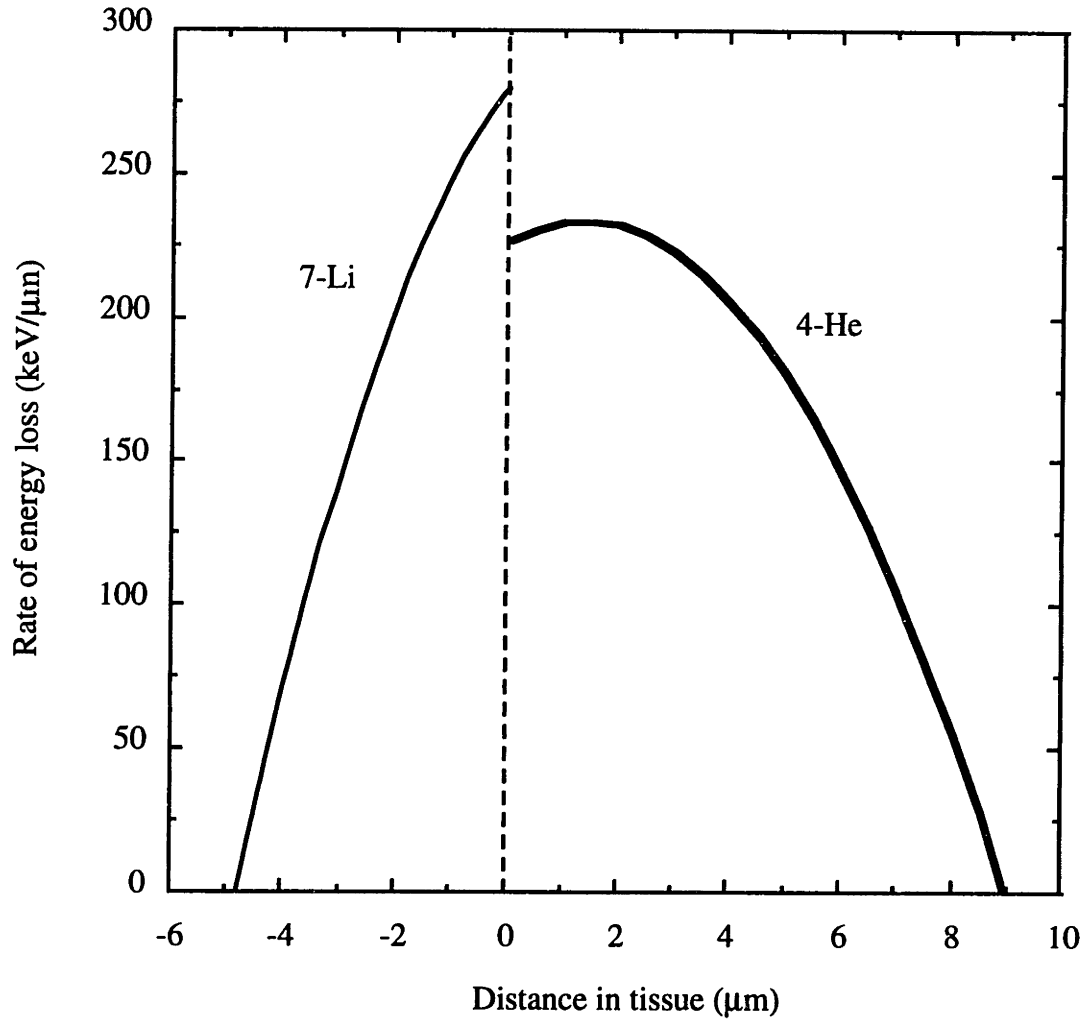

Figure 1.1. Rate of energy loss[8] for the α and Li-7 ions, the reaction products of the B-10 (n,α)Li-7 reaction. These heavy charged particles are densely ionizing. In tissue, the ranges of the α and Li-7 are 9 and 5 μm, respectively.

the thermal neutron kerma for the B-10(n,α)Li-7 reaction is also large, 8.7 E-12 cGy cm^2 per ppm of B-10 (refer to Chapter 3). For comparison, the thermal neutron kerma[9] in muscle tissue, effectively all from the N-14(n,p)C-14 reaction, is 2.7 E-11 cGy cm^2 (refer to Chapter 3). The muscle kerma, then, is equivalent to 3 ppm B-10. With only 30 ppm B-10 in tumor, 90% of the thermal neutron kerma is from the B-10 reaction, not from reactions with other tissue components.

The α and Li-7 reaction products, both densely ionizing, have a high relative biological effectiveness (RBE) and a low oxygen enhancement ratio (OER).[10] The RBE is defined as the ratio $D_x/D_{B\text{-}10}$, where D_x and $D_{B\text{-}10}$ are the doses from x-rays (often 250 kV_p x-rays) and the B-10 reaction needed for an equivalent biological effect.[10] The RBE is dependent on the linear energy transfer (LET) of the charged particles depositing the dose, with a peak in the RBE occurring at LET's around 100 keV/μm.[10] As shown in figure 1.1, the α and Li-7 reaction products have energy-averaged LET's in this range and, therefore, have relatively high RBE's. The OER is the ratio of doses under hypoxic to aerated conditions needed for equivalent biological effects.[10] With relatively low OER's, the α and Li-7 reaction products are more effective in killing hypoxic tumor cells than less densely ionizing radiations such as x-rays. One or two particles passing through the nucleus cause irreparable cell damage.[10,11]

Early clinical trials of BNCT at Brookhaven National Laboratory and at MIT

Clinical trials using BNCT for high-grade gliomas in the early 1950's and 1960's were not successful.[12,13] These early trials were carried out using thermal neutron beams from reactors at Brookhaven National Laboratory (BNL) and at MIT. Several B-10 loaded drugs (borax, sodium pentaborate, p-carboxyphenylboronic acid) were tried. Forty-five patients were treated at BNL; 18 were treated at MIT. Slatkin[12] has reviewed some of the early work at BNL and presented a new dosimetric analysis of the 1959-1961 clinical trials. Choi[13] has also reviewed the early clinical trials at BNL, as well as the

clinical trials at MIT. Dose estimates are presented along with pathological findings. The reader is referred to references 12-14 for details of these initial clinical trials of BNCT.

The early trials of BNCT were unsuccessful for four major reasons. First, the radiobiology of the B-10 reaction was not well known. For the first 10 patients treated at BNL, for example, the RBE for the B-10 reaction was thought to be 20,[13] a factor of 5-10 too high. The dose equivalent given to these patients, therefore, was much lower than had been thought. Second, the B-10 delivery agents did not provide sufficiently high tumor-to-blood ratios, which were around 1 to 1. The high concentration of B-10 in the blood resulted in high doses (sometimes greater than 100 Gy) to the capillary endothelium, which caused swelling and failure of the vessels.[13] Third, the B-10 concentration of the patient's blood was not measured before the irradiation. At the time, there was no method that was sufficiently rapid and sensitive to do this. The B-10 concentration could only be estimated and could not reflect any variability from patient to patient. Finally, the B-10 dose distribution within the patient was poor due to the use of thermal neutron beams. The thermal neutron flux profile in a hydrogenous phantom produced by an incident thermal neutron beam has a shape typical of that shown in figure 1.2. Thermal neutrons do not penetrate well into tissue; the half value layer is 1.5-2.0 cm. Since the dose deposited for the B-10 reaction is proportional to the amount of B-10 present and the thermal neutron flux, the B-10 dose with thermal neutron beams is very high at the surface and drops off rapidly with depth within the body. Tumors deeper than 3-4 cm cannot be given a therapeutic dose without giving unacceptably high doses near the surface. A troublesome side effect with patients in the second series of clinical trials at BNL, for example, was intractable radiation dermatitis of the scalp, sometimes with ulceration.[12] In the MIT trials that came later, the dermatitis was avoided by reflecting the scalp and skull before the patient was irradiated.[13] The reflection was possible to do at MIT because the neutron beam comes down from the ceiling and the MIT therapy

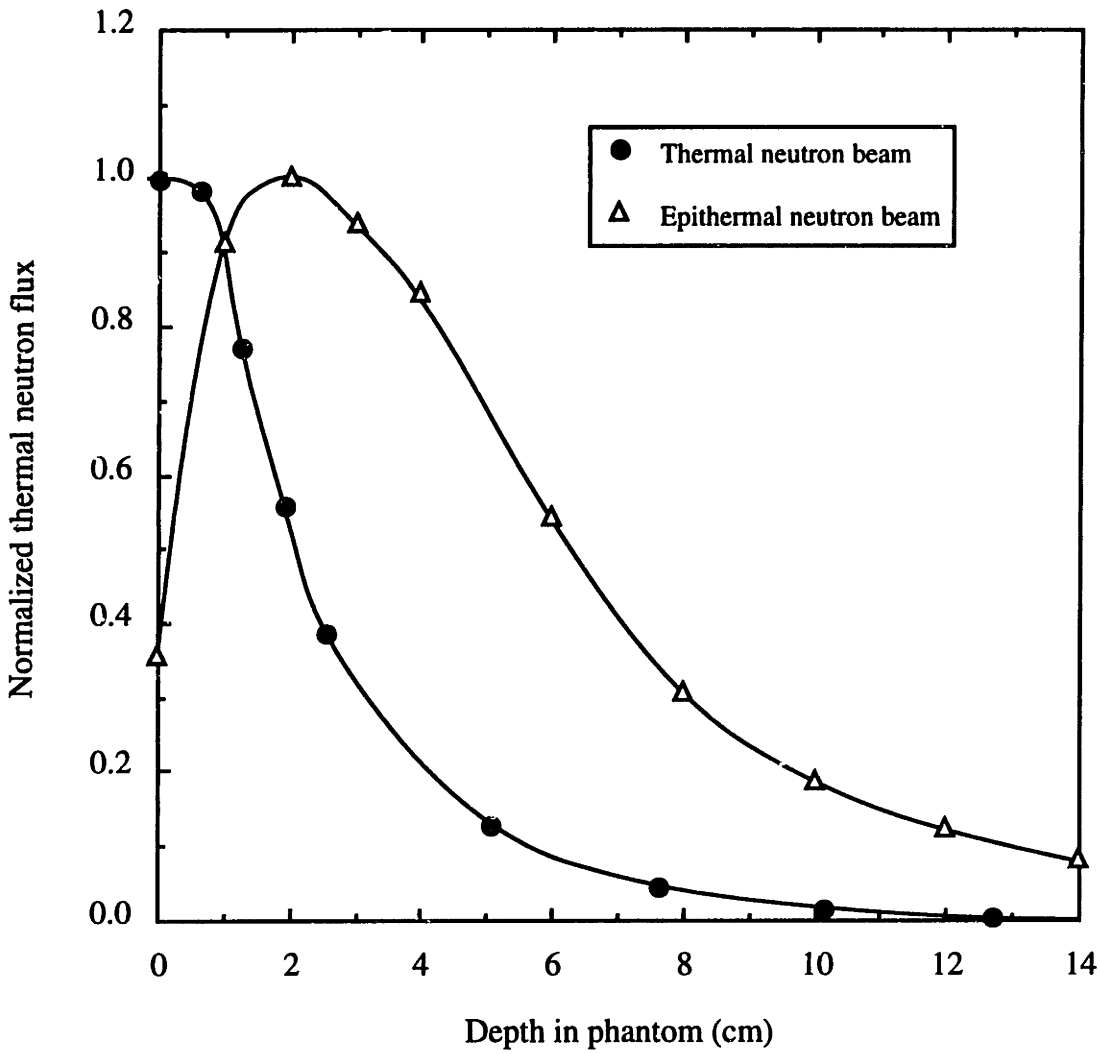

Figure 1.2. Thermal neutron flux profiles in phantom for typical thermal and epithermal neutron beams.[13] For thermal neutron beams, the thermal neutron flux peaks at or within the first few millimeters of the surface, and then drops rapidly with distance. For epithermal neutron beams, the thermal flux peaks around 2 cm and falls off more gradually with distance. The drop in the thermal flux at the surface is important for skin sparing.

beam is located in a sterile operating room. Reflection of the scalp and skull not only reduced radiation dermatitis, but allowed the thermal neutron beam to penetrate more deeply into the brain. Still, in attempting to give therapeutic doses at depth, doses at the surface of the brain were very high, with resulting radiation necrosis in many patients.[13] Reflection or craniotomies also had some medical risks, including infection and death.[13] The last clinical irradiations for BNCT in the U.S. were in 1961.

Clinical trials of BNCT in Japan

In the mid-1960's, a new B-10 drug, sodium mercaptoundecahydrododecaborate (BSH), was synthesized; this drug would enter glioma tissue freely, but would not cross the blood brain barrier.[12] Most important, BSH showed higher tumor-to-blood ratios (from 1-3:1) than the previous B-10 delivery agents if the BSH is delivered by common carotid artery. The higher tumor-to-blood ratio results in much lower endothelial doses.[13] BSH was used in the next clinical trials for brain tumors, which were carried out in Japan and led by Dr. Hiroshi Hatanaka.[12,13] Some 120 patients have been treated, including about 50 patients with grade-III/IV gliomas. Clinically, the tumor is first debulked and then one week is allowed for the blood brain barrier to heal. BSH (30-80 mg B-10 per kg body weight) is administered by an infusion pump into the internal carotid or common carotid artery. A craniotomy is performed before the irradiation. A "ping pong ball" is used to keep the brain from collapsing into the tumor cavity and to increase the penetration of the thermal neutron beam.[13] The reported results have been encouraging. For shallow tumors in which the thermal neutron beam is most effective, patients with grade III/IV gliomas had five year survival rates of 60%, and 10 year survival rates of 10%.[1] In contrast, five year survival rates for grade III/IV gliomas treated with state-of-the-art photon therapy is only 2%.[15] While the new drug, BSH, results in a lower endothelial dose relative to earlier drugs that had lower tumor-to-blood

ratios, the use of a thermal neutron beam is still a disadvantage since it requires a craniotomy and the thermal neutrons do not penetrate deeply.

In addition to the BNCT treatments for high grade gliomas, Dr. Yutaka Mishima in Japan has, since 1971, treated 5 cases of extracranial melanoma by BNCT.[16,17] His results are also encouraging. Dr. Mishima uses a different B-10 loaded drug, l-p-boronophenylalanine (BPA), and a thermal neutron beam to treat relatively superficial melanomas that are not amenable to standard surgery or radiotherapy.

New England Medical Center / Massachusetts Institute of Technology BNCT Program

The BNCT program at New England Medical Center / Massachusetts Institute of Technology (NEMC/MIT) is now in its sixth year. A major difference between this program's upcoming clinical trials and those of previous clinical trials is that we plan to irradiate the body using an epithermal neutron beam in which most of the neutrons have energies between 0.5 eV and 20 keV. In epithermal neutron beams, most of the thermal neutrons (0-0.5 eV) have been removed by absorption while most of the higher energy neutrons (greater than 20 keV) have been removed by moderation or filtering.[4,18] Epithermal neutron beams result in a much different thermal neutron flux profile in patients. The thermal neutron flux profile in a hydrogenous phantom produced by an incident epithermal neutron beam has a shape typical of that shown in figure 1.2.[13] For an epithermal neutron beam, the thermal neutron flux peaks around 2 cm and falls off more gradually with distance. This shape is far preferable to that of thermal neutron beams. For epithermal neutron beams, the drop in flux near the surface is important for sparing of the skin and scalp. The more gradual drop of flux results in a more uniform dose-depth distribution.

The goal of epithermal neutron beam design is to generate a sufficiently wide and intense beam of epithermal neutrons, with minimal contamination from thermal and fast neutrons, or from photons. The design and dosimetry of these beams at the MITR-II

reactor was a major task of this thesis. The neutron source, fission, produces neutrons in the energy range 0-15 MeV. In Chapter 2, it is shown that there is a useful range of neutrons that can be used in BNCT which will result in good penetration and high tumor-to-healthy tissue dose ratios. Thermal neutrons, and neutrons above 20 keV, should be reduced to low levels. Fast neutrons are non-selective in that they will deposit dose equally in healthy tissue and in tumor tissue. This is a drawback as the goal of BNCT is to deliver a selectively and significantly higher dose to tumor cells through the B-10 reaction. Gamma rays are also produced during fission, as well as from decaying fission products and their daughters. Additional gamma rays are produced by neutron capture reactions. Gamma rays are also non-selective. Their presence will reduce the average tumor-to-healthy tissue dose ratio. The gamma rays, therefore, need to be reduced to a low level as well. Within the patient, incident epithermal neutrons thermalize and generate a photon field from the H-1(n,γ)H-2 reaction. This photon field cannot be reduced. (Some reduction may be achievable by partially deuterating the patient such as by replacing cerebral water with heavy water. Dr. Hatanaka has done this, not to reduce the photon dose, but to improve the penetrability of the thermal neutron beam.[19])

The longer range goal of the NEMC/MIT project is Phase I and II clinical trials of BNCT for grade III/IV gliomas. Phase I trials involve dose escalation, evaluation of safety and maximum acceptable toxicity, and pharmacokinetics in human subjects, but involve no requirement or criteria for assessing anti-tumor activity. Phase II trials involve attempts at limited therapeutic efficacy in human subjects using dose levels established as safe or acceptable in the Phase I study, and the specific evaluation of anti-tumor activity. The gliomas will be treated using an epithermal neutron beam through the intact scalp and skull; a craniotomy or scalp reflection will not be needed.

The grade III/IV glioma trials will be preceded, however, by a Phase I trial of BNCT for subcutaneous peripheral melanoma, and will run concurrently with a Phase II trial of BNCT for subcutaneous peripheral melanoma. Epithermal neutron beams will

also be used in the melanoma trials. The reasons for starting with the Phase I melanoma trial are twofold. First, there continues to be an uncertainty regarding the biological effects of the B-10 dose (B-10 RBE) and of the neutrons in the epithermal neutron beam (neutron RBE). A dose escalation schedule would be safer for the patient if the tissues at risk were the extremities rather than the scalp or brain. Second, the potential for BNCT to extend the survival and quality of life is as important for melanoma patients as for grade III/IV glioma patients. Alternative therapies available to control the CNS disease component in melanoma patients are as ineffectual as with grade III/IV glioma patients.[20]

The annual incidence of malignant melanoma in the U.S. is about 23,000 cases; the annual death rate is 7,500.[20] Metastasis to the CNS is a serious complication of malignant melanoma, accounting for about 4,200 symptomatic presentations annually. At autopsy, however, the incidence of CNS metastases is 36-90% of all diagnosed melanomas. About 4000 melanoma patients, therefore, who die each year with CNS involvement could be palliated employing BNCT to the CNS.

There is now at the MITR-II a fully equipped and clinically usable medical irradiation room.[21,22] Entering from the ceiling of this medical room through shutters and collimators is an optimized, large area, epithermal neutron beam that can be used to treat deeply seated tumors with an average tumor-to-healthy tissue dose ratio of 2 (refer to Chapter 5). This beam has been fully characterized by state-of-the-art in-phantom mixed field dosimetry (refer to Chapter 3) and by Monte Carlo simulation[23] using the continuous energy Monte Carlo transport code MCNP.[24] Monte Carlo based clinical treatment planning methods have been developed to ensure accurate and safe dose delivery to patients.[25,26] A highly sensitive and accurate prompt gamma B-10 analysis facility for quantitating B-10 concentrations in blood, urine, and other tissues down to sample sizes of 0.05 g (i.e., equivalent to small punch biopsy samples) has been developed.[27,28] The prompt gamma system will be used to measure the patient's B-10 blood level before the neutron irradiation. A unique, high-resolution alpha-track

autoradiographic capability for examining B-10 distributions in frozen tissue sections at the subcellular level with 1-2 micron spatial resolution and ≈0.1 ppm sensitivity has been developed.[29] A DOE funded interinstitutional BPA biodistribution study to evaluate B-10 labeled l,p-boronophenylalanine as a potentially suitable compound for delivery of B-10 to human melanoma and glioblastoma tumors has been carried out.[29,30] The prompt gamma system was used to measure the B-10 concentrations of the patient's blood and urine samples; alpha-track autoradiography was used to measure the B-10 concentrations of the patient's tumor and healthy tissue samples. Extensive BNCT animal survival studies that unequivocally demonstrated the activity of BPA in producing long-term survival of mice carrying highly refractory GL261 intracranial brain tumors have been completed.[29,31] BPA animal toxicity studies have been completed according to FDA requirements and guidelines; these studies have contributed to the award of an Investigation New Drug (IND) to use BPA in combination with a neutron irradiation in a phase-I clinical trial. Finally, 11 federal and institutional approvals, and the legal indemnity agreements between NEMC and MIT, required to initiate a phase-I BNCT clinical study of subcutaneous peripheral melanoma have been obtained.

Scope of thesis

The work in this thesis was dedicated towards developing the mixed field dosimetry needed to accurately measure the radiation doses (thermal and fast neutron, photon, and B-10) within realistic phantoms, to design and dosimetrically characterize an epithermal neutron beam that has sufficient quality and intensity to be used clinically, to make modifications to the medical room in preparation for clinical trials, to improve a prompt gamma neutron activation analysis system for the measurement of low ppm B-10 levels in blood, urine, and tissue samples, and finally to use the prompt gamma system to measure the B-10 levels in blood and urine samples from patients who volunteered in the BPA human biodistribution study.

An overview of the MITR-II reactor, the methods used in designing epithermal neutron beams, and general aspects of mixed field dosimetry are provided (Chapter 2). Included is a description of the different phantoms that were used to characterize the beams, a discussion of the RBE's, and a discussion of how the dosimetric results are presented.

A clinical protocol for the mixed field dosimetry has been developed (Chapter 3). The mixed field dosimetry was especially challenging as it was necessary to measure the separate neutron and photon doses in a mixed field in which the spectra were not well known and in which the dose rates were comparable. The photon and fast neutron doses are measured with ionization chambers using the dual chamber technique. The thermal neutron and B-10 doses are calculated by measuring the thermal neutron flux and multiplying the flux by the appropriate kerma. The thermal neutron flux is measured with gold foils using the cadmium difference technique. The electrometer and ionization chambers have been calibrated by the University of Wisconsin Accredited Dosimetry Calibration Laboratory (Appendix B). The dosimetry protocol and the experimental technique have been carefully reviewed by Professor Steven Goetsch of U.C.L.A., an expert on mixed field dosimetry (Appendix A). Four sets of Procedures on the dosimetry were written (Appendix D); they were reviewed and approved pursuant to MITR Technical Specification No. 6.5.

Over 20 different epithermal neutron beams have been designed, installed, and characterized in air and along a central axis in realistic phantoms (Chapter 4). As-built drawings for some of the beam components have been provided (Appendix C). A new head phantom was made. Some beams were characterized with more than one phantom, with different delimiters, or were characterized in off-axis positions as well as along the central axis. In two of these beams, the experimentally determined central and off-axis data were compared with dosimetry generated by MCNP.[23,24] One of these beams, the M67 beam, was selected as the beam that would be used in the initial clinical trials.

The clinical beam, along with its delimiter and whole body shields, is described in detail (Chapter 5). Dosimetry is provided assuming the tissue of interest is muscle or brain. Centerline and off-axis dosimetry is also provided for the clinical beam. These experimental results have been compared with those generated by MCNP. A normalization factor has been determined for each dose component; these normalization factors are used in the treatment planning software.

Whole body doses have been estimated (Chapter 5). Some aspects of in-vivo dosimetry have been addressed. Health physics related doses, including the doses that will be received by personnel setting up the patient, during the irradiation of the patient, and during a potential medical emergency with the patient, have also been investigated.

Many modifications were made to the medical room in preparation for clinical trials (Chapter 6). These include painting the ceiling with thermal neutron absorbing paints to reduce activation and designing a new lead shutter that would reduce the dose rates inside the medical room from a health physics perspective.

A prompt gamma neutron activation analysis system has been improved and set up to analyze ppm levels of B-10 in blood, urine, and tissue samples (Chapter 7). The system is unique in that it uses a Bragg diffracted neutron beam. As required by the FDA as part of the human BPA biodistribution study, this prompt gamma system was successfully intercalibrated with the prompt gamma system at Brookhaven National Laboratory.

As part of an interinstitutional study to determine the biodistribution and pharmacokinetics of BPA in humans, about 70 blood and urine samples from 6 cancer patients were analyzed for B-10 (Chapter 7). This work, performed under an IND application to the FDA, was needed to obtain an amendment to the IND; the amendment approves the use of BPA for clinical treatment of patients by BNCT in the phase-I trial.

For the first patient irradiation to run smoothly, practice runs were carried out. These usually involved personnel from the Nuclear Reactor Laboratory, Reactor

Operations, Radiological Protection Office, clinicians and medical physicists from T-NEMC, and students working on the project. Minutes of the practice runs are provided (Appendix E).

Finally, recommendations for further work are provided (Chapter 8). These include obtaining additional dosimetric information to better estimate the patient's whole body dose, reducing the patient's whole body with additional shielding, reducing the beam-off dose rates in the medical room through improved shielding, and, after several patients are irradiated, to review and modify the dosimetry Procedures so the prescribed radiation dose is delivered with improved safety and accuracy.

Next, Chapter 2 provides an overview of the MITR-II reactor and a discussion of the methods used in the design and dosimetry of the epithermal neutron beams.

References

1..R. F. Barth, A. H. Soloway, and R. G. Fairchild, "Boron neutron capture therapy for cancer," Sci. Amer., 100-107 (October, 1990).

2. R. F. Barth, A. H. Soloway, and R. G. Fairchild, "Boron neutron capture therapy of cancer," Cancer Res. **50**, 1061-1070 (1990).

3. G. Locher, "Biological effects and therapeutic possibilities of neutrons," Am. J. Roentgenology **71**, 279-291 (1936).

4. R. M. Brugger, G. Constatine, O. K. Harling, and F. J. Wheeler, "Rapporteurs' Report," in *Neutron Beam Design, Development, and Performance for Neutron Capture Therapy*, (O. K. Harling, John A. Bernard, Robert G. Zamenhof, eds., Plenum Press, New York, 1990).

5. D. Gabel, "Radiobiological Considerations Concerning the Development of Compounds for Boron Neutron Capture Therapy," Fifth International Symposium on Neutron Capture Therapy for Cancer, Columbus, Ohio, (1992).

6. F. W. Walker, J. R. Parrington, and F. Feiner, *Nuclides and Isotopes*, 14th ed. (General Electric Co., San Jose, California, 1989).

7. C. M. Lederer, Virginia Shirley, *Table of Isotopes, 7*th ed. (Lawrence Berkeley Laboratory, Wiley-Interscience Publication, John Wiley & Sons, Inc., N.Y., 1978).

8. D. Gabel, S. Foster, and R. Fairchild, "The Monte Carlo simulation of the biological effect of the $^{10}B(n,\alpha)^{7}Li$ reaction in cells and tissues and its implication of boron neutron capture therapy," Rad. Res. **111**, 14-25 (1987).

9. ICRU Report 46, *Photon, Electron, Proton and Neutron Interactions Data for Body Tissues*, (International Commission on Radiation Units and Measurements, Bethesda, Maryland, 1992).

10. Eric J. Hall, *Radiobiology for the Radiologist*, 3rd ed., (J. B. Lippincott Co., New York, NY, 1988).

11. T. R. Munro, "The relative sensitivity of the nucleus and cytoplasm of the Chinese hamster fibroblasts," Rad. Res. **42**, 451-470 (1970).

12. D. N. Slatkin, "A history of boron neutron capture therapy of brain tumors," Brain **114**, 1609-1629 (1991).

13. Jong-Ho Richard Choi, *Development and Characterization of an Epithermal Beam for Boron Neutron Capture Therapy at the MITR-II Research Reactor*, (Ph.D. Thesis, Massachusetts Institute of Technology, 1991).

14. L. E. Farr, W. H. Sweet, J. S. Robertson, C. G. Foster, H. B. Locksley, and D. L. Sutherland, "Neutron capture therapy with boron in the treatment of glioblastoma mulitforme," Am. J. Roentgenology **71**, 279-293 (1954).

15. Vincent DeVita, Samuel Hellman, and Steven Rosenberg, *Cancer: Principles and Practice of Oncology*, (J. B. Lippincott Co., Philadelphia, 1982).

16. Y. Ujeno, K. Akuta, H. Hatanaka, Y. Mishima, Y. Oda, and Y. Nakagawa, "Clinical Experience of BNCT for Brain and Skin Tumors at Kyoto University Reactor," in *Progress in Neutron Capture Therapy for Cancer* (Barry J. Allen, Douglas E. Moore, Baiba V. Harrington, eds., Plenum Press, New York, 1992).

17. Y. Mishima, M. Ichihashi, C. Honda, M. Shiona, T. Nakagawa, H. Obara, J. Hiratsuka, et al, "Advances in the Control of Human Cutaneous Primary and Metastatic Melanoma by Thermal Neutron Capture Therapy," in *Progress in Neutron Capture Therapy for Cancer* (Barry J. Allen, Douglas E. Moore, Baiba V. Harrington, eds., Plenum Press, New York, 1992).

18. F. J. Wheeler, D. K. Parsons, D. W. Nigg, D. E. Wessol, "Physics Design for the Brookhaven Medical Research Reactor Epithermal Neutron Source," in *Neutron Beam Design, Development, and Performance for Neutron Capture Therapy*, (O. K. Harling, John A. Bernard, Robert G. Zamenhof, eds., Plenum Press, New York, 1990).

19. H. Hatanaka, K. Sano, and H. Yasukochi, "Clinical Results of Boron Neutron capture Therapy," in *Neutron Beam Design, Development, and Performance for Neutron Capture Therapy*, (O. K. Harling, John A. Bernard, Robert G. Zamenhof, eds., Plenum Press, New York, 1990).

20. Eugene Braunwald, Kurt Isselbacher, Robert Petersdorf, Jean Wilson, and Anthony Fauci, *Harrison's Principles of Internal Medicine*, 11th ed., (McGraw-Hill Co., New York, NY, 1987).

21. R. G. Zamenhof, H. Madoc-Jones, O. Harling, D. Wazer, S. Saris, J. Yanch, G. Solares, and G. Rodgers, "The Neutron Capture Research Program at the New England Medical Center and Massachusetts Institute of Technology," in *Progress in Neutron Capture Therapy for Cancer* (Barry J. Allen, Douglas E. Moore, Baiba V. Harrington, eds., Plenum Press, New York, 1992).

22. J. R. Choi, R. G. Zamenhof, J. C. Yanch, R. Rogus, and O. K. Harling, "Performance of the Currently Available Epithermal Neutron Beam at the Massachusetts Institute of Technology," in *Progress in Neutron Capture Therapy for Cancer* (Barry J. Allen, Douglas E. Moore, Baiba V. Harrington, eds., Plenum Press, New York, 1992).

23. E. L. Redmond II, J. C. Yanch, and O. K. Harling, "Monte Carlo simulation of the Massachusetts Institute of Technology research reactor" Nuc. Tech, (Accepted for publication, 1994).

24. J. F. Briesmeister, ed, "MCNP - A General Monte Carlo Code for Neutron and Photon Transport (Version 3A)," LA-7396-M, Rev. 2, (Los Alamos National Laboratory, 1986).

25. R. G. Zamenhof, S. D. Clement, O. K. Harling, et al, "Monte Carlo Based Dosimetry and Treatment Planning for Neutron Capture Therapy of Brain Tumors," in *Neutron Beam Design, Development, and Performance for Neutron Capture Therapy*, (O. K. Harling, John A. Bernard, Robert G. Zamenhof, eds., Plenum Press, New York, 1990).

26. R. G. Zamenhof, J. Brenner, J. Yanch, et al, "Treatment Planning for Neutron Capture Therapy of Glioblastoma Multiforme Using and Epithermal Neutron Beam from

the MITR-II Research Reactor and Monte Carlo Simulation," in *Progress in Neutron Capture Therapy for Cancer* (Barry J. Allen, Douglas E. Moore, Baiba V. Harrington, eds., Plenum Press, New York, 1992).

27. R. Rogus, O.K. Harling, I. Olmez, and S. Wirdzek, "Boron-10 prompt gamma analysis using a diffracted neutron beam," in *Progress in Neutron Capture Therapy for Cancer*, (Barry Allen, Douglas Moore, Baiba Harrington, eds., Plenum Press, New York, 1992).

28. O. K. Harling, J-M Chabeuf, F. Lambert, and G. Yasuda, "A prompt gamma neutron activation analysis facility using a diffracted beam," Nucl. Inst. Methods, (Accepted for publication, 1994).

29. Guido Solares, *High Resolution Alpha Track Autoradiography and Biological Studies of Boron Neutron Capture Therapy*, (Ph.D. Thesis, Massachusetts Institute of Technology, 1991).

30. J. A. Coderre, "A Phase-I Biodistribution Study of p-Boronophenylalanine," in *Boron Neutron Therapy: Toward Clinical Trials of Glioma Treatment*, (D. Gabel and Ray Moss, eds., Plenum Press, New York, 1992).

31. S. C. Saris, G. R. Solares, D. E. Wazer, G. Cano, S. E. Kerley, M. A. Joyce, L. S. Adelman, O. K. Harling, H. Madoc-Jones, and R. G. Zamenhof, "Boron neutron capture therapy for murine malignant gliomas" Can. Res. **52**, 4672-4677 (1992).

CHAPTER 2 OVERVIEW OF THE MITR-II REACTOR, BEAM DESIGN, AND DOSIMETRY

2.1 GENERAL DESCRIPTION OF THE MITR-II REACTOR

An isometric view of the MITR-II reactor is shown in figure 2.1. The reactor is rated at 5 MW thermal and routinely operates in the 4-5 MW range 100 hours a week. The core is light water cooled and D_2O moderated. The fuel elements are 66.7 cm long and consist of 15 flat, grooved aluminum plates with a 93% enriched uranium/aluminum meat. Power is controlled by 6 shim blades on the outside of the core and an automatic regulating rod located on one corner of the hexagonally shaped core.

A system of four shutters is used to turn the beam on and off. Usually the H_2O and D_2O shutters are filled, and the lead and boral shutters are closed. With the beam off, personnel can work inside the medical room with the reactor at full power. The dose rates in some areas of the medical room are quite high (2000 mrem/hr, mostly from fast neutrons), however, so the time personnel spend inside the room is limited. Health physics information is provided in Chapter 5. To open the beam for a therapeutic irradiation, the H_2O and D_2O shutters are emptied, and the lead and boral shutters are slid sideways. The H_2O shutter takes 2 minutes to open or close. The D_2O shutter takes 3 minutes to open and 13 minutes to close. The lead and boral shutters take several seconds to open or close. The boral shutter is retracted so that it lies completely outside the beam. The lead shutter was constructed with a 15" hole through it; the hole, or beam aperture, can be seen in figure 2.1. Special inserts, called collimators, have been made which are inserted into the hole in the shutter. The collimators function to improve the

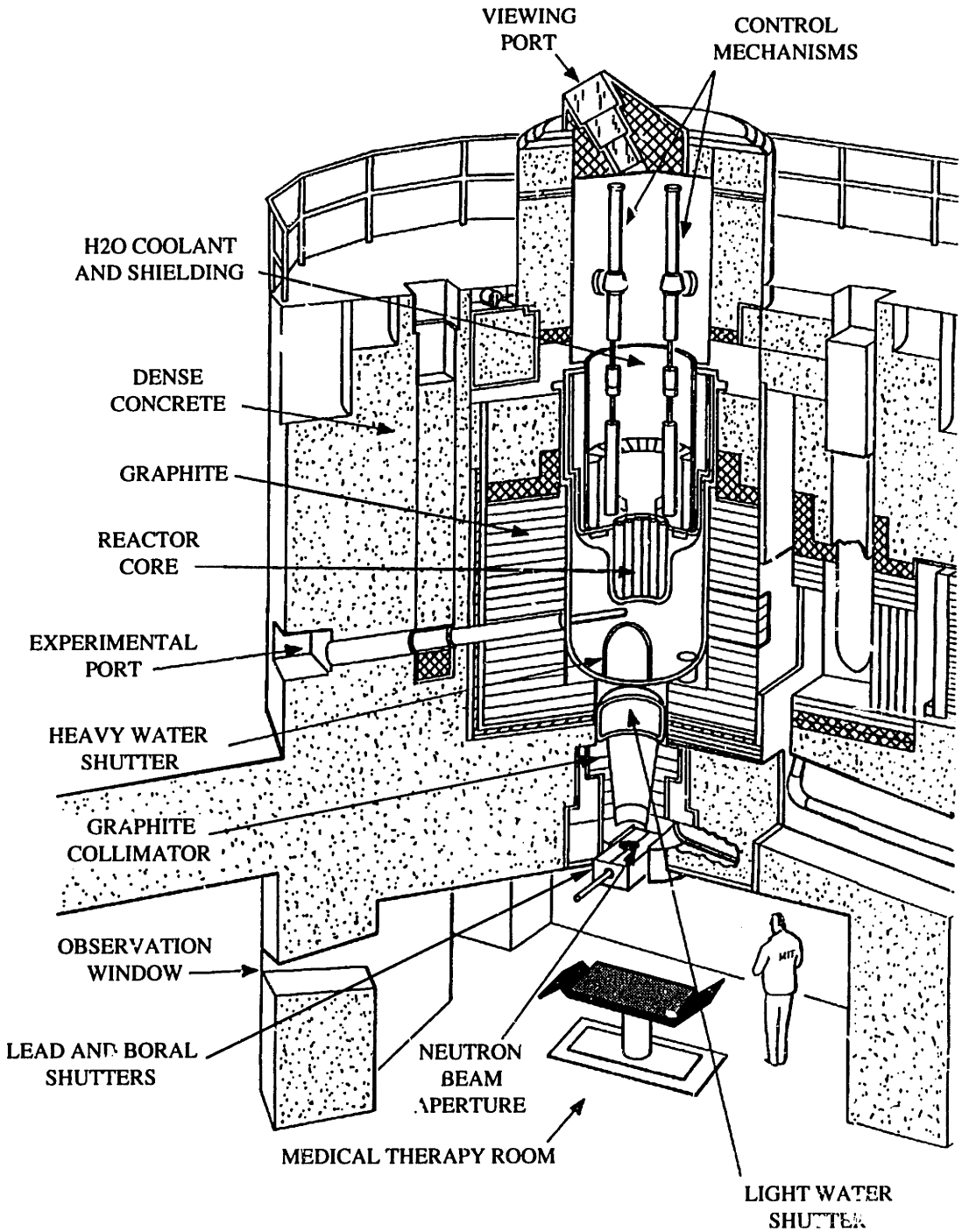

Figure 2.1. Isometric view of the MITR-II reactor and its medical irradiation facility. The reactor is rated at 5 MW. The H_2O and D_2O shutters can be voided. The boral shutter can be slid out of the beam. The lead shutter can slide sideways to position the collimator in the beam.

quality of the epithermal neutron beam, and will be discussed in Chapter 4. When the lead shutter is opened, it slides sidewise and positions the collimator in the main beam.

2.2 EPITHERMAL NEUTRON BEAM DESIGN

The goal of epithermal neutron beam design is to generate a sufficiently wide and intense beam of epithermal neutrons, with minimal contamination from thermal and fast neutrons, or from photons. The neutron source, fission, produces neutrons in the energy range 0-15 MeV. Gamma rays are also produced during fission, as well as from the decaying fission products and their daughters. Additional gamma rays are produced by neutron capture reactions.

Regarding the neutron component of the beam, a series of Monte Carlo based ideal beam studies[1-3] have shown that there is a useful range of neutrons, from 1 eV to about 20 keV, which would result in relatively high tumor-to-healthy tissue dose ratios and which would have the ability to treat deep seated tumors (6-7 cm deep) with excellent skin sparing. An ideal beam is defined as a monoenergetic, photon-free source of neutrons with a user-specified size, shape, and angular dependence.[4] A Monte Carlo based ideal beam study on the dosimetric effects of beam size and collimation has been reported.[4] Thermal neutrons are not useful; they reduce skin sparing and reduce the depth at which tumors can be treated. Fast neutrons, with energies significantly above 20 keV, are also not useful; they add significantly to the fast neutron dose (refer to figure 5.23), which is caused primarily by recoil protons in elastic collisions with hydrogen. Fast neutrons are non-selective in that they will deposit dose equally in healthy tissue and in tumor tissue. This is a drawback as the goal of BNCT is to deliver a selectively and significantly higher dose to tumor cells through the B-10 reaction. The thermal and fast neutrons in the beam, therefore, need to be reduced to a low level.

Photons are also non-selective in that they will deposit dose equally in healthy tissue and in tumor tissue. Their presence will reduce the average tumor-to-healthy tissue dose ratio. The photons in the beam, therefore, need to be reduced to a low level as well.

Removing the higher energy neutrons from the beam while transmitting a useful flux of neutrons in the useful energy range is the major task in epithermal neutron beam design. Photons in the beam can be removed more easily with materials such as lead or bismuth, although with a loss in the intensity of the useful epithermal neutrons.

Two general approaches have been used to remove the higher energy neutrons from fission sources - the moderator method and the filter method.[5,6] In the moderator method, a sufficient amount of appropriate moderator is positioned near the core. The moderator thermalizes the higher energy neutrons, and the energy loss of the higher energy neutrons is much greater than that of the lower energy neutrons. The spectrum is softened without greatly reducing the intensity of neutrons in the useful energy range. Effective moderators include D_2O, Al, Al_2O_3, and C.[6-12] Light water, often used in reactors, moderates too rapidly for effective spectrum shaping.

In the filter method, elements with windows in their cross sections are positioned more towards the patient than towards the core. Windows are regions in the cross section that are significantly lower than at other energies. Effective neutron filters include sulfur, aluminum, argon, and titanium.[6-12] These elements have large s-wave scattering resonances in the keV range. The cross sections for sulfur and aluminum are shown in figure 2.2.[13] Neutrons emerging from the core and moderator in the direction of the patient pass through the filter. The higher energy neutrons are more likely to be scattered. Many of these scattered neutrons are effectively lost from the beam; however, because the upper part of the MITR-II beam is wide (30-40 cm) some scattered neutrons, if scattered in the forward direction, will not be lost from the beam and will add to the fast neutron dose in the patient. Also, some neutrons that have scattered out of the beam can undergo a subsequent scattering and be scattered back into the beam. Neutrons in the

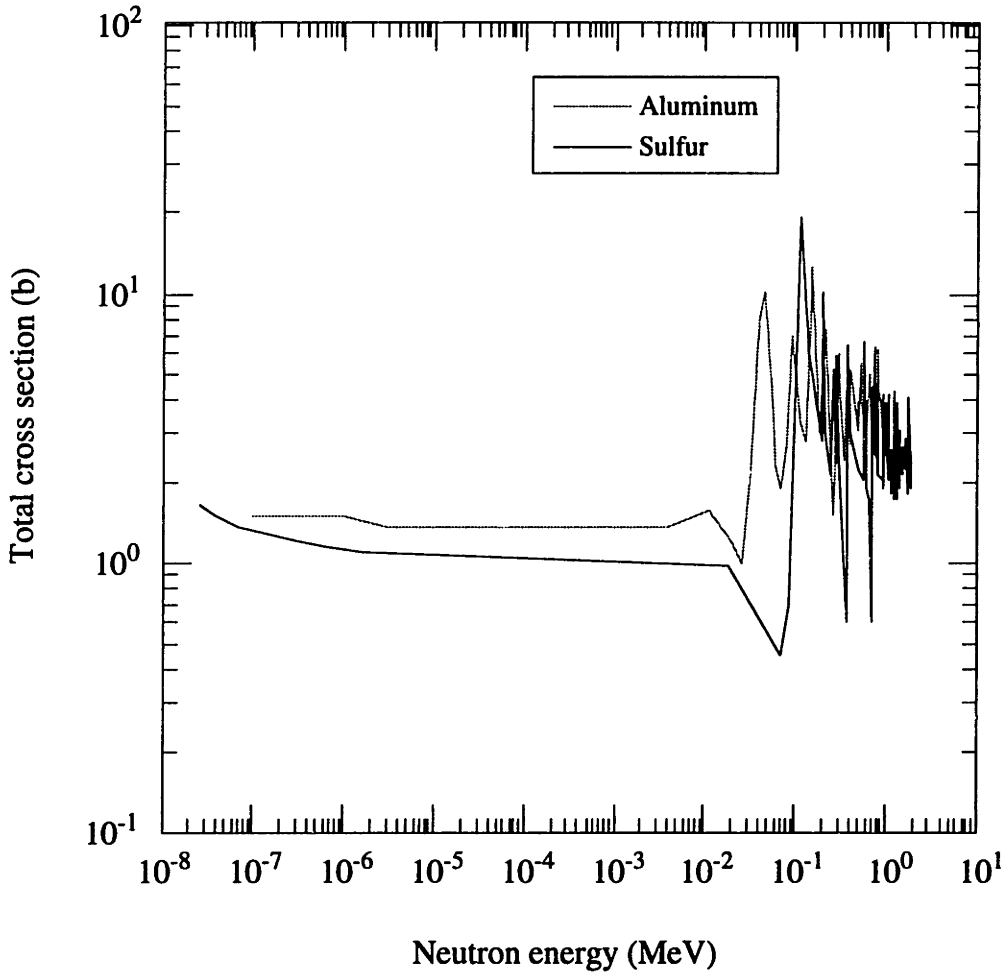

Figure 2.2. Total cross sections for sulfur and aluminum.[13] The cross sections are flat from thermal energy to 10 keV. Above 10 keV, these elements have large s-wave scattering resonances. Neutrons above 10 keV are more likely to be scattered from the beam. The large window at 80 keV in sulfur can be shadowed with aluminum, which has a resonance at about the same energy.

lower energy range are more likely to pass through the filter and reach the patient. With sulfur and aluminum, for example, neutrons above 10 keV are more likely to be scattered out of the beam. Also, the large window at 80 keV in sulfur can be shadowed with aluminum, which has a resonance at about the same energy.

The filter and moderator methods are often used together.[2,5] That is, some moderator (D_2O, Al, Al_2O_3, C) is used near the core to soften the spectrum and the moderator is followed by one or more filters to further reduce the fast neutron contamination.

A cross sectional view of the MITR-II is shown in figure 2.3. Filters can be positioned inside the graphite collimator and within the hole in the horsecollar. Filters can also be used inside the collimator. In this study, generally sulfur and aluminum have been used in these regions. The epithermal neutron beams at the MITR-II reactor are both moderated and filtered. There is at least 24 cm of D_2O just below the core. The mean free path of neutrons in D_2O is 2.6 cm for 0-1 MeV neutrons and increases to 5.5 cm for 5 MeV neutrons. There is a significant amount of scattering and moderation, therefore, in the D_2O.

Beam design by our group has been a step-by-step process. A particular beam is installed and fully characterized by measuring the thermal flux, photon, and fast neutron doses in realistic phantoms. Then, the beam is modified in some way in an attempt to improve the quality of the beam by reducing the photon and fast neutron contamination relative to the useful epithermal neutron flux. Decisions on how to modify the beam are based on Monte Carlo calculations, simple removal cross section considerations, previous experimental results, or a combination of these. Results of the new beam are then compared with previous Monte Carlo and experimental results to gain a better understanding of the radiation transport.

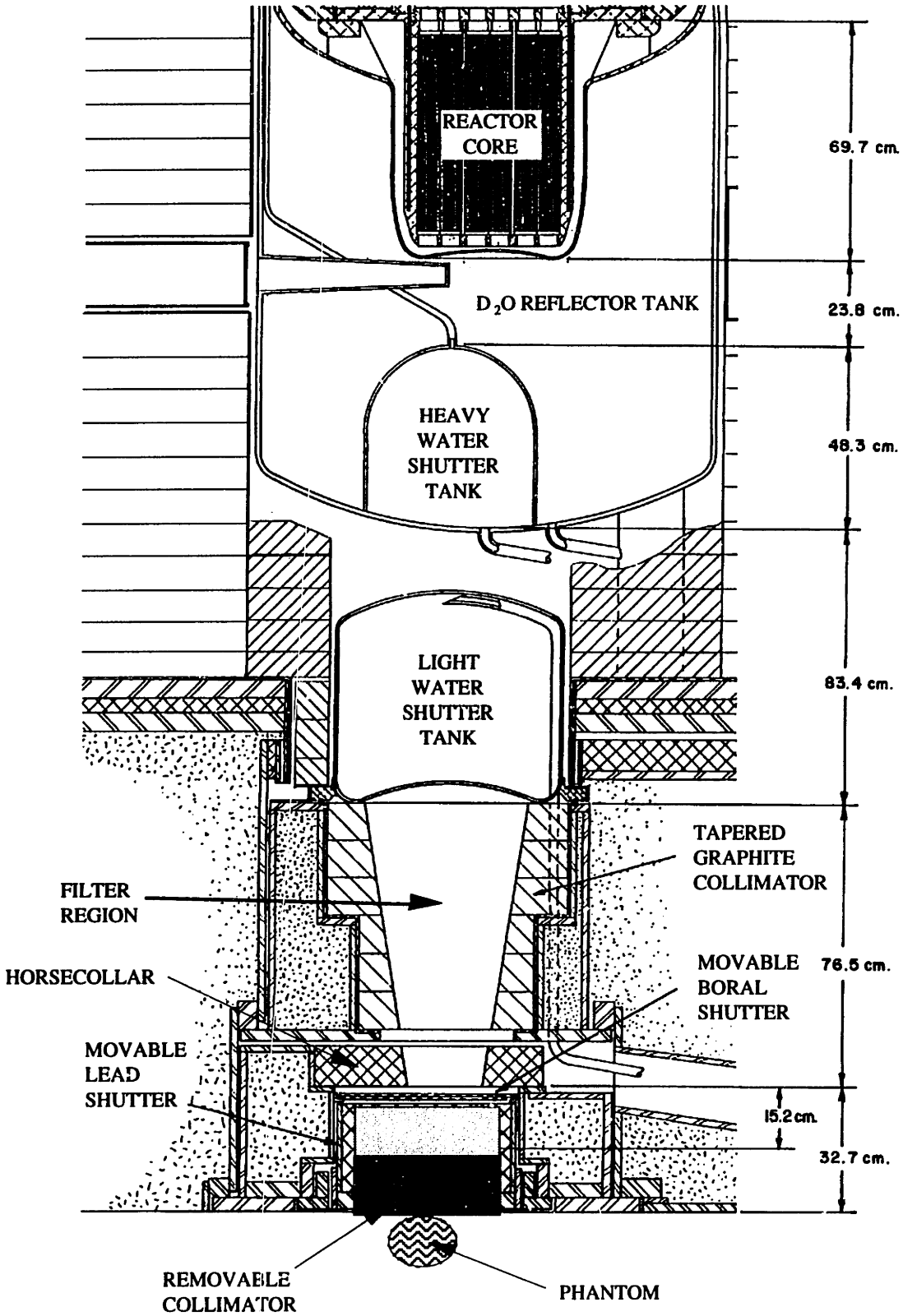

Figure 2.3. Cross sectional view of the MITR-II medical therapy beam showing the shutters, the region where filters can be placed, and the positioning of the phantom.

2.3 EPITHERMAL NEUTRON BEAM DOSIMETRY

Four separate radiation dose components must be measured - the photon and fast neutron doses, and the thermal neutron and B-10 doses. The method used to measure these doses is discussed in detail in Chapter 3. Discussed here is a brief overview of several methods that can be used to measure the photon or fast neutron doses in a mixed field. The thermal neutron and B-10 doses are determined by measuring the thermal neutron flux with gold foils and multiplying the flux by the kerma factor (refer to Chapter 3).

2.3.1 Dual ionization chamber technique

Our group measures the photon and fast neutron doses using the dual ionization chamber technique[14,15] with realistic phantoms. A carbon graphite ionization chamber, which is relatively insensitive to neutrons, is used to determine the photon dose. A similar ionization chamber, but made with a tissue equivalent material that is about equally sensitive to photons and fast neutrons, is used to determine the total photon and fast neutron dose. The fast neutron dose is found by subtraction. A method to calculate the separate photon and fast neutron doses has been developed which accounts for the actual neutron and photon sensitivities of the chambers and the kerma match to the tissue of interest.

The carbon graphite chamber is flushed with CO_2 while the tissue equivalent chamber is flushed with a tissue equivalent gas. In practice, clinical fast neutron dosimetry relies on and is based on measurements made with tissue equivalent ionization chambers flushed with tissue equivalent gas.[16] The chambers can be calibrated at an AAPM Accredited Dosimetry Calibration Laboratory and so carry traceable calibrations. Our group uses chambers that have thimbles about 1 cm in diameter. These chambers are

small enough so that the doses can be determined with an adequately fine grid for most locations within a phantom.

2.3.2 Tissue equivalent calorimeters

Tissue equivalent calorimeters[14] would come closest to being a direct measurement of the total photon and fast neutron dose. They can be made absolute, either intrinsically or by means of electrical heating calibration. They are about equally sensitive to photons and neutrons. The temperature rise as a result of energy deposition, however, is very small. With the dose rates of interest in BNCT therapy (less than 10 rads/min from photons and fast neutrons), thermal leakage would limit the accuracy and precision of the method. Even in very high dose rate applications, calorimetry is cumbersome and is better suited for calibration of other instruments.[16] Measurements are time consuming; this would be a major disadvantage if the doses needed to be determined at many positions within a phantom.

2.3.3 TLD's

TLD's are useful in determining the photon dose[14]; they have been used by the BNCT group at Brookhaven National Laboratory.[17] They are useful over a wide range of doses, and have no dose rate dependence. They are cheap, reusable, and are commercially available in small sizes. They are accurate to within several percent[14] and can be calibrated in Co-60 beams. TLD-700's ($\approx$ 100% Li-7) have a low neutron to gamma sensitivity ratio and a low response to thermal neutrons. TLD's might be most useful when determining the photon dose in three dimensions within a phantom. The TLD's could be positioned within the phantom and then the phantom given a single irradiation. This would be quicker than determining the photon dose at each position one by one using an ionization chamber, for example.

2.3.4 G-M Counters

Miniature stainless-steel G-M counters have extremely low neutron-to-gamma sensitivity ratios.[14] Some G-M counters are small enough (1 cm^3) so that the exposure rate in a phantom can be measured with minimal perturbation of the radiation field. The thermal neutron response can be suppressed with a shield of Li-6 fluoride. Count rates are limited; exposure rates would need to be determined at a low power level and then scaled.

2.3.5 Silicon diodes

These detectors are much more sensitive to damage by fast neutrons than by photons.[14] Their response per unit dose in tissue is flat (±20%) for neutrons between 300 keV - 14 MeV. They have been used to measure the fast neutron dose in a dog head phantom.[18]

2.3.6 Spectral measurements

The neutron spectrum can be measured in several ways including high resolution proton recoil, spectrum modification, and multisphere spectrometry.[19,20] These measurements are difficult and time consuming to carry out and provide only in-air information. They may be useful in a beam design effort. They are difficult to use, however, to determine the fast neutron doses within a phantom.

2.3.7 Bubble detectors

Bubble detectors consist of an elastic polymer throughout which droplets of superheated liquid have been dispersed.[21,22] When the droplets are struck by fast neutrons, they form small gas bubbles which remain fixed in the polymer. After receiving a neutron dose, the bubbles are counted visually or with an optical reader. Alternatively, the neutron dose rate can be measured in real time with the use of an

acoustical reader that senses and counts the number of "pops" that are emitted as the gas bubbles are formed. The response is dependent on the neutron energy. A set of 6 bubble detectors with different neutron energy thresholds can be used to quickly measure the neutron spectrum in a low resolution sense. Fine structure in the spectrum, such as that due to resonance scatterers, could not be resolved by the method.

To our knowledge, bubble detectors have not been used in epithermal neutron beam dosimetry. They may, however, be useful in low resolution spectral measurements or in determining the fast neutron dose rates in air.

2.4 DESCRIPTION OF PHANTOMS

Several phantoms were used in this work. They were designed to mimic various parts of the body in that the thermal flux as well as the photon and fast neutron doses within the phantom would be similar to those within an actual patient. The most important parameter for neutron transport is the hydrogen atom density. Hydrogen attenuates and thermalizes the incident epithermal neutron flux, and the thermal neutron capture reaction H-1(n,γ)H-2 induces a significant photon flux within the phantom. The materials used in the phantoms were selected to match their hydrogen densities to those of brain or muscle. The compositions of brain and muscle, and of the materials used in the phantoms are shown in table 2.1. They will be referred to later. The size and shape of the phantoms were also chosen to match the body part in which the doses were to be estimated.

Initially, a simple polyethylene or water filled cylinder was used. These crudely represented the human head, but were used mainly for beam design work. Later, more anthropomorphic phantoms were made. These include water filled ellipsoidal phantoms that were based on Snyder's [23] original MIRD shapes and sizes as well as even more

Table 2.1 Densities and hydrogen contents for brain and muscle and for several phantom materials.

Material	Density (g/cm^3)	Hydrogen (weight percent)	Hydrogen ($atoms/cm^3$)
Water	1.00	11.1	6.63E+22
Average brain *	1.047	10.6	6.63E+22
ICRU muscle *	1.04	10.2	6.34E+22
Plexiglas	1.18	8.05	5.67E+22
Lucite	1.17	8.05	5.63E+22
Wax-130 [27]	0.845	13.25	6.69E+22
Paraffin [27]	0.865	14.2	7.34E+22

* Complete compositions are provided in tables 3.3 and 3.4.

realistic head phantoms with noses, ears, and necks. The Medical Internal Radiation Dose (MIRD) Committee of the Society of Nuclear Medicine is charged with responsibility for providing guidance and information to the nuclear medicine community on calculating the radiation doses from radionuclides. Phantoms of other parts of the body, including the leg, thigh, and groin were also made. These phantoms are discussed briefly below.

2.4.1 Cylindrical water head phantom

The cylindrical water phantom[24] is shown in figure 2.4. The phantom is made from an acrylic tube with 0.32 cm thick walls. The top plate is 0.16 cm thick acrylic and the bottom plate is 0.64 cm thick acrylic. As shown in table 2.1, water has a hydrogen atom density about equal to that of average brain and only 1.7% higher than ICRU muscle. Thirteen holes were machined out of the bottom plate and fitted with guide pieces made out of 2.5 cm diameter acrylic rods. There are two hexagonal arrays of tubes with radii of 3 and 6 cm. There is also a tube on the central axis of the phantom. Radiation detectors can be positioned almost anywhere within the phantom. The tubes are 1.27 cm in diameter, thin walled, and 30 cm long. Rubber O-rings prevent leakage. A small hole was drilled in the top of the phantom to allow air bubbles to escape and to allow water to escape when a tube was being inserted. The tubes were fitted with plastic end caps inside the phantom to form a water proof barrier. During the ionization chamber measurements, a chamber is inserted into one of the tubes. The other tubes are withdrawn to the bottom of the phantom. Dose rates can be measured anywhere along the line that defines the central axis of the tube. For the foil measurements, the gold or cadmium covered gold foils are positioned and taped to a thin plastic rod. The rod is then inserted into a tube, and the tube filled with water. A plastic end cap is attached to the bottom of the tube to keep the water inside the tube. The cylindrical water phantom was used for much of the initial beam design work, up to beam M47.

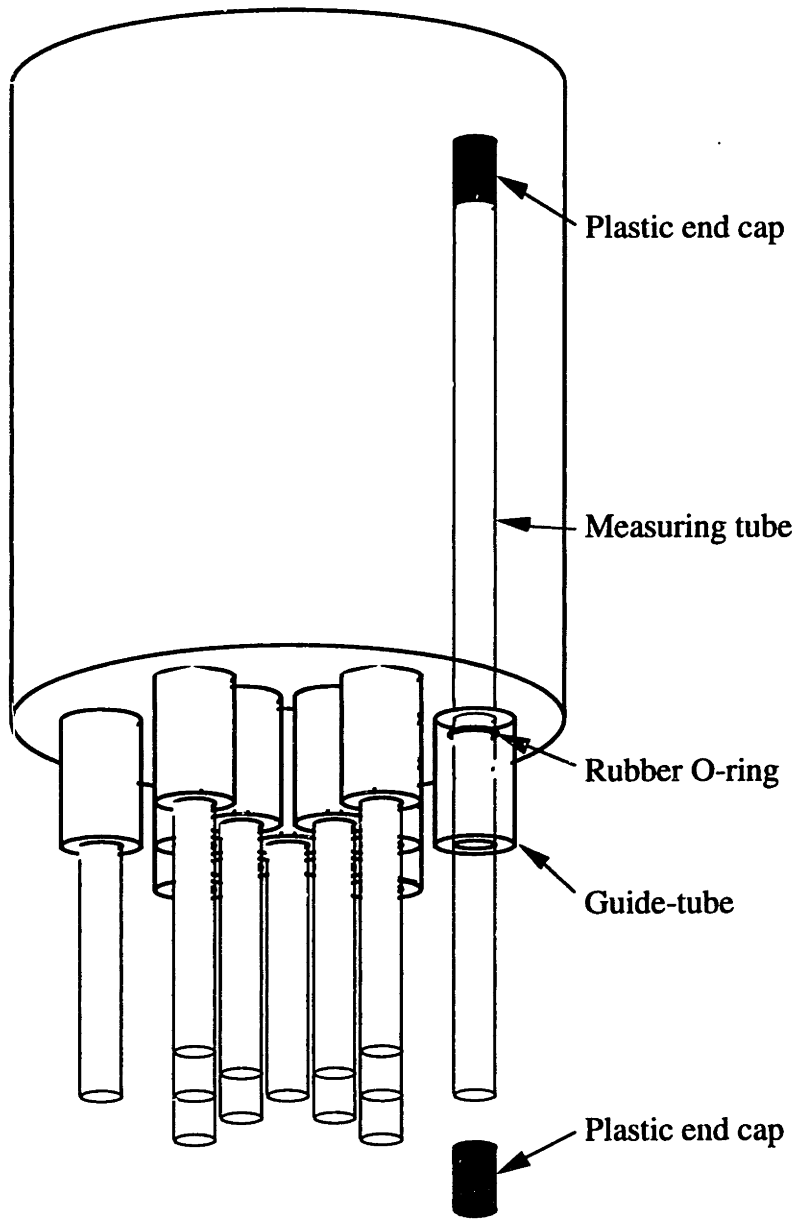

Figure 2.4. Cylindrical water filled head phantom. The cylinder is 18 cm in diameter and 20 cm high. This phantom was used for much of the initial beam design effort. The cylinder and endcaps are thin walled acrylic. There are 12 tubes in 2 hexagonal arrays and a tube along the centerline.

2.4.2 Ellipsoidal water filled head phantoms

Three ellipsoidal water filled head phantoms were made, in small, medium, and large head sizes. Details of their design and construction can be found in Moulin[25] and Roberts.[26] A schematic of the medium sized ellipsoidal water filled head phantom is shown in figure 2.5. The dimensions of the medium sized phantom is based on the Snyder model.[23] In one design, a 0.1" thick curved piece of Plexiglas forms the top part of the phantom; acrylic plates form the bottom half. The curved Plexiglas piece was made by first heating a sheet of Plexiglas to about 100 C in an oven. The hot Plexiglas was flexible and was pressed over a wood mold.[26] Excess Plexiglas was trimmed while still hot. The shell was then glued to the base using formaldehyde. The butyrate tubes and tube array are the same as those of the cylindrical phantom. A pair of O-rings was used for each tube. A Teflon fill tube enters through the acrylic plates. A Teflon overflow tube exits from the top of the phantom.

2.4.3 Ellipsoidal head phantom made with a casting resin shell

The original head phantom made by Moulin, and which had a Plexiglas shell, was broken by accident. It was decided to replace it with a new design that would be of higher quality and easier to make. The original design worked very well, but had some drawbacks in the method of construction. Forming the Plexiglas shell was difficult; excess material resulted in creases which had to be smoothed out or trimmed. Also, the seam between the shell and the acrylic base was prone to water leaks. An improved method of making the shell was developed as part of this thesis research.

In the new design a casting resin, not Plexiglas, was used to make the ellipsoidal shells of the phantom. The acrylic plates forming the base of the phantom were the same as those made by Moulin. To make the shells, the ellipsoidal wood mold made by Roberts[26] was first sprayed with a mold release (Fluoroglide, Norton Co., Wayne, N.J.). Then, a sheet of Saran Wrap was placed over the mold, taking care to eliminate most of

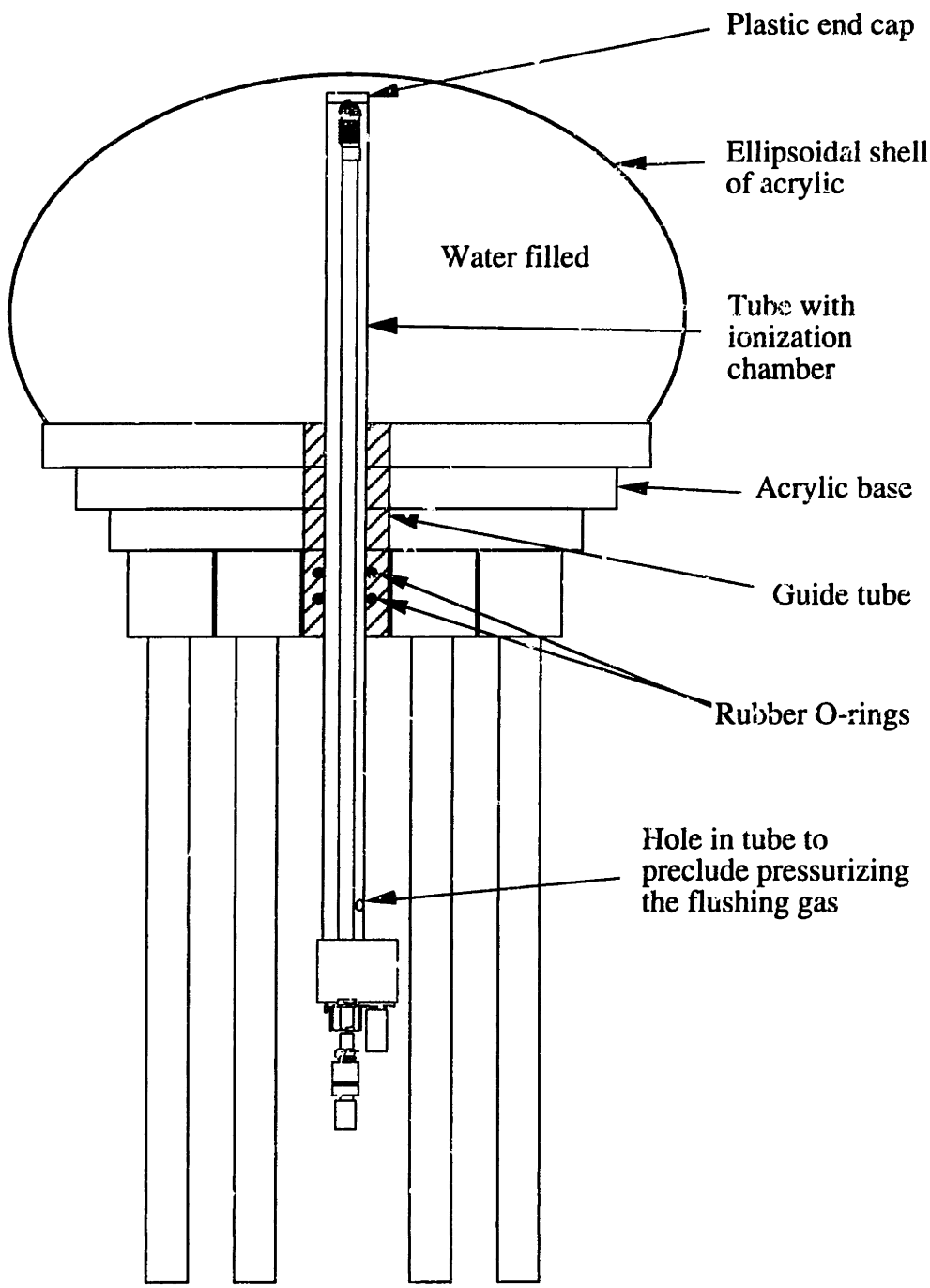

Figure 2.5. Ellipsoidal water filled head phantom showing positioning of the ionization chamber in the center tube. The top part of the phantom is a thin sheet of Plexiglas that was heated and formed over a mold. When the chamber is snapped into the tube, the chamber's thimble is at the top of the tube. A hole in the bottom of the tube precludes pressurization. The new head phantom has a ellipsoidal shell made of casting resin that is strengthened with quartz fibers.

the creases. On top of this was placed an approximately 0.1" thick mat of quartz wool or cloth (Quartz Plus, Inc., Concord, Ma.). The mat from the supplier was 0.2" thick. This mat was gently separated into two 0.1" thick pieces. Excess mat was wrapped underneath the wood mold and taped down.

Then, the liquid resin was prepared. About 30 drops of catalyst were added to 50 ml of resin (Castin'craft clear liquid plastic casting resin, ETI, Fields Landing, Ca), and the mixture thoroughly stirred. The mixture was then poured over the mat. This was repeated 3 times, until a total of about 200 ml of resin was used. It's important not to compress the quartz mat as then the resin does not soak into the mat. Quartz mat was used to strengthen the shell. Quartz has no B-10 or other impurities that could cause flux depression or lead to activation.

The resin takes half a day to one day to hardened sufficiently. A heat lamp may be used to speed the process. Then, the excess material is trimmed away. A hot air gun is used to heat the resin and soften it, and then scissors are used to trim the excess. After this, the mold is clamped down, and the shell separated from the mold.

The shell was then sanded with a power sander, starting with 40 grit sandpaper (an aluminum oxide sandpaper), then 60, 100, 150, and 220 grit. The inside surface of the phantom was sanded by hand. Finally, the shell was sprayed with a resin spray. This improved the appearance of the shell and made it a little easier to see through it. The top shell of the phantom is half an ellipsoid. The bottom half starts out as half an ellipsoid as well; then, about half the material is removed so the bottom half can be attached to the acrylic base. The excess material is removed with a belt grinder.

Two sets of templates for the shells, one based on the inside diameters and the other on the outside diameters, were cut out of cardboard. These were used to ensure that the dimensions of the shells were correct. Errors were generally less than 3 mm, or about 1-2% of the diameter. The thicknesses of the shells were measured at several places with

a micrometer; the thicknesses varied from 0.100-0.115". The density was measured to be 1.20 g/cm^3. Acrylic, for comparison, has a density of 1.19 g/cm^3.

The shells were glued together, and to the acrylic base, with a solvent cement formulated for joining acrylic (Weld.On 3, IPS, Inc, Gardena, Ca). Tests showed the phantom to be water tight. The phantom was tested for neutron activation when it was first used with the M67 beam. No activity was detected with a survey meter after a one-hour irradiation.

The new quartz mat - resin based phantom design is easier and quicker to make than the Plexiglas design. The quartz mat - resin shell is likely to be stronger than the Plexiglas shell; a drop test, though, showed that a pure resin shell breaks when dropped from a height of 1 foot. It was concluded that if the phantom falls, or is knocked over, the shell will probably break. The resin shell is not transparent like the Plexiglas shell. This is not a drawback, however. The inside of the phantom can be clearly seen by looking in through the acrylic plates on the bottom.

2.4.4 Partial body phantoms

The partial body phantoms were developed to investigate the dosimetry for metastatic melanoma within different parts of the body, including the groin, thigh, and leg. Details of their design and construction can be found in Yam.[27] A sketch of the leg phantom is shown in figure 2.6. The groin phantom was made of paraffin and the thigh phantom was made of Wax-130 (Polygon Co., S. Boston, Ma.). The hydrogen densities of these materials are shown in table 2.1. To make these phantoms, a Plaster of Paris cast of the body part was made. The cast was then filled in layers, about 1" thick, with melted paraffin or wax. The model for these plaster molds was a 66 kg, 177 cm tall man. Holes were drilled through the phantoms so the tubes and detectors could be inserted. One of the phantoms underwent a CT scan. Small cracks and voids were visible, but they would not affect the dosimetry, which is dependent on the macroscopic density of the material

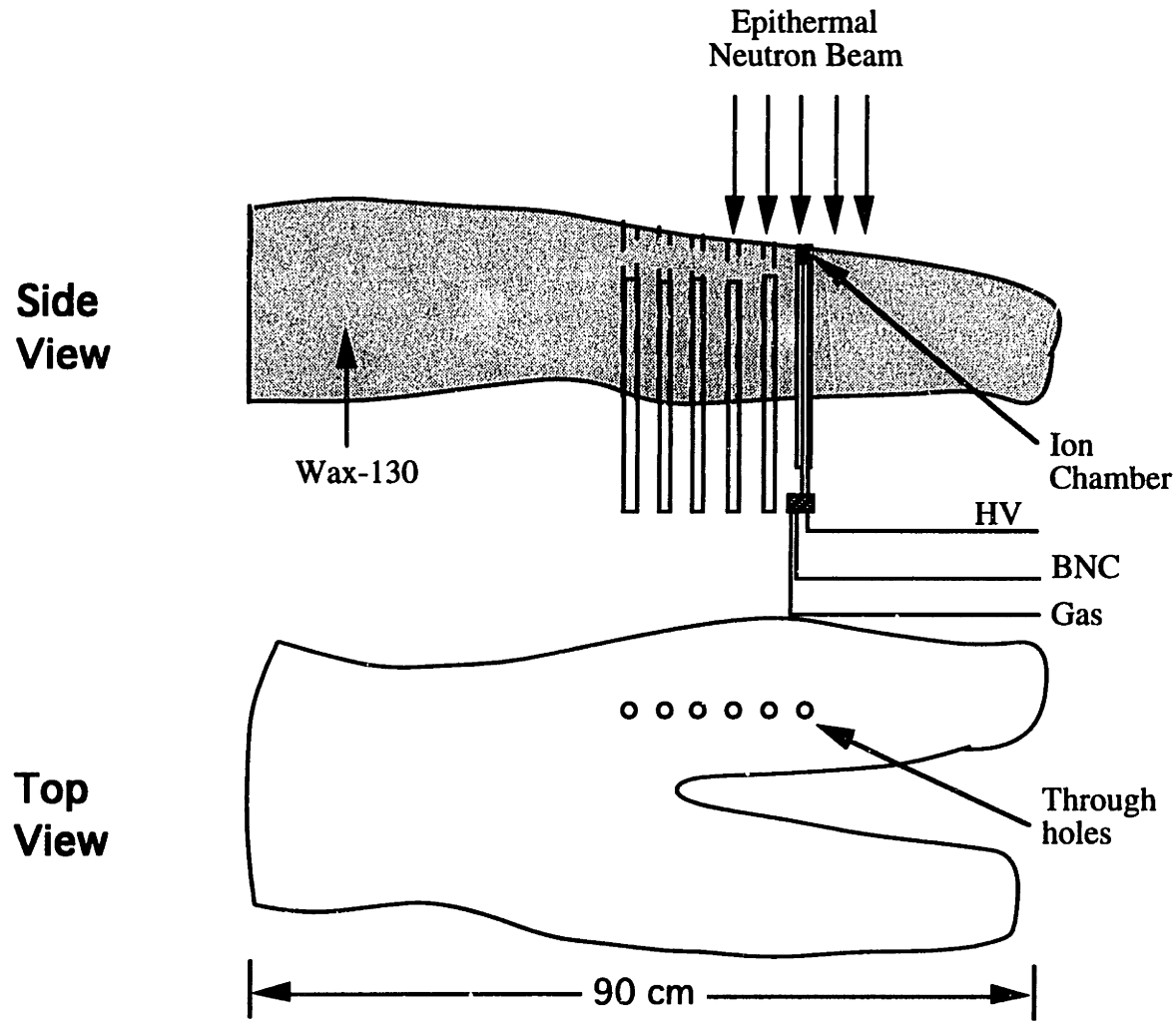

Figure 2.6. Leg phantom made of Wax-130. Holes were drilled through the phantom so the doses could be measured from the knee to the groin. These phantoms were developed to investigate the dosimetry for metastatic melanoma within different parts of the body.

and its hydrogen content. For the gold foil irradiations, the tubes were filled with water. For the chamber irradiations, the chambers were inserted into the butyrate tubes as usual. When a tube was pulled down through the phantom, plugs of paraffin or wax were inserted from the top to fill the air space above the tube.

2.5 SELECTION OF RBE'S FOR THE VARIOUS RADIATION COMPONENTS

Each component of the dose has been assigned a relative biological effectiveness (RBE) value. For the B-10 delivery agent BPA, RBE's were assumed (for most of the results presented in this thesis) to be 4.0 for the B-10 dose, 2.3 for the fast neutron dose, 2.3 for the thermal neutron dose, and 0.5 for the photon dose. These RBE's were drawn from available radiobiological data,[28-30] and have been used by our group as a likely set of RBE's for the past two years.[31] The photon RBE of 0.5 was chosen since it was assumed that the therapy would be fractionated. A result is also reported (refer to Chapter 5) assuming a pessimistic thermal and fast neutron RBE of 4.0. It is shown that a adequate therapeutic ratio can be achieved even under the conditions of a less favorable, but conceivable, thermal and fast neutron RBE. More accurate information about RBE's in BNCT irradiation therapies will undoubtedly be developed in the future. Tumor and healthy tissue B-10 concentrations, 30 and 7.5 ppm respectively, are illustrative of concentrations and concentration ratios which our group have experimentally observed for BPA.[31,32]

For the B-10 delivery agent BSH, RBE's were assumed to be 2.3 for the B-10 dose, 1.6 for the fast neutron dose, 1.6 for the thermal neutron dose, and 1.0 for the photon dose. These RBE's were drawn from available radiobiological data and have been generally agreed upon by the international BNCT community. [5,32-36] Tumor concentrations of 30 ppm are reasonable, along with tumor-to-blood ratios of three-to-

one.[5,32] The critical cell population with BSH appears to be the capillary endothelial cells.[5,32] Microdosimetric analyses of the B-10 reaction in the microvasculature have shown that the dose received by the endothelial cells is much less than that predicted from the concentration of B-10 in blood.[32,34-36] Estimated dose absorption factors, or "compound factors" of 0.33 have been reported. That is, the endothelial cells receive 1/3 the dose predicted from the concentration of B-10 in blood. Due to the geometry of the microvasculature and the short range of the α and Li-7, 2/3 of the energy from a B-10 reaction in blood is deposited in the blood. Accounting for the 3:1 tumor-to-blood ratio, and a compound factor of 0.33, an effective background level of B-10 has generally been assumed to be 10 times lower than the tumor concentration, or 3 ppm B-10. A minimum background level of 0 ppm has been assumed.

2.6 PRESENTATION OF DOSIMETRIC RESULTS

Dosimetric results are generally presented in the form of RBE-weighted dose rate versus depth-in-phantom plots. Sample plots for BSH and BPA are shown in figures 2.7 and 2.8. Each plot illustrates the individual thermal neutron, fast neutron, photon, and 30 ppm B-10 doses. The 30 ppm B-10 total tumor dose is the sum of the four individual components.

For BSH, the minimum and maximum background doses are also given. The minimum background dose is the sum of thermal neutron, fast neutron, and photon doses. This is the dose that healthy tissue would receive if it contained no B-10. The maximum background dose is the sum of the thermal neutron, fast neutron, and photon doses, plus that due to 3 ppm B-10. This is the dose that healthy tissue would receive if it contained a B-10 concentration of 3 ppm.

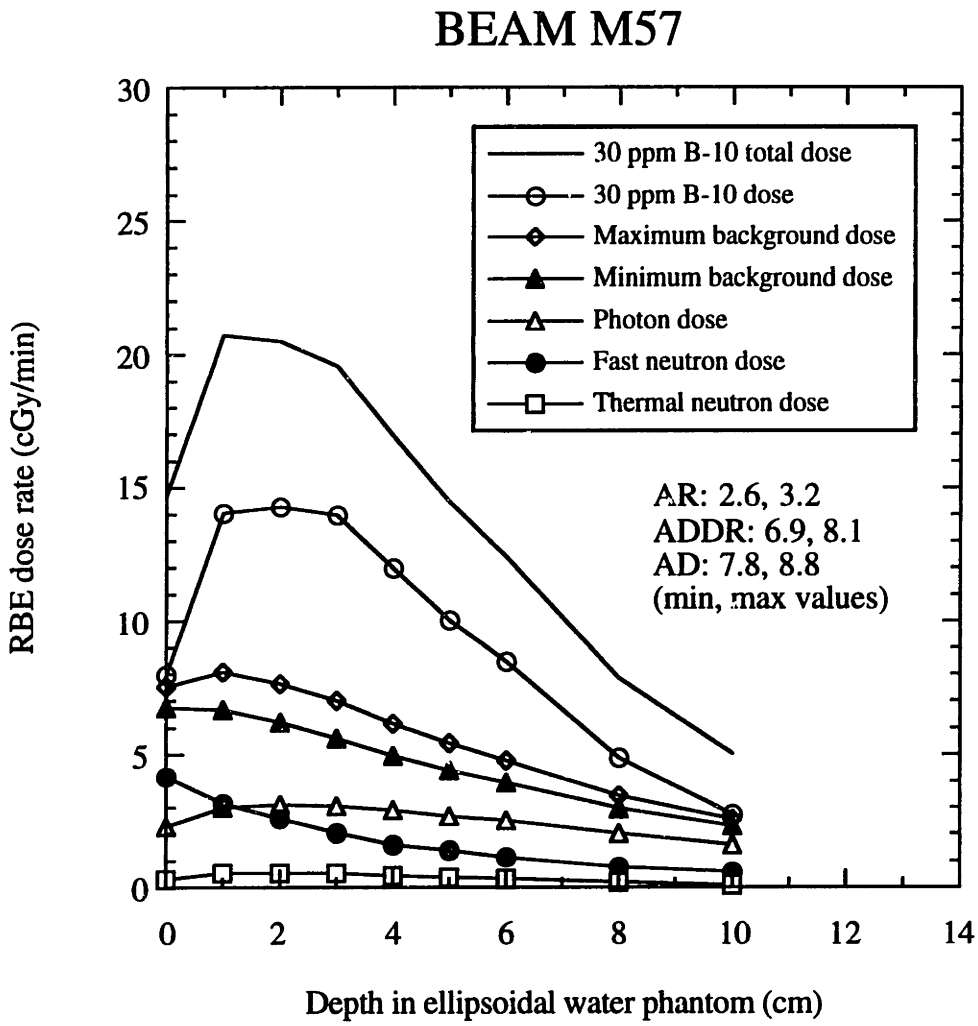

Figure 2.7. Sample dose versus depth plot. These doses are for the M57 beam (no delimiter) and BSH. The M57 beam was an earlier beam configuration. The current beam is M67.

Unilateral irradiation.
Phantom: Medium sized, ellipsoidal, water filled, center tube.
Reactor power: 5 MWn.
RBE's: 2.3 for B-10, 1.6 for neutrons, 1.0 for photons (BSH).
B-10 concentrations: 30 ppm for tumor, 3 ppm for maximum background, 0 ppm for minimum background.
In-air data: D_{fn} = 3.4 cGy/min
D_{γ} = 1.2 cGy/min

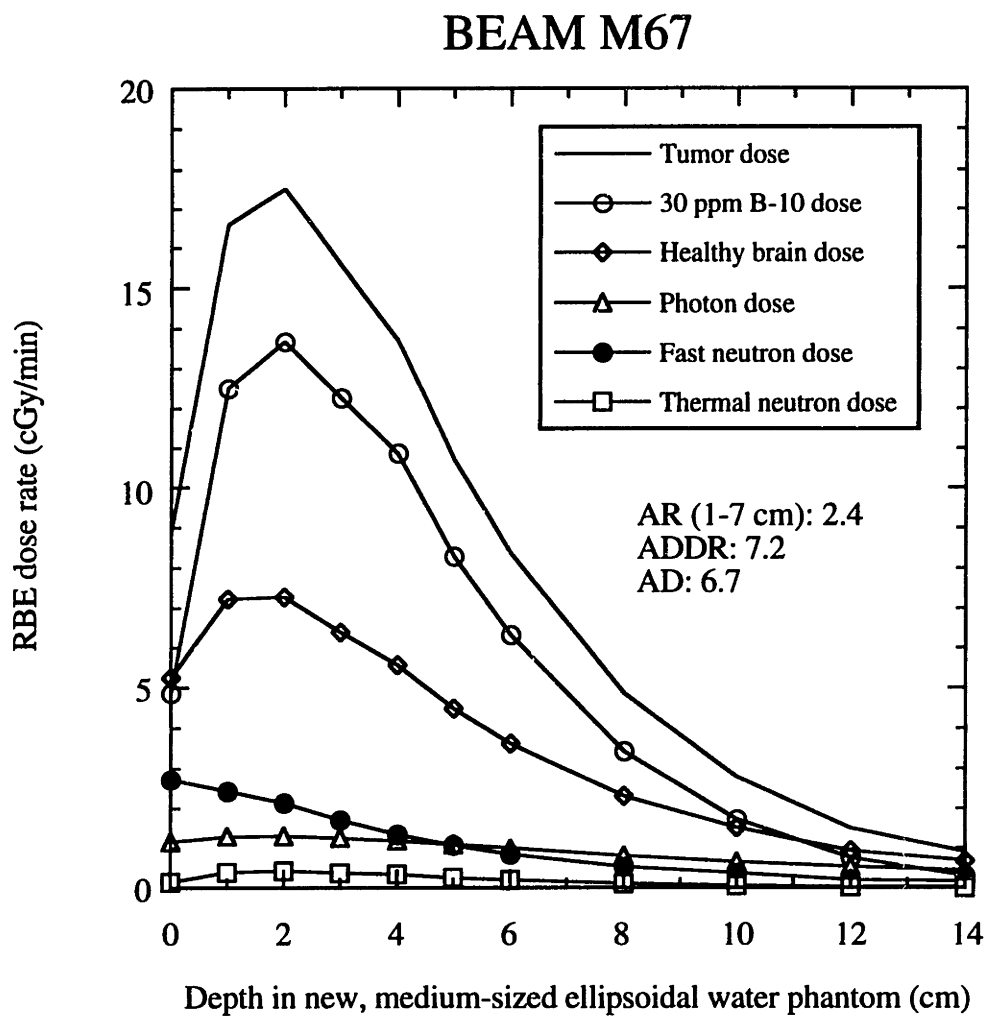

Figure 2.8. Sample dose versus depth plot. These doses are for the M67, delimiter #3 beam and BPA. This is the current beam configuration.

Unilateral irradiation.
Phantom: Medium sized, casting resin ellipsoidal, water filled, center tube.
Delimiter: #3, 15 cm diameter hole.
Reactor power: 5 MWn.
RBE's: 4.0 for B-10, 2.3 for neutrons, 0.5 for photons (BPA).
B-10 concentrations: 30 ppm for tumor, 7.5 ppm for healthy brain.
In-air data: $D_{fn} = 2.5$ cGy/min
$D_{\gamma} = 0.85$ cGy/min
$D_{30ppm\ B\text{-}10} = 1.2$ cGy/min

For BPA, there is a single curve for healthy tissue (brain or muscle). The healthy tissue dose is the sum of the thermal neutron, fast neutron, and photon doses, plus that due to 7.5 ppm B-10. For BPA, then, it is assumed that tumor has 30 ppm B-10 and that healthy tissue has 7.5 ppm B-10.

Three parameters have been used to summarize the overall quality and intensity of each beam. They are the advantage ratio (AR), advantage depth (AD), and the advantage depth dose rate (ADDR).[5] The advantage ratio is defined as the quotient of the integral of the total therapeutic dose and the integral of the total background dose. It is the ratio of tumor dose to healthy tissue dose, on average. The integral extends from the surface of the phantom to the advantage depth. For BSH, the upper limit is the maximum advantage depth. The advantage depth is defined as the depth in phantom where the total therapeutic dose equals the background dose in phantom. It is an indicator of how effective the beam would be at treating deeply seated tumors. For BSH, minimum and maximum AD's are defined by using the background determined with 3 and 0 ppm B-10, respectively, in healthy tissue, and 30 ppm B-10 in tumor. The advantage depth dose rate is the total therapeutic dose rate at the advantage depth, or equivalently, the maximum dose rate to healthy tissue.

ADDR values are scaled to a reactor power of 5 MW_n as measured by Channel 7, one of the reactor control instruments (a compensated ionization chamber). All advantage parameters are based on RBE-weighted doses.

Additional dosimetric information is generally given along with the dose versus depth plot. These include the mode of irradiation (unilateral or bilateral), phantom used, reactor power, RBE's, and B-10 concentrations. In unilateral irradiations, the body is irradiated from one side only. In bilateral irradiations, the body is first irradiated from one side and then irradiated equally from the other side. For the bilateral results reported in this thesis, it was assumed that the part of the body being irradiated was symmetrical relative to the beam; that is, a bilateral irradiation would result in a symmetrical dose

distribution within the body. In-air doses (photon and fast neutron doses, and 30 ppm B-10 doses) are given as well.

The thermal and epithermal fluxes versus depth in phantom are also given.

2.7 CLINICAL DOSIMETRY

One of the beams that was designed and characterized in this study, the M67 beam, was selected as the beam that will be used for clinical trials. The dosimetry for this beam is discussed in detail in Chapter 5. Delimiters and whole body shields were designed and used with this beam; many of the earlier beams did not have this additional shielding. Centerline and off-axis dosimetry was obtained for this beam. Experimental results were compared with those generated by MCNP. Whole body doses were determined. Some aspects of in-vivo dosimetry were investigated with this beam.

Pursuant to MITR Technical Specification No. 6.5, a set of Procedures was written and followed during the characterization of this beam. The electrometer and ionization chambers used to characterize this beam were calibrated at the University of Wisconsin Accredited Calibration Laboratory. The overall errors associated with the doses were determined. The calculations and experimental technique used to determine the doses for this and the other beams was reviewed and approved by an outside expert in mixed field dosimetry.

2.8 SUMMARY

This chapter gave an overview of the MITR-II reactor, and brief description of epithermal neutron beam design and dosimetry. The reactor was described along with the

system of shutters that is used to turn the beam on and off. The positioning of the moderator and filtering materials was also discussed. The two general approaches to epithermal neutron beam design - the moderator method and the filter method - were discussed. Epithermal neutron beam dosimetry and the various radiation detectors that can be used in this dosimetry were reviewed. The phantoms, including the head and partial body phantoms, were described. Doses reported in this thesis are all RBE-weighted; the selection of the RBE's used for BSH and BPA was discussed. Sample dose-versus-depth plots were provided for BSH and BPA, along with a description of the advantage parameters used to describe the beam dosimetry. Finally, the additional work needed for clinical dosimetry was reviewed.

In the next chapter, the protocol for mixed field dosimetry of the epithermal neutron beams is described in detail. In Chapter 4, the dosimetric results for the beams characterized as part of this thesis are presented.

REFERENCES

1. S. D. Clement, J. R. Choi, R. G. Zamenhof, J. C. Yanch, and O. K. Harling, "Monte Carlo Methods of Neutron Beam Design for Neutron Capture Therapy at the MITR-II Research Reactor (MITR-II)," in *Neutron Beam Design, Development, and Performance for Neutron Capture Therapy*, (O. K. Harling, John A. Bernard, Robert G. Zamenhof, eds., Plenum Press, New York, 1990).

2. R. M. Brugger and W. H. Herleth, "Intermediate Energy Neutron Beams from the MURR," in *Neutron Beam Design, Development, and Performance for Neutron Capture Therapy*, (O. K. Harling, John A. Bernard, Robert G. Zamenhof, eds., Plenum Press, New York, 1990).

3. J. C. Yanch, X-L. Zhou, R. E. Shefer, R. E. Klinowstein, and G. L. Brownell, "Design of an Accelerator-Based Epithermal Neutron Beam for Boron Neutron Capture Therapy," in *Progress in Neutron Capture Therapy for Cancer* (Barry J. Allen, Douglas E. Moore, Baiba V. Harrington, eds., Plenum Press, New York, 1992).

4. J. C. Yanch and O. K. Harling, "Dosimetric effects of beam size and collimation of epithermal neutrons for boron neutron capture therapy," Rad. Res. **135**, 131-145 (1993).

5. R. M. Brugger, G. Constatine, O. K. Harling, and F. J. Wheeler, "Rapporteurs' Report," in *Neutron Beam Design, Development, and Performance for Neutron Capture Therapy*, (O. K. Harling, John A. Bernard, Robert G. Zamenhof, eds., Plenum Press, New York, 1990).

6. F. J. Wheeler, D. K. Parsons, D. W. Nigg, D. E. Wessol, "Physics Design for the Brookhaven Medical Research Reactor Epithermal Neutron Source," in *Neutron Beam Design, Development, and Performance for Neutron Capture Therapy*, (O. K. Harling, John A. Bernard, Robert G. Zamenhof, eds., Plenum Press, New York, 1990).

7. G. Constatine, "Neutron Capture Therapy Beam Design at Harwell," in *Neutron Beam Design, Development, and Performance for Neutron Capture Therapy*, (O. K. Harling, John A. Bernard, Robert G. Zamenhof, eds., Plenum Press, New York, 1990).

8. B. V. Harrington, "A Calculational Study of Tangential and Radial Beams in HIFAR for Neutron Capture Therapy," in *Neutron Beam Design, Development, and Performance for Neutron Capture Therapy*, (O. K. Harling, John A. Bernard, Robert G. Zamenhof, eds., Plenum Press, New York, 1990).

9. O. Aizawa, "Research on Neutron Beam Design for BNCT at the Musashi Reactor," in *Neutron Beam Design, Development, and Performance for Neutron Capture Therapy*, (O. K. Harling, John A. Bernard, Robert G. Zamenhof, eds., Plenum Press, New York, 1990).

10. W. A. Neuman, "Neutron Beam Studies for a Medical Therapy Reactor," in *Neutron Beam Design, Development, and Performance for Neutron Capture Therapy*, (O. K. Harling, John A. Bernard, Robert G. Zamenhof, eds., Plenum Press, New York, 1990).

11. J. R. Choi, R. G. Zamenhof, J. C. Yanch, R. Rogus, O. K. Harling, "Performance of the Currently Available Epithermal Neutron Beam at the Massachusetts Institute of Technology Research Reactor (MITR-II)," in *Progress in Neutron Capture Therapy for Cancer* (Barry J. Allen, Douglas E. Moore, Baiba V. Harrington, eds., Plenum Press, New York, 1992).

12. R. L. Moss, F. Stecher-Rasmussen, K. Ravensberg, G. Constatine, and P. Watkins, "Design, Construction, and Installation of an Epithermal Neutron Beam for BNCT at the High Flux Reactor at Petten," in *Progress in Neutron Capture Therapy for Cancer* (Barry J. Allen, Douglas E. Moore, Baiba V. Harrington, eds., Plenum Press, New York, 1992).

13. Victoria McLane, Charles Dunford, and Philip Rose, *Neutron Cross Sections, Volume 2, Neutron Cross Section Curves*, (National Nuclear Data Center, Brookhaven National Laboratory, Upton, New York, Academic Press, NY, 1988).

14. Frank H. Attix, *Introduction to Radiological Physics and Radiation Dosimetry*, (John Wiley & Sons, New York, NY, 1986).

15. ICRU Report 26, *Neutron Dosimetry for Biology and Medicine*, (International Commission on Radiation Units and Measurements Bethesda, Maryland, 1977).

16. ICRU Report 45, *Clinical Neutron Dosimetry. Part I: Determination of Absorbed Dose in a Patient Treated by External Beams of Fast Neutrons*, (International Commission on Radiation Units and Measurements, Bethesda, Maryland, 1989).

17. S. K. Saraf, J. Kalef-Ezra, R. G. Fairchild, B. H. Laster, S. Fiarman, and E. Ramsey, "Epithermal Beam Development at the BMRR: Dosimetric Evaluation," in *Neutron Beam Design, Development, and Performance for Neutron Capture Therapy*, (O. K. Harling, John A. Bernard, Robert G. Zamenhof, eds., Plenum Press, New York, 1990).

18. V. Benary, R. G. Fairchild, J. Kalef-Ezra, D. Greenberg, Y. Kamen, S. Fiarman, and L. Wielopolski, "Dose Measurements and Calculations in the Epithermal Neutron Beam as the Brookhaven Medical research Reactor (BMRR)," in *Progress in Neutron Capture Therapy for Cancer* (Barry J. Allen, Douglas E. Moore, Baiba V. Harrington, eds., Plenum Press, New York, 1992).

19. C. A. Perks, G. Constatine, and H. Delafield, "Review of Techniques Developed at Harwell Laboratory for Neutron and Gamma-Ray Characterization of Filtered Neutron Beams for Boron Neutron Capture Therapy," in *Progress in Neutron Capture Therapy for Cancer* (Barry J. Allen, Douglas E. Moore, Baiba V. Harrington, eds., Plenum Press, New York, 1992).

20. G. F. Knoll, *Radiation Detection and Measurement*, 2nd ed. (John Wiley & Sons, NY, 1989).

21. BTI Bubble Technology Industries, Product literature on bubble detector neutron spectrometer, bubble neutron dosimeter, and automatic bubble counter.

22. Personal communication, Nathan D. Lee, BTI Bubble Technology Industries, Chalk River, Ontario, Canada.

23. W. S. Snyder, M. R. Ford, G. G. Warner, and H. L. Fisher, "Estimates of Absorbed Fractions for Monoenergetic Photon Sources Uniformly Distributed in Various Organs of a Heterogeneous Phantom," MIRD, J. Nucl. Med. Suppl #3, pamphlet #5, (1969).

24. Jong-Ho Richard Choi, *Development and Characterization of an Epithermal Beam for Boron Neutron Capture Therapy at the MITR-II Research Reactor*, (Ph.D. Thesis, Massachusetts Institute of Technology, 1991).

25. Damien Moulin, *Design and Construction of Ellipsoidal Head Phantoms for Boron Neutron Capture Therapy*, (Report #MITNRL-042, Nuclear Reactor Laboratory, Massachusetts Institute of Technology, 1990).

26. Kevin A. Roberts, *Mixed Field Dosimetry in Realistic Head Phantoms Using an Epithermal Beam at the MITR-II*, (M.S. Thesis, Massachusetts Institute of Technology, 1990).

27. Chun-Shan Yam, *Design of Patient Positioning System, Body Phantom, and Patient Shielding for the Boron Neutron Capture Therapy Project at MITR-II*, (Master's Thesis, Massachusetts Institute of Technology, 1993).

28. G. R. Morgan, A. J. Mill, D. J. Roberts, S. Newman, and P. D. Holt, "The radiobiology of 24 keV neutrons," Br. J. Radiol. **61**, 1127 (1988).

29. H. Fukuda, T. Kobayashi, T. Matsuzawa, "RBE of a thermal neutron beam and the B-10(n,α)Li-7 reaction on cultured B-16 melanoma cells," Int. J. Radiat. Biol. **1**, 167 (1987).

30. J. A. Coderre, "Experimental determination of RBE values for the B-10(n,a)Li-7 reaction using BPA or BSSB in the rat 9L gliosarcoma model," (International workshop and plenary meeting - Toward Clinical Trials of Glioma with BNCT, Petten, The Netherlands, September 18-20, 1991).

31. O. Harling, R. Rogus, J. M. Chabeuf, S. Yam, F. Lambert, J. Yanch, "Final Preparations for Clinical Trials as the MIT Reactor and the New England Medical Center," Fifth International Symposium on Neutron Capture Therapy for Cancer, Columbus, Ohio, (1992).

32. Guido R. Solares, *High Resolution Alpha Track Autoradiography and Biological Studies of Boron Neutron Capture Therapy*, (Ph.D. Thesis, Massachusetts Institute of Technology, 1991).

33. R. G. Zamenhof, S. D. Clement, O. K. Harling, J. F. Brenner, D. E. Wazer, H. Madoc-Jones, and J. C. Yanch, "Monte Carlo Dosimetry and Treatment Planning for Neutron Capture Therapy for Brain Tumors," in *Neutron Beam Design, Development, and Performance for Neutron Capture Therapy*, (O. K. Harling, John A. Bernard, Robert G. Zamenhof, eds., Plenum Press, New York, 1990).

34. J. B. Davis, J. B. Little, K. Ayyangar, and A. R. Reddy, "Relative Biological Effectiveness of the B-10(n,α)Li-7 Reaction in HeLa Cells," Rad. Res. **43**, 534-553 (1970).

35. R. A. Rydin, O. L. Deutsch, and B. W. Murray, "The Effect of Geometry on Capillary Wall Dose for Boron Neutron Capture Therapy," Phys. Med. Biol.. **21**, 134 (1976).

36. K. Kitao, "A Method for Calculating the Absorbed Dose Near the Interface from the B-10(n,α)Li-7 Reaction," Rad. Res. **61**, 304-315 (1975).

CHAPTER 3 PROTOCOL FOR MIXED FIELD DOSIMETRY OF THE EPITHERMAL NEUTRON BEAMS

3.1 INTRODUCTION

In this chapter, the method that is used to measure and calculate the radiation doses is described in detail. The dosimetry of these epithermal neutron beams is different from that of fast neutron beams used for fast neutron therapy. In BNCT using epithermal neutron beams, the incident radiation field consists primarily of neutrons with energies from 0.5 eV to 10 keV. In addition, the incident field has some higher energy neutrons, with energies up to 15 MeV, and some photons. The incident epithermal neutrons thermalize within the patient and generate a photon field from the H-1(n,γ)H-2 reaction. Finally, most of the tumor dose and a significant fraction of the healthy tissue dose, is a result of the B-10(n,α) Li-7 reaction. In BNCT dosimetry, therefore, separate macroscopic doses, including those from thermal and fast neutrons, photons, and the B-10(n,α)Li-7 reaction, must be determined. Our group has been using and investigating this type of dosimetry for several years.[1] An outside review of this dosimetry protocol is provided in Appendix A (also, refer to Chapter 5.8).

The photon and fast neutron doses are measured with ionization chambers using the dual chamber technique. The thermal neutron flux is measured with gold foils using the cadmium difference technique. The thermal neutron and B-10 doses are determined by the kerma factor method using the measured thermal neutron flux. The accuracy of the four dose components depends on the quality of the experimental technique, and on the calculations and assumptions that are used to convert the experimental data into absorbed

doses. The experimental methodology as well as the calculations and assumptions that are used to calculate these doses is presented. The analysis emphasizes areas of BNCT dosimetry that are considerably different from those of fast neutron therapy dosimetry. Sample calculations are provided. If experimental data were needed for a particular sample calculation, these data were drawn from the characterization of the M57 beam. Sources of error in the experimental method and calculations are discussed. The overall uncertainty in the calculated doses is provided.

3.2 MATERIALS AND METHODS

3.2.1 Photon and fast neutron doses

The photon and fast neutron doses are determined using the dual ionization chamber technique[2] with realistic phantoms. In practice, clinical fast neutron dosimetry relies on and is based on measurements made with tissue equivalent ionization chambers flushed with tissue equivalent gas.[3] A carbon graphite chamber flushed with CO_2 is usually used to determine the accompanying photon dose. The dual chamber method is accurate and convenient. The chambers are small enough so that the doses can be determined almost anywhere throughout a phantom. Tissue equivalent calorimeters probably give smaller uncertainties for the total dose in some situations, but are too cumbersome for routine use and are better suited for calibration of other instruments.[3]

Experimental Method

Equipment

Two ionization chambers are used: an A-150 tissue equivalent chamber (Far West IC-18) and a carbon graphite chamber (Far West IC-18G). A schematic of the chambers is shown in figure 3.1. The tissue equivalent chamber has an OD of 9.59 mm and a wall

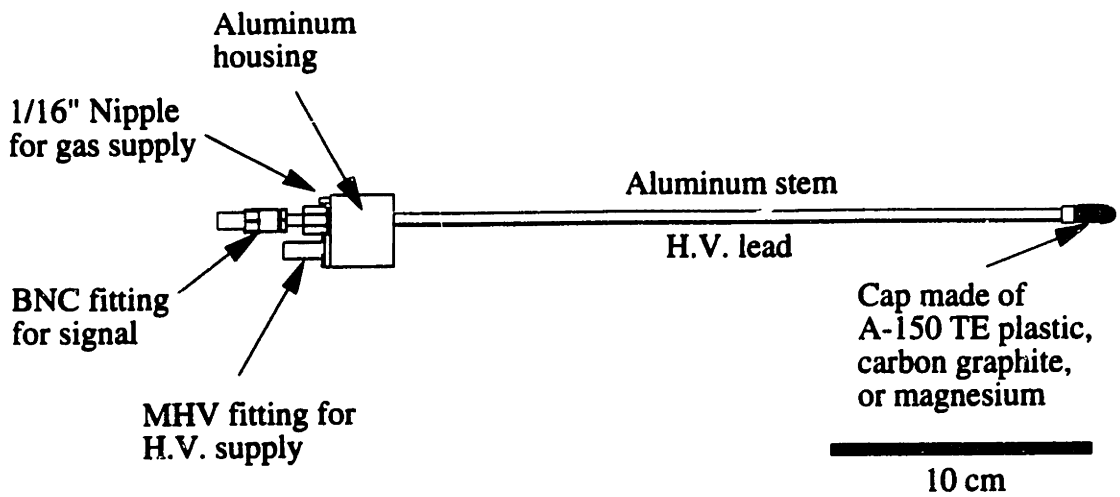

Figure 3.1. Schematic of the ionization chambers used in this study. These Far West chambers are fully guarded, three terminal designs.

thickness of 2.51 mm. The carbon graphite chamber has an OD of 7.87 mm and a wall thickness of 1.65 mm. The tissue equivalent wall provides transient charged particle equilibrium for photons up to 0.7 MeV and charged particle equilibrium for neutrons up to 15 MeV. Similarly, the carbon graphite wall provides transient charged particle equilibrium for photons up to 0.8 MeV and charged particle equilibrium for neutrons up to 17 MeV. These chambers were calibrated at an AAPM Accredited Calibration Laboratory. Details on this calibration are discussed later in the chapter.

The tissue equivalent chamber is flushed with tissue equivalent gas (64.4% CH_4, 32.4% CO_2, and 3.2% N_2 by partial pressure) and the carbon graphite chamber is flushed with CO_2. The tissue equivalent gas (Matheson Co., Gloucester) is of high quality, and is certified and analyzed. The CO_2 gas (Middlesex Welding, Cambridge) is from the reactor's CO_2 system. This gas has a purity of at least 99.98%. The impurities are mostly nitrogen, a little oxygen, and a trace of argon. A separate tank of CO_2 gas (Matheson Co., Coleman Instrument Grade, 99.99% purity), not dependent on the reactor's CO_2 system, was purchased and is now used exclusively. This Coleman CO_2 is a high quality, certified gas. Tygon tubing connects the chambers to the gas supply. The chambers and tubing are purged for 15 minutes at about 100 cc/min, and then the flow rate is set to 20 cc/min using an air calibrated flowmeter (Matheson PG-1111 or PG-1121). The temperature and pressure of the flushing gases are measured with a thermometer and barometer. The temperature and pressure are needed to correct the mass of gas within the sensitive volume of the chamber to standard conditions.

The chamber voltage is +250 volts (Canberra HV Supply #2861A or equivalent), which is in the plateau region and is the voltage recommended by the manufacturer. Ionic recombination during the measurements was assumed to be negligible. Fast neutron and photon dose rates are generally less than 10 rad/min and the irradiation is continuous, not pulsed. The electrometer is a Keithley 616 or 617. The Keithley 617 was calibrated at an AAPM Accredited Calibration Laboratory. Details on this calibration are discussed later

in the chapter. The signal lead is a low noise triax cable with a triax fitting on the electrometer end and a BNC fitting on the chamber end (the chambers have female BNC's for the signal). The signal and voltage cables are about 7 meters long. The background current, with voltage applied to the chambers but with no radiation field, is less than 1E-14 amperes. Typical currents measured during the dosimetric characterizations are around 1E-12 amperes. Racetrack timing is used. Charge is collected for about 1 minute and the charge and time interval recorded. These measurements are repeated twice and the 3 results are averaged.

Design and construction of buildup caps

The walls of our ionization chambers are not thick enough to provide charged particle equilibrium for Co-60. Buildup caps, therefore, were recently designed and machined to bring the chambers to equilibrium thickness. The buildup caps were needed to properly calibrate the chambers in the Co-60 beam used at the Calibration Laboratory. Also, the buildup caps were used during the later in-air measurements in our beams.

The thimbles of the carbon graphite, tissue equivalent, and magnesium chambers are described in table 3.1. Buildup caps were machined out of Plexiglas rod. A 2.057" length of 0.502" OD rod weighed 7.935 g; the calculated density is 1.189 g/cm^3. The buildup caps were designed to just fit over the chamber thimble, but without impeding the flow of the flushing gas. The thicknesses of the caps were designed to provide a total thickness (thimble plus cap) of about 0.52 g/cm^2, which is the Co-60 equilibrium thickness of polystyrene.[2] The buildup caps are described in table 3.2. Note that the total thickness of the magnesium chamber is 0.690 g/cm^2; the walls of this buildup cap are thicker than needed. The walls can be turned down to a 0.187 cm thickness, which will give a total thickness of 0.52 g/cm^2. Alternatively, the buildup cap for the tissue equivalent chamber can be used with the magnesium chamber.

Table 3.1. Description of chamber thimbles.

Chamber	Wall material	Density (g/cm^3)	OD (cm)	Wall thickness (cm)	Wall thickness (g/cm^2)
Carbon graphite	graphite	2.1*	0.787	0.165	0.347
Tissue equivalent	A-150 plastic	1.127	0.960	0.251	0.283
Magnesium	magnesium	1.735	0.787	0.168	0.291

* Nominal value.

Table 3.2. Description of buildup caps.

Chamber	Cap OD (cm)	Cap ID (cm)	Cap thickness (cm)	Cap length (cm)	Cap thickness (g/cm^2)	Total thickness (thimble + cap) (g/cm^2)
Carbon graphite	1.069	0.785	0.142	1.669	0.169	0.516
Tissue equivalent	1.328	0.960	0.184	1.900	0.219	0.502
Magnesium	1.463	0.792	0.335	1.704	0.399	0.690

All cap dimensions as built.

A factory built cap (Far West?) of what appears to be A-150 plastic is also available. The volume of the cap has been measured by the water displacement technique. The volume is 3.0 cm^3 and the weight is 3.312 g; the calculated density is 1.104 ± 5% g/cm^3. This cap has a wall thickness of 0.342 cm, or 0.377 g/cm^2.

It would be instructive to measure the degree to which the buildup caps affect the in-air measurements taken inside the medical room. This could best be done by positioning a chamber 2 cm below the beam, and then taking a measurement. Then, the buildup cap could be slid over the thimble without disturbing the positioning of the chamber, and the measurement repeated. This would need to be done with both the carbon graphite and tissue equivalent chambers.

Sealing the carbon graphite ionization chamber

During an on-site visit to review our experimental technique, Dr. Steven Goetsch, Department of Radiation Oncology, UCLA School of Medicine, recommended that we investigate the possibility of sealing the carbon graphite chamber. His Group has documented influx of air into the sensitive volume of the chamber by diffusion through the porous graphite, which affects the calibration of the chamber.[34] The carbon graphite chamber, therefore, was sealed by spraying the outside of the thimble with a thin coat of lacquer (Tru-Test Interior/Exterior HI-Q Lacquer, #1355 Clear). This should preclude any possibility of air diffusing from the outside of the thimble into the sensitive volume. The lacquer was first tested by PGNAA. No additional peaks from B-10, cadmium, gadolinium, or other elements that could affect the response of the chamber in a neutron field were seen. Only additional hydrogen prompt gammas were found.

The carbon graphite chamber was tested to be certain that the exposure calibration was left unaffected by the lacquer. Exposure rates measured at the Cs-137 source were 0.5376 ± 1% R/min before the chamber was sprayed and 0.5364 ± 1% R/min after the

chamber had been sprayed and dried. The lacquer, therefore, has no measurable effect on the chamber's calibration.

Reference phantoms

Measurements are made within a water filled, ellipsoidal head phantom[4,5] or a wax, partial body phantom.[6] The head phantom is constructed of a thin ellipsoid of acrylic on the top 2/3 of the phantom and acrylic plates on the bottom 1/3. The dimensions of the phantom are based on the Snyder model.[7] The head phantom is shown positioned in the beam in figure 3.2. The partial body phantoms are made by first making a mold with Plaster of Paris and then filling the mold in layers with Wax-130 (Polygon Co., S. Boston, Ma.). The mold is then cut off, leaving a wax phantom that closely matches the size and shape of the actual body part. The partial body phantoms are similarly positioned, but are supported on the sides or ends with a different support. The phantoms can be accurately positioned, within several millimeters, relative to the beam centerline. The position of any phantom is the same for both chambers.

Watertight butyrate tubes are inserted from the bottom of the phantoms and allow the gold foils or ionization chambers to be positioned within the phantoms. With the head phantom, usually only one tube is inserted into the phantom at a time; the rest of the tubes are almost fully withdrawn to minimize perturbation of the radiation field. When gold foils are used, the tube containing the gold foils is filled with water. The ionization chambers are inserted into the bottom of the tubes. An 1/8" hole has been drilled through the side of the tubes, near the bottom so that there is no water leakage, to prevent pressurization of the tubes by the fill gas. A close up an ionization chamber positioned within the head phantom is shown in figure 3.3.

Measurements are generally made within a phantom at depths of 1, 2, 3, 4, 5, 6, 8, and 10 cm. The fast neutron and photon doses are also determined on the top of the phantom. This information allows these doses to be interpolated through the top 1 cm

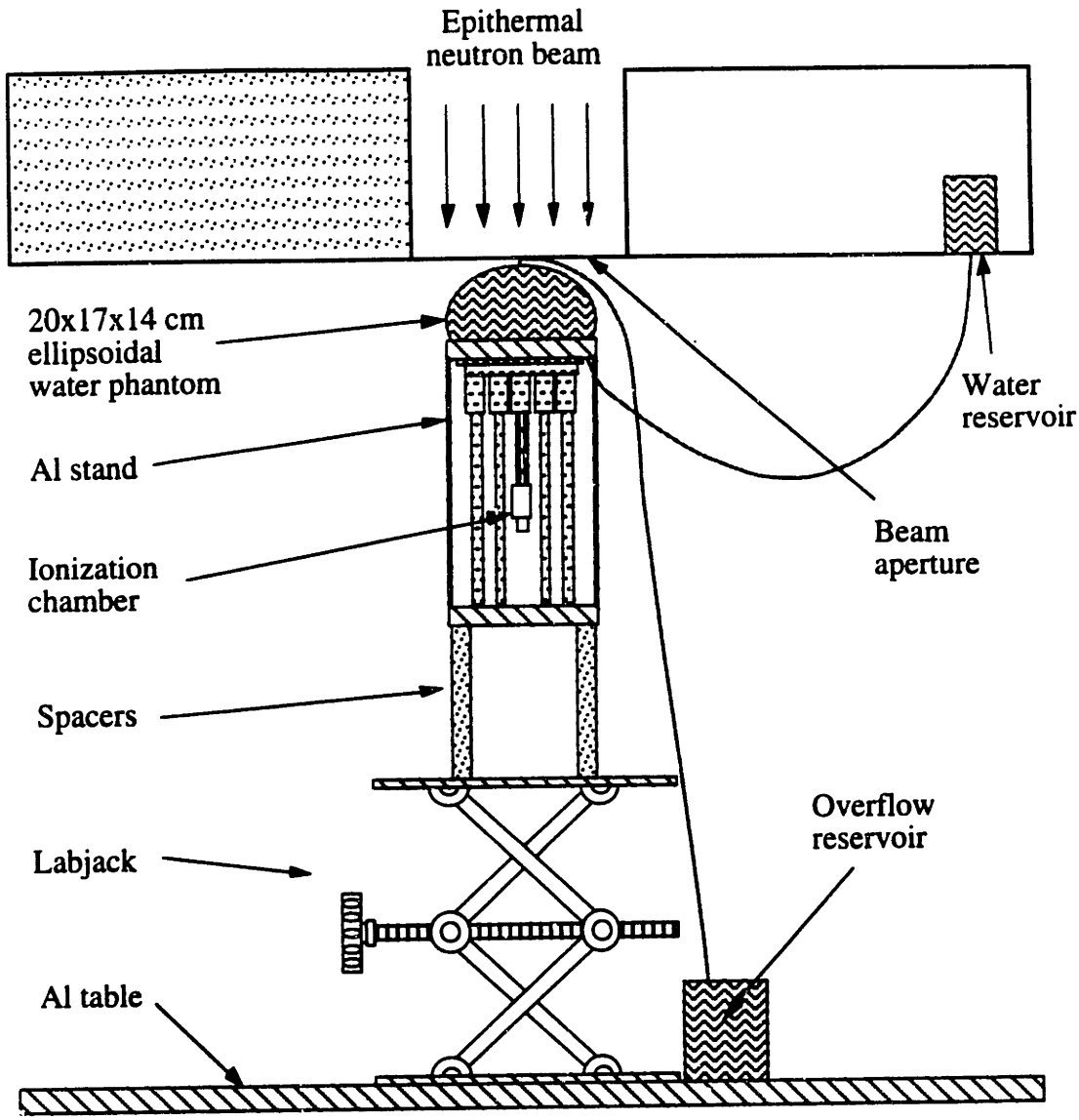

Figure 3.2. Experimental setup for positioning the head phantom in the beam. One of the ionization chambers is shown inserted into the center tube. Fiduciary marks on the bottom of the lead shutter or delimiter were used to position the phantom. The height of the phantom was adjusted with the labjack: the gap between the top of the phantom and the bottom of the shutter or delimiter was measured with a spacer bar.

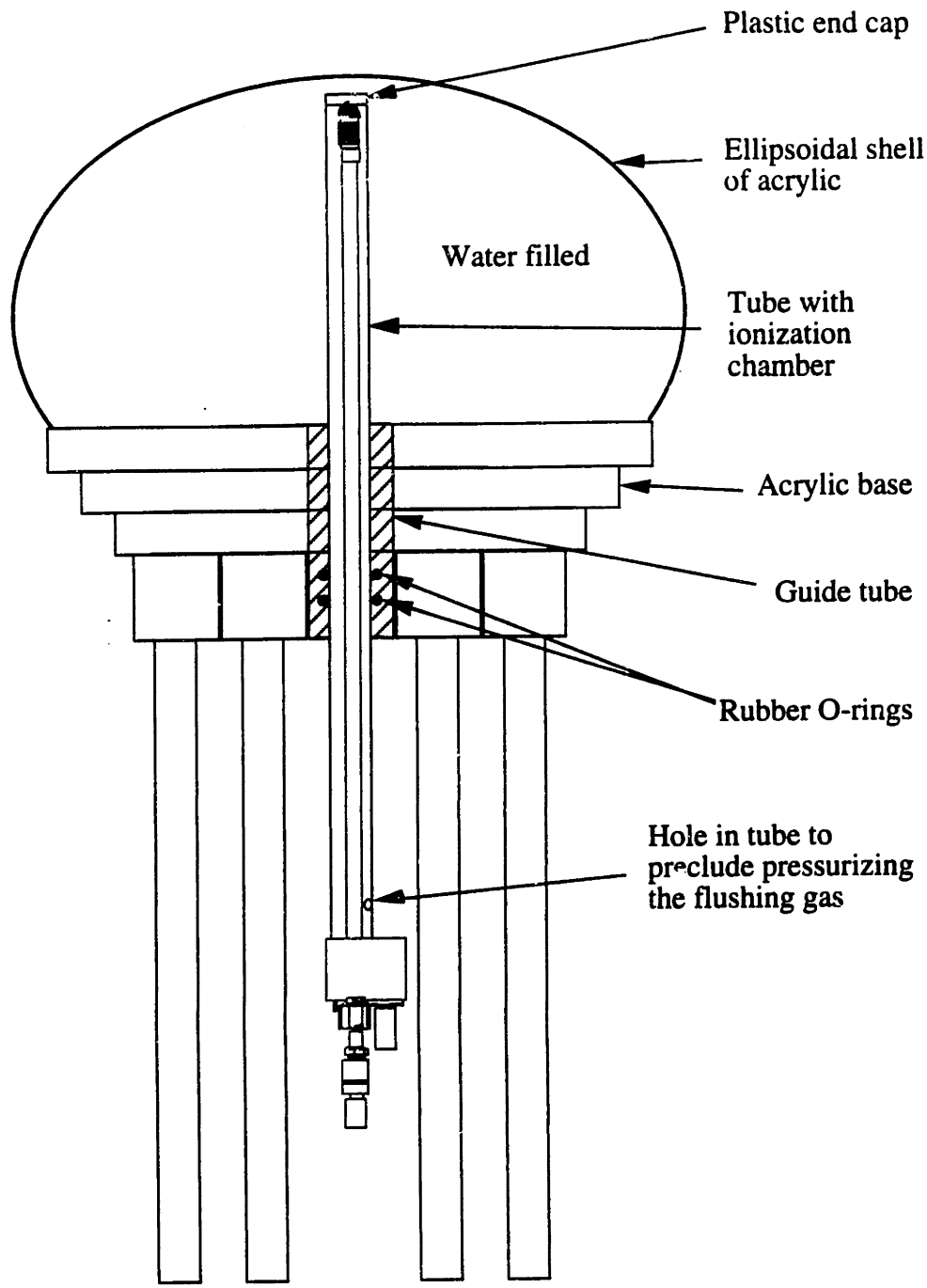

Figure 3.3. Close up of head phantom showing positioning of the ionization chamber in the center tube. When the chamber is snapped into the tube, the chamber's thimble is at the top of the tube. A hole in the bottom of the tube precludes pressurization.

layer of the phantom where measurements in phantom are difficult. Sufficient data have been collected to formulate general trends in the depth-dose shapes near the surface. The fast neutron and photon doses are also determined in air, without the phantom being present. The in air measurements are useful for beam comparisons, but do not accurately predict the relative performance at depth in tissue. Doses in air have also been measured at locations outside the main beam as well.

Reference compositions

The compositions of the phantoms were chosen so that the neutron and photon scattering and absorption interactions that occur within the phantom would be similar to those that would occur within a human head or the body. The compositions of brain, water, and a tissue equivalent liquid are shown in table 3.3. Also shown are the compositions of ICRU and ICRP muscle, A-150 tissue equivalent plastic, and tissue equivalent gas; these compositions will be referred to later in this chapter. The most important parameter for neutron transport is the hydrogen atom density. Hydrogen attenuates and thermalizes the incident epithermal neutron flux, and the thermal neutron capture reaction H-1(n,γ)H-2 induces a significant photon flux within the phantom. As shown in table 3.4, the hydrogen atom densities of water and brain agree to less than 1%; the hydrogen atom densities of Wax-130 and muscle agree within 4%. Photon transport is also important; the energy-absorption coefficients for water and brain are shown in table 3.4. Agreement is within 4 %. The energy-absorption coefficient of Wax-130 is not known; however, with its low effective Z it should be close to that of muscle.

Water is often used as the reference phantom material for neutron dosimetry in tissue.[3] The difference in doses measured in water and in tissue equivalent liquid of density 1.07 g/cm^3 is less than 1% for 2-12 cm depths in a deuterium-on-tritium beam (mean neutron energy about 15 MeV) or a 15 MeV deuteron-on-beryllium beam (mean

Table 3.3. Elemental compositions of reference materials.

Element	Ave. brain[8]	Water	ICRU muscle	ICRP muscle	Tissue equiv. liquid	A-150 plastic	Tissue equiv. gas
H	10.6	11.11	10.2	10.06	10.20	10.13	10.2
C	14.0		12.3	10.78	12.01	77.55	45.6
N	1.8		3.5	2.77	3.54	3.51	3.5
O	72.6	88.89	72.9	75.48	74.25	5.23	40.7
Other	1.0		1.1**	0.91		3.58 (Ca, F)	
Total	100.0	100.0	100.0	100.0	100.0	100.0	
Density (g/cm^3)		1.00		1.04		1.127	1.046E-3

* All values are in weight percent.

** From Na, Mg, P, S, K, and Ca.

Data for ICRU muscle, ICRP muscle, TE liquid, A-150 plastic, and TE gas have been extracted from several sources and are published in Attix,[2] Appendix B.3.

Table 3.4. Hydrogen densities and photon attenuation coefficients for brain, water, muscle, and Wax-130.

	Average brain	Water	ICRU muscle	Wax-130[6]
Density (g/cm^3)	1.047	1.00	1.04	0.842
H (weight percent)	10.6	11.1	10.2	13.15
H ($atoms/cm^3$)*	6.68 E22	6.69 E22	6.39 E22	6.61 E22
μ_{en} (cm^{-1}) at 1 MeV	0.0320	0.0309	0.0318	-
μ_{en}/ρ (cm^2/g) at 1 MeV	0.0306	0.0309	0.0306	-

* For comparison, the hydrogen density of a tissue equivalent liquid described by Goodman[9] is 6.57 E22 atoms/cm^3.

Note: The mass energy-absorption coefficients, μ_{en}/ρ, were taken from Attix,[2] Appendix D; the coefficients for brain and muscle were assumed to be equal to that of ICRU striated muscle.

neutron energy about 8 MeV). ICRU has recommended that water be used as the reference phantom material for this type of fast neutron dosimetry.[3]

In-Air Dosimetry

As already mentioned, the tissue equivalent and carbon graphite chambers are not adequately thick to provide charged particle equilibrium for photons above about 0.7 MeV. Without the buildup caps, then, the doses measured in-air and at the top of the phantom are only estimates. The method of dosimetry presented here excludes such interface effects.

After the buildup caps were made, the in-air measurements were made with the buildup caps. These in-air measurements are expected to be quite accurate. Charged particle equilibrium, however, still does not exist as many of the photons have energies well above that of Co-60. The correction for this is small. It is noted that these measured doses would be the doses under equilibrium conditions, not the doses that would be present in a small sample of tissue at that location or in the surface layer of a phantom or a patient. An extrapolation chamber could be used to obtain this information, if needed.

Calculations and assumptions

The dual chamber technique involves a calibration of the ionization chambers, several correction factors, a calculation of neutron to gamma sensitivity ratios, and some other parameters. With our method, the following calculations and assumptions are used to convert the ionization chamber currents into separate neutron and photon doses.

Equations for Dosimeter Response

The equations for the responses of the tissue equivalent and carbon graphite ionization chambers in a mixed neutron and photon field can be written[2]

$$\dot{Q}_{TE} = A_{TE}\,\dot{D}_{\gamma} + B_{TE}\,\dot{D}_{n} \qquad (3.1)$$

$$\dot{Q}_{CG} = A_{CG}\,\dot{D}_{\gamma} + B_{CG}\,\dot{D}_{n} \qquad (3.2)$$

where $\dot{Q}_{TE}$, $\dot{Q}_{CG}$ = the corrected currents of the tissue equivalent and carbon graphite ionization chambers due to the mixed field (C/min),

A_{TE}, A_{CG} = the responses of the tissue equivalent and carbon graphite chambers per unit of absorbed dose in the tissue of interest from photons (C/cGy),

B_{TE}, B_{CG} = the responses of the tissue equivalent and carbon graphite chambers per unit absorbed dose in the tissue of interest from neutrons (C/cGy),

$\dot{D}_{\gamma}$, $\dot{D}_{n}$ = the photon and neutron dose rates in the tissue if interest (cGy/min).

In this thesis, the tissues of interest are either brain or muscle. The corrections to the currents, as measured by the electrometer, are discussed later.

The responses of the two ionization chambers to neutrons and photons is different; therefore, the above two equations are independent and can be solved simultaneously for the separate neutron and photon doses. The solutions are

$$\dot{D}_{\gamma} = \frac{B_{TE}\,\dot{Q}_{CG} - B_{CG}\,\dot{Q}_{TE}}{B_{TE}\,A_{CG} - B_{CG}\,A_{TE}} \qquad (3.3)$$

$$\dot{D}_{n} = \frac{A_{TE}\,\dot{Q}_{CG} - A_{CG}\,\dot{Q}_{TE}}{A_{TE}\,B_{CG} - A_{CG}\,B_{TE}} \qquad (3.4)$$

The ratio B/A of a dosimeter is called the neutron to gamma sensitivity ratio. This ratio is the sensitivity of an ionization chamber to neutrons relative to its sensitivity to the radiation used for calibration. By convention, this sensitivity is referenced to the dose that would occur under charged particle equilibrium conditions in a small sphere of muscle tissue (generally 0.52 g/cm^2 in radius) centered at the dosimeter midpoint with the dosimeter absent. The units g/cm^2 arise since the radius (cm) has been multiplied by the density (g/cm^3) of the material. The sensitivities for brain in this thesis, however, are referenced not to muscle tissue but to brain. The nitrogen content of brain is about half that of muscle; therefore, the neutron dose in brain can be significantly less than that in muscle for thermal neutrons and for epithermal neutrons up to about 100 eV.

In equations 3.1 and 3.2, the values for A_{TE} and A_{CG} were determined by an exposure calibration with Co-60. The values for B_{TE} and B_{CG} could theoretically be determined by a neutron calibration, but this is done only rarely and was not done here. Instead, for the tissue equivalent chamber, the ratio B/A was determined by applying the Bragg-Gray relation, which was assumed to be valid for both neutron and photon irradiations. The B/A ratio for the carbon graphite chamber was taken from a previously published value for this chamber.[10] The B/A ratio for the carbon graphite chamber is consistent with other theoretically and experimentally determined values published in the literature. The B/A ratios for these chambers were multiplied by their A values to determine their B values. Finally, the values of $\dot{Q}_{TE}$ and $\dot{Q}_{CG}$ in equations 3.1 and 3.2 are not used directly. Several correction factors are applied first. The determination of the A and B values, and the correction factors for the currents, are discussed in more detail later.

Calibration of the Ionization Chambers

The values of A_{TE} and A_{CG} were determined by a Co-60 exposure calibration at an AAPM Accredited Dosimetry Calibration Laboratory. The chambers were calibrated

with the buildup caps. Ionic recombination during the calibrations was assumed to be negligible. During the calibration, the chambers were open to the air. Results of this calibration, and of the previous calibrations for these chambers, are shown in table 3.5. Calibration data sheets for the current calibration are provided in Appendix B.

In the actual dosimetry measurements the tissue equivalent chamber is flushed with tissue equivalent gas while the graphite chamber is flushed with CO_2; therefore, an air-to-gas calibration factor was needed for each chamber. This factor was determined experimentally. Each chamber was exposed to a Cs-137 beam, and the current measured while the chamber was open to the air and while being flushed with the appropriate gas. This gives the exposure calibrations with the appropriate gas. The flow rate of the gases used during these measurements was 20 cc/min, which is the same as that used during the actual dosimetric measurements. The experimentally determined current ratios ($\dot{Q}_{gas}$ / $\dot{Q}_{air}$) were 1.57 for the tissue equivalent chamber and 1.19 for the carbon graphite chamber. The theoretical ratios are calculated as 1.57 and 1.17, respectively.

A Procedure, PM 3.14.2.6 Calibration and Stability Check of Ionization Chambers and Electrometers, has been written which provides a standard method for checking the calibration and stability of the ionization chambers (refer to Chapter 5.6). This Procedure is attached in Appendix D. In the Procedure, each ionization chamber is exposed to a Cs-137 at a fixed distance using a positioning jig. The exposure rates are measured and compared with previously measured exposure rates to assure that the calibration has not changed.

Calibration of the Keithley 617 Electrometer

The Keithley 617 electrometer was also calibrated at an AAPM Accredited Dosimetry Calibration Laboratory (University of Wisconsin). It was calibrated in a range about 1E-10 C, which is typical of the amount of charge collected during the actual measurements with the epithermal beams. Calibration data sheets for the this calibration

Table 3.5. Calibration data for the ionization chambers.

Model	Wall material	Calibrated by	Date	Air calibration (R/C)	Gas calibration (R/C)	Ratio of air to gas calibration
SN-131-TG	TE	Far West	1975	2.19 E 10	1.93 E 10	1.135
		Far West	1981	2.5 E 10	2.18 E 10	1.147
		Zamenhof/ Choi	1989	2.58 E 10	(2.22 E 10) (a)	1.162
		AAPM Cal Lab, U of Wisconsin	1993	2.538 E 10	2.127 E 10 (b)	1.193 (c)
I32-CG	CG	Far West	1975	1.94 E 10	1.33 E 10	1.459
		Far West	1981	1.96 E 10	1.25 E 10	1.568
		Far West	1988	2.23 E10		
		Zamenhof/ Choi	1989	2.17 E 10	(1.36 E 10) (a)	1.596
		AAPM Cal Lab, U of Wisconsin	1993	2.128 E 10	1.358 E 10 (b)	1.567 (c)

(a) During this calibration the chambers were open to the air. The gas exposure calibration was estimated from the air calibration.
(b) These gas calibration constants were determined from the air calibration constants and the ratio of air to gas calibrations as determined experimentally.
(c) These ratios were determined experimentally by measuring the exposure rates at the Cs-137 source with the chambers open to the air and with the appropriate flushing gas at a flow rate of 20 c/min. The theoretical ratios are 1.17 for the TE/TE chamber and 1.57 for the CG/CO_2 chamber, at low flow rates.

Notes: 1. "Air calibration" means that the exposure calibration constants were determined with the chambers open to the air. "Gas calibration" means the exposure calibration constants with the tissue equivalent chambers flushed with methane based tissue equivalent gas, and the carbon graphite chambers flushed with CO_2. Gas flow rates were 5 cc/min for the Far West calibrations. 2. Buildup caps were used in all the calibrations. 3. The calibration irradiation facilities had exposure calibrations that were traceable to a Standards Laboratory. 4. The calibrations are referenced to 22 °C and 760 mm Hg.

are provided in Appendix B. The Procedure 3.14.2.6 discussed above also provides a check on the calibration of the electrometer. Details can be found in the Procedure. A separate Procedure, PM 3.14.2.5 Cross-Calibration of Electrometers, has also been written and is provided in Appendix D. This Procedure provides a standard method for calibrating the Keithley 616 electrometer against the Keithley 617 electrometer. The Keithley 616 electrometer, then, could be used as the field instrument. The Keithley 617 was stored in a cabinet and was used only in the dosimetry of the most important beams. The beam that will be used clinically (M67) was characterized with the Keithley 617.

Exposure to Dose Conversion

The exposure calibration constants were converted to dose calibration constants. The absorbed dose at the center of an equilibrium sphere of tissue, 0.52 g/cm^2 in radius, from a free space exposure X is:[2]

$$D = 0.873\ \beta\ A_c\ X\ (\mu_{en} / \rho)_{air}^{tissue} \qquad (3.5)$$

where
- D = dose in brain or muscle (cGy),
- β = transient charged particle equilibrium constant,
- A_c = effective displacement correction factor,
- X = exposure (R),
- $(\mu_{en} / \rho)_{air}^{tissue}$ = mass energy-absorption coefficient for tissue divided by the mass energy-absorption coefficient for air.

The transient charged particle equilibrium constant, β, accounts for the fact that the dose at depth in a phantom caused by incident neutrons and photons is actually slightly higher than the collision kerma at the same depth. The effective displacement factor, A_c, accounts for the fact that the positioning the ionization chamber in the phantom

actually requires removing some phantom material that would normally be there. β is close to 1.004 ($\beta_{tis} \approx \beta_{brain} \approx \beta_{muscle}$) and A_c for these chambers is approximately 0.99. It was assumed that the mass energy-absorption coefficient of brain is equal to that of muscle tissue. The tissue-to-air mass energy-absorption coefficient is energy dependent. It is believed that in our therapy beam most of the photons penetrating the head are prompt gammas from lead (7.4 MeV + continuum), bismuth (4.1 MeV + continuum), and hydrogen (2.2 MeV), as well as gammas from inelastic scattering (several MeV). For photons in this energy range, the tissue-to-air ratio is about 1.10.[2]

Neutron to Gamma Sensitivity Ratio of the Tissue Equivalent Chamber

An equation for the neutron to gamma sensitivity ratio of the tissue equivalent chamber, derived by an application of the Bragg-Gray relation, has been presented by Attix.[2] The derivation is carried out for a particular photon and neutron energy. The sensitivity ratio is strongly dependent on the neutron energy, and an effective value is best obtained by appropriate weighting over the differential neutron spectrum.

If $(Q_\gamma)_{TE}$ is the charge produced in the tissue equivalent ionization chamber when it is given the same photon irradiation that deposits D_γ (cGy) in a small equilibrium sphere of tissue then

$$A_{TE} \equiv \frac{(Q_\gamma)_{TE}}{D_\gamma} \qquad (C/cGy) \qquad (3.6)$$

This value is just the inverse of the brain or muscle dose calibration constant. The value is the same for brain or muscle since it was assumed that they have the same mass energy-absorption coefficients. Under transient charged particle equilibrium and conditions in which the Bragg-Gray relation is valid, Attix has derived an equation for the neutron to gamma sensitivity ratio. The result is:

$$\left(\frac{B}{A}\right)_{TE,i} = \frac{(F_n)_i^{TE}}{\left(\frac{\mu_{en}}{\rho}\right)_i^{TE}} \frac{(\overline{W}_\gamma/e)_g\,(\overline{S_\gamma/\rho})_g^{TE}}{(\overline{W}_n/e)_g\,(\overline{S_n/\rho})_g^{TE}} \qquad i = \text{brain, muscle} \qquad (3.7)$$

where $(F_n)_i^{TE}$ = neutron kerma factor ratio of tissue equivalent plastic to tissue i,

$\left(\frac{\mu_{en}}{\rho}\right)_i^{TE}$ = mass energy-absorption coefficient ratio of A-150 tissue equivalent plastic to tissue i,

$(\overline{W}_\gamma/e)_g$ = value of $\overline{W}/e$, the average energy needed to produce an ion pair, for photons in tissue equivalent gas (29.3 J/C),

$(\overline{W}_n/e)_g$ = value of $\overline{W}/e$ for neutrons in tissue equivalent gas,

$(\overline{S_\gamma/\rho})_g^{TE}$ = mass collision stopping power ratio of tissue equivalent plastic to tissue equivalent gas for electrons,

$(\overline{S_n/\rho})_g^{TE}$ = mass collision stopping power ratio of tissue equivalent plastic to tissue equivalent gas for neutron secondaries.

In this equation, the dependence of the sensitivity ratio on the tissue of interest (brain or muscle) is written explicitly. The mass energy-absorption coefficient ratio is effectively the same for brain and muscle. The kerma factor ratio, however, is significantly different for muscle and brain. The sensitivity ratio is weakly dependent on the photon energy. It is moderately dependent on the neutron energy for brain, however, since there is a nitrogen mismatch between brain and A-150 plastic, and the nitrogen kerma becomes significant at lower neutron energies. As well, the sensitivity ratio changes with neutron energy since $(\overline{W}_n/e)_g$ increases rapidly as the neutron energy drops below about 20 keV.

The compositions of tissue equivalent gas and A-150 plastic are so similar (table 3.3) that the neutron and photon ratios of the mass collision stopping powers are both close to unity.[2] For 0.01 - 10 MeV neutrons, more than 90% of the kerma is attributable to H. Also, the weight percentage of hydrogen in tissue equivalent gas and A-150 plastic differ by only 0.7%. The carbon and oxygen percentages are very different. However, their elemental kermas are not very different, and they contribute less than 10% of the dose. The ratio of the neutron mass collision stopping powers, therefore, was assumed to be 1.0. The photon mass collision stopping power is Z dependent. The effective Z's, however, are similar and so the ratio of the electron stopping powers was assumed to be 1.0.

The ratio of the mass energy-absorption coefficients of the tissue equivalent material to brain is also nearly unity. While the compositions of carbon and oxygen are considerably different, their mass energy-absorption coefficients are within several percent for photon energies between 0.2 and 8 MeV.

Equation 7 then simplifies to

$$\left(\frac{B}{A}\right)_{TE,i} = \left(F_n\right)_i^{TE} \frac{(\overline{W}_\gamma/e)_g}{(\overline{W}_n/e)_g} \tag{3.8}$$

The neutron kerma factors, or their ratios, have been tabulated as a function of neutron energy for several elements and mixtures.[11] We determined the kerma factors for A-150 plastic, average brain, and ICRU muscle from their elemental compositions. These energy dependent kerma factors are shown in figure 3.4. For a differential neutron spectrum, the average kerma is obtained by integrating over the spectrum.

The reciprocal of the $\overline{W}$ ratio in equation 3.8 has been computed by Goodman as a function of neutron energy over the range 0.1 - 20 MeV.[12] These data are shown in figure 3.5. Charged particle spectra were calculated theoretically for a methane based

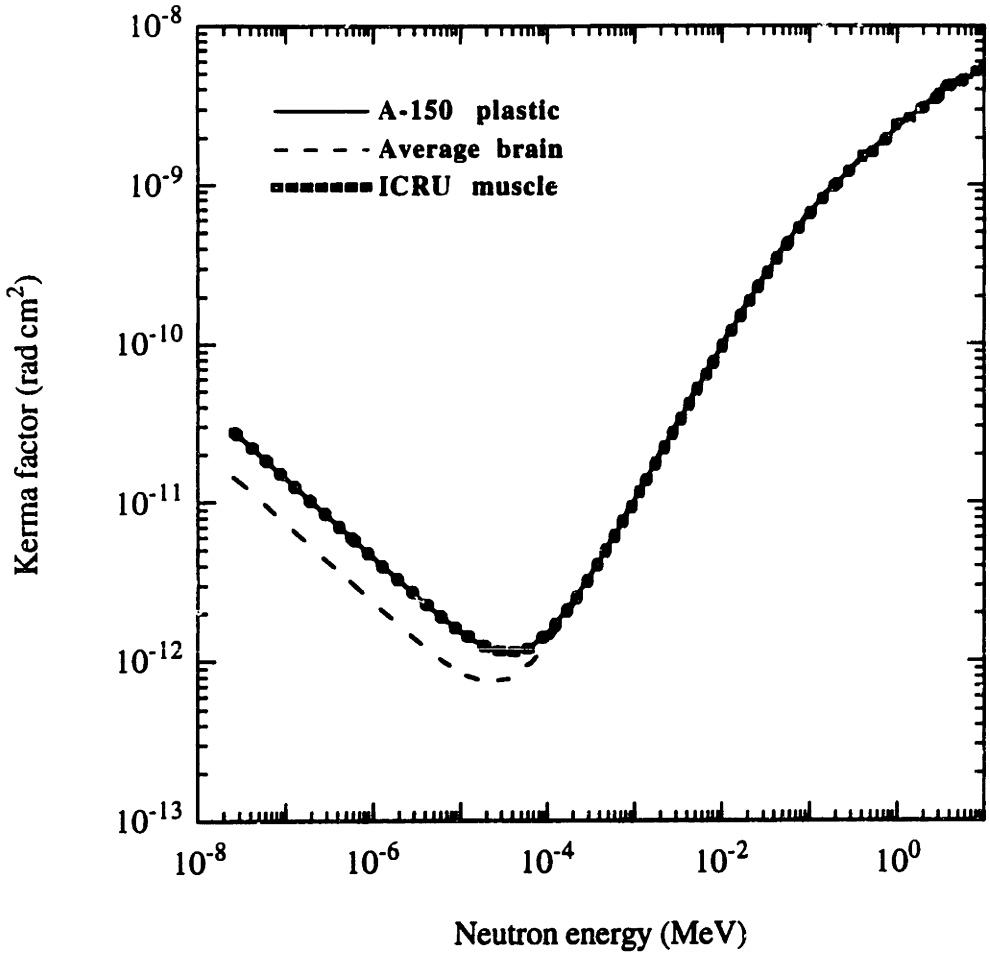

Figure 3.4. The energy dependent kerma factors for A-150 plastic, average brain, and ICRU muscle. There is a near perfect match between A-150 plastic and ICRU muscle. From thermal energies to 100 eV, average brain has a lower kerma than A-150 plastic because average brain has a lower nitrogen content.

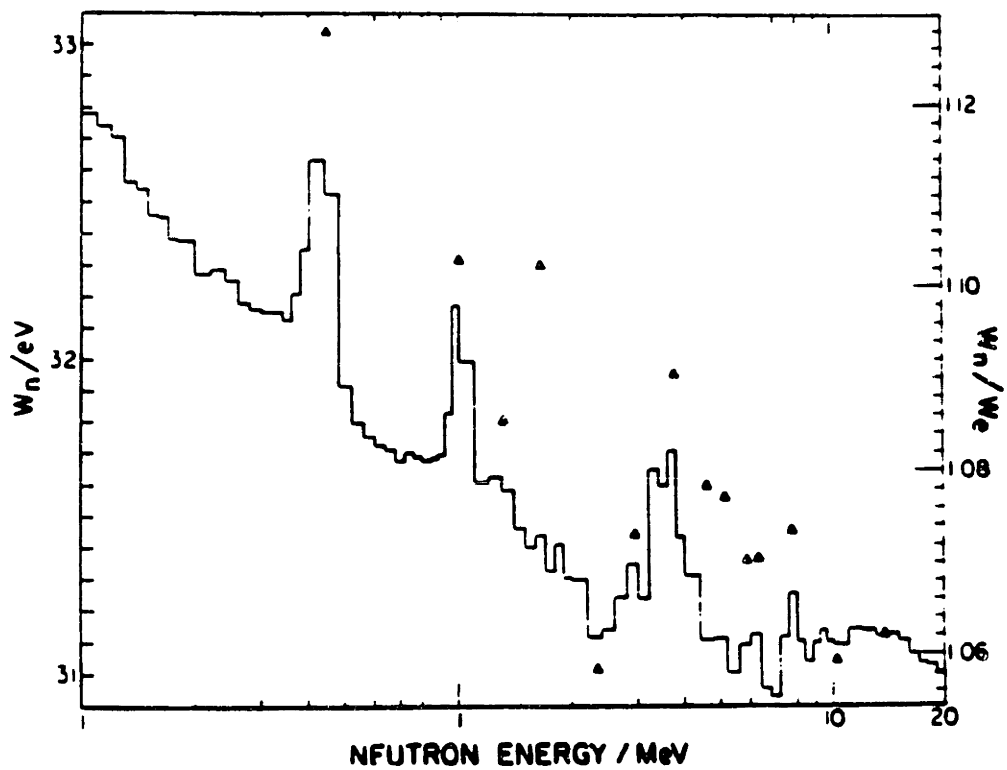

Figure 3.5. $\overline{W}_n$ and $\overline{W}_n/\overline{W}_\gamma$ for tissue equivalent gas. The solid line is for an energy bin average. The triangles are point values at resonances or minimums. From Goodman.[12]

tissue equivalent gas mixture and the relative kermas contributed by the various types of charged particles were determined. Then these spectra were combined with an evaluation of available experimental data on $\overline{W}$ for the secondaries to compute $\overline{W}_n$ as a function of neutron energy. In the 0.1 - 10 MeV energy range, the ratio $\overline{W}_n/\overline{W}_\gamma$ increases about 3% per energy decade.

$\overline{W}_p$ for hydrogen has been measured in the range 3.7 to 48 keV per atom by Leonard.[13] These data, along with other researcher's data, are shown in figure 3.6. In Leonard's work, H^+ and H_2^+ ions were accelerated and then allowed to enter an ionization chamber through a differentially pumped aperture. The chamber was filled with a tissue equivalent gas mixture. A large increase in $\overline{W}_p$ is seen for energies below 20 keV and it appears that $\overline{W}_p$ becomes infinite as the hydrogen energies approach 1 keV. Leonard proposed that as the velocity of the ions becomes comparable to or less than the velocity of the electron in the first Bohr orbit of hydrogen, an increased amount of energy is deposited by elastic coulomb collisions with the atoms as a whole. This means that no current would be collected for recoil protons that have energies less than 1 keV. This information is also important in assessing the biological damage caused by lower energy neutrons (< 1 keV).

For epithermal neutron beam dosimetry, the neutron sensitivity factor should be averaged over the neutron spectrum, which extends from epicadmium energies up to 15 MeV. Later it will be shown that the thermal neutron response of the chambers is subtracted out. This requires a large extrapolation of the Goodman $\overline{W}$ data or use of the Leonard data.

For neutron spectra typical of fast neutron therapy applications, a value $\overline{W}_n/\overline{W}_c = 1.06 \pm 0.02$ was recommended by Goodman.[12] $\overline{W}_c$ refers to the $\overline{W}$ value for the photon energy of the calibration field. The European protocol for fast neutron therapy also recommends a value of 1.06.[3] A value of 1.05 was recommended in ICRU Report #26.[14] If no spectral information is available, ICRU Report #45 recommends a value of

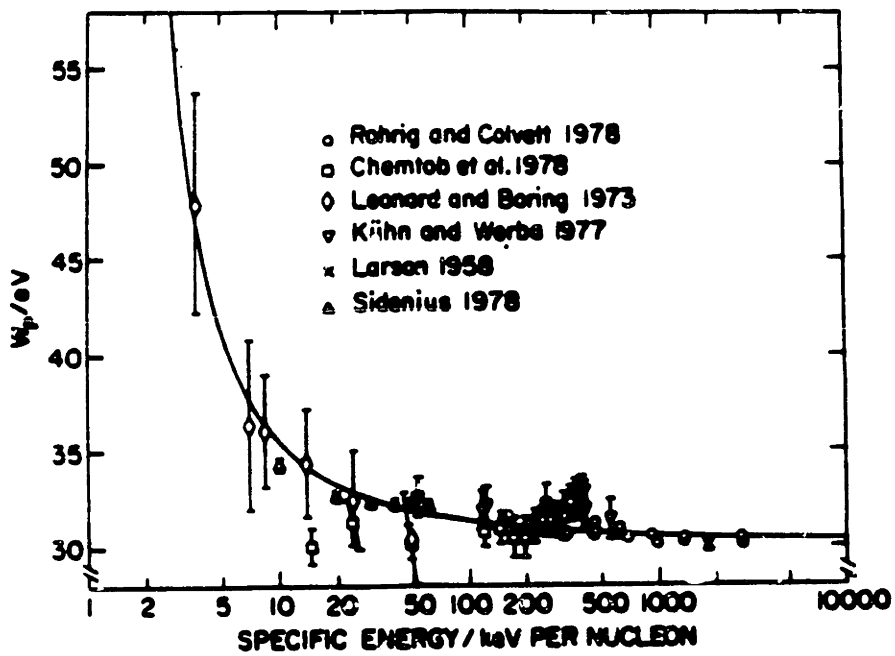

Figure 3.6. $\overline{W}_p$ for tissue equivalent gas as determined by several investigators, including the low energy data of Leonard. From Goodman.[12]

1.06 ± 0.02, for spectra typical of therapy applications.[3] These recommended values are for neutron beams that are generally in the 1 to 20 MeV range.

$(B/A)_{TE}$ for brain and muscle as a function of neutron energy are shown in figures 3.7 and 3.8. In each figure, one curve was calculated using the data of Goodman and an extrapolation of those data. The other curve was calculated using an empirical fit to the data of Leonard and others as provided by Goodman. For the neutron sensitivity factor curve obtained with the Goodman data, the increase in $(B/A)_{TE}$ for brain at lower energies is a result of the nitrogen kerma mismatch between the A-150 plastic and brain. A-150 plastic has about twice the amount of nitrogen as brain and so over responds in the lower energy range where the nitrogen kerma increases to a significant level. For the neutron sensitivity factor curves obtained with the Leonard data, the sensitivity factor drops rapidly as the neutron energy drops below 20 keV. This is due to the rapid increase in $\overline{W}_p$. For muscle, $(B/A)_{TE}$ obtained with the Goodman data declines steadily because of the assumed linear increase in the $\overline{W}_n/\overline{W}_\gamma$ ratio.

The values for $(B/A)_{TE,i}$ used in our dosimetry protocol are 0.92 for brain and 0.95 for muscle. These numbers were obtained by averaging the $(B/A)_{TE,i}$ over the range 0.1 to 10 MeV. Obtaining some spectral information about the beam would reduce the uncertainty in the $(B/A)_{TE}$ values. Their uncertainties must be kept in mind and additional information in the future (such as spectral data and $\overline{W}$ ratios in the lower energy range) can be used to determine an improved value.

Neutron to Gamma Sensitivity Ratio of the Carbon Graphite Chamber

If $(Q_\gamma)_{CG}$ is the charge produced in the carbon graphite ionization chamber when it is given the same photon irradiation that deposits D_γ (cGy) in a small equilibrium sphere of tissue, then

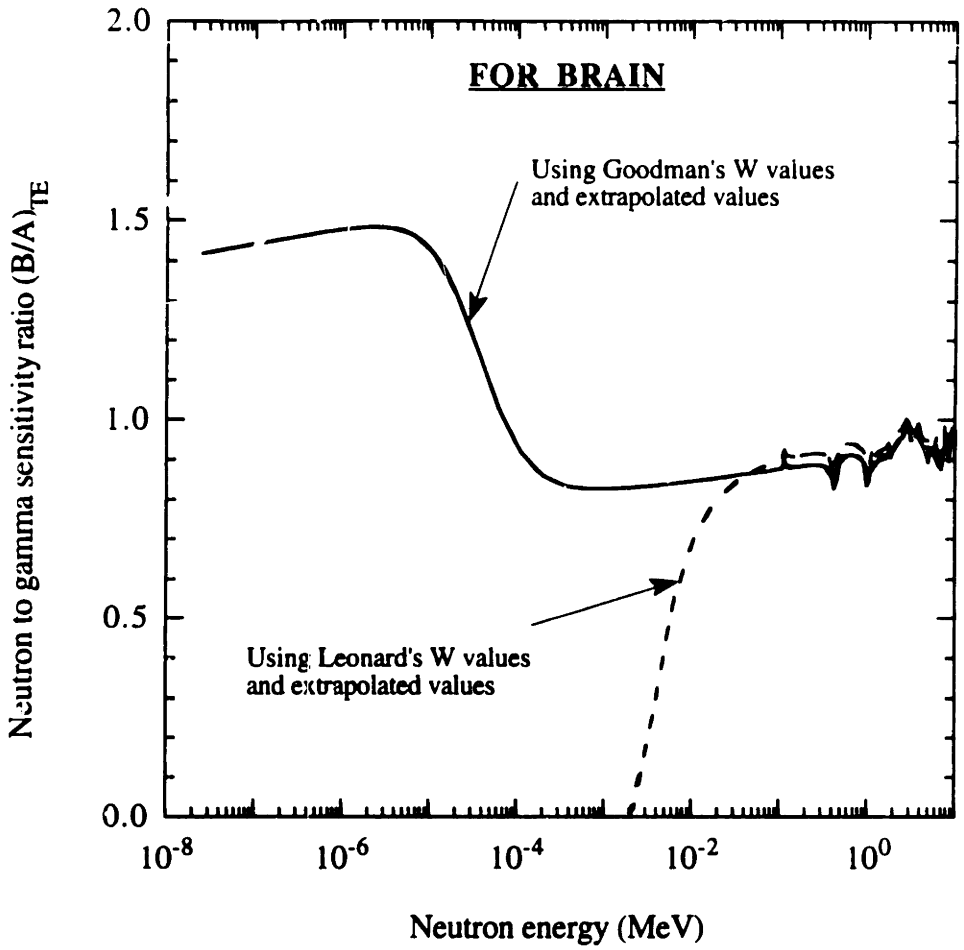

Figure 3.7. The neutron to gamma sensitivity ratio for brain and the tissue equivalent chamber as a function of neutron energy. The rise in the sensitivity factor below 100 eV (using Goodman's W values) is a result of the mismatch between the nitrogen contents of brain and A-150 plastic. The drop in the sensitivity factor below 20 keV (using Leonard's W values) is a result of a rapidly rising W_p.

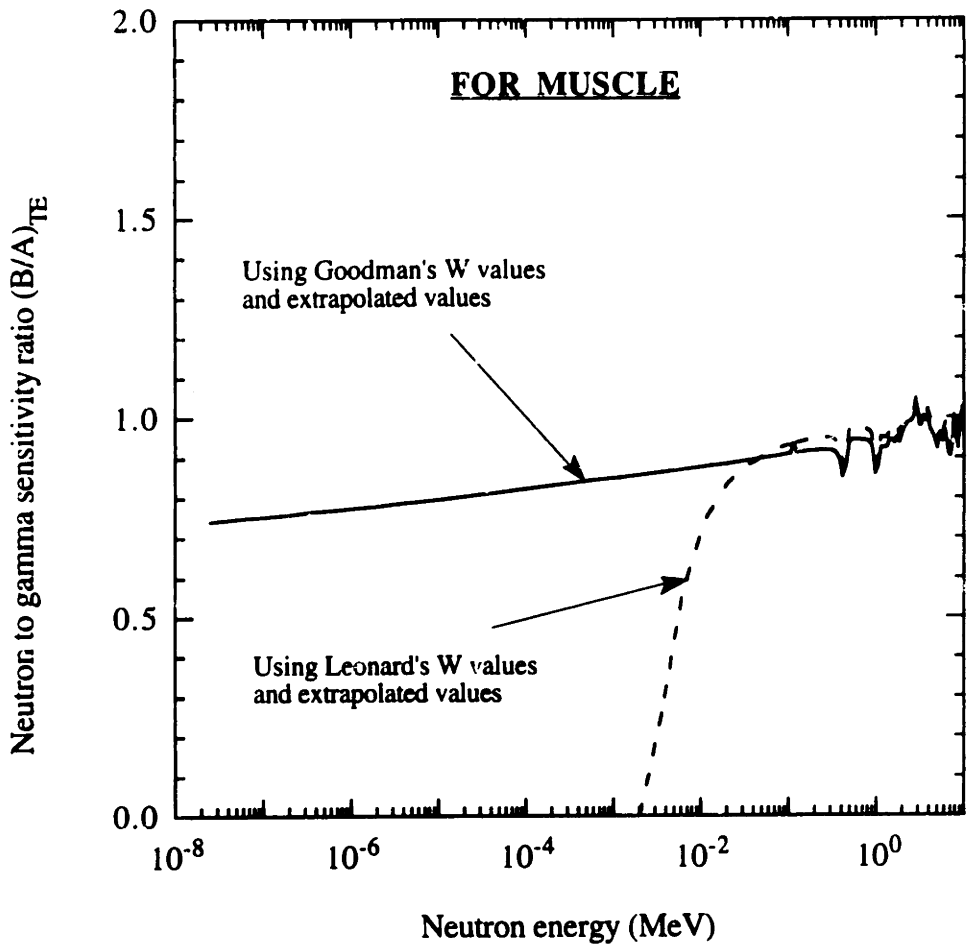

Figure 3.8. Same as figure x, but for muscle. With the close match between muscle and A-150 plastic, the sensitivity ratio (using Goodman's W values) declines steadily with decreasing neutron energy because of the assumed linear increase in the $\overline{W}_n/\overline{W}_\gamma$ ratio. The drop in the sensitivity factor below 20 keV (using Leonard's W values) is a result of a rapidly rising W_p, as was seen previously with brain.

$$A_{CG} \equiv \frac{(Q_\gamma)_{CG}}{D_\gamma} \qquad (C/cGy) \qquad (3.9)$$

As with the tissue equivalent chamber, A_{CG} is just the inverse of the dose calibration constant. Again following Attix,[2] the equation corresponding to equation 3.7 could be used to calcul..te B/A for the carbon graphite chamber. However, this result would be expected to be less accurate than determining this ratio experimentally using the narrow beam lead filtration method (provided that the spectrum of the calibration source matched the spectrum of the radiation field in which the dose is to be measured).

The neutron sensitivities of various graphite chambers filled with CO_2 have been calculated theoretically and measured experimentally by several investigators.[14] The sensitivities are smooth functions of energy in the 0-10 MeV range, ranging from about 0.03 at 0.5 MeV to 0.12 at 10 MeV. The actual value for our beams is uncertain, but it is not critical to know this number accurately. An error analysis on the sensitivity of the calculated doses to the selected neutron sensitivity of the carbon graphite chamber is provided in reference 14. A value of 0.044 is used, based on a spectral analysis of a largely thermal neutron beam used by Ashtari.[10] She spectrum weighted this value (but excluded the thermal part of the spectrum) and her thermal beam spectra were probably significantly different from those of the epithermal beams considered here. The actual value for our epithermal neutron beams might be somewhat higher.

The neutron spectrum changes throughout the phantom. Therefore, the values of B/A for both chambers depend on position within the phantom. This effect was not accounted for. Spectrum effects such as these are also not accounted for in fast neutron therapy dosimetry protocols. The magnitude of this effect could be estimated by measuring or calculating the neutron spectrum at several depths within the phantom and

then calculating the spectrum weighted values of B/A. The photon and fast neutron doses, however, are probably affected by less than 10%.

Returning to equations 3.3 and 3.4, the four constants (A_{TE}, B_{TE}, A_{CG}, and B_{CG}) are obtained as discussed above. The ionization chamber currents are measured experimentally. However, some corrections to these currents are needed before they are used in these equations.

Temperature and Pressure Corrections

The mass of gas in the sensitive volume of the chamber depends on the temperature and pressure; therefore, the chamber currents are corrected to standard conditions. The following equation is used:

$$f_{T,P} = \frac{T + 273°}{22° + 273°} \frac{29.92}{P} \qquad (3.10)$$

where $f_{T,P}$ = correction factor for temperature and pressure,

T = the temperature of the gas in the sensitive volume of the chamber (C),

P = pressure of the gas in the sensitive volume of the chamber (inches of Hg).

No correction was made for the relative humidity; this correction is less than 0.3% (32). The barometric pressure is measured by a barometer in the control room. The pressure drop across the containment is negligible. The temperature is measured with a thermometer. This correction factor, $f_{T,P}$, is multiplied by the ionization chamber current as measured by the electrometer to obtain the current corrected for pressure and temperature. Temperature corrections have been less than 1%; pressure corrections about 1%.

Flow Rate of Chamber Gas

The gas flow rate affects the pressure within the sensitive volume of the chamber. Increasing the flow rate increases the chamber pressure; this results in higher currents as shown in figure 3.9. The gas flow rate was determined to have a large effect on the calculated doses, especially the fast neutron dose. The flow rate, therefore, is carefully controlled and monitored (20 ± 2 cc/min).

Previously, the chambers were calibrated either in air or with a gas flow rate of 5 cc/min (Far West calibrations). Therefore, a correction factor, f_{flow}, was applied to the experimental data which is obtained at 20 cc/min. As shown in figure 3.9, the correction factor for the tissue equivalent chamber is 1/1.02 = 0.98. The correction factor for the carbon graphite chamber is 1/1.007 = 0.993.

In the most recent calibrations at the University of Wisconsin Accredited Dosimetry Calibration Laboratory, the chambers were calibrated in air. The calibrations in the appropriate flushing gases were determined experimentally, at a flow rate of 20 cc/min, as discussed previously. The f_{flow} factor, then, is not needed as it is already incorporated into the method used to determined the calibrations with the appropriate flushing gas. The flow rate during the characterization of the beams was 20 cc/min.

Power History Correction Factor

In conventional radiation therapy, the fast neutron or photon sources are designed to have a known intensity and energy distribution. When reactors are the neutron source, the intensity and energy distribution of the neutrons and photons may change somewhat depending on the current operating conditions of the reactor. These changes in the source may be caused by changing xenon concentrations in core and by the positioning of the control rods, as well as by buildup of gamma emitting radionuclides produced by radiative capture reactions. For our reactor's epithermal neutron beam, the variation in

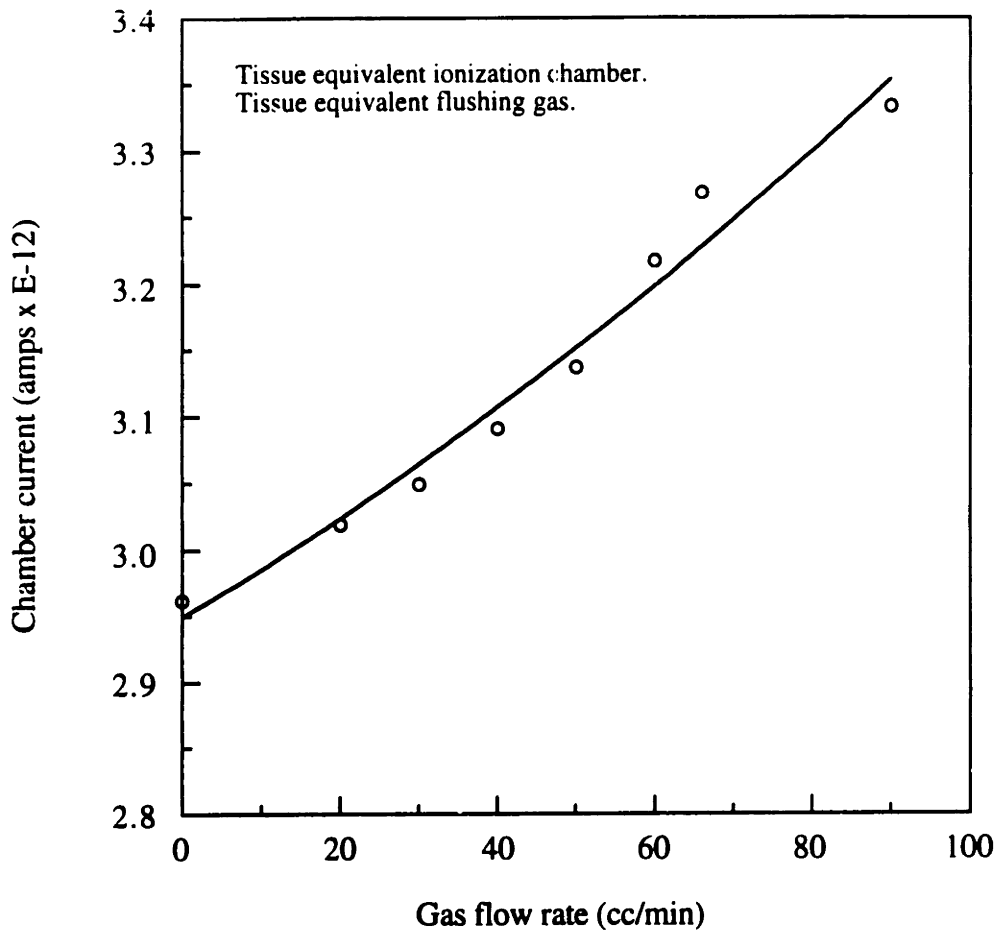

Figure 3.9. The ionization chamber current increases with the flow rate of the flushing gas. Higher flow rates apparently increase the pressure within the sensitive volume of the chamber. In this study, a flow rate of 20 cc/min was used, which gives 2% more current than using the tissue equivalent gas at a very low flow rate. A similar curve was obtained experimentally with the carbon graphite chamber flushed with CO_2. A 0.7% increase was seen in this case.

the source has up to a 10% [1] affect on the delivered dose components; corrections can be applied to the measured doses if the variation in the incident radiation fields is measured. Measurements taken with the two chambers should be taken at nearly the same time so the neutron and photon fields are the same for both detectors.

The power history correction factor, f_{hist}, accounts for the change in chamber currents as a function of time after reactor startup. For one beam, these factors were determined by Choi.[1] He followed the outputs of two radiation detectors, a fission chamber that was surrounded by a shield of Li-6 carbonate that was black to thermal neutrons, and a tissue equivalent ionization chamber positioned at a 1 cm depth in an ellipsoidal water phantom, over a period of two weeks. He found that for a given reactor power, the neutron dose rate falls about 5% over a few day period, while the gamma dose rate first rapidly increases by about 5% then drops about 7% over the next few days. Using the uncorrected currents from measurements taken over a several day period, the fast neutron dose was underestimated by about a factor of two.

Although beam-specific, the power history correction factors have been used for other beams as well. These factors are useful, but do have limits. They would be expected to change with position in the phantom, are not directly applicable to in-air measurements, and were not obtained with the two chambers themselves.

Currently, an attempt is made to take ionization chamber measurements under steady-state conditions. Then the power history correction factors for both chambers are equal to 1. A check of the steady-state condition is made for the more important dosimetric measurements. After one of the chambers has been used to measure the currents at various positions within a phantom, a process that takes about 5 hours, the chamber is returned to the first position and the current re-measured. If the reactor has been under near steady-state conditions, these currents have been found to repeat within 1%. A repeat measurement is also made with the other chamber.

Thermal Neutron Response of the Chambers

When high energy neutrons thermalize in tissue, the thermal neutrons can be absorbed by N-14. The reaction is N-14(n,p)C-14, and E_p = 0.58 MeV. Kinetic energy carried off by the proton and C-14 adds to the dose. In clinical fast neutron radiotherapy and in most neutron radiobiological experiments, the fast neutron dose is enormous relative to the N-14 dose. The response of the tissue equivalent ionization chamber from the N-14 reaction, therefore, is negligible. In BNCT, an effort is made to reduce the fast neutron dose to a low level. Under these circumstances, the response of the tissue equivalent ionization chamber from the thermal neutrons might be up to 10% of the total response. It is desirable to subtract the current caused by thermal neutrons from the total current, first, because there is a significant nitrogen kerma mismatch between A-150 plastic and brain, and second. because the neutron spectrum, particularly the thermal flux, changes rapidly throughout the phantom.

The thermal response of both chambers has been experimentally determined by Ashtari.[10] We extracted the data from table 9.9 of that reference, columns 3 and 6, and averaged the thermal responses calculated with the D_2O shutter open and closed. These averaged values are 1.50 E -20 (C/min)/(n/cm^2-sec) for the carbon graphite chamber and 4.77 E -20 (C/min)/(n/cm^2-sec) for the tissue equivalent chamber.

A quick and easy experiment was designed and carried out so that we could get our own rough estimate of the thermal flux response. The experimental set up is shown in figure 3.10. The currents of the chambers were measured with and without a thin bag of Li-6 carbonate surrounding the thimble of the chamber. The chambers were positioned side by side in air just below the collimator of the M62 beam. Three discs, each 17.8 cm diameter by 0.63 cm thick, were positioned on top of one another below the bismuth so that the bottom piece was flush with the bottom of the collimator. The sensitive volumes of the chambers were 2 cm below the bottom of the collimator. The currents were measured. Then, a small bag of Li-6 carbonate was placed over the thimbles of the

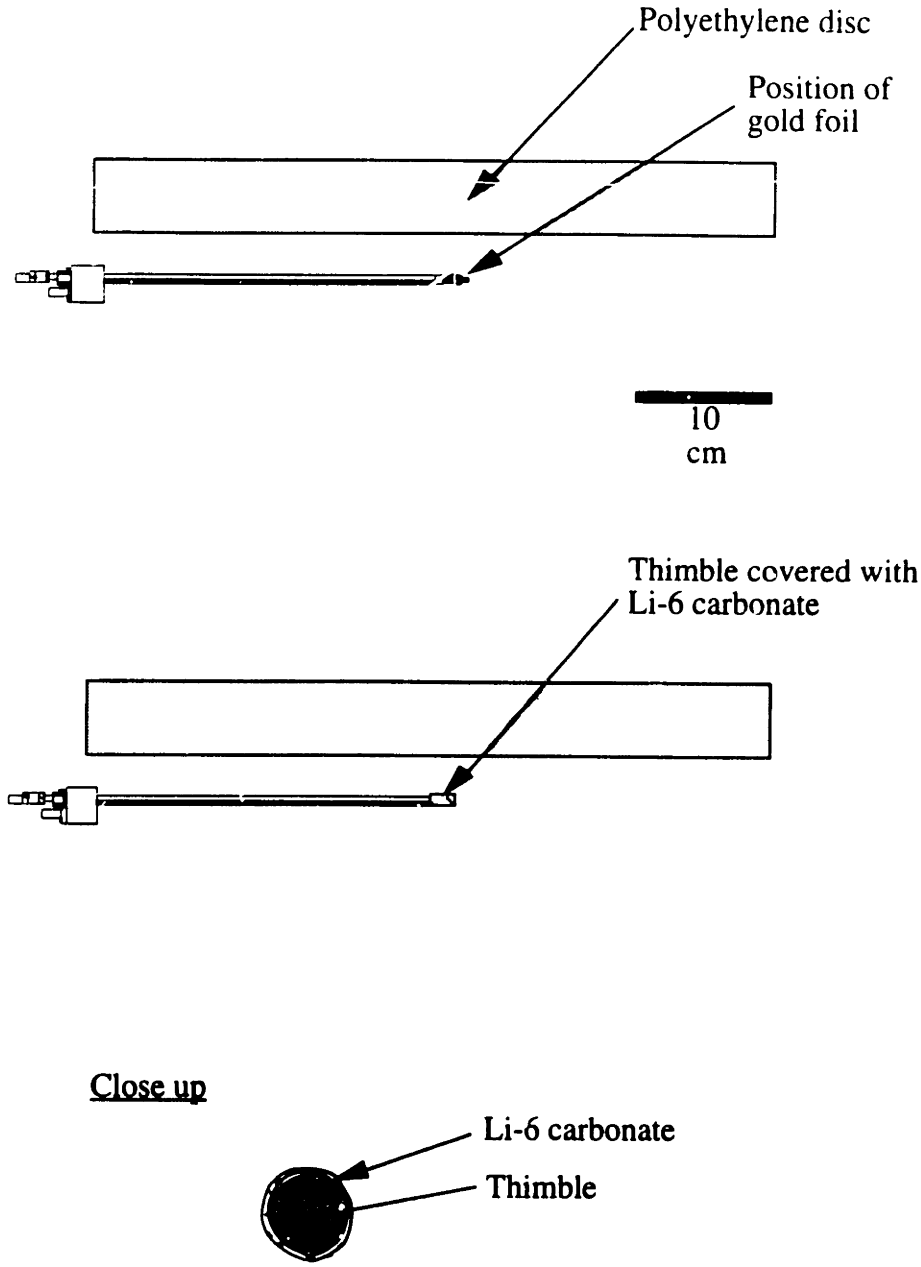

Figure 3.10. Setup for experimentally determining the thermal neutron response of the ionization chambers. The polyethylene disc was used to increase the thermal flux. The current of the chamber was measured with and without the Li-6 carbonate cover, which was black to thermal neutrons.

chambers. The bag was thin plastic, about 0.002" thick, and the Li-6 carbonate was 2.1 mm thick. This thickness would be expected to reduce the thermal flux by a factor of 25. This amount of Li-6 carbonate also causes a slight attenuation of the photon and fast neutron doses as seen by the chambers. About 2% of 1 MeV neutrons would scatter; however, most of this scattering is off oxygen with little reduction in neutron energy. Fast neutron attenuation, therefore, was assumed to be negligible. Attenuation of 2 MeV photons was estimated at 0.6%; this effect would be expected to reduce the current of the graphite chamber by 0.48%. Only a 0.36% reduction would be expected for the tissue equivalent chamber since, in this experiment, the gamma component of the dose was 70% of the total gamma and fast neutron dose. The thermal response of the two chambers can be calculated by subtracting the currents with and without the Li-6 absorber and dividing this by the thermal flux. The thermal flux at the chamber positions was measured by the usual gold foil technique. The thermal flux was measured with the chambers in position. A summary of the results is shown in table 3.6.

The calculated value for the carbon graphite chamber is actually slightly negative. It was assigned a value of 0, which is well within the experimental uncertainties for this measurement. There might be some backscatter from the Li-6 carbonate beneath the thimble; this would tend to raise the calculated value for the response.

The calculated value for the tissue equivalent chamber, shown in table 3.6, is in the expected range. The accuracy of this number is ±100%.

Theoretically, the thermal response of the carbon graphite chamber should be very low; the thermal neutron absorption cross section of carbon is only 0.0035 barns. A trace impurity such as B-10, with a high absorption cross section for a charged particle emission reaction, however, could lead to a higher response. If the composition of the chamber is known, the thermal response can be calculated theoretically. A-150 plastic has 3.51 weight percent nitrogen; therefore, the 0.025 eV N-14 kerma factor is 2.73E-11 cGy/n-cm^2. Since the neutron calibration of the tissue equivalent chamber is 4.29 E-11

Table 3.6. Experimental data used to calculate the thermal neutron response of the carbon graphite and tissue equivalent ionization chambers.

Chamber	Current without Li-6 absorber (C/min)	Current with Li-6 absorber (C/min)	Current with Li-6 absorber, corrected for photon and fast neutron attenuation (C/min)	Col 2 - Col 4 divided by the thermal flux (C/min per n/cm^2-sec)
CG/CO_2	1.186e-10	1.183e-10	1.189e-10	≈ 0
TE/TE	1.019e-10	1.000e-10	1.0037e-10	4.68e-20

Note: The thermal flux was measured at 3.28E7 n/cm2-sec. The currents and thermal flux are for P = 4.0 MWn.

C/cGy, the expected response for this chamber is 2.73E-11 cGy/n-cm^2 x 4.29 E-11 C/cGy x 60 sec/min, which is equal to 7.03 E-20 (C/min)/(n/cm^2-sec). This is about 50% higher than the experimentally determined response.

The current produced in the chambers from the thermal flux is:

$$\dot{Q}_\phi = f_\phi \, \phi_{2200} \qquad (3.11)$$

where $\dot{Q}_\phi$ = current under standard conditions from the thermal neutron response of the chamber (C/min),

f_ϕ = thermal response correction factor (C/min) / (n/cm^2-sec),

ϕ_{2200} = the 2200 m/sec neutron flux (n/cm^2-sec).

The experimental method used to determine ϕ_{2200} is discussed later in this chapter. Equation 10 is used to calculate the currents produced by the thermal flux for each of the chambers. Generally, these currents were less than 3% of the total current for the carbon graphite chamber and less than 8% for the tissue equivalent chamber. The thermal neutron induced currents are highest near the top of the phantom where the thermal flux is highest.

Reactor Power

Measurements have been made at various reactor powers, from 100 kWn to 5 MWn. The subscript "n" is used to indicate neutronic power, as distinguished from the reactor thermal power. The reactor neutronic power is measured by a compensated ionization chamber. The current of this chamber is displayed on Channel 7 in the control room. All chamber data are normalized to 5 MWn using the Channel 7 reading taken with all the shutters closed. Cycling the H_2O or D_2O shutters changes the Channel 7 reading. Implicit in this normalization is that the current from the compensated ionization chamber

scales linearly with the intensity of the therapy beam. It is possible, however, that fuel burnup, shim bank height, xenon concentrations, or a core refueling could affect this linearity relation. A beam monitor, which will measure the incident thermal and epithermal neutron fluxes as well as the photon exposure, is being installed. This monitor will be able to measure and record the changes in the incident radiation field from day to day and week to week.

The equation used to normalize the measured data to 5 WM_n is:

$$f_{RP} = 5MW_n / P \qquad (3.12)$$

where f_{RP} = the scale factor for reactor power, and

P = the reactor power (MW_n) during the experiment as measured by Channel 7.

With these corrections to the current, the separate neutron and photon doses can be calculated using equations 3.3 and 3.4.

Sample calculation for D_γ and D_n

The photon and neutron doses are now calculated for the M57 beam at a depth of 1 cm. The experimental conditions were: temperature = 25.6 C, pressure = 30.01" Hg, reactor power = 4.42 MW_n for both chambers; power history correction factors were 0.991 during the tissue equivalent chamber measurements and 0.986 during the carbon graphite chamber measurements; raw chamber currents were 2.28 E-10 C/min for the tissue equivalent chamber and 2.21 E-10 C/min for the carbon graphite chamber. Corrected currents were calculated from

$$I = \frac{1}{f_{flow}} f_{hist}\, f_{T,P}\, I_{meas} - f_{\phi}\, \phi_{5MWn} \frac{1}{f_{RP}} \qquad (3.13)$$

where I_{meas} = the current measured by the electrometer.

For the tissue equivalent chamber,

$$I = \frac{1}{1.02}\, 0.991\, \frac{25.6 + 273}{22 + 273}\, \frac{29.92}{30.01}\, 2.28\text{ E-10 C/min}$$

$$- 4.77\text{ E-20}\, \frac{\text{C/min}}{\text{n/cm}^2\text{-sec}}\, 3.94\text{ E 8 n/cm}^2\text{-sec}\, \frac{1}{5\text{ MWn} / 4.42\text{ MWn}}$$

I = 2.07 E -10 C/min at 4.42 MWn, or 2.34 E-10 C/min at 5 MWn.

For the carbon graphite chamber,

$$I = \frac{1}{1.007}\, 0.986\, \frac{25.6 + 273}{22 + 273}\, \frac{29.92}{30.01}\, 2.21\text{ E-10 C/min}$$

$$- 1.50\text{ E-20}\, \frac{\text{C/min}}{\text{n/cm}^2\text{-sec}}\, 3.939\text{ E 8 n/cm}^2\text{-sec}\, \frac{1}{5\text{ MWn} / 4.42\text{ MWn}}$$

I = 2.13 E-10 C/min at 4.42 MWn, or 2.41 E-10 C/min at 5 MWn.

The photon and neutron doses are determined using these corrected currents in equations 3.3 and 3.4, using the appropriate values of A and B.

$$D_{\gamma} = \frac{4.29\text{ E-11}\, \frac{C}{cGy}\, 2.41\text{ E-10}\, \frac{C}{min} - 3.33\text{ E-12}\, \frac{C}{cGy}\, 2.34\text{ E-10}\, \frac{C}{min}}{4.29\text{ E-11}\, \frac{C}{cGy}\, 7.62\text{ E-11}\, \frac{C}{cGy} - 3.33\text{ E-12}\, \frac{C}{cGy}\, 4.67\text{ E-11}\, \frac{C}{cGy}}$$

$D_\gamma = 3.07$ cGy/min

$$D_n = \frac{4.67\text{ E-}11\ \frac{C}{cGy}\ 2.41\text{ E-}10\ \frac{C}{min} - 7.62\text{ E-}11\ \frac{C}{cGy}\ 2.34\text{ E-}10\ \frac{C}{min}}{4.67\text{ E-}11\ \frac{C}{cGy}\ 3.33\text{ E-}12\ \frac{C}{cGy} - 7.62\text{ E-}11\ \frac{C}{cGy}\ 4.29\text{ E-}11\ \frac{C}{cGy}}$$

$D_n = 2.11$ cGy/min

3.2.2 Thermal neutron doses

N-14 Dose

The two important interactions of thermal neutrons with brain tissue are: N-14(n,p)C-14 and H-1(n,γ)H-2. The dose from the H-1 prompt gammas is included in the measured photon dose as measured by the dual chamber technique. The recoiling deuterium adds to the kerma, but this effect is negligible and the deuterium does not have sufficient energy to ionize. The dose from the N-14(n,p)C-14 reaction is calculated using the kerma factor method. The equation is:[2]

$$D \overset{CPE}{=} K = \Phi F_n \qquad (3.14)$$

or for dose rates,

$$\dot{D} \overset{CPE}{=} \dot{K} = \phi F_n \qquad (3.14b)$$

where $D, \dot{D}$ = dose (cGy) or dose rate (cGy/min),

$K, \dot{K}$ = kerma (cGy) or kerma rate (cGy/min),

Φ, ϕ = neutron fluence (cm^{-2}) or flux (n/cm^2-sec),

F_n = kerma factor (cGy cm^2 /n),

CPE = under charged particle equilibrium conditions.

CPE exists for a volume υ if each charged particle of a given type and energy leaving υ is replaced by an identical particle entering υ, in terms of expectation values.[2] CPE equilibrium will not exist near biological inhomogeneities such as between bone and brain since the atomic composition and density change. Also, CPE will not exist for B-10 since it is not uniformly distributed and, as such, requires a microdosimetric analysis.

For a single neutron energy, type of target atom, and kind of interaction, the kerma factor is calculated from the following equation :[2]

$$F_n = 1.602\ E\text{-}8\ \sigma\ N_t\ m^{-1}\ E_{tr} \qquad (3.15)$$

where σ = interaction cross section (cm^2),

N_t = number of target atoms in the sample,

m = mass of the sample (g),

E_{tr} = total kinetic energy (MeV) given to charged particles per interaction.

Tables of kerma factors for several elements, compounds, and mixtures can be found in Caswell et al.[11] For a continuous neutron spectrum, weighted kerma factors are found by integrating the cross section and energy transferred over the differential spectrum.

To determine the N-14 dose from thermal neutrons, the 0.025 eV kerma factor for N-14 was calculated and multiplied by the 2200 m/sec flux that was determined experimentally using gold foils. N-14 is not a 1/v absorber; however, a non 1/v factor was not found in the literature surveyed. It is most likely between 0.9 and 1.1. For this

reaction, the 2200 m/sec cross section is 1.83 barns[15] and the energy transferred is 0.62 MeV.[2] Since the nitrogen content of ICRU muscle and average brain are 3.5 and 1.8 weight percent, respectively, the kerma factors calculated using equation 3.15 are 2.724E-11 and 1.401 E-11 cGy cm^2/n. For nitrogen, Caswell reports a 0.025 eV kerma factor of 0.785 E-9 cGy cm^2/n. For 3.5 and 1.8 weight percent nitrogen, then, the kerma factors are 2.75 E-11 and 1.41 E-11 cGy cm^2/n, which agree well with the values calculated above.

Sample calculation for the N-14 dose from thermal neutrons

At 1 cm, the 5 MW_n 2200 m/sec flux is 3.94 E 8 n/cm^2-sec. The N-14 dose is:

D = 1.401 E-11 cGy cm^2 / n x 3.94 E 8 n/cm^2-sec x 60 sec/min

= 0.331 cGy/min

Boron-10 Dose

The B-10 dose is also calculated using the kerma factor method. In the B-10(n,α) Li-7 reaction, 6.5% of the reactions lead directly to the ground state of Li-7; 93.5% of the reactions lead to the 0.4776 MeV excited state of Li-7, which decays immediately by emission of a Doppler broadened 0.4776 MeV prompt gamma.[16] The energy is broadened because the excited Li-7 is in motion during emission of the prompt gamma. The Q value for the reaction leading to the ground state of Li-7 is 2.79 MeV.[17] The average energy transferred in this reaction is 2.343 MeV. The 2200 m/sec cross section for this reaction is 3838 barns.[15] For a 1 ppm concentration of B-10, the kerma factor calculated using equation 3.15 is 8.66 E-12 cGy cm^2/n. For elemental boron, Caswell

reports a 0.025 eV kerma factor of 0.159 E -5 cGy cm^2/n.[11] Since the cross section for B-11 is only 5 millibarns and the energy transferred in the B-11 reaction is small, the kerma factor for boron comes almost exclusively from B-10. The Caswell kerma factor, corrected for the atomic abundance of B-10 (20%) and for a 1 ppm concentration of B-10 is 8.59 E -12 cGy cm^2/n. This agrees well with the value calculated above.

Sample calculation for the B-10 dose from thermal neutrons

At 1 cm, the 5 MW 2200 m/sec flux is 3.94 E 8 n/cm^2-sec. The B-10 dose for 30 ppm B-10 is

$$D = 8.66\text{ E-12 cGy cm}^2\text{/n-ppm B-10} \times 3.94\text{ E 8 n/cm}^2\text{-sec} \times 60\text{ sec/min} \times 30\text{ ppm B-10}$$

$$= 6.14\text{ cGy/min}$$

3.2.3 2200 m/sec flux

Experimental method

Gold foils (5 - 10 mg, 0.002" thick) are weighed to within 1%. The foils are irradiated bare and with cadmium covers (0.020" thick). For phantom irradiations, several gold foils are positioned along a thin plastic rod and then taped in place. Bare foils are positioned every centimeter while cadmium covered foils are positioned every 2 cm. Positioning the cadmium covered foils 2 cm apart has been shown to not reduce the activation of the foil from the other cadmium covers. The rod is inserted into one of the butyrate tubes discussed in the reference phantom section. The tube is filled with water

and then capped. The other tubes are nearly fully withdrawn to minimize any perturbation of the radiation field. The phantom is positioned in the beam and then the shutters are opened to irradiate.

The gold reaction is Au-197(n,γ) Au-198. The 2200 m/sec cross section is 98.8 barns.[15] The half-life of Au-198 is 2.696 days; it emits 411 keV photons in 95.5% abundance.[18] The activity of the gold foils is determined with either a HPGE or Ge(Li) detector. These detectors are energy calibrated, and are efficiency calibrated with a National Institute of Standards and Technology (NIST) Standard Mixed Radionuclide Source (SRM 4275C-45). The Standard Source[19] consists of a thin deposit, about 6 mm in diameter, on a polyester tape. This source, then, looks much like a thin gold foil. The standard source is placed about 5" from the detector face to minimize coincidence summing errors.[19,20] The efficiency at 411 keV is then determined at this distance. Figure 3.11 shows one of the efficiency curves. To speed up the counting process, the foils are positioned close to the detector surface. The efficiency at this position is determined by counting a gold foil at the 5" distance and then counting the same foil at the close distance. This gives a ratio of count rates that can be multiplied by the efficiency at 5" to determine the efficiency at the close distance. Positioning errors, even when the foil is close to the detector surface, affects the count rates by less than 1%.

Calculations and assumptions

The 2200 m/sec neutron flux is determined by the cadmium difference technique.[21] A cadmium correction factor has been included. Following Knoll,[22] the thermal neutron flux is proportional to the saturated activity of a foil per unit mass:

$$\phi = \frac{MW}{A_v \sigma} \frac{A_{sat}}{m} \qquad (3.16)$$

where ϕ = neutron flux averaged over the foil surface (n/cm^2-sec)

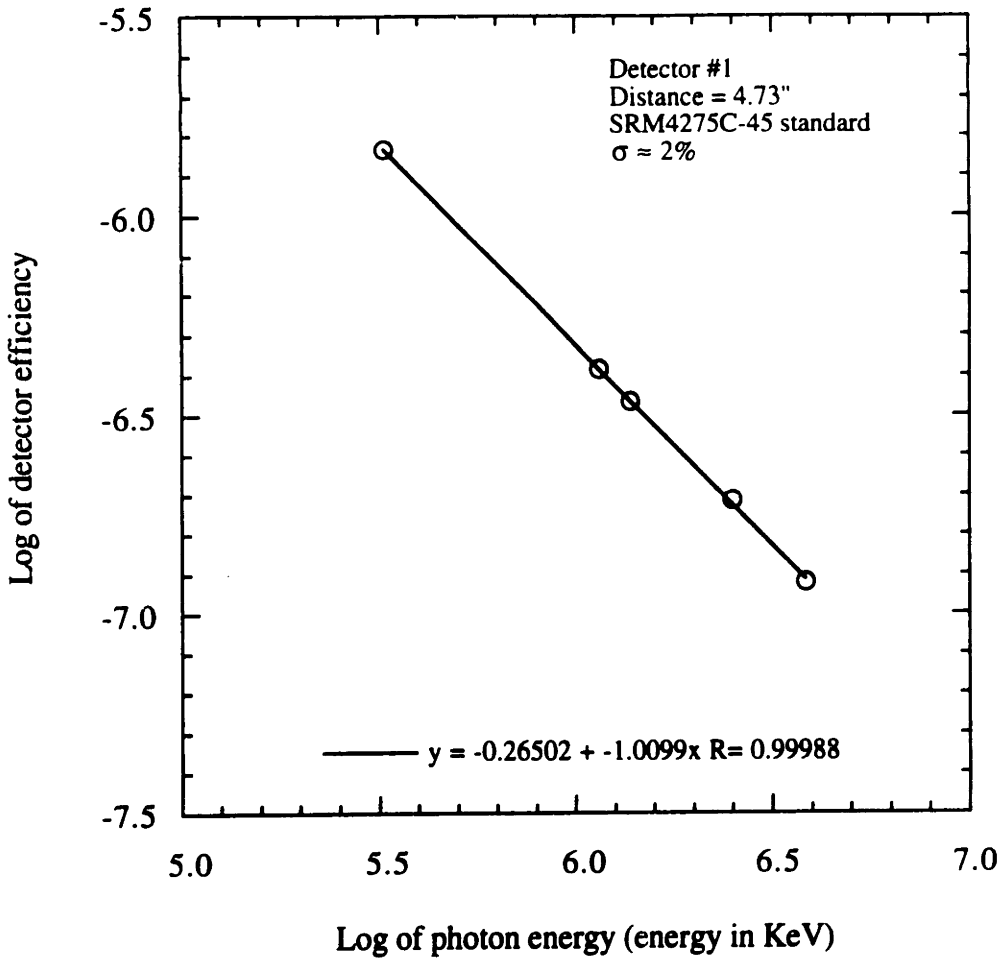

Figure 3.11. A typical efficiency-energy plot obtained with the SRM4275C standard and a Ge(Li) detector. A linear, least-squares fit to the data provides the efficiency at 411 keV, the decay gamma energy of Au-198. Summing effects at this source-to-detector distance are negligible. The detector efficiency was determined every time gold foils needed to be counted.

MW = molecular weight (g/mole)

A_v = Avogadros number (atoms per mole)

σ = microscopic activation cross section averaged over the spectrum (cm^2)

m = mass of the foil (g)

and where

$$A_{sat} = \frac{\lambda C}{\varepsilon (1 - e^{-\lambda t_0}) (e^{-\lambda t_1} - e^{-\lambda t_2})} \qquad (3.17)$$

where λ = decay constant (sec^{-1}),

t_0 = irradiation time (sec),

C = net number of counts (with the background subtracted) obtained with a radiation detector between times t_1 and t2, where the start of irradiation is time zero,

ε = overall counting efficiency.

The overall counting efficiency is the number of counts detected of a particular radiation divided by the number of radiations of that type which were actually emitted. It accounts for self-absorption (ε_a), detector efficiency (ε_d), and abundance of the detected radiation ($\varepsilon_{\%}$). This analysis assumes that the flux is constant during the irradiation and that burnup is negligible, both valid assumptions.

It is desirable to calculate the separate thermal and epithermal fluxes. Bare foils are activated by thermal and epithermal neutrons while cadmium covered foils are activated only by epithermal neutrons. The 2200 m/sec flux, therefore, can be calculated from:

$$\phi_{2200} = \frac{MW}{A_v \sigma_{2200}} \left[\left(\frac{A_{sat}}{m}\right)_{bare} - F_{Cd} \left(\frac{A_{sat}}{m}\right)_{Cd} \right] \qquad (3.18)$$

where the A_{sat}/m ratios are calculated from bare and cadmium covered foils and σ_{2200} is the 2200 m/sec absorption cross section. The thermal neutron self-shielding factor is small (< 1%). Thermal neutron flux depression caused by the presence of the other foils has been shown by Harling[23] to be small.

The flux calculated this way by using the 2200 m/sec cross section is more accurately called the 2200 m/sec flux, not the thermal flux. Also, the cadmium covers absorb some neutrons with energies above the cadmium cut off. This is accounted for by the F_{Cd} term. For 0.020" thick Cd covers, a value of 1.02 for F_{Cd} has been recommended.[24] The first term in equation 3.18 is proportional to the total reaction rate while the second term is proportional to the reaction rate caused by epicadmium neutrons. Subtracting the second term from the first leaves the reaction rate caused by sub-cadmium neutrons. This includes a significant reaction rate from neutrons above the normal Maxwellian distribution (5 kT or 0.13 eV for room temperature, 293 K, neutrons) but below the cadmium cut off (≈ 0.5 eV).

The activation of a 1/v detector in the energy range 5 kT to 0.5 eV can be calculated.[21] This information, however, was not needed and was not obtained. The goal was to obtain an accurate reaction rate for B-10 and an approximate reaction rate for N-14. Boron-10 is a 1/v absorber so its reaction rate can be determined accurately from the 2200 m/sec flux and its 2200 m/sec cross section. N-14 is not a 1/v absorber so a non-1/v factor should be applied. The non-1/v factor was not found in the literature surveyed. The dose from N-14, however, is small so its reaction rate does not have to be determined as accurately as that of B-10.

Sample Calculation for ϕ_{2200} Using Gold Foils

For gold, the molecular weight is 196.97 g/mole, the absorption cross section σ_{2200} is 98.8 barns, and the half life is 2.696 days (λ = 2.975 E -6 sec^{-1}). Using data with the M57 beam at the top of the phantom, m_{bare} was 0.00487 g, and m_{Cd} was 0.00544 g. The foils were irradiated for 1 hour in separate irradiations and were counted several days later. For the bare foil, t_o = 0.0417 days, t_1 = 4.94722 days, t_2 = 4.94792 days, and the number of counts was 5490. For the cadmium covered foil data, see Appendix B. F_{Cd} was taken as 1.02 [24,25]. This is a reasonable value for our foils and cadmium covers. The 411 keV gamma was detected. Its abundance, $e_{\%}$, is 95.5% (21). The detector efficiency, e_d, at 411 keV was determined to be 6.50% for foils on the detector surface.

There is some self-absorption of the 411 keV gammas in the foil itself. The attenuation from scattering and absorption was estimated using the following equation:

$$\varepsilon_a = e^{-\left(\frac{\mu}{\rho}\right)_{Pb} \rho_{Au} x}$$

where $(\mu/\rho)_{Pb}$ is the mass attenuation coefficient for lead at 411 keV and x is half the thickness of the foil. The coefficient for lead was used since it was available and would be expected to be very close to that of gold. For an attenuation coefficient of 0.233 g/cm^2, gold density of 19.29 g/cm^3, and foil thickness of 0.002" (0.0051 cm), e_a = 0.989.

Inserting these values into equation 3.17 gives

$$\left(\frac{A_{sat}}{m}\right)_{bare} = \frac{2.975 \text{ E-6 } sec^{-1} \text{ 5490 counts / 4.87 mg}}{0.989 \times 0.955 \times 0.0650 \times (1 - e^{-0.257 days^{-1} 0.0417 \text{ days}}) (e^{-0.257 days^{-1} 4.94722 \text{ days}} - e^{-0.257 days^{-1} 4.94792 \text{ days}})}$$

$$\left(\frac{A_{sat}}{m}\right)_{bare} = 1.03E5 \sec^{-1} mg^{-1}$$

A similar calculation was done for the cadmium covered foil; the result was 4.20 E 4 sec^{-1} mg^{-1}. Then, equation 3.18 gives

$$\phi_{2200} = \frac{196.97 \text{ g } \frac{1000 \text{ mg}}{\text{g}}}{6.02 \text{ E } 23 \text{ atoms } 98.8 \text{ E } -24 \text{ cm}^2/\text{atom}} \left[1.03 \text{ E } 5 \frac{1}{\sec \text{ mg}} - 1.02 \text{ x } 4.20 \text{ E } 4 \frac{1}{\sec \text{ mg}}\right]$$

$$= 1.98 \text{ E } 8 \text{ n /cm}^2\text{-sec}$$

Cadmium Ratio

The cadmium ratio is a simple parameter that indicates in a gross sense the neutron energy spectrum. It is defined as:

$$CdR = (Asat/m)_{bare} / (Asat/m)_{Cd} \qquad (3.19)$$

The cadmium ratio, expressed this way, depends on the thickness of the foil. There is a large energy self-shielding in the gold resonance. For a 0.002" thick foil, the resonance self-shielding factor, F_{res}, is 0.28.[25] A plot of F_{res} versus foil thickness is provided in figure 3.12. This factor was derived assuming an isotropic flux. Using the resonance self-shielding factor, the cadmium ratio can be corrected to that value which would theoretically be obtained with an infinitely thin foil.

3.2.4 Epithermal neutron flux

It is not essential that the epithermal neutron flux be measured in order to obtain the doses in phantom. However, the epithermal neutron flux is useful in describing the

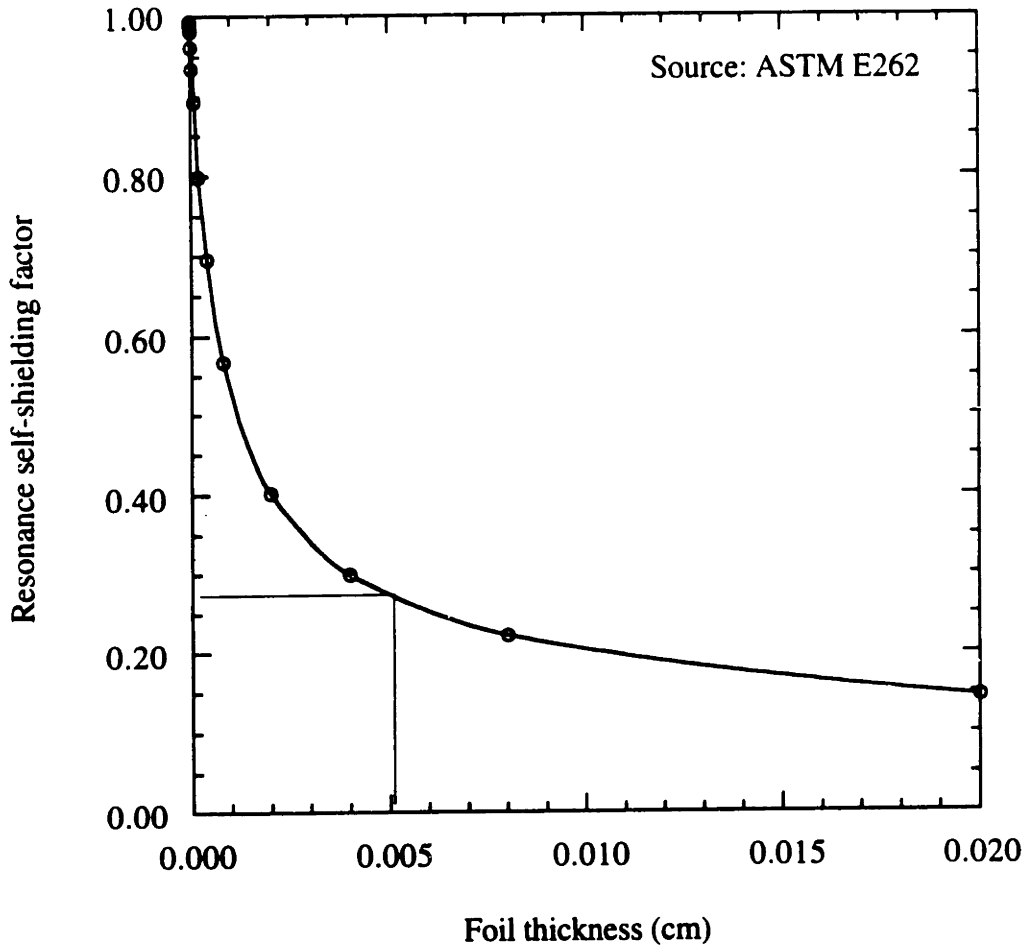

Figure 3.12. Theoretical self-shielding factors for gold foils as provided in ASTM E262. Experimentally determined values were within 2% of the theoretical factors. Gold foils used in this study were 0.002" (0.0051 cm) thick, and so had a resonance self-shielding factor of about 0.28.

intensity of useful epithermal neutrons in a beam, or the intensity below a delimiter used to confine the beam to a particular treatment area. It is also used in two simple parameters that describe the general quality of a beam, that is, how contaminated the epithermal beam is with incident photons and fast neutrons. The parameters are given as the ratio of photon and fast neutron dose rates per unit epithermal neutron flux, all measured in air.

Experimental Method

The epithermal neutron flux is determined by irradiating cadmium covered gold foils. The basic experimental method is the same as that used to determine the 2200 m/sec flux.

Calculations and Assumptions

The epithermal neutron flux is calculated using the known resonance integral and assuming a 1/E slowing down spectrum. The cadmium correction factor and resonance self-shielding factor, discussed previously, are accounted for. From equation 3.16, it is seen that

$$\frac{A_{sat}}{m} = \frac{A_v}{MW} \sigma \phi \qquad (3.20)$$

Recall that σ is the activation cross section already averaged over the neutron spectrum. The saturated activity induced in a cadmium covered foil from a differential spectrum $\phi(E)$ is then

$$\left(\frac{A_{sat}}{m}\right)_{Cd} = \frac{A_v}{MW} \int_{0.5\ eV}^{1\ MeV} \sigma(E)\ \phi(E)\ dE \qquad (3.21)$$

where $\sigma(E)$ = energy dependent activation cross section (cm^2),

$\phi(E)$ = differential neutron spectrum (n/cm^2-sec-eV).

The negligible contribution to the activity from neutrons in the energy range 1-15 MeV has been neglected; the limits in the integral were chosen to be the same as those often used in the definition of the resonance integral, which will be used later. To integrate equation 3.21, the energy dependence of $\phi(E)$ in this energy range must be estimated. For hydrogenous materials, the spectrum shape is usually approximated as $1 / E^{(1+\alpha)}$, at least outside of any absorption resonance. α is an empirical parameter. The scalar flux density, $\phi(E)$, can be calculated analytically for an infinite homogeneous medium under the assumption that moderation is by scattering that is isotropic in the center of mass.[26] When the moderation is by hydrogen only, or when there is no or weak absorption, $\phi(E)$ is found to behave generally as 1/E. The 1/E behavior is modified slightly by absorption of neutrons with energies above E and by significant changes in the scattering cross section with energy. It was assumed that

$$\phi(E) = \frac{\phi_o}{E} \tag{3.22}$$

where ϕ_o is a constant. That is, $\alpha = 0$. What's more, there is no additional information that could be used to make a better estimate of α. Substituting this spectrum shape into the integral gives

$$\left(\frac{A_{sat}}{m}\right)_{Cd} = \frac{A_v}{MW} \int_{0.5\ eV}^{1\ MeV} \frac{\sigma(E)\ \phi_o}{E}\, dE \tag{3.23}$$

Pulling out ϕ_o,

$$\left(\frac{A_{sat}}{m}\right)_{Cd} = \frac{A_v \phi_o}{MW} \int_{0.5\ eV}^{1\ MeV} \frac{\sigma(E)}{E}\, dE \qquad (3.24)$$

$$\left(\frac{A_{sat}}{m}\right)_{Cd} = \frac{A_v \phi_o}{MW} RI \qquad (3.25)$$

where the integral is just the resonance integral (RI) for an ideal infinitely dilute detector. Solving for ϕ_o,

$$\phi_o = \frac{\left(\frac{A_{sat}}{m}\right)_{Cd} MW}{A_v\, RI} \qquad (3.26)$$

So,

$$\phi(E) = \frac{\left(\frac{A_{sat}}{m}\right)_{Cd} MW}{A_v\, RI} \frac{1}{E} \qquad (3.27)$$

The epithermal flux is,

$$\phi_{EPI} = \frac{\left(\frac{A_{sat}}{m}\right)_{Cd} MW}{A_v\, RI} \int_{0.4\ eV}^{10\ keV} \frac{1}{E}\, dE \qquad (3.28)$$

The limits of integration are somewhat arbitrary. Integrating and applying the limits,

$$\phi_{EPI} = \frac{10.1 \left(\frac{A_{sat}}{m}\right)_{Cd} MW}{A_v\, RI} \qquad (3.29)$$

For integration limits of 0.4 eV and 10 keV, the integration constant is 10.1, as seen in the above equation. For integration limits of 0.4 eV and 100 keV, the constant is 12.4, which shows the sensitivity of ϕ_{EPI} to the integration limits.

There is a large resonance self-shielding for the foils used in this study. To account for resonance self-shielding, the right hand side of equation 3.29 is divided by F_{res}, the resonance self-shielding factor. Also, the right hand side is multiplied by F_{Cd} to account for attenuation of resonance neutrons by the cadmium cover. The final equation is,

$$\phi_{EPI} = \frac{10.1\ F_{Cd}\ \left(\frac{A_{sat}}{m}\right)_{Cd}\ MW}{A_v\ RI\ F_{res}} \qquad (3.30)$$

Sample Calculation for the Epithermal Flux

The epithermal flux is calculated at the top of the phantom with the M57 beam. $(A_{sat}/m)_{Cd}$ was previously calculated to be 4.195 E 4 sec^{-1} mg^{-1}. The resonance integral of gold is 1560 barns (19). Therefore,

$$\phi_{EPI} = \frac{10.1 \text{ x } 1.02 \text{ x } 4.20 \text{ E } 4\ \frac{1}{\text{sec mg}}\ 196.97 \text{ g } 1000\ \frac{\text{mg}}{\text{g}}}{6.02 \text{ E } 23 \text{ atoms } 1560 \text{ E } -24 \text{ cm}^2/\text{atom } 0.28}$$

$$= 3.24 \text{ E } 8 \text{ n/cm}^2\text{-sec}$$

or 3.66 E 8 n/cm^2-sec at 5 MW.

Most of the reaction rate in the gold foil is from resonance neutrons.

3.3 RESULTS

As an example, the dose distribution measured for a unilateral irradiation of the head phantom is shown in figure 3.13. Each component of the dose has been assigned

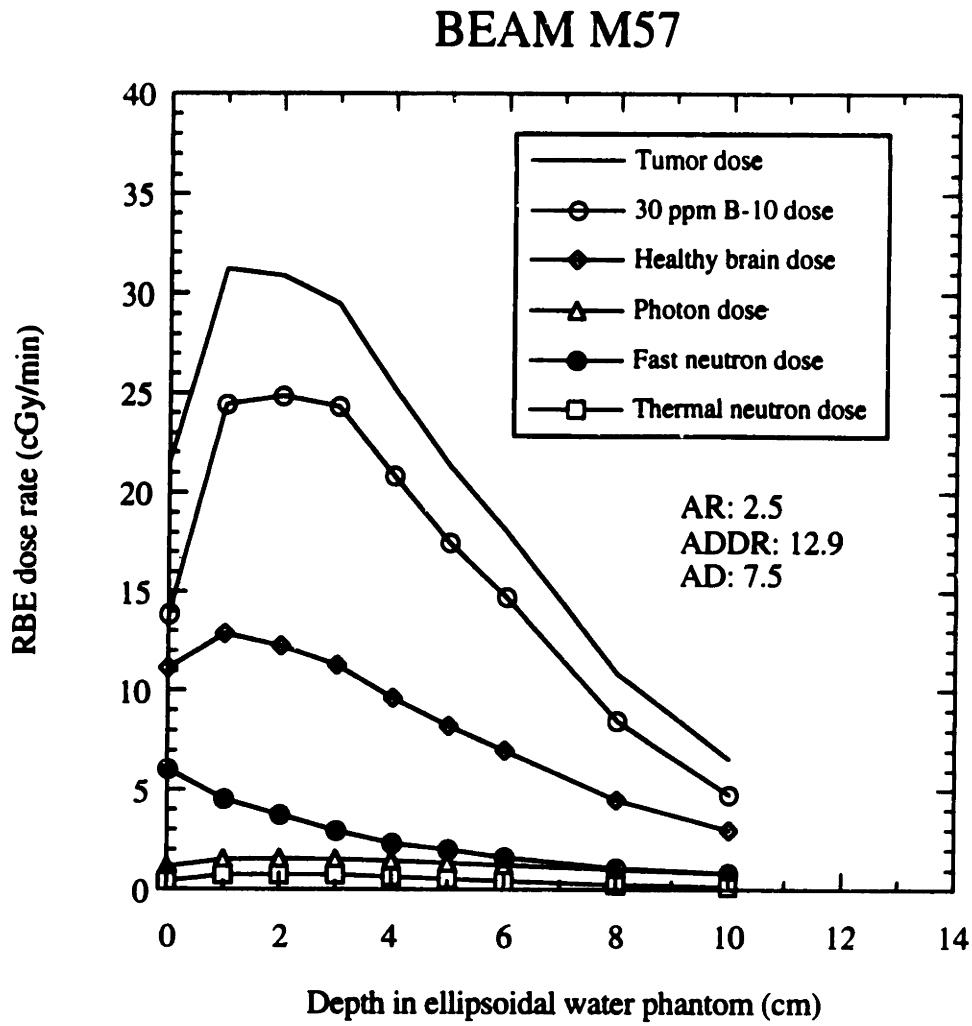

Figure 3.13. Dose-depth plot for the M57 beam. The dose rates are for a unilateral irradiation of s standard sized head phantom. The dose rates have been scaled to a reactor power of 5 MWn. The photon and fast neutron dose rates measured in air at the beam exit were 0.60 and 4.9 RBE cGy/min, respectively.

an relative biological effectiveness (RBE) value: 4.0 for the B-10 dose, 2.3 for the fast neutron dose, 2.3 for the thermal neutron dose, and 0.5 for the photon dose. These RBE's were drawn from available radiobiological data,[27-31] and have been used by our group as a likely set of RBE's for the past two years. The photon RBE of 0.5 was chosen since it was assumed that the therapy would be fractionated. More accurate information about RBE's in BNCT irradiation therapies will undoubtedly be developed in the future; however, for the purposes of this thesis the chosen RBE's provide a useful illustration. The tumor and healthy tissue B-10 concentrations are illustrative of concentrations and concentration ratios which we have experimentally observed for boronophenylalanine.[32] Separate curves are shown for the thermal neutron, fast neutron, and photon doses. The dose to healthy tissue is the sum of these three background doses plus that caused by 7.5 ppm of B-10 that is assumed to be in healthy tissue. The dose to tumor is the sum of the same three background doses plus that caused by 30 ppm of B-10 that is assumed to be in tumor. More uniform dose distributions result with bilateral irradiations.

3.4 DISCUSSION

As shown in figure 3.13, the B-10 and thermal neutron doses peak at about 2 cm. These two dose components are lower near the surface since there is little incident thermal flux. The fast neutron dose is highest at the surface, and drops off with a half-thickness of 3 cm. Since the incident photon field is low, the photon dose peaks at several cm's depth within the phantom due to the H-1(n,γ)H-2 reaction.

The neutron energy spectrum in air or in the phantom have not been measured. Spectral weighting of the kermas and $\overline{W}$ values, therefore, were only roughly estimated. The neutron to gamma sensitivity ratios were assumed to be constant and not to change

with depth inside the phantom; this assumption is generally used in fast neutron therapy dosimetry. Interface effects, such as occur between air and skin and between bone and brain, have not been accounted for.

The kerma of tumor is usually taken as that of ICRU muscle tissue.[3] For subcutaneous melanoma, we make the same assumption; however, for glioblastoma multiforme and intra-cranial metastatic melanoma, we assume that the tumor kerma is equal to that of brain.

The estimated errors in the thermal neutron flux and in the photon and fast neutron doses are shown in tables 3.7 and 3.8. For the thermal flux, the systematic error is small (±2%). The major experimental error is in the reactor power, that is, in the intensity of the beam. The absolute accuracy of the reactor power is ±5%.[33] This error is based on the calibration of a compensated ionization chamber, an error associated with the positioning of the chamber, and periodic intercomparisons of the reactor thermal power as determined by a heat balance with the current collected by the chamber. The other major source of experimental error is counting statistics. This error, ±4% as listed in the table, can be reduced to ±2% with longer irradiations or longer counting times. Other sources of error are due to uncertainties in the basic nuclear data, the accuracy and precision of the balances used to weigh the foils, and shutter timing error. The overall uncertainty in the thermal neutron flux is estimated as ±7%.

For the photon and fast neutron doses, the systematic errors are higher than those for the thermal flux. Most important are the uncertainties in the neutron to gamma sensitivity ratios and the thermal neutron responses of the chambers, especially those of the tissue equivalent chamber. A sensitivity analysis was done; results are shown in figures 3.14-3.17. The photon and fast neutron doses were calculated for a range of neutron to gamma sensitivity ratios and thermal neutron responses.

The ranges used to estimate the uncertainties listed in table 3.8 are: neutron to gamma sensitivity of the carbon graphite chamber, 0.01-0.08; neutron to gamma

Table 3.7. Estimated uncertainties in the determination of the thermal flux in phantom.

Source	Uncertainty in thermal flux (%)
Au-197 thermal neutron absorption cross section	±0.2
Au-198 411 keV photon abundance	±0.3
Self-absorption of 411 keV photons in foil	±0.2
Detector efficiency	±3.0
Foil mass	±1.0
Beam intensity	±5.0
Irradiation time	±0.4
Positioning of phantom	±0.5
Positioning of foils in phantom	±1.5
Effect of other foils	-1.0
Counting statistics	±4.0
Total error	**±7.4**

Table 3.8. Estimated uncertainties in the determination of the photon and fast neutron doses in phantom.

Source	Uncertainty in doses (%)
Electrometer	±0.5
Calibration of chambers	±2.0
Neutron sensitivity factor of CG chamber*	±3% for the photon dose
	±4% for the fast neutron dose
Neutron sensitivity factor of TE chamber*	±1% for the photon dose
	±6% for the fast neutron dose
Thermal neutron response of CG chamber	±2% for the photon dose
	±3% for the fast neutron dose
Thermal neutron response of TE chamber	±1% for the photon dose
	±13% for the fast neutron dose
Temperature, pressure, and gas flow rate	±2.0
Displacement correction factor	±0.3
Positioning of chambers	±2.0
Reactor power	±5.0
Power history	±2.0
Total error	**±9% for the photon dose**
	±17% for the fast neutron dose

* Includes uncertainties in the ratios of the mass energy-absorption coefficients, $\overline{W}$ values, and kerma values, as well as uncertainties in the differential neutron spectrum.

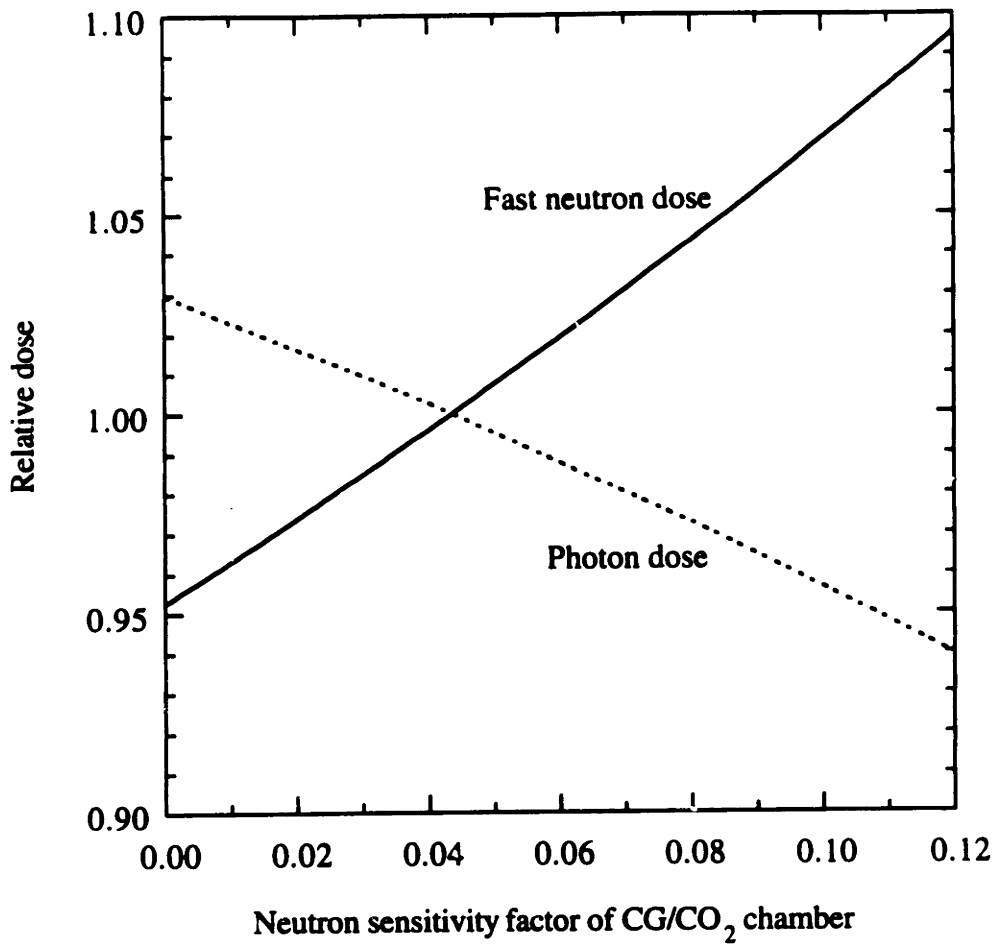

Figure 3.14. Variation in the calculated photon and fast neutron doses as a function of the carbon graphite chamber's neutron sensitivity factor. A nominal value of 0.0437 was assumed . If the true value is higher, the calculated photon dose would be lower and the calculated fast neutron dose would be higher.

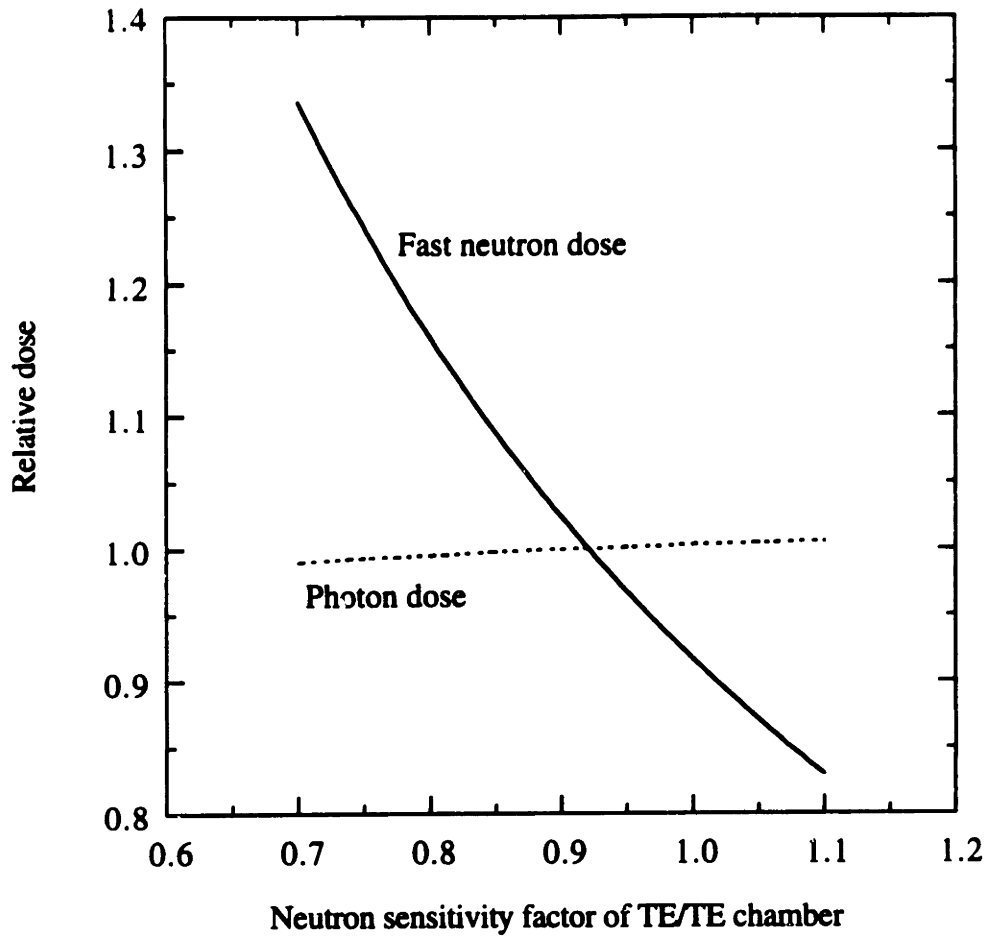

Figure 3.15. Variation in the calculated photon and fast neutron doses as a function of the tissue equivalent chamber's neutron sensitivity factor. A nominal value of 0.92 was assumed . The fast neutron dose is strongly dependent on the sensitivity factor. If the true value is higher, the calculated photon dose would be slightly higher and the calculated fast neutron dose would be significantly lower.

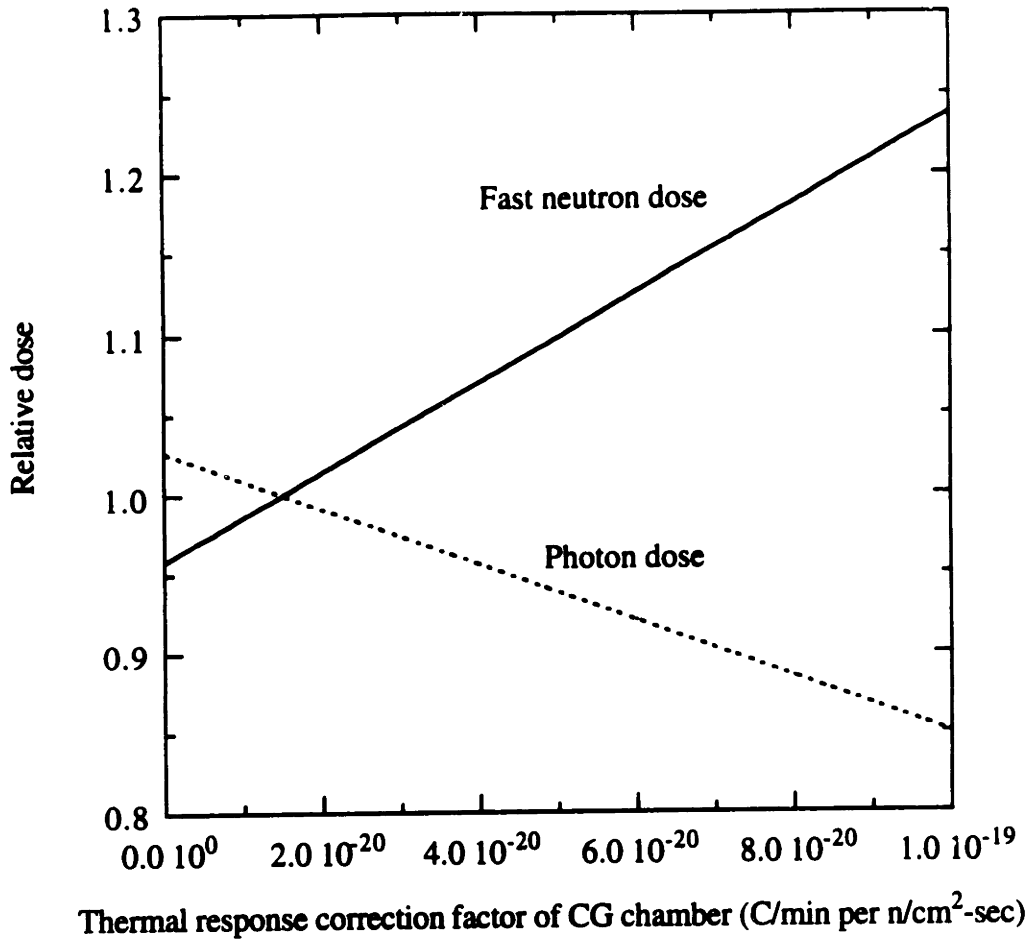

Figure 3.16. Variation in the calculated photon and fast neutron doses as a function of the carbon graphite chamber's response to thermal neutrons. A nominal response of 1.50 E -20 (C/min)/(n/cm^2-sec) was assumed . If the true response is higher, the calculated photon dose would be lower and the calculated fast neutron dose would be higher.

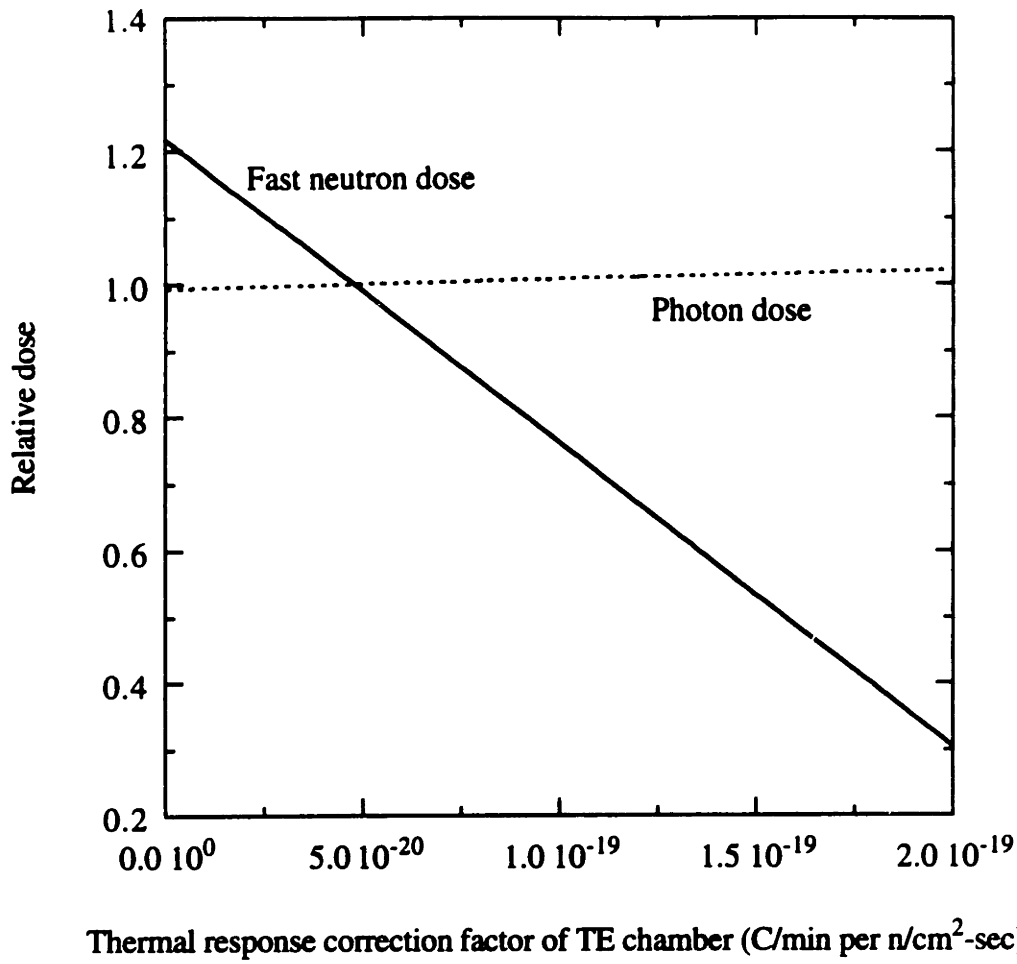

Figure 3.17. Variation in the calculated photon and fast neutron doses as a function of the tissue equivalent chamber's response to thermal neutrons. A nominal response of 4.77 E -20 (C/min)/(n/cm^2-sec) was assumed . If the true response is higher, the calculated photon dose would be slightly higher and the calculated fast neutron dose would be significantly lower.

sensitivity of the tissue equivalent chamber, 0.85-0.95; thermal response of the carbon graphite chamber, 1.5 E-20 ±50% (C/min)/(n/cm^2-sec); thermal response of the tissue equivalent chamber, 4.77 E-20 ±50% (C/min)/(n/cm^2-sec).

Once again the major experimental error is the uncertainty in the absolute reactor power. The overall uncertainty in the photon dose is estimated as ±9%; the overall uncertainty in the fast neutron dose is estimated as ±17%.

Our group has found these methods of dosimetry very useful. Using the realistic phantoms we have developed, the various dose components can be measured in three dimensions, with a grid spacing of 1-2 cm. These methods seem appropriate in the dosimetry of any epithermal neutron beam, regardless of the type of beam or neutron source.

References

[1]Jong-Ho Richard Choi, *Development and Characterization of an Epithermal Beam for Boron Neutron Capture Therapy at the MITR-II Research Reactor*, (Ph.D. Thesis, Massachusetts Institute of Technology, 1991).

[2]Frank H.Attix, *Introduction to Radiological Physics and Radiation Dosimetry*, (John Wiley & Sons, New York, NY, 1986).

[3]ICRU Report 45, *Clinical Neutron Dosimetry. Part I: Determination of Absorbed Dose in a Patient Treated by External Beams of Fast Neutrons*, (International Commission on Radiation Units and Measurements, Bethesda, Maryland, 1989).

[4]Damien Moulin, *Design and Construction of Ellipsoidal Head Phantoms for Boron Neutron Capture Therapy*, (Report #MITNRL-042, Nuclear Reactor Laboratory, Massachusetts Institute of Technology, 1990).

[5]Kevin Roberts, *Mixed Field Dosimetry in Realistic Head Phantoms Using an Epithermal Beam at MITR-II,* (Master's Thesis, Massachusetts Institute of Technology, 1990).

[6]Chun-Shan Yam, *Design of Patient Positioning System, Body Phantom, and Patient shielding for the Boron Neutron Capture Therapy Project at MITR-II*, (Master's Thesis, Massachusetts Institute of Technology, 1993).

[7]W. Snyder, M. Ford, G. Warner, and H. Fisher, Jr., "Estimates of absorbed fractions for monoenergetic photon sources uniformly distributed in various organs of a heterogeneous phantom," MIRD, J. Nucl.Med, Suppl. No. 3, Pamphlet 5 (1969).

[8]Rodney A. Brooks, Giovanni DiChiro, and Mark Keller, "Explanation of cerebral white-gray contrast in computer tomography," J. Comp. Asst. Tomog. **4**, No. 4, 489-491 (1980). Brain composition is an average of gray and white matter as calculated by R. Zamenhof.

[9]L.J. Goodman, "A modified tissue equivalent liquid," Health Physics **16**, 763 (1969).

[10]M. Ashtari, *Biological and Physical Studies of Boron neutron Capture Therapy*, (Ph.D. Thesis, Massachusetts Institute of Technology, 1982).

[11]R. S. Caswell, J.J. Coyne, "Kerma factors for neutron energies below 30 MeV," Rad. Res. **83**, 217-254 (1980).

[12]L. J. Goodman, J. J. Coyne, "W_n and neutron kerma for methane-based tissue-equivalent gas," Rad. Res. **82**, 13-26 (1980).

[13]B. E. Leonard, J. W. Boring, "The average energy per ion pair, W, for hydrogen and oxygen ions in a tissue equivalent gas," Rad. Res. **55**, 1-9 (1973).

[14]ICRU Report 26, *Neutron Dosimetry for Biology and Medicine*, (International Commission on Radiation Units and Measurements, Bethesda, Maryland, 1977).

[15]F. W. Walker, J. R. Parrington, F. Feiner, *Nuclides and Isotopes*, 14th ed, (General Electric Co., San Jose, California, 1989).

[16]R. Rogus, O.K. Harling, I. Olmez, and S. Wirdzek, "Boron-10 prompt gamma analysis using a diffracted neutron beam," in *Progress in Neutron Capture Therapy for Cancer*, (Barry Allen, Douglas Moore, Baiba Harrington, eds., Plenum Press, New York, 1992).

[17]F. W. Walker, J. R. Parrington, and F. Feiner, *Nuclides and Isotopes*, 14th ed. (General Electric Co., San Jose, California, 1989). Q value based on mass defects.

[18]C. M. Lederer, Virginia Shirley, *Table of Isotopes*, 7th ed. (Lawrence Berkeley Laboratory, Wiley-Interscience Publication, John Wiley & Sons, Inc., N.Y., 1978).

[19]National Institute of Standards and Technology, Certificate for Standard Reference Material 4275C, Radioactivity Standard, Office of Standard Reference Materials, Gaithersburg, Md.

[20]G. J. McCallum, G. E. Coote, "Influence of source-detector distance on relative intensity and angular correlation measurements with Ge(Li) spectrometers," Nucl. Instr. and Meth.**130**, 189-197 (1975)

[21]ASTM Standard E262-86(e1), *Standard method for determining thermal neutron reaction and fluence rates by radioactivation techniques*, (1987).

[22]G. F. Knoll, *Radiation Detection and Measurement*, 2nd ed. (John Wiley & Sons, NY, 1989).

[23]Personal communication, Professor Otto Harling, Director, Nuclear Reactor Laboratory, Massachusetts Institute of Technology, Cambridge, Ma.

[24]This value was suggested by R. Fairchild, Brookhaven National Laboratory.

[25]M. Brose, "Zur Messung und Berechnung der Resonanzabsorption von Neutronen in Goldfolien," Nukleonik **6**, 134 (1964).

[26]Allan F. Henry, *Nuclear Reactor Analysis*, (The MIT Press, Cambridge, Massachusetts, 1975).

[27]G. R. Morgan, A. J. Mill, D. J. Roberts, S. Newman, and P. D. Holt, "The radiobiology of 24 keV neutrons," Br. J. Radiol. **61**, 1127 (1988).

[28]H. Fukuda, T. Kobayashi, T. Matsuzawa, "RBE of a thermal neutron beam and the B-10(n,α)Li-7 reaction on cultured B-16 melanoma cells," Int. J. Radiat. Biol. **1**, 167 (1987).

[29]J. A. Coderre, "Experimental determination of RBE values for the B-10(n,a)Li-7 reaction using BPA or BSSB in the rat 9L gliosarcoma model," (International workshop and plenary meeting - Toward Clinical Trials of Glioma with BNCT, Petten, The Netherlands, September 18-20, 1991).

[30]R. G. Fairchild, S. K. Saraf, J. Kalef-Ezra, and B. H. Laster, "Comparison of measured parameters from a 24 keV and a broad spectrum epithermal neutron beam for

neutron capture therapy: an identification of consequential parameters," Med. Phys. **17**, 1045 (1990).

[31]S. Hornsey, "Experimental central nervous system injury from fats neutrons," In: P. H. Gutin, S. A. Leibel, and G. E. Shelin, eds, *Radiation Injury to the Nervous System*, (Raven Press Ltd., New York, 1991).

[32]Guido Solares, *High Resolution Alpha Track Autoradiography and Biological Studies of Boron Neutron Capture Therapy*, (Ph.D. Thesis, Massachusetts Institute of Technology, 1991).

[33]Personal communication, Dr. John Bernard, Director of Reactor Operations, Massachusetts Institute of Technology, Cambridge, Ma.

[34]D. W. Pearson, F. H. Attix, P. M. DeLuca Jr, S. J. Goetsch, and R. P. Torti, "Ionisation error due to porosity in graphite ionisation chambers," Phys. Med. Biol. **23**, No. 2, 333-338 (1990).

CHAPTER 4 EPITHERMAL NEUTRON BEAM DESIGN, INSTALLATION, AND DOSIMETRY

4.1 INTRODUCTION

In this chapter, the various beams that were designed and characterized are discussed. In each case a figure of the beam is provided, along with the relevant dose versus depth plots. The beam that will be used for the clinical irradiations, the M67 beam, is presented here, but is presented in more detail in Chapter 5.

4.2 BEAM M47

The first beam characterized as part of this thesis was the M47 beam. This beam was the result of several years work effort by members of our group. Overall, this beam was the best available at the time, and it was selected as the beam that would be used for the first set of glioblastoma patients. As this beam was to be used for actual irradiations of people, an independent dosimetric evaluation of the beam was needed.

The beam is shown in figure 4.1. Results are shown in figures 4.2 and 4.3. The results of the independent evaluation showed that the original dosimetry presented by Choi needed to be revised. The thermal neutron flux had been overestimated because the diode detectors that were used to count the gold foils had not been properly efficiency calibrated. An efficiency of exactly 4% had been used (efficiency for the 411 keV decay gamma of Au-198 with the foil placed on the top of the detector), while the detector efficiencies actually

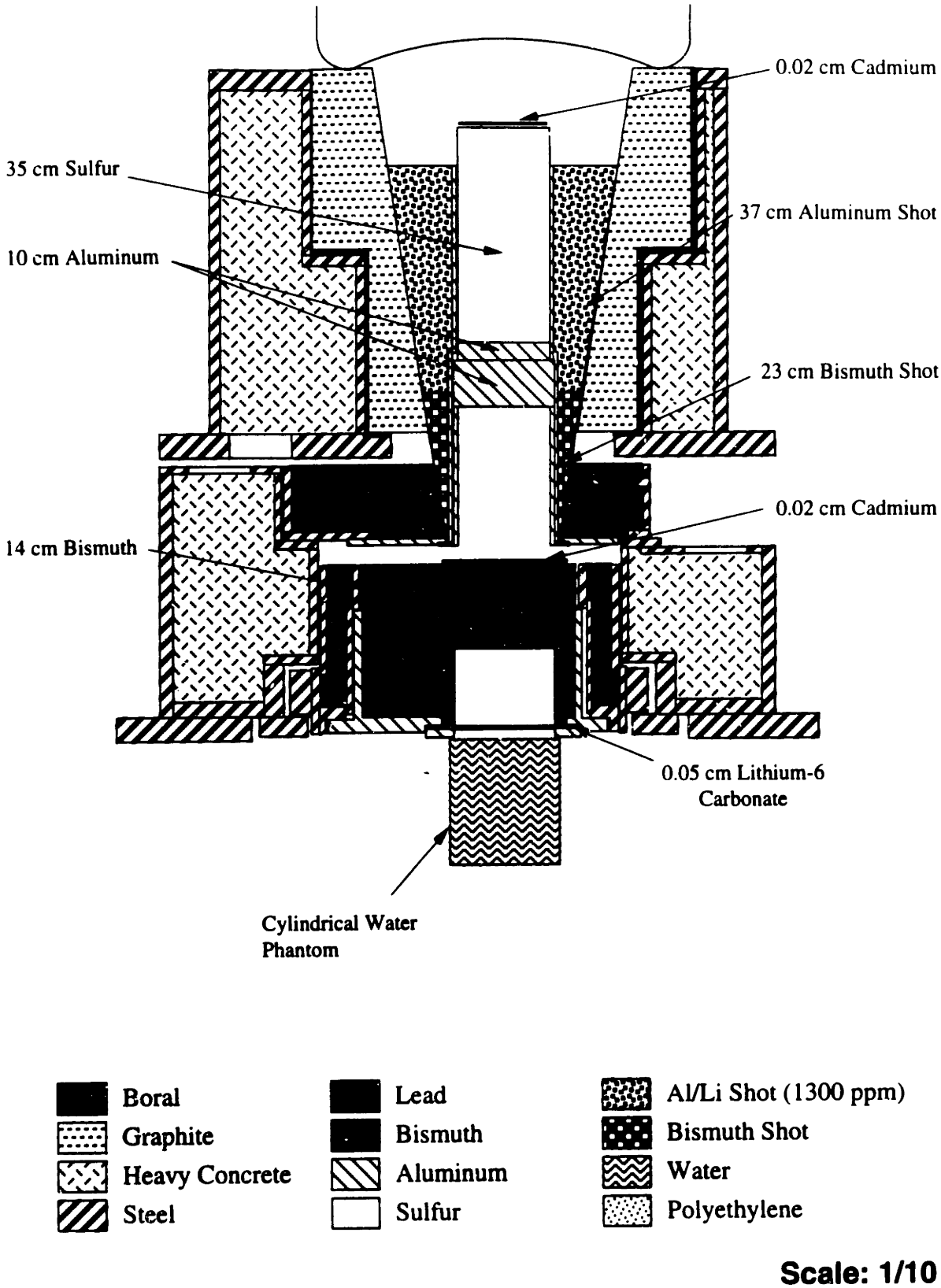

Figure 4.1. Cross sectional view of the M47 beam. This is the only beam in this thesis in which the cylindrical water phantom was used.

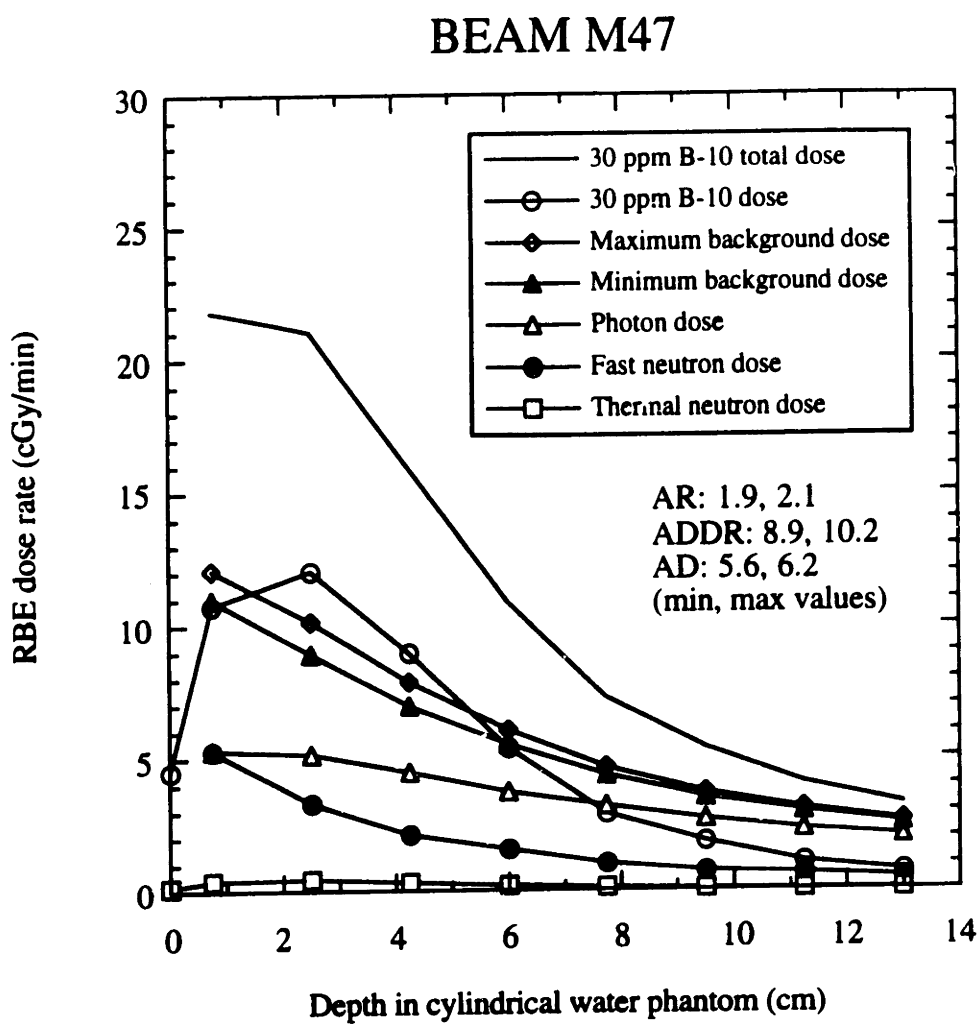

Figure 4.2. Doses measured in phantom for the M47 beam and BSH.

Unilateral irradiation.
Phantom: Cylindrical, water filled, center tube.
Reactor power: 5 MWn.
RBE's: 2.3 for B-10, 1.6 for neutrons, 1.0 for photons.
B-10 concentrations: 30 ppm for tumor, 3 ppm for maximum background, 0 ppm for minimum background.

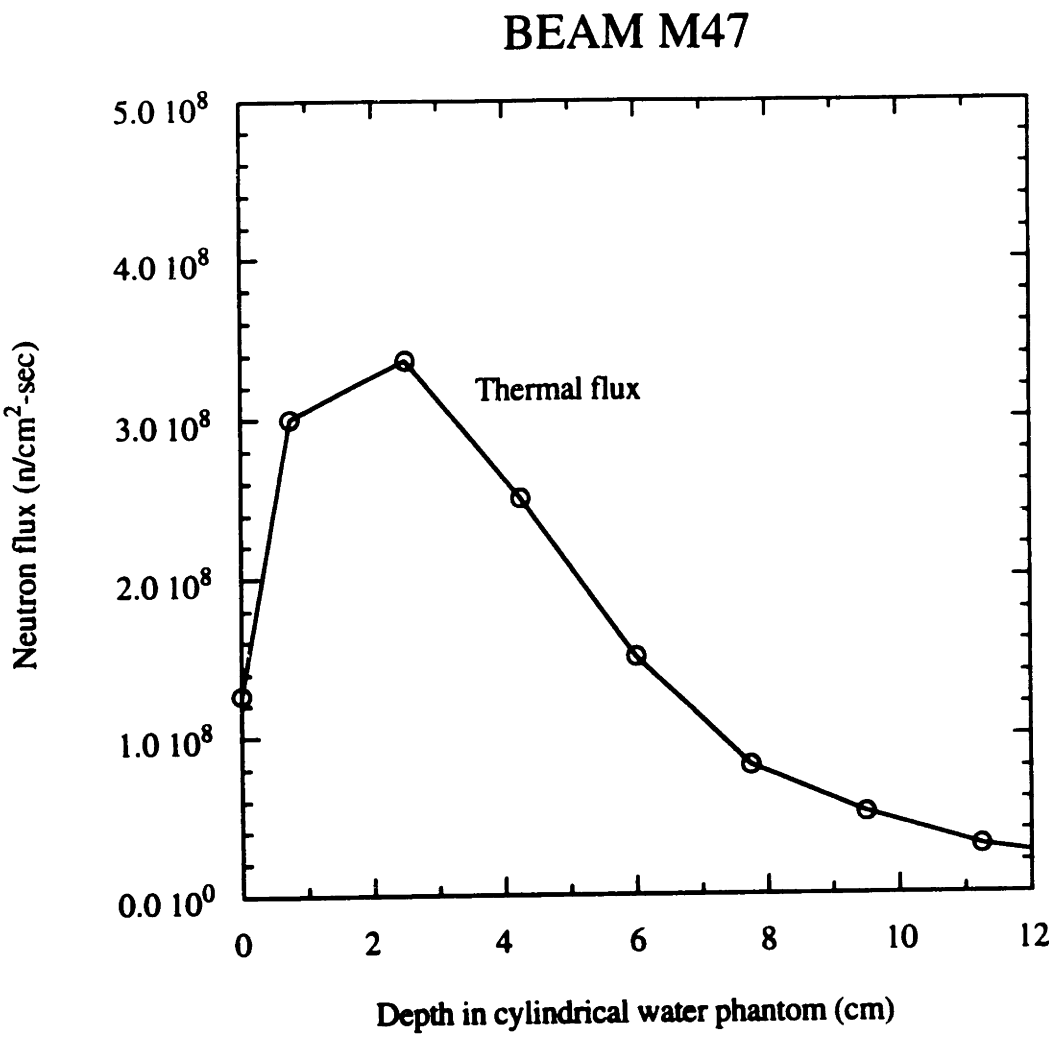

Figure 4.3 Thermal flux measured in phantom for the M47 beam.

Unilateral irradiation.
Phantom: Cylindrical, water filled, center tube.
Reactor power: 5 MWn.

varied from 6-8%, depending on the detector. A method to determine the efficiency was worked on; this method is presented in Chapter 3.

The experimental method and the calculations used to convert the raw experimental data into doses were reviewed. This review led to some changes in the calculations and some improvements in the experimental method.

With the new dosimetry, the quality of the M47 beam was worse than had been thought. The original AR was greater than 3, but the maximum AR as determined with the independent evaluation was only 2.1. The revised AR determined by Choi was 2.3.[1] The maximum AD of this beam was now only 6.2 cm, slightly short of the desired 7 cm.

4.3 EFFECTIVENESS OF SULFUR AND ALUMINUM AS FILTERS

Owing to this setback, it was decided to experimentally determine the effectiveness of sulfur and aluminum as fast neutron filters in our beam. This could be done quickly, and it was hoped that these results could be used to design an improved beam. The photon and fast neutron dose rates, and the epithermal flux, were measured in air with up to 9" of sulfur or aluminum beneath the collimator of an otherwise filterless beam. Effective attenuation coefficients were determined to see which filter material was more effective in reducing the fast neutron dose relative to the epithermal flux.

The experimental setup is shown in figure 4.4. The photon and fast neutron dose rates were measured with the usual dual chamber technique. The chambers were surrounded by a small bag of Li-6 carbonate to eliminate the thermal response of the chambers. A fission chamber (transmission pancake type, 4" diameter, labeled MIA), wrapped with a 0.020" thick sheet of cadmium, was used to measure the epithermal flux. The thermal flux was not measured.

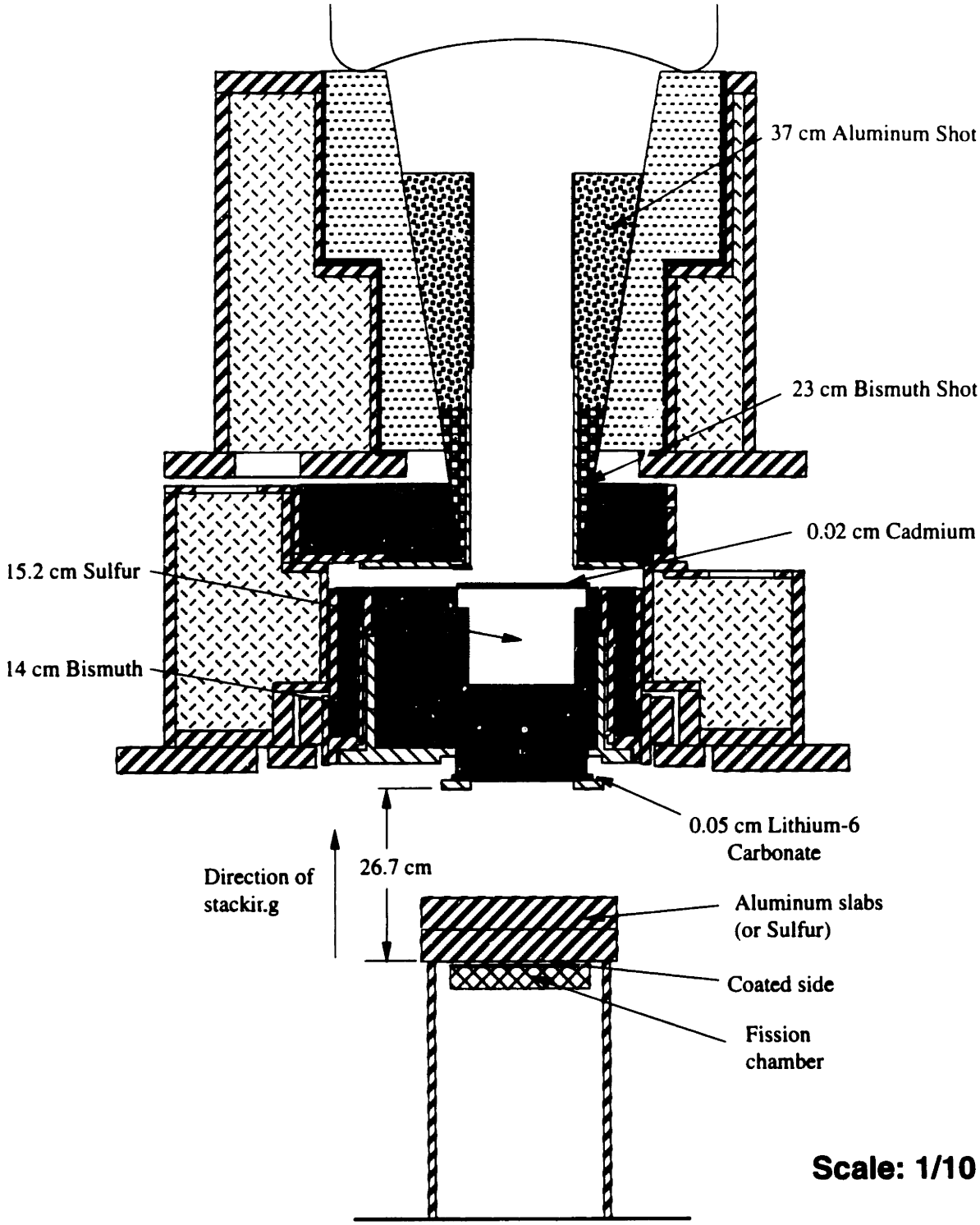

Figure 4.4. Experimental set up to test the effectiveness of sulfur and aluminum as filters. Data were taken at a reactor power of 100 kW_n so that the fission chamber would not be overloaded. All shutters were open. This is the M52 beam, but with the sulfur and aluminum removed from the stovepipe.

The fluxes and dose rates were measured with various amounts of sulfur and aluminum in the beam. The sulfur (2.0 g/cm^3) filters were discs that were 11 1/2" in diameter and 2" thick. The aluminum filters were rectangular plates, 12"x12"x2".

Two sets of ionization chamber data were obtained. In the first set, measurements were made with both chambers using a single electrometer. Switching signal cables introduced a transient electrical response to the system. Time constraints did not allow the system to completely equilibrate before the next current reading was made. The resulting data showed oscillations. Therefore, this experiment was repeated. One chamber was used to measure all filter configurations. Then, the other chamber was connected, allowed to equilibrate, and then used to measure all the filter configurations again. These data showed no oscillations. Only the second set of data is provided here.

Attenuation curves for the epithermal flux, fast neutron and gamma doses are shown in figures 4.5, 4.6, and 4.7. A least squares exponential fit was made for each data set. The first data point (0") of the dose attenuation curves was not used in the curve fit; this data point is not shown in the figures. The slope for 2" of filter was less than that for the longer filters. Since the filters used in this work were much longer than 2", the 0" data points were excluded as including them would result in a lower attenuation coefficient than would be expected with long filters. From the slopes of these curves, the measured effective attenuation coefficients were determined. These are shown in table 4.1. Similar attenuation coefficients, but incorporating the 0" data points, were reported by Choi.[1] The theoretical attenuation coefficients are shown in table 4.2. Finally, the effectiveness of a sulfur and aluminum composite filter is shown in figure 4.8.

The attenuation data were fit well with exponential curves. The effective attenuation coefficients for the epithermal flux were about 1/2 of the theoretical linear attenuation coefficients. Similarly, the effective attenuation coefficients for the fast neutron doses were about 1/3 of the linear attenuation coefficients. This probably indicates some broad beam character of the beam and filters. First, the beam itself is large relative to the size of the

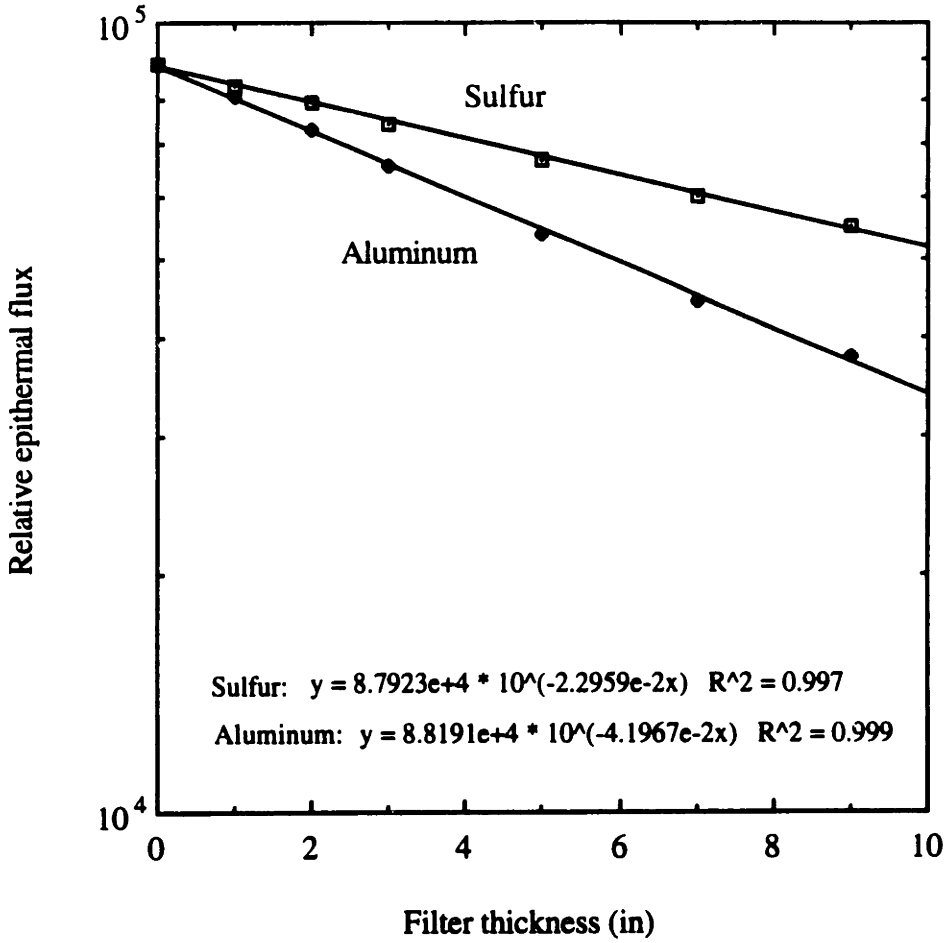

Figure 4.5. Attenuation of the epithermal flux in sulfur and aluminum as measured with the experimental set up shown in figure 4.4.

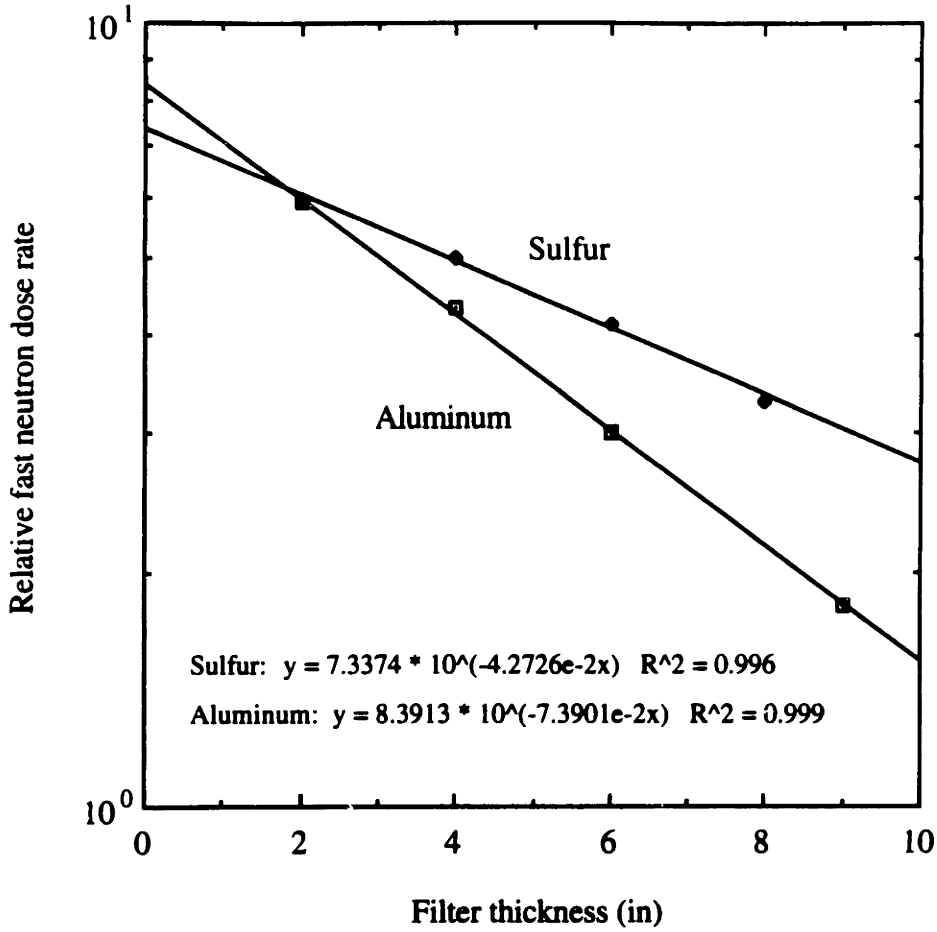

Figure 4.6. Attenuation of the fast neutron dose rate in sulfur and aluminum as measured with the experimental set up shown in figure 4.4. The carbon graphite and tissue equivalent ionization chambers were used in place of the fission chamber. The data point at 0" (not shown) was not included in the exponential curve fit. The slope of the sulfur curve appears to increase with filter thickness.

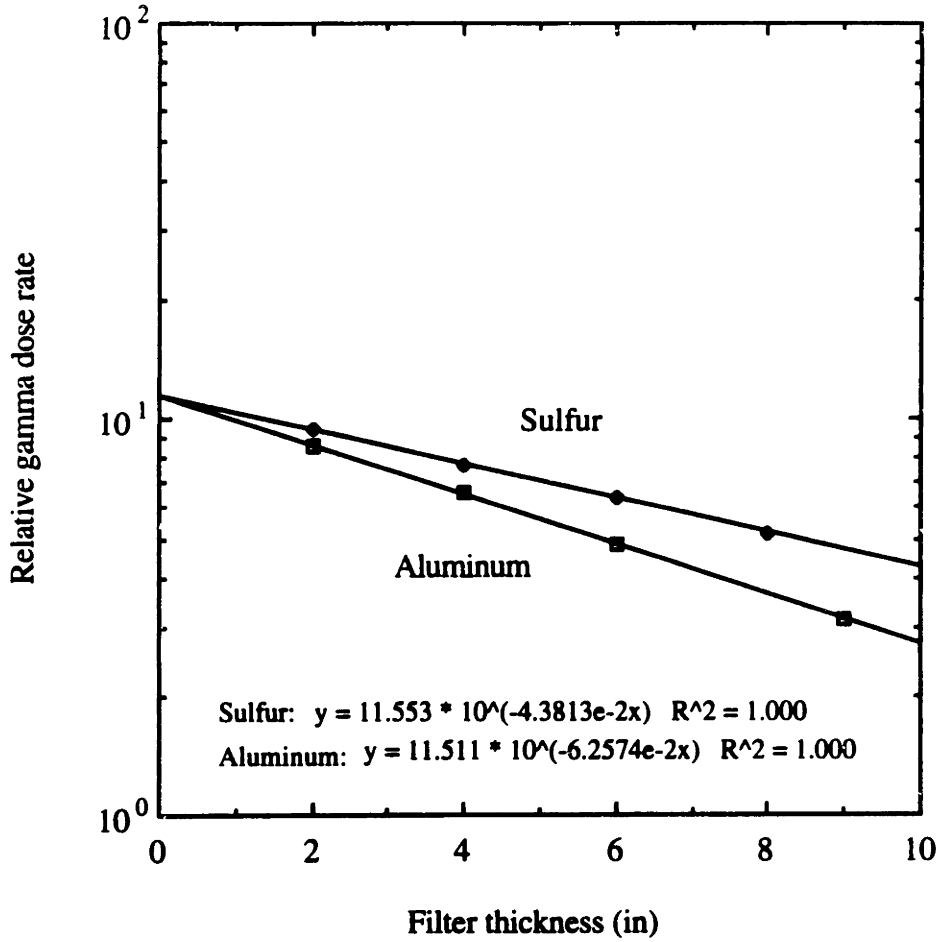

Figure 4.7. Attenuation of photons in sulfur and aluminum as measured with the experimental set up shown in figure 4.4. The carbon graphite and tissue equivalent ionization chambers were used in place of the fission chamber. The data point at 0" (not shown) was not included in the exponential curve fit.

Table 4.1. Measured effective attenuation coefficients. *

Filter material	Epithermal flux	Fast neutron dose	Photon dose
Sulfur	0.0208	0.0387 **	0.0397
Aluminum	0.0381	0.0670	0.0567

* Values in cm^{-1}.

** Using the 6 and 8" data points, this value is 0.0448 cm^{-1}.

Table 4.2. Theoretical linear attenuation coefficients.

Filter material	Density (g/cm^3)	σ_s^{epi} (b)	σ_s^{fast} (b)	μ^{epi} (cm^{-1})	μ^{fast} (cm^{-1})
Sulfur	2.0	1.1	~3.0	0.0413	0.113
Aluminum	2.7	1.35	~3.8	0.0813	0.229

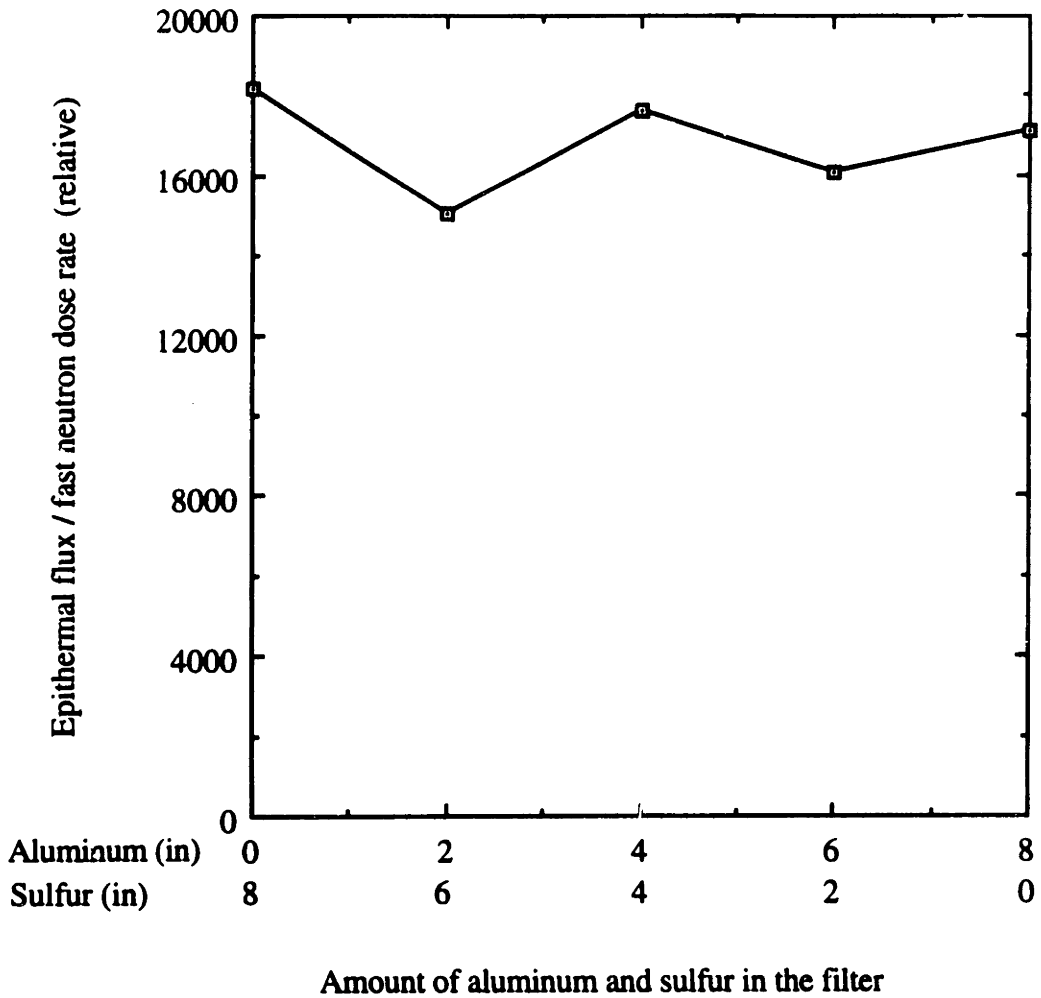

Figure 4.8. The effectiveness of a sulfur and aluminum composite filter was determined. The total thickness of filter was held constant at 8". None of the composite filters were better than sulfur or aluminum when used alone.

detectors. Second, the fission and ionization chambers were positioned just below the sulfur and aluminum filters; therefore, a sizable fraction of the neutrons and photons that scattered in the filter still reach the detectors. This fraction depends on the thickness of the filter. This was not a narrow beam geometry where the measured attenuation coefficient would be expected to approach the theoretical linear attenuation coefficients. With one exception, however, the slopes of the attenuation curves did not increase with longer filters. This is interesting as there might be a canceling of spectral and geometrical effects. The beam hardens with longer filters. Also, prompt gammas are produced within the filters, which lowers the effective photon attenuation coefficient. A more precise, quantitative analysis of these effects was not done.

The slope of the fast neutron attenuation curve for sulfur appears to increase with distance. Using just the 6 and 8" data, the slope gives an effective fast neutron dose attenuation coefficient of 0.0448 cm^{-1}. This is 16% higher than the value of 0.0387 cm^{-1} listed in table 4.1. This higher value would be more appropriate to use with the long (about 20") sulfur filters that have been used in this work.

Perhaps the most important parameter that was determined by these experiments was the ratio of the epithermal flux to fast neutron dose attenuation coefficients. Lower ratios are better. The ratios are 0.54 for sulfur and 0.57 for aluminum. Although these ratios are comparable, the higher photon attenuation per unit epithermal flux attenuation of sulfur makes sulfur a slightly better filter. Note, however, that only about half as much aluminum is needed as sulfur.

The effectiveness of a sulfur and aluminum composite filter is shown in figure 4.8. Nothing is gained by using a composite filter.

The method used to measure the effective attenuation coefficients worked well. Attenuation coefficients were measured only in the range 0-9". Although the slopes were very linear, some care should be used in extrapolating these data well beyond 9".

A similar attenuation experiment was done in which the amount of D_2O in the D_2O shutter was varied. Results of this experiment have been reported by Choi.[1] It was concluded that adding D_2O to the beam would just reduce the intensity of the beam, and would not improve the quality of the beam.

4.4 BEAM M55

At this time, it was proposed that the quality and intensity of the beam could be improved by widening the beam. A wider beam would scatter many fast neutrons that might otherwise be transmitted through the region directly surrounding a smaller beam. Also, a wider beam would transmit more useful epithermal neutrons that might otherwise be removed by scattering or absorption in this same region. A wider beam could later be delimited, if needed. It was concluded that a larger filter would be difficult to install, but that as a first step a wider collimator should be built. The then used M47 type collimator probably scattered and absorbed much of the useful flux. This collimator had 25 cm of lead, much more than needed, with only a 16 cm diameter hole through it. Also, boral plates were embedded in the lead region and one boral plate rested on top of the collimator.

The M55 beam, which incorporates the new, wider collimator, is shown in figure 4.9. Results are shown in figures 4.10 and 4.11. This beam was significantly better than previous beams. Relative to the M53 beam, which used the old collimator, the M55 beam had 25% more thermal flux in phantom and about the same fast neutron dose rate. The higher gamma dose in phantom was related to the higher thermal flux and some increase in incident gammas. The maximum AD, 8.1 cm, of the M55 beam was very good, even though the epithermal flux at the collimator exit would be expected to be nearly isotropic in the downward direction. Previously, members of our own group had though that a high AD was possible only with a highly collimated beam.

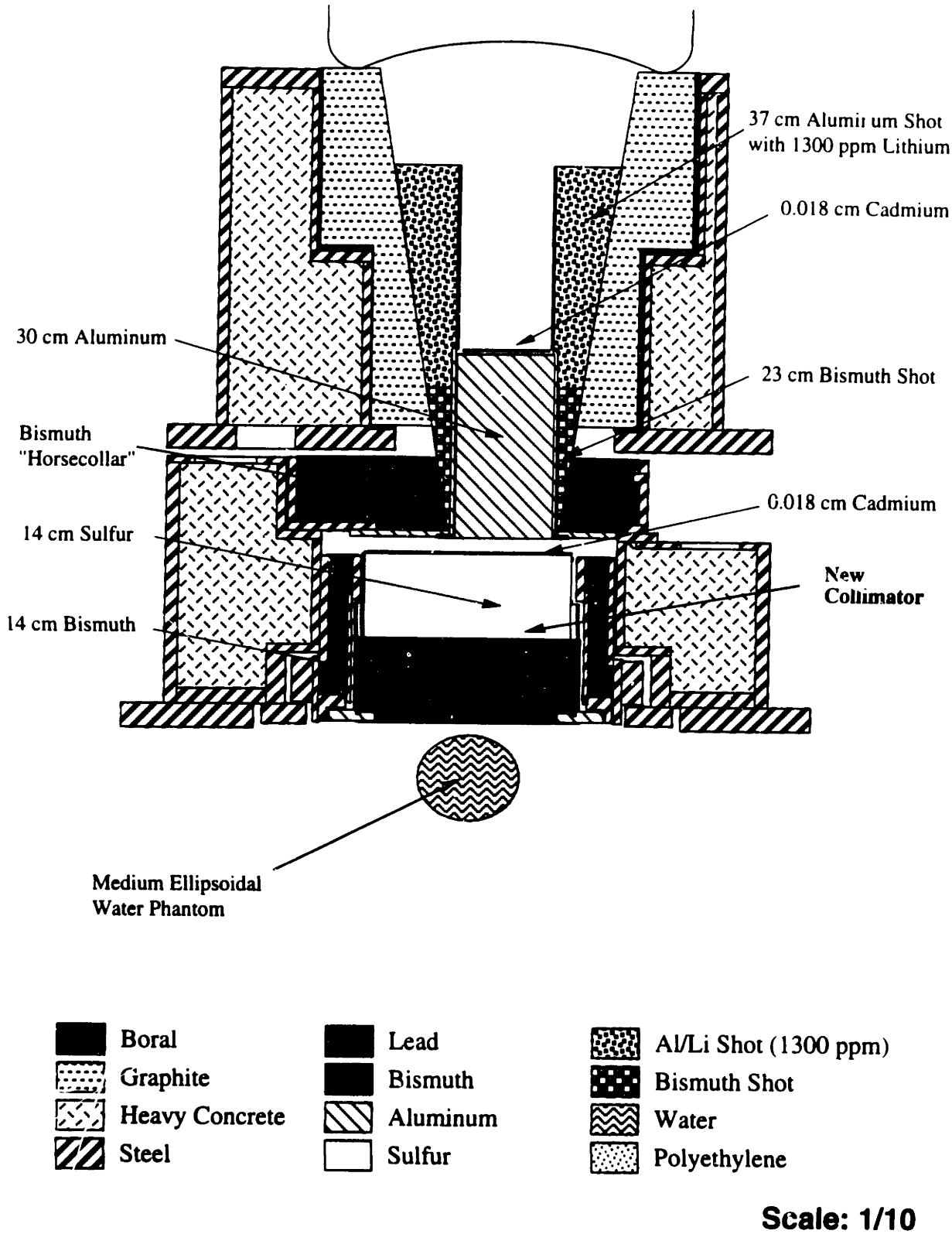

Figure 4.9. Cross sectional view of the M55 beam. The new, wider collimator and the ellipsoidal water phantom were used with this beam.

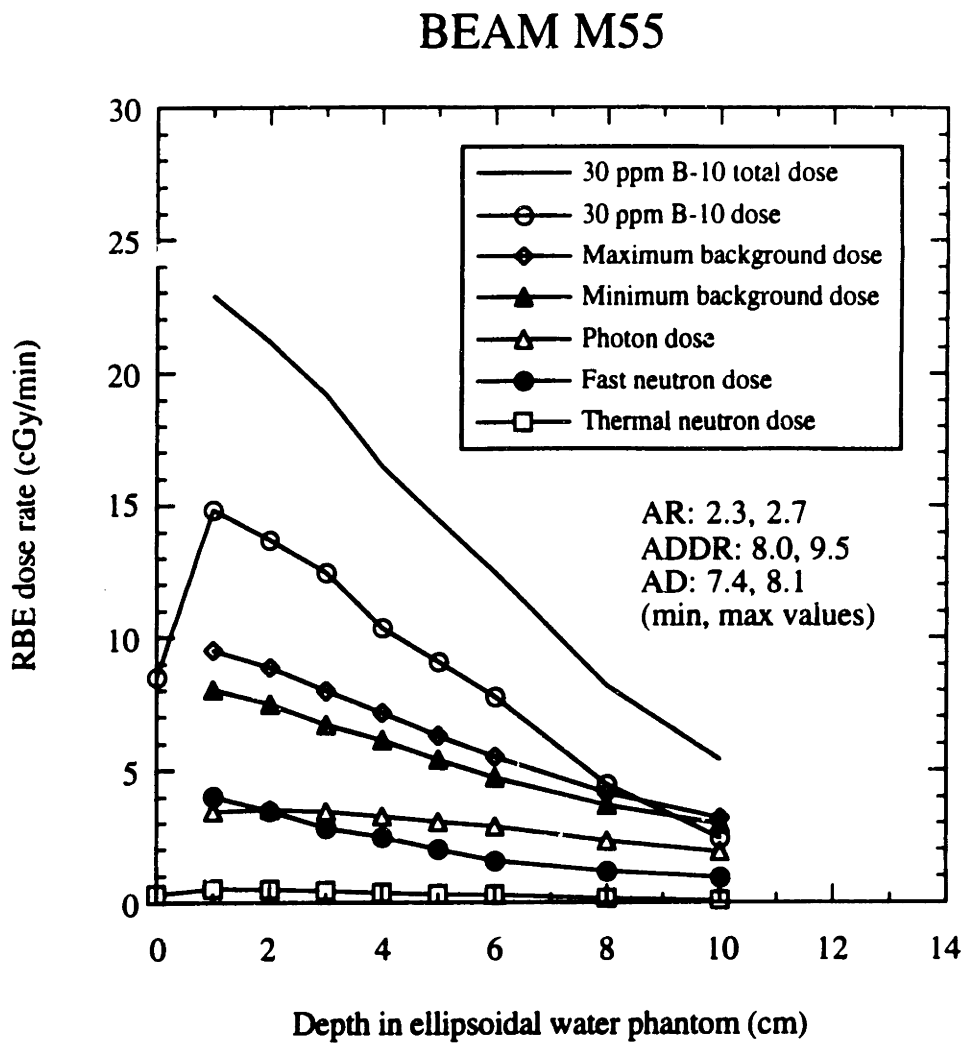

Figure 4.10. Doses measured in phantom for the M55 beam and BSH.

Unilateral irradiation.
Phantom: Medium sized, ellipsoidal, water filled, center tube.
Reactor power: 5 MWn.
RBE's: 2.3 for B-10, 1.6 for neutrons, 1.0 for photons.
B-10 concentrations: 30 ppm for tumor, 3 ppm for maximum background, 0 ppm for minimum background.
In-air data: D_{fn} = 4.2 cGy/min
D_{γ} = 1.6 cGy/min

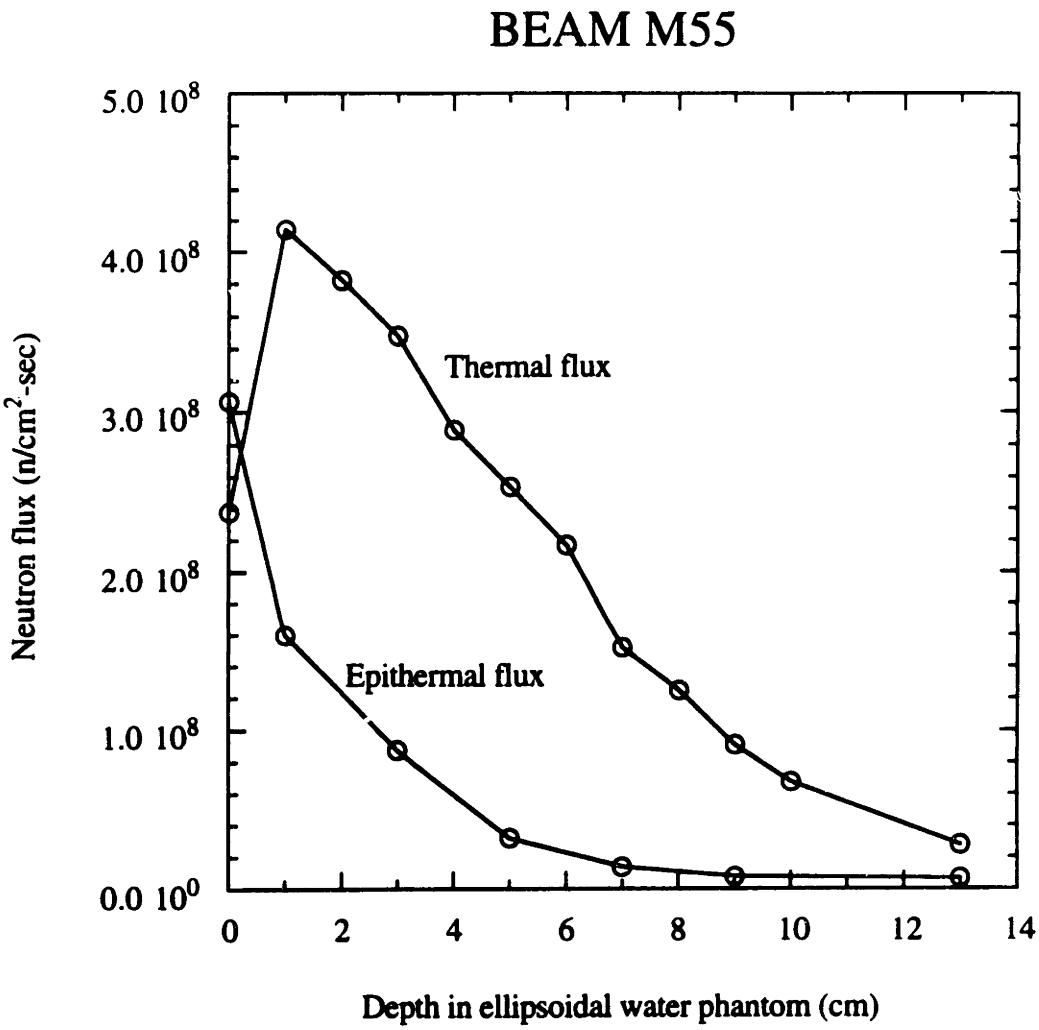

Figure 4.11. Thermal and epithermal fluxes measured in phantom for the M55 beam.

Unilateral irradiation.
Phantom: Medium sized, ellipsoidal, water filled, center tube.
Reactor power: 5 MWn.

Additional measurements were taken to more completely characterize this beam. First, the doses on top of the phantom were measured. To do this, the chambers were positioned as shown in figure 4 12. Also, the doses were determined in air. That is, the doses were determined at the bottom of the collimator without the phantom being present. The positioning of the chambers for these measurements is also shown in figure 4.12. Gold and cadmium covered gold foils were also used in air.

The in-air measurements were useful for several reasons. First, the incident photon dose is determined. In-phantom measurements give the total photon dose from incident photons plus that from prompt gammas in hydrogen. With the in-air data, the contribution that each of these components makes to the photon dose in phantom can be estimated.

Second, the epithermal flux in air is determined. Then, the in-air photon dose rate per unit epithermal flux, and the in-air fast neutron dose rate per unit epithermal flux can be calculated. These two ratios are useful as simple descriptions of a beam, and may be used to compare beams in an approximate fashion.

Third, the thermal flux in air is determined. The incident thermal flux affects the shape and magnitude of the thermal flux in phantom, especially in the first few centimeters near the top of the phantom.

Another additional measurement taken with this beam was to map the incident epithermal flux just below the collimator. Cadmium-covered gold foils were positioned as shown in figure 4.13. Relative intensities are shown in the figure. The intensity of the beam is roughly uniform, with an area of relatively high intensity below the filter and towards the back of the filter (top part of the figure). It was decided to continue positioning the phantoms below the centerline of the collimator, even though this position would be expected to lead to a slightly higher non-uniformity of the dose distribution in phantom and perhaps a few percent lower intensity of the beam in phantom.

The original dosimetry on this beam was done by Choi.[1] Because the quality of this beam at first appeared so good, it was decided to use this beam for clinical irradiations

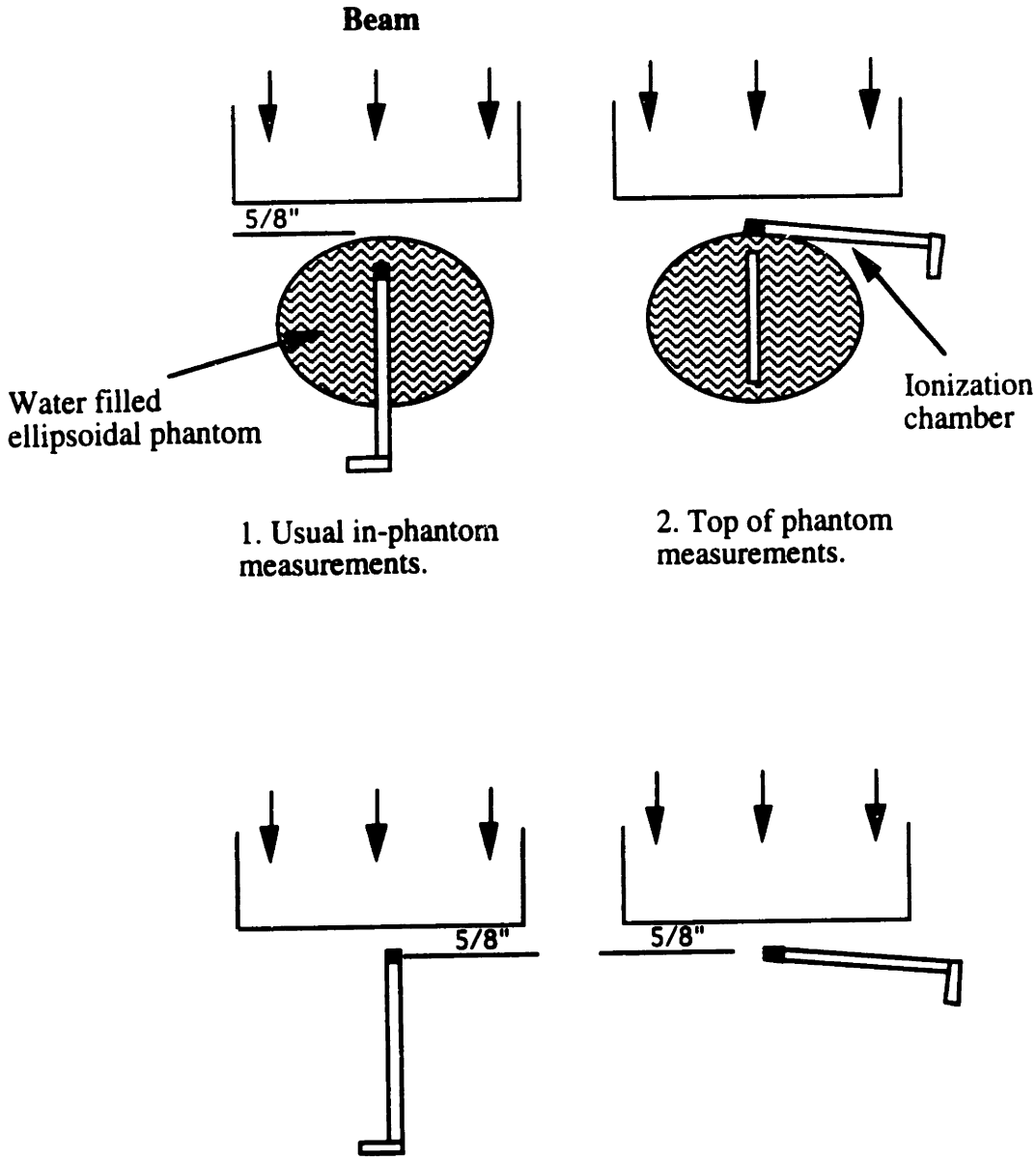

Figure 4.12. Positioning of the ionization chambers for the different types of measurements. The in-air measurements are taken with the ionization chamber nearly horizontal. One measurement was made with the vertically positioned chamber; this measurement gave about the same results as with the horizontally positioned chamber. The distance between the bottom of the beam and the top of the phantom varied slightly from beam to beam.

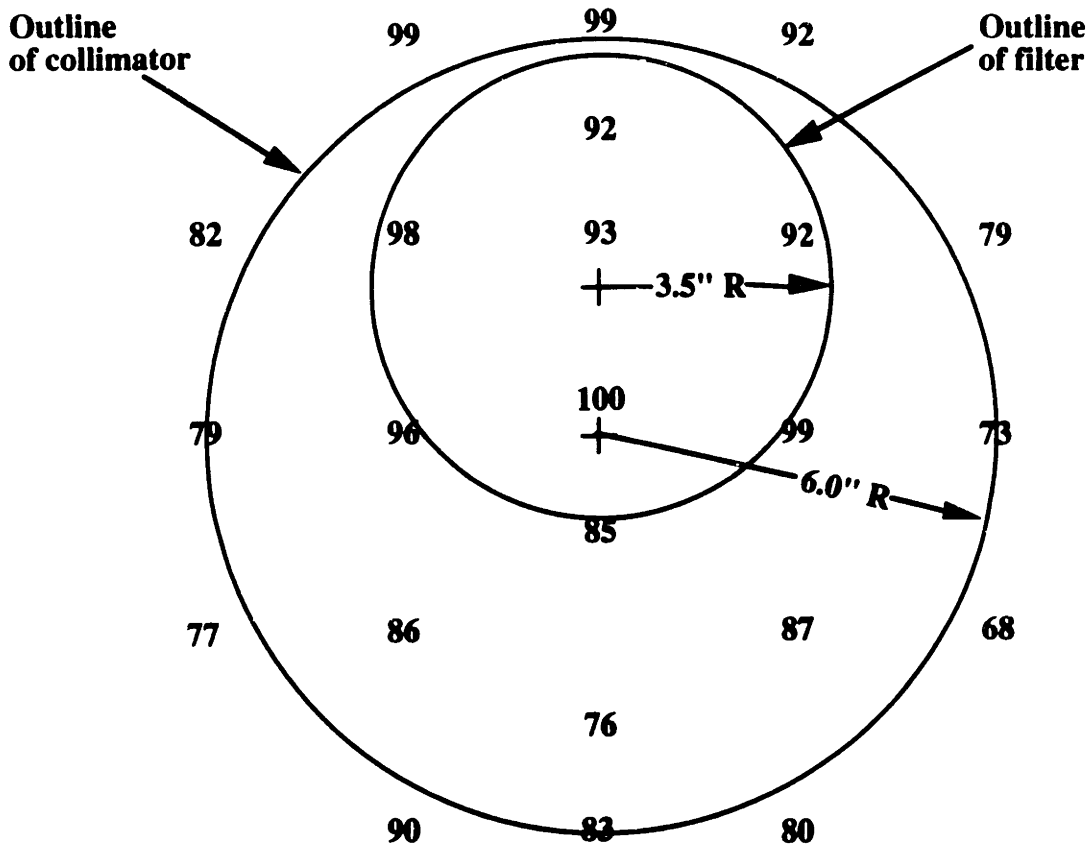

Figure 4.13. The epithermal flux below the M55 beam was mapped with cadmium-covered gold foils in air. The values shown are normalized to 100%, which occurred at the centerline of the collimator. The beam is large and roughly uniform, with slightly higher intensity below the filter and towards the back of the beam.

of patients with glioblastoma. As this beam was to be used for actual irradiations of people, an independent dosimetric evaluation of the beam was needed.

The results of the independent evaluation are shown in figure 4.14. These are compared with those originally presented by Choi[1] in figure 4.15. In the original dosimetry, the photon dose was 15-20% higher while the fast neutron dose was about 10% lower at 1 cm where the fast neutron dose is highest, and increased to a factor of 2 lower at depth. The reasons for the difference were found - the neutron and photon components of the beam change slightly with time after reactor start up. To most accurately measure the fast neutron dose, the carbon graphite and tissue equivalent chambers must be used at the same position before there is a significant change in the radiation field seen by the phantom.. This effect is discussed in detail by Choi.[1]

The next beam, M56, had the same filter (30 cm of aluminum) as M55, but used the old M53 collimator. The poorer performance of the M56 beam showed that the improved performance of the M55 beam was attributable to the new collimator. It was concluded that there was significant attenuation of useful flux in the lead and boral of the old collimator.

4.5 BEAM M57

With the results of the M55 beam, there was renewed interest in widening the upper filter part of the beam. It was proposed that there was significant attenuation of useful flux in the bismuth shot and in the bismuth horsecollar immediately surrounding the beam. Removing the bismuth shot and increasing the diameter of the hole in the horsecollar, or alternatively replacing these materials with a good filter such as aluminum or sulfur would be expected to improve the beam. There were some arguments against the expanded filter design. It was proposed that a larger beam would have a lower intensity than the original

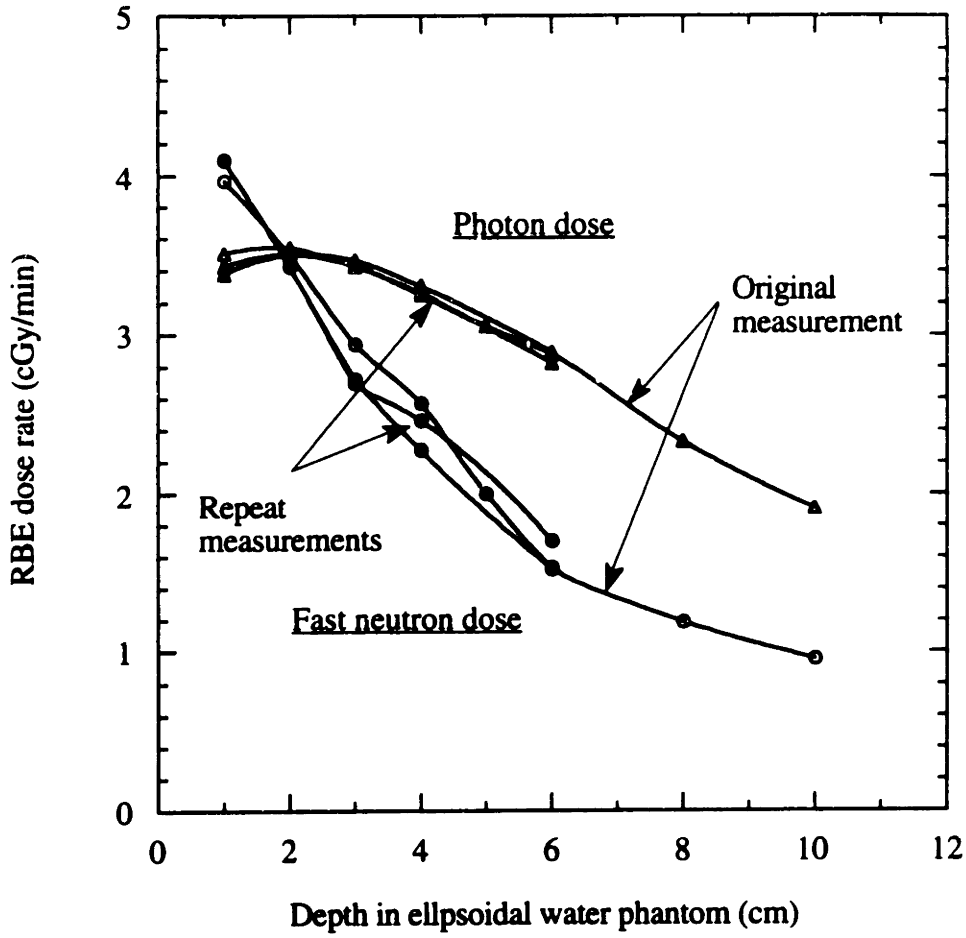

Figure 4.14. The repeatability of the dual chamber technique was tested by twice re-measuring the M55 beam with the ellipsoidal water phantom. The photon doses repeated within 1-2% of the average, while most of the fast neutron doses repeated within 3-4% of the average.

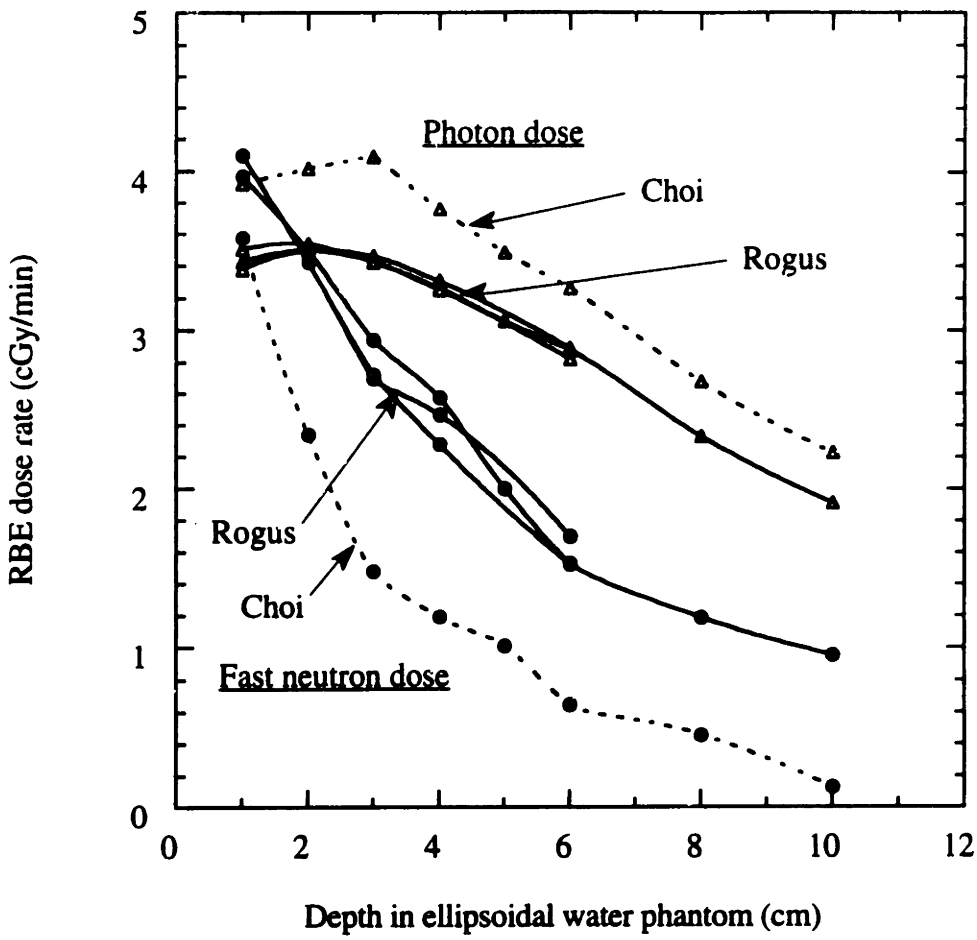

Figure 4.15. Comparison of the original data presented by Choi and by Rogus. This data is for the M55 beam, ellipsoidal water phantom. This beam was measured 3 times by Rogus. Repeated measurements agreed well. Choi's original photon doses were 15-20% higher than those of Rogus. Choi's original fast neutron doses were roughly 10% lower at 1 cm and increased to a factor of 2 lower at depth.

beam, and that the beam's design, construction, and installation would require much work. However, the decision was made to move ahead.

The fundamental change made with the M57 beam was to increase the diameter of the beam from 7 to 9 inches by installing a horsecollar with a larger aperture. This increases the area of the beam by 65%, and was expected to increase the thermal flux in phantom by about 35%. The increase in flux was expected to be less than the increase in area since the additional neutrons, being further from the centerline, would have to travel through a longer distance of bismuth and would subtend less of a solid angle relative to the phantom.

New upper aluminum and sulfur filters were designed and built, as well as a stovepipe that the filters are inserted into. A new horsecollar was also designed and built. Additional supporting structures such as retaining rings and bars were built. A new aluminum liner was made and high purity aluminum shot was bought. Some assistance with machining was provided by the NRL machine shop. The frame of the horsecollar was made by an outside company, as our own machine shop did not have a lathe big enough to swing this piece. The lead was poured by a local smelter. Molds were made for the bismuth inserts, and the bismuth was poured here.

Drawings and other information on the new components are on file at the Reactor Operations Office. Several drawings, needed to understand the important filtering capacity of the beams, are included in Appendix A of this report.

Installing the horsecollar required removing a large amount of shielding from beneath the reactor. The lead shutter, outer plug, and old horsecollar had to be removed. The old shot and the aluminum liner were removed. A new liner was installed. The new horsecollar was installed, and then the outer plug and lead shutter were reinstalled. The new aluminum shot was added to the cone region using a blower, as shown in figure 4.16.

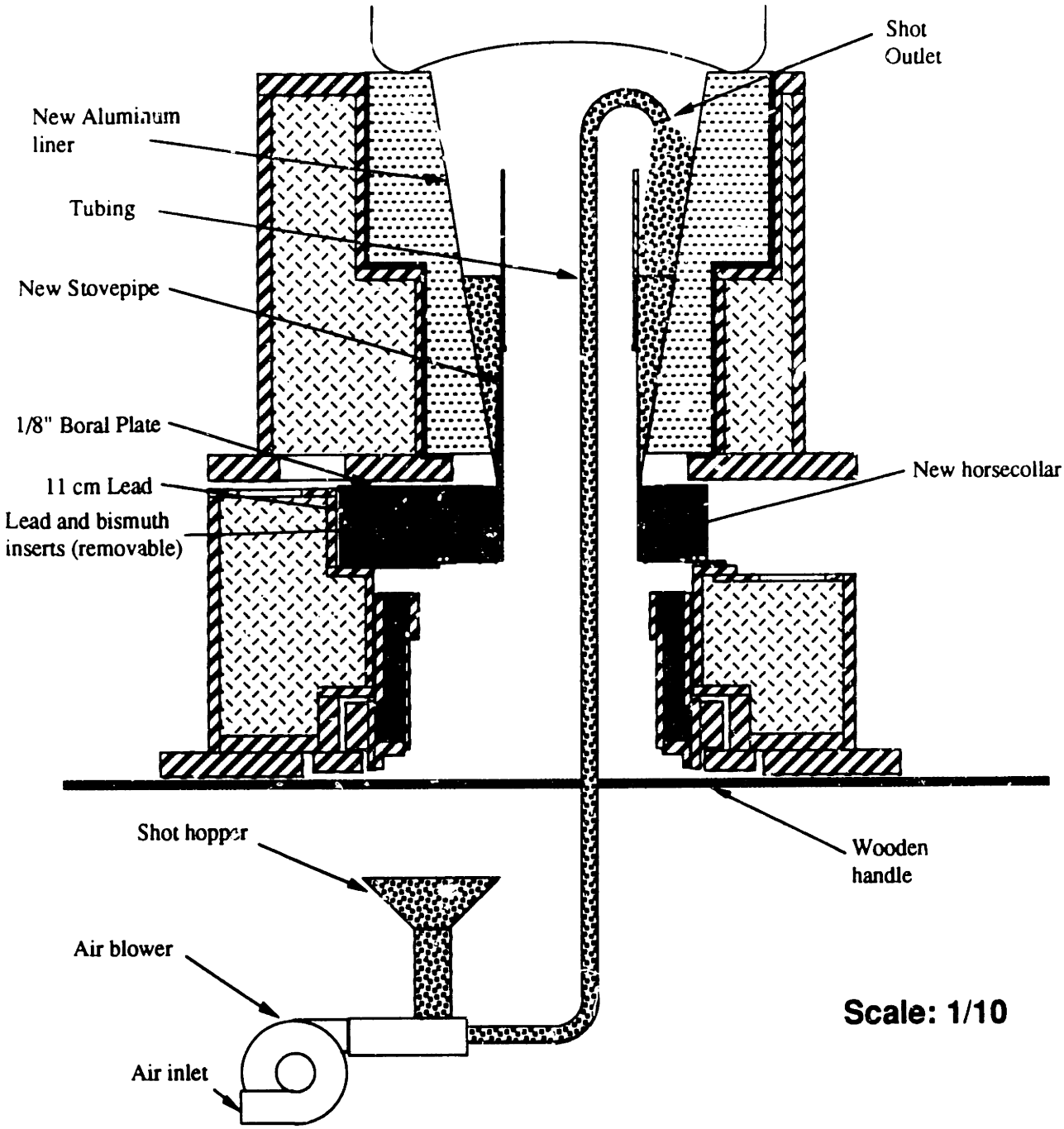

Figure 4.16. 46 cm of pure aluminum shot was added to the cone region using the blower and tubing shown. About 10 shots were added to the hopper at a time, adding too many shots clogged the tubing. The wooden handle allowed the tubing to be rotated without exposing the body to a high radiation area caused by streaming down the empty stovepipe and collimator.

Personnel from Reactor Operations, Radiological Protection Office, Maintenance, and the Machine Shop were all involved. With careful planning, the installation went smoothly and safely.

The first wider diameter beam characterized was M57. The new sulfur filter was used since it had been concluded from the aluminum and sulfur attenuation experiments discussed earlier that sulfur was a moderately better filter than aluminum. Experimentally determined attenuation coefficients for the epithermal flux, fast neutron dose, and photon dose were used to estimate the height of sulfur that would give the same thermal flux in phantom as the 30 cm of aluminum used in the M55 beam. The result was 48 cm of sulfur, plus the aluminum endcaps of the filter. This filter was predicted to give the same thermal flux in phantom, but 33% less fast neutron dose and gamma dose in air relative to the M55 beam. These predicted intensities, however, did not account for the increase in beam area. The larger beam area of the M57 beam was expected to result in an even higher flux in phantom.

The M57 beam is shown in figure 4.17. Results of the characterization are shown in figures 4.18-4.21. As shown, the photon and fast neutron doses were consistent with those expected based on the effective attenuation coefficients. However, the thermal flux in phantom was only about 10% higher than in the M55 beam. This was significantly less than expected. It was postulated that a boral plate on top of the new horsecollar was responsible for some reduction in epithermal flux. It was also postulated that the boral plate could partially explain the relatively low cadmium ratio of this beam as well. Monte Carlo simulations with and without the boral plate indeed predicted that the boral would reduce the thermal flux in phantom by 15%.[2] This 15% effect, and the actually measured 10% increase, sum to 25%. This is reasonably close to the anticipated 35% increase.

Another explanation for the lower thermal flux is that the sources for the two beams were different. The fuel loading configuration of the M57 beam was a three dummy core with the dummies in the center of the core. Different core configurations would be

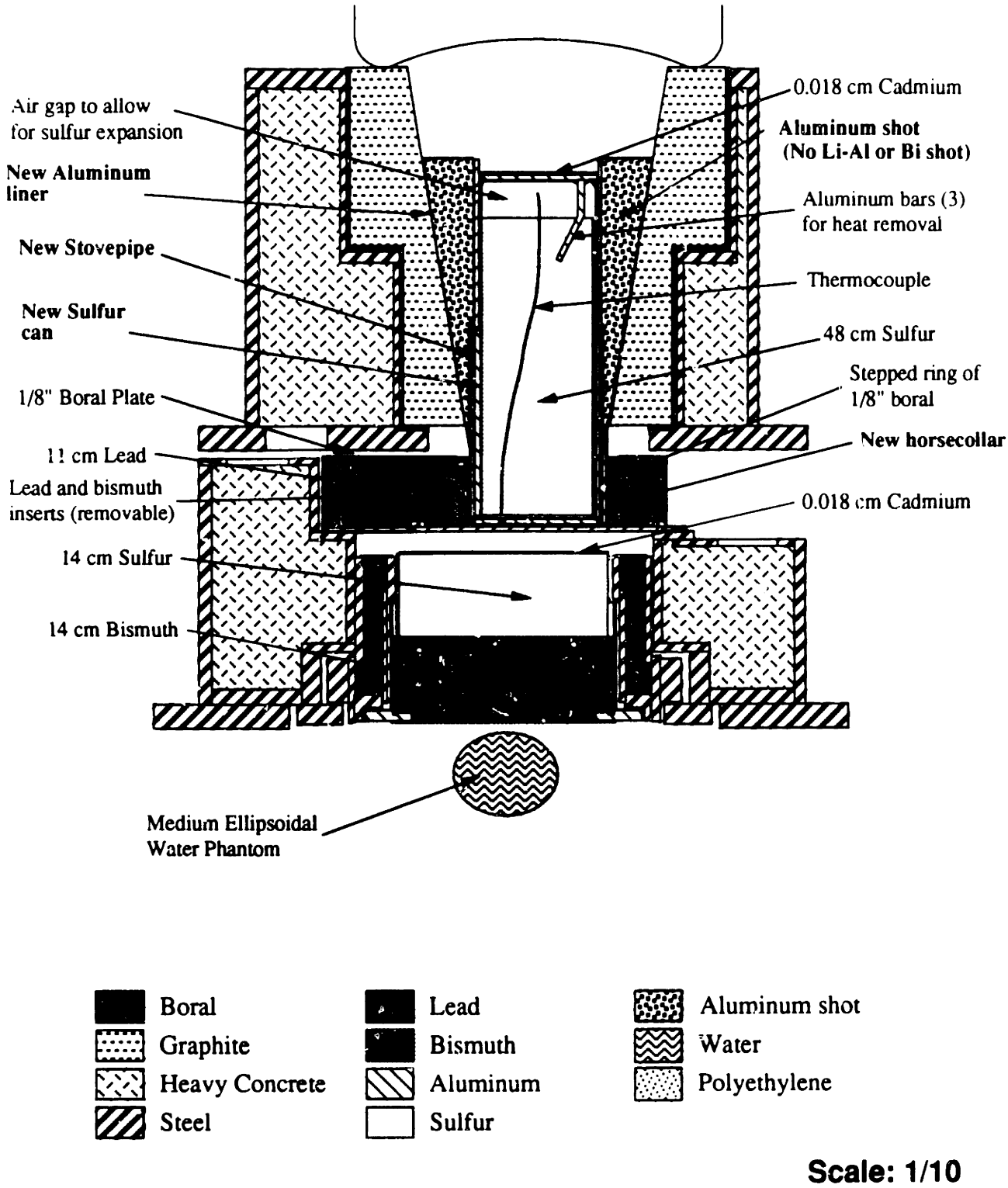

Figure 4.17. Cross sectional view of the M57 beam. Note the new shot, stovepipe, filters, and horsecollar. The new horsecollar has inserts that can be easily removed to widen the beam even more.

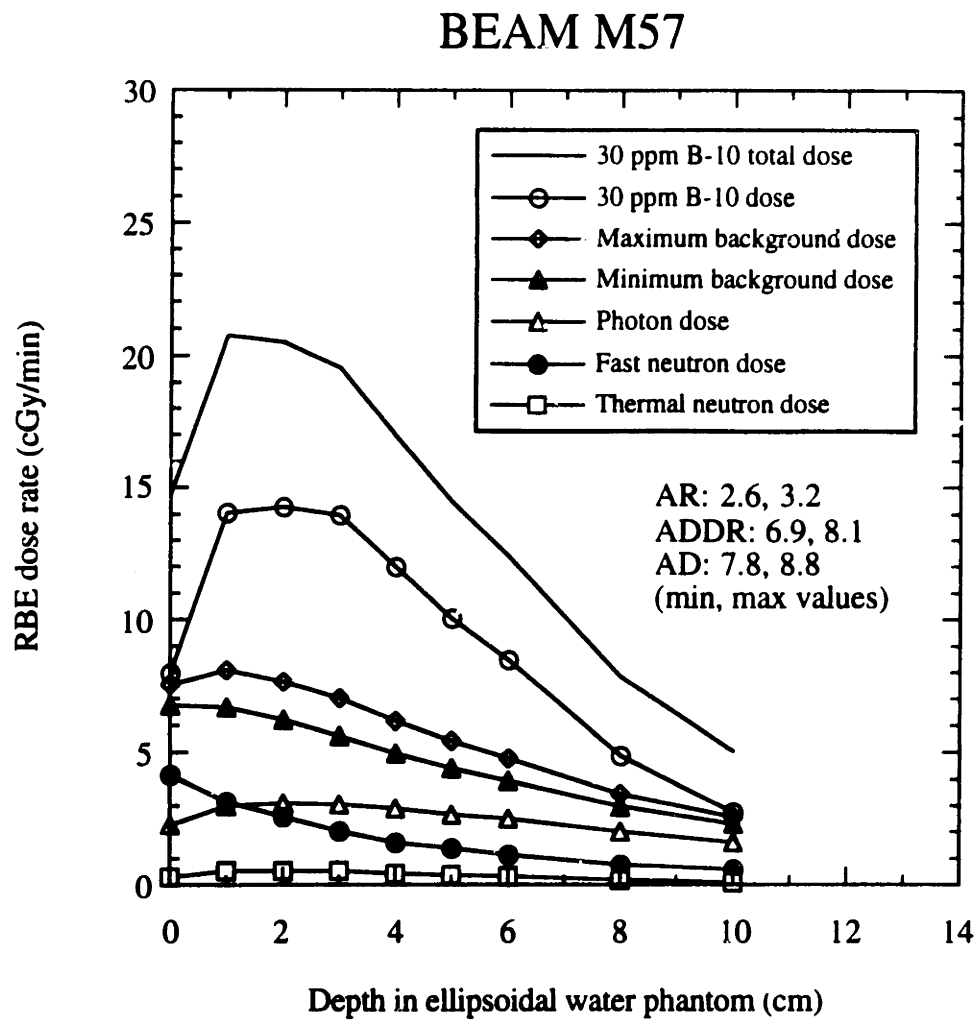

Figure 4.18. Doses measured in phantom for the M57 beam and BSH.

Unilateral irradiation.
Phantom: Medium sized, ellipsoidal, water filled, center tube.
Reactor power: 5 MWn.
RBE's: 2.3 for B-10, 1.6 for neutrons, 1.0 for photons.
B-10 concentrations: 30 ppm for tumor, 3 ppm for maximum background, 0 ppm for minimum background.
In-air data: D_{fn} = 3.4 cGy/min
D_{γ} = 1.2 cGy/min

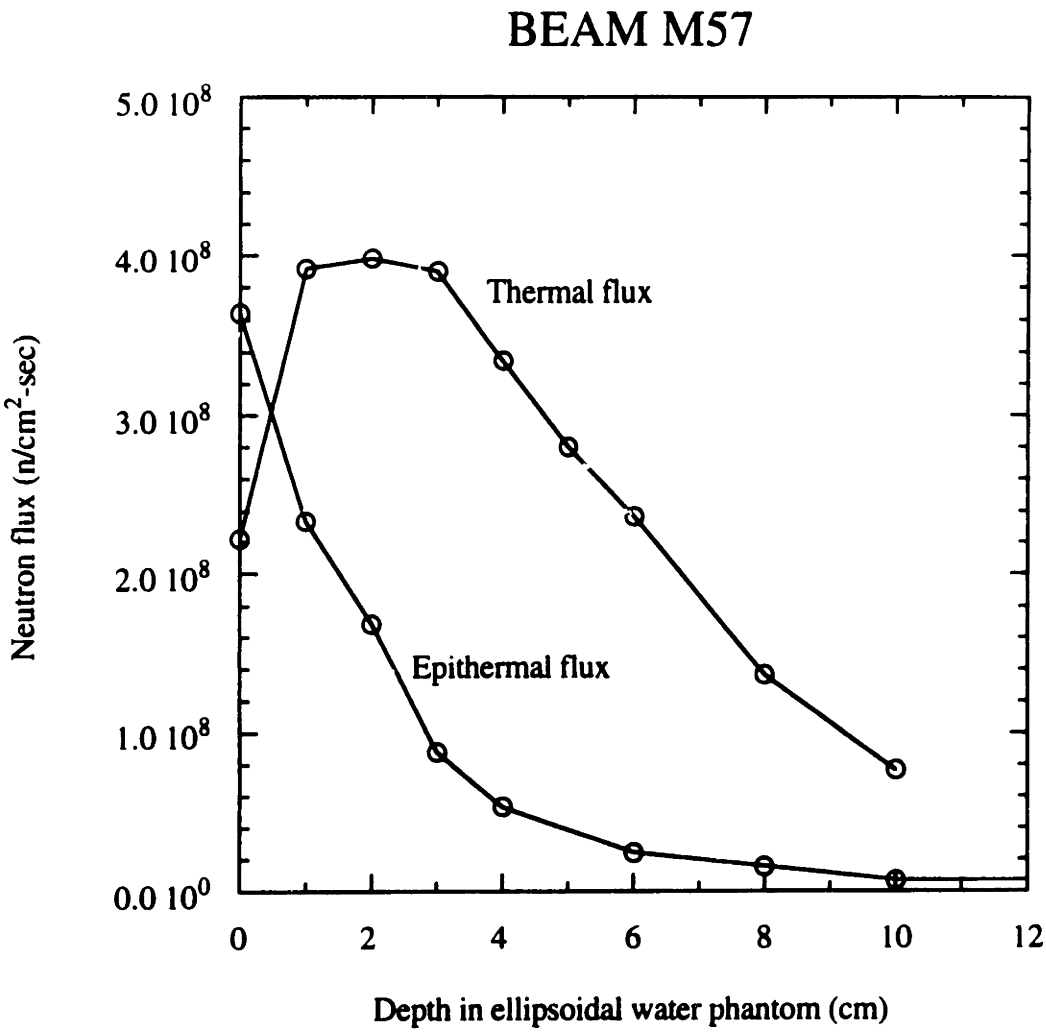

Figure 4.19. Thermal and epithermal fluxes measured in phantom for the M57 beam.

Unilateral irradiation.
Phantom: Medium sized, ellipsoidal, water filled, center tube.
Reactor power: 5 MWn.

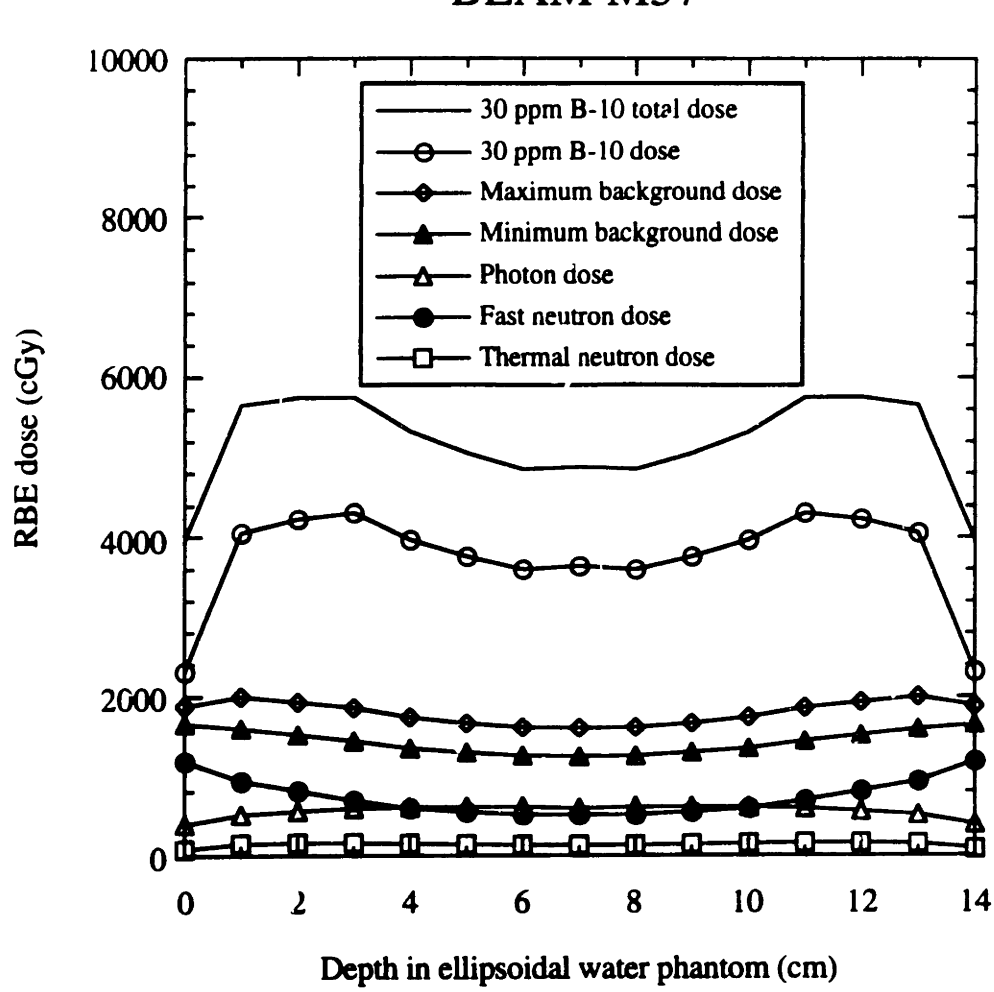

Figure 4.20. Doses measured in phantom for the M57 beam and BSH, assuming a bilateral irradiation. The doses were normalized so that the maximum dose to healthy tissue was 2000 RBE cGy.

Bilateral irradiation.
Phantom: Medium sized, ellipsoidal, water filled, center tube.
Reactor power: 5 MWn.
RBE's: 2.3 for B-10, 1.6 for neutrons, 1.0 for photons.
B-10 concentrations: 30 ppm for tumor, 3 ppm for maximum background, 0 ppm for minimum background.
Maximum dose: 2000 RBE cGy to healthy tissue.

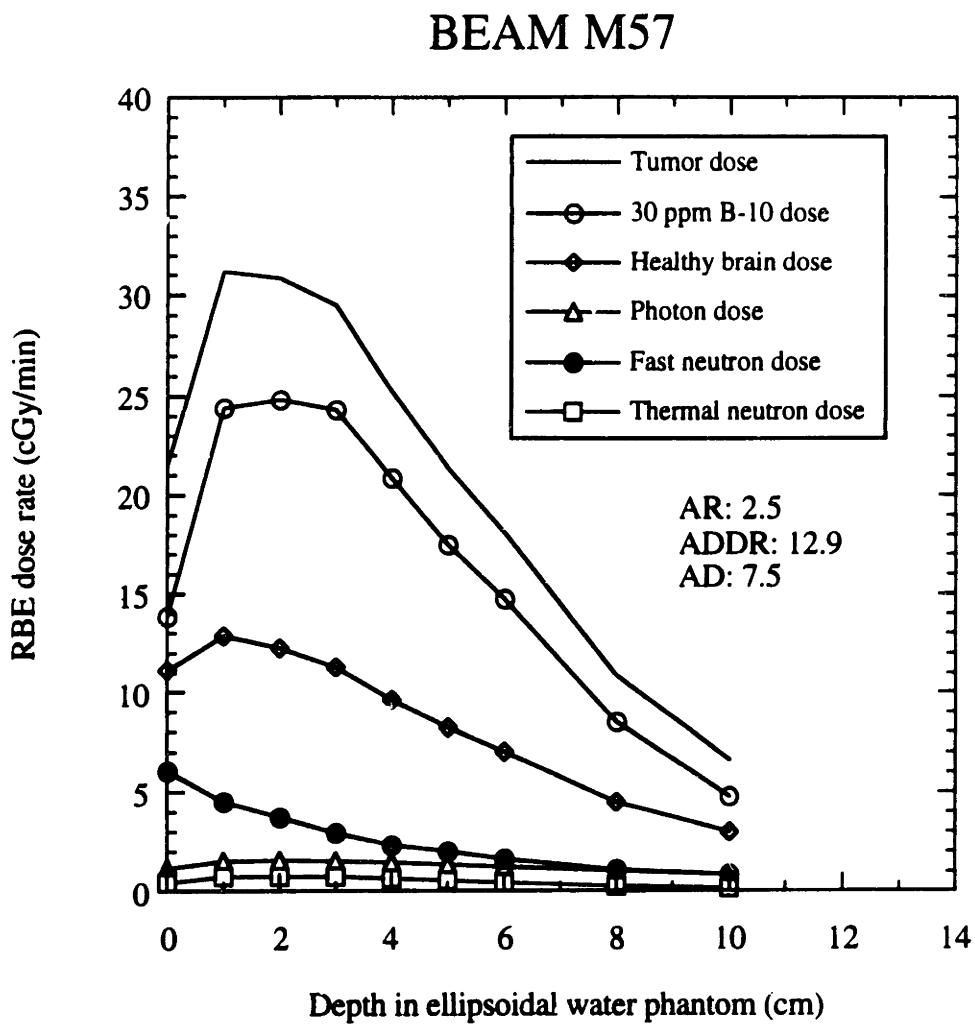

Figure 4.21. Doses measured in phantom for the M57 beam and BPA.

Unilateral irradiation.
Phantom: Medium sized, ellipsoidal, water filled, center tube.
Reactor power: 5 MWn.
RBE's: 4.0 for B-10, 2.3 for neutrons, 0.5 for photons.
B-10 concentrations: 30 ppm for tumor, 7.5 ppm for healthy brain.
In-air data: D_{fn} = 4.9 cGy/min
D_{γ} = 0.60 cGy/min

expected to change the effective axial or radial spatial distribution of epithermal flux. The neutron spectrum as seen by the filters might also change. The effects of changes in fuel loading have not been investigated experimentally.

These issues aside, the M57 beam was by far the best beam to date. It has a high maximum AR (3.2), excellent maximum AD (8.9 cm), and acceptable ADDR's (6.8 and 8.1 RBE cGy/min). This beam is characterized by a deeply penetrating thermal flux with a desirable drop near the surface so that the background doses do not increase at the surface. The incident photon dose was measured in air at only 1.2 RBE cGy/min.

Figure 4.20 shows the uniformity of this beam under conditions of a bilateral irradiation with fractionation. An effective photon RBE of 0.5 was assumed. In this irradiation the maximum dose to healthy brain would be at the tolerable limit of 2000 RBE cGy. The maximum dose to healthy brain limits the dose that can be delivered to tumor. For this beam, the healthy brain dose is relatively uniform; therefore, the dose to tumor is not limited by an undesirable peak in the dose to healthy brain. It should also be noted that the dose to tumor at the midline is only 18% less than the maximum dose to tumor which occurs at 2-3 cm. These figures are valid only for BSH.

A dose plot valid for BPA, the B-10 drug that will be used in clinical trials at MIT, is shown in figure 4.21. For BPA, the B-10 concentration is assumed to be 30 ppm in tumor and 7.5 ppm in healthy brain. Also, the RBE's were taken to be 4.0 for the B-10 reaction, 2.3 for fast neutrons and the N-14(n,p) reaction, and 0.5 for photons (refer to Chapter 2).

This was the first dose-in-phantom result determined specifically for BPA. Only a single curve is given for healthy brain, in contrast to the maximum and minimum background curves given previously for BSH. Also, only a single parameter is given for the AD and ADDR.

An engineering and safety concern with this beam was what temperature the sulfur filter would reach with the beam on. Using a thermocouple placed within and near the top

of the sulfur filter, the temperature was measured twice for this beam. Results are reported in Appendix B.

4.6 BEAM M58

Since the thermal flux in phantom of the M57 beam was less than expected, a more direct comparison of the new, larger diameter beam with the smaller diameter beam was made. Using a 30 cm aluminum filter, a direct comparison with the M55 beam was possible. The M55 beam also had an upper filter of 30 cm aluminum, and both beams had the same lower collimator.

The M58 beam is shown in figure 4.22. Results are provided in figures 4.23 and 4.24. In-air measurements showed the M58 beam to have a marginally lower incident fast neutron and photon doses and a slightly lower thermal flux, relative to the M55 beam. The epithermal fluxes were also similar. In-phantom measurements showed that the M58 beam had the same thermal flux at depth but a slightly lower flux in the first 2 cm. This is partially attributable to the higher incident thermal flux of the M55 beam. The M58 beam had marginally lower fast neutron and photon doses in phantom. The total tumor dose, therefore, is more uniform with the M58 beam than with the M55 beam. The M58 beam also has a marginally better AR and a 0.5 cm higher AD. The ADDR's for the M58 beam are also slightly lower; the minimum ADDR is lower since the incident photon and fast neutron doses are lower while the maximum ADDR is lower because of these effects and the lower incident thermal flux.

These results, along with those of the M57 beam, proved that the full 35% increase in thermal flux predicted for the larger diameter beam would not be realized. However, the boral plates embedded in and on top of the horsecollar probably caused about a 15% reduction in the in-phantom thermal flux. Also, these results indicated that there was more

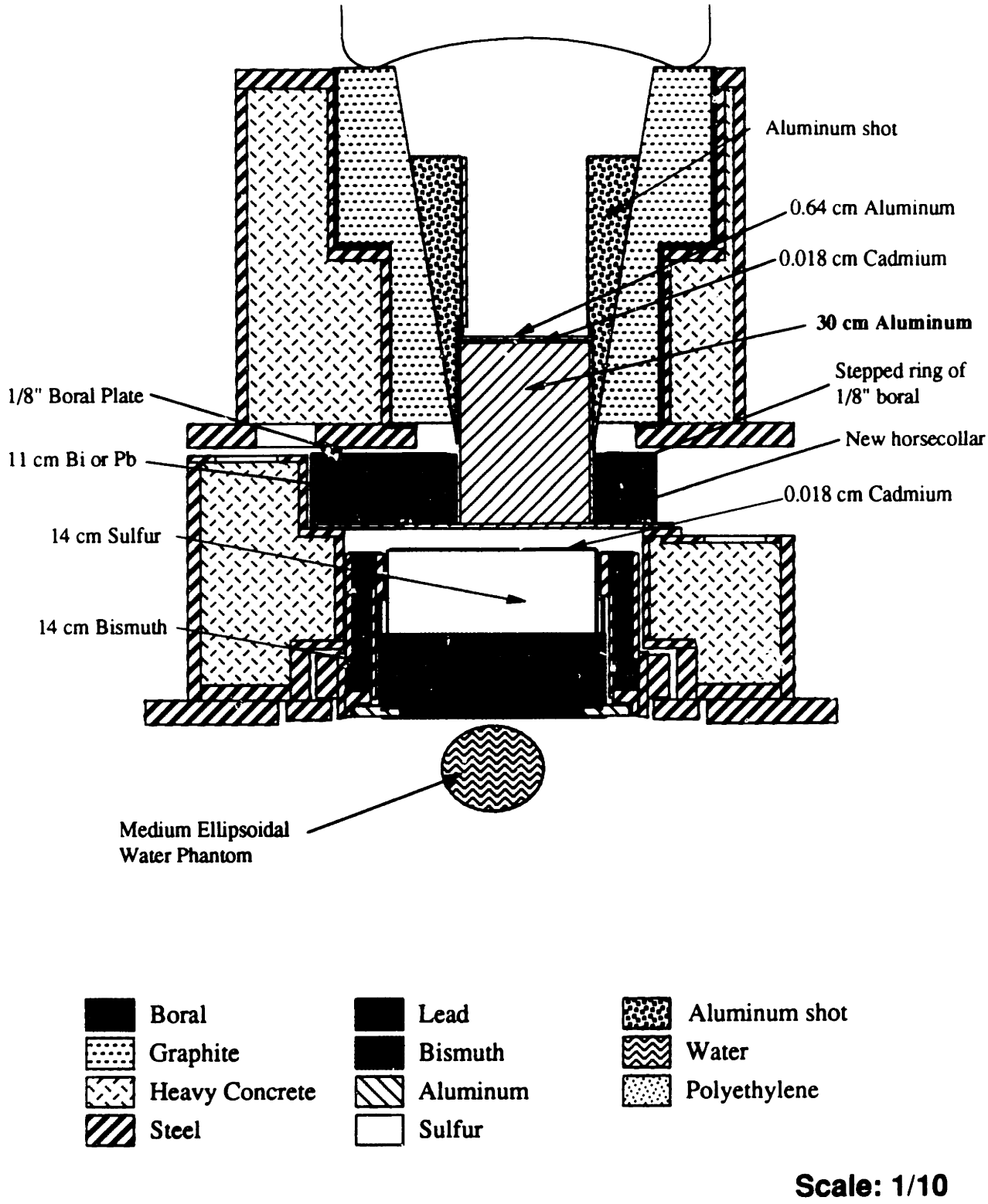

Figure 4.22. Cross sectional view of the M58 beam. The new aluminum filter was used in this beam.

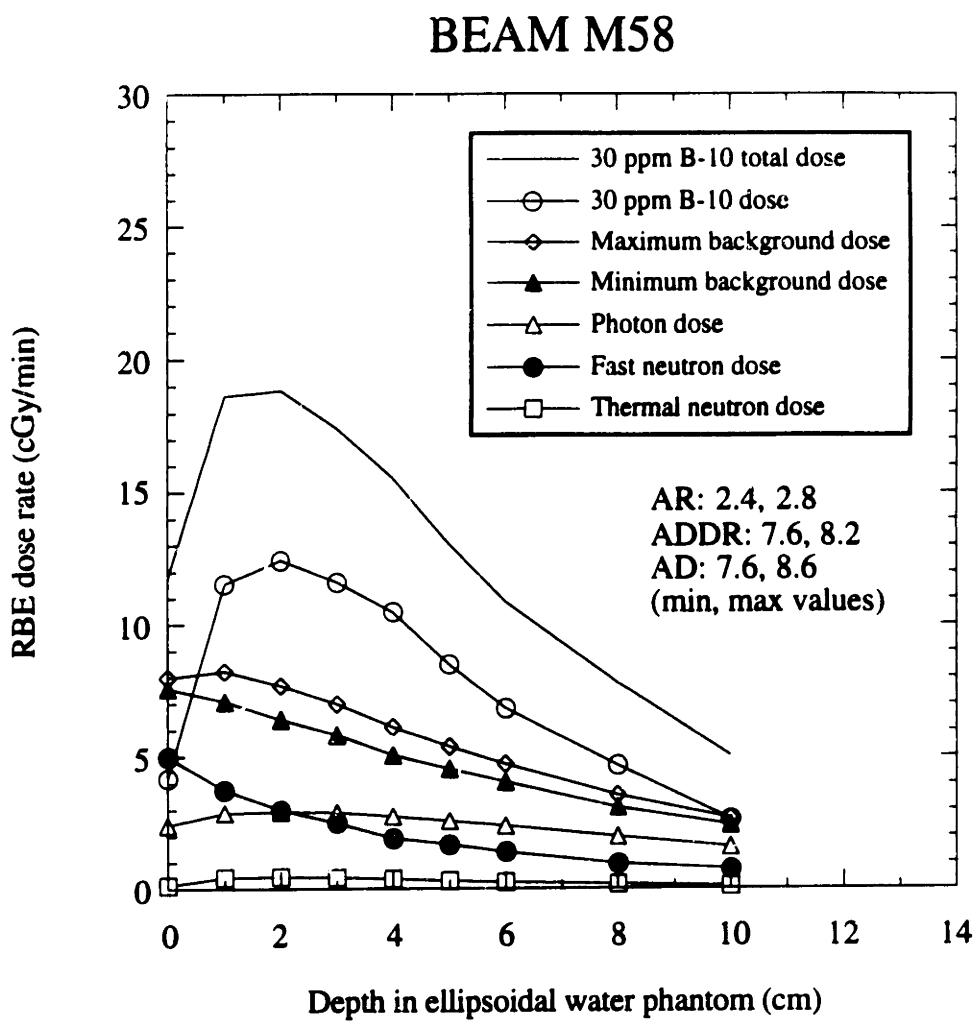

Figure 4.23. Doses measured in phantom for the M58 beam and BSH.

Unilateral irradiation.
Phantom: Medium sized, ellipsoidal, water filled, center tube.
Reactor power: 5 MWn.
RBE's: 2.3 for B-10, 1.6 for neutrons, 1.0 for photons.
B-10 concentrations: 30 ppm for tumor, 3 ppm for maximum background, 0 ppm for minimum background.
In-air data: D_{fn} = 4.2 cGy/min
D_{γ} = 1.4 cGy/min

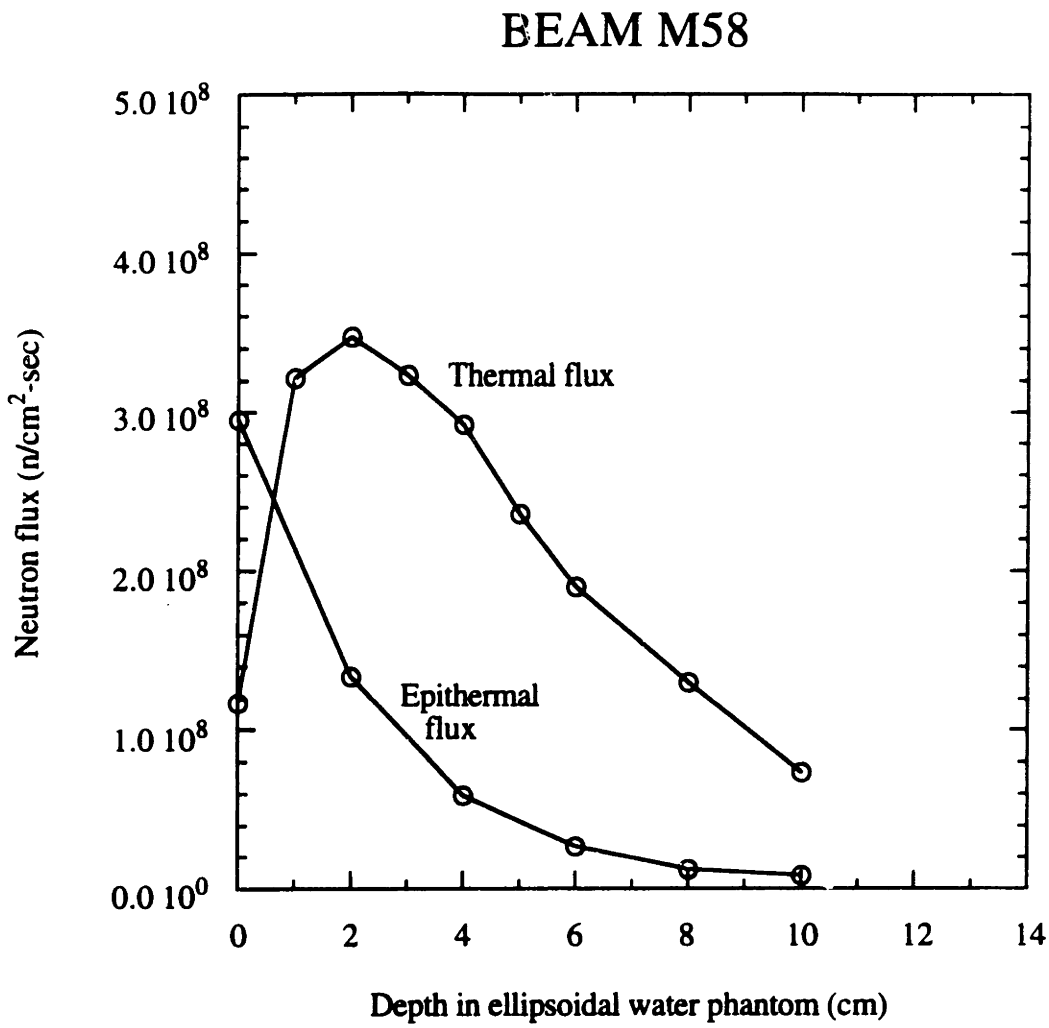

Figure 4.24. Thermal and epithermal fluxes measured in phantom for the M58 beam.

Unilateral irradiation.
Phantom: Medium sized, ellipsoidal, water filled, center tube.
Reactor power: 5 MWn.

filter in the beam line. The aluminum shot now in place has a significantly higher packing density (about 45%) than the lithiated aluminum shot (packing density about 34%) it replaced; the higher density could account for the remainder of the reduction in intensity.

Finally, it is interesting to compare the M58 with M57 beams. The same lower collimators were used, but the M58 beam had 30 cm of aluminum while the M57 beam had 48 cm of sulfur. These heights of filter resulted in beams of comparable intensity, so the better performance of the M57 beam proves that sulfur is a significantly better filter. It should be kept in mind though that a significant fraction of the beam passes through the aluminum shot. Much of the M57 beam, therefore, is filtered by both sulfur and aluminum.

Experiments with Beam M58 and Additional Bismuth

At this time, another approach to increase the intensity of the beam was sought. Since bismuth in the lower collimator is a good neutron scatterer, removing some of this bismuth would increase the beam's intensity. Some bismuth is needed as a photon shield, but its high neutron scattering cross section (about 10 barns for all neutron energies) would be expected to reduce the intensity of the epithermal neutron beam rather rapidly. Designing and building a new collimator would be expensive and time consuming. Therefore, an experiment was designed to determine the doses and epithermal flux with various amounts of bismuth that would be added below the collimator of the M58 beam. These data could then be extrapolated backward somewhat, that is, they could be used to estimate the doses that would be expected with less bismuth in the beam.

The experimental set up is shown in figure 4.25. Results are shown in figure 4.26. This experiment demonstrated that the bismuth greatly reduces the intensity of the beam and that adding more bismuth below the collimator reduces the epithermal flux, fast neutron

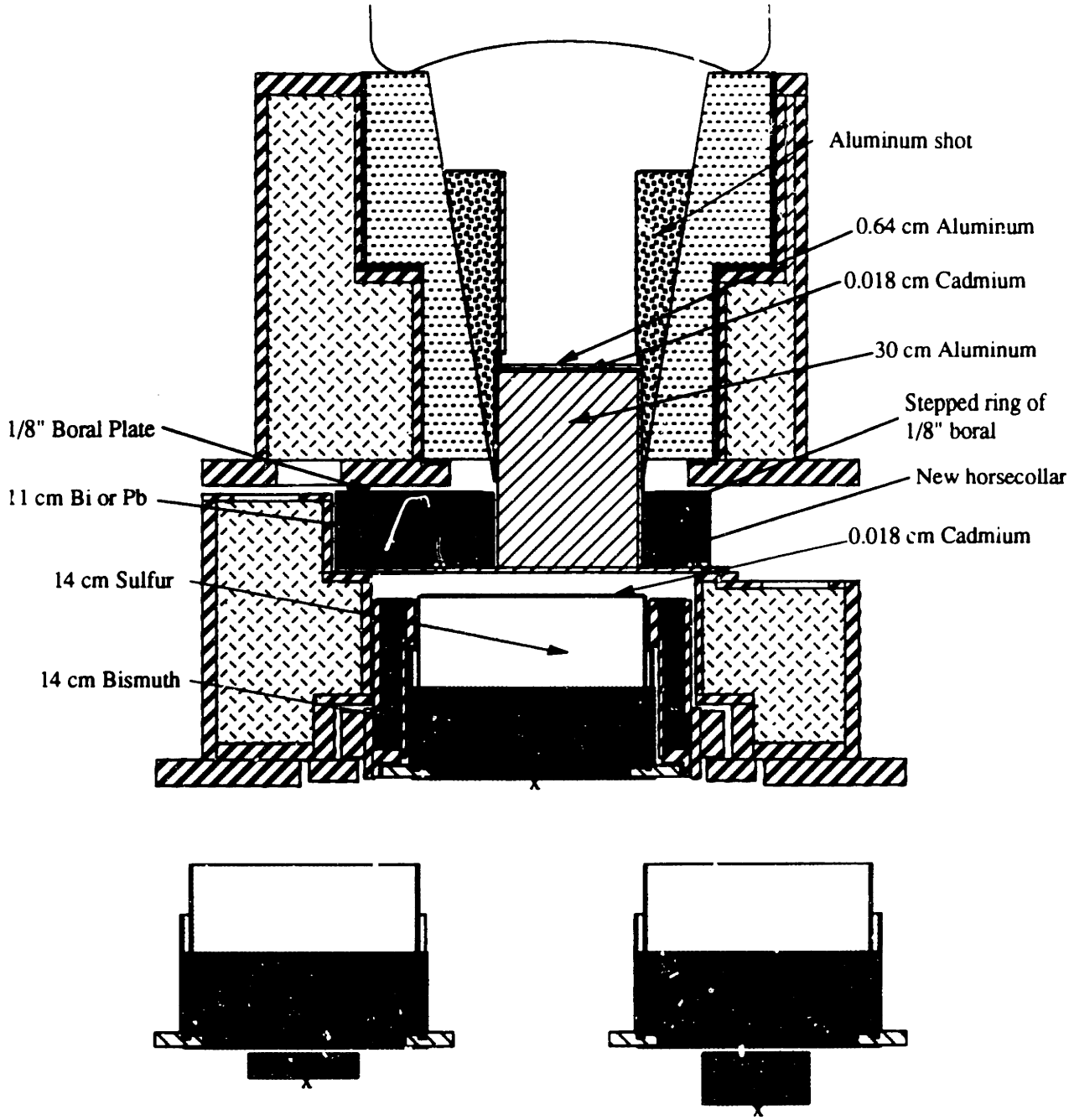

Figure 4.25. Circular slabs of bismuth were added below the collimator as shown. The doses and epithermal fluxes were measured at the positions marked with an "x". Results are shown in figure 4.26.

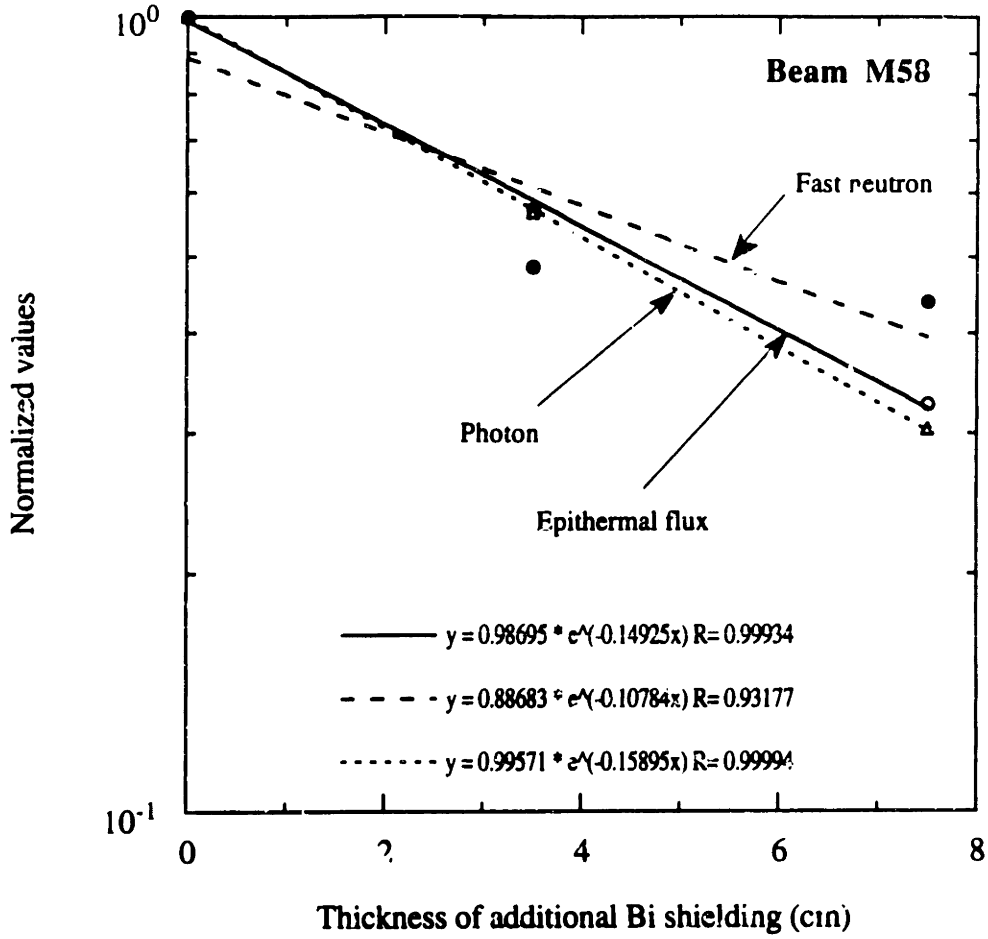

Figure 4.26. Additional amounts of bismuth were added below the centerline of the collimator as shown in figure 4.25. Measurements were then made in air below the added bismuth. The epithermal flux, photon dose, and fast neutron dose dropped exponentially at roughly the same rate. Note, however, that the error bars on the fast neutron dose rates are about ±20%. Closed circles: fast neutron dose, open circles: epithermal flux, open triangles: photon dose.

dose rate, and photon dose rate by roughly the same rates. It was estimated that the intensity of the M58 beam, as well as other beams, could be increased about 50% by removing 3 cm of the bismuth from the bottom of the collimator; the quality of the beam would not be expected to change since sufficient bismuth would be left to attenuate any incident photons. That is, removing 3 cm of bismuth might result in all 3 radiation components to increase by 50%, so the ratios of epithermal flux per incident photon or fast neutron would remain unchanged.

Alternatively, the higher intensity of the beams with less bismuth would permit more filter to be used; this would result in relatively lower fast neutron doses. Only a few centimeters of bismuth could be removed; removing more bismuth would eventually result in a rapid rise in the incident photon dose.

To better understand the effects of removing bismuth, a theoretical analysis of the neutron interactions in bismuth was made. Previously, the photon interactions in the bismuth were a priority. Neutron interactions, however, are equally important.

The neutron density in phase space $N(\underline{r}, \underline{\Omega}, E)$ in the bismuth depends on the incoming density and on the double differential scattering cross section

$$\sigma_\alpha (E \rightarrow E', \mu) = \sigma_\alpha(E)\, f_\alpha(E \rightarrow E', \mu) \qquad \alpha = \text{elastic, inelastic}$$

where $f_\alpha(E \rightarrow E', \mu)\, dE'\, d\mu$ is the probability that a neutron with initial energy E scatters into $dE'\, d\mu$, where $\mu = \cos \theta$.

Looking at these terms one by one,

1. $\sigma_\alpha(E)$. This defines the probability of scattering or the scattering reaction rate. The total cross section for bismuth is constant at 9 barns from 0.1 eV to 100 keV. A broad dip to 4 barns occurs at 1.3 MeV. Inelastic scattering probably occurs after some threshold in

the MeV range. The actual inelastic scattering cross section for bismuth was not found in the literature surveyed.

2..Changes in energy. Elastic scattering of neutrons by heavy nuclei such as bismuth results in negligible change in neutron energy. Inelastic scattering, however, results in very large reductions in energy. The liquid drop model with neutrons boiling off the compound nucleus was used to estimate the average energy loss. When a 7 MeV neutron is inelastically scattered off bismuth, the average energy of the scattered neutron is only 1.2 MeV.

3. Changes in direction. At low energies (eV to keV), a partial wave analysis shows that only s-wave scattering occurs (kR = 0.002 at 1 eV and 0.18 at 10 keV). This elastic scattering is therefore isotropic in the CMCS. Since A is large, it's also isotropic in the LAB. At higher energies (100 keV - 10 MeV), kR is 0.58 to 5.8. Therefore, there is an increasing amount of p-wave scattering. This p-wave scattering has a large forward component in the CMCS, and for bismuth a large forward component in the LAB as well. The inelastic scattering that occurs at higher energies is nearly isotropic.

From this information, we could expect several transport phenomena to occur during transmission of the beam through the bismuth collimator. For useful neutrons (0.5 eV to 30 keV), the interactions are almost entirely elastic scattering that is isotropic in the LAB. The intensity of the neutrons would be expected to drop roughly exponentially due to leakage. This can be thought of as a broadening of the beam or as scattering out of the beam.

For high energy neutrons (1 - 10 MeV), there are three potentially competing effects. First, inelastic scattering greatly reduces the neutron energy and would result in a lower fast neutron dose. This would be beneficial if in fact inelastic scattering occurs to

any significant extent. Second, elastic scattering of these high energy neutrons is forward peaked in the LAB. For 1 MeV neutrons, about 40% of the neutrons scatter into the forward p steradians (as opposed to 25% for an isotropic scatterer). This is detrimental since the higher transport mean free path means that these neutrons would be attenuated less than the useful neutrons. Third, neutrons above 300 keV have a lower total cross section. This is also detrimental since these neutrons would be attenuated less than the useful epithermal neutrons.

In summary, removing several centimeters of bismuth:

1. Should increase the useful epithermal flux. With 3 cm less bismuth, it's estimated that the epithermal flux would increase by 56%.
2. Might reduce the relative fast neutron dose in tissue because of
    a. Forward scattering of high energy neutrons.
    b. Less scattering of high energy neutrons.

With more bismuth, the beam should harden because of these two effects. Removing some bismuth, therefore, might reduce the fast neutron dose relative to the useful epithermal flux.

3. Might increase the relative fast neutron dose in tissue because of additional moderation in bismuth by inelastic scattering.
4. Might not result in a relative increase in incident photons. Removing 1-2 cm of bismuth would be expected to increase all 3 intensities (photon dose, fast neutron dose, epithermal flux) by the same amount. However, if sufficient bismuth is removed, a point would be reached when the photon contribution would increase at a higher rate than the others.

The associated error on the fast neutron dose rates in figure 4.26 are about ±20%; therefore, it was not possible to determine whether item 2 or 3 is more important.

Later, beginning with the M61 beam, 4.3 cm of bismuth was removed from the bottom of the collimator.

4.7 BEAM M58A

The M58A beam is shown in figure 4.27. In this beam the phantom was positioned under the centerline of the upper filter, not the lower collimator as is usually done. The phantom was also rotated 90 degrees so that the major axis of the phantom was perpendicular to the movement of the lead shutter. The beam itself was the same as the M58 beam. Previous results with the M55 beam epithermal flux map showed that the epithermal flux in air was slightly higher beneath the centerline of the upper filter. Positioning the phantom under the centerline of the upper filter, therefore, might result in a slightly higher flux in phantom.

The thermal flux was determined throughout the phantom; however, the fast neutron and photon doses were only determined at three positions. Results are shown in figures 4.28 and 4.29. The thermal flux, fast neutron, and photon doses of the M58A beam were essentially the same as those of the M58 beam. The differences in the various dose components between M58A and M58 are less than experimental error.

Although the intensity of this beam was no higher than before, the information gained from the M58A beam was quite useful. Previously, no data had been obtained on how the doses change with positioning of the phantom in the beam. In this case, the phantom was positioned 6 cm further towards the back of the beam.

4.8 BEAM M59

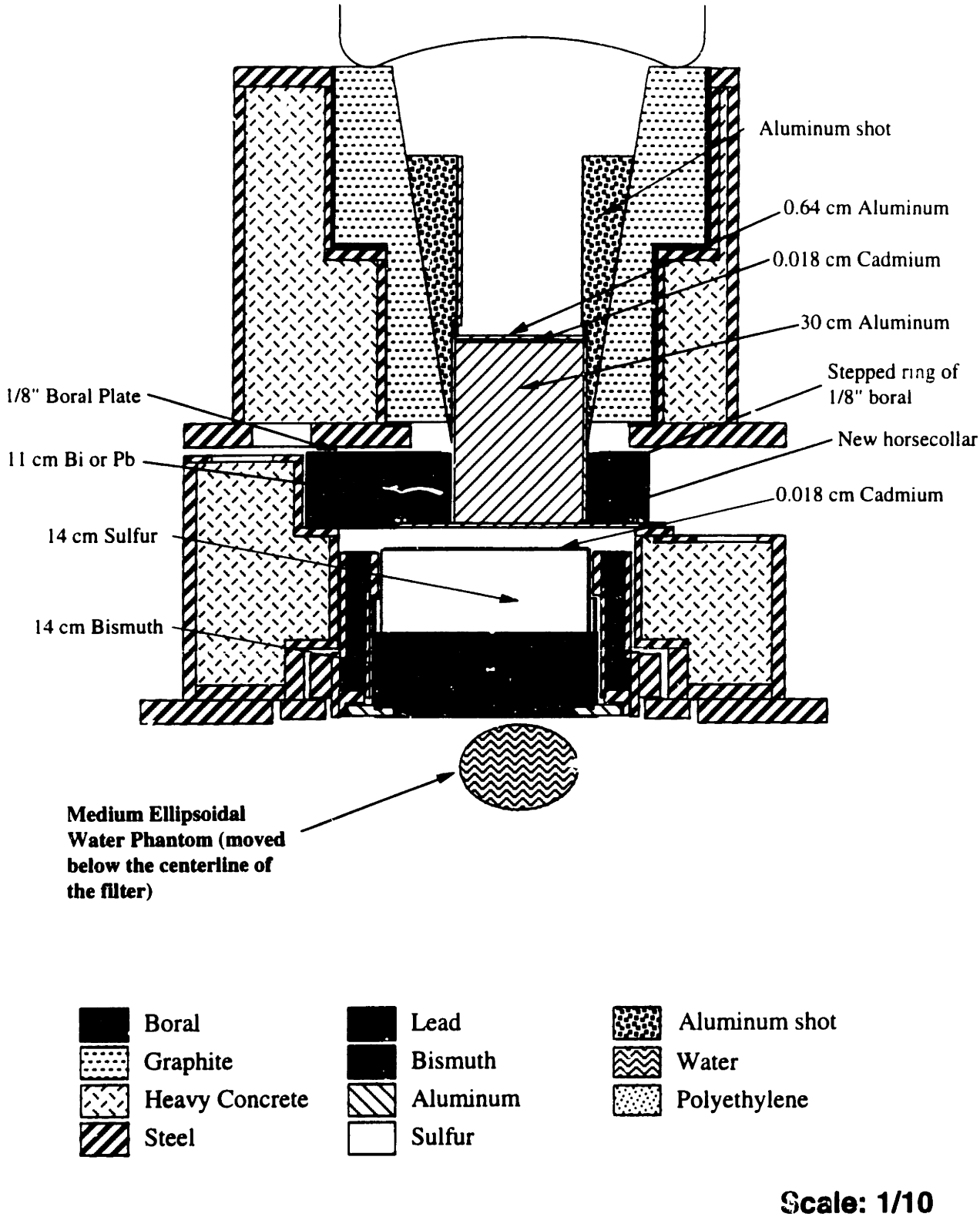

Figure 4.27. Cross sectional view of the M58A beam. The phantom was below the centerline of the upper filter, not the centerline of the collimator.

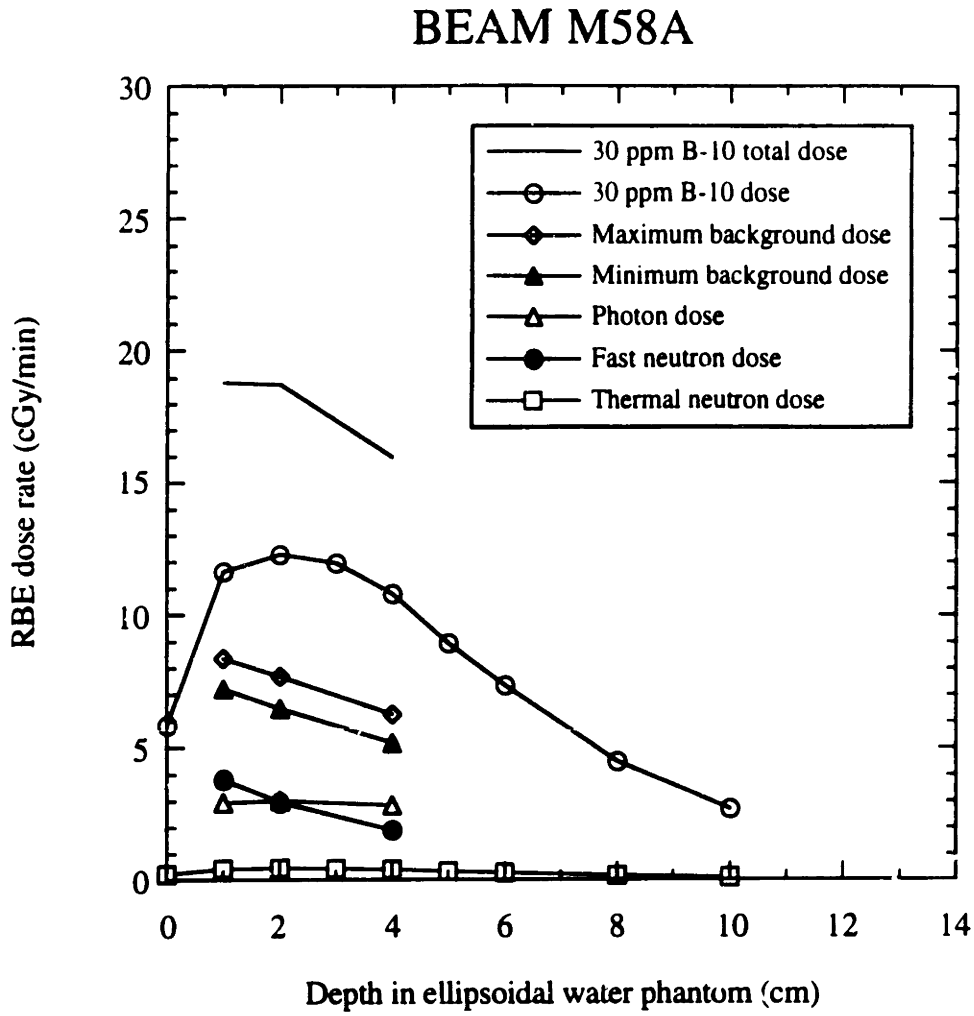

Figure 4.28. Doses measured in phantom for the M58A beam and BSH. The thermal flux was measure as usual, but the chambers were only used at the 3 depths shown. This provided sufficient dosimetric data for comparison with the M58 beam.

Unilateral irradiation.
Phantom: Medium sized, ellipsoidal, water filled, center tube.
Reactor power: 5 MWn.
RBE's: 2.3 for B-10, 1.6 for neutrons, 1.0 for photons.
B-10 concentrations: 30 ppm for tumor, 3 ppm for maximum background, 0 ppm for minimum background.
In-air data: D_{fn} = 4.2 cGy/min
D_{γ} = 1.4 cGy/min
Phantom position: Under centerline of filter.

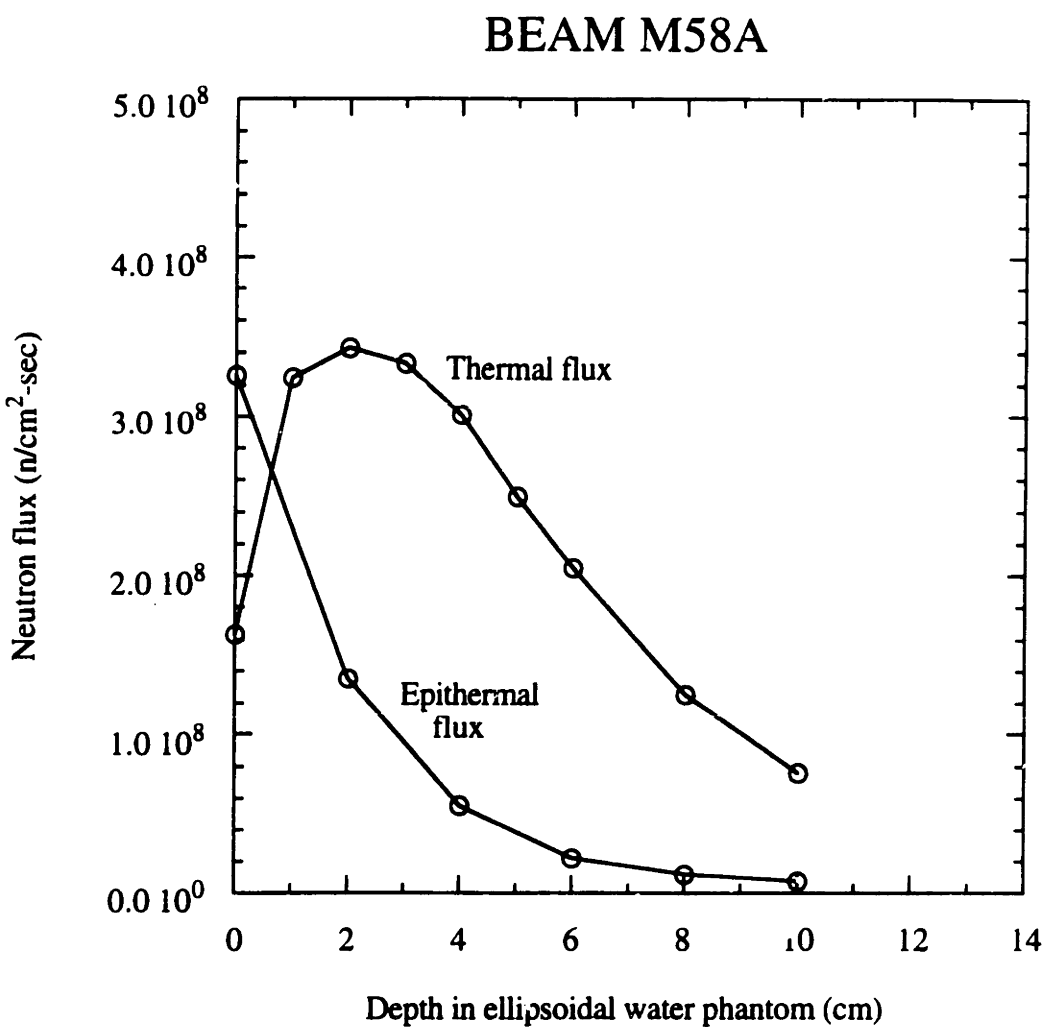

Figure 4.29. Thermal and epithermal fluxes measured in phantom for the M58A beam. These fluxes were within experimental error of the fluxes measured for the M38 beam.

Unilateral irradiation.
Phantom: Medium sized, ellipsoidal, water filled, center tube.
Reactor power: 5 MWn.
Phantom position: Under centerline of collimator.

In this beam the aluminum upper filter was replaced with the sulfur filter, and the cadmium on top of the collimator was removed. The goal was to use the somewhat better sulfur filter, and to increase the thermal flux in phantom by increasing the incident thermal flux. The experimental data for this beam were taken by Choi.

The beam is shown in figure 4.30. Results are shown in figures 4.31 and 4.32. The thermal flux is much higher than in the M58 beam and it peaks at the surface. Relative to the M57 beam, the thermal flux increased by a factor of 4 near the surface and factor of 2 at 10 cm. The AD was still high, however, at 8.3 cm. Even with the higher thermal flux the AR was only 3.3. The incident photon dose rate was not measured in this beam; however, it can be estimated. Extracting data from table 4.5, the induced photon dose per peak ϕ_{th} in phantom is 2.41E-9 RBE cGy/min per n/cm^2-sec (photon RBE assumed to be 0.5). Multiplying this by 1.3E9 n/cm^2-sec, the peak thermal flux for the M59 beam, gives an estimated induced photon dose of 3.1 RBE cGy/min. The peak photon dose measured in phantom was 7.8 RBE cGy/min. The difference between these two dose rates, or 4.7 RBE cGy/min, is the estimate of the incident photon dose rate. This is about 4 times higher than that measured with the M57 beam.

Removing the cadmium allows thermal neutrons to penetrate into the lower collimator. Absorption in the lower structures probably resulted in prompt gammas that significantly increased the incident photon dose.

4.9 BEAM M60

This beam was intermediate between the M57 and M59 beams. The M57 beam had a 0.007" sheet of cadmium on top of the collimator that absorbs 90% of the thermal neutrons. The M59 beam had no cadmium on top of the collimator. With the M60 beam, a 0.004" sheet of cadmium was used.

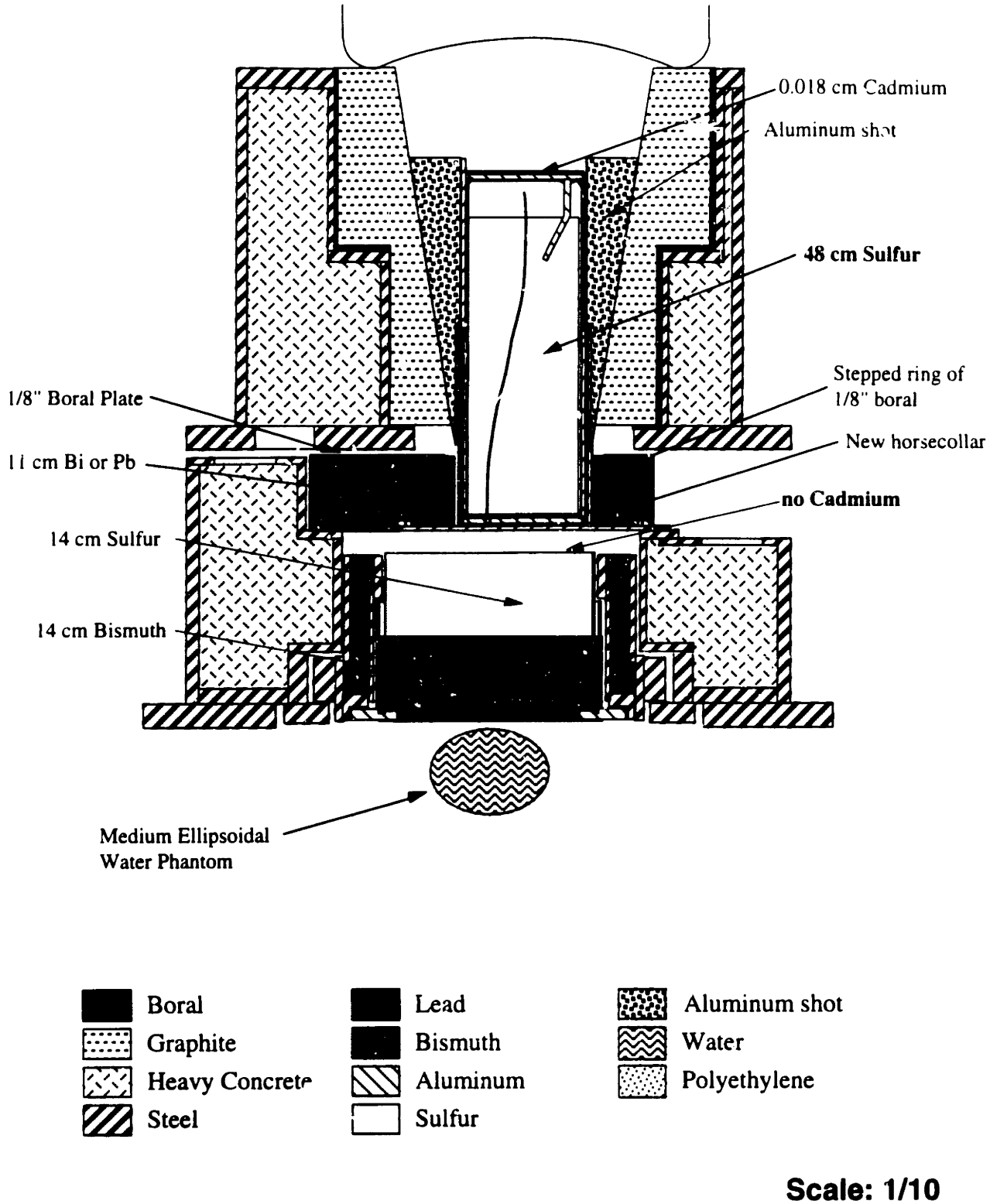

Figure 4.30. Cross sectional view of the M59 beam. The new, sulfur filter was used and the cadmium that had been above the collimator was removed.

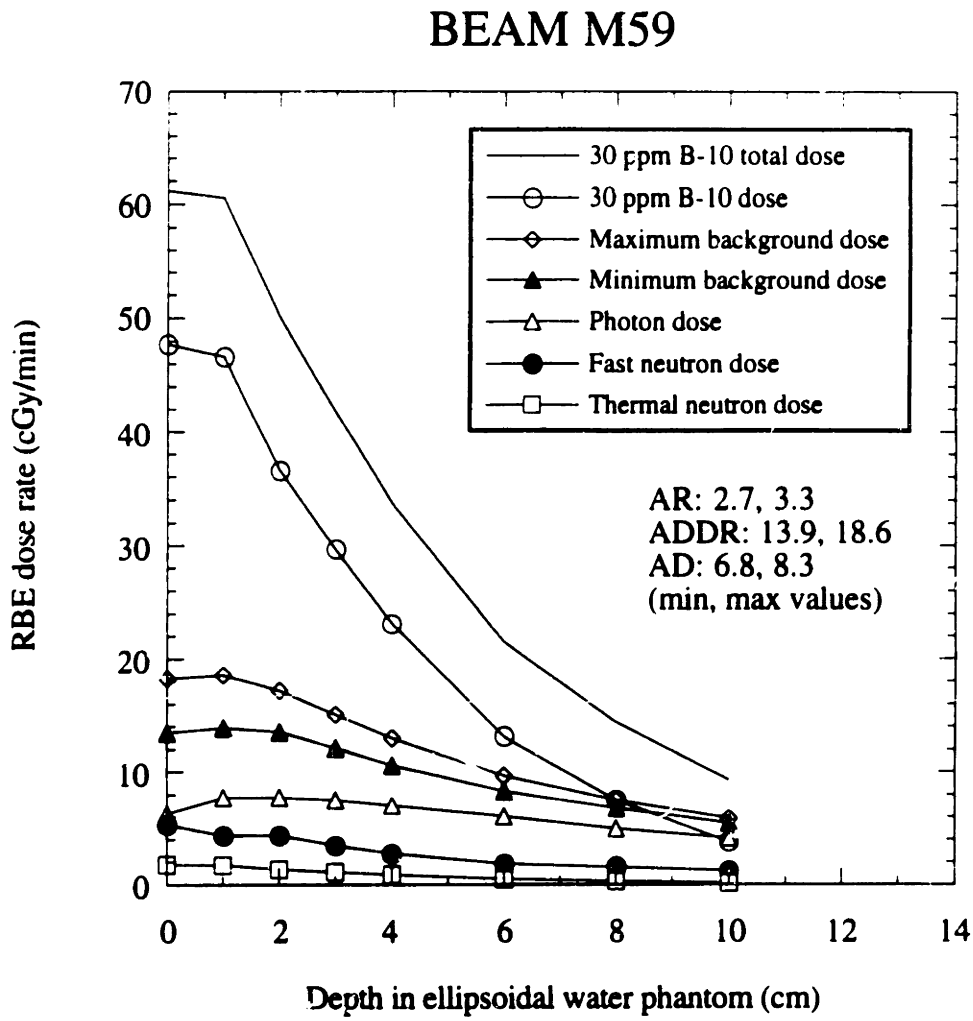

Figure 4.31. Doses measured in phantom for the M59 beam and BSH.

Unilateral irradiation.
Phantom: Medium sized, ellipsoidal, water filled, center tube.
Reactor power: 5 MWn.
RBE's: 2.3 for B-10, 1.6 for neutrons, 1.0 for photons.
B-10 concentrations: 30 ppm for tumor, 3 ppm for maximum background, 0 ppm for minimum background.

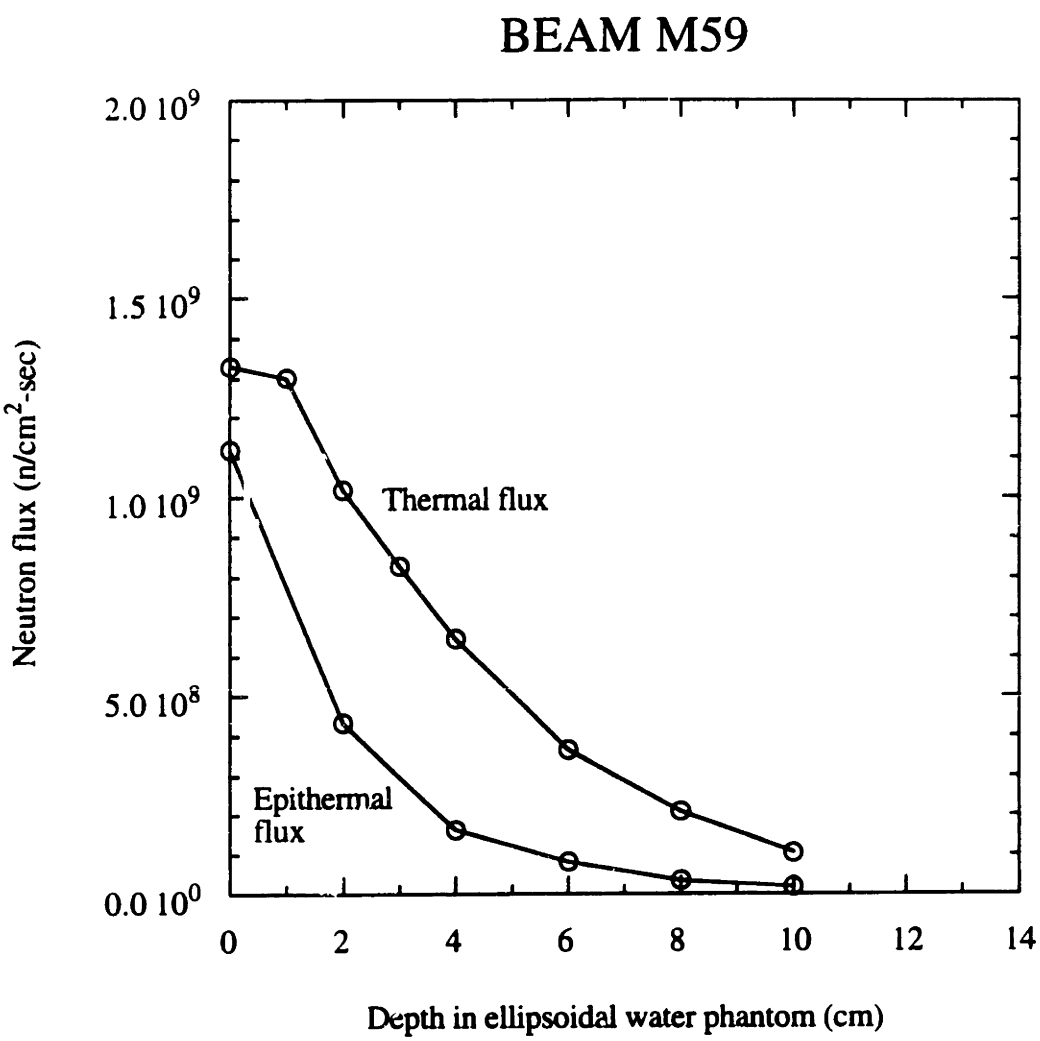

Figure 4.32. Thermal and epithermal fluxes measured in phantom for the M59 beam.

Unilateral irradiation.
Phantom: Medium sized, ellipsoidal, water filled, center tube.
Reactor power: 5 MWn.

The beam is shown in figure 4.33. Results are shown in figures 4.34 and 4.35. With this beam, the incident thermal flux was increased only slightly. Relative to the M57 beam, the M60 beam had 20% more thermal flux in the first 2 cm, and about the same flux at greater depths. This result was expected. The thinner sheet of cadmium allows about 2.8 times as many thermal neutrons to penetrate the cadmium. A 50% increase in thermal flux was expected at the surface, based on the M61 beam results; experimentally, a 40% increase was measured.

Unlike the M59 beam's flux, the M60 beam's flux drops at the surface. The AD (8.4 cm) of this beam was good, but the AR was marginally less than that of the M57 beam. This was because the incident photons increased from additional prompt gammas produced lower in the collimator, as determined with an in-air measurement. The increase in incident gammas was not as much as in the M59 beam.

The results of the M57, M59, and M60 beams show that the beam can be tailored somewhat and that one beam might be preferred for some particular situation. In general, though, it is clear that during this time the M57 beam was the best epithermal beam for deep seated therapy. It has a more uniform dose distribution, ample skin sparing, high AR, and excellent AD.

4.10 BEAM M61

In this beam, 4.3 cm of bismuth were removed from the bottom of the collimator and an additional 7 cm of aluminum was added on top of the sulfur filter. It was hoped that the additional aluminum filter could be placed in the beam, with a resultant reduction in the fast neutron dose relative to the incident epithermal flux, without losing intensity. The beam is shown in figure 4.36. Results are shown in figures 4.37, 4.38, and 4.39. The quality and intensity of this beam are similar to that of the M57 beam. The thermal fluxes

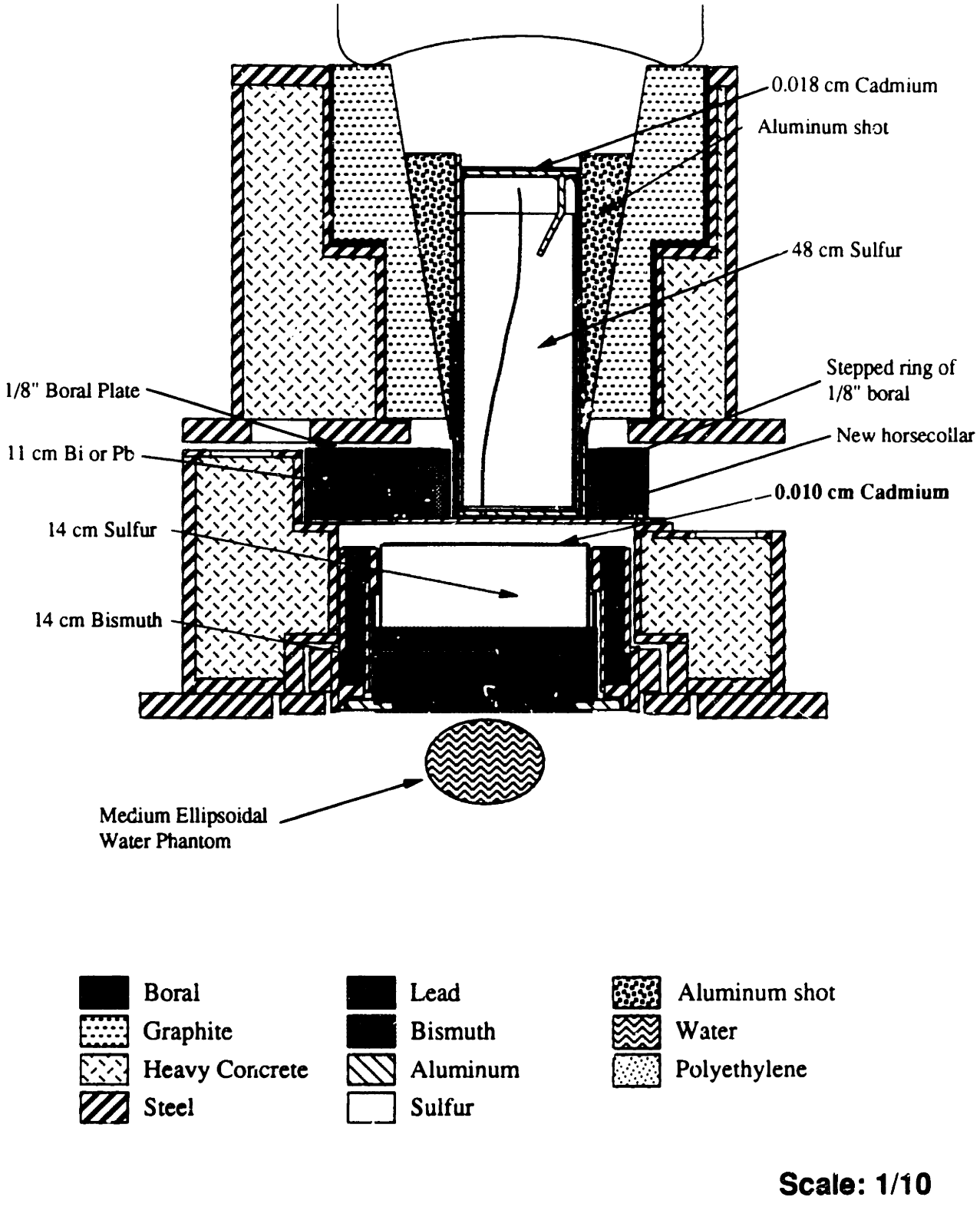

Figure 4.33. Cross sectional view of the M60 beam. A 0.010 cm layer of cadmium was added back to the top of the collimator.

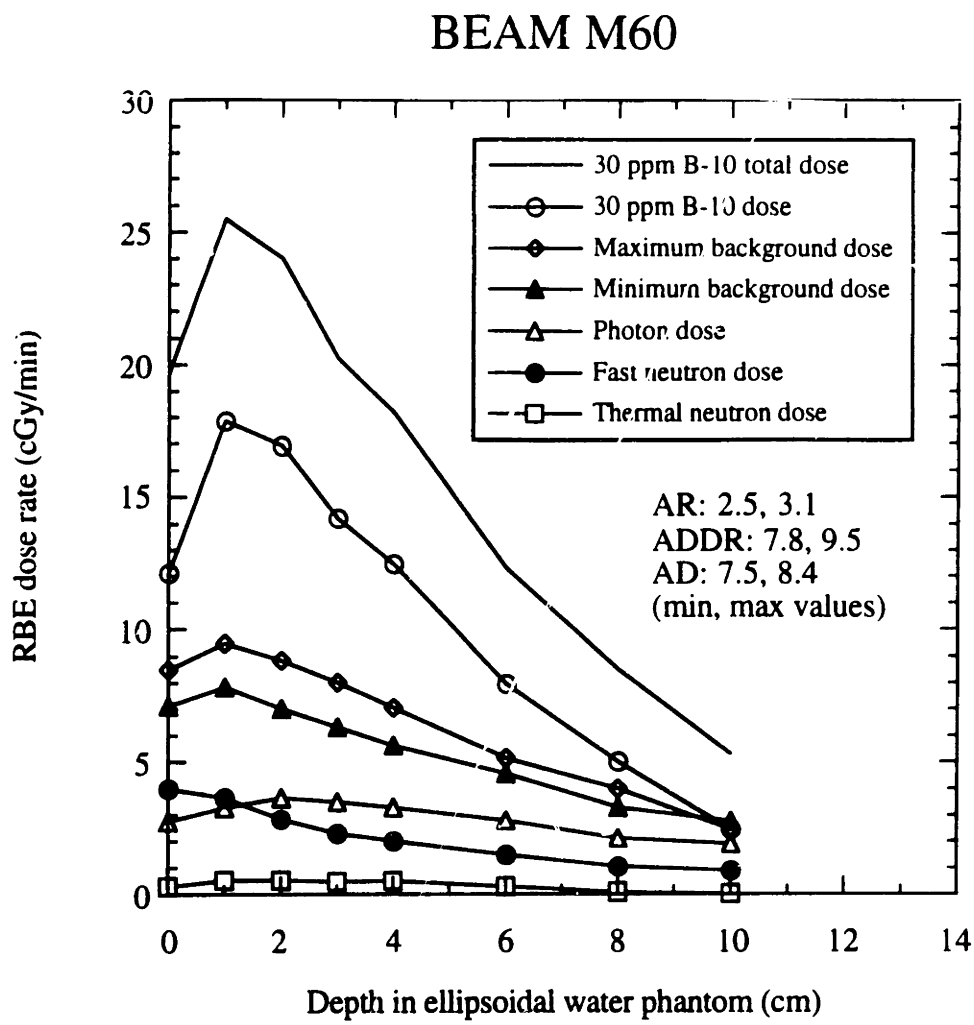

Figure 4.34. Doses measured in phantom for the M60 beam and BSH.

Unilateral irradiation.
Phantom: Medium sized, ellipsoidal, water filled, center tube.
Reactor power: 5 MWn.
RBE's: 2.3 for B-10, 1.6 for neutrons, 1.0 for photons.
B-10 concentrations: 30 ppm for tumor, 3 ppm for maximum background, 0 ppm for minimum background.

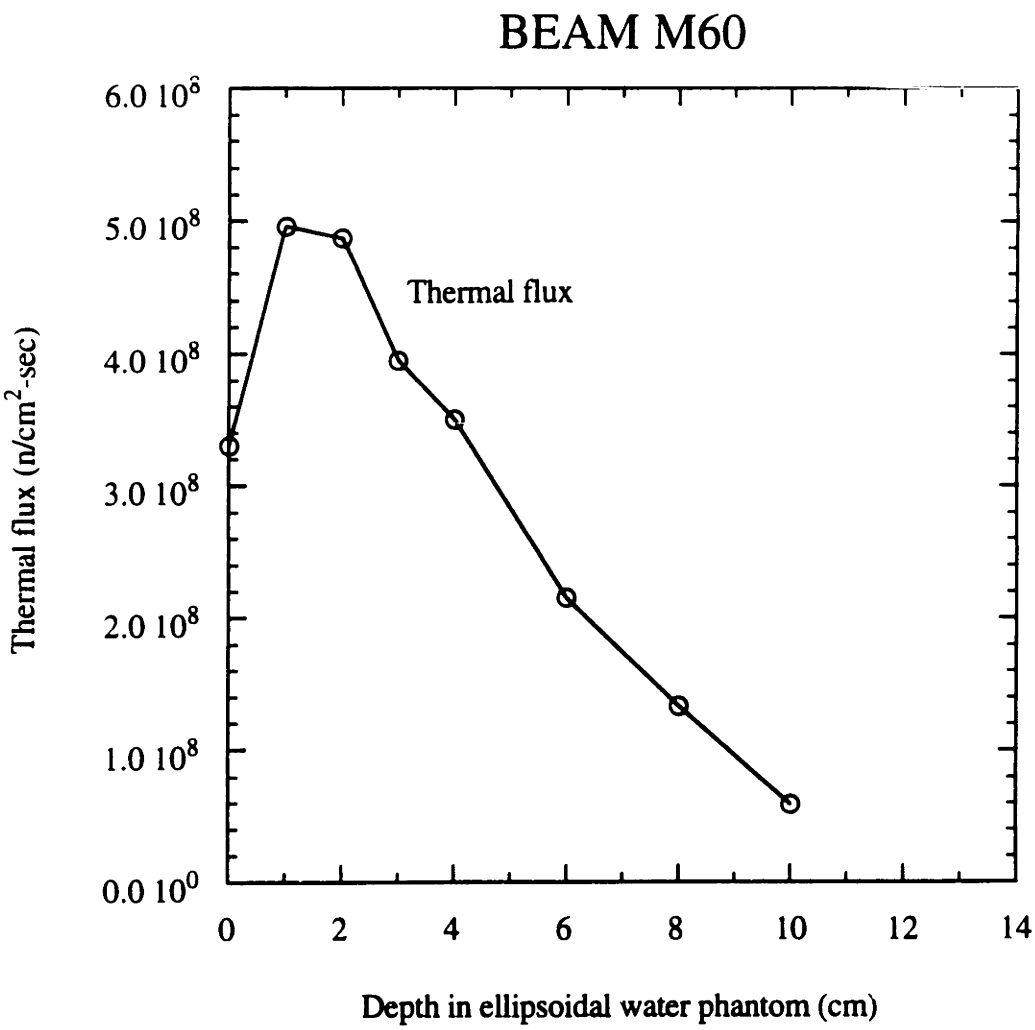

Figure 4.35. Thermal flux measured for the M60 beam.

Unilateral irradiation.
Phantom: Medium sized, ellipsoidal, water filled, center tube.
Reactor power: 5 MWn.

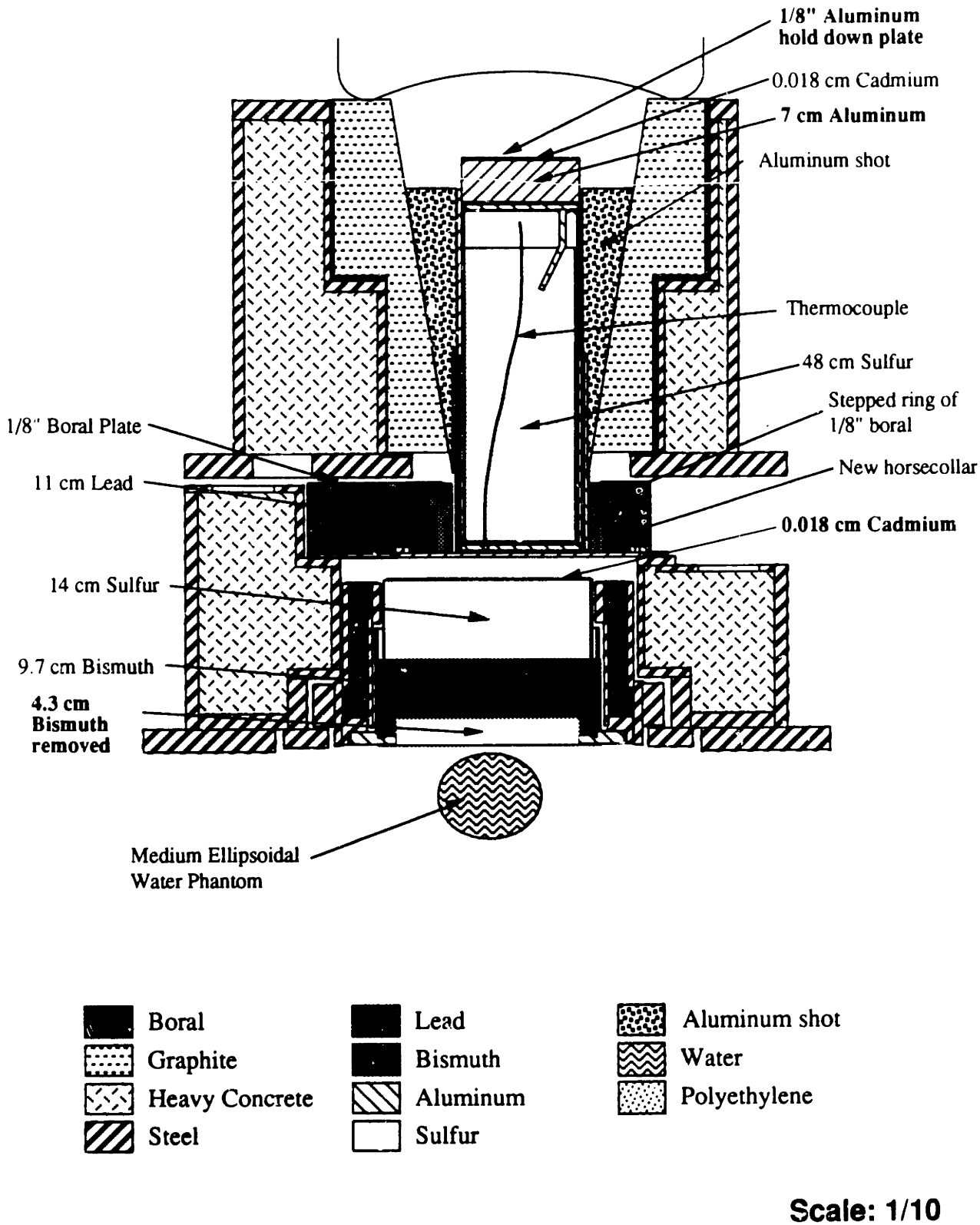

Figure 4.36. Cross sectional view of the M61 beam. Aluminum was added above the sulfur filter, bismuth was removed from the collimator, and the usual thickness of cadmium was used above the collimator.

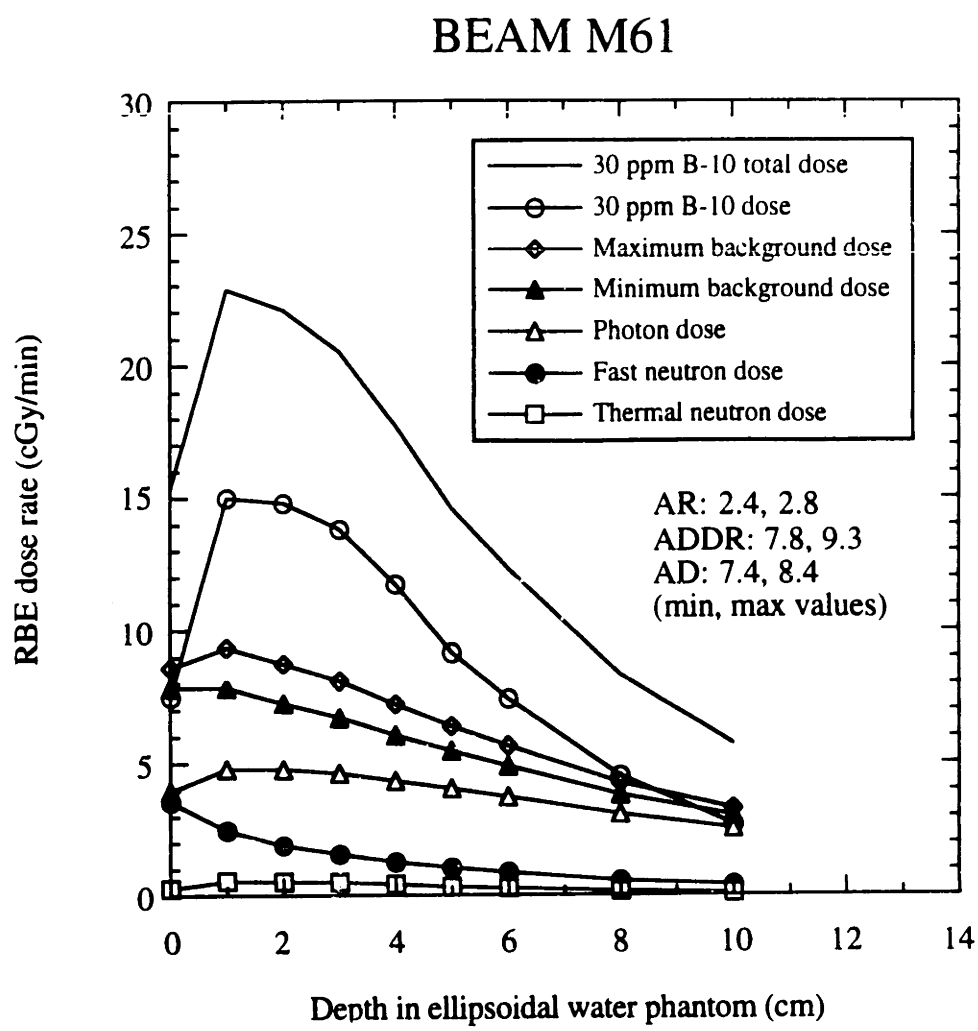

Figure 4.37. Doses measured in phantom for the M61 beam and BSH.

Unilateral irradiation.
Phantom: Medium sized, ellipsoidal, water filled, center tube.
Reactor power: 5 MWn.
RBE's: 2.3 for B-10, 1.6 for neutrons, 1.0 for photons.
B-10 concentrations: 30 ppm for tumor, 3 ppm for maximum background, 0 ppm for minimum background.
In-air data: D_{fn} = 3.3 cGy/min
D_{γ} = 2.8 cGy/min
$D_{30ppm\ B\text{-}10}$ = 2.2 cGy/min

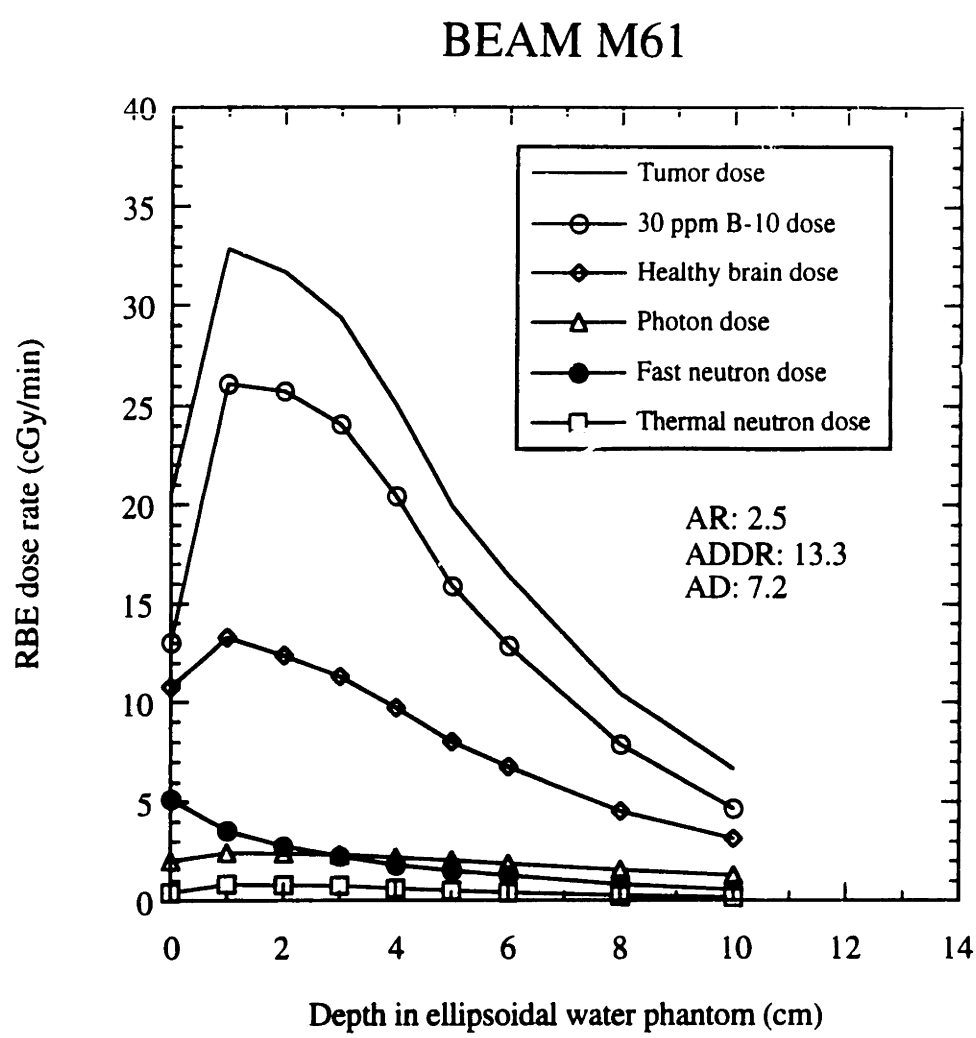

Figure 4.38. Doses measured in phantom for the M61 beam and BPA.

Unilateral irradiation.
Phantom: Medium sized, ellipsoidal, water filled, center tube.
Reactor power: 5 MWn.
RBE's: 4.0 for B-10, 2.3 for neutrons, 0.5 for photons.
B-10 concentrations: 30 ppm for tumor, 7.5 ppm for healthy brain.
In-air data: D_{fn} = 4.7 cGy/min
D_{γ} = 1.4 cGy/min
$D_{30ppm\ B\text{-}10}$ = 3.8 cGy/min

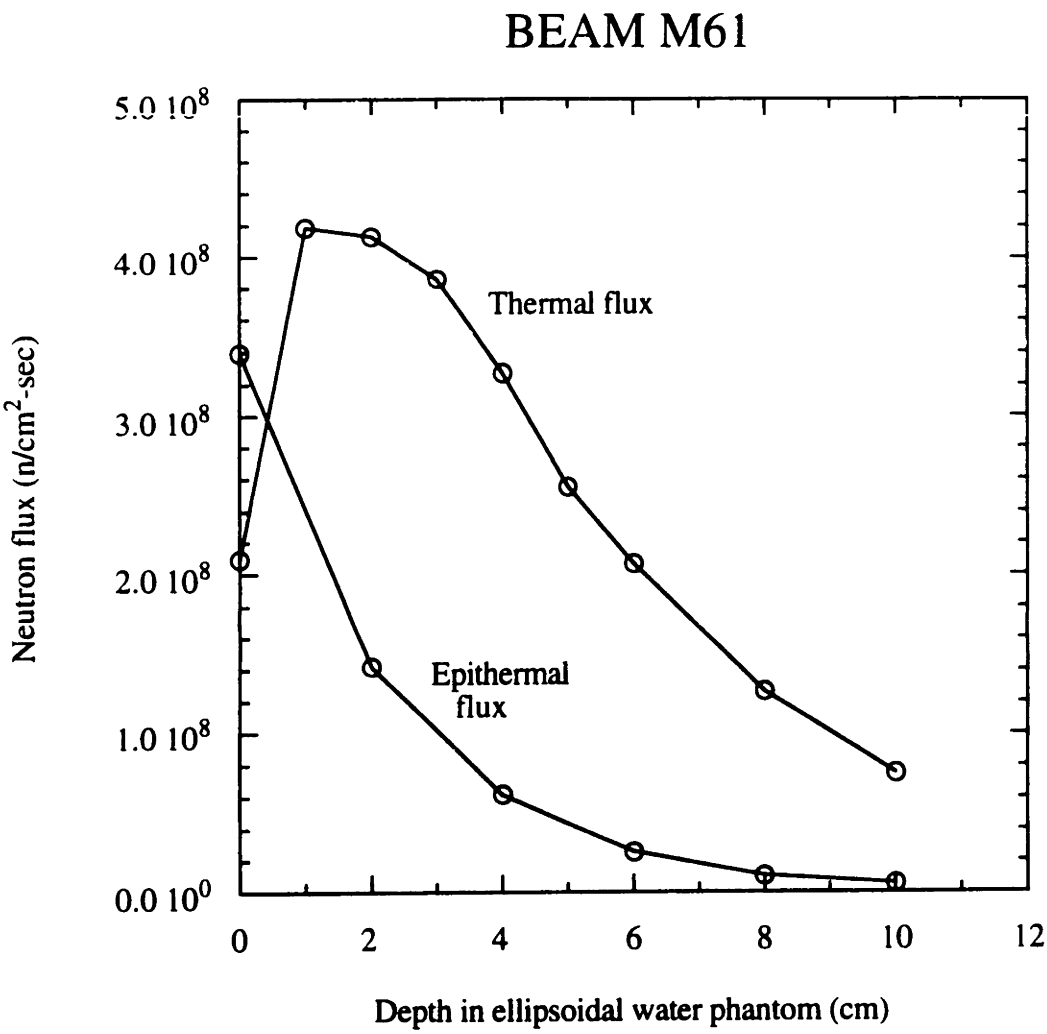

Figure 4.39. Thermal and epithermal fluxes measured in phantom for the M61 beam.

Unilateral irradiation.
Phantom: Medium sized, ellipsoidal, water filled, center tube.
Reactor power: 5 MWn.

in phantom were nearly identical in the two beams. The in-air thermal and epithermal fluxes were similar. Removing the bismuth from the collimator was estimated to increase the epithermal flux by a factor of about 2 based on the previously described attenuation experiment with bismuth. Therefore, the additional 7 cm of aluminum filter appeared to reduce the epithermal flux by about a factor of two. The fast neutron dose to epithermal flux ratio decreased by 29%. Thus the goal of improving this ratio was achieved, and achieved without losing intensity of thermal flux in phantom. With less bismuth, however, a substantial penalty was taken with the higher incident photon dose.

4.11 BEAM M62

In this beam, an additional 12 cm of aluminum shot was added to the cone region as shown in figure 4.40. Adding additional filter in this region would be expected to reduce the fast neutron dose from those neutrons that would otherwise not pass through the central stovepipe region of the filter. The shot was added to the very top of the stovepipe. Thermal neutrons diffusing down the cone region could be captured and produce prompt gammas close to the phantom. With less bismuth in the lower collimator, these prompt gammas could increase the incident photon dose. It was decided, therefore, to remove the thermal neutrons at the top of the cone by using aluminum shot that had been plated with cadmium. Cadmium plated shot was used since adding a sheet of cadmium above the shot is not easily done. The cadmium plating was done by F. M. Callahan Co (Malden, Ma). The shot was first flashed with 0.00005" of nickel and then cadmium plated at about 0.001".

It was desired to remove about 90% of the incident thermal flux with the cadmium plated shot. An attenuation experiment was done using the 4DH1 thermal neutron beam. The experimental setup consisted of passing a small, thermal neutron beam through various

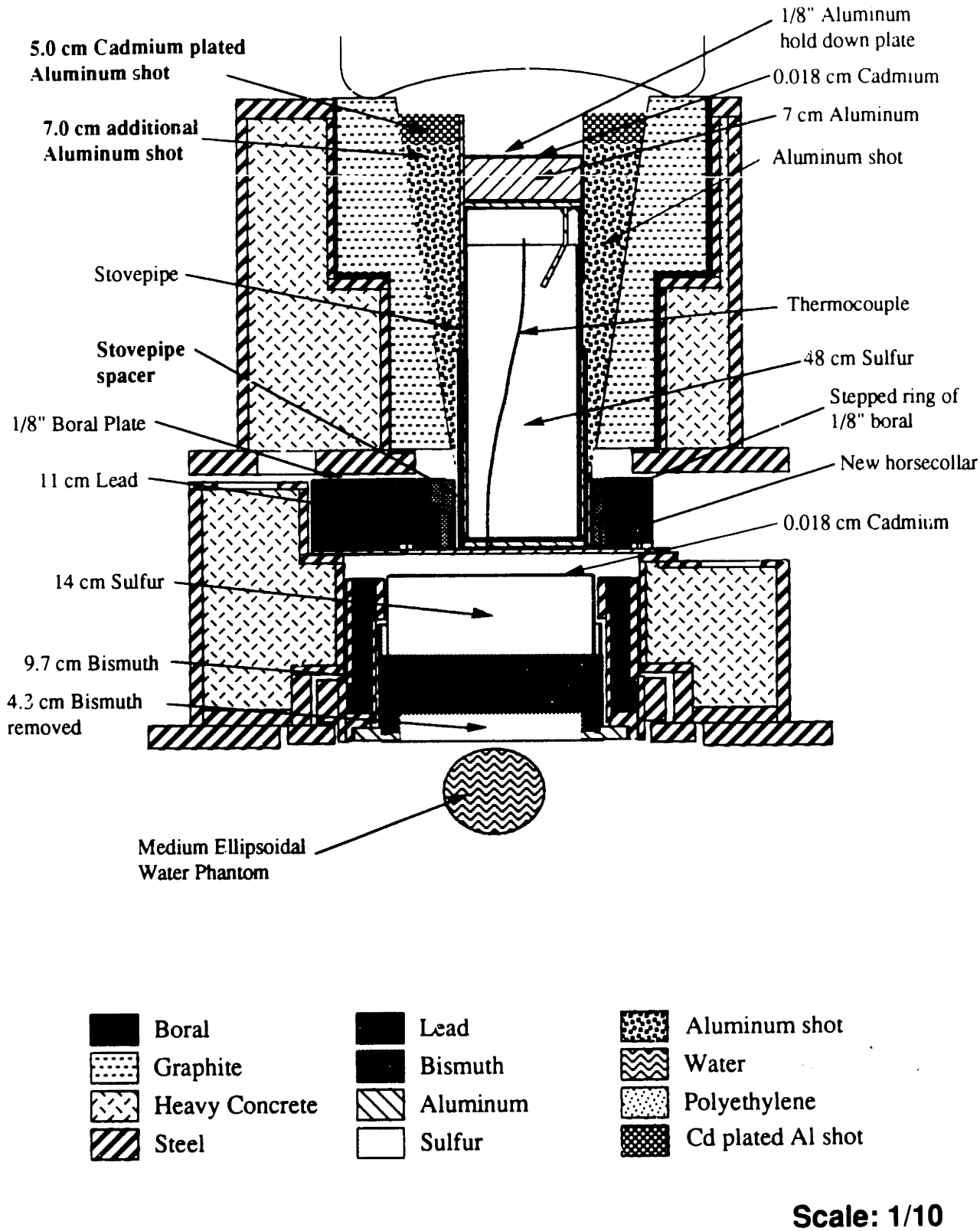

Figure 4.40. Cross sectional view of the M62 beam. The stovepipe was extended with the spacer and additional aluminum and cadmium plated aluminum shot were airlifted into the cone region.

thicknesses of shot. The thermal flux was measured with a BF_3 tube. Results are shown in figure 4.41. With these results, it was decided to add 7.0 cm of pure aluminum shot and then add 5.0 cm of the cadmium plated aluminum shot on top of the cone shaped region.

Results of the beam characterization are shown in figures 4.42-4.45. The quality of this beam was about equal to that of the M61 beam. The epithermal flux was reduced by only 13%, and there was only a 7% improvement in the fast neutron dose to epithermal flux ratio. These data demonstrate that most of the useful epithermal neutrons that reach the phantom pass through the region occupied by the 7 cm aluminum filter and not through the surrounding shot. The M62 beam had very little incident thermal flux, and so there is a large drop in the thermal flux near the surface of the phantom. The cadmium plated aluminum shot absorbed thermal neutrons that otherwise would have diffused through the shot, sulfur filter, and collimator.

The M57, M61, and M62 beams are compared in tables 4.3 and 4.4. In table 4.5, the incident photon dose measured in air was subtracted from the photon dose averaged over the first 3 cm of phantom. For beam M57, about 38% of the photon dose in phantom is caused by the incident photons. For beam M62, this number is 54%, due to having less bismuth in the collimator. Also seen in the table is that the induced photon dose scales with the peak thermal flux in phantom. This result is expected since dose rate scale linearly with the source intensity.

It is also interesting to compare these data with those presented earlier by Yanch and Clement[3] as part of their ideal beam studies. For a 20 keV beam,[1] they reported a B-10 dose to induced photon dose in phantom of 7.5, using their RBE's of 2.3 for the B-10 reaction and 1.0 for the photon dose, and a B-10 concentration of 30 ppm. For our current RBE's of 4.0 and 0.5, this ratio becomes 26.1. The M57, M61, and M62 beams have a ratio of about 24.5. Thus, there is good agreement between the induced photon doses calculated by MCNP and those measured experimentally.

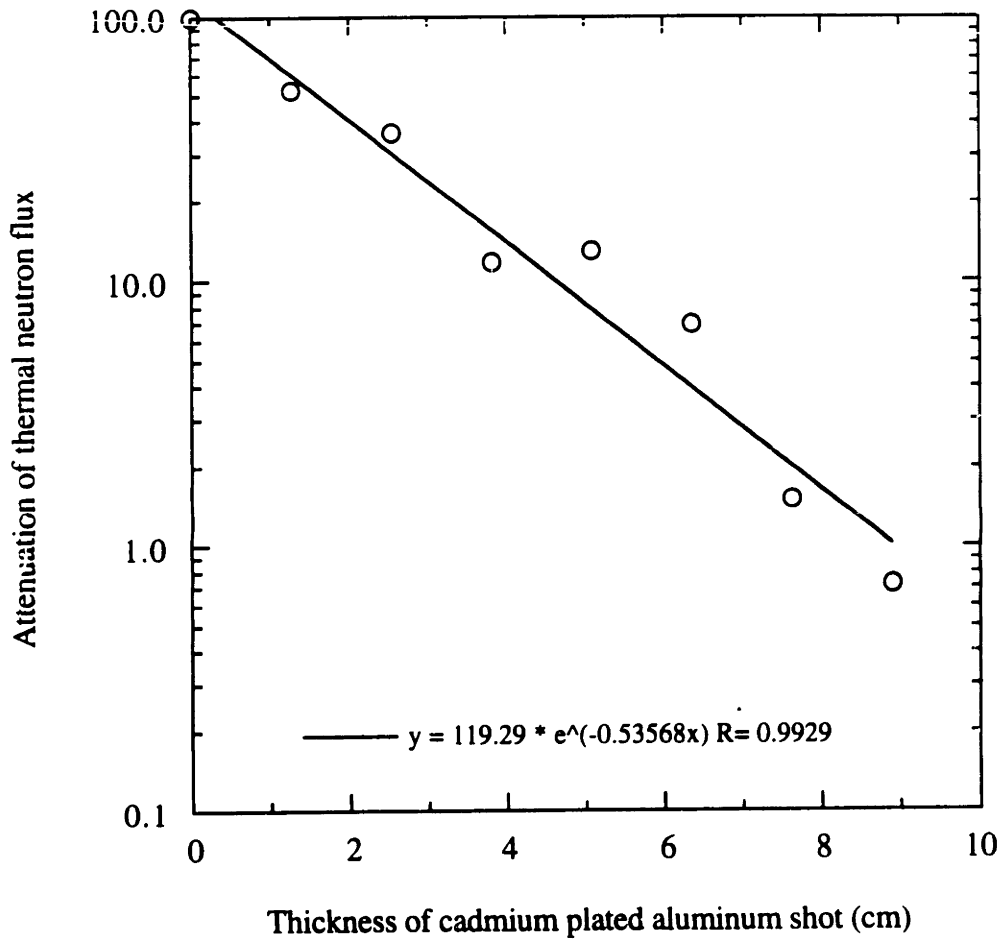

Figure 4.41. To determine the thickness of cadmium plated aluminum shot that was needed for the M62 beam, a transmission attenuation experiment was done using the 4DH1 thermal neutron beam. A BF_3 tube was used to measure the thermal flux. 5 cm of shot gave more than 90% attenuation of the thermal flux.

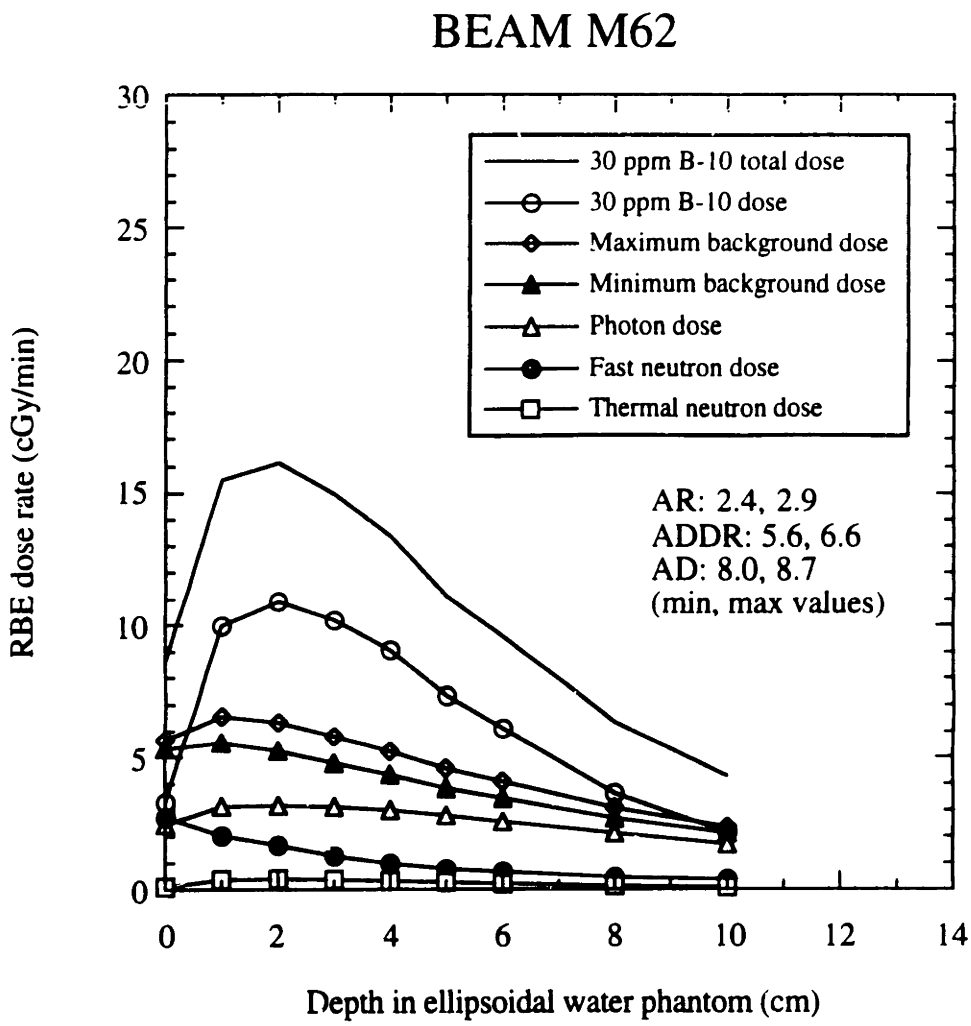

Figure 4.42. Doses measured in phantom for the M62 beam and BSH.

Unilateral irradiation.
Phantom: Medium sized, ellipsoidal, water filled, center tube.
Reactor power: 5 MWn.
RBE's: 2.3 for B-10, 1.6 for neutrons, 1.0 for photons.
B-10 concentrations: 30 ppm for tumor, 3 ppm for maximum background, 0 ppm for minimum background.
In-air data: D_{fn} = 2.4 cGy/min
D_{γ} = 1.7 cGy/min
$D_{30ppm\ B\text{-}10}$ = 0.52 cGy/min

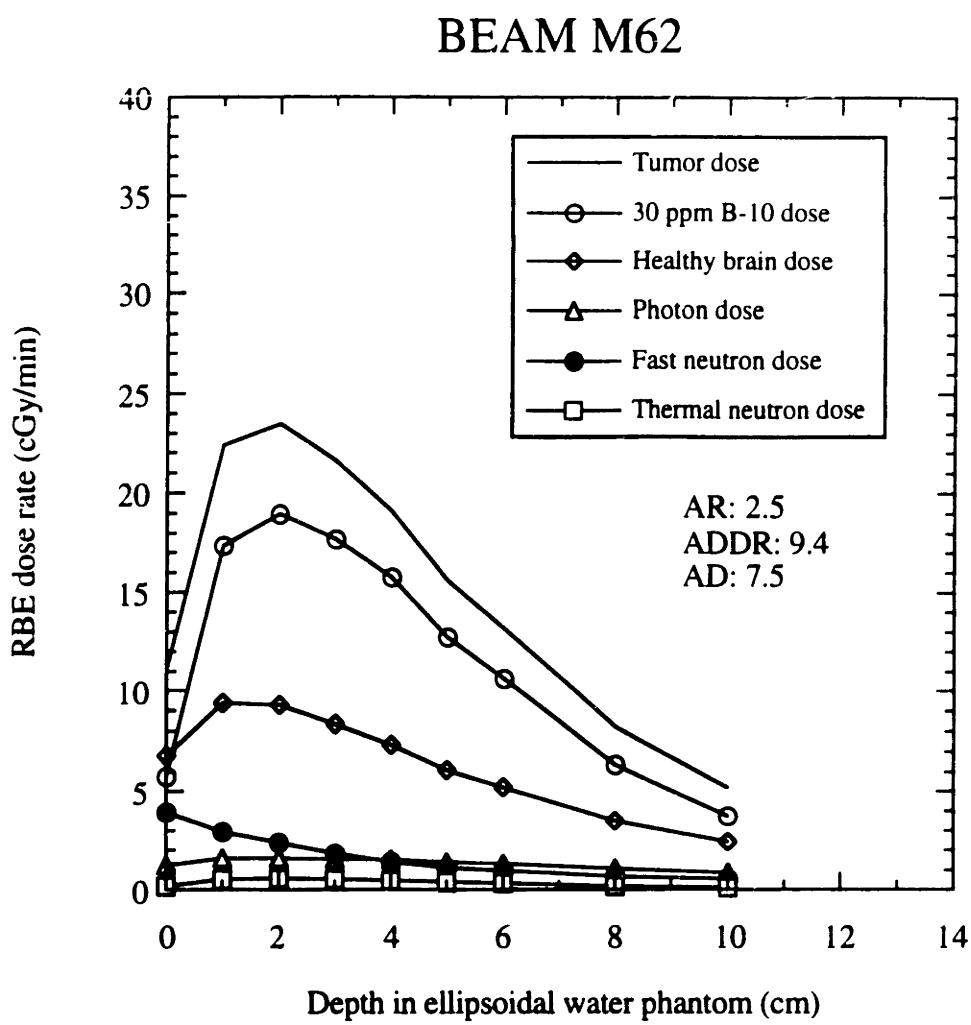

Figure 4.43. Doses measured in phantom for the M62 beam and BPA.

Unilateral irradiation.
Phantom: Medium sized, ellipsoidal, water filled, center tube.
Reactor power: 5 MWn.
RBE's: 4.0 for B-10, 2.3 for neutrons, 0.5 for photons.
B-10 concentrations: 30 ppm for tumor, 7.5 ppm for healthy brain.
In-air data: D_{fn} = 3.5 cGy/min
D_{γ} = 0.85 cGy/min
$D_{30ppm\ B\text{-}10}$ = 0.90 cGy/min

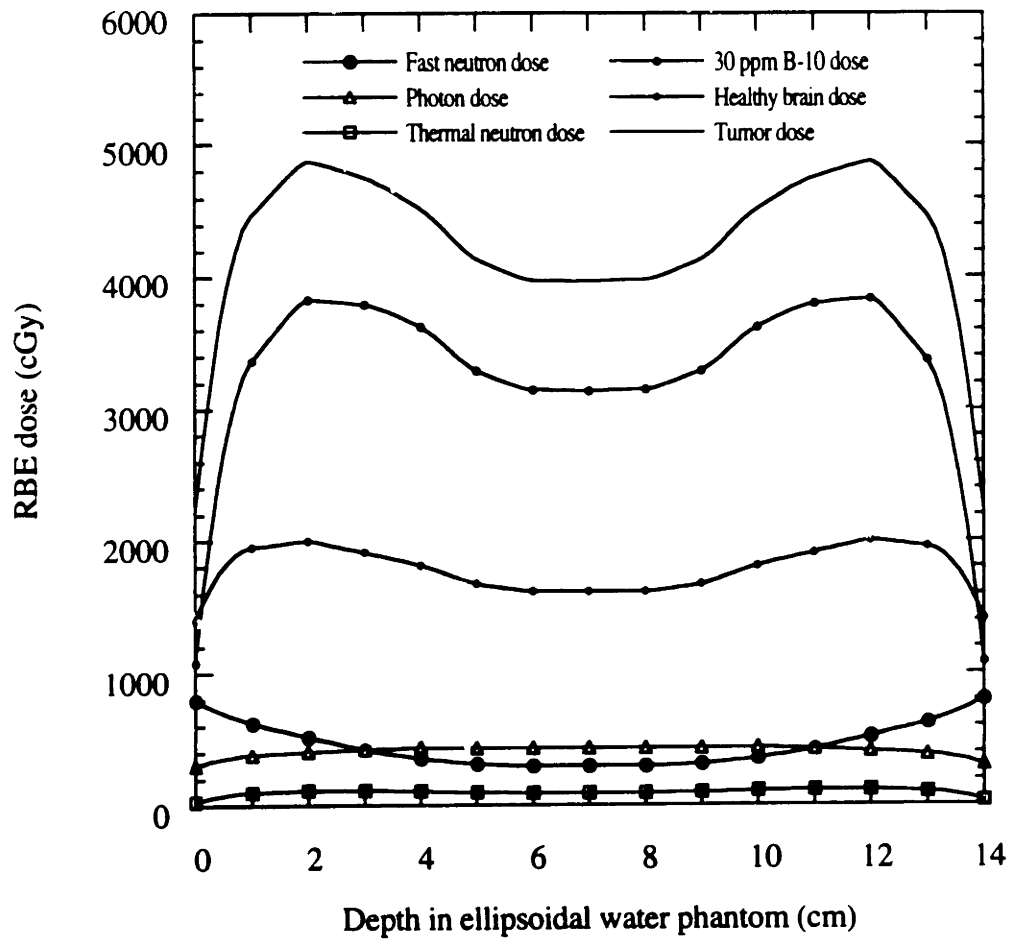

Figure 4.44. Bilateral irradiation dose distribution calculated from the unilateral irradiation doses measured for the M62 beam and BPA.

Bilateral irradiation.
Phantom: Medium sized, ellipsoidal, water filled, center tube.
Reactor power: 5 MWn.
RBE's: 4.0 for B-10, 2.3 for neutrons, 0.5 for photons.
B-10 concentrations: 30 ppm for tumor, 7.5 ppm for healthy brain.
Maximum dose: 2000 RBE cGy to healthy tissue.
AR = 2.44.

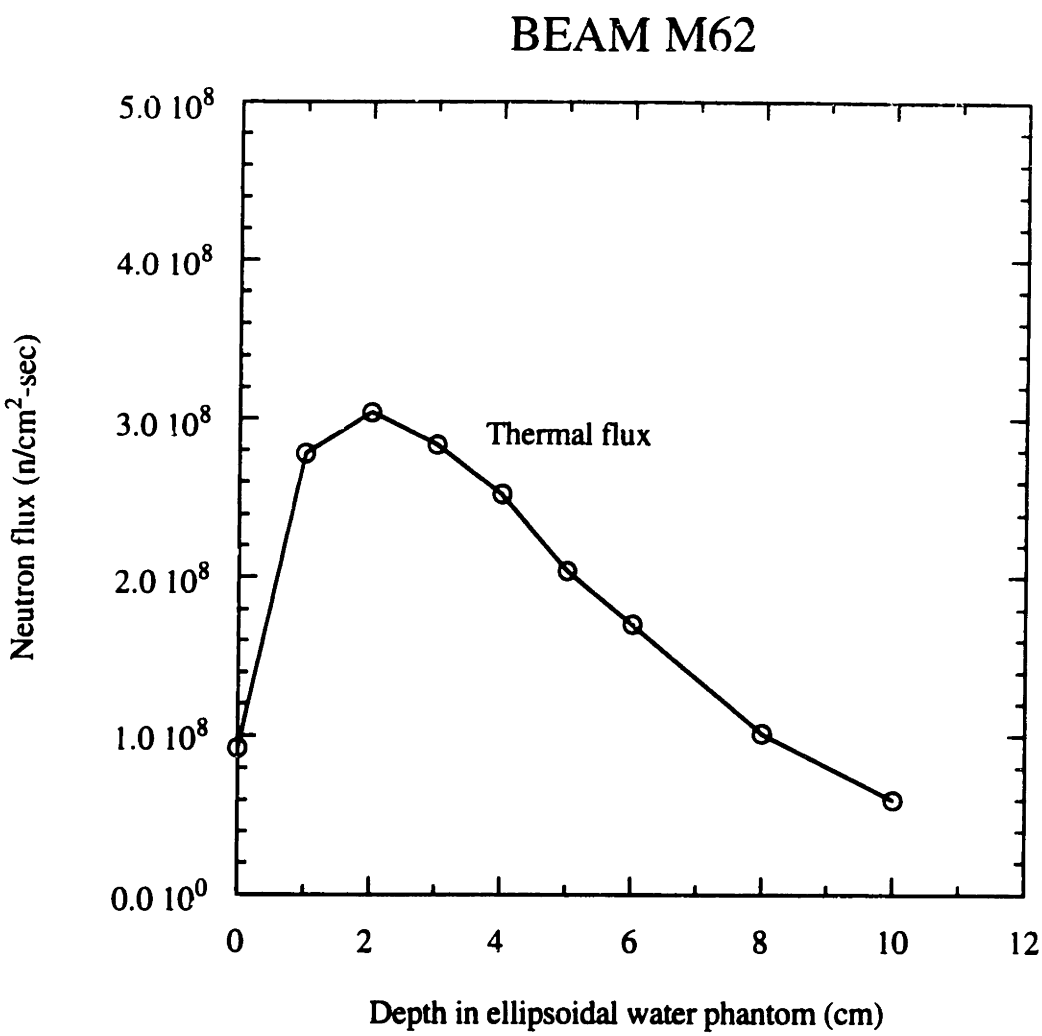

Figure 4.45. Thermal flux measured in phantom for the M62 beam.

Unilateral irradiation.
Phantom: Medium sized, ellipsoidal, water filled, center tube.
Reactor power: 5 MWn.

Table 4.3. Flux and dose data, in air, for several beams.

Beam	ϕ_{epi} (n/cm^2-sec)	ϕ_{th} (n/cm^2-sec)	D_{fn} (RBE cGy/min)	D_{γ} (RBE cGy/min)	D_{fn}/ϕ_{epi} (RBE cGy per n/cm^2)	D_{γ}/ϕ_{epi} (RBE cGy per n/cm^2)
M62	1.99E8	1.44E7	3.49	0.851	2.93E-10	7.13E-11
M61	2.24E8	6.03E7	4.70	1.415	3.50E-10	1.05E-10
M57	2.30E8	6.11E7	4.87	0.600	3.52E-10	4.35E-11

RBE's: fast neutron, 2.3; photon, 0.5. All fluxes and doses measured in air.

Table 4.4. Flux and dose data, in phantom, for several beams.

Beam	ϕ_{epi} (n/cm^2-sec)	ϕ_{th} (n/cm^2-sec)	D_{fn} (RBE cGy/min)	D_{γ} (RBE cGy/min)	D_{fn}/ϕ_{epi} (RBE cGy per n/cm^2)	D_{γ}/ϕ_{epi} (RBE cGy per n/cm^2)
M62	2.36E8	2.89E8	2.38	1.58	1.68E-10	1.11E-10
M61	2.41E8	4.06E8	2.86	2.37	1.98E-10	1.64E-10
M57	2.99E8	3.93E8	3.73	1.53	2.08E-10	8.52E-11

RBE's: fast neutron, 2.3; photon, 0.5.
The thermal flux, photon, and fast neutron doses were averaged over 1-3 cm depth. The epithermal flux was averaged over 0-2 cm depth.

Table 4.5. Summary of incident and induced photon doses.

Beam	D_γ in air (RBE cGy/min)	D_γ in phantom (RBE cGy/min)	ϕ_{th} peak in phantom (n/cm^2-sec)	D_γ induced col 3 - col 2 (RBE cGy/min)	D_γ induced per ϕ_{th} peak in phantom (RBE cGy per n/cm^2)
M62	0.854	1.59	3.04E8	0.74	4.07E-11
M61	1.42	2.41	4.19E8	0.99	3.93E-11
M57	0.600	1.57	3.98E8	0.97	4.03E-11

Note: Photon RBE = 0.5.

4.12 BEAM M63

Adding the cadmium plated aluminum shot with the M62 beam reduced the incident thermal flux by a factor of 4 relative to the M61 beam. The lower incident thermal flux also resulted in a large drop in the thermal flux near the surface of the phantom. With the M63 beam, it was decided to determine how much thermal flux could be recovered, if needed. To find out, the cadmium sheet on top of the collimator was removed. This beam is shown in figure 4.46. Measurements were only made in air. The results are: D_{fn} = 3.8 cGy/min, D_{γ} = 1.1 cGy/min, and $D_{30ppm\ B\text{-}10}$ = 8.4 cGy/min (RBE's of 2.3, 0.5, 4.0). Compared with the M62 beam, the M63 beam has about the same fast neutron dose, 35% higher photon dose, and an incident thermal flux about 10 times as high. Sufficient thermal flux, therefore, could be recovered if needed.

What's interesting is that the incident photon dose only increases by 35% even with a factor of 10 increase in the incident thermal flux. Prompt gammas originating in the collimator and surrounding lead, therefore, are not causing most of the incident photon dose. With only 9.7 cm of bismuth now in the collimator, most of the incident photons are originating from above the collimator. This is easy to show experimentally. With the M62 beam, for example, the incident photon dose was measured with all the shutters open. Then, the boral shutter was closed and the photon dose remeasured. Closing the boral shutter eliminates most of the thermal flux within the collimator, but the photon dose dropped by only 22%. More than 3/4 of the incident photons, therefore, originate from prompt gammas formed above the collimator or from core gammas directly.

4.13 BEAM M64

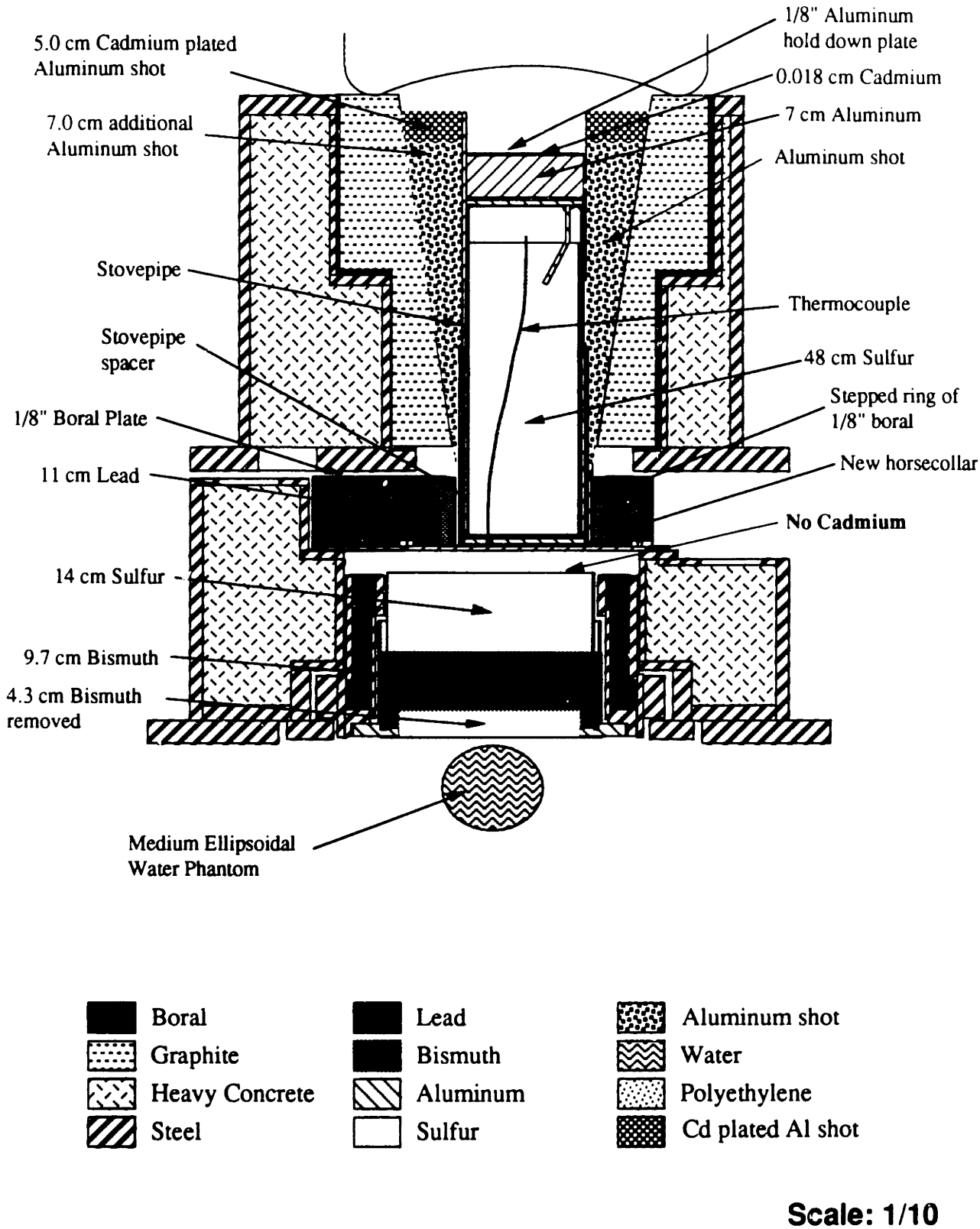

Figure 4.46. Cross sectional view of the M63 beam. In this beam, there was no cadmium on top of the collimator.

In this beam, it was decided to test another filter material - titanium. Titanium has two 30 barn resonances at 3 and 4 keV, a wide, 110 barn resonance at 18 keV, and several additional resonances in the keV range. Titanium (ASTM B 265 Grade 2) was purchased from Tico Titanium, Inc. (Farmington Hills, Mi). Three 1/8" thick plates (0.95 cm total) by 23 cm diameter were placed on top of the collimator as shown in figure 4.47. Otherwise, this beam is the same as the M62 beam. The 3/8" thickness of titanium would greatly reduce neutrons in the energy range 12-25 keV (factor of 10) and the energy ranges of the higher keV resonances. About 20% of the useful neutrons in the energy range 1 eV to 1 keV, as well as in the 1-5 MeV range, would scatter once within the titanium. Not all of these scattered neutrons would be lost from the beam; therefore, their attenuation would be somewhat less than 20%. The collimator was dropped 1 cm to allow clearance for the boral shutter.

Results are show in figures 4.48 and 4.49. The AR and AD of this beam are the same as those for the M62 beam, while the ADDR is about 11% less. The fast neutron dose rate and the thermal flux in phantom were about 15% lower with the M64 beam. These results are consistent with the expected scattering of useful epithermal neutrons and of MeV neutrons in the titanium filter. These results proved that neutrons in the energy range 12-25 keV do not make a significant contribution to the fast neutron dose.

4.14 BEAM M65

The M65 beam is shown in figure 4.50. This beam is a thermal beam, not an epithermal beam, and was installed so that other researchers on our BNCT project could continue with a series of thermal neutron beam irradiations of mice. The configuration of this beam is presented here for documentation, and to show how an epithermal beam can be rapidly converted to a thermal neutron beam. In this beam, all the filters were removed

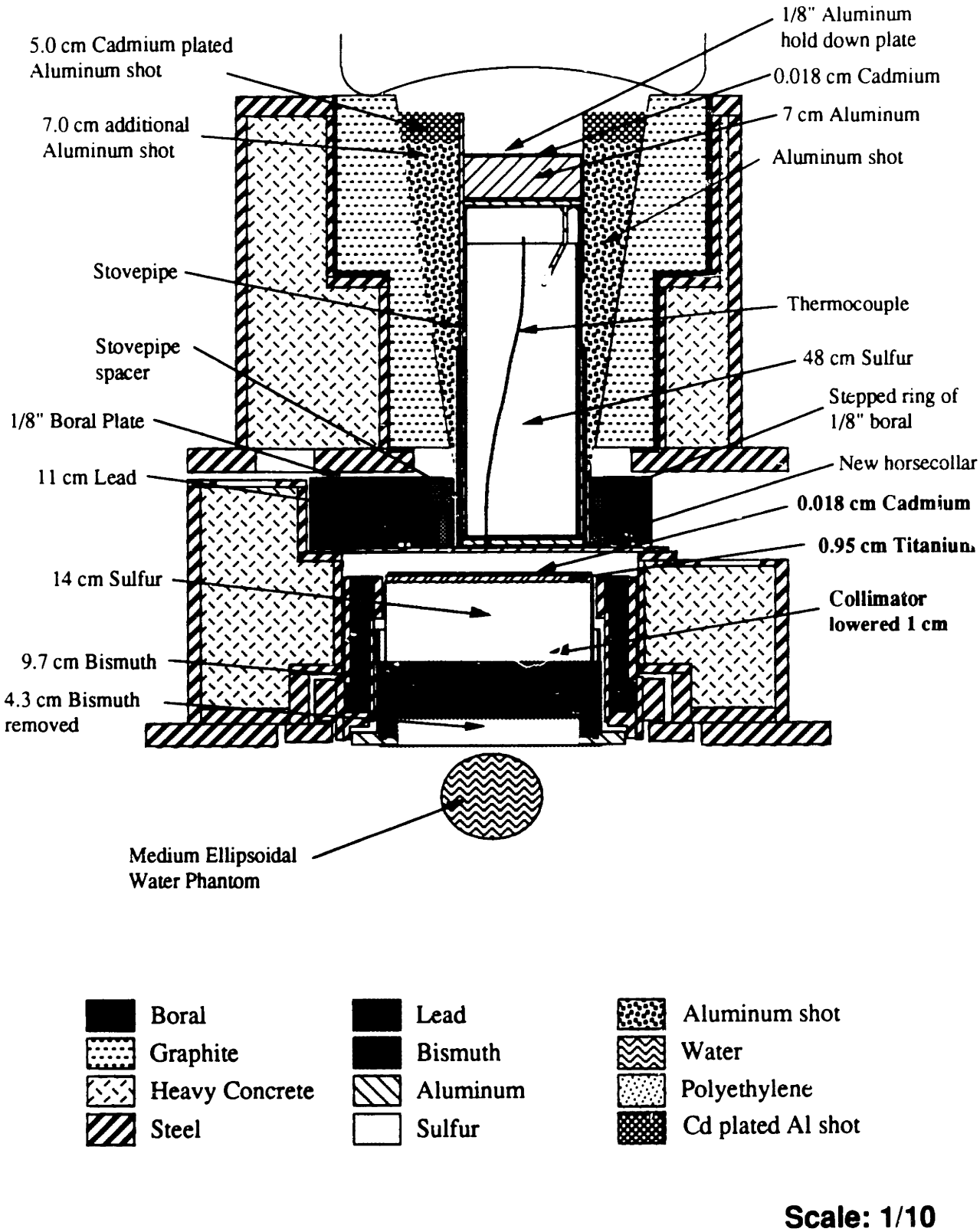

Figure 4.47. Cross sectional view of the M64 beam. Titanium was added above the collimator, which was lowered 1 cm to allow the boral shutter to clear.

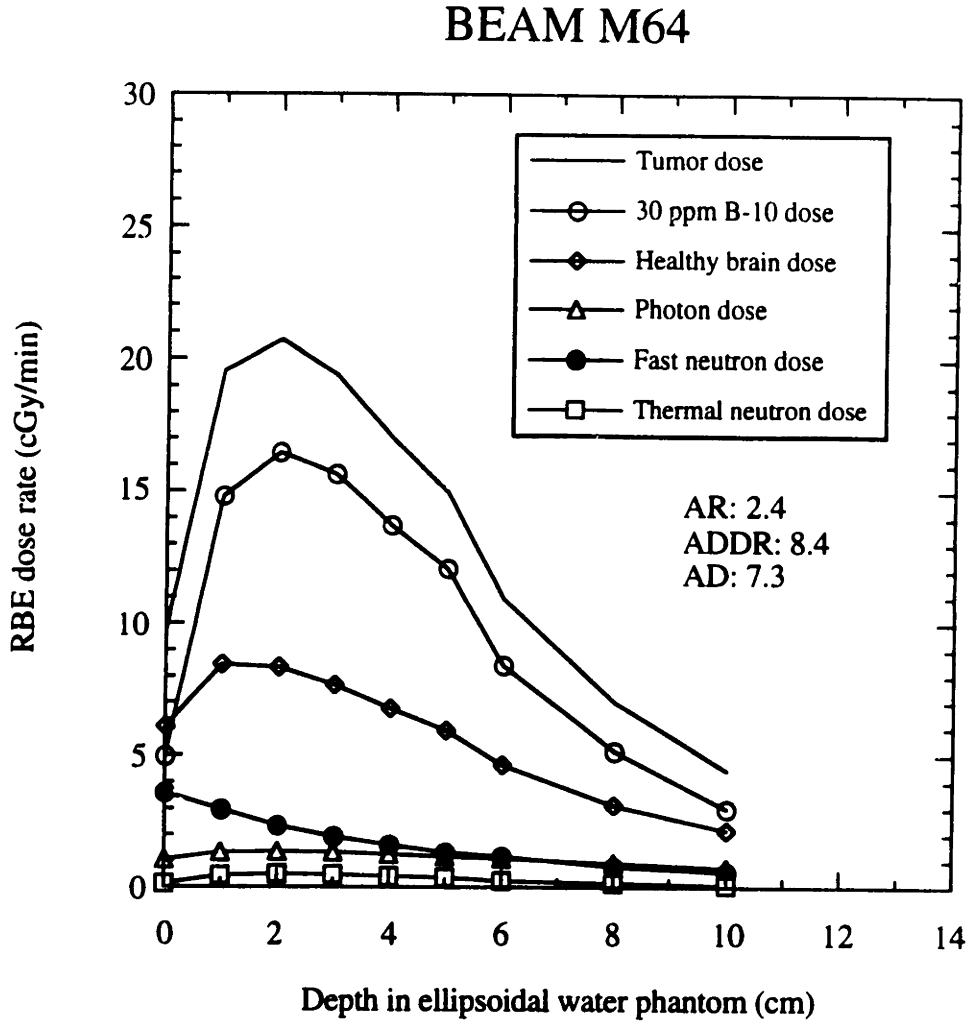

Figure 4.48. Doses measured in phantom for the M64 beam and BPA.

Unilateral irradiation.
Phantom: Medium sized, ellipsoidal, water filled, center tube.
Reactor power: 5 MWn.
RBE's: 4.0 for B-10, 2.3 for neutrons, 0.5 for photons.
B-10 concentrations: 30 ppm for tumor, 7.5 ppm for healthy brain.
In-air data: D_{fn} = 3.2 cGy/min
D_{γ} = 0.75 cGy/min
$D_{30ppm\ B\text{-}10}$ = 0.89 cGy/min

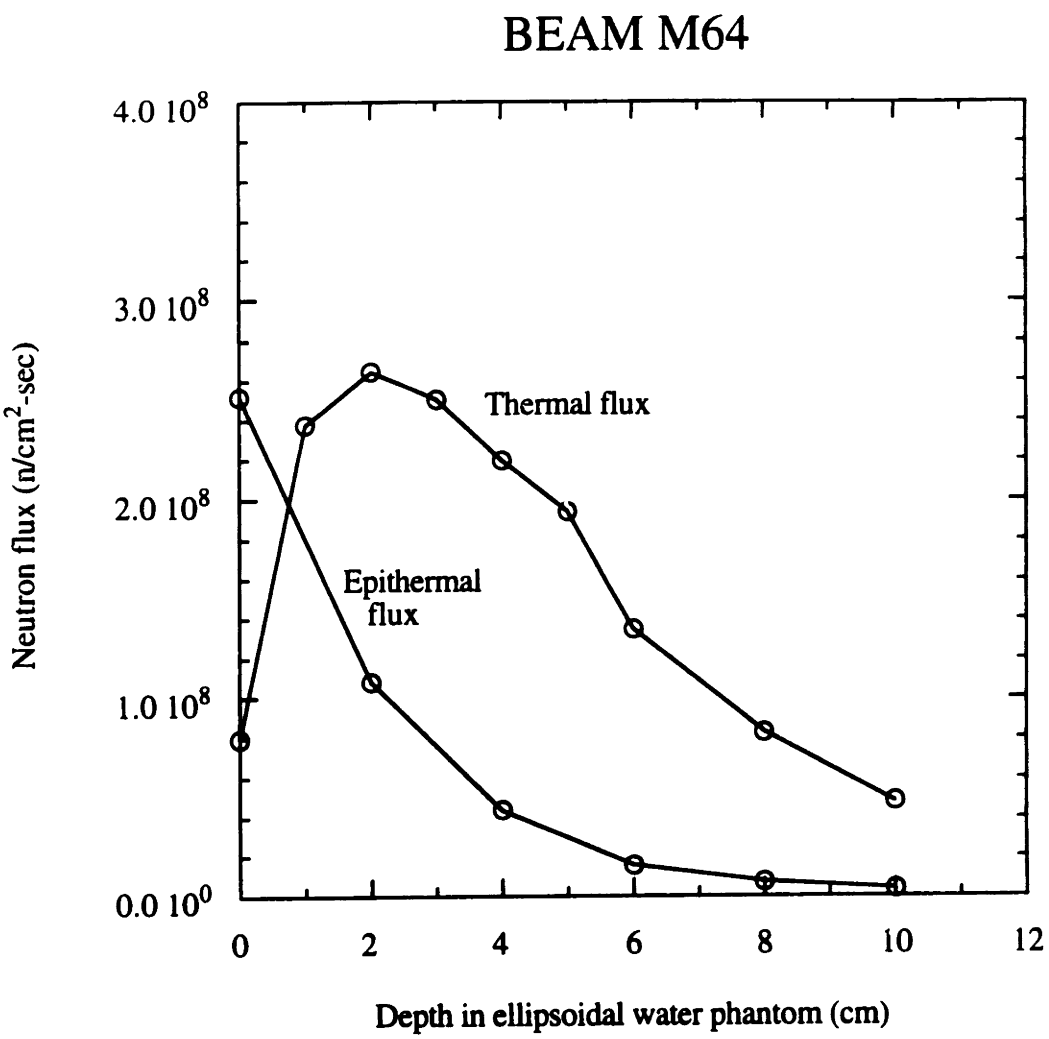

Figure 4.49. Thermal and epithermal fluxes measured in phantom for the M64 beam.

Unilateral irradiation.
Phantom: Medium sized, ellipsoidal, water filled, center tube.
Reactor power: 5 MWn.

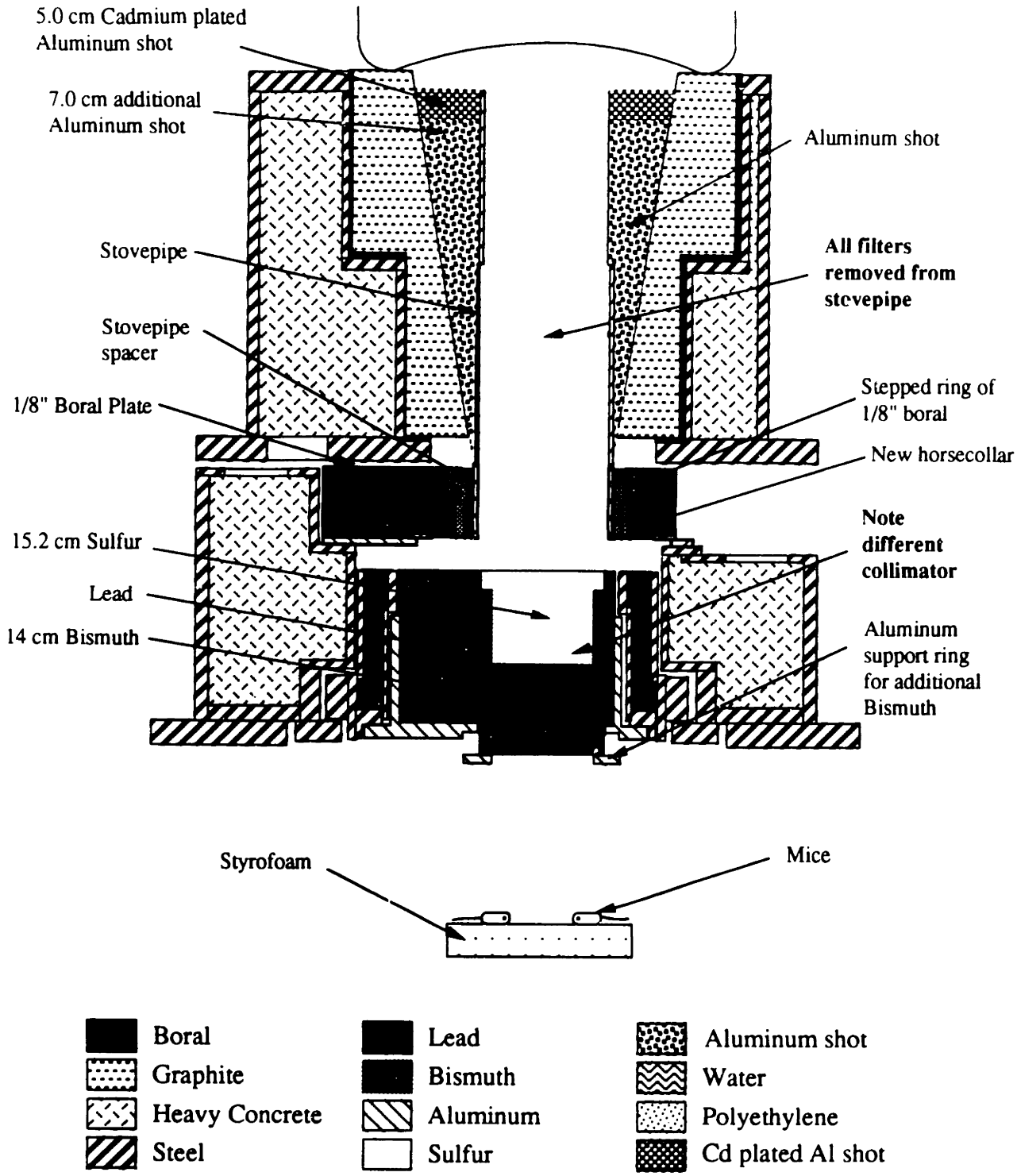

Figure 4.50. Cross sectional view of the M65 beam. This is a thermal neutron beam. It was used for many of the mouse irradiations carried out by our group to test the efficacy of BNCT.

from the central stovepipe, and a different collimator was installed into the lead shutter. There is no cadmium above the collimator. Two circular rings of bismuth are bolted to the bottom of the collimator with a support ring. It takes two people about 2-3 hours to convert to a thermal beam. Assistance from the Radiological Protection Office is needed at times. Also, it is preferable that the reactor be shut down for at least one day before the beam is changed.

It is noted that this beam is different from the thermal beam used initially in the mouse irradiation studies. The major difference is that this beam has additional aluminum shot and the cadmium plated shot at the top of the cone region.

Fluxes and doses were measured in air, 27 cm below the bottom of the bismuth, on the centerline of the collimator. At 4.5 MWn, the thermal flux was 1.4E9 n/cm^2-sec, the photon dose was 12.2 RBE cGy/min, and the fast neutron dose was 2.07 RBE cGy/min. RBE's were 1.6 for fast neutrons and 1.0 for photons.

4.15 BEAM M62 - SUPPLEMENTAL

Because the titanium filter tested in the M64 beam did not improve the quality of the beam, it was decided to return to the M62 beam. A review of the previous beams concluded that the M62 beam would be the best for the initial clinical trials in the treatment of deep seated melanoma. It was decided, therefore, to obtain additional dosimetric information on this beam.

1. Fall off of fluxes and doses with distance below the lead shutter

The fluxes and doses were measured in air at several distances below the lead shutter, shown as positions 1, 2, and 3 in figure 4.51. The reference plane is the bottom of

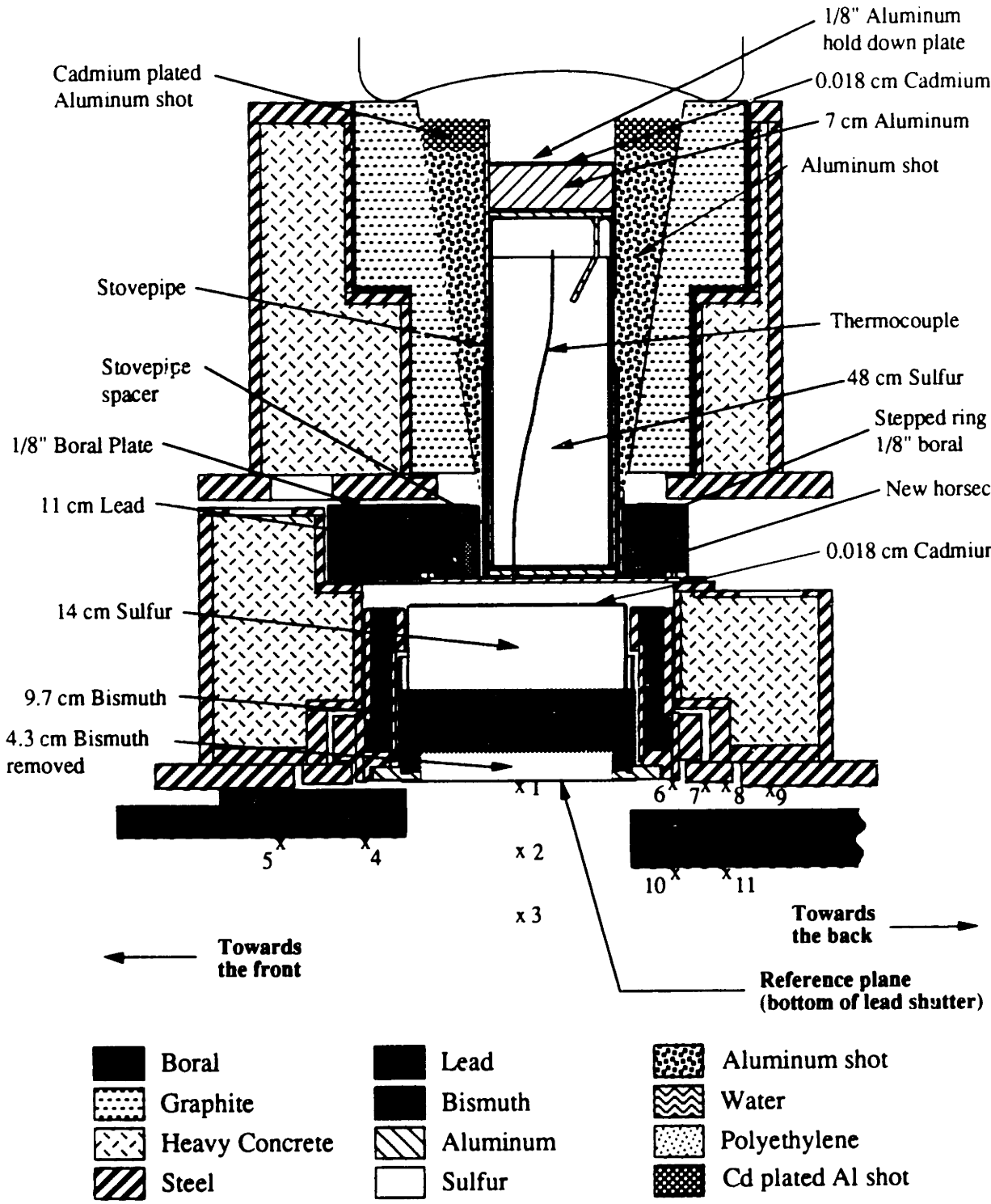

Scale: 1/10

Figure 4.51. Cross sectional view of the M62 beam showing the bioshields and the positions where dose and flux measurements were taken. The reference plane is the bottom of the lead shutter. The bioshield on the right was removed to measure at positions 6-9.

the lead shutter. This information was important as it had been determined that there might be a gap of up to 4" between the part of the body that was to be treated and the bottom of the lead shutter. Test with mock patients showed that some part of the patient's body would contact one of the bioshields or the whole body shield, leaving a gap between the plane of the lead shutter and the part of the patient's body that was to be irradiated. This gap would significantly reduce the intensity of the beam. Results are shown in figure 4.52. The fluxes and doses fall off rapidly and at about the same rate. A 10% reduction is seen at a gap of 1", and a 30% reduction at 3". It's important, therefore, to position the patient as close as possible to the bottom of the lead shutter.

2. Fall off of fluxes and doses along the lead shutter and perpendicular to the lead shutter

This information was needed to estimate the whole body doses that a patient would receive, and to provide the information needed to design a whole body shield and delimiter for the beam that would minimize the whole body dose. Results for positions along the lead shutter and perpendicular to the lead shutter are shown in figures 4.53 - 4.56. The fluxes and doses were measured 1/2" below the lead shutter. The beam intensity was highest below the centerline of the collimator. The intensity dropped to half this value at about 18 cm from the centerline, both along the lead shutter and perpendicular to the lead shutter. The symmetry between the fluxes measured beneath the half moon and back bioshield is noted.

The fluxes and doses were also measured above the back bioshield, shown as positions 6-9 in figure 4.51. To do this, the first section of the back bioshield was removed. With this section of bioshield removed, the patient could be positioned just below the lead shutter. Results are shown in figures 4.55 and 4.56. The fluxes and fast neutron dose were 1-2 times higher above the bioshield. The photon dose was about 10 times higher. No hot spots from streaming were seen. These results show that removing

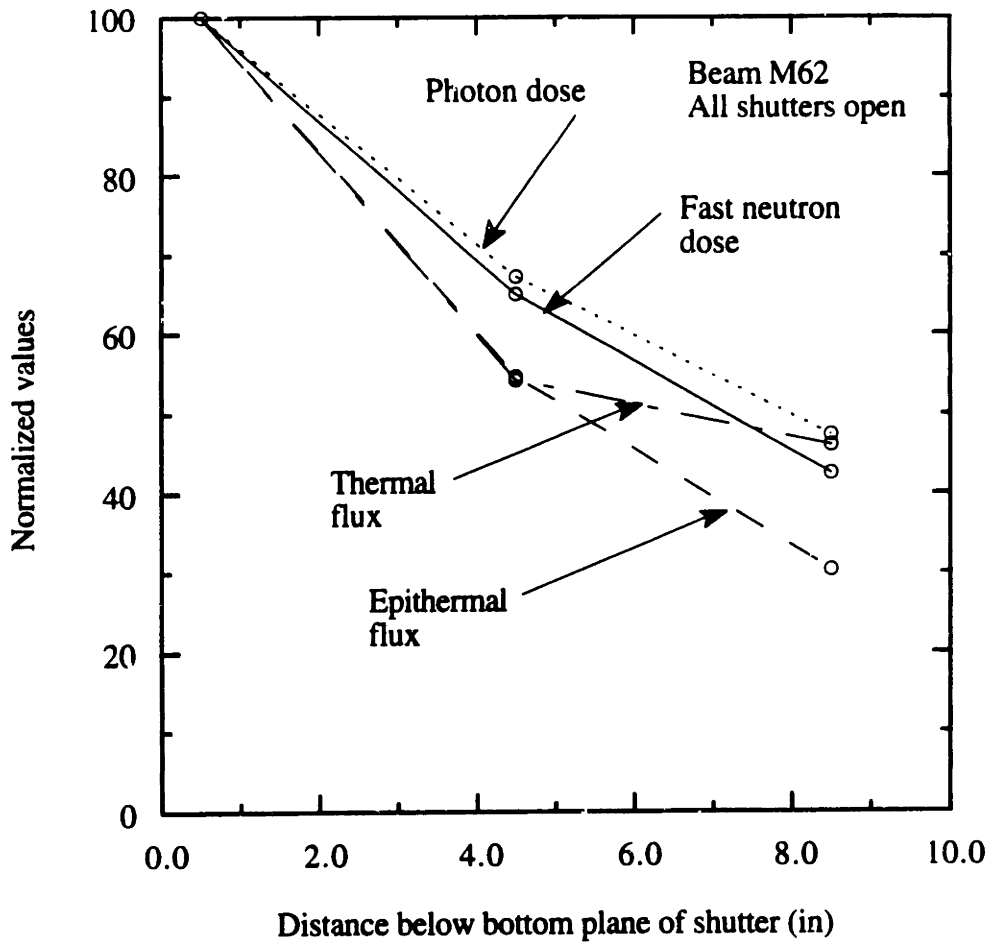

Figure 4.52. The doses and fluxes were measured at 3 positions below the plane of the lead shutter, shown as positions 1, 2, and 3 in Figure 4.51. These data are for the M62 beam with all the shutters open. The epithermal flux falls off at a slightly faster rate than the others. A substantial drop in intensity is seen with distance below the collimator. With the bioshields in place, the groin or armpit areas of some patients might be 1-3 inches below the collimator.

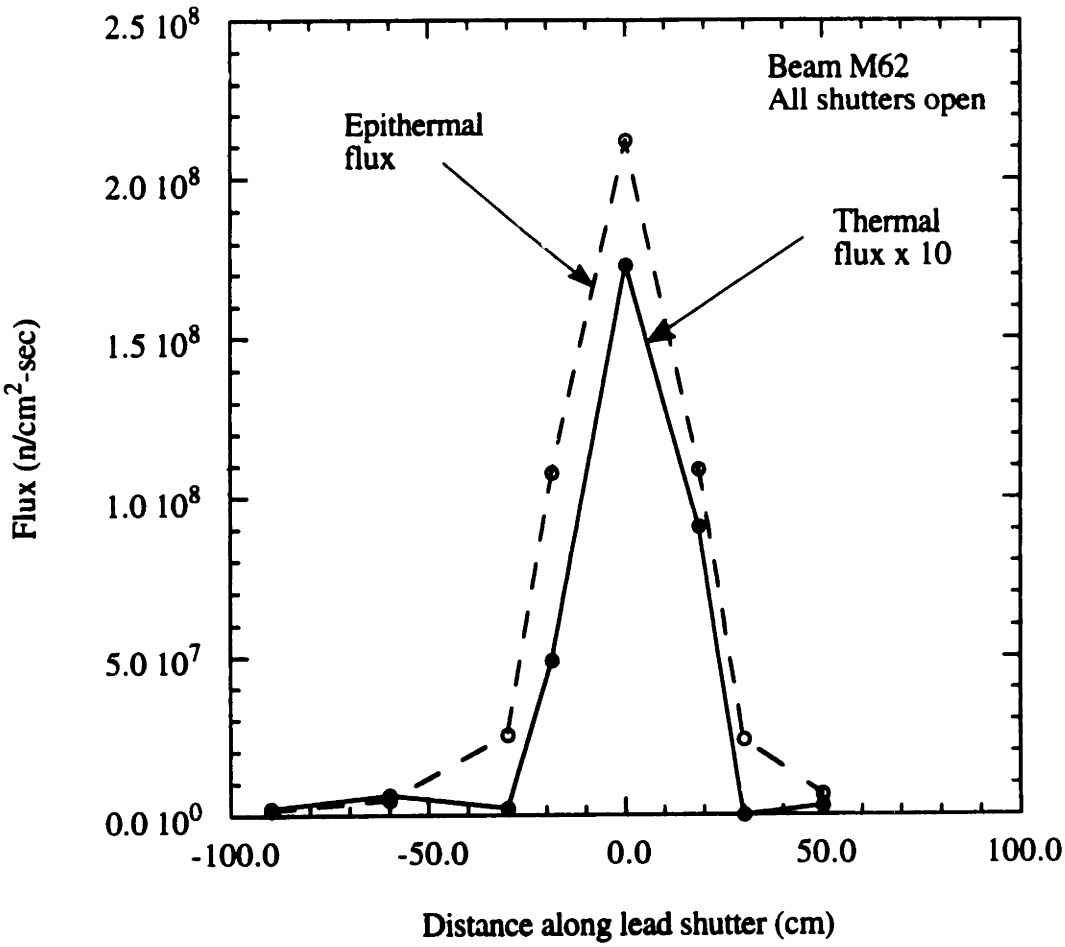

Figure 4.53. Thermal and epithermal fluxes measured 1.2 cm below the lead shutter from the left of the beam to the right. The reference plane is the bottom of the lead shutter. The thermal fluxes have been multiplied by 10. Phantom: none. Reactor power: 5 MWn.

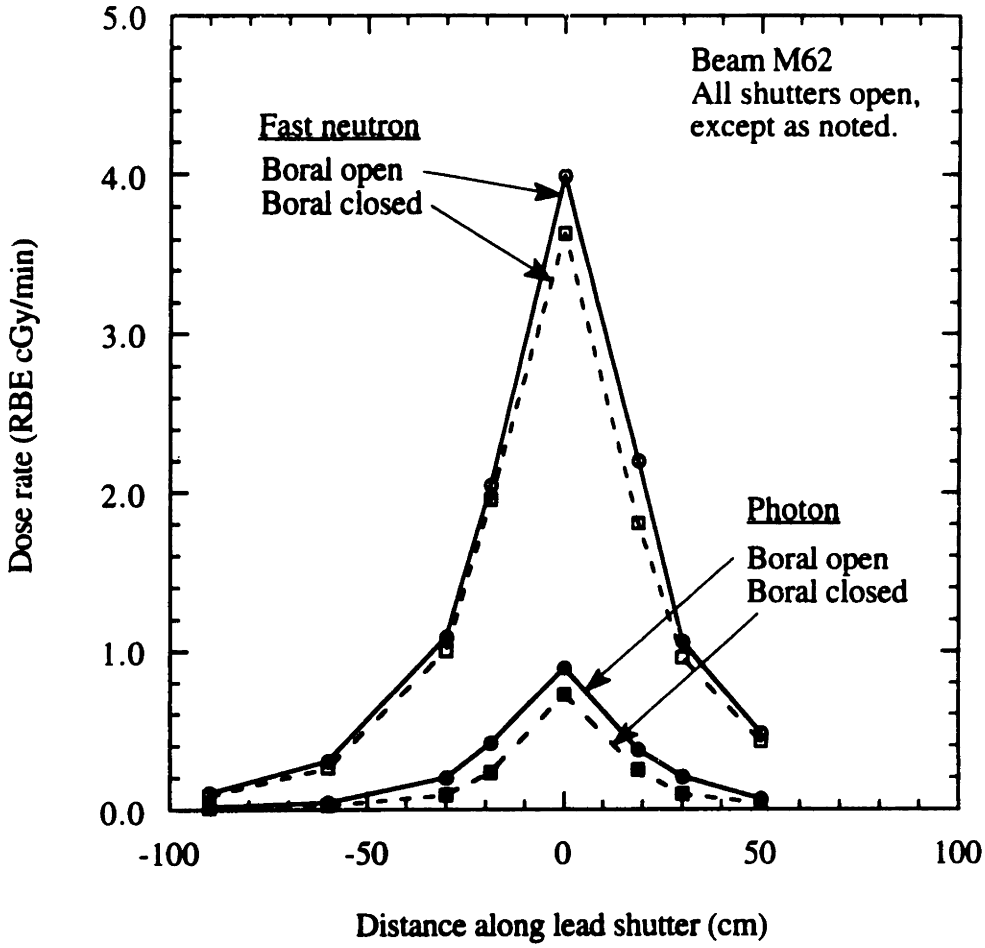

Figure 4.54. Photon and fast neutron doses measured 1.2 cm below the lead shutter from the left of the beam to the right. The reference plane is the bottom of the lead shutter. Phantom: none. Reactor power: 5 MW_n. RBE's: 2.3 for the fast neutron dose, 0.5 for the photon dose.

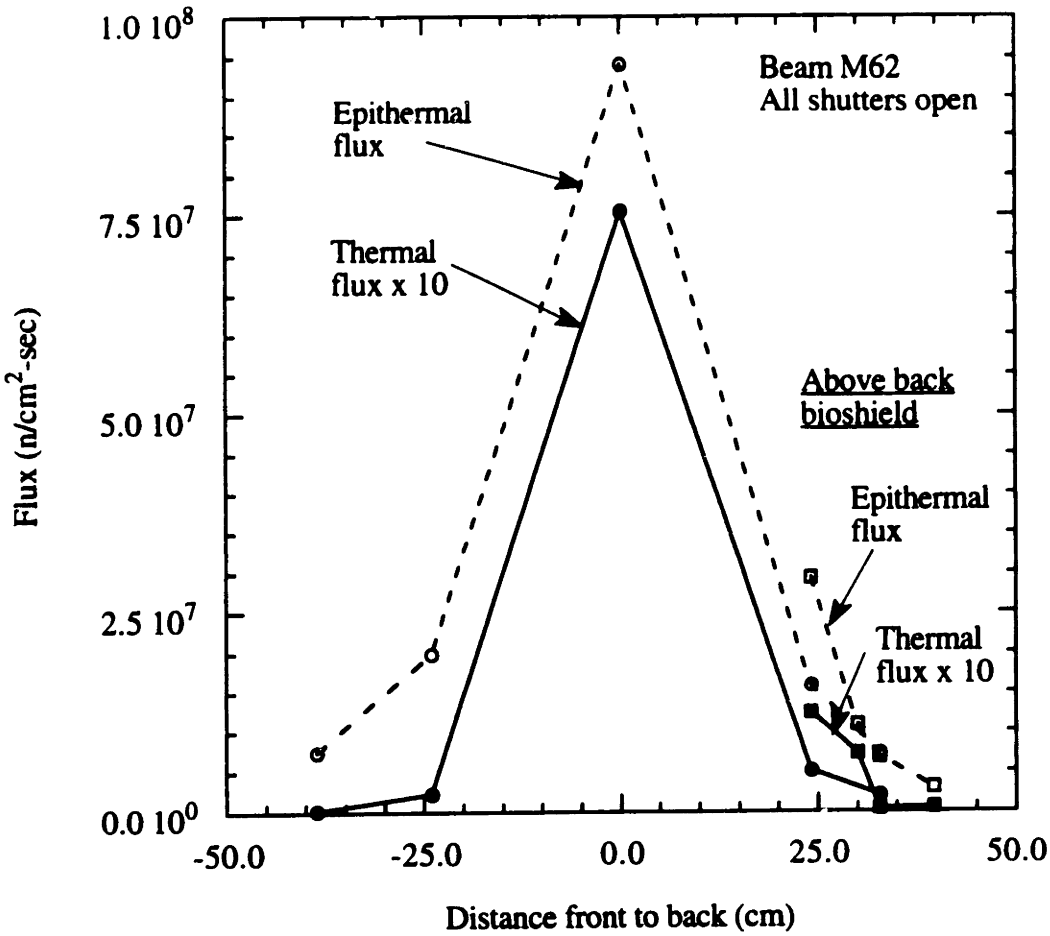

Figure 4.55. Thermal and epithermal fluxes measured from the front of the beam to the back, shown as positions 5, 4, 2, 10, and 11 in figure 4.51. The reference plane is the bottom of the lead shutter. Fluxes above the back bioshield, positions 6-9, are also shown. The thermal fluxes have been multiplied by 10. Phantom: none. Reactor power: 5 MWn.

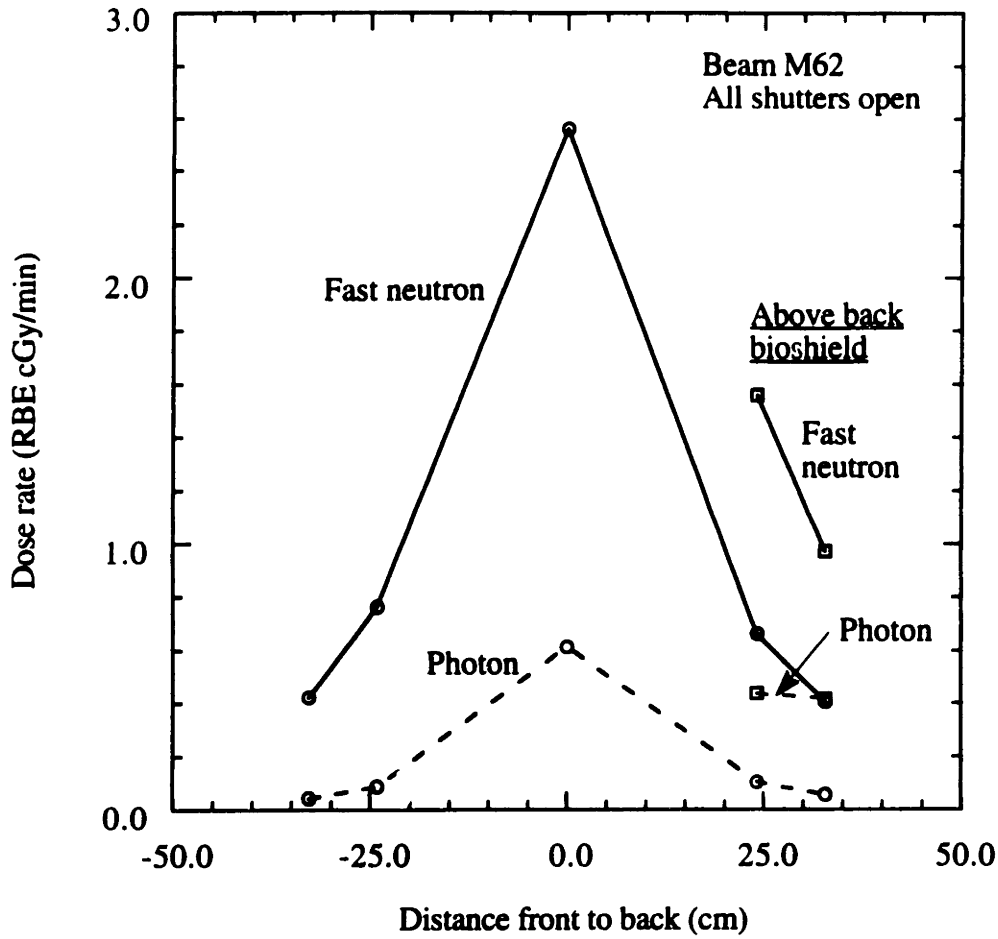

Figure 4.56. Photon and fast neutron doses measured from the front of the beam to the back, shown as positions 5, 4, 2, 10, and 11 in figure 4.51. The reference plane is the bottom of the lead shutter. Doses above the back bioshield, positions 6 and 8, are also shown. Phantom: none. Reactor power: 5 MWn. RBE's: 2.3 for the fast neutron dose, 0.5 for the photon dose.

the back bioshield to better position the patient would result in a substantially higher whole body dose. It's informative to compare the values at positions 1 and 6. At position 6, the thermal flux is 10 times lower while the epithermal flux is 6 times lower. However, the fast neutron and photon dose rates are only 2.5 and 2.1 times lower. Therefore, the patient's body in area 6 will receive a substantial dose (roughly 890 RBE cGy over a treatment that gives a maximum dose of 2000 RBE cGy to healthy tissue in the treatment area) from fast neutrons and photons at the surface. This assumes that the same body part is positioned in that location for each treatment. The whole body doses that would be received during an irradiation are discussed in more detail in chapter 5.

Health physics surveys were also made with the back bioshield removed. These are discussed in Chapter 6.

Flux and dose data for the positions shown in figure 4.51 are summarized in table 4.6.

3. Effects of whole body shields and delimiters

With the fluxes and dose rates in the general beam area now known, a whole body shield and beam delimiter were designed and made. Two inch thick slabs of borated polyethylene were available in the reactor laboratory; it was decided to cut these to size (14 1/16" x 43") and use them as the whole body shield. Two rails were made to support the slabs. The rails were bolted to the bioshields on either side of the lead shutter.

A beam delimiter was also designed and made. The delimiter was 60 cm x 36 cm, 2" thick, with a 20 cm diameter whole in the center. It was made by melting paraffin and pouring the melt into a mold layer by layer.[4] Sufficient Li_2CO_3 was added such that the thermal neutron capture rate was 10 times higher in the lithium than in the hydrogen. This was done to suppress production of hydrogen prompt gammas that would increase the

Table 4.6. Flux and dose data measured for the M62 bioshield study.

Position	Thermal flux (n/cm^2-sec)	Epithermal flux (n/cm^2-sec)	Fast neutron dose (RBE cGy/min)	Photon dose (RBE cGy/rnin)
Below centerline of collimator				
1	1.39E7	1.72E8	3.93	0.913
2	7.56E6	9.41E7	2.56	0.615
3	6.42E6	5.23E7	1.67	0.433
Below half moon				
4	2.35E5	1.99E7		
5	2.68E4	7.53E6		
Above back bioshield				
6	1.24E6	2.93E7	1.56	0.435
7	7.24E5	1.08E7		
8	4.19E4	6.81E6	0.970	0.416
9	5.86E4	3.03E6		
Below back bioshield				
10	5.10E5	1.58E7	0.663	0.102
11	2.09E5	7.27E6	0.404	0.055

Notes: Data have been normalized to a reactor power of 5 MWn. RBE's were assumed to be 2.3 for fast neutrons and 0.5 for photons. These data were obtained with all shutters open as they would be during a radiation treatment. Refer to Figure 4.51 for the locations where these fluxes and doses were measured. The reference plane is the bottom of the lead shutter.

gamma dose to the patient. The delimiter is supported by the same railing that supports and positions the whole body shields.

Fluxes and doses were measured in air with and with out the whole body shields and delimiter in place. These are shown in figures 4.57 and 4.58. The delimiter has little effect on the epithermal fluxes near the centerline of the hole in the delimiter (0 and -5 cm). Beneath the delimiter (-15 cm), however, the epithermal flux is about a factor of 10 lower. With the delimiter, the thermal flux is higher near the centerline of the hole. This is due to the generation of thermal flux in the delimiter near the hole. Underneath the delimiter, the thermal flux is lower due to attenuation of the epithermal flux and absorption of thermal neutrons within the delimiter itself.

At 0 cm, 70 % of the drop in the fast neutron dose with the delimiter is attributed to being 5.1 cm further below the bismuth shield. The remaining 30% is due to the shielding of the delimiter. At -15 cm, the fast neutron dose without the delimiter was measured at 2.43 RBE cGy/min, and would be expected to be 2.04 RBE cGy/min 5.1 cm further down. The fast neutron dose measured at that position was 0.706 RBE cGy/min. The delimiter, therefore, reduced the fast neutron dose by a factor of 2.9. A factor of 2.7 was expected based on the attenuation of the fast neutron dose in the water filled head phantom.

A similar analysis was done for the photon doses. With the delimiter, the photon dose was 5% higher than expected at 0 cm, and 13% higher at -15 cm. These data indicate that there is a slight increase in the incident photon field due to hydrogen prompt gammas that are produced in the delimiter itself. (These hydrogen prompt gammas could be reduced further by adding more Li_2CO_3 or LiF to the paraffin, but then the effectiveness of the delimiter in reducing the fast neutron dose would be reduced as hydrogen is displaced.)

This delimiter was effective in reducing the fast neutron dose by a factor of 2.9 without greatly increasing the incident photon field. It performed as expected. However, the surface dose to the patient, 5 cm outside the edge of the treatment area, would still be rather high. The fast neutron dose alone would be roughly 125 RBE cGy, if that part of

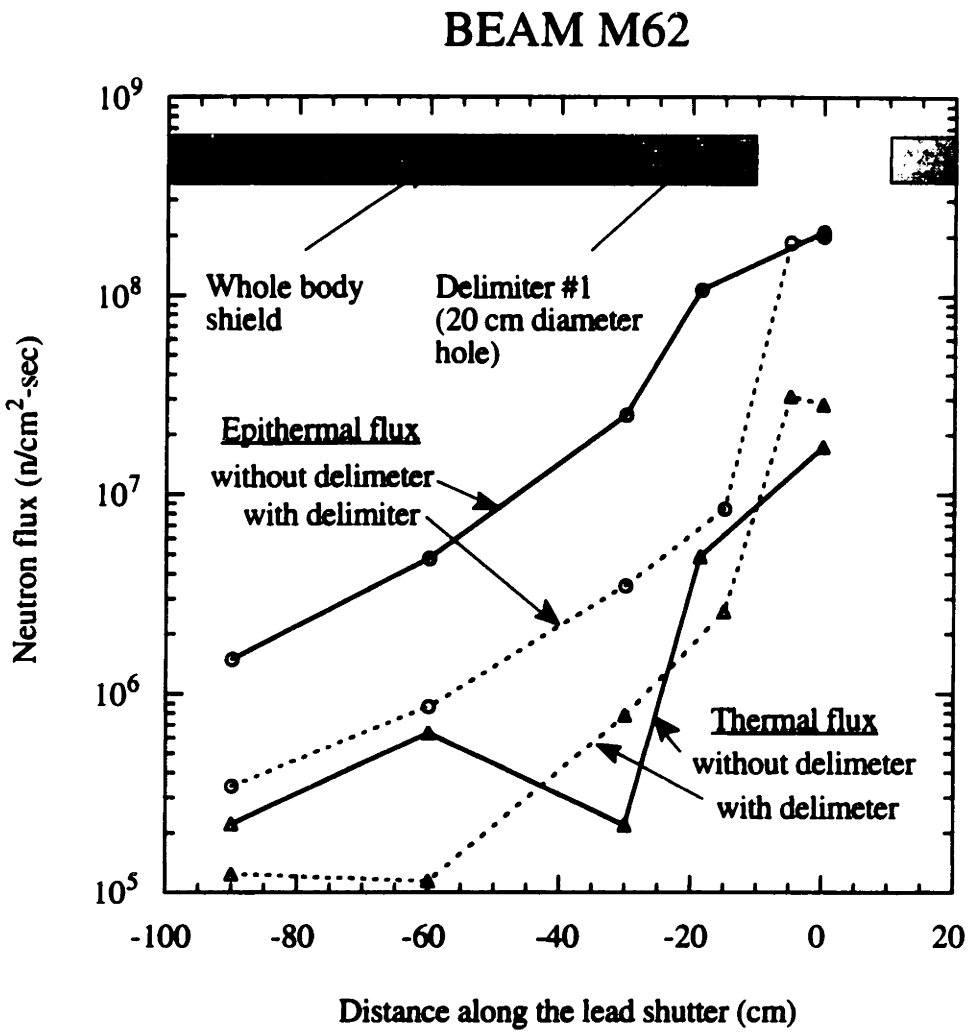

Figure 4.57. Comparison of thermal and epithermal fluxes with and without delimiter #1. The doses were measured in air 1.3 cm below the lead shutter or delimiter. The delimiter did not affect the epithermal flux near the centerline of the hole, but reduced it a factor of 10 below the delimiter. Phantom: none. Reactor power: 5 MWn.

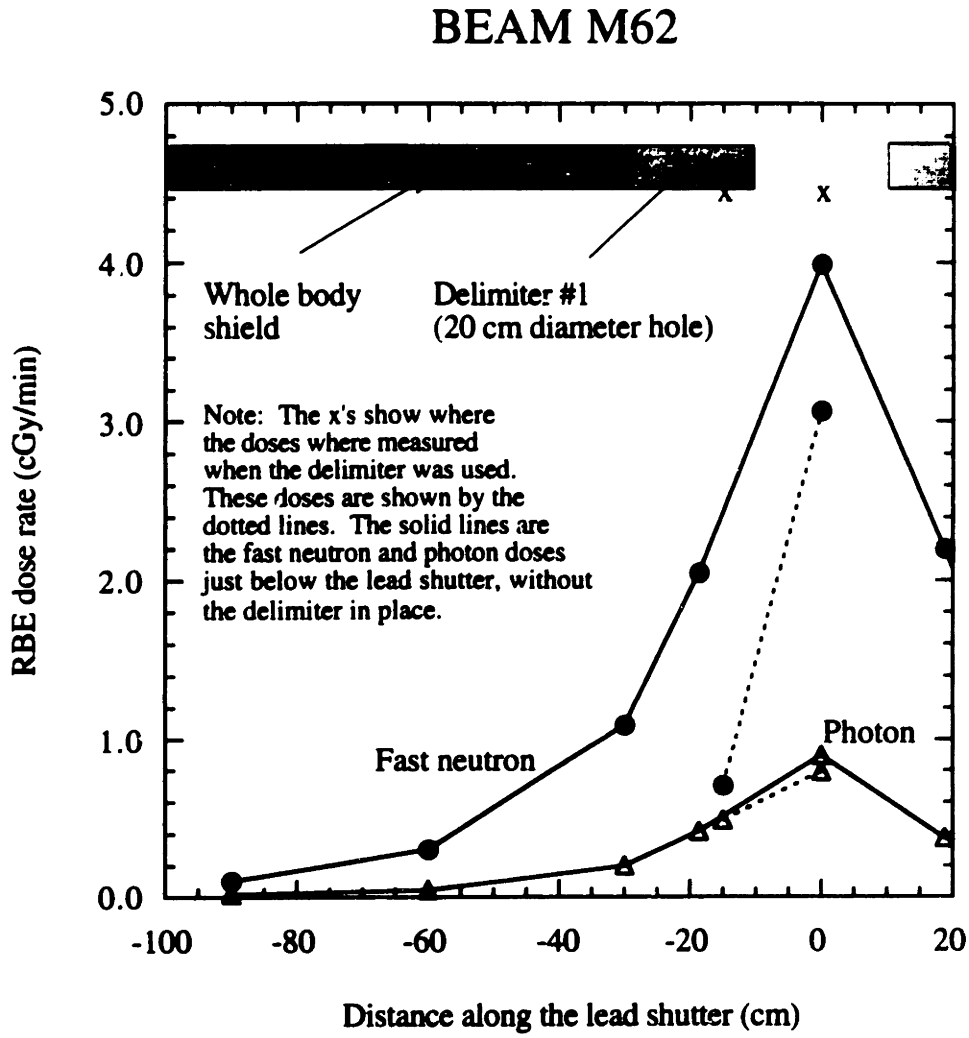

Figure 4.58. Comparison of photon and fast neutron doses with and without delimiter #1. The doses were measured in air 1.3 cm below the lead shutter or delimiter. The fast neutron dose is reduced by a factor of 2.9 below the delimiter. Phantom: none. Reactor power: 5 MWn. RBE's: 2.3 for the fast neutron dose, 0.5 for the photon dose.

the body were positioned in the same place for all fractions. This assumes a maximum healthy tissue dose of 2000 RBE cGy in the treatment area.

Fluxes and doses were also measured in a half-body Wax-130 phantom, described in Chapter 2, with the whole body shields and delimiter in place. The phantom was positioned so that the mid-thigh was under the centerline of the delimiter. The knee was touching the bottom of the delimiter. The fluxes and doses were measured at 0 and 2 cm depth from the mid-thigh up to the pelvis. Results are shown in figures 4.59 and 4.60. The fluxes are attenuated very rapidly by the delimiter, both at the surface and at the 2 cm depth.

The photon and fast neutron doses fall off more gradually below the delimiter. Most of the photon dose results from prompt gammas generated within the phantom. The delimiter, then, would not be expected to be effective in rapidly attenuating the photon dose. The fast neutron dose is attenuated more rapidly than the photon dose. Some of this attenuation appears to be due to the delimiter. However, a similar off axis attenuation experiment without the delimiter was not done.

4.16 BEAM M62 - GROIN IRRADIATION

At this time, it was thought that the first patients who would be treated would have deep seated melanoma of the groin region. Therefore, it was decided to make a new phantom, and measure the radiation doses in the groin region. A new wax phantom, extending from the chest to the knees, was made.[4] This phantom is described in Chapter 2. A hole was drilled through the groin so that the gold foils and ionization chambers could be positioned. The chambers were inserted into a butyrate tube as usual. When the tube was pulled down through the phantom, plugs of wax were inserted from the top to fill the air space above the tube.

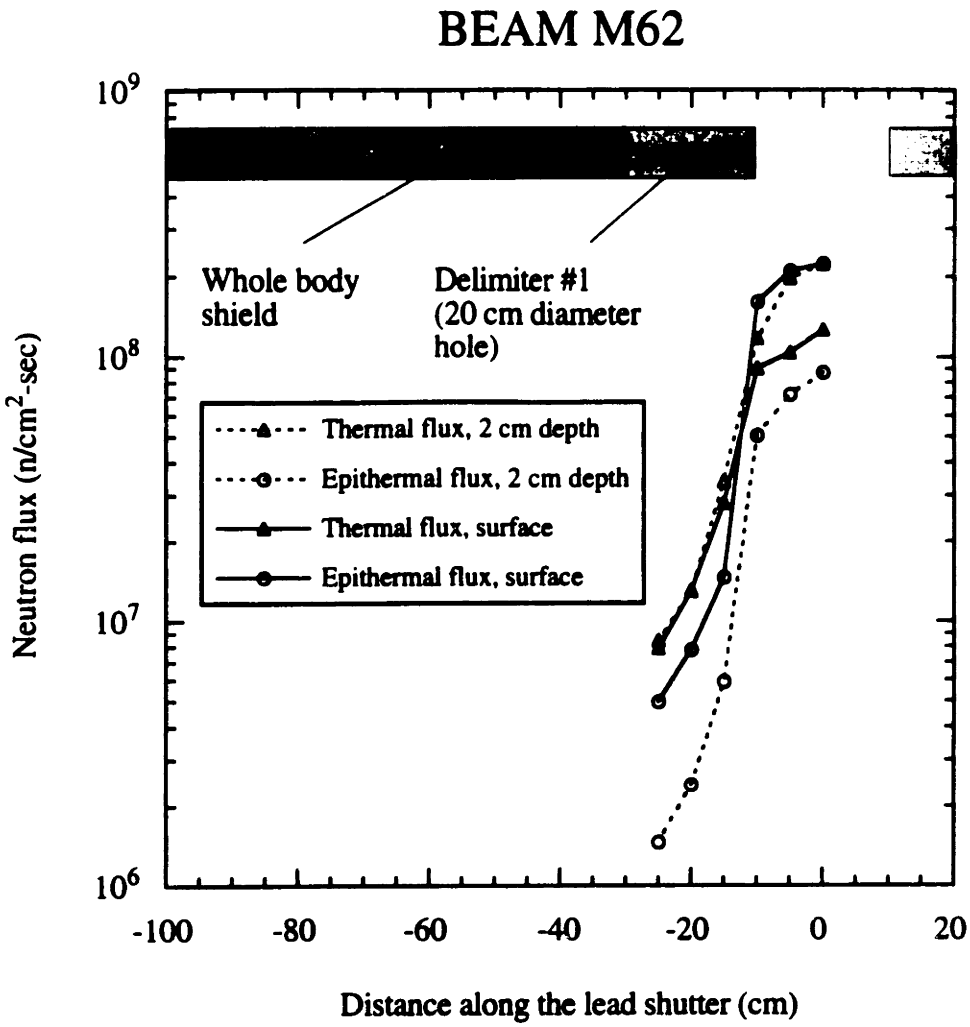

Figure 4.59. Measured thermal and epithermal fluxes in the mid-thigh of the half-body wax-130 phantom while using delimiter #1. The beam centerline is at 0 cm. These doses were measured towards the left of the beam centerline. The fluxes drop rapidly below the delimiter. Refer to figure 4.51. Reactor power: 5 MWn.

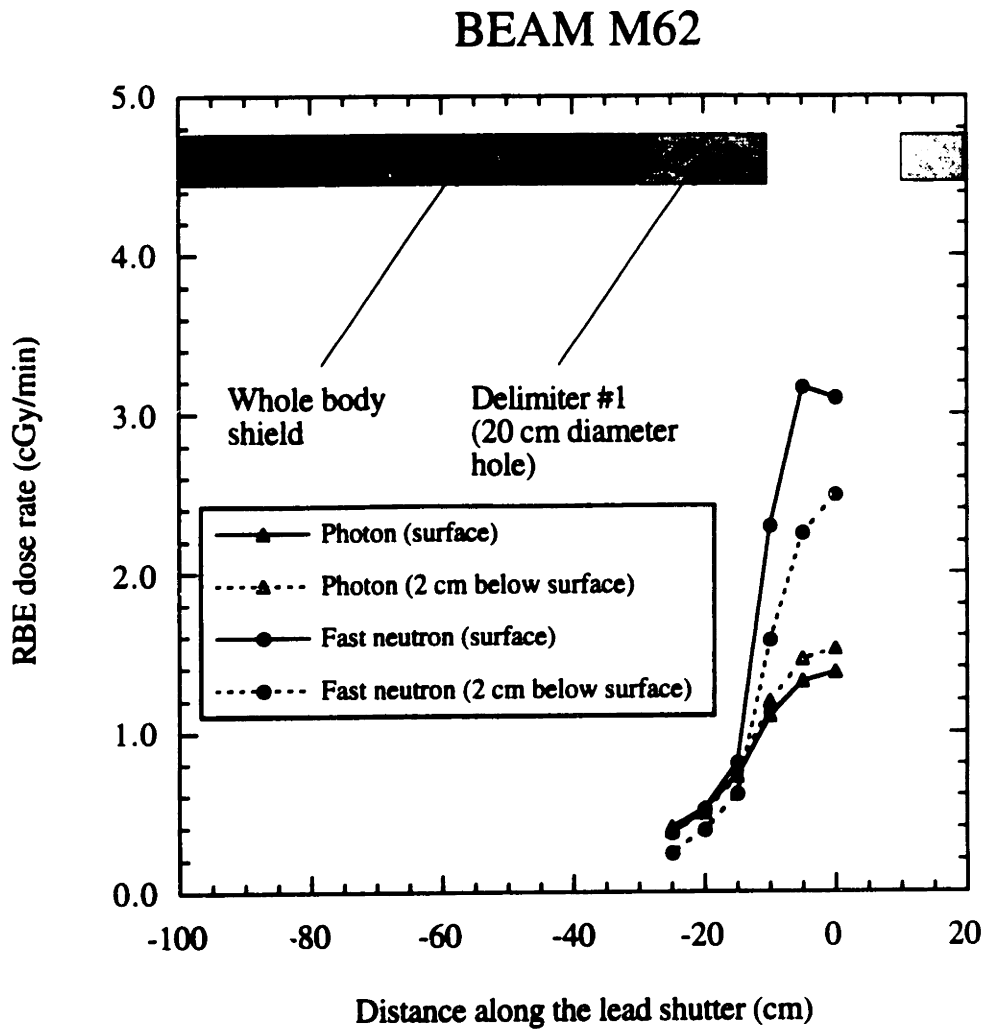

Figure 4.60. Measured photon and fast neutron doses in the mid-thigh of the half-body wax-130 phantom while using delimiter #1. The beam centerline is at 0 cm. These doses were measured towards the left of the beam centerline. These doses fall off much more gradually than the fluxes. Refer to figure 4.51. Reactor power: 5 MW_n. RBE's: 2.3 for the fast neutron dose, 0.5 for the photon dose.

The beam and groin phantom are shown in figure 4.61. Delimiter #1 (20 cm diameter) was used with this characterization. Results are shown in figures 4.62 and 4.63. These results were compared with those of the M62 beam using the head phantom. There were several differences. First, the intensities of the radiation components are about 15-20% less in the groin phantom. This loss in intensity can be attributed to the delimiter and the additional 2" between the phantom and the bottom of the delimiter. Second, the thermal flux does not drop off as much at the surface of the groin phantom. The half body phantom is flat on the top, not sharply curved like the head phantom, so the higher level of thermal flux at the surface is expected. The additional hydrogenous material at the top of the groin phantom moderates the incident epithermal neutron and so acts as a thermal neutron source. The thermal neutron source at the to of the phantom would add to the thermal flux at the top of the phantom. Finally, the thermal flux falls off more rapidly with depth in the groin phantom. This also seems mostly due to the different size and shape of the phantom. The additional hydrogenous material at the top of the groin phantom attenuates the epithermal flux more rapidly; therefore, there will be less thermal flux generated at depth. The faster drop off in the thermal flux leads to a significantly lower AD (5.8 cm) in the groin phantom.

Because the fast neutron dose relative to the thermal flux in the groin phantom was higher than expected based on the previous results in the head phantom, it was decided to repeat the chamber measurements at the top and at the 1 cm depth inside the groin phantom. Results are shown in figure 4.64. The photon and fast neutron doses repeated well. It was concluded that the differences in the doses measured with the M62 beam and the head phantom and with the M62 beam, delimiter #1, and the groin phantom are due in fact to using the delimiter and the differences in the phantoms.

4.17 BEAM M62 - MID-THIGH IRRADIATION

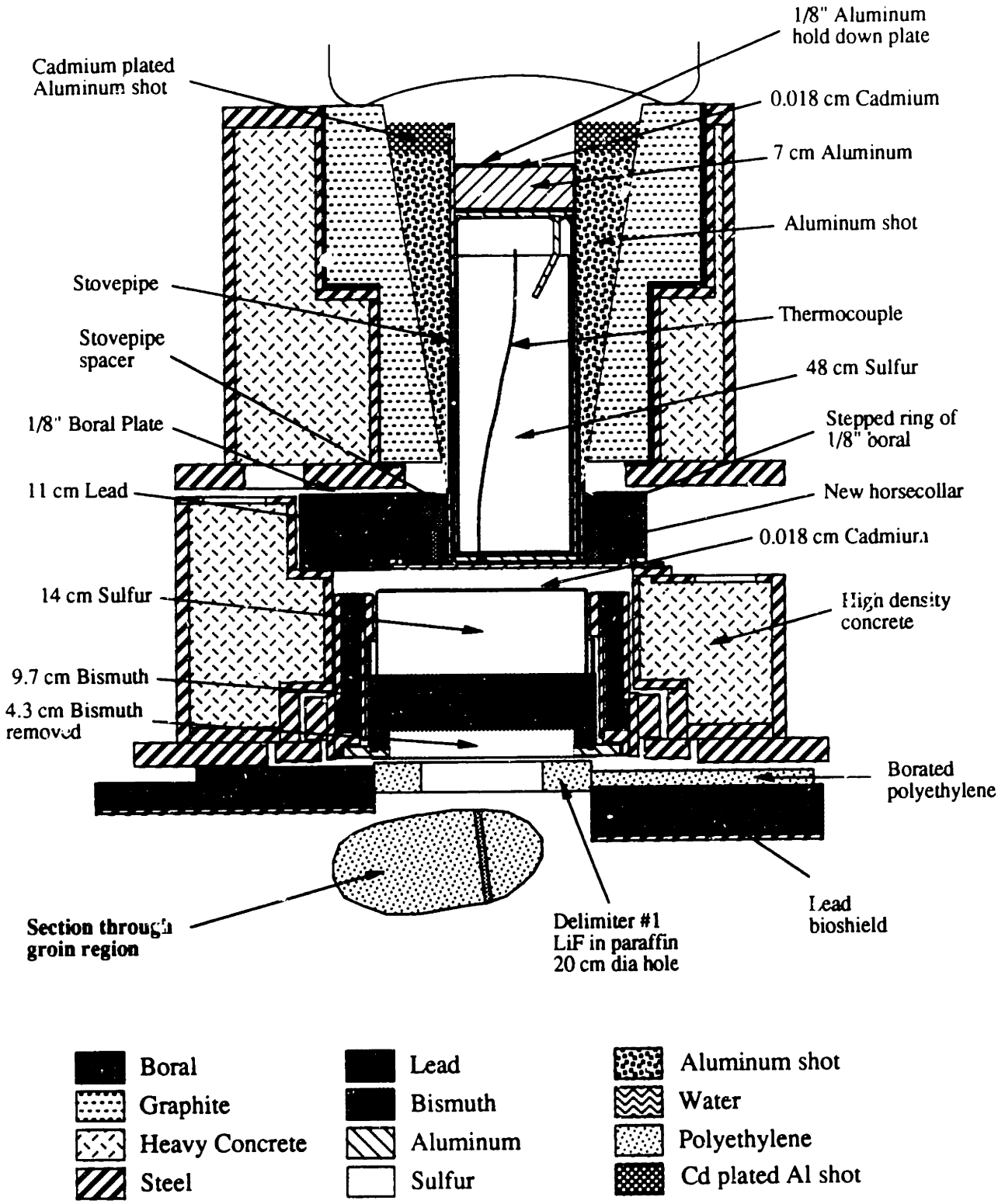

Figure 4.61. Cross section for the M62 beam, delimiter #1, and the groin phantom. The phantom was positioned so the left groin was centered below the beam.

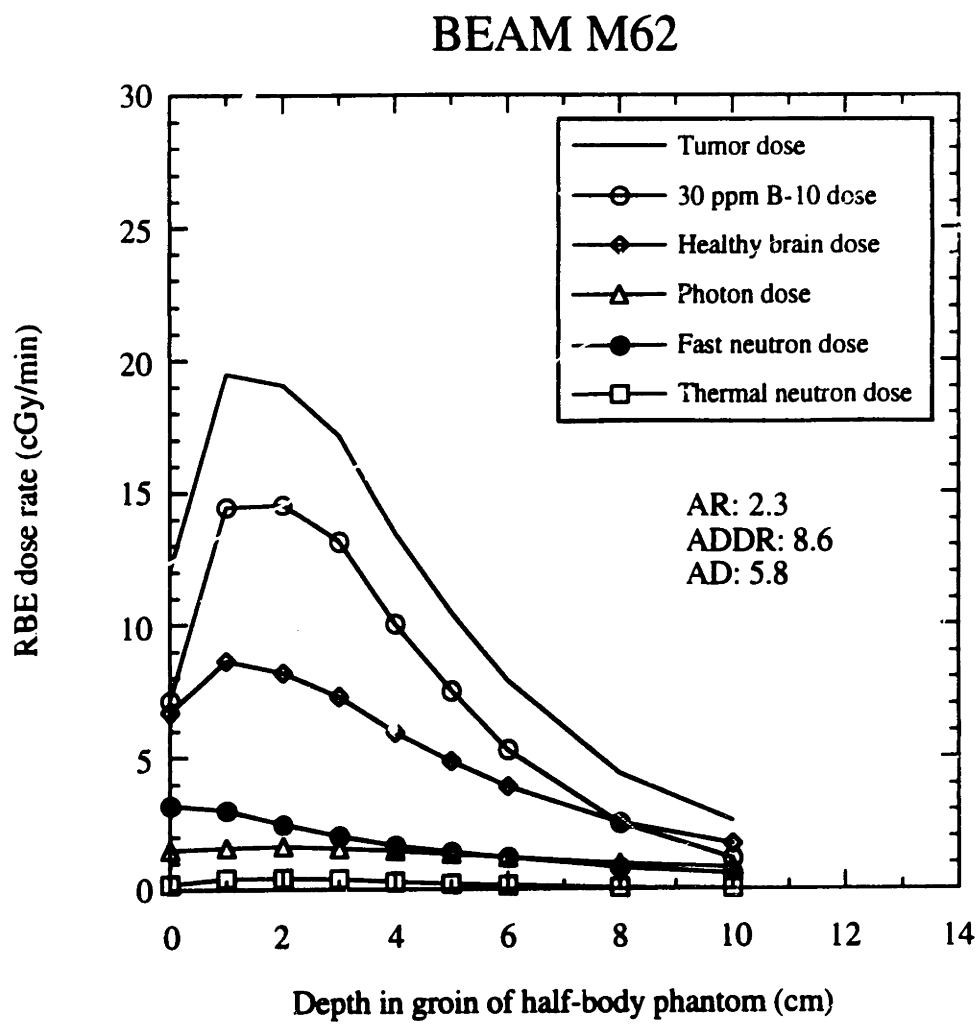

Figure 4.62. Doses measured in the groin phantom for the M62, delimiter #1 (20 cm diameter hole) beam and BPA.

Unilateral irradiation.
Phantom: Wax half-body, center tube through groin.
Delimiter: #1. LiF in paraffin, 5.1 cm thick, 20 cm diameter hole.
Reactor power: 5 MWn.
RBE's: 4.0 for B-10, 3.2 for neutrons, 0.5 for photons.
B-10 concentrations: 30 ppm for tumor, 7.5 ppm for healthy brain.
In-air data: D_{fn} = 3.1 cGy/min
D_{γ} = 0.79 cGy/min
$D_{30ppm\ B\text{-}10}$ = 1.8 cGy/min

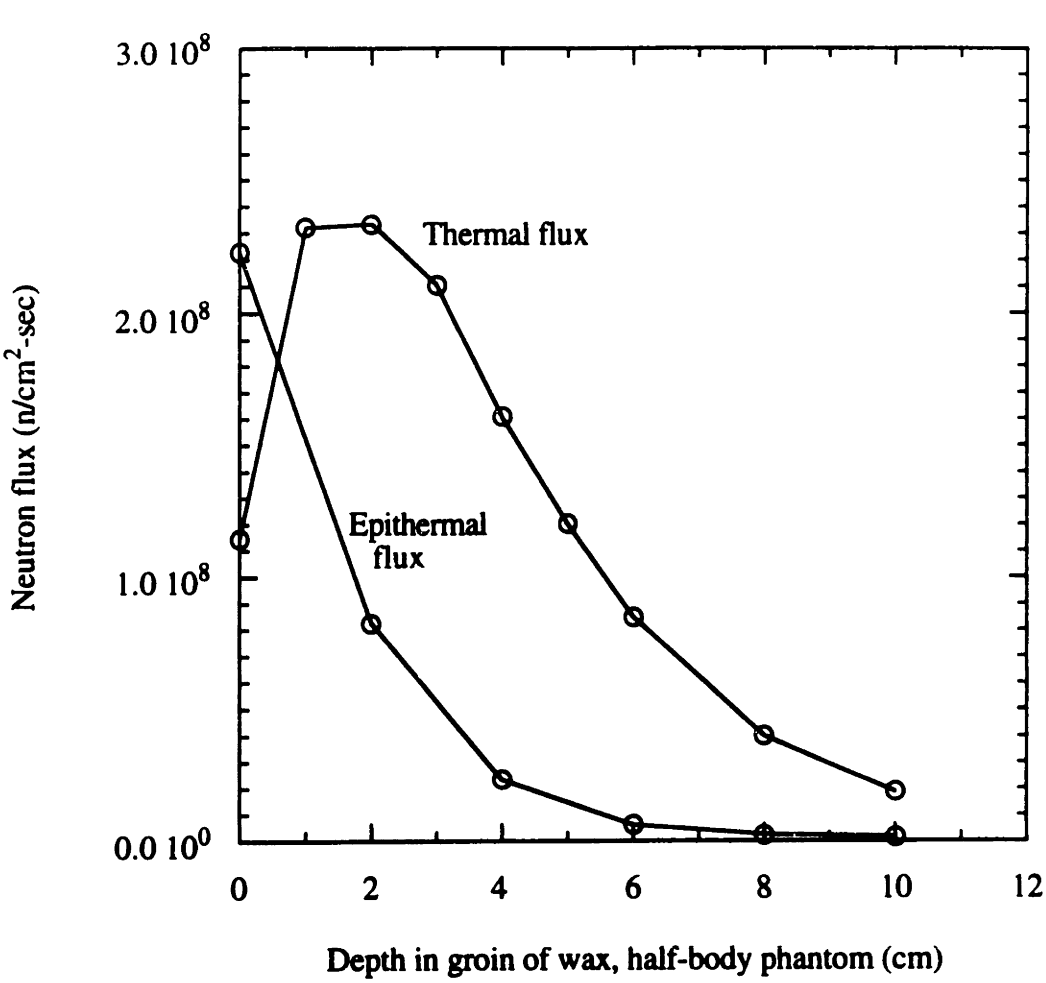

Figure 4.63. Thermal and epithermal fluxes measured in the groin phantom for the M62, delimiter #1 beam.

Unilateral irradiation.
Phantom: Wax half-body, center tube through groin.
Delimiter: #1. LiF in paraffin, 5.1 cm thick, 20 cm diameter hole.
Reactor power: 5 MWn.

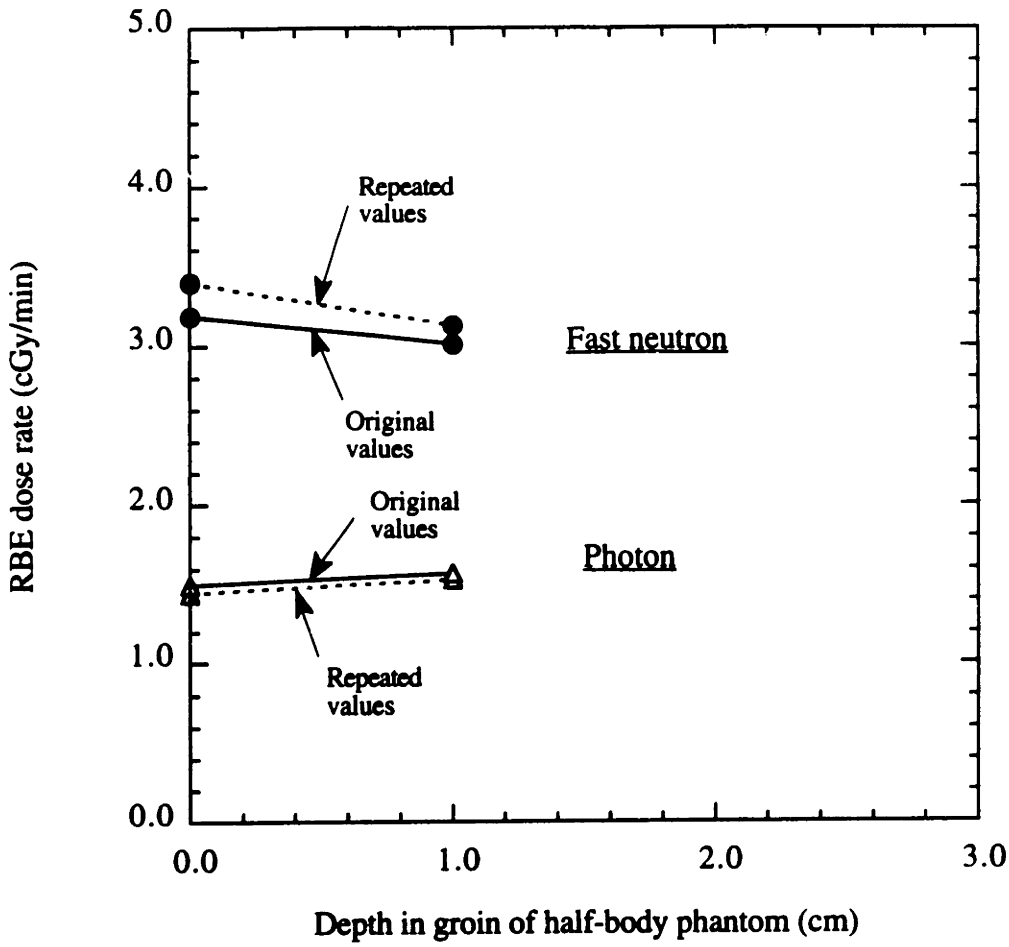

Figure 4.64. Repeat measurement data for the M62, delimiter #1, groin phantom beam and BPA. The photon and fast neutron doses repeated well, especially since the dosimetry was repeated at a later date and the phantom had to be re-positioned.

Unilateral irradiation.
Phantom: Wax half-body, center tube through groin.
Delimiter: #1. LiF in paraffin, 5.1 cm thick, 20 cm diameter hole.
Reactor power: 5 MWn.
RBE's: 4.0 for B-10, 2.3 for neutrons, 0.5 for photons.
B-10 concentrations: 30 ppm for tumor, 7.5 ppm for healthy brain.

At this time, it was decided to obtain dose information for an irradiation of the mid thigh. Irradiations of the groin would result in high doses to the lower abdominal organs, bladder wall, and genitals. Irradiation of more distal areas would result in much lower doses to these areas. A new Wax-130 phantom, extending from the chest to the knees, was made.[4] This phantom is described in Chapter 2. A hole was drilled through the mid-thigh so that the gold foils and ionization chambers could be positioned.

The beam and thigh phantom are shown in figure 4.65. Results are shown in figures 4.66 and 4.67. These results are similar to those obtained with the groin phantom. The most important difference is that the thermal flux falls off more gradually with depth in the phantom, probably because there is less hydrogenous material at the top of this phantom than at the top of the groin phantom. Less attenuation of the epithermal flux leads to a higher thermal flux at depth. This leads to a slightly higher AD with the thigh phantom.

4.18 BEAM M66

With these data available, it was decided to modify the M62 beam in two ways. First, the bottom and sides of the collimator were painted with a Li-6 enriched (96 atom % Li-6) carbonate latex paint to reduce the thermal flux within the collimator and the incident thermal flux. Li-6 was used since thermal neutron capture does not produce any prompt gammas of significance. 2.0 g of the enriched Li-6 carbonate were used for every 5 cc of paint - carbonate mixture. Four to five coats of this paint were found to attenuate the thermal flux by 90%, as measured by an attenuation transmission experiment using the usual 4DH1 thermal neutron beam. An attenuation curve for this paint is shown in figure 4.68. Part of the lead shutter around the collimator was also painted with the Li-6 paint.

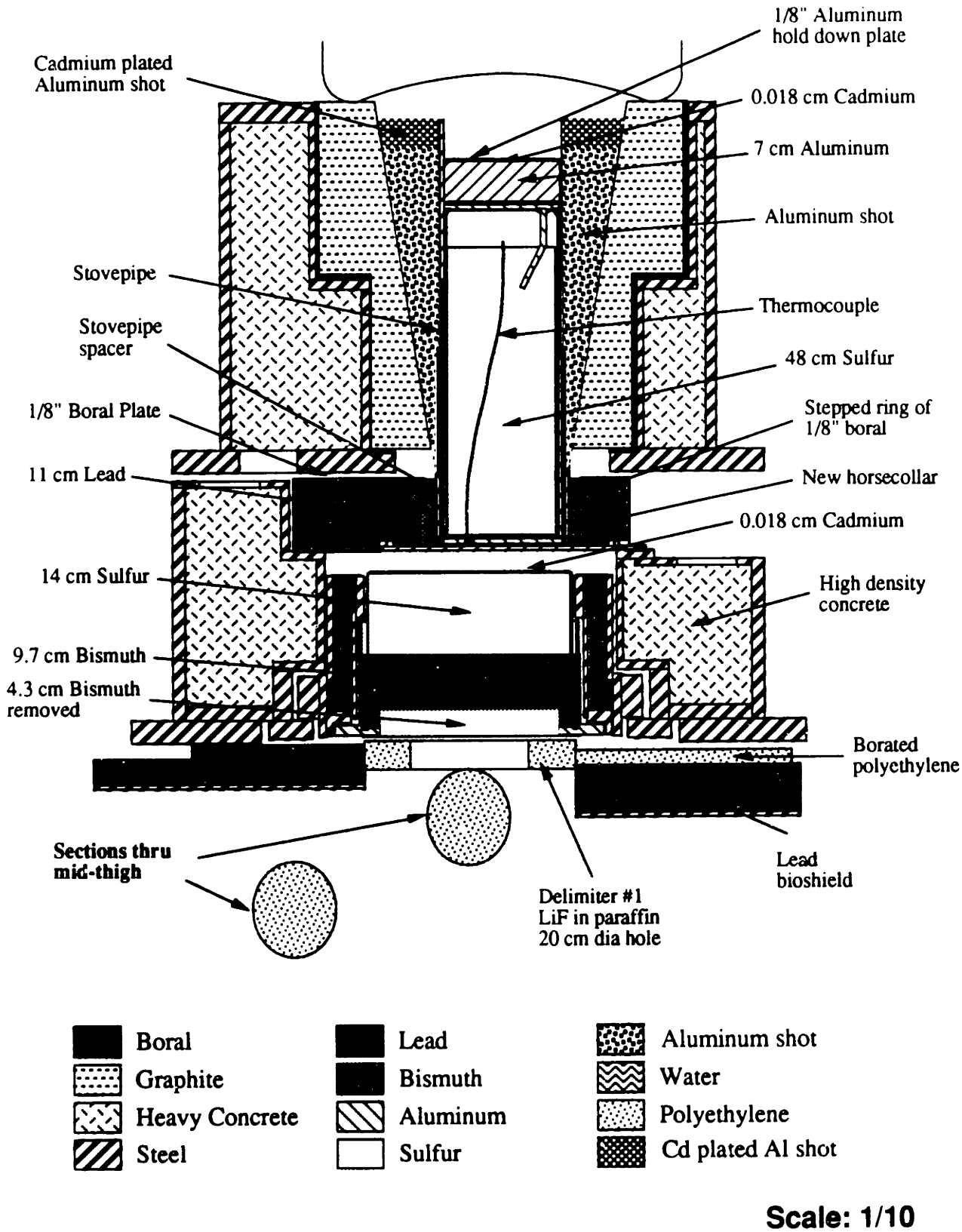

Figure 4.65. Cross sectional view of the M62 beam, delimiter #1, and the thigh phantom. The phantom was positioned so the left thigh was below the beam.

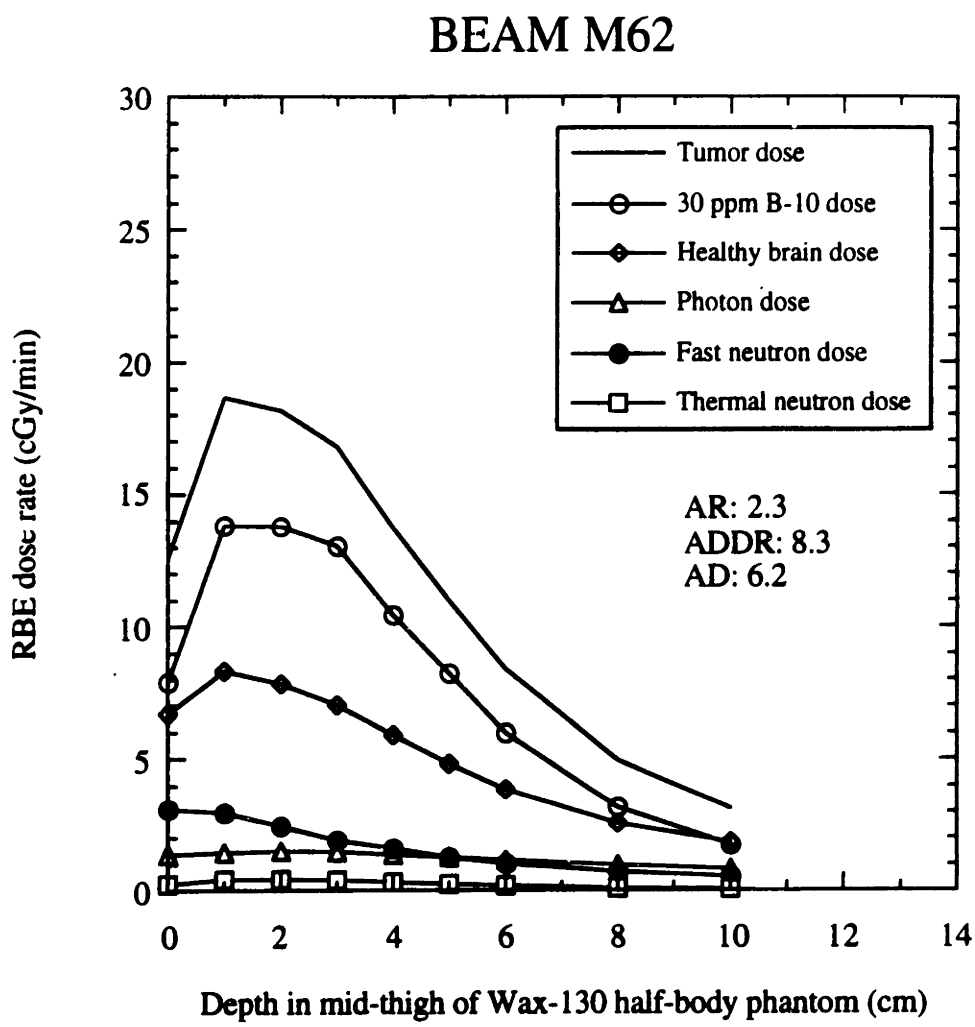

Figure 4.66. Doses measured in the thigh phantom for the M62, delimiter #1 beam and BPA.

Unilateral irradiation.
Phantom: Wax-130 half-body, center tube through mid-thigh.
Delimiter: #1. LiF in paraffin, 5.1 cm thick, 20 cm diameter hole.
Reactor power: 5 MWn.
RBE's: 4.0 for B-10, 2.3 for neutrons, 0.5 for photons.
B-10 concentrations: 30 ppm for tumor, 7.5 ppm for healthy brain.
In-air data: D_{fn} = 3.1 cGy/min
D_{γ} = 0.79 cGy/min
$D_{30ppm\ B\text{-}10}$ = 1.8 cGy/min

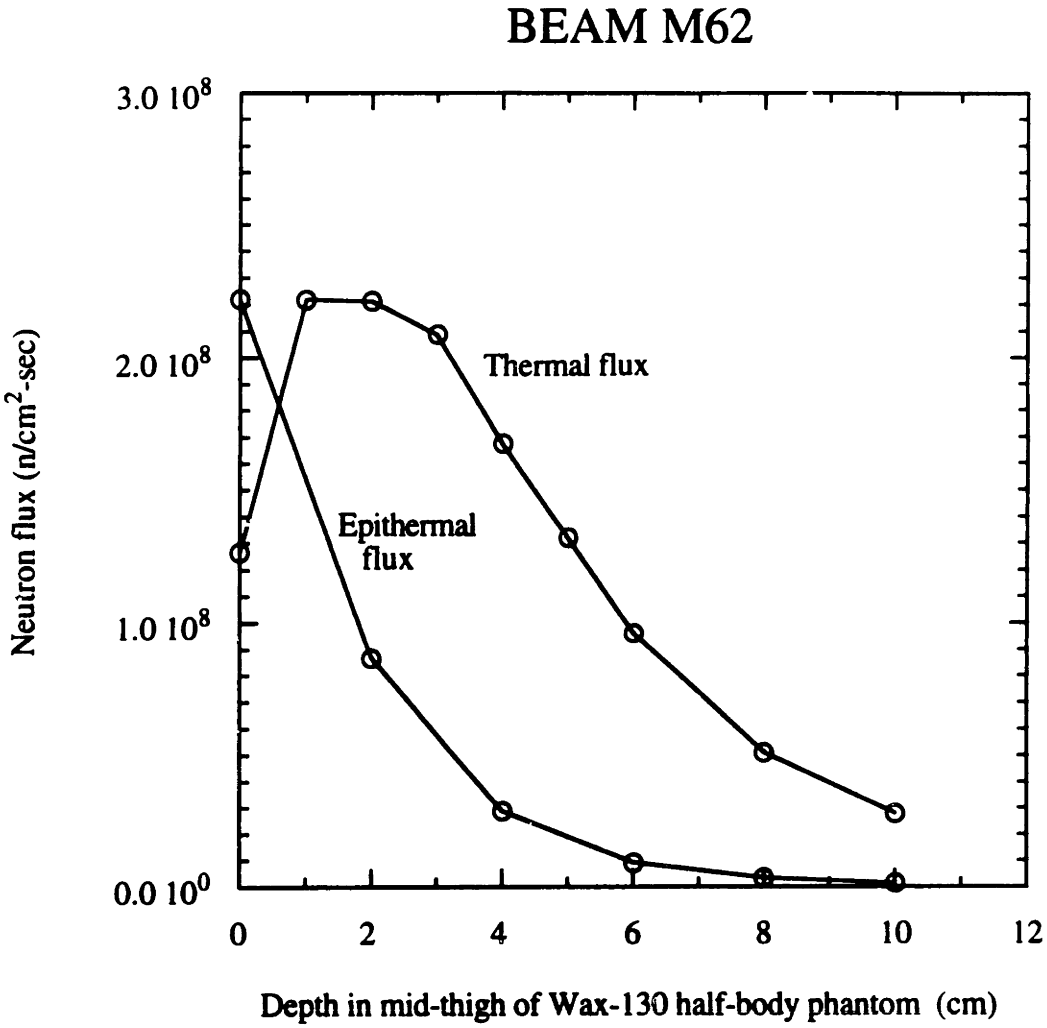

Figure 4.67. Thermal and epithermal fluxes measured in the thigh phantom for the M62, delimiter #1 beam.

Unilateral irradiation.
Phantom: Wax-130 half-body, center tube through mid-thigh.
Delimiter: #1. LiF in paraffin, 5.1 cm thick, 20 cm diameter hole.
Reactor power: 5 MWn.

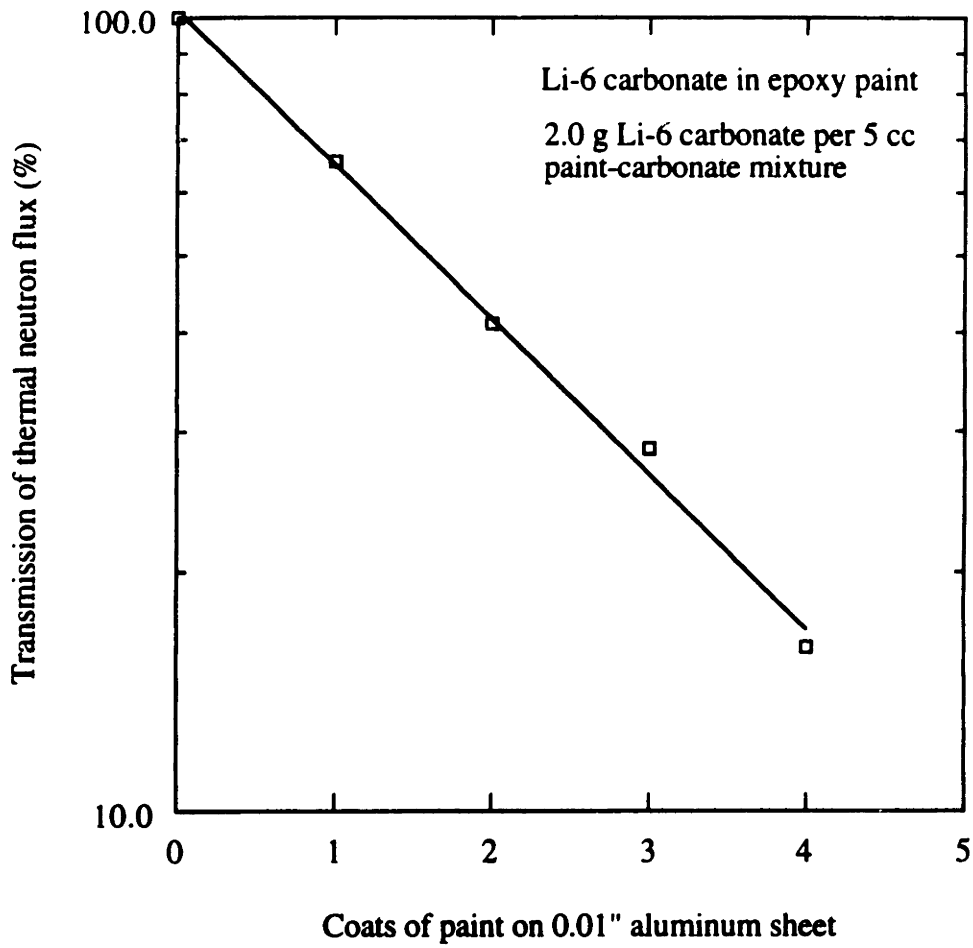

Figure 4.68. Attenuation of the thermal neutron flux in a Li-6 carbonate loaded paint. These data were obtained with a transmission experiment where a nearly pure thermal neutron beam was passed through the painted surfaces. Five coats gave about 90% attenuation.

The rest of the bottom of the lead shutter was painted with 10 coats of a B_4C loaded paint. This attenuates the thermal neutron flux by more than a factor of 10. Capture in B-10 produces prompt gammas, but these do not add significantly to the patient's dose. B_4C was used to paint most of the lead shutter since it is much cheaper than Li-6 carbonate. The areas where the lead shutter was painted are shown in figure 4.69.

The second change was with the delimiter. A new delimiter (delimiter #3) was used with the M66 beam. This delimiter[4] was also 2" thick, 35.7 cm wide, and 60 cm long. It had a smaller, 15 cm diameter hole, however. Also, LiF was added to a concentration of 0.147 g natural LiF per cm^3 of mixture throughout most of the delimiter, and twice this concentration around the periphery of the hole.

The M66 beam is shown in figure 4.70. Results are shown in figures 4.71-4.73. Some off axis data were obtained with this beam. The intensity of this beam was about 30% less than the M62 beam. A 20% loss was expected since the phantom was an additional 2" below the lead shutter owing to the presence of the delimiter. An additional 10% loss in intensity from scattering and absorption within the delimiter itself is reasonable. Also, the additional Li-6 that was painted on the bottom and sides of the collimator would be expected to reduce the incident epithermal flux by several percent. The thermal flux in phantom fell off faster than that in the M62 beam. This is attributed to the more directional quality of the beam and less contribution from the sides of the phantom.

Results of a MCNP run for the M66 beam are shown in figure 4.74 .[5,6] There is excellent agreement for the 30 ppm B-10 and thermal neutron doses; that is, the thermal flux as determined by the two methods are well matched (the KERMA factors used to convert the thermal flux to thermal neutron in brain and B-10 doses were essentially the same). The fast neutron dose plotted for MCNP is that contribution from neutrons with energies greater than 40 keV. There is good agreement between the fast neutron doses determined by MCNP and experiment at depths greater than 1 cm; however, MCNP predicts a significantly higher fast neutron dose in the first centimeter of the phantom. This

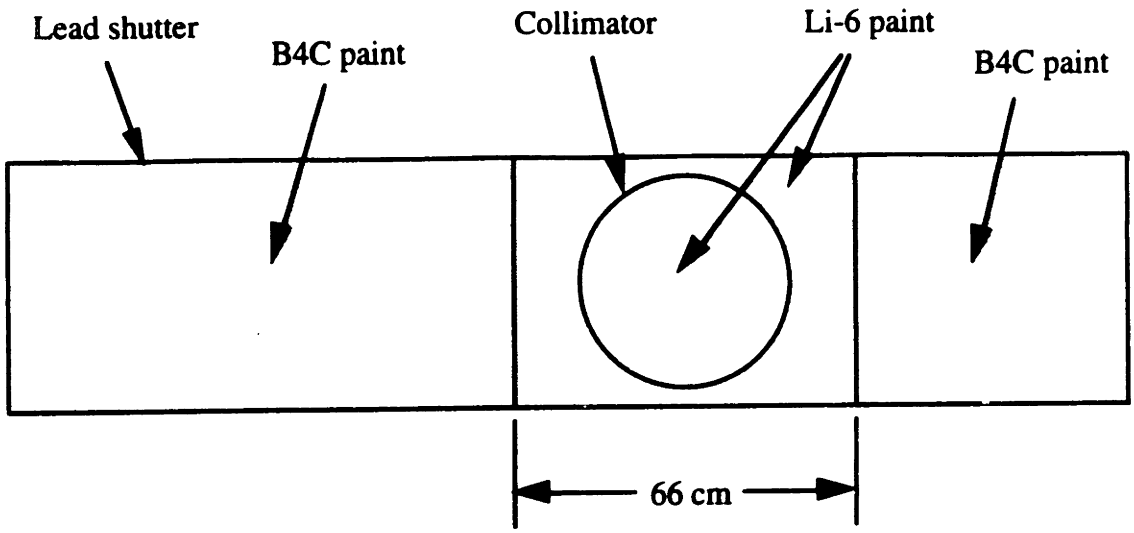

Scale: 1/15

Figure 4.69. Bottom of the lead shutter showing where the Li-6 and B_4C loaded paints were applied. Five coats of the Li-6 carbonate paint and 10 coats of the B_4C paint were applied. These give a factor of 10 reduction in the thermal flux.

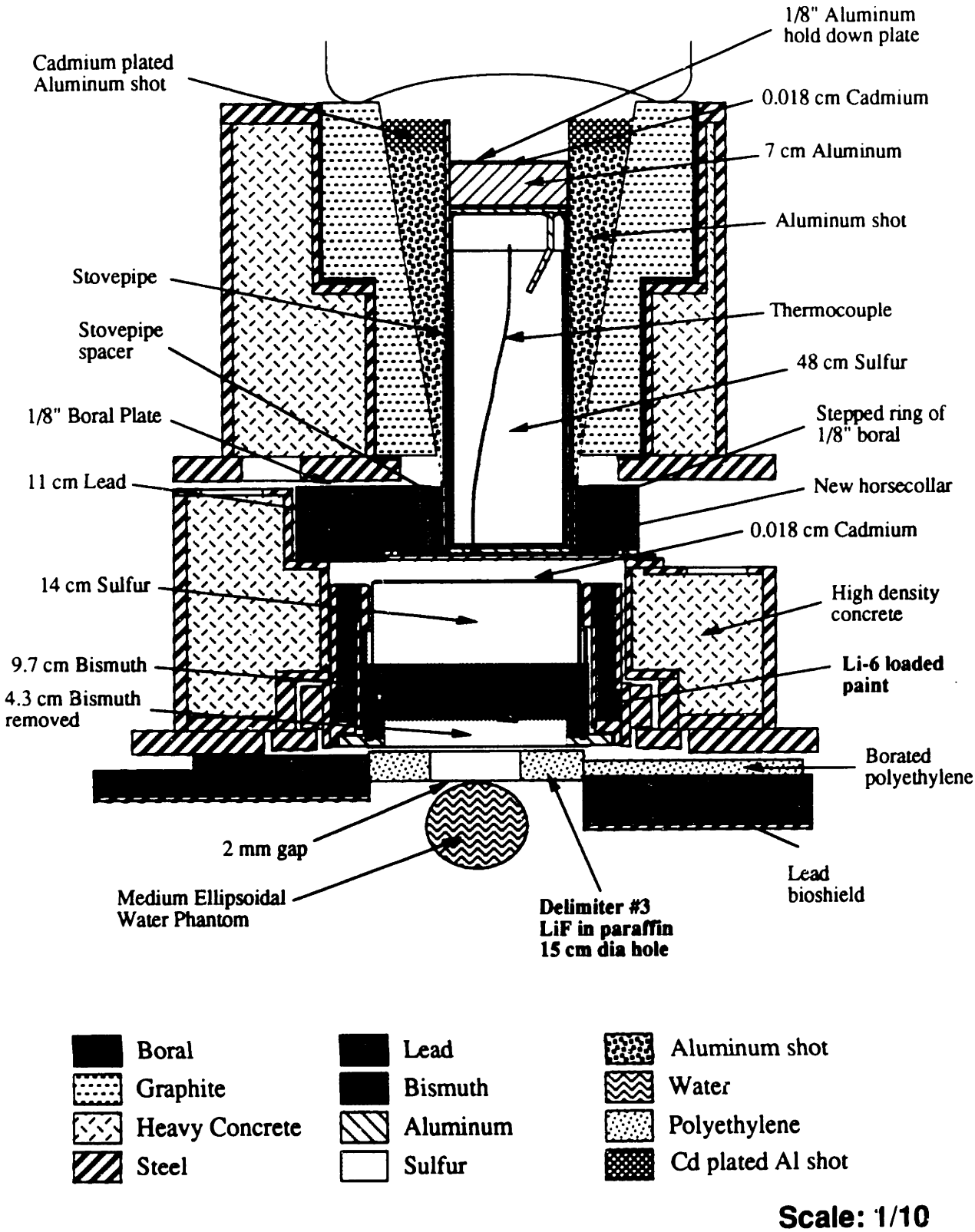

Figure 4. 70. Cross sectional view of the M66, delimiter #3 beam. The sides and bottom of the collimator were painted with 5 coats of the Li-6 paint. Delimiter #3 has a 15 cm diameter hole.

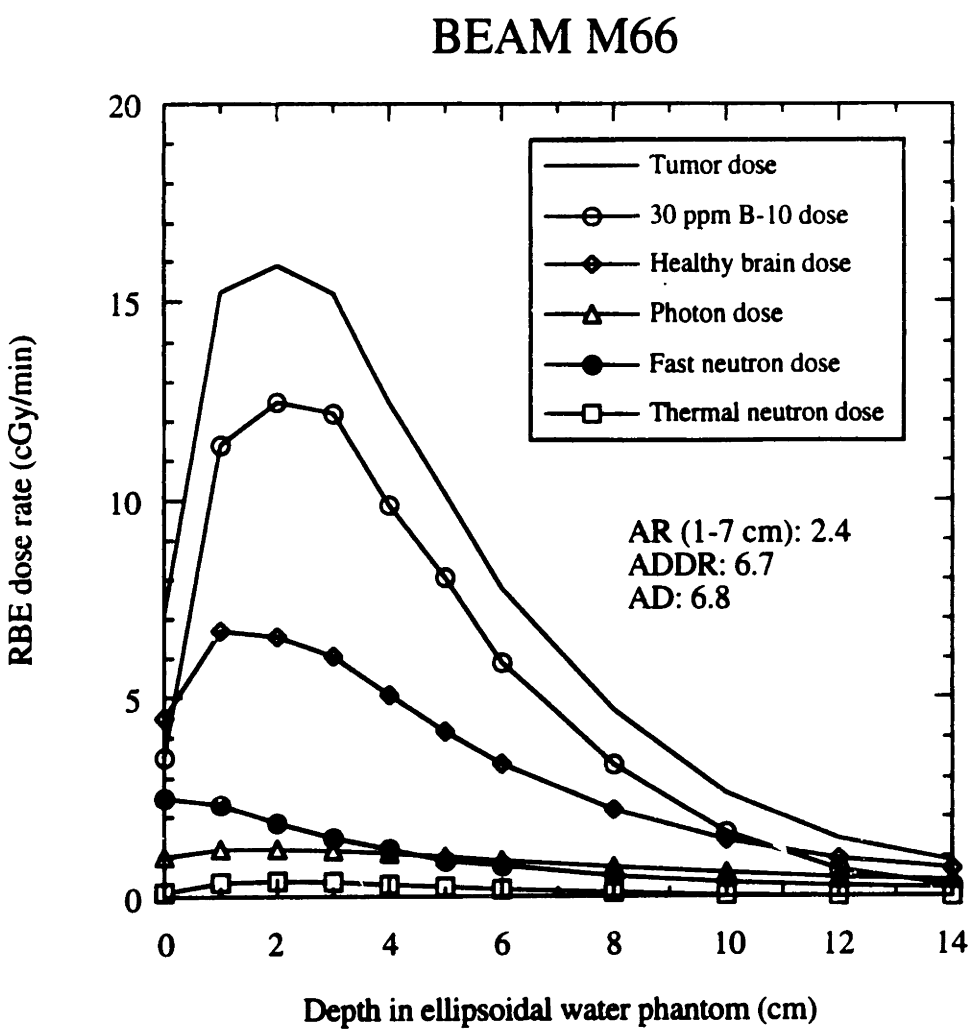

Figure 4.71. Doses measured in phantom for the M66, delimiter #1 beam and BPA.

Unilateral irradiation.
Phantom: Medium sized, ellipsoidal, water filled, center tube.
Delimiter: #3, 15 cm diameter hole.
Reactor power: 5 MWn.
RBE's: 4.0 for B-10, 2.3 for neutrons, 0.5 for photons.
B-10 concentrations: 30 ppm for tumor, 7.5 ppm for healthy brain.
In-air data: $D_{fn} = 2.4$ cGy/min
$D_{\gamma} = 0.82$ cGy/min
$D_{30ppm\ B\text{-}10} = 0.68$ cGy/min

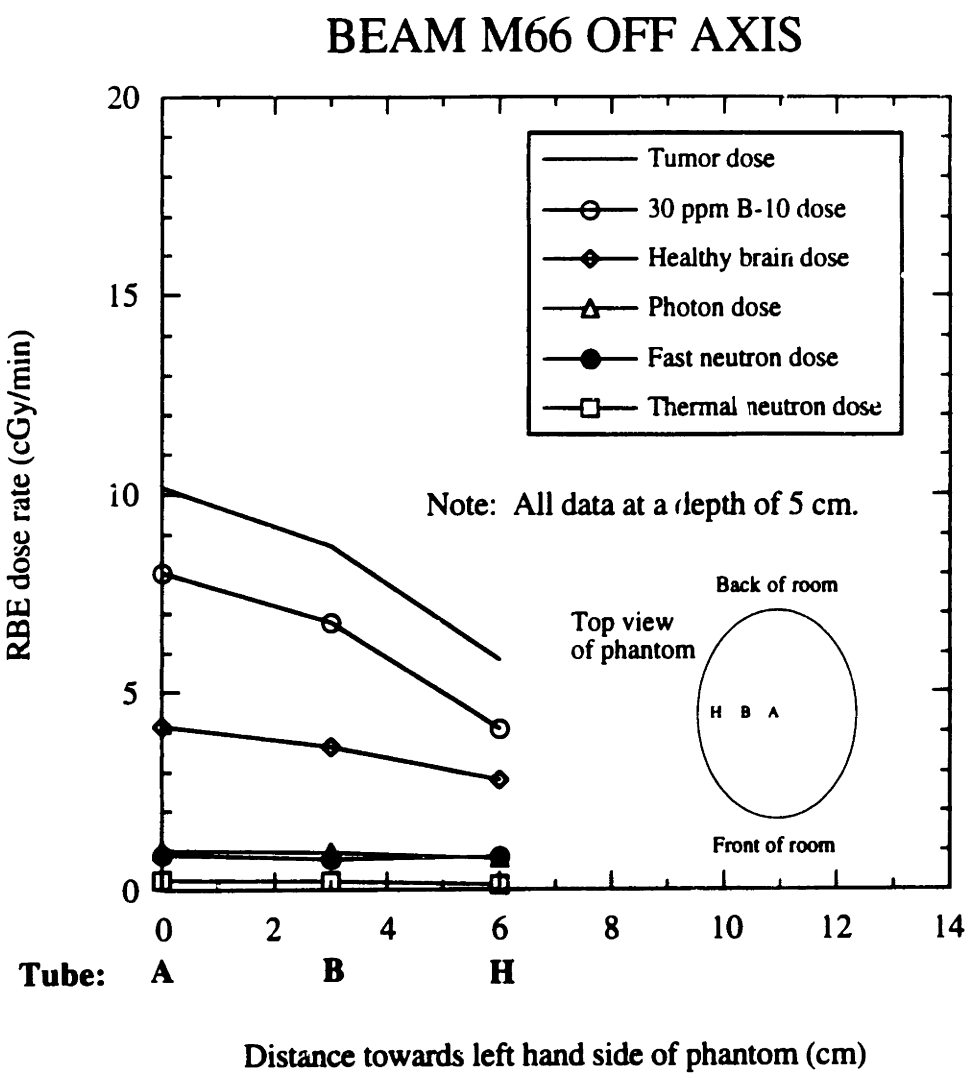

Figure 4.72. Off axis doses measured in phantom for the M66, delimiter #3 beam and BPA.

Unilateral irradiation.
Phantom: Medium sized, ellipsoidal, water filled, center tube.
Delimiter: #3, 15 cm diameter hole.
Reactor power: 5 MWn.
RBE's: 4.0 for B-10, 2.3 for neutrons, 0.5 for photons.
B-10 concentrations: 30 ppm for tumor, 7.5 ppm for healthy brain.
In-air data: D_{fn} = 2.4 cGy/min
D_{γ} = 0.82 cGy/min
$D_{30ppm\ B\text{-}10}$ = 0.68 cGy/min

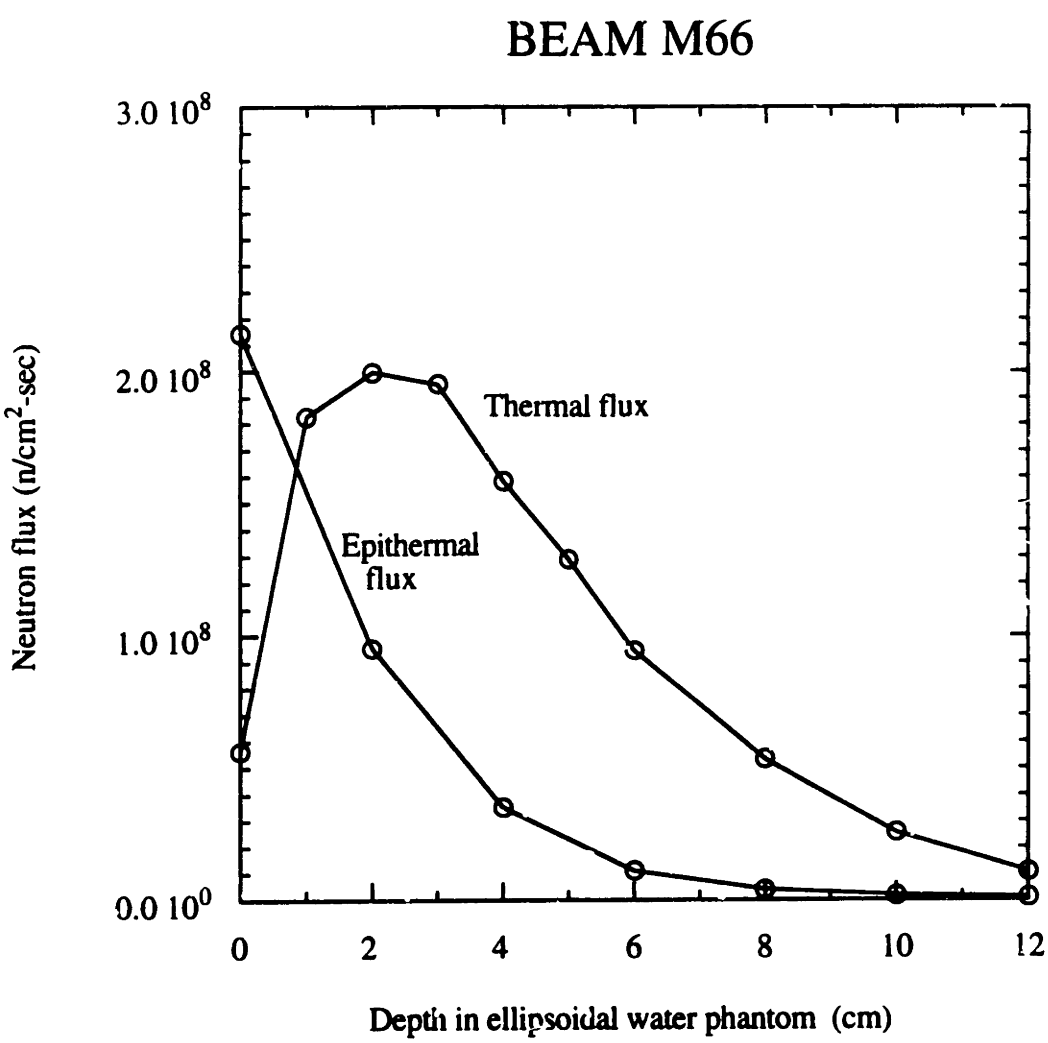

Figure 4.73. Thermal and epithermal fluxes measured in phantom for the M66, delimiter #1 beam.

Unilateral irradiation.
Phantom: Medium sized, ellipsoidal, water filled, center tube.
Delimiter: #3, 15 cm diameter hole.
Reactor power: 5 MWn.

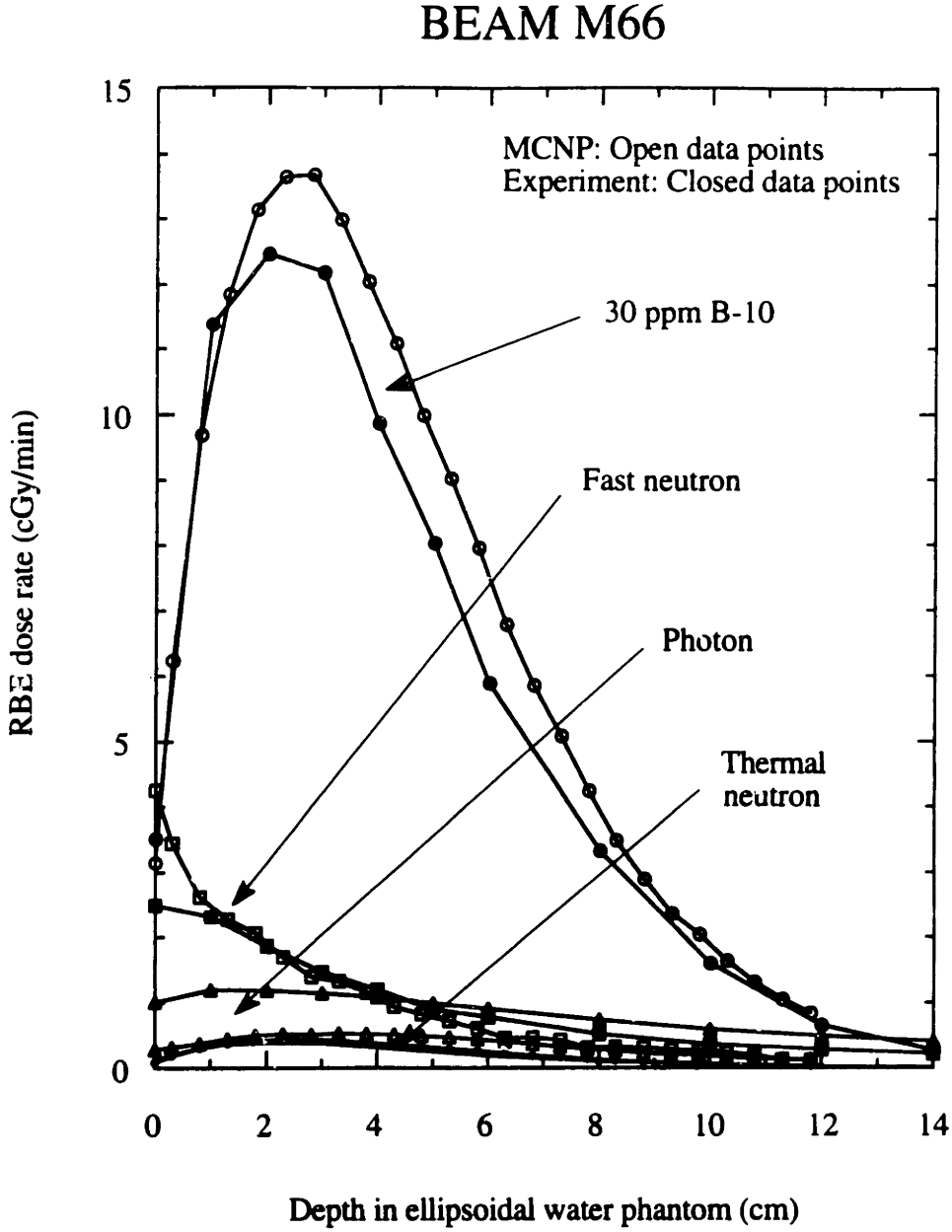

Figure 4.74. Comparison of MCNP and experimental data for the M66, delimiter #3 beam. Agreement was excellent. The N-14 kerma for brain was used in both calculations. The MCNP fast neutron dose was calculated for neutrons with energies above 40 keV. The MCNP fast neutron dose rises rapidly at the surface.

Unilateral irradiation.
Phantom: Medium sized, ellipsoidal, water filled, center tube.
Delimiter #3, 15 cm diameter hole.
Reactor power: 5 MWn.
RBE's: 4.0 for B-10, 2.3 for neutrons, 0.5 for photons.
B-10 concentrations: 30 ppm in tumor, 7.5 ppm in healthy brain.

effect is discussed in more detail in Chapter 5.3.2. The experimentally determined photon dose is higher than that determined by MCNP. At the surface, it is 3.7 times higher (1.01 versus 0.274 RBE cGy/min). At depth, however, it is only 2.2 times higher (1.08 versus 0.516 RBE cGy/min at 4 cm, for example). This is because the MCNP runs, as set up, do not account for photons coming from the core or for prompt gammas other than those produced in the phantom itself. The photon dose as determined by MCNP, therefore, underestimates the actual photon dose especially near the surface of the phantom where the incident photons make the greatest contribution. The incident photon dose rate has been measured in air. When this incident contribution is added to the MCNP values, there is reasonable agreement with the photon dose determined experimentally within the phantom. For example, at the surface MCNP underestimates the photon dose by 0.74 RBE cGy/min. The measured incident photon dose rate was 0.82 RBE cGy/min, which agrees closely with the above underestimate.

Off-axis data as determined by MCNP is shown in figure 4.74. These doses can be compared with those off axis doses determined experimentally as shown in figure 4.72. The B-10 dose as determined by MCNP is about 10% higher than that determined experimentally. The shapes of the curves are similar. The fast neutron doses as determined by MCNP agree very well with those determined experimentally.

4.19. BEAM M67

While the lower intensity of the M66 beam relative to the M62 beam could be reasonably explained by the additional space between the phantom and the lead shutter and by the presence of the delimiter itself, the Li-6 paint on the bottom of the collimator might reduce the intensity as well. With the M67 beam, then, this Li-6 paint was removed from

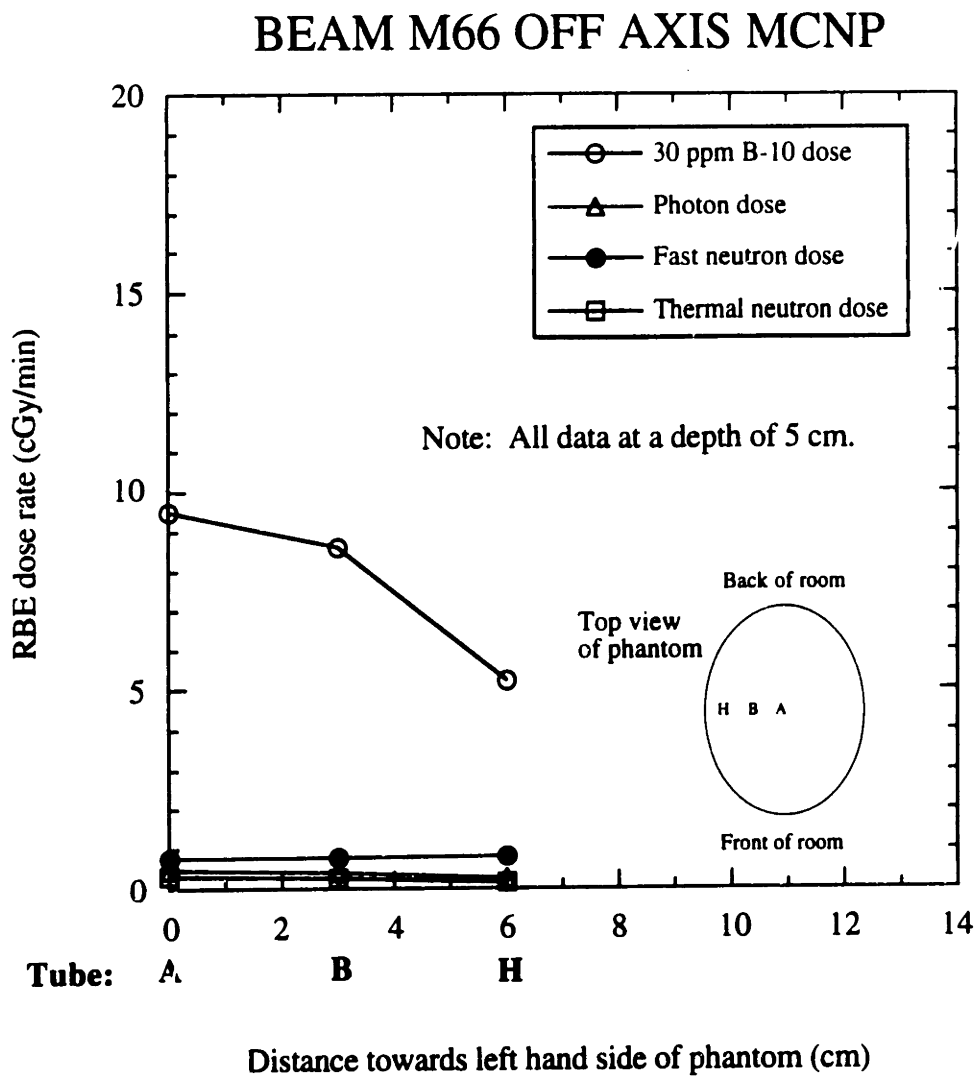

Figure 4.75. Off axis doses calculated by MCNP for the M66, delimiter #3 beam and BPA.

Unilateral irradiation.
Phantom: Medium sized, ellipsoidal, water filled, center tube.
Delimiter: #3, 15 cm diameter hole.
Reactor power: 5 MWn.
RBE's: 4.0 for B-10, 2.3 for neutrons, 0.5 for photons.
B-10 concentrations: 30 ppm for tumor, 7.5 ppm for healthy brain.

the bottom of the collimator. The paint was not removed from the sides of the collimator or from the bottom of the lead shutter.

The M67 beam is shown in figure 4.76. Results are shown in figures 4.77-4.79. Off-axis data were taken for this beam as well. The M67 beam was characterized with a new ellipsoidal phantom. The other phantom was broken. The new phantom is identical to the old one except that the shell was made with a casting resin, not Plexiglas. The new phantom is described in Chapter 2. The dose distributions determined with the two phantoms are expected to be the same. Another change was that the phantom with the M67 beam was positioned 1 cm below the bottom of the delimiter. This was done since it was thought that the patient's body might be more reasonably positioned with at least 1 cm gap between it and the delimiter. In the MCNP run that accompanied this beam, the phantom was also positioned 1 cm below the delimiter.

The thermal flux in the first few centimeters of the phantom is about 5% higher than that measured with the M66 beam, even though the phantom was positioned 8 mm lower in the M67 beam. A few percent of the incident epithermal flux, therefore, may have been removed by the Li-6 paint. The M67 beam, however, is almost identical to the M66 beam. The shapes and intensities of the various dose components are very close. The incident thermal flux is about twice as high with the M67 beam, as can be seen from the in-air B-10 dose rates. This makes little difference in the thermal flux profile, however, as most of the thermal flux is generated from the incident epithermal flux.

Off- axis doses, as shown in figure 4.78, have shapes comparable to those obtained with the M66 beam.

Results of a MCNP run[6] for the M67 beam are shown in figure 4.80. There is excellent agreement for the 30 ppm B-10 and thermal neutron doses. The fast neutron dose plotted for MCNP is that contribution from neutrons with energies greater than 40 keV. As with the B-10 dose, there is excellent agreement between the fast neutron doses determined by MCNP and experiment, except near the surface as was discussed previously with the

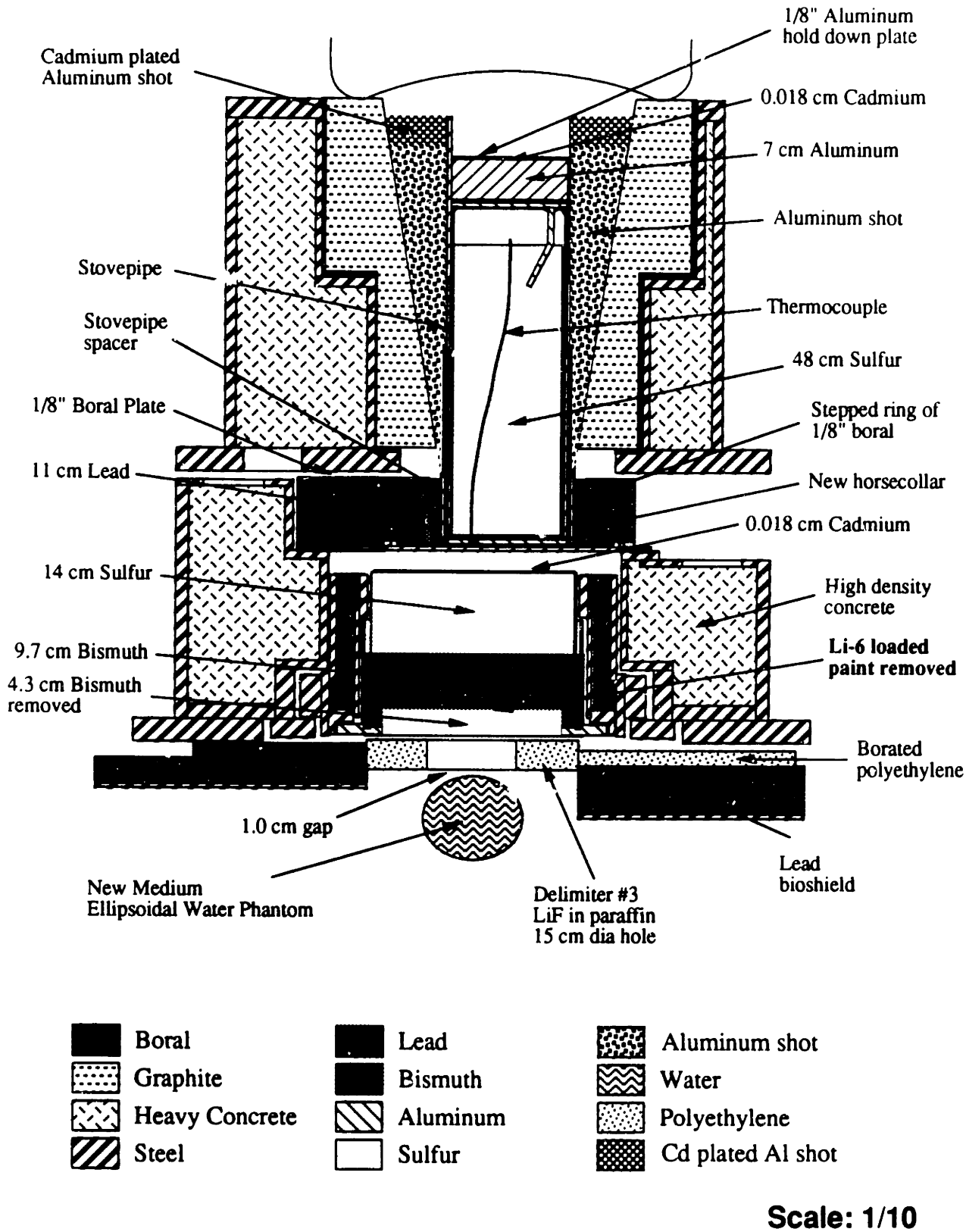

Figure 4.76. Cross sectional view of the M67, delimiter #3 beam. The Li-6 paint on the bottom of the collimator was removed. The new head phantom, essentially identical to the old one, was used with this beam.

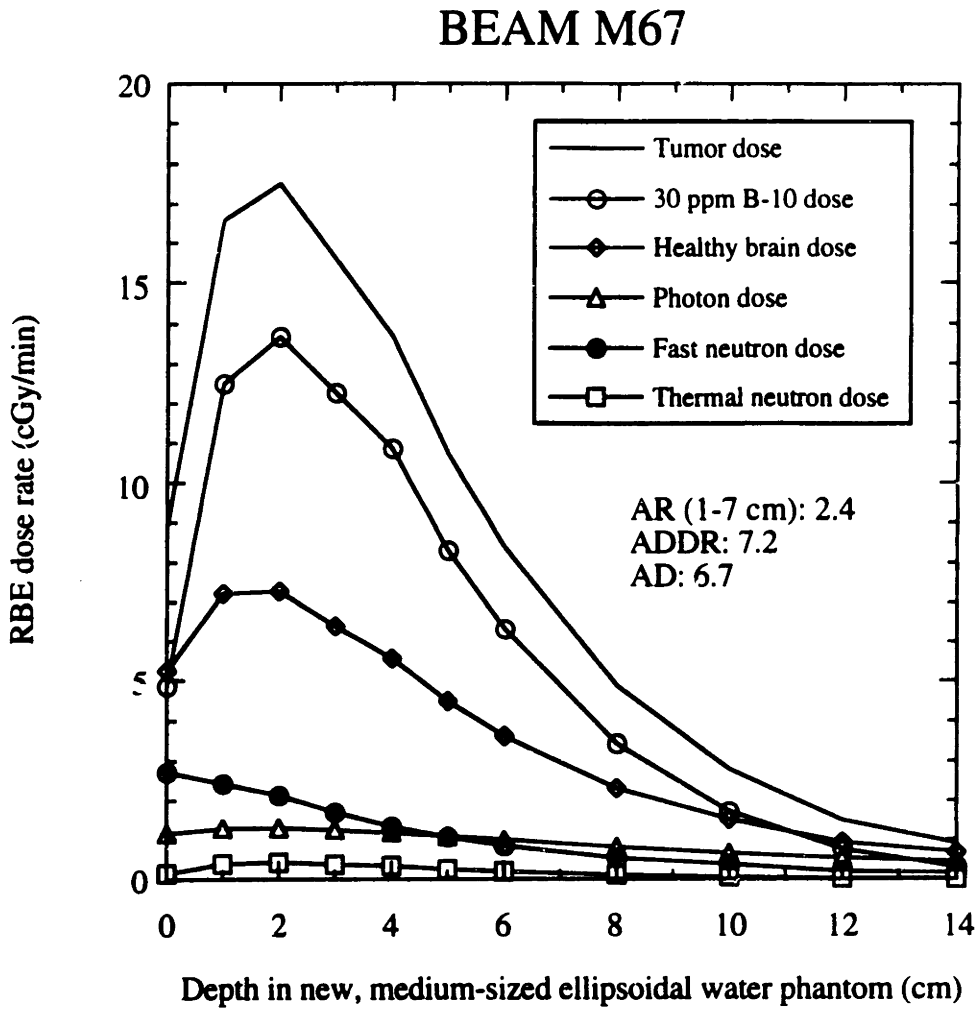

Figure 4.77. Doses measured in the new phantom for the M67, delimiter #3 beam and BPA.

Unilateral irradiation.
Phantom: Medium sized, casting resin ellipsoidal, water filled, center tube.
Delimiter: #3, 15 cm diameter hole.
Reactor power: 5 MWn.
RBE's: 4.0 for B-10, 2.3 for neutrons, 0.5 for photons.
B-10 concentrations: 30 ppm for tumor, 7.5 ppm for healthy brain.
In-air data: D_{fn} = 2.5 cGy/min
D_{γ} = 0.85 cGy/min
$D_{30ppm\ B\text{-}10}$ = 1.2 cGy/min

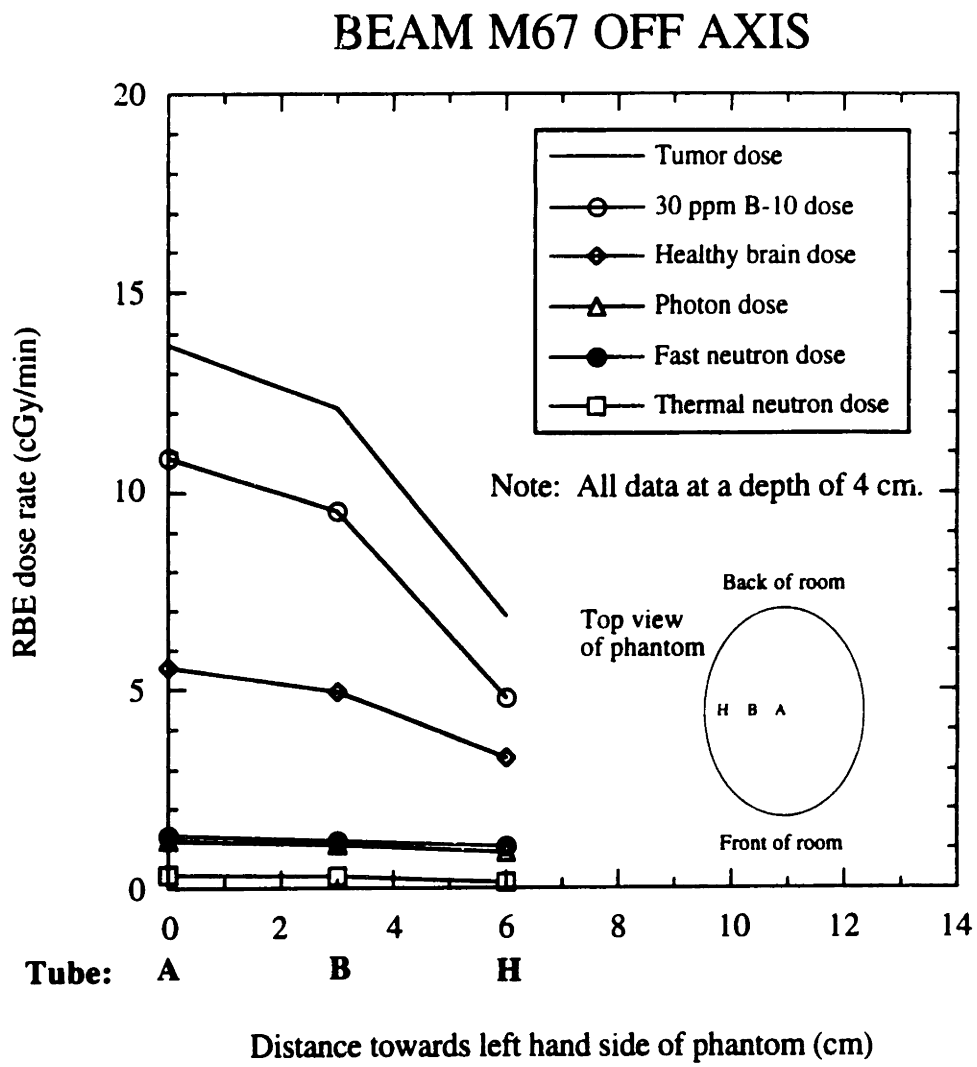

Figure 4.78. Off axis doses measured in phantom for the M67, delimiter #3 beam and BPA.

Unilateral irradiation.
Phantom: New medium sized, ellipsoidal, water filled, center tube.
Delimiter: #3, 15 cm diameter hole.
Reactor power: 5 MWn.
RBE's: 4.0 for B-10, 2.3 for neutrons, 0.5 for photons.
B-10 concentrations: 30 ppm for tumor, 7.5 ppm for healthy brain.
In-air data: $D_{fn} = 2.5$ cGy/min
$D_{\gamma} = 0.85$ cGy/min
$D_{30ppm\ B\text{-}10} = 1.2$ cGy/min

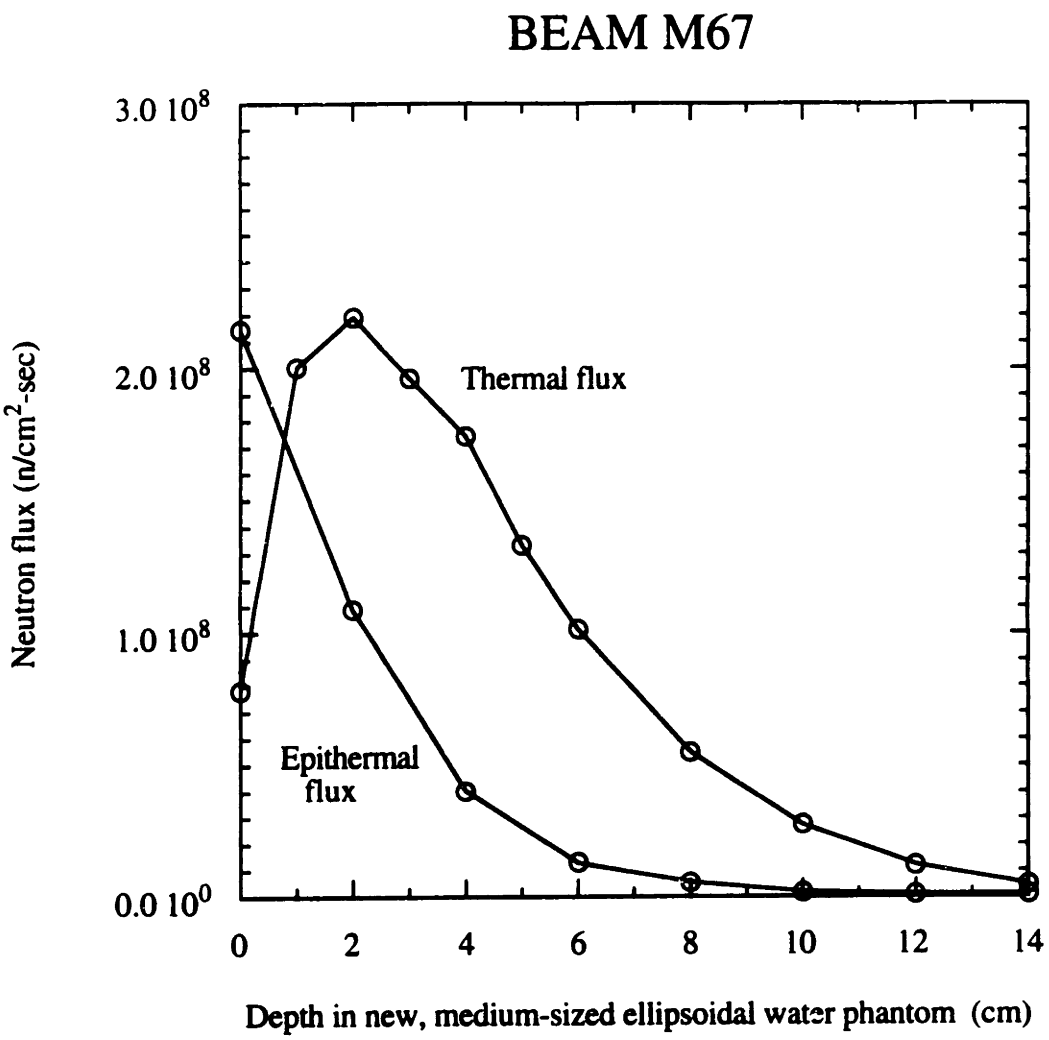

Figure 4.79. Thermal and epithermal fluxes measured in the new phantom for the M67, delimiter #3 beam.

Unilateral irradiation.
Phantom: New medium sized, ellipsoidal, water filled, center tube.
Delimiter: #3, 15 cm diameter hole.
Reactor power: 5 MWn.

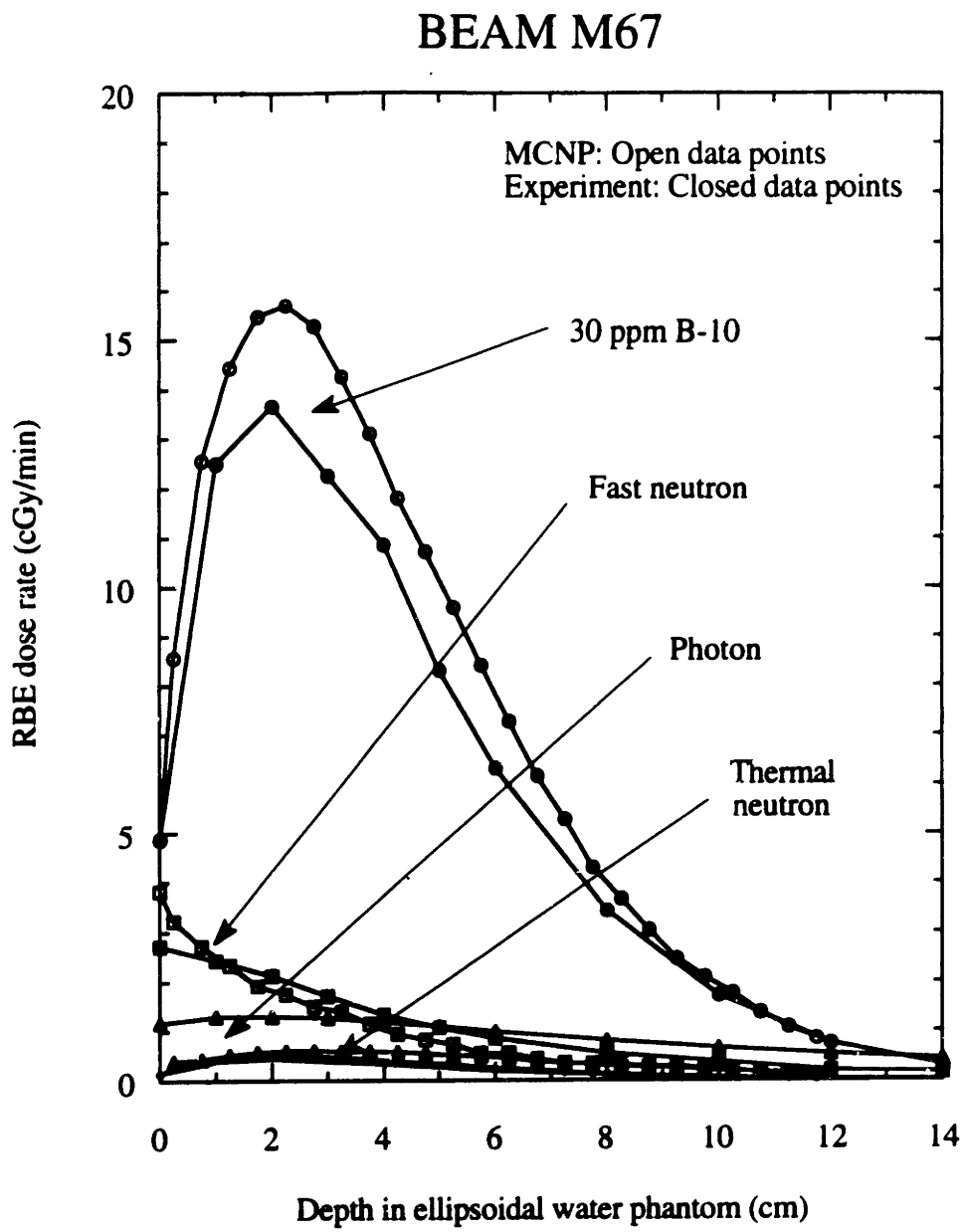

Figure 4.80. Comparison of MCNP and experimental data for the M67, delimiter #3 beam. Agreement was excellent. The N-14 kerma for brain was used in both calculations. The MCNP fast neutron dose was calculated for neutrons with energies above 40 keV. The MCNP fast neutron dose rises at the surface.

Unilateral irradiation.
Phantom: Medium sized, ellipsoidal, water filled, center tube.
Delimiter #3, 15 cm diameter hole.
Reactor power: 5 MWn.
RBE's: 4.0 for B-10, 2.3 for neutrons, 0.5 for photons.
B-10 concentrations: 30 ppm in tumor, 7.5 ppm in healthy brain.

M66 beam results. Comparing the two photon doses, the experimentally determined photon dose is higher than that determined by MCNP as discussed with the M66 beam. The incident photon dose rate has been measured in air. When this incident contribution is added to the MCNP values, there is reasonable agreement with the photon dose determined experimentally within the phantom. For example, at the surface MCNP underestimates the photon dose by 0.80 RBE cGy/min. The measured incident photon dose rate was 0.85 RBE cGy/min, which agrees closely with the above underestimate.

Off-axis data as determined by MCNP is shown in figure 4.81. These doses can be compared with those determined experimentally as shown in figure 4.78. The B-10 dose as determined by MCNP is about 10% higher than that determined experimentally. The shapes of the curves are similar. The fast neutron doses as determined by MCNP agree well with those determined experimentally except in the first centimeter of the phantom. This is discussed in more detail in Chapter 5.3.2.

The experimentally determined AR of the M67 beam is good at 2.4. The AD is reasonable at 6.7 cm, even with the 15 cm diameter delimiter. The ADDR is adequate; 35 minutes per fraction would be needed for a 4 fraction, unilateral treatment that delivers a total healthy tissue dose of 1000 RBE cGy.

A summary of the beams that were characterized for this thesis is provided in table 4.7.

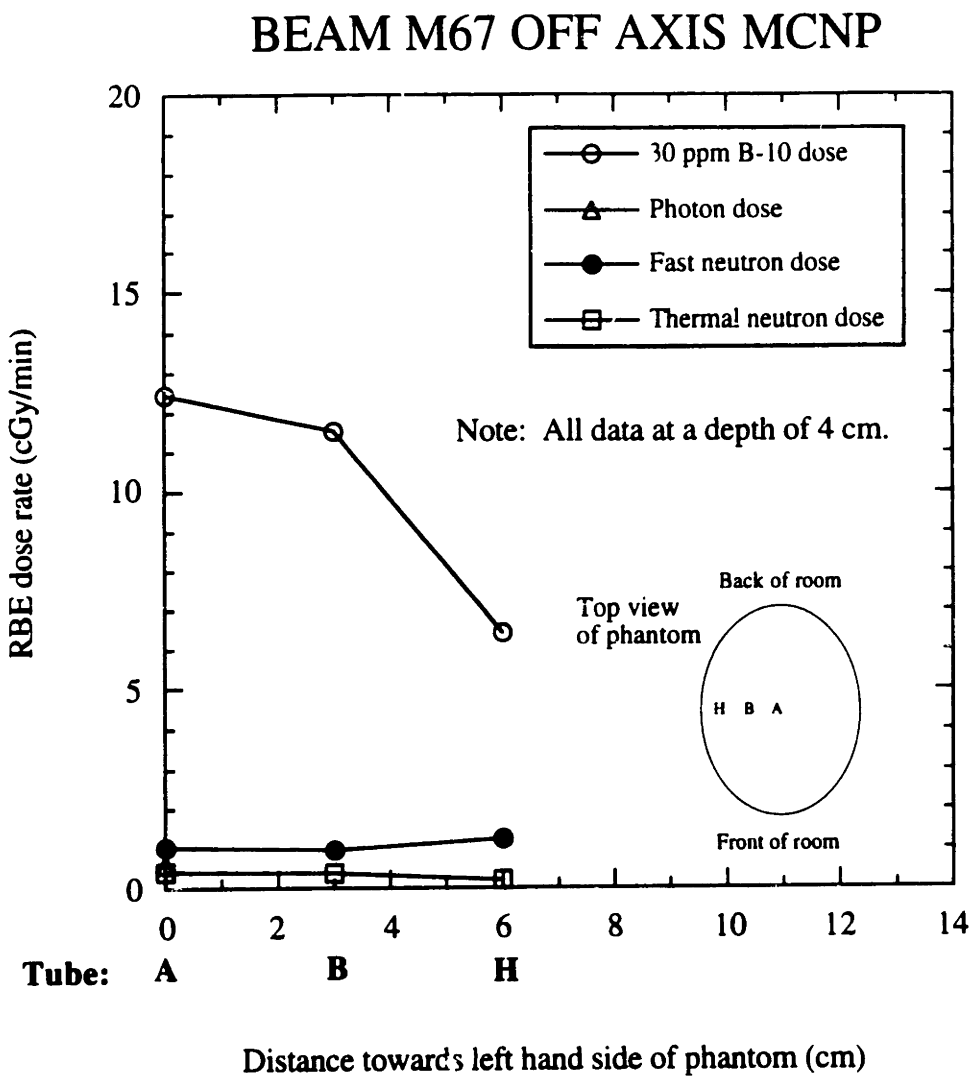

Figure 4.81. Off axis doses calculated by MCNP for the M67, delimiter #3 beam and BPA.

Unilateral irradiation.
Phantom: Medium sized, ellipsoidal, water filled, center tube.
Delimiter: #3, 15 cm diameter hole.
Reactor power: 5 MWn.
RBE's: 4.0 for B-10, 2.3 for neutrons, 0.5 for photons.
B-10 concentrations: 30 ppm for tumor, 7.5 ppm for healthy brain.

Table 4.6. Summary of the beams that were characterized*.

* Values for BSH assume: RBE's of 2.3 for B-10, 1.6 for neutrons, and 1.0 for photons. B-10 concentration of 30 ppm in tumor. Minimum values assume 3 ppm B-10 in healthy tissue; maximum values assume 0 ppm B-10 in healthy tissue.

Values for BPA assume: RBE's of 4.0 for B-10, 2.3 for neutrons, and 0.5 for photons. A fractionated treatment is assumed. B-10 concentration of 30 ppm in tumor and 7.5 ppm in healthy tissue. Unlike BSH, only a single value is given for each parameter for BPA since only one concentration of B-10 in healthy tissue (7.5 ppm) is assumed.

ADDR values scaled to a reactor power of 5 MW_n. All advantage parameters are based on RBE weighted doses.

BEAM	DESCRIPTION	AR*	ADDR* (RBE cGy/min)	AD* (cm)
M47	Stovepipe: 0.02 cm Cd, 35 cm S, 10 cm Al. Cone: 37 cm Al shot, 23 cm Bi shot. Collimator: 0.02 cm Cd, 14 cm Bi, 0.05 cm Li-6 carbonate. Phantom: Cyl water (18 cm dia x 20 cm).	BSH: 1.9, 2.1	8.9, 10.2	5.6, 6.2
M55	Stovepipe: 0.018 cm Cd, 30 cm Al. Cone: 37 cm Al shot, 23 cm Bi shot. Collimator: New wide collimator, 0.018 cm Cd, 14 cm S, 14 cm Bi. Phantom: Med ellip water.	BSH: 2.3, 2.7	8.0, 9.5	7.4, 8.1

M57	Stovepipe: New larger dia pipe, 0.018 cm Cd, new larger dia S filter - 48 cm S, Cone: 46 cm Al shot. Horsecollar: New Pb and Bi collar. Collimator: Wide collimator, 0.018 cm Cd, 14 cm S, 14 cm Bi. Phantom: Med ellip water.	BSH: 2.6, 3.2 BPA: 2.5	6.9, 8.1 12.9	7.8, 8.8 7.5
M58	Stovepipe: Larger dia pipe, 0.018 cm Cd, new larger dia Al filter - 30 cm Al, Cone: 46 cm Al shot. Horsecollar: Pb and Bi collar. Collimator: Wide collimator, 0.018 cm Cd, 14 cm S, 14 cm Bi. Phantom: Med ellip water.	BSH: 2.4, 2.8	7.6, 8.2	7.6, 8.6
M58A	Note: Moved phantom to below centerline of collimator.	-	-	-
M59	Stovepipe: Larger dia pipe, 0.018 cm Cd, larger dia S filter - 48 cm S, Cone: 46 cm Al shot. Horsecollar: Pb and Bi collar. Collimator: Wide collimator, no Cd, 14 cm S, 14 cm Bi. Phantom: Med ellip water.	BSH: 2.7, 3.3	13,9, 18.6	6.8, 8.3
M60	Stovepipe: Larger dia pipe, 0.018 cm Cd, larger dia S filter - 48 cm S, Cone: 46 cm Al shot. Horsecollar: Pb and Bi collar. Collimator: Wide collimator, 0.010 cm Cd, 14 cm S, 14 cm Bi. Phantom: Med ellip water.	BSH: 2.5, 3.1	7.8, 9.5	7.5, 8.4

M61	Stovepipe: Larger dia pipe, 0.018 cm Cd, 7 cm Al, larger dia S filter - 48 cm S, Cone: 46 cm Al shot. Horsecollar: Pb and Bi collar. Collimator: Wide collimator, 0.018 cm Cd, 14 cm S, 9.7 cm Bi. Phantom: Med ellip water.	BSH: 2.4, 2.8 BPA: 2.5	7.8, 9.3 13.3	7.4, 8.4 7.2
M62	Stovepipe: Larger dia pipe, 0.018 cm Cd, 7 cm Al, larger dia S filter - 48 cm S, Cone: 5.0 cm Cd plated Al shot, 53 cm Al shot. Horsecollar: Pb and Bi collar. Collimator: Wide collimator, 0.018 cm Cd, 14 cm S, 9.7 cm Bi. Phantom: Med ellip water.	BSH: 2.4, 2.9 BPA: 2.5	5.6, 6.6 9.4	8.0, 8.7 7.5
M62G	Stovepipe: Larger dia pipe, 0.018 cm Cd, 7 cm Al, larger dia S filter - 48 cm S, Cone: 5.0 cm Cd plated Al shot, 53 cm Al shot. Horsecollar: Pb and Bi collar. Collimator: Wide collimator, 0.018 cm Cd, 14 cm S, 9.7 cm Bi. Delimiter: #1, 20 cm dia hole. Phantom: Groin half-body wax.	BPA: 2.3	8.6	5.8

M62T	Stovepipe: Larger dia pipe, 0.018 cm Cd, 7 cm Al, larger dia S filter - 48 cm S, Cone: 5.0 cm Cd plated Al shot, 53 cm Al shot. Horsecollar: Pb and Bi collar. Collimator: Wide collimator, 0.018 cm Cd, 14 cm S, 9.7 cm Bi. Delimiter: #1, 20 cm dia hole. Phantom: Thigh half-body wax-130.	BPA: 2.3	8.3	6.2
M63	Stovepipe: Larger dia pipe, 0.018 cm Cd, 7 cm Al, larger dia S filter - 48 cm S, Cone: 5.0 cm Cd plated Al shot, 53 cm Al shot. Horsecollar: Pb and Bi collar. Collimator: Wide collimator, no Cd, 14 cm S, 9.7 cm Bi. Phantom: Med ellip water.	-	-	-
M64	Stovepipe: Larger dia pipe, 0.018 cm Cd, 7 cm Al, larger dia S filter - 48 cm S. Cone: 5.0 cm Cd plated Al shot, 53 cm Al shot. Horsecollar: Pb and Bi collar. Collimator: Wide collimator, 0.018 cm Cd, 0.95 cm Ti, 14 cm S, 9.7 cm Bi. Phantom: Med ellip water.	BPA: 2.4	8.4	7.3

M65	Stovepipe: Larger dia pipe - empty. Cone: 5.0 cm Cd plated Al shot, 53 cm Al shot. Horsecollar: Pb and Bi collar. Collimator: Note different collimator, 15.2 cm S, 14 cm Bi. Phantom: None. Note: A thermal beam used for mouse irradiations.	-	-	-
M66	Stovepipe: Larger dia pipe, 0.018 cm Cd, 7 cm Al, larger dia S filter - 48 cm S. Cone: 5.0 cm Cd plated Al shot, 53 cm Al shot. Horsecollar: Pb and Bi collar. Collimator: Wide collimator, 0.018 cm Cd, 14 cm S, 9.7 cm Bi, Li-6 paint on bottom of Bi. Deliiniter: #3, 15 cm dia hole. Phantom: Med ellip water.	BPA: 2.4	6.7	6.8
M67	Stovepipe: Larger dia pipe, 0.018 cm Cd, 7 cm Al, larger dia S filter - 48 cm S. Cone: 5.0 cm Cd plated Al shot, 53 cm Al shot. Horsecollar: Pb and Bi collar. Collimator: Wide collimator, 0.018 cm Cd, 14 cm S, 9.7 cm Bi, no Li-6 paint on bottom of Bi. Delimiter: #3, 15 cm dia hole. Phantom: Med ellip water.	BPA: 2.4	7.2	6.7

References

1. Jong-Ho Richard Choi, *Development and Characterization of an Epithermal Beam for Boron Neutron Capture Therapy at the MITR-II Research Reactor*, (Ph.D. Thesis, Massachusetts Institute of Technology, 1991).

2. Personal communication, Professor Jacquelyn Yanch.

3. S. D. Clement, J. R. Choi, R. G. Zamenhof, J. C. Yanch, and O. K. Harling "Monte Carlo Methods of Neutron Beam Design for Neutron Capture Therapy at the MIT Research Reactor (MITR-II)," in *Neutron Beam Design, Development, and Performance for Neutron Capture Therapy*, (O. K. Harling, John A. Bernard, Robert G. Zamenhof, eds., Plenum Press, New York, 1990).

4. Chun-Shan Yam, *Design of Patient Positioning System, Body Phantom, and Patient shielding for the Boron Neutron Capture Therapy Project at MITR-II*, (Master's Thesis, Massachusetts Institute of Technology, 1993).

5. E. L. Redmond II, J. C. Yanch, and O. K. Harling, "Monte Carlo simulation of the Massachusetts Institute of Technology research reactor" Nuc. Tech, (Accepted for publication, 1994).

6. Personal communication, Everett Redmond, graduate student, MIT Nuclear Engineering Department.

CHAPTER 5 DESCRIPTION AND DOSIMETRY OF THE BEAM SELECTED FOR CLINICAL TRIALS

5.1 INTRODUCTION

In this chapter, the beam selected for clinical trials is discussed in detail. This includes a description of the filtering materials in the beam, and the delimiters and whole body shields that are used to minimize the radiation doses to the patient outside of the treatment area. Dosimetry is provided assuming the tissue of interest is muscle or brain. Centerline and off-axis dosimetry is provided. Experimental results are compared with those generated by the Monte Carlo based neutron and photon transport code MCNP.[13] Whole body doses are provided. Some aspects of in-vivo dosimetry are discussed. Also discussed are several Procedures related to dosimetry that were written pursuant to MITR Technical Specification No. 6.5. Health physics issues, including the doses that will be received while setting up the patient, during the irradiation of the patient, and during a potential medical emergency with the patient, are discussed. Finally, an outside review of the dosimetry used to characterize this and the other beams is briefly discussed.

5.2 DESCRIPTION OF BEAM, WHOLE BODY SHIELDS, AND DELIMITERS

The beam selected for clinical trials, the M67 beam, is shown in figure 5.1. The cone region is filled with pure aluminum shot, with 5.0 cm of cadmium-plated aluminum shot on top. Inside the stovepipe is a 7 cm aluminum plug with a sheet of cadmium on top, an aluminum hold-down plate for the cadmium, and the sulfur filter which is filled

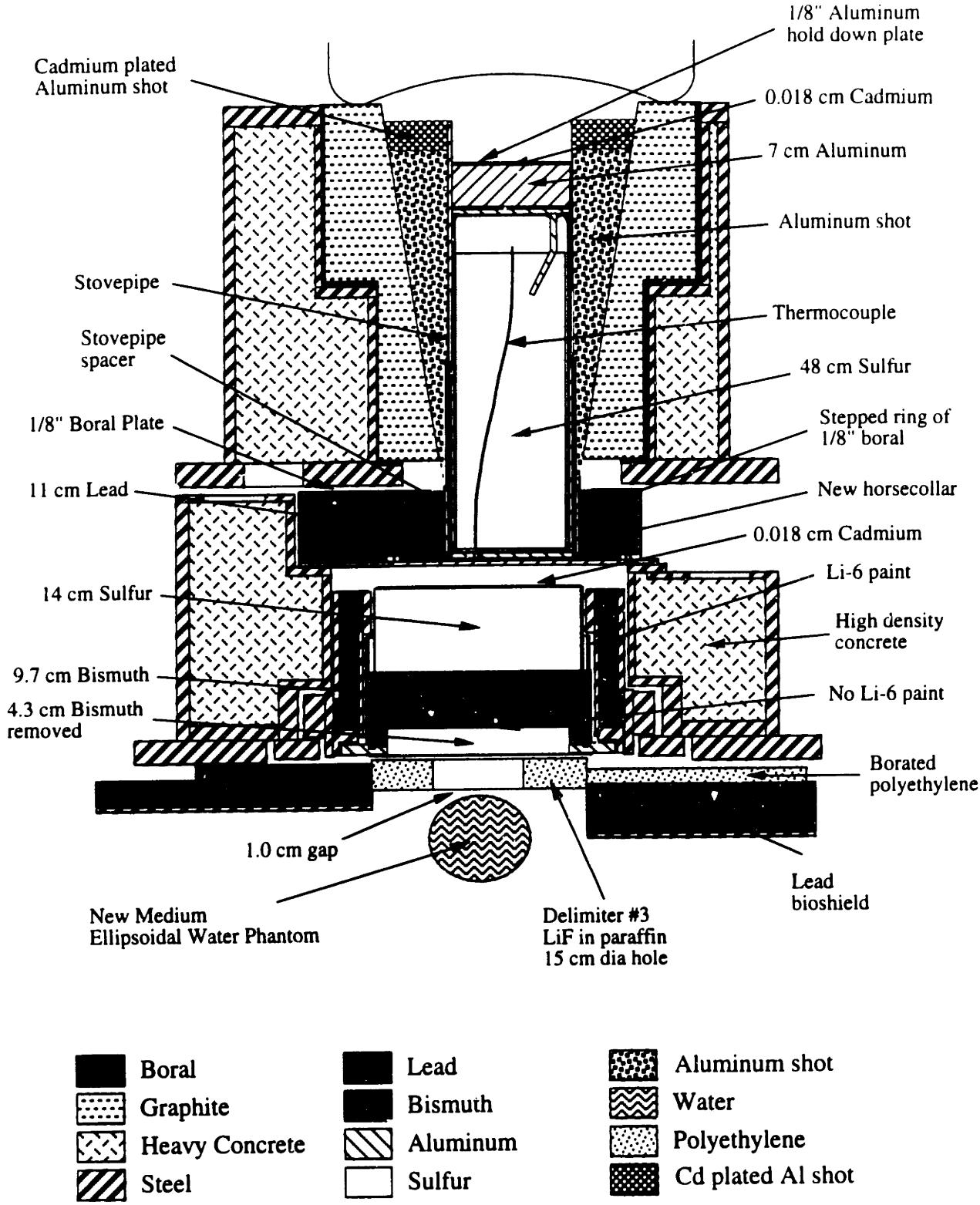

Figure 5.1. Cross sectional view of the clinical beam. This is the M67 beam with delimiter #3 (15 cm diameter). The standard size, ellipsoidal, water filled head phantom was used to characterize this beam.

with 48 cm of sulfur. The collimator is the wide collimator (33 cm diameter), with 14 cm of sulfur and 9.7 cm of bismuth.

The delimiter[1] used in this beam, delimiter #3, is shown in figure 5.2. The purpose of the delimiter is to reduce the dose to the patient outside the main beam. The delimiter is a 2" thick slab of lithiated paraffin with a 15 cm diameter hole in the middle. The hole in the delimiter is centered below the collimator, not the upper filter or stovepipe section. Lithium in the form of LiF was added to the delimiter to suppress prompt gammas which would increase the patient's photon dose. Sufficient lithium was added such that the thermal neutron capture rate in the region around the hole was 20 times higher in the lithium than in the hydrogen; further away from the hole, half as much lithium was added. The effectiveness of a 20 cm diameter delimiter in reducing the various incident radiation components is discussed in Chapter 4. Delimiter #3, which has a 15 cm diameter hole, provides the same shielding beneath the delimiter itself; however, the full intensity of the beam is confined to the smaller, 15 cm diameter hole. The incident epithermal flux and, therefore, the thermal flux that would be generated within the patient outside the main beam, is reduced by a factor of 10 by the delimiter. The fast neutron dose is reduced by a factor of 2.9. The incident photon dose is reduced only slightly. The delimiter is supported by railings that are bolted to the bioshields.

A whole body shield extends along the full length of the lead shutter, about 0.5 cm below the bottom plane of the shutter. This shield consists of two 2" thick slabs of borated polyethylene, 14 1/16" wide and 43" long. There is one slab on either side of the delimiter. These slabs are supported on the same railings that support the delimiter.

The bottom of the lead shutter is painted as shown in figure 5.3. Five coats of a Li-6 carbonate loaded paint have been applied around the collimator. The bismuth on the bottom of the collimator, however, is not painted. Ten coats of a B_4C loaded paint have been applied to the rest of the lead shutter. These paints absorb at least 90% of the incident thermal neutrons (refer to figures 4.68 and 6.1). They were applied primarily to

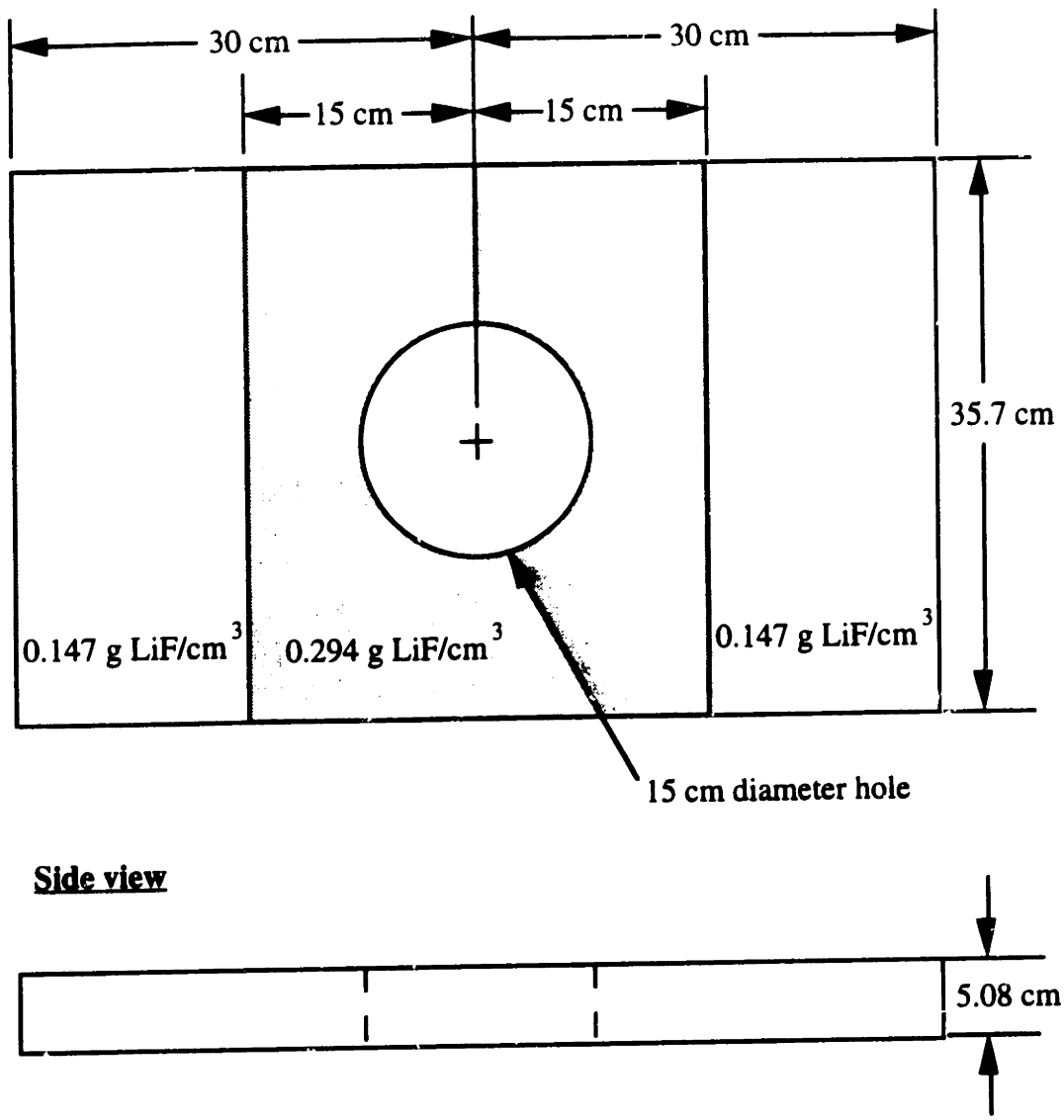

Figure 5.2. Delimiter #3, which was used in the M67 clinical beam. This delimiter was made of lithiated paraffin. It has a 15 cm diameter hole in the center. Lithium in the form of LiF was added to suppress prompt gammas, which would increase the patient's photon dose.

Bottom view

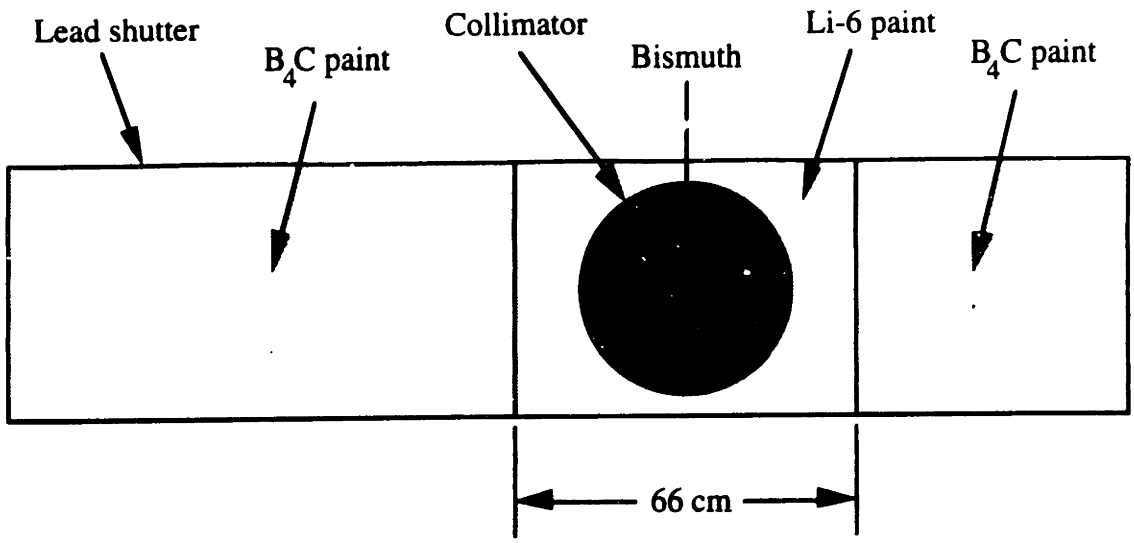

Scale: 1/15

Figure 5.3. Bottom view of the lead shutter showing where the Li-6 and B_4C loaded paints were applied for the M67 beam. Five coats of the Li-6 carbonate loaded paint and 10 coats of the B_4C loaded paint were applied. These paints give a factor of 10 reduction in the thermal flux. There was no paint on the bottom of the bismuth collimator. Delimiter #3 is 60 cm long, so the Li-6 painted region on the bottom of the lead shutter extends 3 cm beyond the delimiter on each side.

reduce activation of components, such as the surgical couch, outside the main beam. The Li-6 based paint was used around the collimator so that prompt gammas, which would increase the patient's dose, would not be produced. Well outside the beam, however, the B_4C paint was used since it is cheaper and prompt gamma production is not sufficiently intense to increase the patient's dose.

5.3 DOSIMETRY OF THE CLINICAL BEAM

5.3.1 Experimental dosimetry

Pursuant to MITR Technical Specification No. 6.5, four separate Procedures related to dosimetry were written and followed for the dosimetric characterization of this beam. They are discussed briefly towards the end of this chapter.

The important parameters used in the calculations of the doses are: For the carbon graphite ionization chamber with CO_2, neutron to gamma sensitivity ratio = 0.0437, calibration = 1.299E10 rads/C, thermal neutron response = 1.50E-20 (C/min)/(n/cm^2-sec). These are valid in determining the doses for muscle or brain. For the tissue equivalent ionization chamber with tissue equivalent gas, neutron to gamma sensitivity ratio = 0.95 for muscle and 0.92 for brain, calibration = 2.034E10 rads/C, thermal neutron response = 4.77E-20 (C/min)/(n/cm^2-sec). The B-10 kerma that was used is 8.66E-12 cGy cm^2/n per ppm B-10. The thermal neutron dose kerma, from the N-14(n,p)C-14 reaction, that was used is 2.724E-11 cGy cm^2/n for muscle and 1.401E-11 cGy cm^2/n for brain. The reader is referred to Chapter 3 for a discussion of these values.

The electrometer and ionization chambers used to measure this beam had been officially calibrated by the University of Wisconsin Accredited Dosimetry Calibration Laboratory. Calibration reports are provided in Appendix B.

This beam was characterized using a standard sized, water filled head phantom (refer to Chapter 2). The head phantom with the shell made of casting resin was used. The phantom was positioned 1 cm below the bottom of the delimiter. This was done since, with most patients, there will often be at least a 1 cm gap between the patient and the bottom of the delimiter. The doses were measured along the central axis of the phantom. Some off-axis doses, at a depth of 4 cm, were also measured.

Results are shown in figures 5.4 - 5.6. Each dose component is RBE weighted; selection of these RBE's is discussed in Chapter 2. Separate doses were calculated using muscle and brain kermas. This was done for a more complete comparison of the experimental results with a companion set of MCNP results. Using muscle kermas, the advantage parameters of this beam are: AR = 2.1, ADDR = 7.7 RBE cGy/min, AD = 6.6 cm. Only a single set of advantage parameters is provided for BPA; healthy tissue was assumed to have 7.5 ppm B-10. This beam has significant skin sparing; the total tumor dose at the surface is about one-half of its maximum value at 2 cm depth. Also, the thermal neutron flux drops off rapidly at the surface. The fast neutron dose falls off with a half-thickness of 3 cm.

Buildup caps were used during the in-air ionization chamber measurements. The in-air fast neutron dose (2.57 RBE cGy/min) is slightly less than that at the top of the phantom (2.74 RBE cGy/min); the phantom itself scatters and reflects back some of the incident fast neutrons, leading to a higher fast neutron dose at the top of the phantom. The in-air photon dose is 0.855 RBE cGy/min; in phantom, it is 1.16 RBE cGy/min at the surface and it reaches a maximum of 1.30 RBE cGy/min. The in-air thermal flux is very small; it is about 5 times lower than that generated at the surface of the phantom from the incident epithermal neutrons.

Using brain kermas, the advantage parameters of this beam are: AR = 2.4, ADDR = 7.4 RBE cGy/min, AD = 6.6 cm. The major difference between the doses in muscle and in brain is the thermal neutron dose. The thermal neutron dose is much lower in

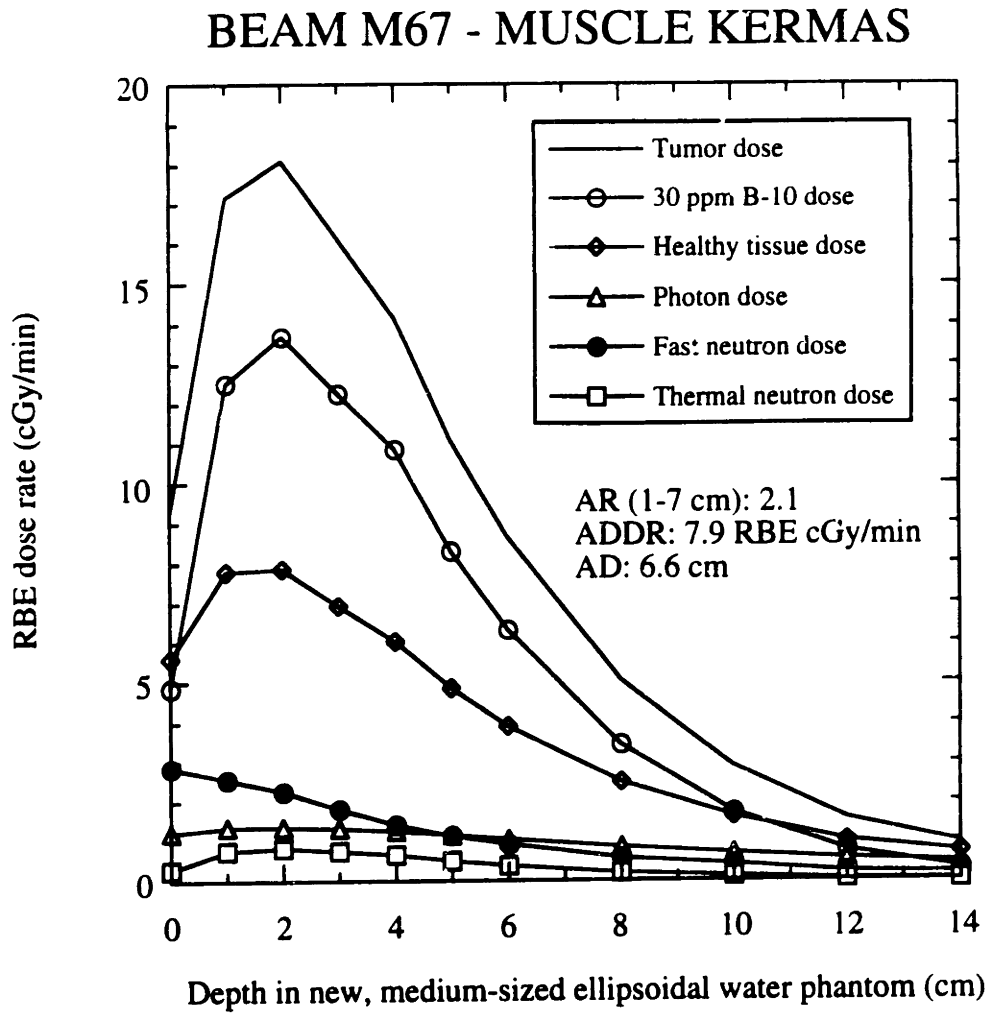

Figure 5.4. Doses measured in the new phantom for the M67, delimiter #3 beam and BPA. These doses were calculated for muscle.

Unilateral irradiation.
Phantom: Standard sized, casting resin ellipsoidal, water filled, center tube.
Delimiter: #3, 15 cm diameter hole.
Reactor power: 5 MWn.
RBE's: 4.0 for B-10, 2.3 for neutrons, 0.5 for photons.
B-10 concentrations: 30 ppm for tumor, 7.5 ppm for healthy brain.
In-air data: D_{fn} = 2.7 cGy/min
D_{γ} = 0.89 cGy/min
$D_{30ppm\ B\text{-}10}$ = 1.2 cGy/min

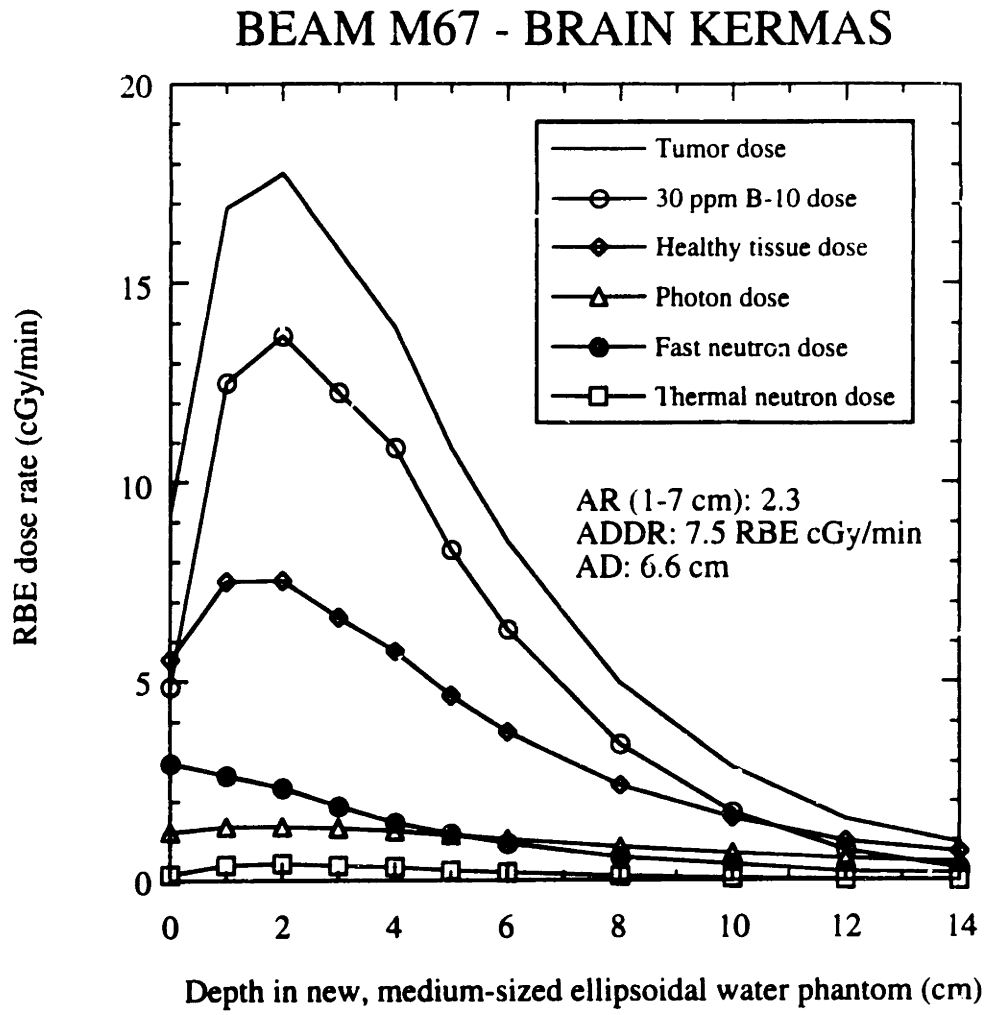

Figure 5.5. Doses measured in the new phantom for the M67, delimiter #3 beam and BPA. These doses were calculated for brain.

Unilateral irradiation.
Phantom: Standard sized, casting resin ellipsoidal, water filled, center tube.
Delimiter: #3, 15 cm diameter hole.
Reactor power: 5 MWn.
RBE's: 4.0 for B-10, 2.3 for neutrons, 0.5 for photons.
B-10 concentrations: 30 ppm for tumor, 7.5 ppm for healthy brain.
In-air data: D_{fn} = 2.8 cGy/min
D_{γ} = 0.89 cGy/min
$D_{30ppm\ B\text{-}10}$ = 1.2 cGy/min

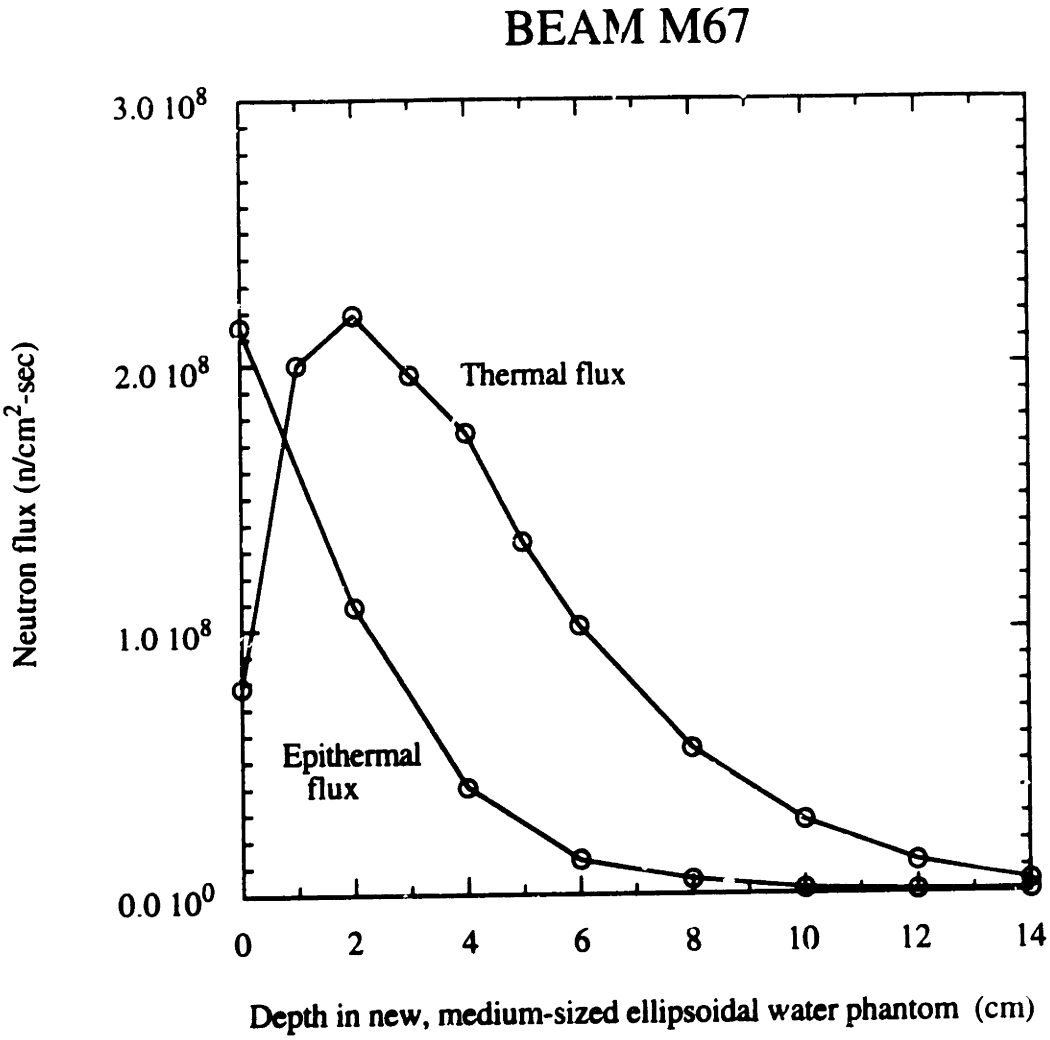

Figure 5.6. Thermal and epithermal fluxes measured in the new phantom for the M67, delimiter #3 beam.

Unilateral irradiation.
Phantom: New standard sized, ellipsoidal, water filled, center tube.
Delimiter: #3, 15 cm diameter hole.
Reactor power: 5 MWn.

brain since brain has less nitrogen (Table 3.3). Brain has a slightly higher fast neutron dose because of its higher hydrogen density.

The peak thermal neutron flux is 2.2E8 n/cm^2-sec.

The dose distribution for an assumed bilateral irradiation is shown in figure 5.7. The doses are symmetrical about the centerline of the phantom. The maximum dose to healthy tissue was normalized to 2000 RBE cGy, the highest dose which is now planned to be delivered to the Phase I melanoma patients. The AR for the bilateral irradiation is 2.2.

The fast neutron RBE is not known with confidence. The bilateral dosimetry, therefore, was redone assuming that the thermal and fast neutron RBE was 4.0, not 2.3. The bilateral dose distribution assuming the pessimistic neutron RBE is shown in figure 5.8. Again, the healthy tissue dose has been normalized to 2000 RBE cGy. It is seen that the AR under these pessimistic conditions is still 2.0; this is compared to the AR of 2.2 using the likely neutron RBE of 2.3. It is concluded that even when using the pessimistically high neutron RBE of 4.0 that the average tumor dose will still be 2.0 times that of the average healthy tissue dose.

Off-axis doses for the M67 clinical beam are shown in figures 5.9 and 5.10. Most noticeable is the drop in the thermal flux at the side of the phantom (tube H). This is attributable to shadowing by the delimiter, and to being closer to the surface of the phantom. The epithermal flux is greatly attenuated in the delimiter so few epithermal neutrons around the outside of the beam strike the sides of the phantom. Also, there is greater likelihood of leakage for thermal neutrons born near the surface of the phantom.

Patients will be irradiated to give a particular maximum dose to healthy tissue. The dose rate to healthy tissue depends on the B-10 concentration in healthy tissue, as well as the photon and fast neutron dose rates. This is shown in figure 5.11, which was calculated using muscle kermas. The fast neutron RBE for this plot was assumed to be 4.0.[2] (For BPA, our group assumes a fast neutron RBE of 2.3. For this plot, however, an

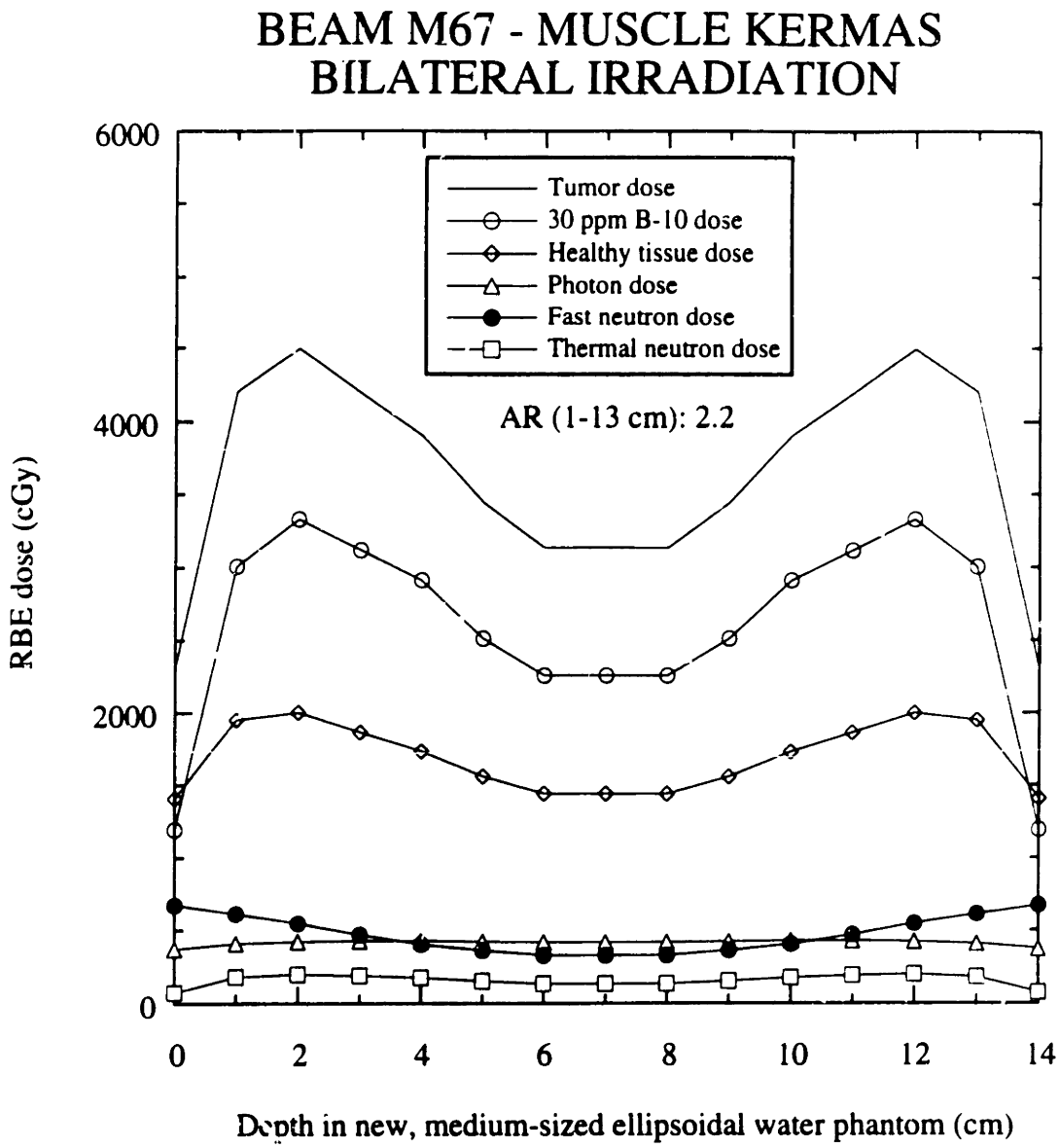

Figure 5.7. Bilateral irradiation dose distribution in the new phantom for the M67, delimiter #3 beam and BPA. These doses were calculated for muscle. The doses were normalized such that the maximum dose to healthy tissue is 2000 RBE cGy.

Bilateral irradiation.
Phantom: Medium sized, casting resin ellipsoidal, water filled, center tube.
Delimiter: #3, 15 cm diameter hole.
Reactor power: 5 MWn.
RBE's: 4.0 for B-10, 2.3 for neutrons, 0.5 for photons.
B-10 concentrations: 30 ppm for tumor, 7.5 ppm for healthy brain.

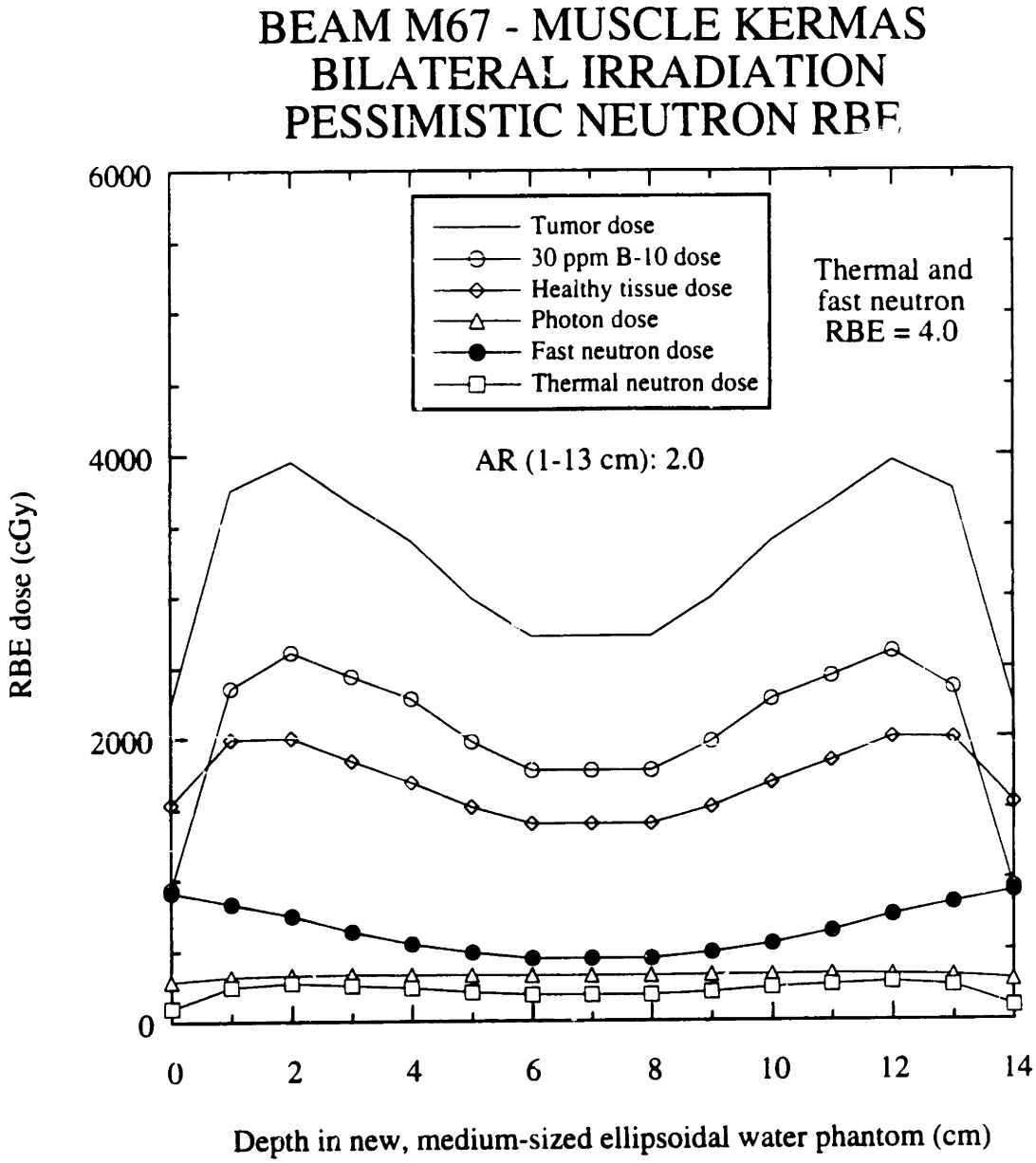

Figure 5.8. Bilateral irradiation dose distribution in the new phantom for the M67, delimiter #3 beam and BPA assuming a pessimistic thermal and fast neutron RBE of 4.0. These doses were calculated for muscle. The doses were normalized such that the maximum dose to healthy tissue is 2000 RBE cGy. The AR was 2.2 using the likely set of RBE's; the AR is 2.0 using these pessimistic RBE's.

Bilateral irradiation.
Phantom: Medium sized, casting resin ellipsoidal, water filled, center tube.
Delimiter: #3, 15 cm diameter hole.
Reactor power: 5 MWn.
RBE's: 4.0 for B-10, 4.0 for neutrons, 0.5 for photons.
B-10 concentrations: 30 ppm for tumor, 7.5 ppm for healthy brain.

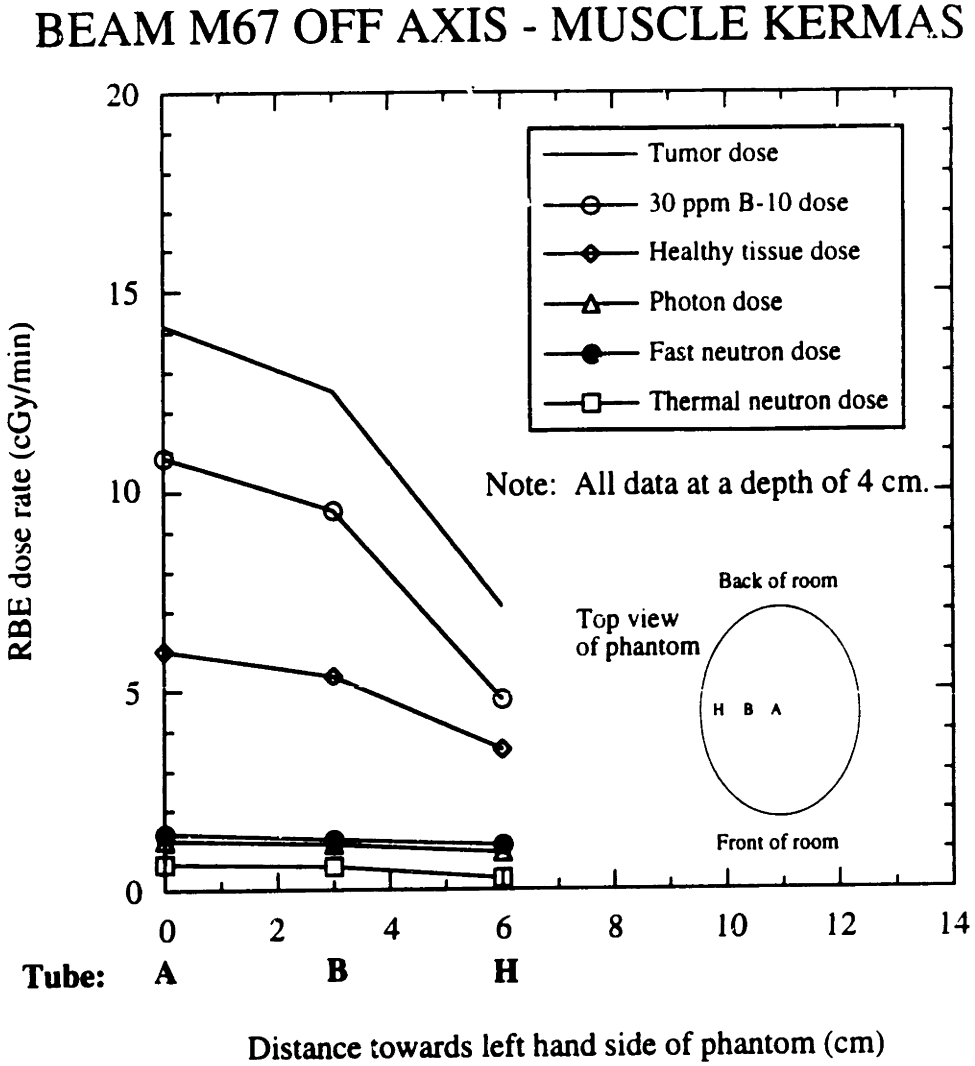

Figure 5.9. Off axis doses measured in phantom for the M67, delimiter #3 beam and BPA. These doses were calculated for muscle.

Unilateral irradiation.
Phantom: New medium sized, ellipsoidal, water filled, center tube.
Delimiter: #3, 15 cm diameter hole.
Reactor power: 5 MWn.
RBE's: 4.0 for B-10, 2.3 for neutrons, 0.5 for photons.
B-10 concentrations: 30 ppm for tumor, 7.5 ppm for healthy brain.
In-air data: $D_{fn} = 2.7$ cGy/min
$D_{\gamma} = 0.89$ cGy/min
$D_{30ppm\ B\text{-}10} = 1.2$ cGy/min

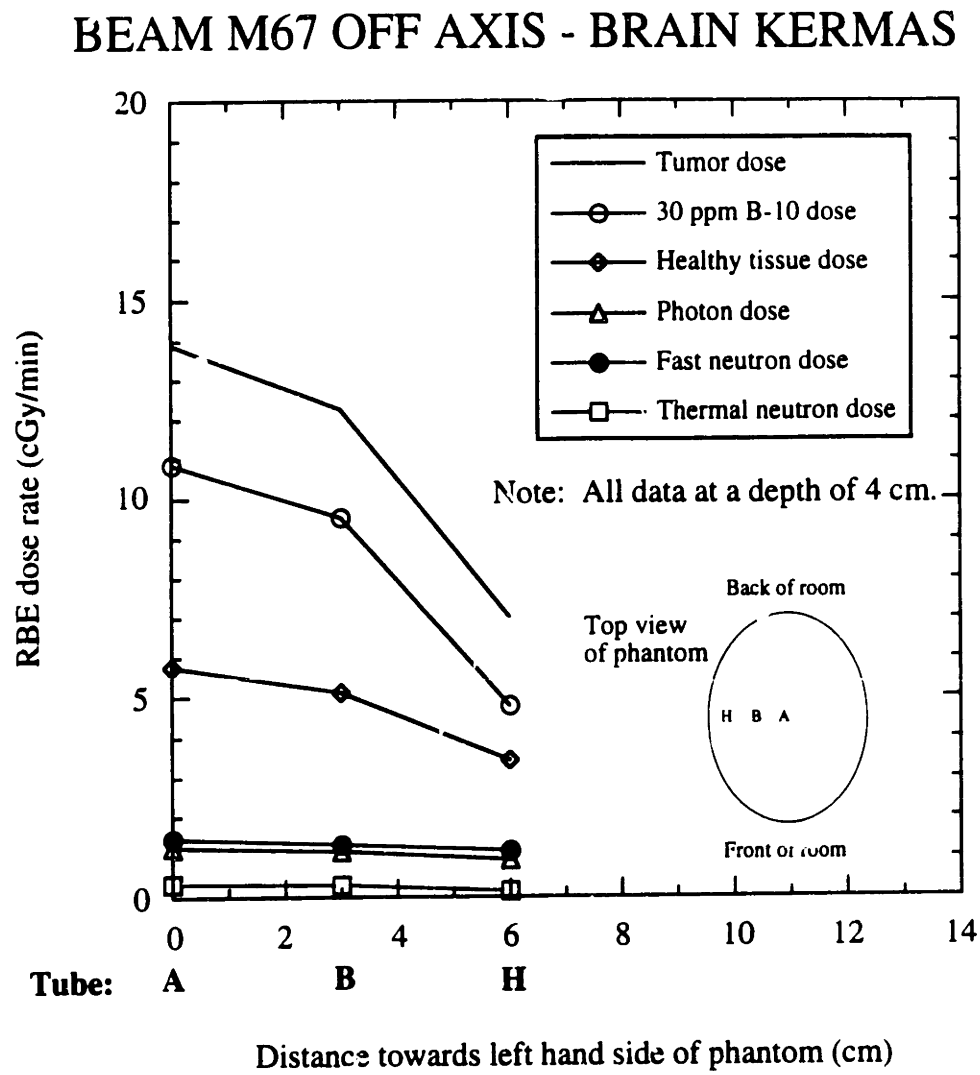

Figure 5.10. Off axis doses measured in phantom for the M67, delimiter #3 beam and BPA. These doses were calculated for brain.

Unilateral irradiation.
Phantom: New medium sized, ellipsoidal, water filled, center tube.
Delimiter: #3, 15 cm diameter hole.
Reactor power: 5 MWth.
RBE's: 4.0 for B-10, 2.3 for neutrons, 0.5 for photons.
B-10 concentrations: 30 ppm for tumor, 7.5 ppm for healthy brain.
In-air data: D_{fn} = 2.8 cGy/min
D_{γ} = 0.89 cGy/min
$D_{30ppm\ B\text{-}10}$ = 1.2 cGy/min

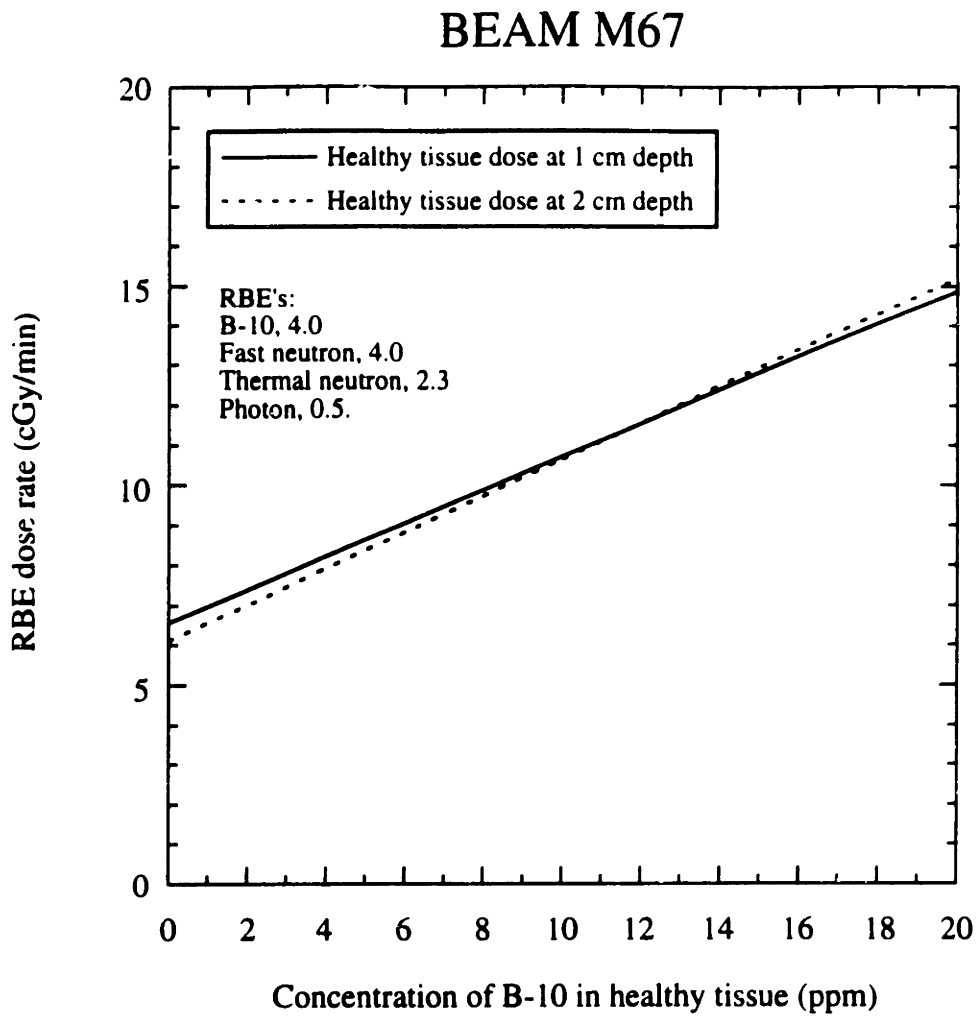

Figure 5.11. Variation in the total dose rate to healthy tissue with the B-10 concentration in healthy tissue. The photon and fast neutron doses were assumed to be independent of the B-10 concentration. The fast neutron RBE was assumed to be 4.0 for this plot. The doses in phantom were calculated using muscle kermas.

Unilateral irradiation.
Phantom: Medium sized, casting resin ellipsoidal, water filled, center tube.
Delimiter: #3, 15 cm diameter hole.
Reactor power: 5 MWn.
RBE's: 4.0 for B-10, 4.0 for fast neutrons, 2.3 for thermal neutrons, 0.5 for photons.
B-10 concentrations: 30 ppm for tumor, variable ppm for healthy tissue.

RBE of 4.0 was assumed. Doses determined with the treatment planning program, which will be discussed next, will be reported assuming a fast neutron RBE of 4.0.) Just before the patient is irradiated, a blood sample will be drawn and its B-10 concentration will be measured within 15 minutes by prompt gamma neutron activation analysis (refer to Chapter 7). The healthy tissue B-10 concentration will then be estimated and figure 5.11 will be used to determine the dose rate to healthy tissue. This is only an approximate method as the dose rates in an actual patient will be different than those in the head phantom. The differences might be large, up to 50% or more, since the patient could be positioned further away from the bottom of the collimator. Also, the patient and phantom have different sizes and shapes and will have different orientations relative to the beam.

5.3.2 Monte Carlo based dosimetry

Monte Carlo based dosimetry and computer-aided treatment planning have been developed to link the experimentally measured doses with the need of the radiation oncologist to synthesize large amounts of dosimetric data into a clinically meaningful treatment plan for each patient.[3,4] In the treatment planning program, called NCTPLAN, Monte Carlo simulation is used to characterize the spatial dose distribution within a patient. The treatment plan incorporates three dimensional computed tomographic image data. The cell volume for the Monte Carlo simulation has been chosen to be 1 cm^3; this volume is a compromise between spatial resolution and computer time. The composition of each cell is assigned to be either bone, muscle, or air; one of these compositions is determined from the average densities in that volume from the computed tomographic images. Dose distributions can be determined along any arbitrary axis or within any arbitrary oriented plane. Figures of merit (AR, AD, ADDR, and others) can also be calculated. The reader is referred to references 3 and 4 for more details on the Monte Carlo based dosimetry and treatment planning.

One step in the treatment planning process is the normalization of the Monte Carlo derived dose rates with those determined experimentally. These normalizations have been done for each of the radiation dose components for the M67 clinical beam. The normalizations minimize the error between the Monte Carlo derived and experimentally measured doses in a least squared sense. For treatment planning, the thermal and fast neutron RBE's were assumed to be 4.0. The normalized Monte Carlo and experimentally derived dose components, along the central axis of the head phantom, are shown in figures 5.12 - 5.16. A companion set of off-axis dose components is shown in figures 5.17-5.21.

The B-10 doses are compared in figure 5.12. For the B-10 dose, the normalization factor is 0.87. Then, the shapes and intensities of the two B-10 dose curves agree well throughout the phantom. The same normalization factor was used for the thermal neutron dose. Again, as shown in figure 5.13, the shapes and intensities of the two thermal neutron dose curves then agree well throughout the phantom.

The fast neutron doses are compared in figure 5.14. The MCNP derived fast neutron dose (0.5 eV - 15 MeV) was calculated by subtracting the thermal neutron dose (0 - 0.5 eV) from the total neutron dose (0 - 15 MeV). The normalization factor is 1.10. The MCNP generated fast neutron dose rate rises more rapidly than the experimentally measured values at the surface of the phantom. Part of this effect is due to spatial averaging, as the grid size of the MCNP run is less than that for the experimental measurement. Also, with the ionization chambers and phantoms used in this work, it is not possible to measure experimentally the doses exactly at the top of the phantom. Instead, the chamber is placed with its centerline 1 cm below the bottom plane of the collimator, and the phantom is raised until it touches the thimble of the chamber. The spatial averaging effect and the difficulty in measuring exactly at the top of the phantom, then, could account for some of the difference between the fast neutron doses at the surface of the phantom.

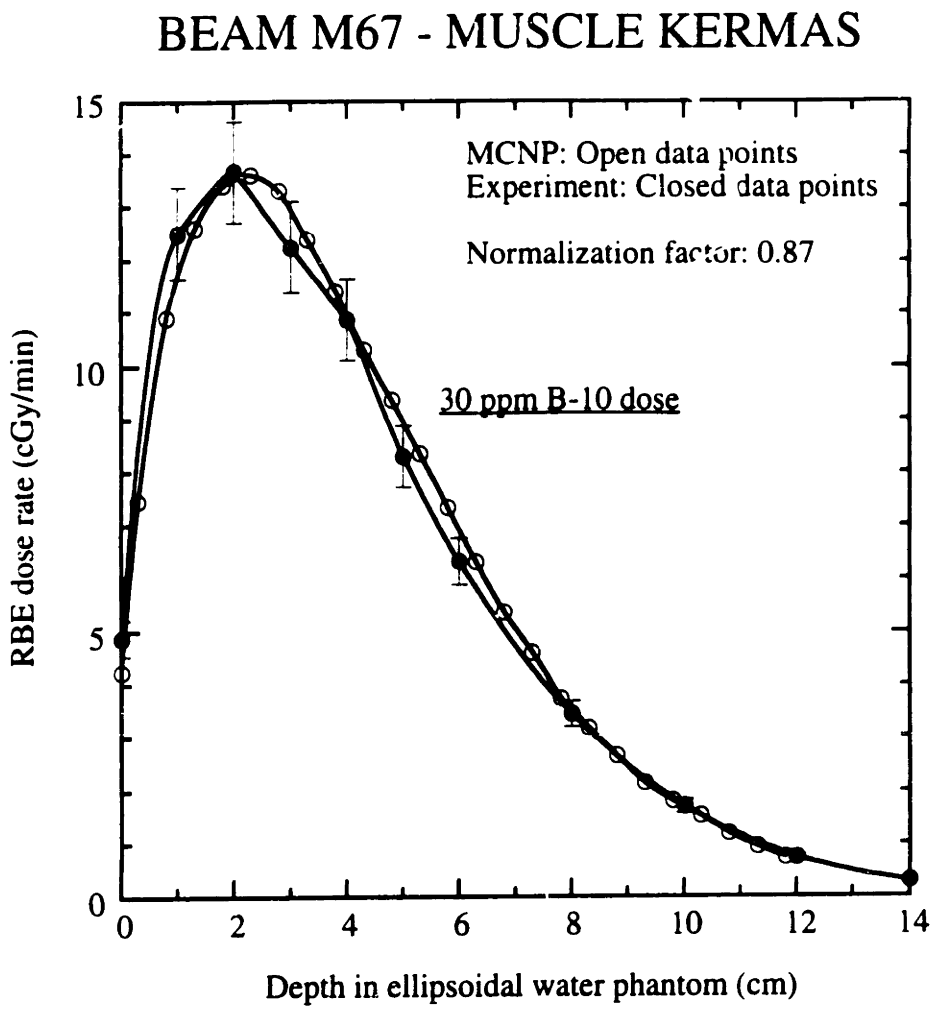

Figure 5.12. Comparison of MCNP generated and experimentally measured B-10 dose rates for the M67, delimiter #3 beam. A normalization factor of 0.87 was multiplied by the original MCNP generated B-10 dose rate. The shapes of the curves agree well. The error bars for the experimental data are for the total uncertainty in the B-10 dose.

Unilateral irradiation.
Phantom: Medium sized, casting resin ellipsoidal, water filled, center tube.
Delimiter: #3, 15 cm diameter hole.
Reactor power: 5 MWn.
RBE's: 4.0 for B-10, 4.0 for neutrons, 0.5 for photons.
B-10 concentrations: 30 ppm for tumor, 7 5 ppm for healthy brain.

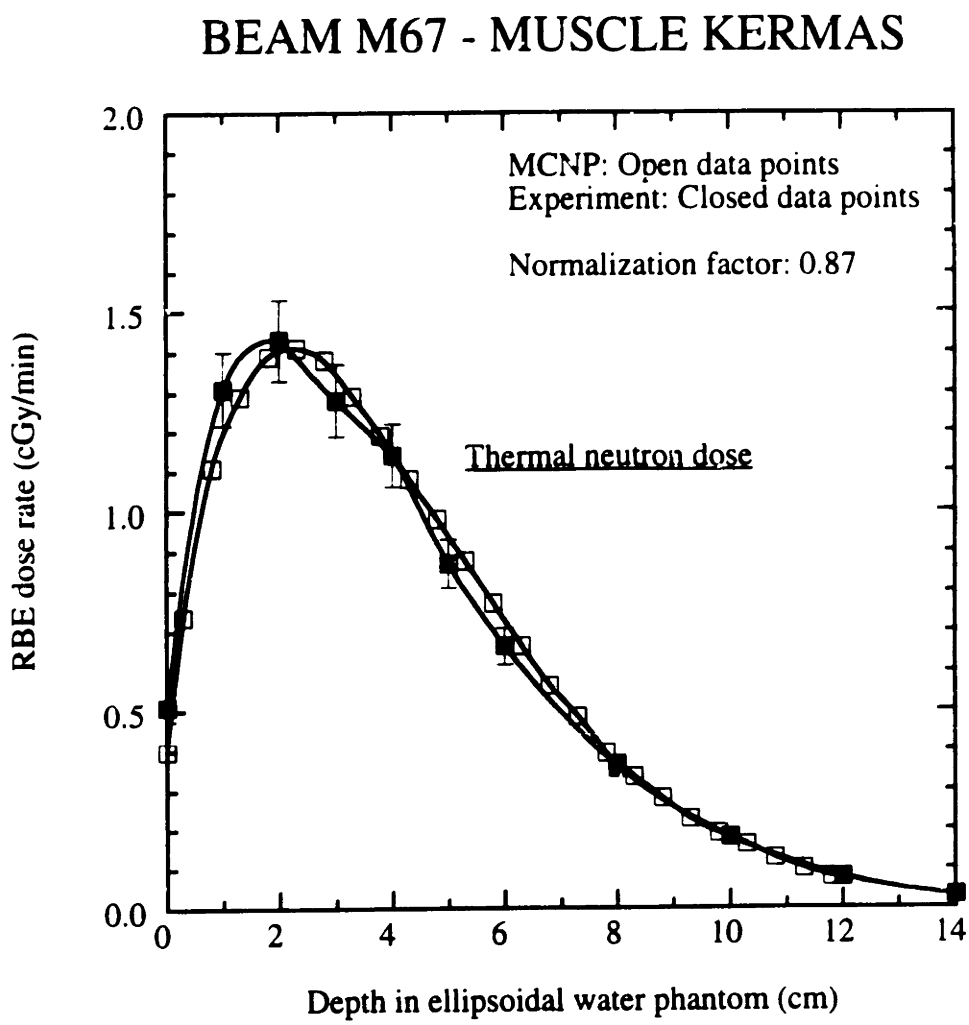

Figure 5.13. Comparison of MCNP generated and experimentally measured thermal neutron dose rates for the M67, delimiter #3 beam. A normalization factor of 0.87 was multiplied by the original MCNP generated thermal neutron dose. The shapes of the curves agree well. The error bars for the experimental data are for the total uncertainty in the thermal neutron dose.

Unilateral irradiation.
Phantom: Medium sized, casting resin ellipsoidal, water filled, center tube.
Delimiter: #3, 15 cm diameter hole.
Reactor power: 5 MWn.
RBE's: 4.0 for B-10, 4.0 for neutrons, 0.5 for photons.
B-10 concentrations: 30 ppm for tumor, 7.5 ppm for healthy brain.

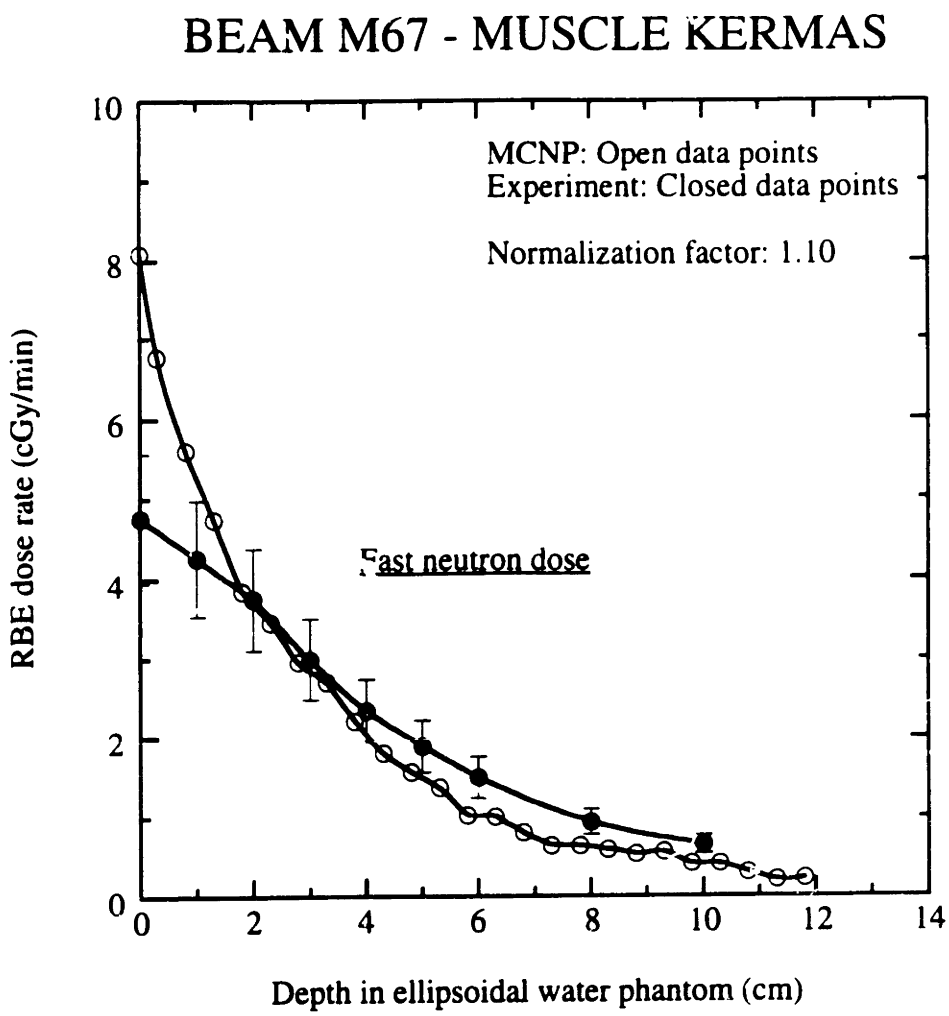

Figure 5.14. Comparison of MCNP generated and experimentally measured fast neutron dose rates for the M67, delimiter #3 beam. A normalization factor of 1.10 was multiplied by the original MCNP generated fast neutron dose rate. The MCNP generated fast neutron dose rate rises more rapidly than the experimentally measured values at the surface of the phantom. The error bars for the experimental data are for the total uncertainty in the fast neutron dose.

Unilateral irradiation.
Phantom: Medium sized, casting resin ellipsoidal, water filled, center tube.
Delimiter: #3, 15 cm diameter hole.
Reactor power: 5 MWn.
RBE's: 4.0 for B-10, 4.0 for neutrons, 0.5 for photons.
B-10 concentrations: 30 ppm for tumor, 7.5 ppm for healthy brain.

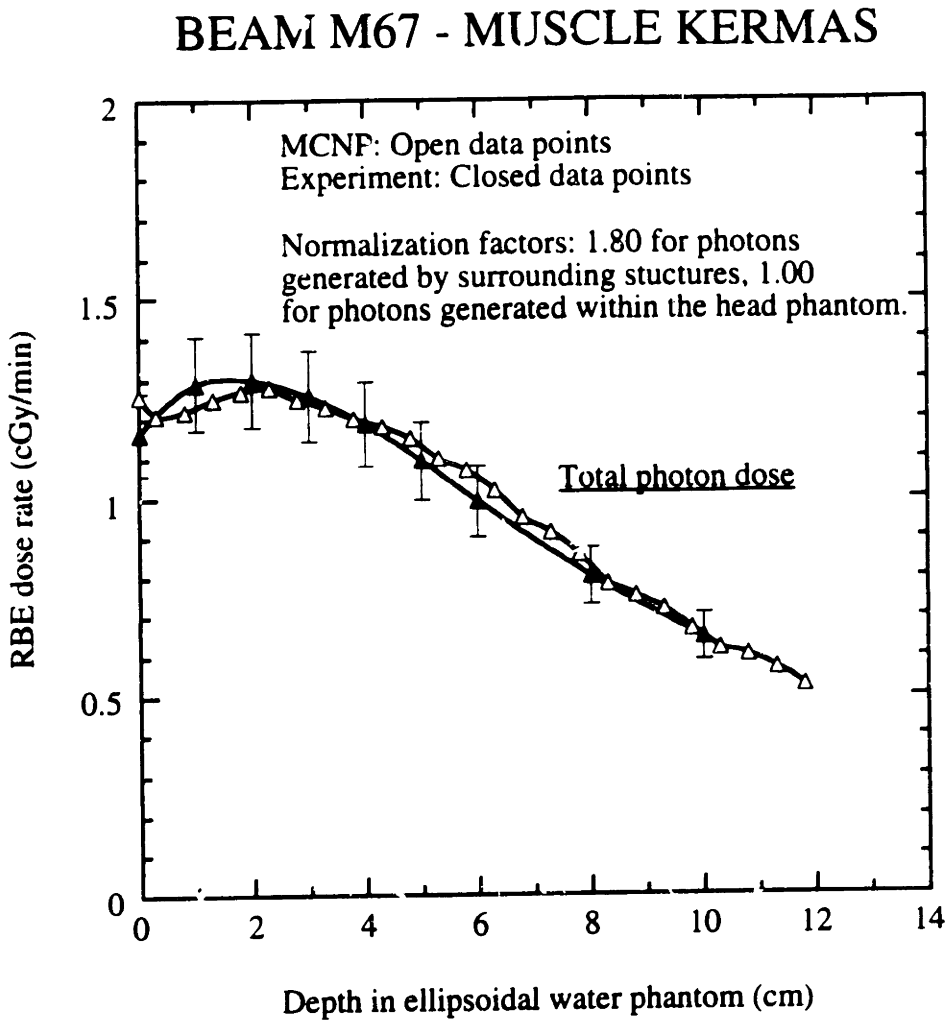

Figure 5.15. Comparison of MCNP generated and experimentally measured photon dose rates for the M67, delimiter #3 beam. A normalization factor of 1.80 was multiplied by the original MCNP generated structural gamma dose; a normalization factor of 1.00 was multiplied by the original MCNP generated phantom induced gamma dose The shapes of the curves agree well. The error bars for the experimental data are for the total uncertainty in the photon dose.

Unilateral irradiation.
Phantom: Medium sized, casting resin ellipsoidal, water filled, center tube.
Delimiter: #3, 15 cm diameter hole.
Reactor power: 5 MWn.
RBE's: 4.0 for B-10, 4.0 for neutrons, 0.5 for photons.
B-10 concentrations: 30 ppm for tumor, 7.5 ppm for healthy brain.

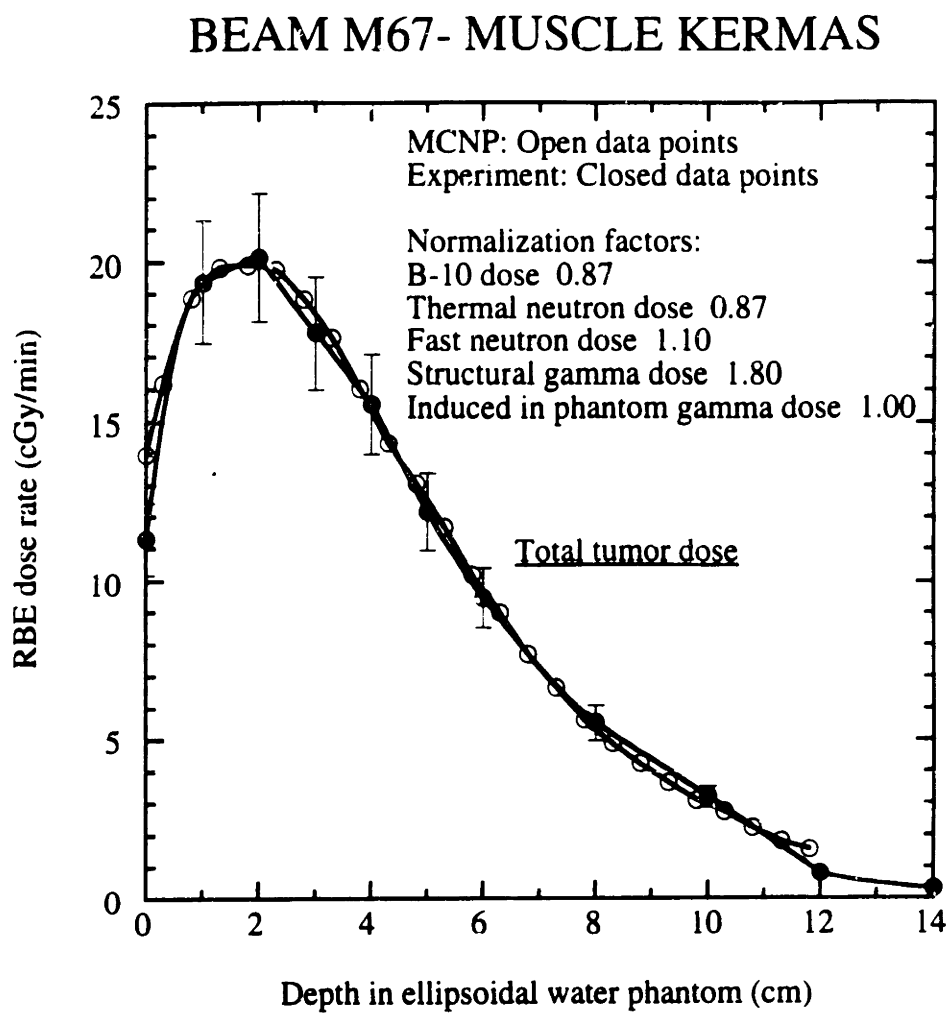

Figure 5.16. Comparison of MCNP generated and experimentally measured total tumor dose rates for the M67, delimiter #3 beam. Normalization factors have been applied tc the separate dose components. The error bars for the experimental data are for the total uncertainty in the total tumor dose.

Unilateral irradiation.
Phantom: Medium sized, casting resin ellipsoidal, water filled, center tube.
Delimiter: #3, 15 cm diameter hole.
Reactor power: 5 MWn.
RBE's: 4.0 for B-10, 4.0 for neutrons, 0.5 for photons.
B-10 concentrations: 30 ppm for tumor, 7.5 ppm for healthy brain.

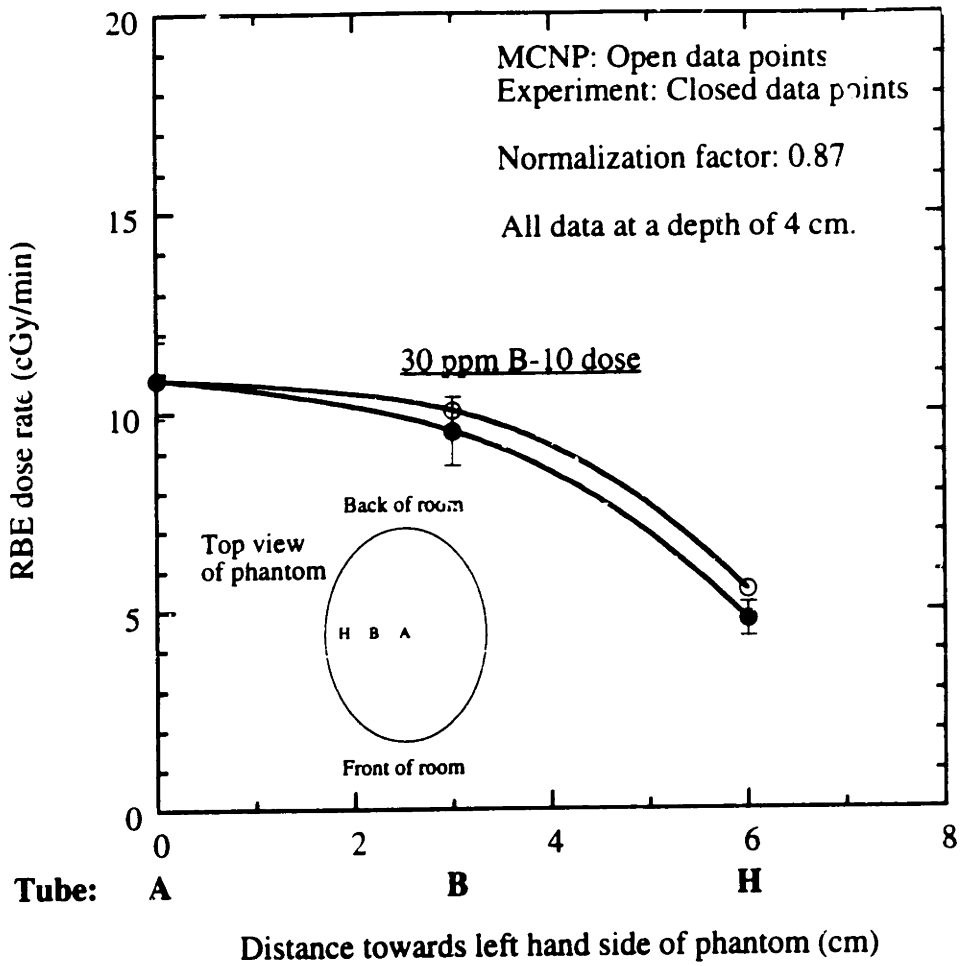

Figure 5.17. Comparison of MCNP generated and experimentally measured B-10 off axis dose rates for the M67, delimiter #3 beam. A normalization factor of 0.87 was multiplied by the original MCNP generated B-10 dose rate. MCNP predicts a slightly higher dose rate towards the side of the phantom. The error bars for the experimental data are for the total uncertainty in the B-10 dose.

Unilateral irradiation.
Phantom: Medium sized, casting resin ellipsoidal, water filled, center tube.
Delimiter: #3, 15 cm diameter hole.
Reactor power: 5 MWn.
RBE's: 4.0 for B-10, 4.0 for neutrons, 0.5 for photons.
B-10 concentrations: 30 ppm for tumor, 7.5 ppm for healthy brain.

BEAM M67 OFF AXIS - MUSCLE KERMAS

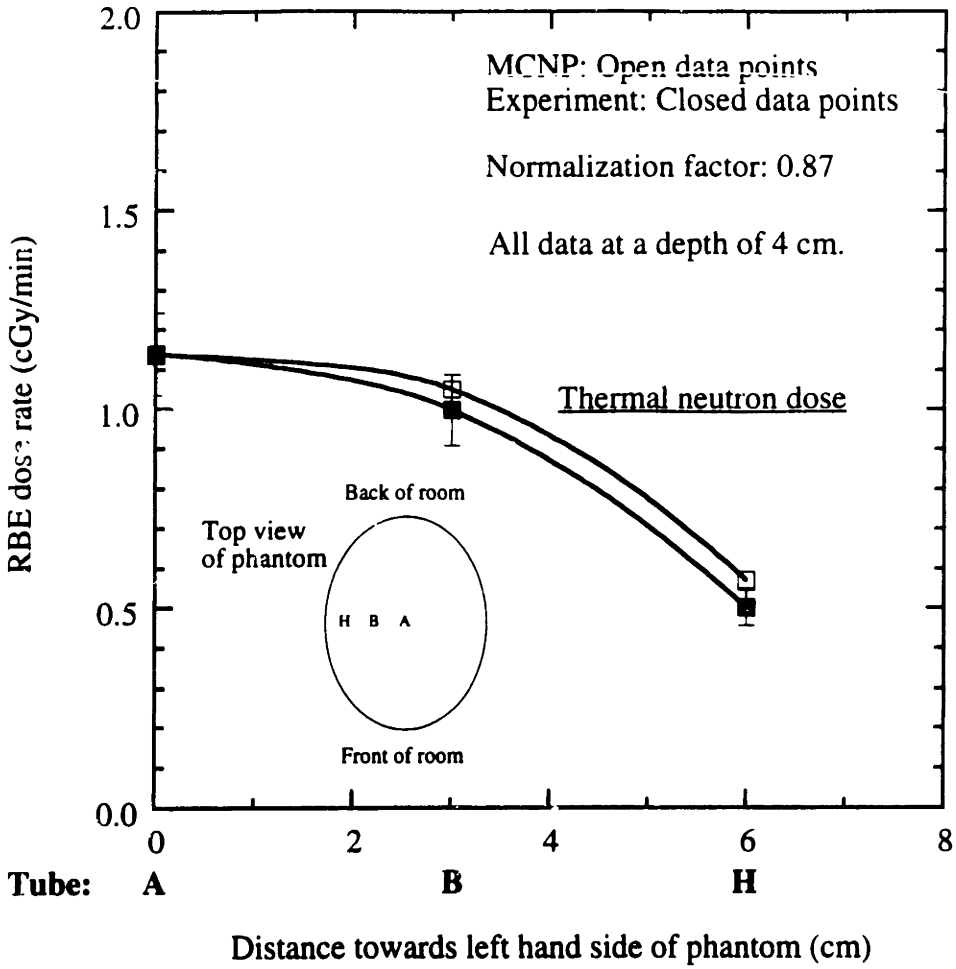

Figure 5.18. Comparison of MCNP generated and experimentally measured thermal neutron off axis dose rates for the M67, delimiter #3 beam. A normalization factor of 0.87 was multiplied by the original MCNP generated thermal neutron dose. The shapes of the curves agree well. The error bars for the experimental data are for the total uncertainty in the thermal neutron dose.

Unilateral irradiation.
Phantom: Medium sized, casting resin ellipsoidal, water filled, center tube.
Delimiter: #3, 15 cm diameter hole.
Reactor power: 5 MWn.
RBE's: 4.0 for B-10, 4.0 for neutrons, 0.5 for photons.
B-10 concentrations: 30 ppm for tumor, 7.5 ppm for healthy brain.

BEAM M67 OFF AXIS - MUSCLE KERMAS

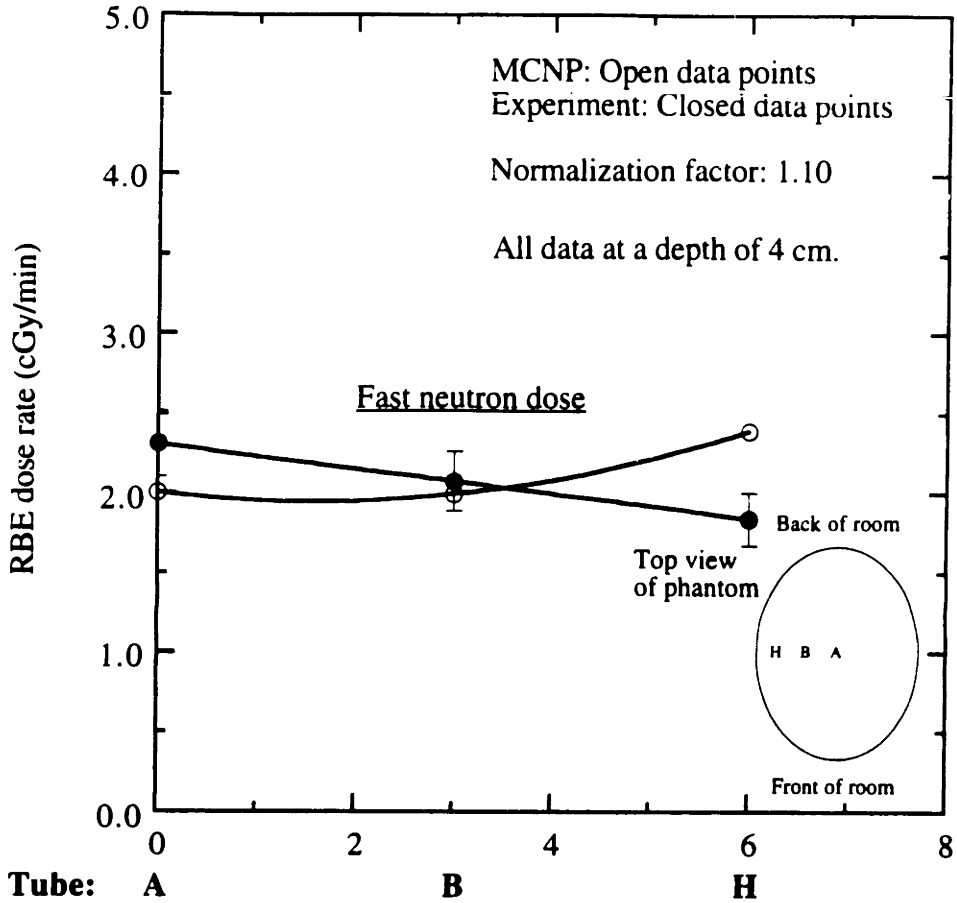

Figure 5.19. Comparison of MCNP generated and experimentally measured fast neutron off axis dose rates for the M67, delimiter #3 beam. A normalization factor of 1.10 was multiplied by the original MCNP generated fast neutron dose rate. The MCNP generated fast neutron dose rate increases at the side of the phantom (tube H), which is closer to the surface; a similar effect was seen with the center tube data at the top of the phantom. The error bars for the experimental data are for the total uncertainty in the fast neutron dose.

Unilateral irradiation.
Phantom: Medium sized, casting resin ellipsoidal, water filled, center tube.
Delimiter: #3, 15 cm diameter hole.
Reactor power: 5 MWn.
RBE's: 4.0 for B-10, 4.0 for neutrons, 0.5 for photons.
B-10 concentrations: 30 ppm for tumor, 7.5 ppm for healthy brain.

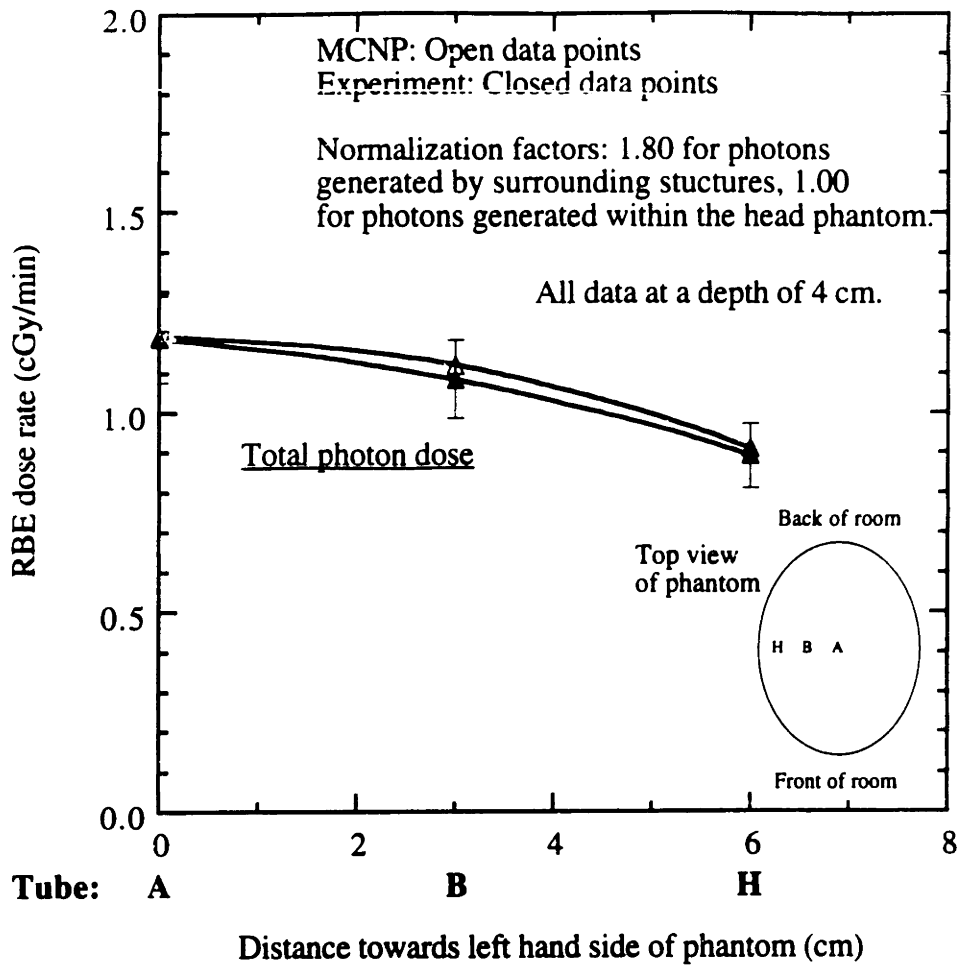

Figure 5.20. Comparison of MCNP generated and experimentally measured off axis photon dose rates for the M67, delimiter #3 beam. A normalization factor of 1.80 was multiplied by the original MCNP generated structural gamma dose; a normalization factor of 1.00 was multiplied by the original MCNP generated phantom induced gamma dose The shapes of the curves agree well. The error bars for the experimental data are for the total uncertainty in the photon dose.

Unilateral irradiation.
Phantom: Medium sized, casting resin ellipsoidal, water filled, center tube.
Delimiter: #3, 15 cm diameter hole.
Reactor power: 5 MWn.
RBE's: 4.0 for B-10, 4.0 for neutrons, 0.5 for photons.
B-10 concentrations: 30 ppm for tumor, 7.5 ppm for healthy brain.

BEAM M67 OFF AXIS - MUSCLE KERMAS

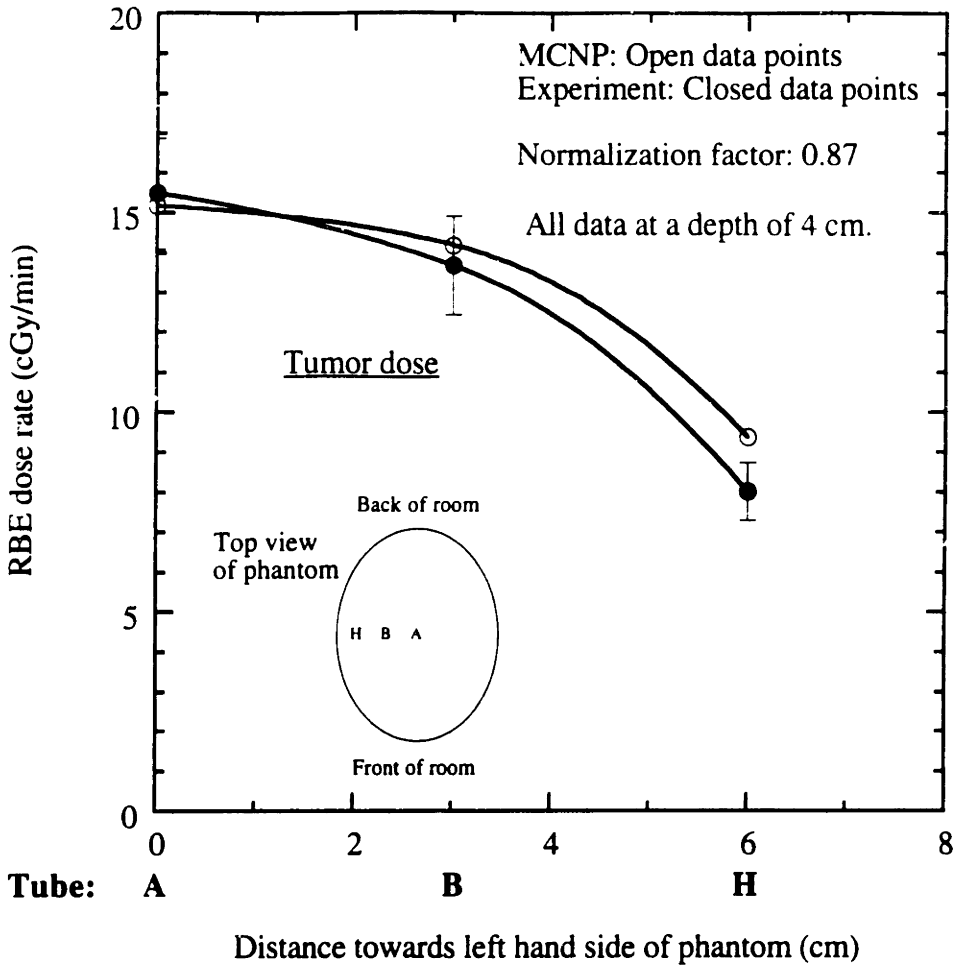

Figure 5.21. Comparison of MCNP generated and experimentally measured total tumor dose rates for the M67, delimiter #3 beam. Normalization factors have been applied to the separate dose components. The error bars for the experimental data are for the total uncertainty in the total tumor dose.

Unilateral irradiation.
Phantom: Medium sized, casting resin ellipsoidal, water filled, center tube.
Delimiter: #3, 15 cm diameter hole.
Reactor power: 5 MWn.
RBE's: 4.0 for B-10, 4.0 for neutrons, 0.5 for photons.
B-10 concentrations: 30 ppm for tumor, 7.5 ppm for healthy brain.

The photon doses are compared in figure 5.15. The MCNP generated photon dose includes induced and structural gammas, but not core gammas. Induced gammas are gammas produced within the phantom itself. Structural gammas are gammas produced in the surrounding structures. The MCNP photon dose, before normalization, was about 50% less than that measured experimentally; this might be because the core gammas were not included in the MCNP calculations. An additional MCNP run, including core gammas, is being worked on.[5] To normalize the two sets of doses, a normalization factor was applied only to the structural gamma component of the MCNP generated photon dose. The induced gamma component was left unchanged. This was done since there is good agreement between the induced photon doses calculated by MCNP and those measured experimentally (refer to the end of the discussion for the M62 beam in Chapter 4). Also, the core gammas that were not included in the MCNP calculations might reasonably be approximated by additional structural gammas. Both core and structural gammas would have a wide range of energies and angles, and be seen as a source primarily in the collimator region.

A normalization factor of 1.80 was applied to the structural gamma component. As shown in figure 5.15, the shapes and intensities of the two curves then agree well throughout the phantom.

Finally, the total tumor doses are compared in figure 5.16. The MCNP generated total tumor dose was obtained by summing the various dose components after they had been normalized. Excellent agreement is found throughout the phantom.

The companion set of off axis doses is shown in figures 5.17 - 5.21. The same normalization factors determined for the central axis doses were applied to the off-axis dose components. Again, there was excellent agreement between the B-10 and thermal neutron doses. The MCNP generated fast neutron dose is significantly higher than the experimentally measured fast neutron dose in tube H. The 4 cm depth position in tube H is near the surface of the phantom. The higher fast neutron dose rate in this position, as

determined by MCNP, is similar to the higher fast neutron doses near the surface of the phantom along the central axis (as shown in figure 5.14). The off-axis photon and total tumor doses also agree well.

These normalization factors have now been incorporated into NCTPLAN. They will be applied to the various dose components so a more accurate dosimetry of the patient is available for treatment planning and for radiological and pathological correlation.

In addition to the dose versus depth profiles, the MCNP runs have been used to determine the neutron current spectrum at the top of the phantom for the M67, delimiter #3 clinical beam.[6] The spectrum is shown in figure 5.22. The overall error associated with each data point is roughly ±10%.[5] The spectrum falls off generally as 1/E. There is a dip in the spectrum at 35 keV, which corresponds to a large resonance in aluminum. Similarly, there is a broad dip in the 80-250 keV range, which corresponds to a large, wide resonance in sulfur.

The integral kerma weighted current, normalized to a maximum value of 1.0, is shown in figure 5.23. Less than 5% of the dose comes from neutrons with energies below 10 keV. Half the dose comes from neutrons with energies above 500 keV.

5.3.3 Error Analysis

The errors associated with the experimentally measured doses presented here are discussed in detail at the end of Chapter 3. For the thermal flux, the systematic error is ±2%. The major experimental error is in accurately knowing the reactor power, that is, in the intensity of the beam. The absolute accuracy of the reactor power is ±5%. The overall uncertainty in the thermal neutron flux is estimated as ±7%. For the photon and fast neutron doses, the systematic errors are higher than those for the thermal neutron flux. Most important are the uncertainties in the neutron to gamma sensitivity ratios and the thermal neutron responses of the ionization chambers. Once again, a major source of

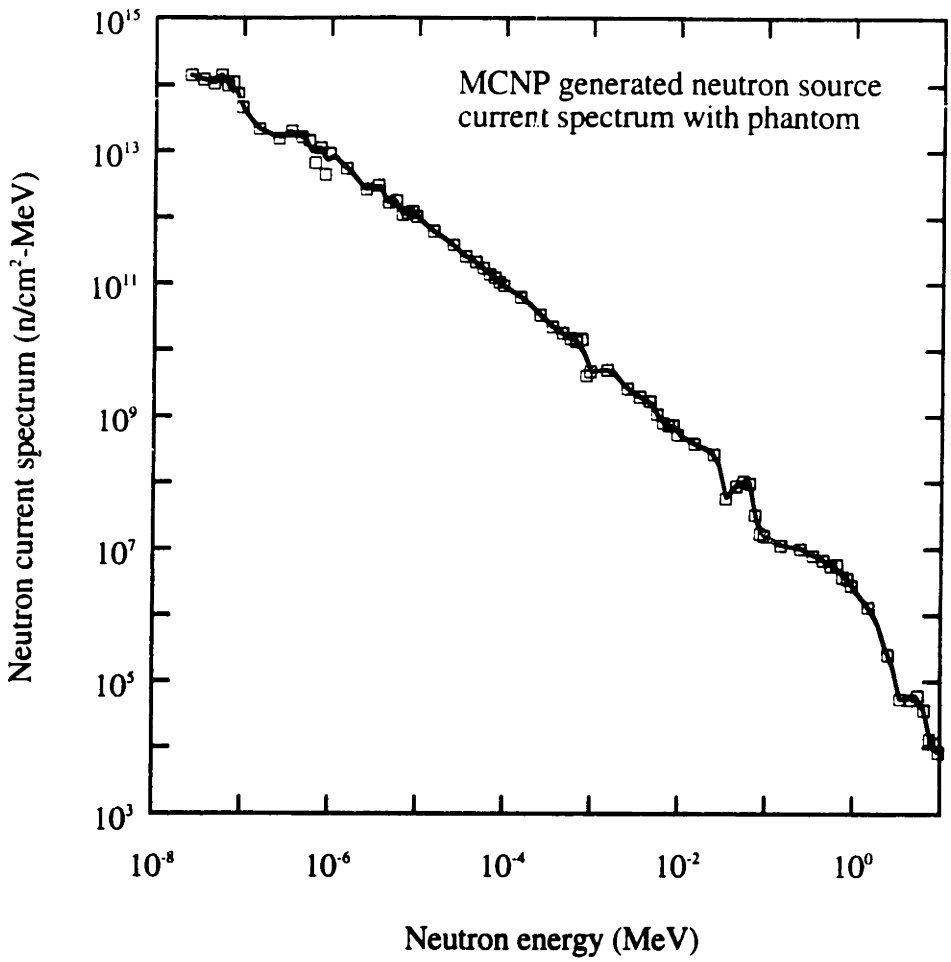

Figure 5.22. MCNP generated neutron spectrum in the medical beam with the ellipsoidal water phantom.[6] This spectrum is for the M67, delimiter #3 beam. The dip in the spectrum at 35 keV corresponds to a large resonance in aluminum. Similarly, a broad dip in the 80-250 keV range corresponds to a large, wide resonance in sulfur.

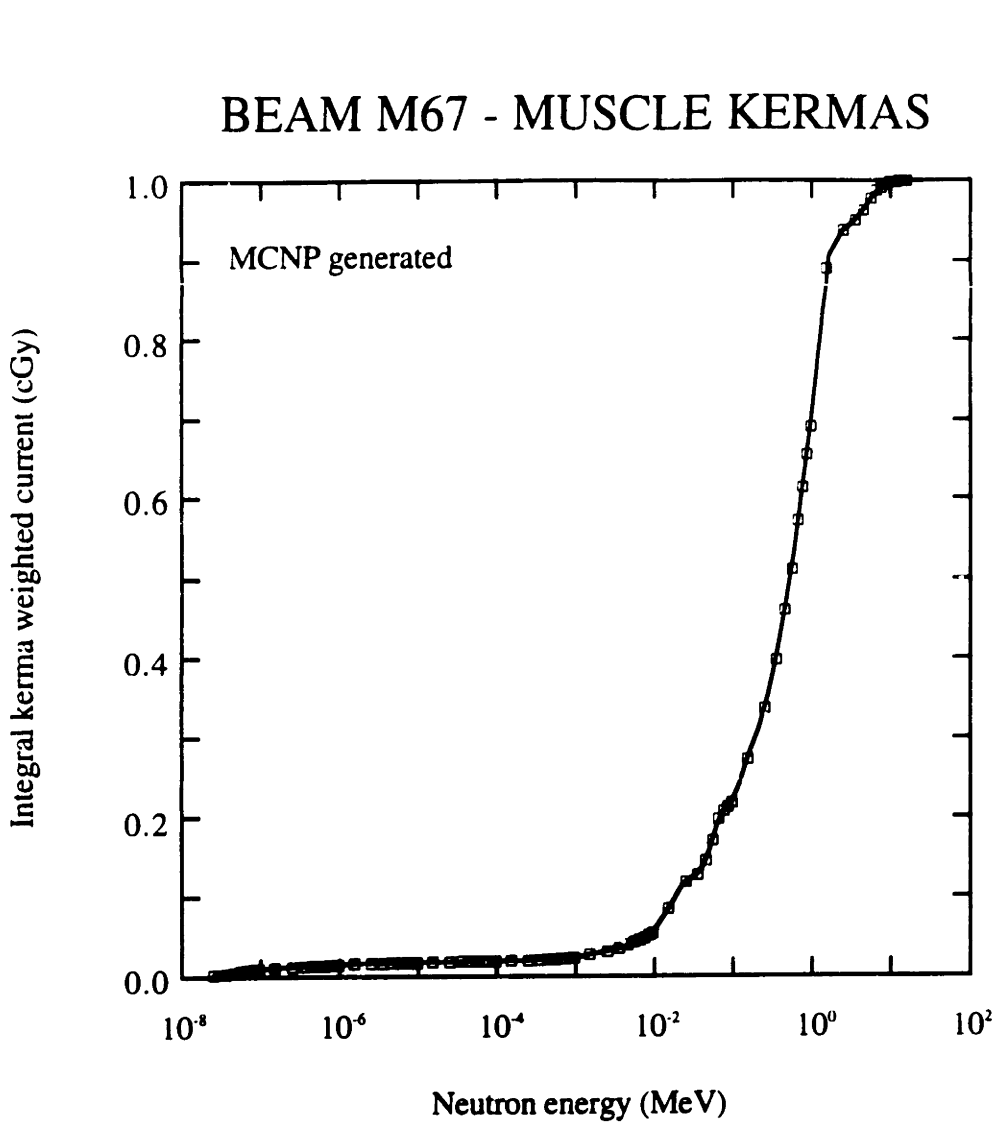

Figure 5.23. MCNP generated integral kerma weighted current in the medical beam with the ellipsoidal water phantom.[6] This spectrum is for the M67, delimiter #3 beam. Half the dose comes from neutrons with energies above 500 keV; 25% comes from neutrons with energies less than 100 keV.

experimental error is the uncertainty in the absolute reactor power, and the several additional sources of error contribute to the total error. The overall uncertainty in the photon dose is estimated as ±9%; the overall uncertainty in the fast neutron dose is estimated as ±17%.

5.4 WHOLE BODY DOSIMETRY

The whole body doses for an assumed BNCT treatment of the mid-thigh have been estimated. These whole body dose estimates are for the M62 epithermal neutron beam, using delimiter #1 (20 cm diameter aperture) around the treatment area and a 2" thick borated polyethylene whole body shield. The whole body doses for the M67 clinical beam using the 15 cm diameter delimiter were estimated from those calculated for the M62 beam. Aside from the different hole size in the delimiter, the only difference between these two beams is that the collimator of the M67 beam was painted with Li-6 and B-10 loaded paints (see Chapter 4) and that the bottom of the lead shutter had likewise been painted. If anything, the paints would have been expected to reduce the structurally produced prompt gammas; however, the incident, in-air photon doses for these two beams were the same so that even this effect is negligible. The whole body doses with the two beams, therefore, are expected to be the same.

The doses delivered throughout the body were estimated from measured fluxes and doses in air, obtained just below the lead shutter, and an estimate of their attenuation with depth inside the body. Measured fluxes and doses within a paraffin half-body phantom were also used in estimating the whole body doses. RBE's were assumed to be 4.0 for the B-10 reaction, 2.3 for fast neutrons and N-14(n,p) protons, and 0.5 for photons (refer to Chapter 2 for more details on the RBE's). The 0.5 value [8] for photons assumes a fractionated treatment.

Dose rates, both maximum and average values, are shown in table 5.1. Dose rates are highest in the treatment zone, and fall-off with distance away from the beam. The rate of fall-off is different for the three dose components.

These dose rates were used to calculate the mass-weighted whole body dose rates, as shown in table 5.2. Average dose rates were calculated to various parts of the body. The mass-weighted whole body dose rate is 0.23 RBE cGy/min, which is 2.5% of the average tumor dose rate. A 250 minute unilateral irradiation would deliver 2000 RBE cGy peak dose to healthy tissue in the treatment zone. The whole body dose, therefore, would be 0.23 x 250, or 57 RBE cGy. This whole body dose is much higher than the several rads of whole body dose delivered to many photon therapy patients.[7] It is comparable, however, to the whole body dose incurred by a patient undergoing a treatment for Hodgkin's disease on a high-energy X-ray linear accelerator.[8]

Finally, the doses were estimated at a 2 cm depth within the abdomen at the level of the hip, as shown in table 5.3. Although the thermal flux in this area is about 40 times lower than that in the treatment area, the potential for high B-10 concentrations, such as in the intestinal epithelium,[9] might still result in a significant dose contribution from the B-10 reaction. The B-10 concentrations in the intestinal epithelium or other organs in this region have not been determined. A range of B-10 concentrations is provided in table 5.3. However, even with a B-10 concentration of 30 ppm, the additional dose due to B-10 for a full treatment (2000 RBE cGy peak dose to healthy tissue in the treatment area) is 88 RBE cGy; this is comparable to the photon dose and twice as high as the fast neutron dose in this region.

These dose estimates are expected to be accurate within roughly a factor of 2. The doses outside the treatment zone are conservative estimates. This conservatism arises because it was assumed that the patient would be positioned within several centimeters of the delimiter or whole body shield; trial runs have shown that much of the patient's body can be positioned more than 5 cm below this shielding, which would

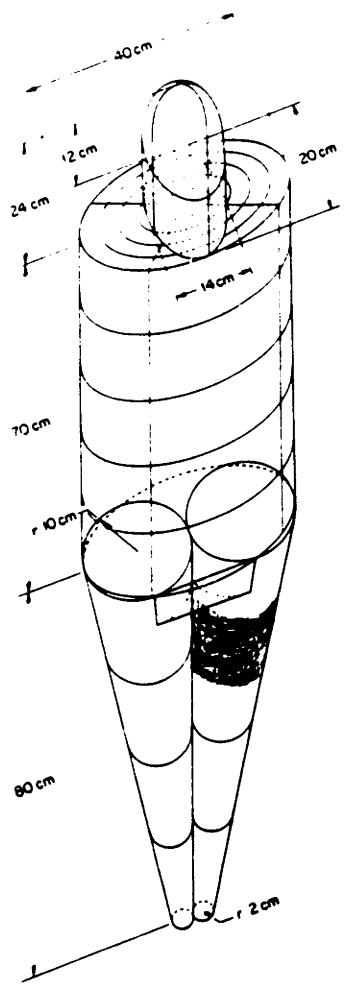

Table 5.1. Estimated dose rates in the whole body for an irradiation of the mid-thigh.

D_{fn} (RBE cGy/min)		D_{γ} (RBE cGy/min)		7.5 ppm D_{B-10} (RBE cGy/min)	
Max	Ave	Max	Ave	Max	Ave
0.010	0.003	0.0050	0.0035	0.0032	0.0016
0.030	0.01	0.015	0.011	0.0058	0.0029
0.13	0.043	0.040	0.028	0.015	0.0075
0.33	0.11	0.30	0.21	0.087	0.044
0.80	0.27	0.70	0.49	0.50	0.25
3.1	**1.0**	**1.5**	**1.1**	**3.5**	**1.75**
0.80	0.27	0.70	0.49	0.50	0.25
0.33	0.11	0.30	0.21	0.087	0.044
0.13	0.043	0.040	0.028	0.015	0.0075

Beam: M62 with delimiter #1 (20 cm diameter aperture).
RBE's: 4.0 for B-10, 2.3 for neutrons and N-14(n,p) protons, and 0.5 for photons.
Note: The rows of dose values correspond to the same vertical position on the MIRD phantom. The treatment zone is shaded on the phantom.

Table 5.2. Components of the mass-weighted total body dose.

Part of body	Mass (kg)	D_{fn} (RBE cGy/min)	D_{γ} (RBE cGy/min)	7.5 ppm B-10 (RBE cGy/min)	Mass weighted total dose rate (RBE cGy/min)
Head	5.1	0.0065	0.0072	0.0023	0.0012
Upper trunk	20.	0.027	0.019	0.0052	0.015
Lower trunk	22.7	0.077	0.12	0.026	0.073
Upper thigh	4.0	0.27	0.49	0.25	0.058
Mid-thigh	3.7	**1.0**	**1.1**	**1.75**	**0.20**
Lower thigh	3.3	0.27	0.49	0.25	0.048
Lower leg	10.9	0.077	0.12	0.026	0.035
Sum (excluding mid-thigh)	69.7	-	-	-	0.23

Beam: M62 with delimiter #1 (20 cm diameter aperture).
RBE's: 4.0 for B-10, 2.3 for neutrons and N-14(n,p) protons, and 0.5 for photons.

Note: The average total dose rate to tumor in the treatment area is 1.0 + 1.1 + 4 x 1.75 = 9.1 RBE cGy/min. The B-10 dose rate is multiplied by 4 since tumor has 4 times the B-10 concentration of healthy tissue. The mass-weighted whole body dose rate is 0.23 RBE cGy/min; this is 2.5% of the average tumor dose rate.

Table 5.3. Estimated doses 2 cm deep within the abdomen at the level of the hip for an irradiation of the mid-thigh.

B-10 concentration (ppm)	D_{fn} (RBE cGy)	D_{γ} (RBE cGy)	$D_{B\text{-}10}$ (RBE cGy)	D_{total} (RBE cGy)
0	45	75	0	120
7.5	45	75	22	142
30	45	75	88	208
100	45	75	292	412
500	45	75	1460	1580
1000	45	75	2920	3040

Beam: M62 with delimiter #1 (20 cm diameter aperture).
RBE's: 4.0 for B-10, 2.3 for neutrons and N-14(n,p) protons, and 0.5 for photons.
Treatment: 250 minute unilateral irradiation, which gives 2000 RBE cGy peak dose to healthy tissue in the treatment area.
Data source: 5 cm extrapolation of doses measured with the half-body phantom that is used for mid-thigh dosimetry.

Note: This table provides very rough estimates of doses that could be produced in the lower abdominal region. Critical cell populations in the small intestine might have relatively high concentrations of B-10. Other organs in this region that could receive significant doses include the genitals, cecum, ascending colon, and sigmoid colon. If the patient is facing down during the irradiation, the ureters and descending colon would receive higher doses.

reduce the doses and might allow additional shielding to be placed between the beam and the patient. The intensity of the beam drops with distance below the lead shutter as shown in figure 4.52. This figure can be used to adjust the whole body dose estimates provided here for the additional distance effect, especially for those parts of the body that are closer to the beam itself. Additional polyethylene shielding could be used with some patients. Half value layers for the epithermal neutron flux and fast neutron dose, based on in-phantom measurements, are 2 and 3 cm, respectively. The half value layer for 1 MeV gammas is 10 cm.[10] These half values can be used to further adjust the whole body doses to account for the additional shielding. Lead or bismuth are much better gamma shields than polyethylene, but there are no plans to use such heavy materials as additional shielding for the patient.

An estimate of the patient's whole body dose will be made for each patient based upon the part of the body that is irradiated and the actual positioning of the patient relative to the beam. The various radiation dose components around the beam are not symmetrical. For example, as one enters the medical room, if the patient is positioned below the lead shutter and towards the left of the beam, the lead shutter will shield the full length of the patient's body. If the patient is to the right of the beam, then the lower part of the patient's body will no longer be shielded by the lead shutter. This area might receive a higher dose than if the patient were positioned on the left hand side of the beam.

A rough estimate of this effect was made by mapping the thermal neutron, fast neutron, and photon doses along the lead shutter with only the lead shutter open (all other shutters closed). Results are shown in figure 5.24. Dose rates are higher beyond the end of the lead shutter.

Patients will be positioned to minimize their whole body dose, and to particularly minimize the dose to the abdominal region. These doses will be estimated for each patient.

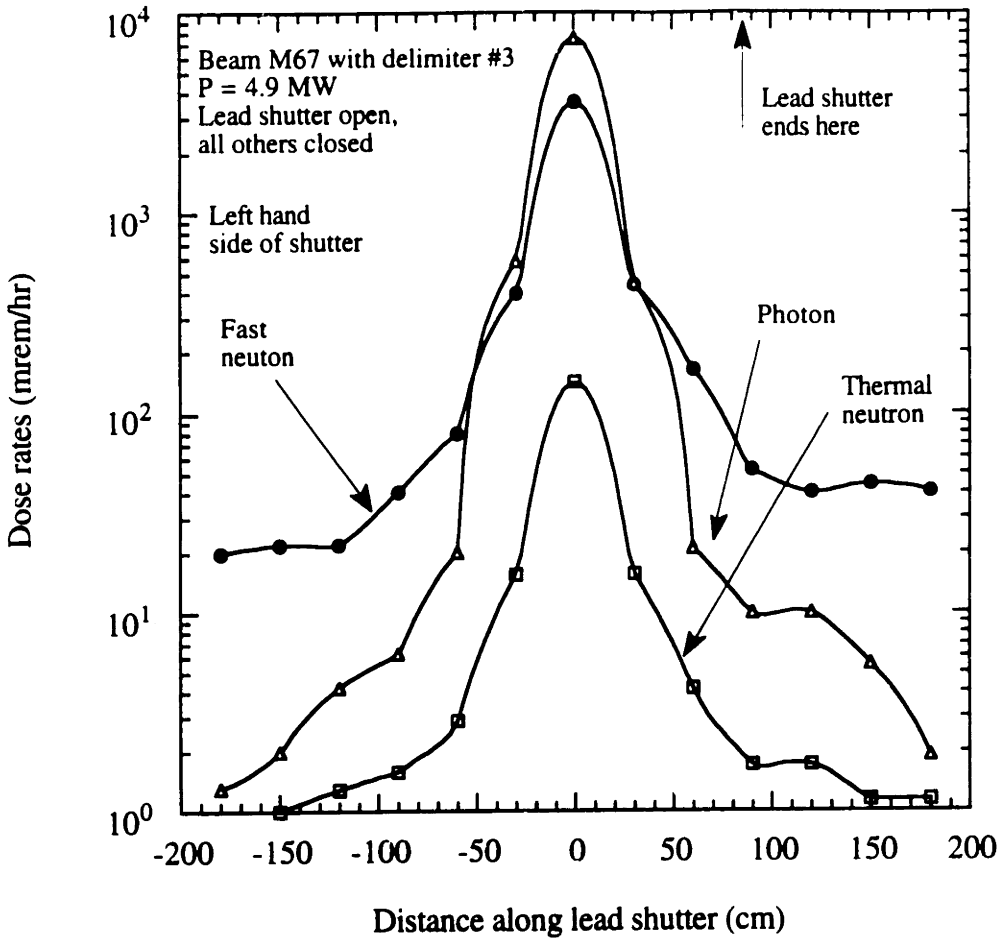

Figure 5.24. Results of a health physics survey for the M67 beam. The dose rates were measured just below the lead shutter. The lead shutter was open, but the other shutters were closed. The 0 cm distance is directly below the upper filter. When the lead shutter is open, it ends at 86 cm. Dose rates are higher on the right hand side beyond the lead shutter. Increases in these doses are seen as bumps near 120 cm, where the lead shutter no longer effectively attenuates the radiations.

5.5 IN-VIVO DOSIMETRY

In-vivo dosimetry serves as a useful check on the doses received by a patient during radiation therapy. For the metastatic melanoma patients, our Group has decided to forgo any in-vivo dosimetry. Instead, the dosimetry for each patient will be determined by NCTPLAN, the Monte Carlo based treatment planning program discussed earlier in the chapter. Initially, however, there were plans to measure the thermal and epithermal fluxes at several positions on the surface of the patient.

The thermal flux is easily measured using gold foils and the cadmium difference technique (refer to chapter 3). A potential problem in using this technique for in-vivo dosimetry, however, is the prompt gammas emitted from the Cd(n,γ) reaction. These prompt gammas would increase the dose to the patient, especially the dose to skin that would be in contact with the cadmium. The dose that patients would receive from the cadmium prompt gammas, therefore, was estimated theoretically. This analysis has shown that prompt gammas from the cadmium would significantly increase the local gamma dose. While this is not an immediate concern with the first patient irradiations, the analysis and results are presented here in case a decision is made in the future to measure the neutron fluxes during an irradiation. As an alternative to the cadmium cover, a Li-6 based cover has been designed in which the epithermal flux can be measured without a local increase in the gamma dose.

Kerma rates at various distances from a cadmium disc, 1.3 cm diameter and 0.05 cm thick, were estimated. This is the same disc size as that used during the beam characterizations. Under charged particle equilibrium conditions, the dose rate is equal to the kerma rate.[11] For gammas of several MeV in tissue, the range of the most energetic electron secondaries is 4 mm.[11] Beyond 4 mm for the cadmium source, then, equilibrium has been established and the dose rate is equal to the kerma rate. At closer distances, the dose rate is less than the kerma rate. The reader is referred to Attix for a detailed

discussion of this effect.[11] The kerma rate was determined using the following equation:[11]

$$\dot{K} = \dot{\Psi} \left(\frac{\mu_{tr}}{\rho}\right)_{tis} \tag{5.1}$$

where $\dot{K}$ = kerma rate (erg/g),

$\dot{\Psi}$ = energy fluence rate (erg/cm^2),

$\left(\frac{\mu_{tr}}{\rho}\right)_{tis}$ = mass energy-transfer coefficient of tissue (cm^2/g).

This equation is valid at a photon energy E; if an energy spectrum is present, the kerma rate is found by integrating the spectrum over the energy dependent mass energy-transfer coefficient. The energy dependent mass energy-transfer coefficient for tissue is known.[11] The energy fluence rate was calculated from the reaction rate in the cadmium and the resultant flux of prompt gammas. It was assumed that all the kerma was caused by the prompt gammas. The dose from decay betas is negligible.

The beam was assumed to be M62, with delimiter #1 (20 cm diameter), used for an irradiation of the mid-thigh. Under these conditions, the thermal flux at the top surface of the thigh is about 1.3E8 n/cm^2-sec at a reactor power of 5 MW$_n$. With the M67 clinical beam, the surface flux is somewhat less than this, depending on the part of the body that is irradiated. The 1.3E8 n/cm^2-sec flux, however, serves as a useful reference. The cadmium disc is black to thermal neutrons; therefore, there is a large depression of thermal flux within the disc. The thermal flux was idealized as a parallel beam of neutrons normally incident on the cadmium disc. Then, the Cd(n,γ) reaction rate is equal to that of the flux times the surface area of the disc. The surface area of the disc, folded in half to cover the gold foil, is 0.63 cm^2; therefore, the reaction rate is 8.23E7 reactions/sec.

The thermal neutron induced prompt gamma spectra for many elements have been measured.[12] Cadmium has 73% abundant 559 keV gammas, 14% abundant 651 keV gammas, and about 200 other gammas with low abundances. A sizable amount of the binding energy made available from neutron absorption is in the continuum, that is, much of the energy is released by hundreds of prompt gammas that are too close in energy (< 1 keV) to be resolved with today's radiation detectors. Individual peaks are not seen in the spectrum; instead a continuum is seen. The average binding energy released by thermal neutron absorption in cadmium is about 9 MeV.[12] Because a large fraction of this energy is released in the continuum, it was assumed that an absorption reaction releases 4.5 photons, each with energy of 2.0 MeV. The mass-energy transfer coefficient is dependent on the photon energy; the 2.0 MeV assumption gives an average, or effective, transfer coefficient. The transfer coefficient for the abundant 559 keV prompt gammas is 20% higher than that at 2.0 MeV, while the transfer coefficient for gammas in the 2-8 MeV range is on average 20% lower.

For 2.0 MeV photons, the mass energy-transfer coefficient of tissue is 0.0259 cm^2/g.[11] Consider a thin section of tissue, small in area, in contact with the cadmium disc. Half the prompt gammas are emitted in the direction of the skin; the other half are emitted away from the skin and are assumed to be lost. Then, the kerma rate can be calculated as

$$\dot{K} = 0.5 \times 1.3E8 \frac{\text{reactions}}{cm^2 sec} \times 4.5 \times 2.0 \text{ MeV} \times 0.0259 \frac{cm^2}{g} \frac{1.6E\text{-}6 \text{ erg}}{1 \text{ MeV}} \frac{1 \text{ cGy}}{100 \text{ erg/g}} \frac{60 \text{ sec}}{\text{min}}$$

$$\dot{K} = 14.5 \text{ cGy/min}$$

This is the kerma rate for tissue in contact with the cadmium. The dose rate is much less under these non-charged particle equilibrium conditions.

The rate of fall-off of kerma from the cadmium disc was calculated theoretically. It was assumed that the cadmium disc was a infinitely thin disc source and that there was no attenuation in the tissue. The geometry is shown in figure 5.25. Then, the rate of fall-off along the axis can be shown to go as $\log (1 + (R/L)^2)$.

The kerma rate far from the cadmium was calculated by assuming a point source with $1/R^2$ attenuation. Then, the kerma rates nearer the cadmium were calculated using the logarithmic fall-off rate above.

The theoretical logarithmic rate of fall-off is shown in figure 5.26. The idealization breaks down as L approaches 0 since the kerma becomes infinite. In this region, a three dimensional model is needed. The kerma fall-off for the M62 beam is shown in figure 5.27. Also shown is the rate of fall off expected for a cadmium disc that has 1/2 the diameter of the original disc.

The rate of fall-off is less than $1/R^2$ in the region very close to the cadmium since it can no longer be considered a point source. Close to the cadmium, the kerma rate is mostly a function of the reaction rate per cm^2 of foil; therefore, as shown in figure 5.27, the kerma rate of the smaller cadmium disc is only slightly less than that of the larger cadmium disc. Far from the cadmium, the kerma rate is mostly a function of the total reaction rate in the cadmium discs; therefore, the cadmium disc with 1/2 the diameter has 1/4 of the kerma rate.

A limit could be placed on the local increase in dose due to the cadmium cover. Then, the size of the cadmium and its distance from the patient can be determined from figure 5.27.

An alternative cover using Li-6 in the form of Li_2CO_3 was tested to see if it could be used in place of the cadmium. Li-6 has a high thermal neutron absorption cross section, but the capture reaction produces almost no prompt gammas. The epithermal flux might then be measured without a local increase in the gamma dose.

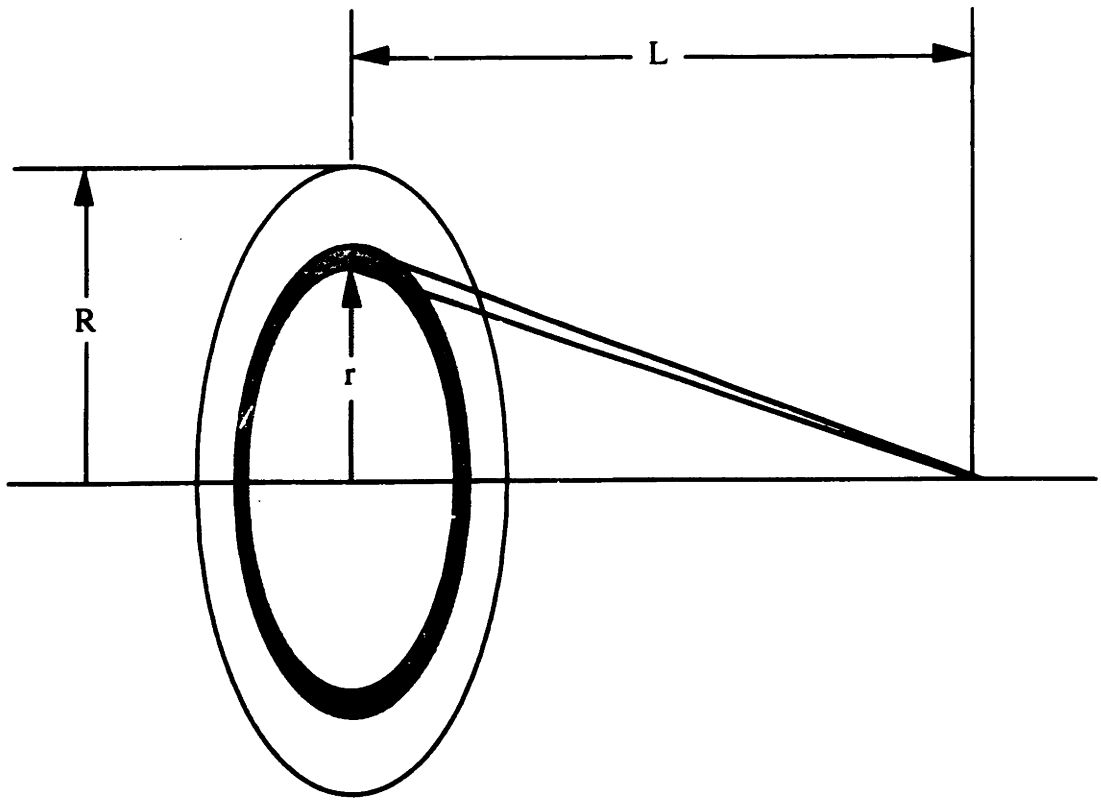

Figure 5.25. Geometry used to estimate the theoretical drop off of the kerma with distance from the cadmium disc.

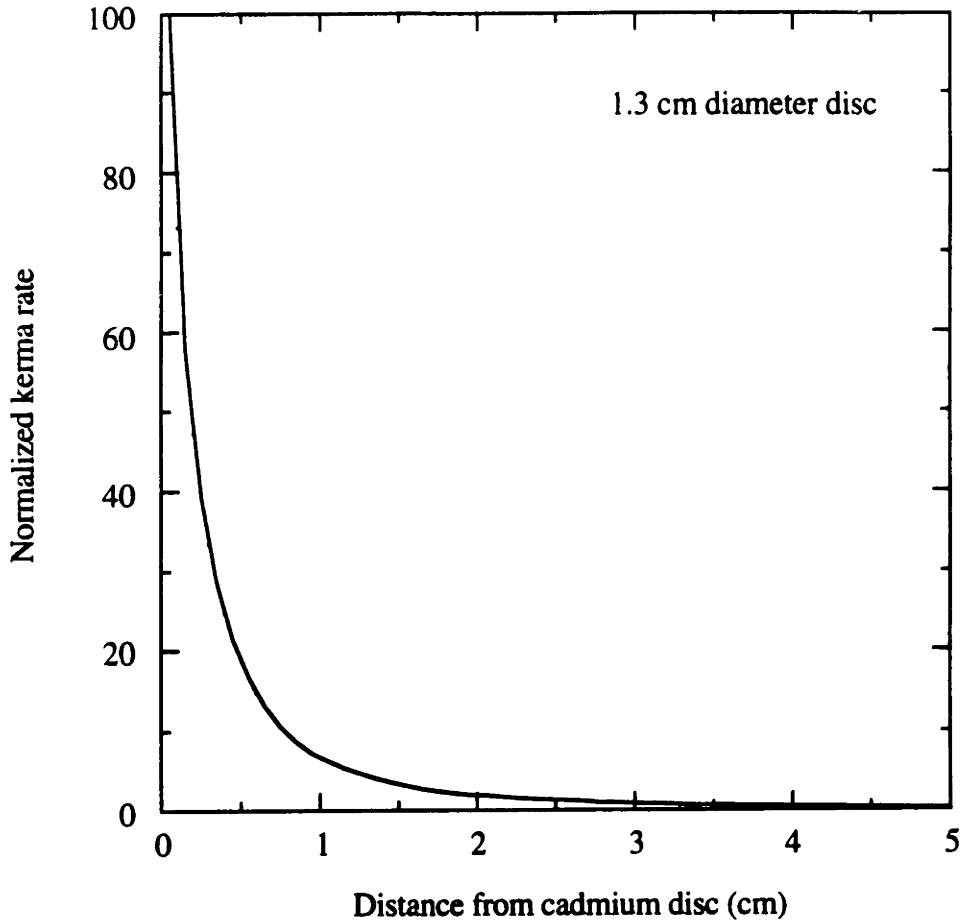

Figure 5.26. The kerma rate drops with distance away from the cadmium disc. The rate of fall-off shown is the logarithmic rate calculated for an infinitely thin disc source.

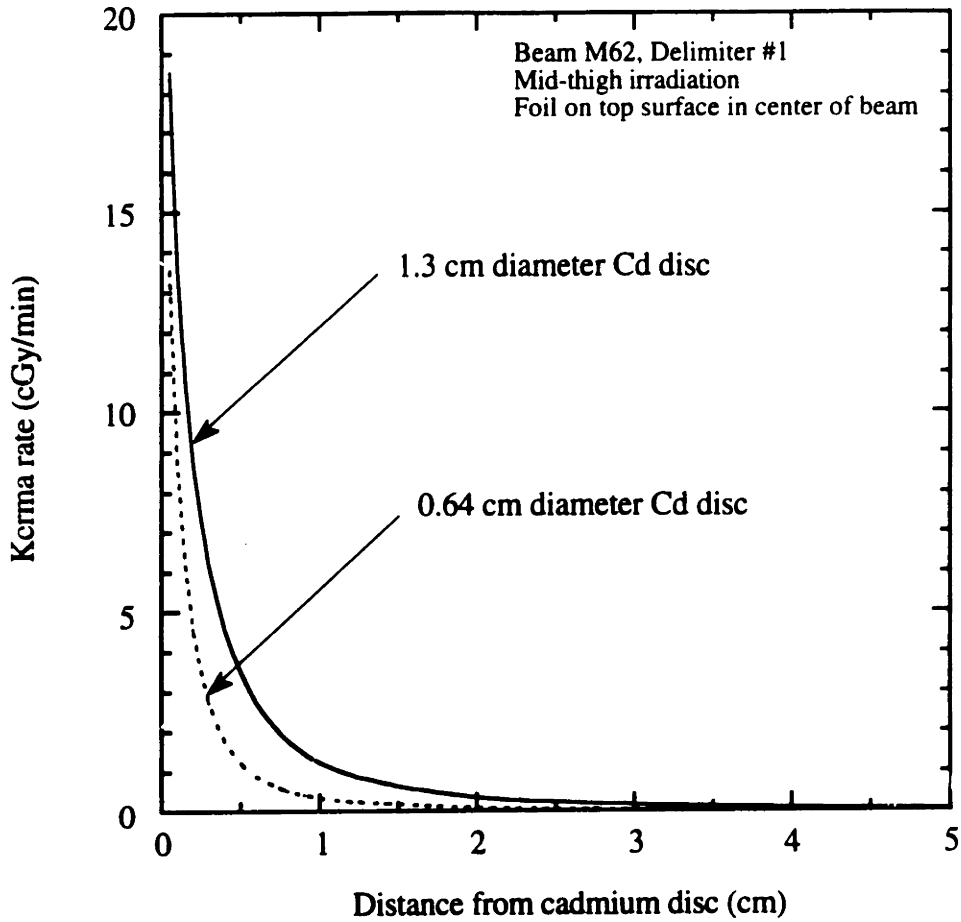

Figure 5.27. The theoretical kerma rate fall-off with distance away from the cadmium cover using the neutron flux from the M62 beam. It was assumed that the cadmium disc was folded in half to envelope the gold foil. The prompt gamma dose is unacceptably high for tissue adjacent to the cadmium. A smaller diameter disc reduces the kerma rate.

Three different Li-6 (93 atom percent) carbonate covers were made. In the first, a special paint was made that consisted of 2 g of Li_2CO_3 per 5 cc of total carbonate-paint mixture. Several layers of the Li-6 loaded paint were applied to both sides of a polyester tape. The attenuation of thermal flux through several layers of the painted tapes was measured experimentally. The painted tapes were inserted into a small, collimated thermal neutron beam. Thermal neutrons passing through the tape were detected with a BF_3 tube. Results are shown in figure 5.28. Seven layers of painted tape attenuated about 99% of the thermal flux. Squares of the tape, 12 mm x 12 mm, were cut. The cover consisted of a stack of 7 of these squares on top of the gold foil and 7 more on the bottom. The total height of the stack was about 10 mm.

The other two covers were made by surrounding the gold foil with Li-6 carbonate powder. The attenuation of thermal and epithermal (5 eV) flux are shown in figure 5.29. 3.4 mm of powder (45% of theoretical solid density) are needed to attenuate 99% of the thermal flux; at this thickness, 28% of the epithermal flux is absorbed and 72% is transmitted. This contrasts with the 98% of the epithermal flux that is transmitted with the usual cadmium covers.

The second Li-6 carbonate cover was a 0.010" thick can, 7.5 mm diameter x 8 mm long, that was filled with Li-6 carbonate powder. The powder was packed down with a rod; the gold foil was positioned in the center of the can. The third Li-6 carbonate was similar to this one, but used a Teflon beaker that was 11 mm diameter x 17 mm long.

These new Li-6 covered gold foils were irradiated along with the usual cadmium covered gold foils. The beam was M62, delimiter #1. The 19 cm diameter, cylindrical polyethylene phantom was used. The covered foils were placed on top of the phantom; the cadmium covered foils were raised about 5 mm above the surface so that the height of the Li-6 and cadmium covered gold foils were the same in all cases. After the irradiations, the foils were counted on a HPGE detector.

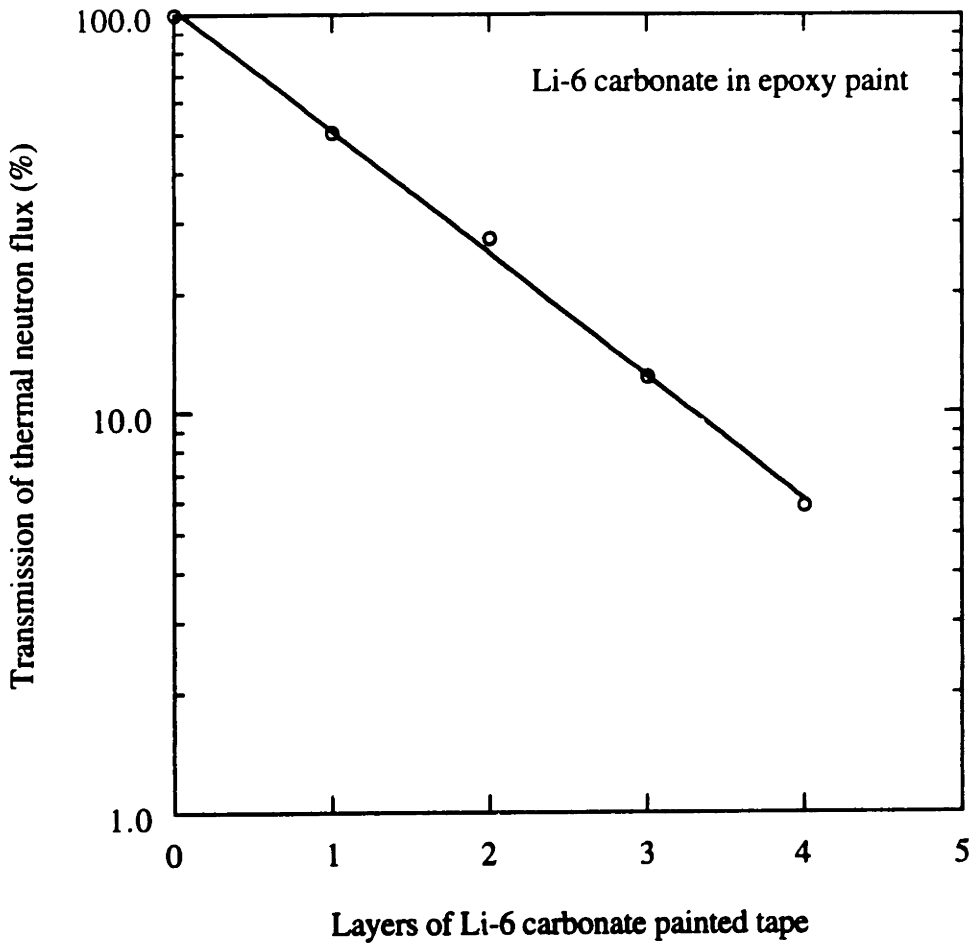

Figure 5.28. Attenuation of thermal neutrons in a Li-6 carbonate painted tape. Data were obtained by the usual transmission attenuation experiment using a thermal neutron beam and BF_3 detector. The thermal neutron beam has some neutrons with energies above the cadmium cut-off. These epicadmium neutrons add to the count rate of the BF_3 detector. Their contribution was determined and subtracted from the total count rate so that the attenuation shown is due only to attenuation of thermal neutrons.

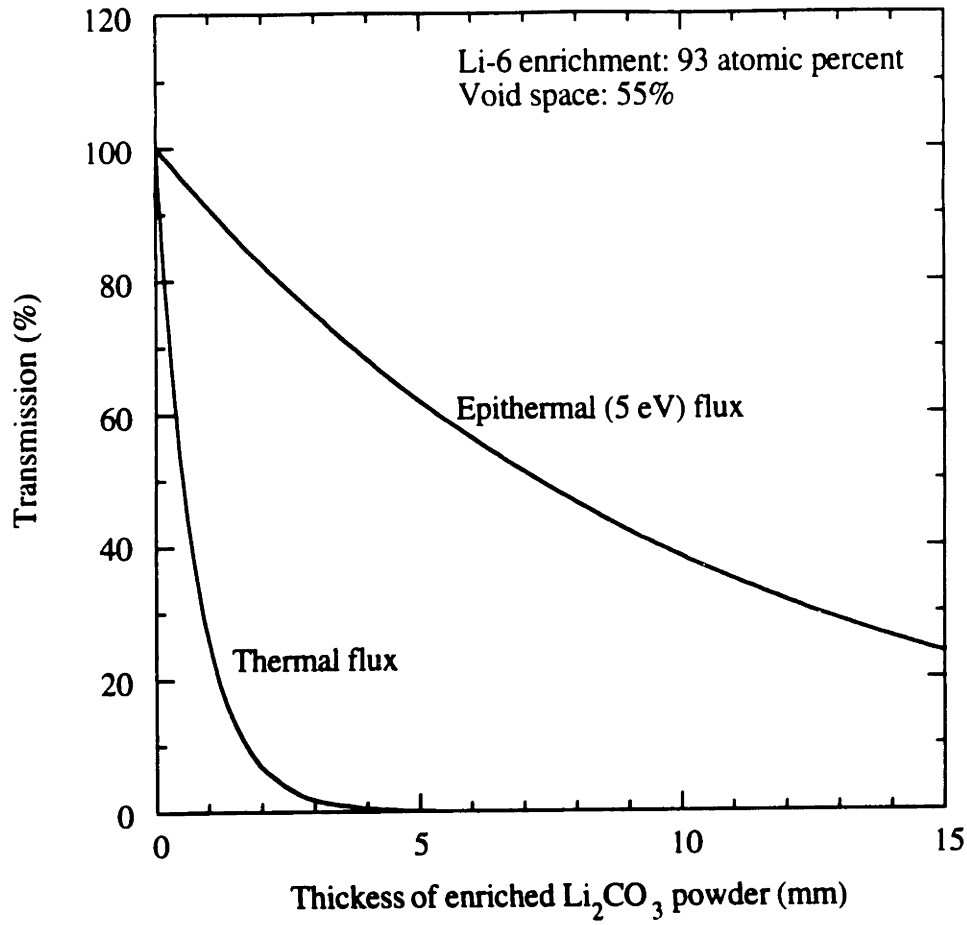

Figure 5.29. Theoretical transmission of thermal and epithermal fluxes through Li_2CO_3 powder.

Results of the foil activations are shown in figure 5.30. The activities per unit mass of foil were normalized to that of the cadmium covered foils.

In all cases the normalized activities of the Li-6 covered foils were less than those of the cadmium covered foils. Most of the activation in the covered gold foils comes from absorption of neutrons in the 5 eV resonance of gold. Li-6 is a 1/v absorber and some attenuation of 5 eV neutrons would be expected. Relative to the cadmium covered foils, the activation was highest in the foil surrounded by the layered paint; some neutrons were probably coming in from the sides of the cover where the effective thickness of the Li-6 might not have been high enough to absorb all the thermal neutrons. Alternatively, the other two Li-6 covers might have a little more Li-6 than needed to attenuate the thermal flux, so that their lower activation is caused by additional attenuation of epithermal flux. Which of these is the case could be determined by irradiating these foils in a high thermal/low epithermal flux. Regardless, the activation with the larger powdered sample cover is only 4% less than that of the smaller sample; therefore, the sensitivity to the size of the cover is small.

The two powdered covers probably have some directional dependence. This dependence could be reduced by making the covers spherical.

It is concluded that Li-6 carbonate covers can be used in place of cadmium. The epithermal and thermal fluxes can be measured in-vivo without a local increase in the photon dose from prompt gammas. A correction to the measured gold foil activities is needed to account for attenuation of epithermal flux in the Li-6 carbonate covers. A set of Li-6 carbonate covers, all the same size and perhaps spherical, could be irradiated with cadmium covered gold foils so that the correction factor is measured for each cover experimentally. Then, the additional error in the calculated thermal and epithermal fluxes using the Li-6 carbonate covers would be only several percent.

An alternative approach to using Cd or Li-6 carbonate covers would be to place the gold foils about 3 cm deep within the tissue, if possible, or within a tissue equivalent

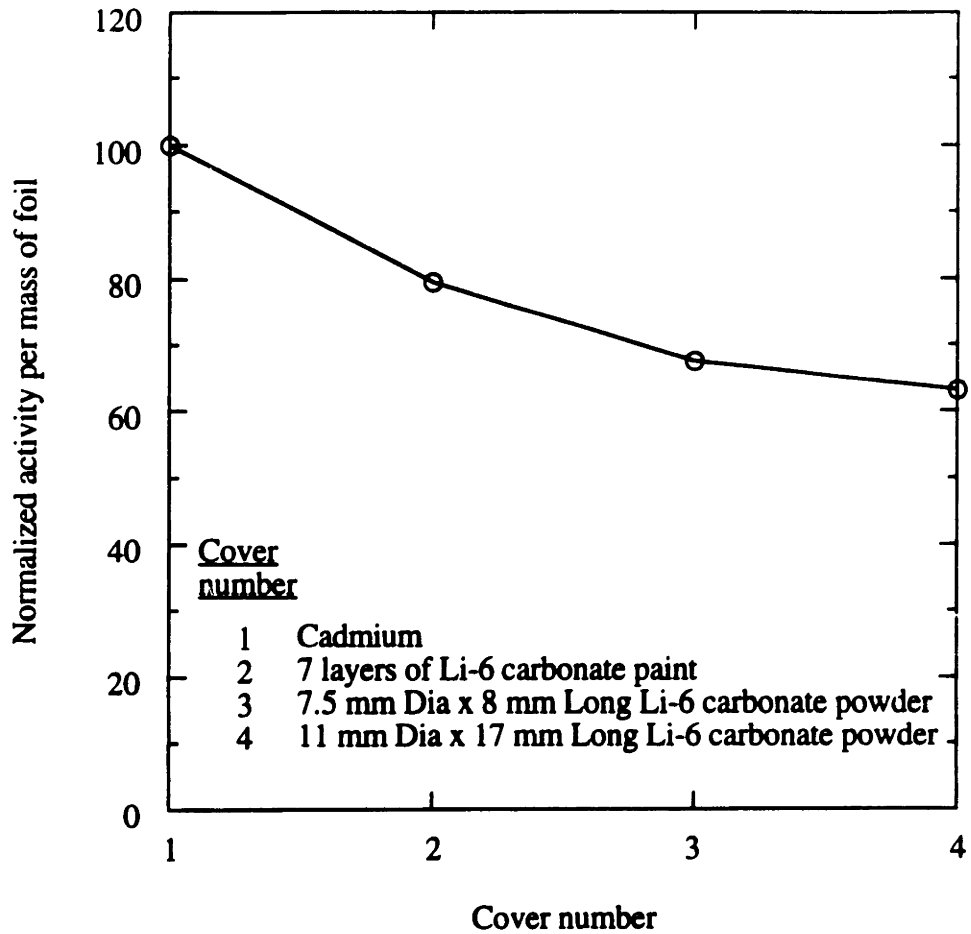

Figure 5.30. Gold foils with the 4 covers shown in the figure were placed on top of a polyethylene phantom and given identical irradiations. The foils were counted on a HPGE detector and the saturated activities per unit mass were calculated. The cadmium covered gold foil has the highest activity; the Li-6 covered foils have lower activities due to absorption of 5 eV neutrons in the 1/v tail of Li-6. A correction term can be applied to the activities of the Li-6 covered foils.

sphere. At this distance, and deeper, the thermal flux is measured directly as the contribution to the gold activity from epithermal neutrons is small (≈ 10% at 3 cm) and can be accounted for in an approximate fashion.

5.6 PROCEDURES

Four Procedures were written and were used in the dosimetry of the M67 clinical beam. They are:

1. PM 3.14.2.4 Characterization of the Medical Therapy Beam
2. PM 3.14.2.5 Cross-Calibration of Electrometers
3. PM 3.14.2.6 Calibration and Stability Check of Ionization Chambers and Electrometers
4. PM 3.14.2.7 Determination of High Purity or Ge(Li) Detector Efficiency

These Procedures are provided in Appendix D. They are discussed briefly here.

1. PM 3.14.2.4 Characterization of the Medical Therapy Beam

This Procedure provides a standard method to determine the dose-depth profiles in phantom and in air. The results of the characterization also serve as a reference for subsequent calibration checks of the beam and for the beam monitor functional checks.

2. PM 3.14.2.5 Cross-Calibration of Electrometers

This Procedure provides a standard method for calibrating a field electrometer against the AAPM Calibrated electrometer.

3. PM.3.14.2.6. Calibration and Stability Check of Ionization Chambers and Electrometers

This Procedure provides a standard method for checking the calibration and stability of both the ionization chambers and the electrometers. The exposure rate at a fixed distance from a known Cs-137 source is measured. Agreement with the previously measured exposure rate ensures that the calibration of the ionization chambers and electrometers has not changed. A calibration jig, shown in figure 5.31, was designed, built, and tested. Exposure rates are repeatable and positioning errors are negligible (less than 1%).

An independent, simple method to rapidly check the calibration of the electrometers was also developed. A known voltage is placed in series with a known resistance to produce a current in the range of interest, around 1E-12 amps. The experimental setup is shown in figure 5.32. The current is measured with the electrometer and compared with its theoretical value. The voltage source is an Analogic DC Voltage Standard, Model AN 3100. It has a range of 0.0001 - 10 volts, in 0.0001 volt increments. It has not been calibrated, but the output voltage agrees well (within 0.2%) with that measured by the Keithley 617 for voltages above 100 mV. This agreement might continue below 100 mV, but in this range the K-617 has only a 2 digit display. Initially, the resistor used was a Kobra 500 MΩ, 1%. Using the K-617, the resistance was measured at 499.9 MΩ. To produce a current of 1E-12 amps, 0.0005 volts was applied. When this was done, however, the current was 5% less than expected. It was hypothesized that the voltage drop of the K-617 was significant relative to the 0.0005 volts applied.

To test this hypothesis, the current was measured over a range of applied voltages, from 0 to 0.5 volts. The lower range of this data is plotted in figure 5.33. The theoretical and measured curves are linear and parallel, but offset. The offset is 26 μV. The measurement error, therefore, decreases as the applied voltage becomes much greater

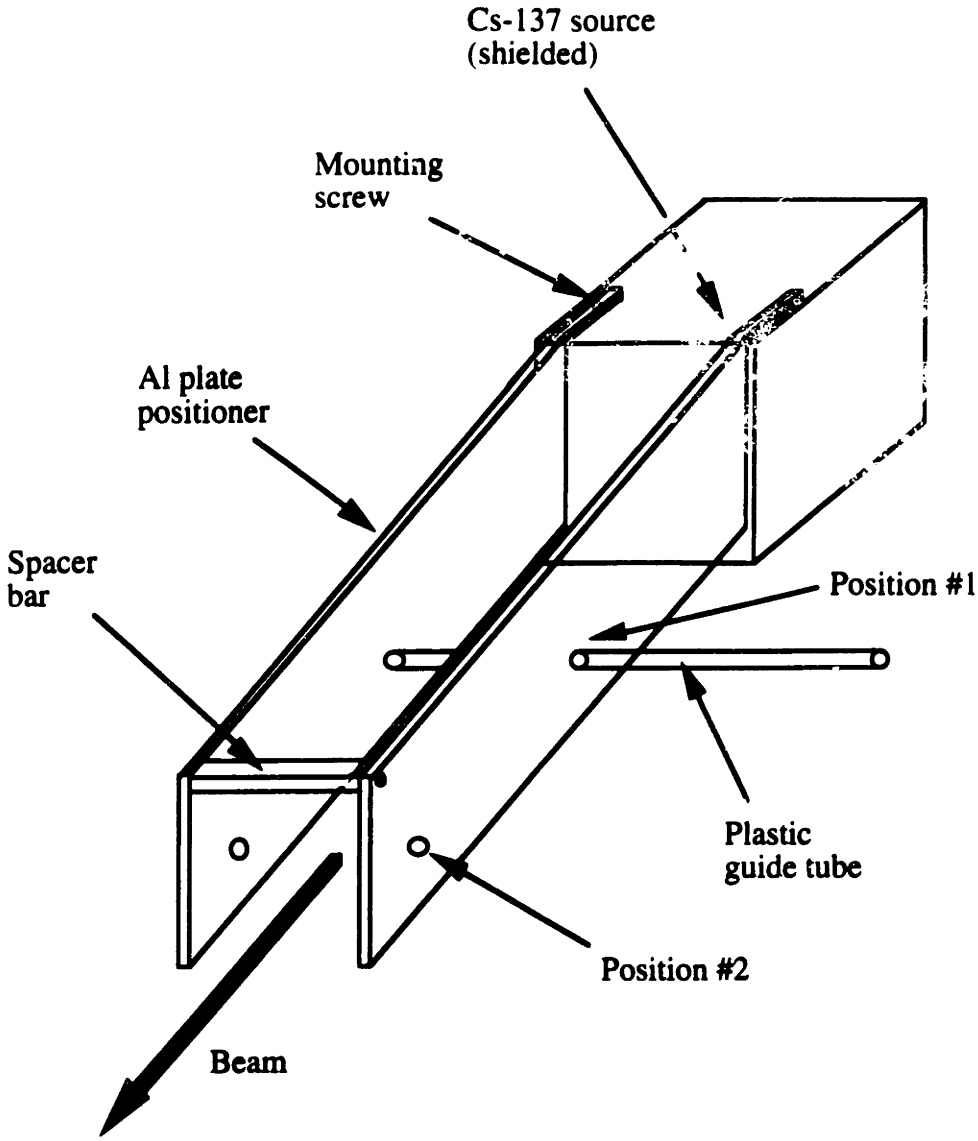

Figure 5.31. Schematic of the ionization chamber positioner. The positioner is secured to the Cs-137 source with two screws. The spacer bar keeps the plates parallel. The ionization chamber is slid into the guide tube. A mark on the tube indicates where the thimble of the chamber is to be positioned, which is in the centerline of the beam.

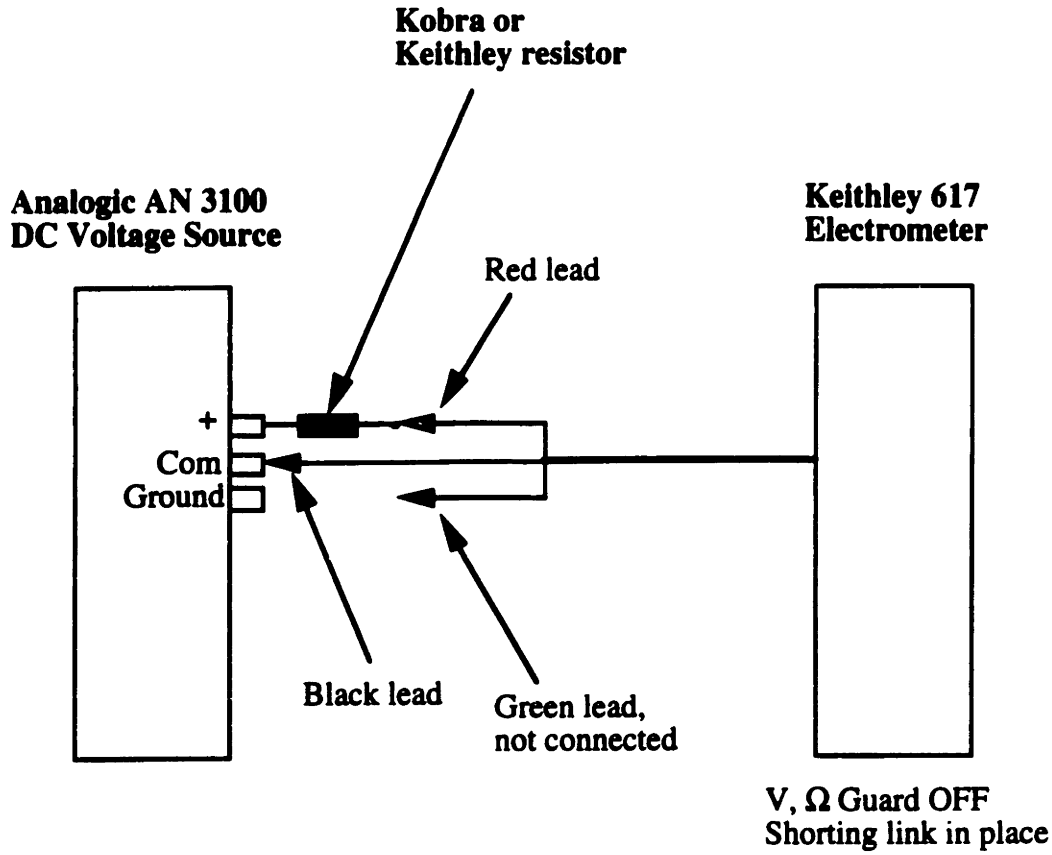

Figure 5.32. Experimental setup to check the calibration of the electrometer. A known voltage is placed in series with a standard resistor to produce a current that is typical of that produced with the ionization chambers. The measured current is compared with the theoretical value to ensure that the calibration of the electrometer has not changed.

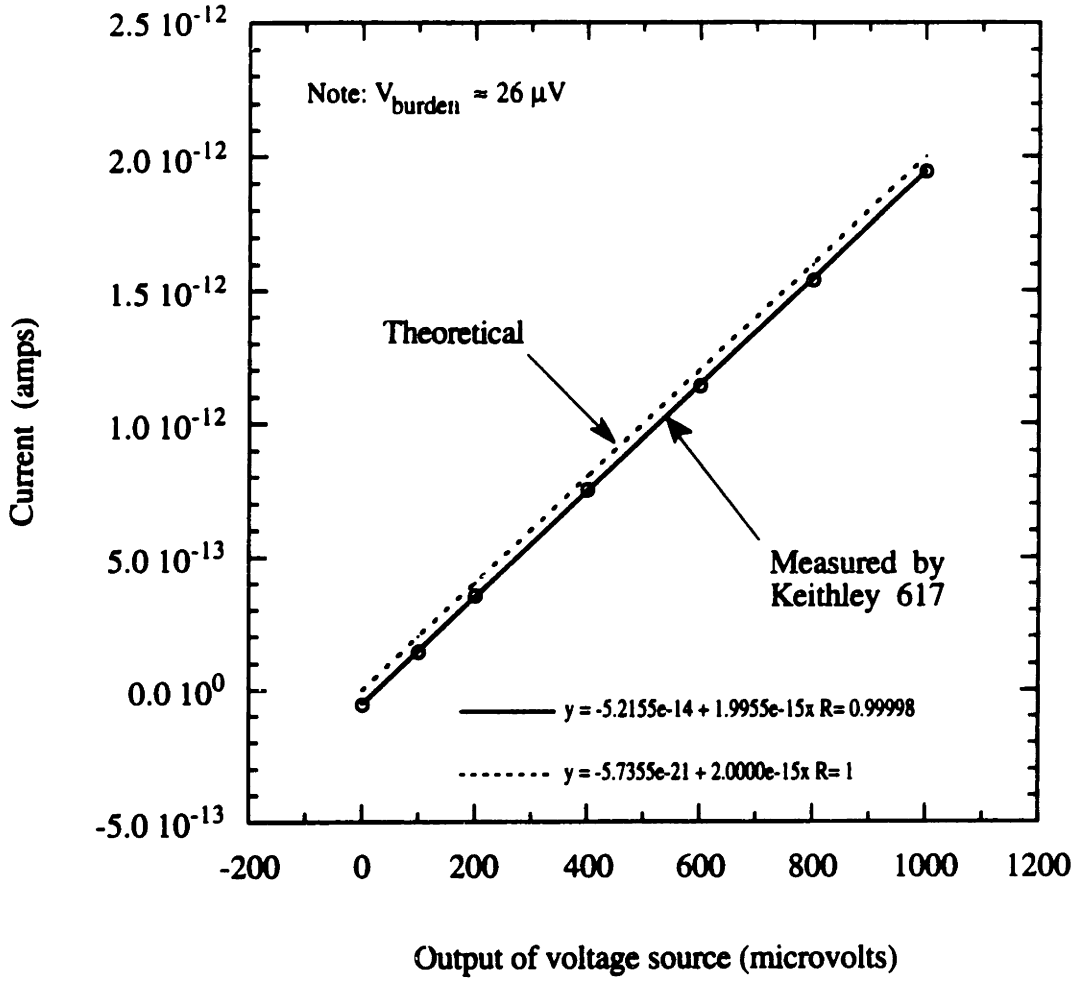

Figure 5.33. Theoretical and experimentally measured currents as a function of the applied voltage. The offset is 26 μV, which is equal to the voltage burden of the electrometer. Unless the voltage applied across the resistor is much higher than the voltage burden, the current measured by the electrometer will be significantly in error.

than the voltage drop of the K-617, as shown in figure 5.34. The measured data, therefore, are consistent with the hypothesis. The measurement error is less than 0.5% at 0.005 volts.

In the final design, the current is produced using either a 10 ±2% or 100 ±2% GΩ resistor (Keithley R-319-10G or R-319-100G). The applied voltage is 0.02 or 0.2 volts, respectively. Then, for the 100 GΩ resistor, the measurement error due to the applied voltage is less than 0.1%. Using the 100 GΩ resistor has the advantage that the voltage output of the source can be checked to 3 digits with the Keithley-617. There have been no handling and contamination problems with these ultra-high resistance resistors.

4. PM.3.14.2.7 Determination of High Purity or Ge(Li) Detector Efficiency

This Procedure provides a standard method for determining the efficiency of a HPGE or Ge(Li) detector that is used to count the gold foils.

5.7 HEALTH PHYSICS

Three sets of health physics measurements were made. In the first set, dose rates were measured inside the medical room with all the shutters closed and the reactor at power. These are the dose rates that personnel would be exposed to while positioning the patient in the beam. In the second set, dose rates were measured outside the room while the beam was on. These are the dose rates that personnel would be exposed to while the patient was being irradiated. In the third set, dose rates were measured inside the medical room just after a minor scram, that is, all-rods-in (ARI), and with all the shutters closing. These are dose rates that personnel would be exposed to during an emergency evacuation of the patient from the medical room.

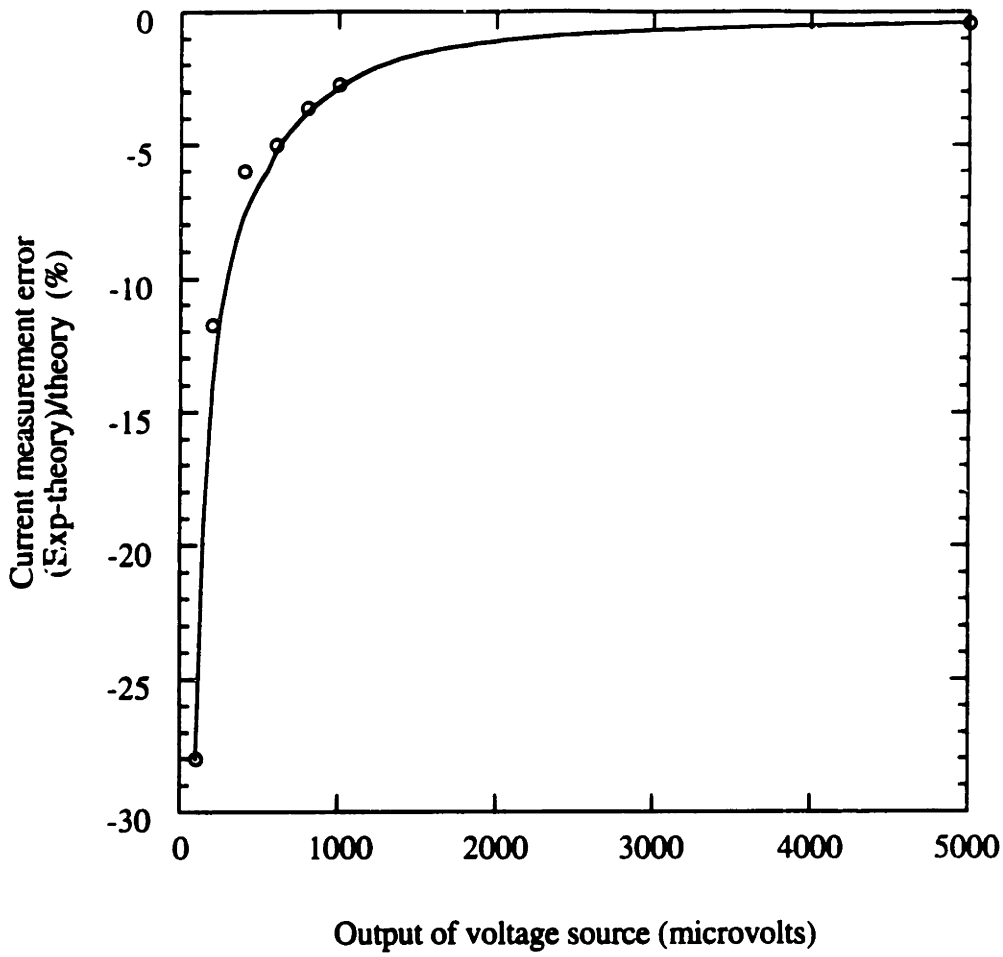

Figure 5.34. The measurement error decreases as the applied voltage greatly exceeds the voltage drop of the Keithley-617 electrometer. In the final design of the calibration circuit, a 100 GΩ resistor is used with an applied voltage of 0.2 volts. Then, the measurement error due to the applied voltage is less than 0.1%.

The thermal and fast neutron dose rates were measured with a bare LiI(Eu) detector and a 10" Bonner sphere, respectively. The gamma ray exposure rates were measured with an air ionization chamber. During these measurements, the aluminum platform and surgical couch were in position below the beam. Boral plates covered the floor and 5 coats of a B_4C loaded paint had been applied to the bottom of the lead shutter.

Results are shown in figures 5.35 and 5.36. The results presented are for the M62, delimiter #1 (20 cm diameter) beam. The dose rates, however, would be about the same for the M67, delimiter #3 (15 cm diameter) clinical beam. Aside from the different hole size in the delimiter, the only difference between these two beams is that the collimator of the M67 beam was painted with Li-6 and B-10 loaded paints (see Chapter 4) and that the bottom of the lead shutter had likewise been painted. These differences would not affect the health physics doses. Dose rates at each position are given as a set of 3 numbers: the photon exposure rate (mR/hr), thermal neutron dose rate (mrem/hr), and the fast neutron dose rate (mrem/hr). The quality factors for the thermal and fast neutron doses are about 10. The doses provided are at shoulder height.

During the patient setup, the reactor power might be lowered to around 0.5 MW_n or less. The dose rates given in figure 5.35 can then be scaled downward. Total dose rates below the lead shutter would still be around 100 mrem/hr at shoulder height and around 300 mrem/hr just below the shutter near the beam.

Personnel viewing the patient during an irradiation would receive about 4 mrem/hr. Personnel at the table and instrument rack would receive about 2 mrem/hr.

If a patient would need emergency medical treatment during an irradiation, the reactor will be scrammed and all the shutters will be closed. The lead and boral shutters close within seconds, but the water shutter takes 2 minutes to fill completely and the heavy water shutter takes 12 minutes to fill completely. Dose rates under the emergency situation were measured by opening the beam for 87 minutes at 4.0 MW_n. Then, the reactor was scrammed and all the shutters were closed. The drop in the exposure rate

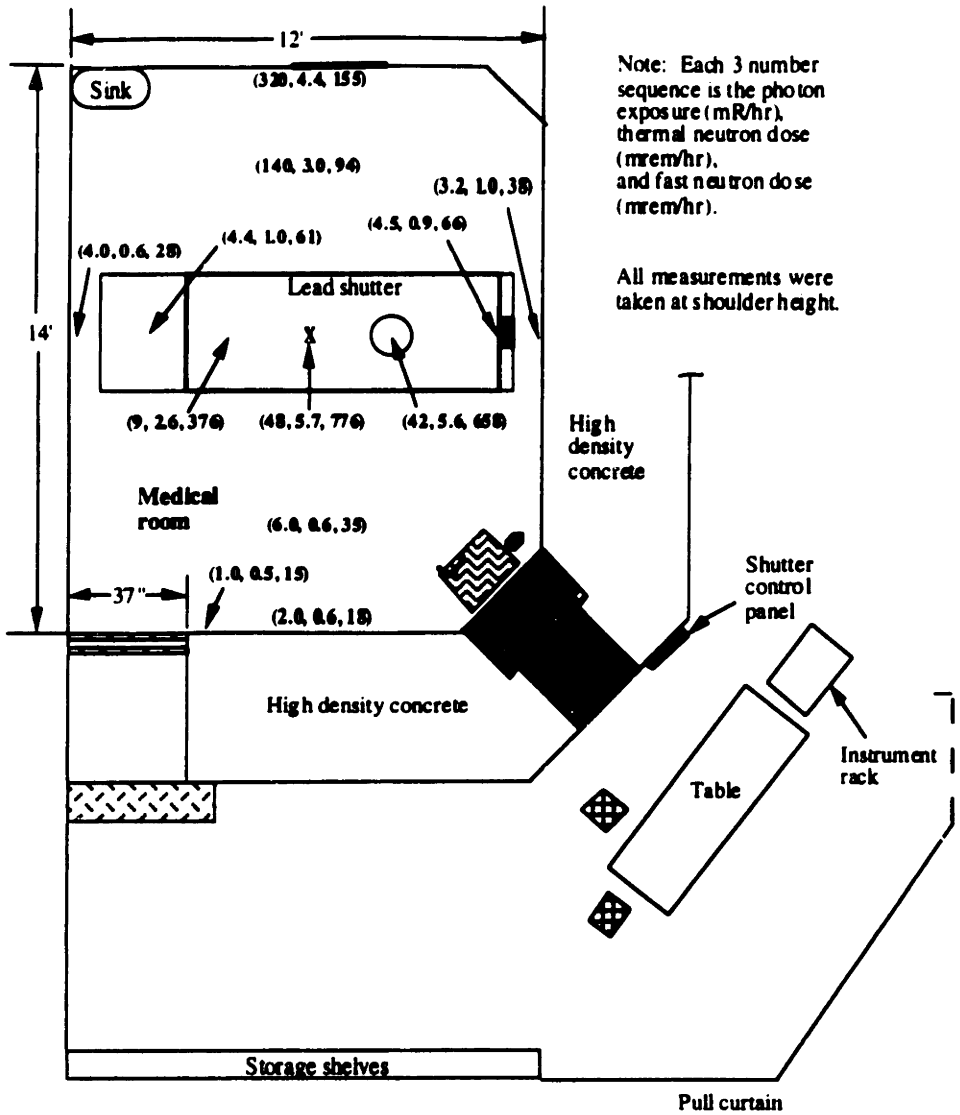

Figure 5.35. Dose rates inside the medical room for the M62, delimiter #1 beam at a power of 4.0 MWn. All shutters were closed. The M67, delimiter #3 clinical beam has similar dose rates (see text). The quality factor for neutrons is about 10. Fast neutron dose rates are high below the beam and collimator. There is photon and fast neutron streaming along the back wall. The lowest dose rates are by the front door.

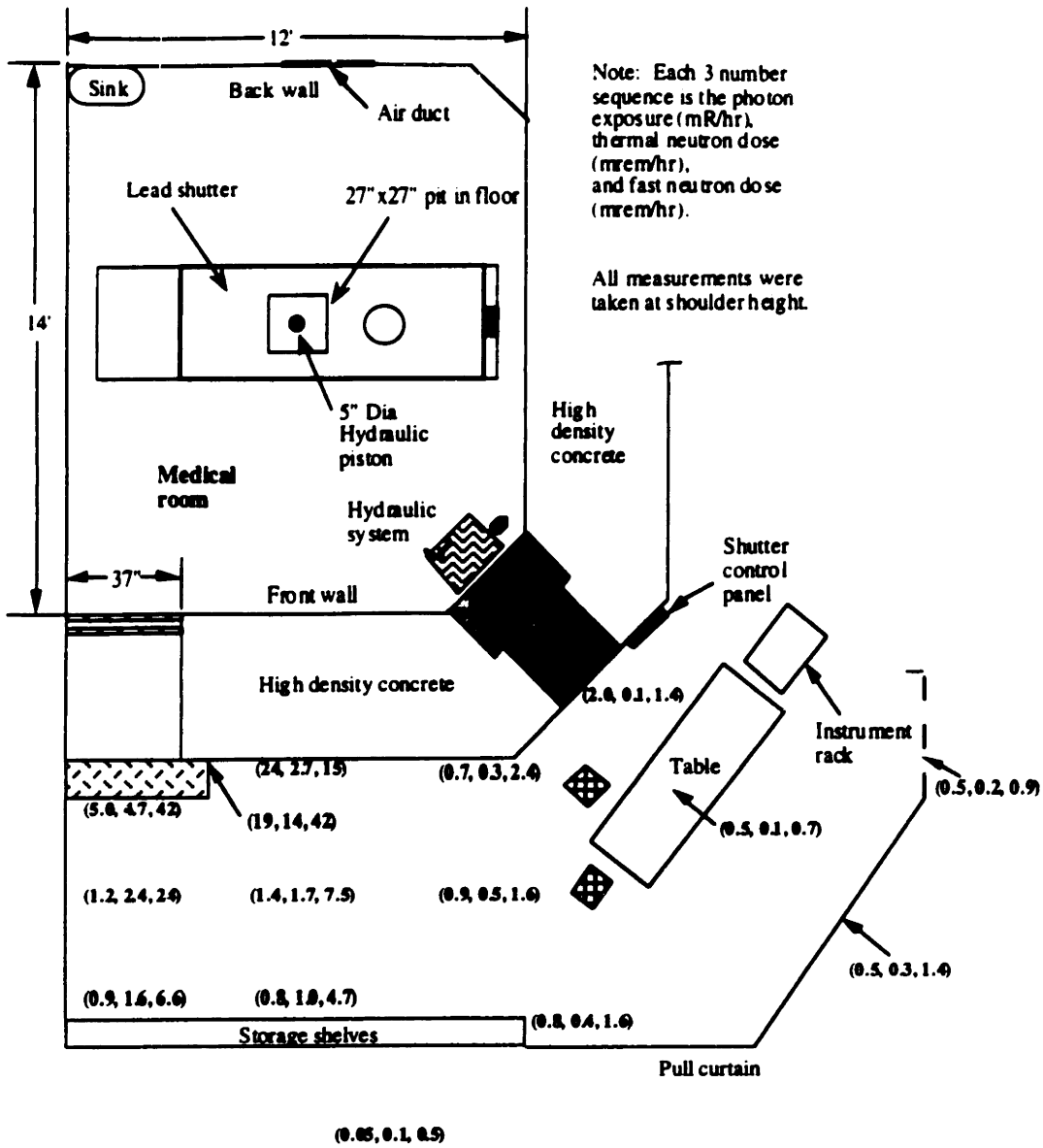

Figure 5.36. Dose rates outside the medical room for the M62, delimiter #1 beam at a power of 4.0 MWn. All shutters were open. The M67, delimiter #3 clinical beam has similar dose rates (see text). The quality factor for neutrons is about 10. Total dose rates are around 3 mrem/hr near the table and view window. Dose rates increase as the shield door is approached. There are some streaming hot spots behind the shield door. Dose rates are much less in the hallway behind the storage shelves.

inside the medical room is shown in figure 5.37. Closing the water shutter is important in reducing the exposure rate. After 60 seconds, the exposure rate was nearly constant at 9 mR/hr. Closing the D_2O shutter reduces the exposure rate by about 2 mR/hr.

Dose rates measured inside the medical room during the emergency entrance conditions are shown in table 5.4. It takes about 9 seconds to open the motorized door and the two inner doors, and enter the medical room. There is a significant fast neutron dose rate inside the medical room during the first minute after ARI. Realistically, it would take about 15 seconds to reach the patient, and by then the fast neutron dose is estimated to be less than 3000 mrem/hr under the filter, based on the fast neutron dose rates measured inside the medical room during the first minute after ARI. Under an emergency situation, the average dose rate from fast neutrons to any personnel is estimated to be less than 10 mrem/min during the first minute. This amounts to a total neutron dose of 10 mrem, as the fast neutron dose is very small after 1 minute provided that the water shutter closes. Average photon exposures are estimated to be less than 10 mR/hr during the first 15 minutes, so total photon exposures are estimated to be less than 3 mR. The total exposure to any emergency personnel, therefore, is estimated to be around 13 mrem.

5.8 OUTSIDE REVIEW OF CLINICAL DOSIMETRY

The dosimetry protocol (Chapter 3) that was used to characterize all the beams, including the clinical beam, has been thoroughly reviewed by Professor Steven Goetsch, of U.C.L.A., an expert on mixed field dosimetry. Dr. Goetsch also visited the MITR-II medical beam facility and reviewed our experimental method. His review is provided in Appendix A. Two suggestions made by Dr. Goetsch were to seal the carbon graphite chamber with lacquer, and to periodically check the calibrations of the ionization

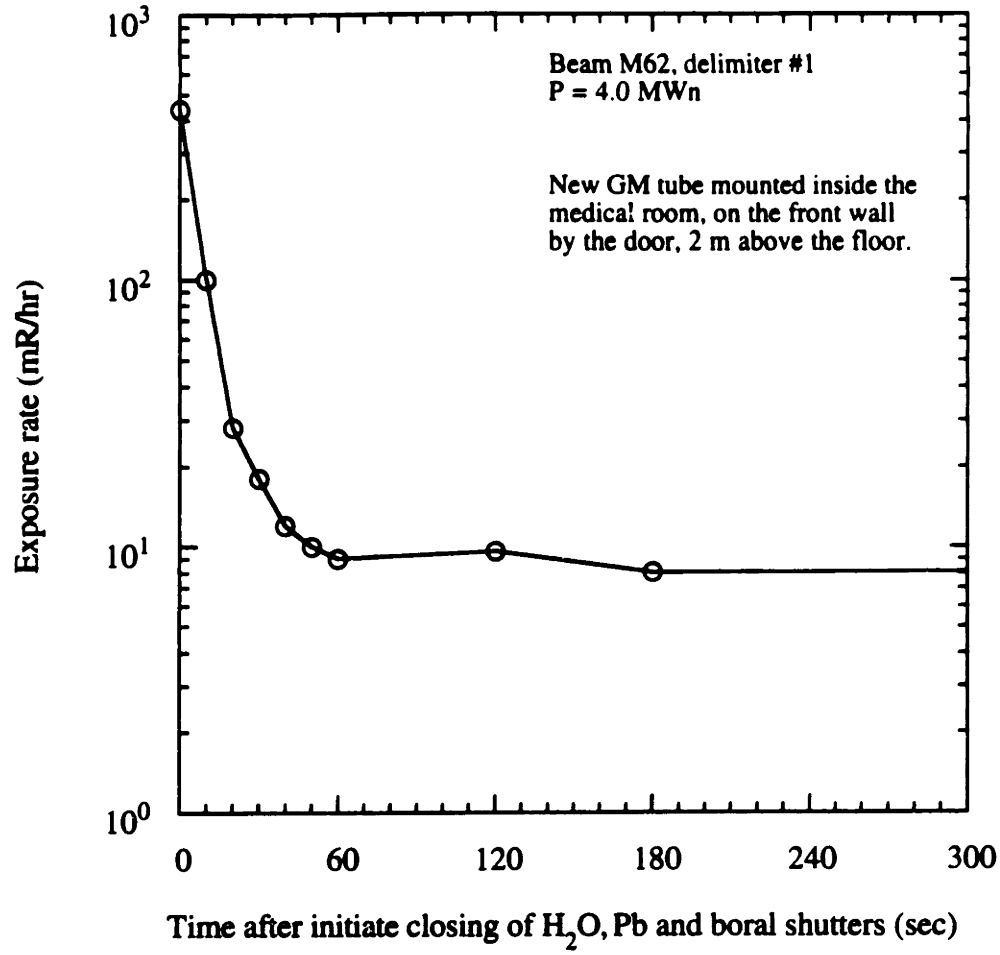

Figure 5.37. Drop in the exposure rate inside the medical room when the water, lead, and boral shutters are closed simultaneously. If the patient would need emergency medical assistance, the rapid drop in the exposure rate would allow medical personnel to enter the room as soon as the shield door opens.

Table 5.4. Dose rates following all-rods-in (ARI) and closing of all shutters.

Time after ARI min:sec	Position	Fast neutron dose rate (mrem/hr)	Photon exposure rate (mR/hr)
0:25	Inside door	94	12
0:30	1 m from couch	329	
0:45	Side of couch, towards front wall	127	100
0:60	Side of couch, towards left wall	19	28
1:30	Side of couch, towards front wall		80
1:52-2:10	Below collimator:		
	Below Bi		260
	Below Al		280
	Below Pb to RHS		180
2:22	Platform		12
3:00	Inside door		2.3
3:45	First back bioshield		10
5-6 minutes	Left wall		2.3
	Back wall		2.7
	Right wall		3.6
	Front wall		2.4
9 minutes	Left wall		1.7
	Back wall		2.2
	Right wall		2.7
	Front wall		1.8
10-11 minutes	Below filter		23
	Below Bi		39
	Below Al		82
	Below Pb on RHS		44
20-21 minutes	Left wall		1.4
	Back wall		1.8
	Right wall		1.9
	Front wall		1.4
21-22 minutes	Below filter		19
	Below Bi		24
	Below Al		46
	Below Pb on RHS		39

These dose rates are for the M62, delimiter #2 beam. Similar dose rates are expected for the M67, delimiter #3 clinical beam; aside from the different hole size in the delimiter, the only difference between these two beams is that the collimator of the clinical beam was painted with Li-6 and B-10 loaded paints and that the bottom of the lead shutter had also been painted. The beam had been open for 87 minutes at a power of 4.0 MWn. Fast neutrons are present during the first minute after ARI. During an emergency evacuation of the patient, personnel would receive less than 10 mrem of fast neutron dose and less than 3 mrem of photon dose.

chambers and electrometer using the Cs-137 source that is on site. The carbon graphite chamber has been sealed, a positioning jig was made for the Cs-137 source check, and a procedure has been written to do the periodic check calibrations.

5.9 SUMMARY

The M67 clinical beam and related dosimetry have been described. For a unilateral irradiation, the advantage parameters for this beam, using muscle kermas, are: AR = 2.1, ADDR = 7.7 RBE cGy/min, and AD = 6.6 cm. The beam has a 5.1 cm thick, 15 cm diameter delimiter, and whole body shields that extend along the full length of the lead shutter. The experimentally determined dose components have been used to normalize the Monte Carlo generated dose components for input into NCTPLAN. A 250 minute unilateral irradiation would deliver 2000 RBE cGy peak dose to healthy tissue in the treatment zone, and a whole body dose of 57 RBE cGy. Although the thermal flux drops rapidly outside the treatment zone, the potential for high B-10 concentrations, such as in the intestinal epithelium, might still result in a significant dose contribution from the B-10 reaction. Judicious positioning of the patient, and use of additional shielding, can reduce the patient's whole body dose by a factor of 2 or more. In-vivo measurement of the thermal flux with bare and cadmium covered gold foils would result in a locally high gamma dose from cadmium prompt gammas. To measure the thermal flux without a local increase in gamma dose, an alternative cover made of Li-6 carbonate has been designed and tested. Four procedures for the clinical dosimetry have been written and completed. A calibration jig for the Cs-137 source and a simple current source were designed and built. Health physics doses were measured under routine and emergency conditions. With the reactor power lowered to 0.5 MWn or less while setting up the patient, routine doses are estimated to be less than 20 mrem. During an emergency

entrance into the medical room to assist the patient, the total dose is estimated to be around 13 mrem. The dosimetry protocol and experimental technique used to characterize the M67 clinical beam has been reviewed and approved by Dr. Steven Goetsch, an outside expert on mixed field dosimetry.

The above discussion of the M67 clinical beam compietes the beam design and dosimetry part of the thesis. In the next chapter, the modifications that were made to the medical room in preparation for clinical trials is discussed.

References

1. Chun-Shan Yam, *Design of Patient Positioning System, Body Phantom, and Patient Shielding for the Boron Neutron Capture Therapy Project at MITR-II*, (Master's Thesis, Massachusetts Institute of Technology, 1993).

2. The fast neutron RBE of 4.0 was recommended by Prof. Robert Zamenhof, New England Medical Center.

3. R. G. Zamenhof, S. D. Clement, O. K. Harling, et al, "Monte Carlo Based Dosimetry and Treatment Planning for Neutron Capture Therapy of Brain Tumors," in *Neutron Beam Design, Development, and Performance for Neutron Capture Therapy*, (O. K. Harling, John A. Bernard, Robert G. Zamenhof, eds., Plenum Press, New York, 1990).

4. R. G. Zamenhof, J. Brenner, J. Yanch, et al, "Treatment Planning for Neutron Capture Therapy of Glioblastoma Multiforme Using and Epithermal Neutron Beam from the MITR-II Research Reactor and Monte Carlo Simulation," in *Progress in Neutron Capture Therapy for Cancer* (Barry J. Allen, Douglas E. Moore, Baiba V. Harrington, eds., Plenum Press, New York, 1992).

5. Personal communication, Everett Redmond, graduate student, MIT Nuclear Engineering Department.

6. MCNP derived spectrum obtained from Everett Redmond.

7. Personal communication, Dr. David Wazer, New England Medical Center.

8. Personal communication, Prof. Robert Zamenhof, New England Medical Center.

9. Oral administration of BPA might result in high B-10 concentrations in the intestinal epithelium. No quantitative information is available on the actual B-10 concentrations in the intestinal epithelium.

10. John C. Villforth, George R. Shultz, *Radiological health Handbook, Revised Edition*, (U. S. Department of Health, Education, and Welfare, Rockville, Md, 1970).

11. Frank H. Attix, *Introduction to Radiological Physics and radiation Dosimetry*, (John Wiley & Sons, New York, NY, 1986).

12. John N. Hamawi, Norman C. Rasmussen, *Neutron Capture Gamma Rays of 75 Elements Listed in Terms of Increasing Gamma-Ray Energy*, MIT Report MITNE-105, 1969.

13. J. F. Briesmeister, ed, "MCNP - A General Monte Carlo Code for Neutron and Photon Transport (Version 3A)," LA-7396-M, Rev. 2, (Los Alamos National Laboratory, 1986).

CHAPTER 6 MODIFICATIONS MADE TO THE MEDICAL ROOM FOR CLINICAL TRIALS

6.1 INTRODUCTION

Many modifications were made to the medical room in preparation for clinical trials. Most important was the design and construction of a system to position the patient in the neutron beam.[1] Additional modifications were also made. These include using thermal neutron absorbing paints to reduce the activation levels within the medical room, designing a shield plug for the lead shutter that would lower the doses to personnel setting up the patient, adding a closed circuit TV camera and mirrors to better view the patient during an irradiation, adding an intercom system so the patient and physician can talk together during the irradiation, improving the appearance of the medical room, among other items. These modifications are discussed in a little more detail in the following pages of this chapter.

6.2 HEALTH PHYSICS

6.2.1 Boral and B_4C loaded paints

To reduce neutron activation, sufficient boral (1/4" thick) was obtained to completely cover the floor. The boral ($48,000 current cost) was very generously provided free of charge by the Army Materials Testing Reactor (Walthain, Ma.). The bottom of the lead shutter and the entire ceiling of the medical room were painted with a thermal neutron absorbing paint. The paint had a concentration of 5 g B_4C powder (1000

mesh) per 6 cc of paint - B_4C mixture. The attenuation of thermal flux in a similar B_4C loaded paint was measured experimentally as shown in figure 6.1. For that paint, B_4C was ground in a mortar and pestle until roughly 40% was in the 20-100 mesh range and 60% was finer than 100 mesh. The experimentally measured attenuation coefficient is less than that predicted theoretically; the theoretical prediction was based on the 2200 m/sec absorption cross section while the actual beam is a thermal neutron beam with a distribution of energies. Also, the experimentally measured attenuation coefficient will be reduced if the B_4C is not distributed uniformly within the paint. The paint actually used in the medical room was made with the finer, 1000 mesh B_4C; this paint absorbs thermal neutrons as well or better than the other paint since the B-10 is more uniformly distributed within the paint made with the finer B_4C. The paint was well mixed with the B_4C, and although the B_4C loaded paint was thicker than the base paint, it was still "paintable" with a brush. From figure 6.1, ten coats of paint made with the coarse B_4C absorbs 90-99% of the incident thermal neutrons. Several samples of the painted ceiling tiles were tested for their effectiveness in absorbing thermal neutrons; all samples gave greater than a factor of 10 attenuation and so the activation within the medical has been greatly reduced.

The surgical couch was also painted with 5 coats of this B_4C loaded paint. Tests showed that the couch and platform will not become significantly activated (<10mR/hr on contact) during a patient irradiation.[1]

6.2.2 NAA of the wallpaper

Wallpaper was applied to the ceiling of the medical room to improve the room's appearance. The wallpaper was tested by NAA and PGNAA before installation to determine if it would become activated. Results (not shown) indicated that the wallpaper would not become significantly activated or cause a significant prompt gamma dose rate in the medical room.

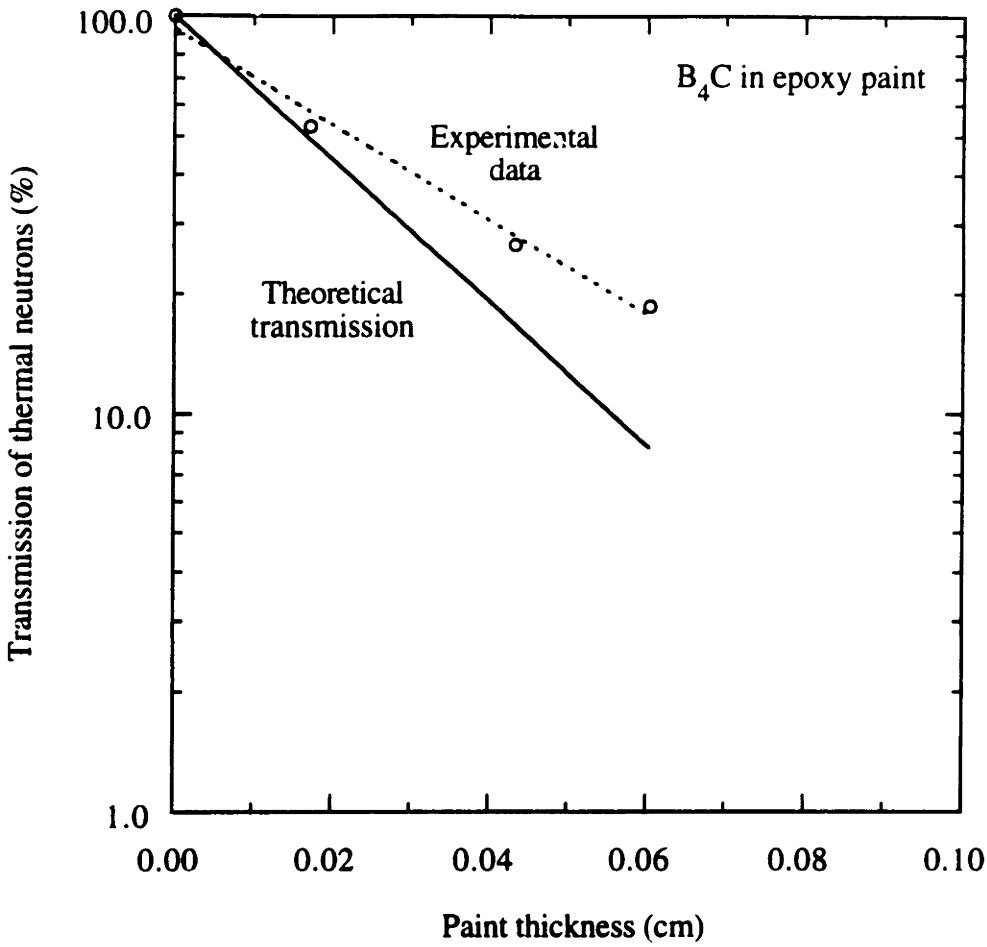

Figure 6.1. Experimentally determined transmission curve with B_4C in epoxy paint. B_4C was ground in a mortar and pestle until roughly 40% was in the 20-100 mesh range and 60% was finer than 100 mesh. Five grams of B_4C was put into a test tube and epoxy paint added to give a total of 6 cm^3 of paint. This paint was well mixed; the consistency of the mixed paint was such that it was "paintable" with a brush. The borated paint was painted on a flat of 0.015" thick Al sheet. A transmission attenuation experiment was done using the nearly pure thermal neutron beam at the 4DH1 beam port. A BF_3 tube was used to measure the thermal neutron flux. The first data point (0 cm) was obtained with an Al sheet that was not painted. The next three data points correspond to 1, 2, and 3 coats of paint. The theoretical curve was calculated from the concentration of B-10 in the paint and the 2200 m/sec absorption cross section of B-10.

6.2.3 NAA of the medical room

At the end of a patient irradiation, the shutters are closed and the reactor power reduced to a low level. Most of the radiation exposure to people entering the room just after an irradiation will be caused by decaying radionuclides in the lower shielding, primarily just below and to the sides of the collimator.

The specific radionuclides that are responsible for the exposure rates were determined by NAA. With the reactor at 4 MWn, the M62 beam was opened for 100 minutes. There was nothing in the beam. Boral was on the floor. At the end of the irradiation, the reactor power was lowered to 0 MWn by an all-rods-in (ARI) shutdown. The HPGE detector from the prompt gamma system was brought into the medical room and positioned on the floor. It was 1.3 meters inside the door. The detector was not shielded. Several counts were taken.

One of the counting results is shown in the table 6.1. This was a 600 second count that was started 3.5 hours after shutdown. Other counts were taken at earlier times, but provided similar spectral data aside from the higher number of counts from Mn-56 that is expected from its short half-life ($T_{1/2}$ = 2.6 hours). The counts provided are net counts and were not corrected for the relative energy efficiency of the detector. The dead time was 14%.

Most of the exposure is caused by Mn-56 and Na-24; they each contribute about the same amount 3.5 hours after shutdown. Mn-56 gives twice the exposure rate as Na-24 just after shutdown. Some of the Na-24 in this experiment might have been produced during irradiations the previous day; a background measurement before the beam was opened for this experiment was not taken. Co-60 and Ar-41 each contribute several percent of the total exposure. The Mn-56 is produced from manganese in the steel surrounding and at the bottom of the collimator. The Co-60 is likely coming from this steel as well. The Na-24 can be produced directly from Na-23, but may be mostly

Table 6.1. Spectrum obtained inside the medical room after an irradiation.

E_γ (keV)	Net area (counts)	Radionuclide	$T_{1/2}$
511.0	13546	Annihilation	-
846.9	132061	Mn-56	2.58 hr
1173.1	1356	Co-60	5.24 yr
1293.6	3600	Ar-41	110 min
1332.4	950	Co-60	5.24 yr
1368.4	45182	Na-24	15.0 hr
1810.7	25724	Mn-56	2.58 hr
2112.8	10305	Mn-56	2.58 hr
2242.6	4654	Na-24 *	15.0 hr

* Single escape peak of the 2753.6 keV gamma of Na-24; this peak was seen when the gain was reduced.
Beam M62, 100 minute irradiation, 3 1/2 hour decay time, 600 second count time. The HPGE detector was on the floor of the medical room.

produced from the fast neutron induced Al-27(n,α)Na-24 reaction. The Ar-41 is from gaseous argon in the air.

6.2.4 Painting the collimator with a thermal neutron absorbing paint

With the results of the NAA, the collimator was painted with a thermal neutron absorbing paint. This was expected to reduce the exposure rates after an irradiation by reducing the activation of Mn-56, and potentially reducing the activation of Na-24. Probably most of the exposure rate in the medical room is caused by activation in the lower part of the collimator and the lower part of the lead shutter near the collimator; radionuclides in the upper part of the collimator and shutter are well shielded.

A Li-6 loaded paint was applied to the bottom 2/3 of the collimator; a B-10 loaded paint was applied to the top 1/3. The Li-6 loaded paint was used on the bottom 2/3 of the collimator since thermal neutron absorption in Li-6 does not produce prompt gammas; prompt gammas produced this close to the patient would increase the patient's gamma dose. The B-10 loaded paint was used on the top 1/3 of the collimator as a cost savings measure. Thermal neutron capture in B-10 produces 93% abundant 478 keV gammas (refer to Chapter 1); however, these gammas are well shielded from the patient by the intervening bismuth.

The Li-6 paint was made of 2 g of Li-6 carbonate per 5 cc of paint-carbonate mixture (refer to figure 4.68 for the thermal neutron attenuation curve for this paint). The B_4C paint was the same as that applied to the ceiling of the medical room, 5 g of B_4C per 6 cc of paint B_4C mixture. Roughly an 80-90% reduction in thermal flux was expected with the amount of paint applied. To measure the effectiveness of the paint in reducing overall activation, radiation surveys were done before and after the collimator was painted.

The M62 beam was opened for 1.5 hours at 4.0 MWn to build up the activation products. Afterwards, the shutters were closed and the reactor power dropped to 50 kW

or less. The area just below the lead shutter was surveyed in 4 places as shown in figure 6.2. Air ionization survey meters were used. At 50 kW, the exposure rates from the core are much lower than those from the activation products that were measured. Similar surveys were done before and after the collimator was painted.

Results of the surveys are shown in figures 6.3 and 6.4.

Exposure rates were lower after the collimator was painted. However, in the non-painted case, there was a 1.5 hour irradiation several hours before the start of the 1.5 hour experimental irradiation. The two sets of data, then, are best compared by normalizing the exposure rates to the exposure rates below the filter. The exposure rates below the filter are a monitor of the activities above the lead shutter, in the beam filter itself and would not be affected by the paint on the collimator. After normalizing, it is seen that the painting was effective in reducing the exposure rates. Exposure rates below the aluminum, lead, and bismuth dropped to 45, 50, and 60% of their original values, respectively. These are at about 40 minutes after closing the shutters.

The previous NAA of the lead shutter showed that at this time about 60-70% of the exposure is caused by Mn-56, with most of the remainder caused by Na-24. If the Na-24 is produced mainly by the fast neutron induced Al-27(n,α)Na-24 reaction, then reducing the thermal flux with the paint would only reduce the Mn-56 component, which is produced by thermal neutron absorption in Mn-55. In this case, a 60-70% reduction in exposure rates would be expected. This is in rough agreement with the 45-60% reduction measured.

6.2.5 GM tube to monitor the exposure rates inside the medical room

A GM tube was purchased and mounted to the front wall of the medical room.[2] A measurement of the exposure rates inside the medical room was required pursuant to the MITR Technical Specification No. 6.5, which covers irradiations of patients in the medical room. The readout of exposure rate is provided at the viewing window.

Bottom view of lead shutter

Note: Lead shutter
in closed position.

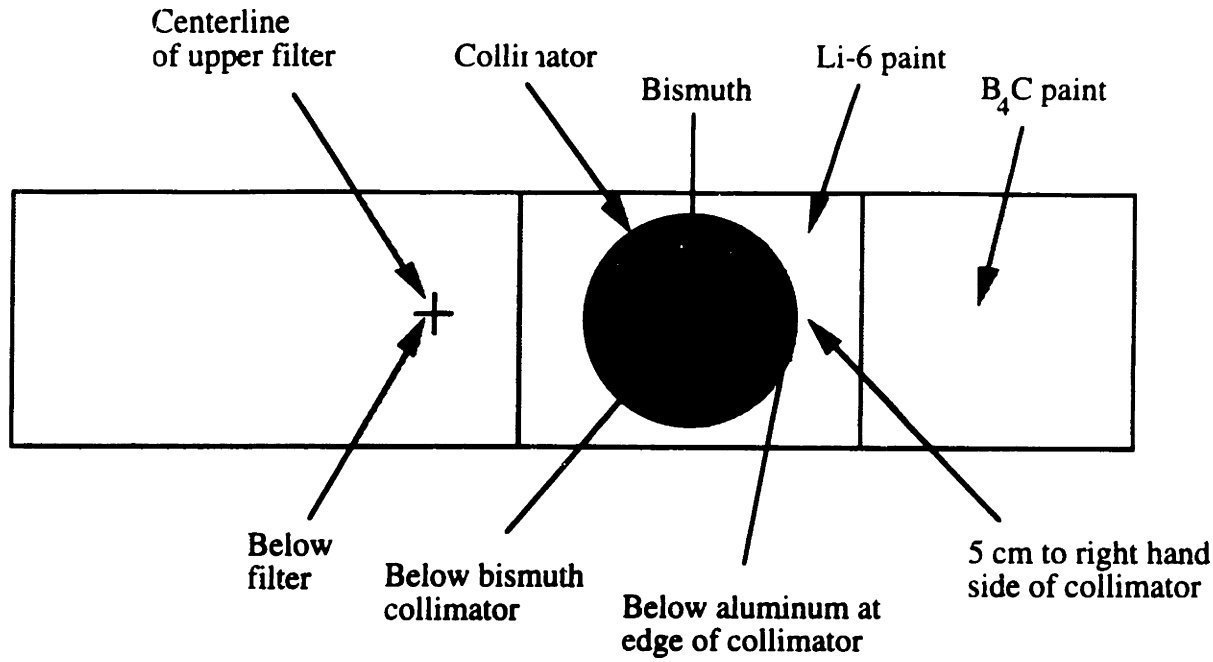

Scale: 1/15

Figure 6.2. Bottom view of the lead shutter showing where the exposure rates were measured to asses the effectiveness of the thermal neutron absorbing paints in reducing activation.

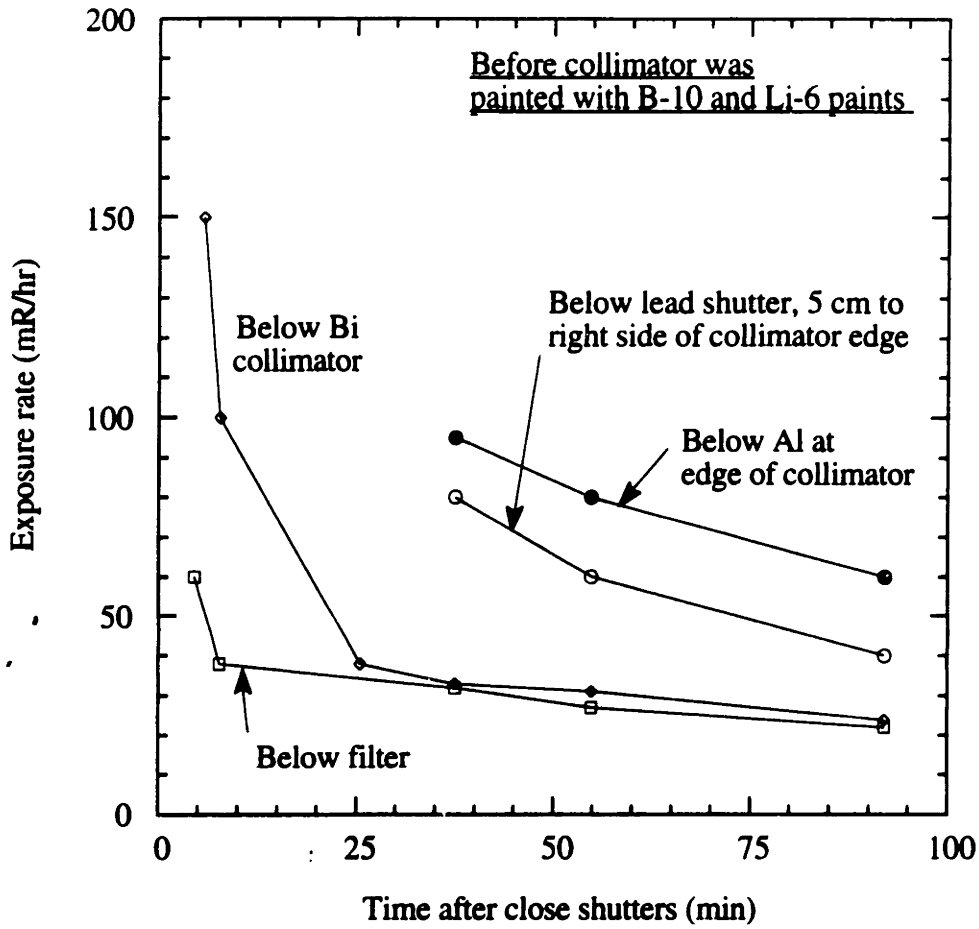

Figure 6.3. Exposure rates for the M62 beam after a 1.5 hour irradiation at 4.0 MW_n to build up activation products. The exposure rates were measured with all the shutters closed. Reactor power was reduced to 50 kW so that radiations from the core were much lower than those from the activation products. The initially high exposure rates below the bismuth collimator may be due to decay of Al-28. The walls and lower flange of the collimator are made of aluminum.

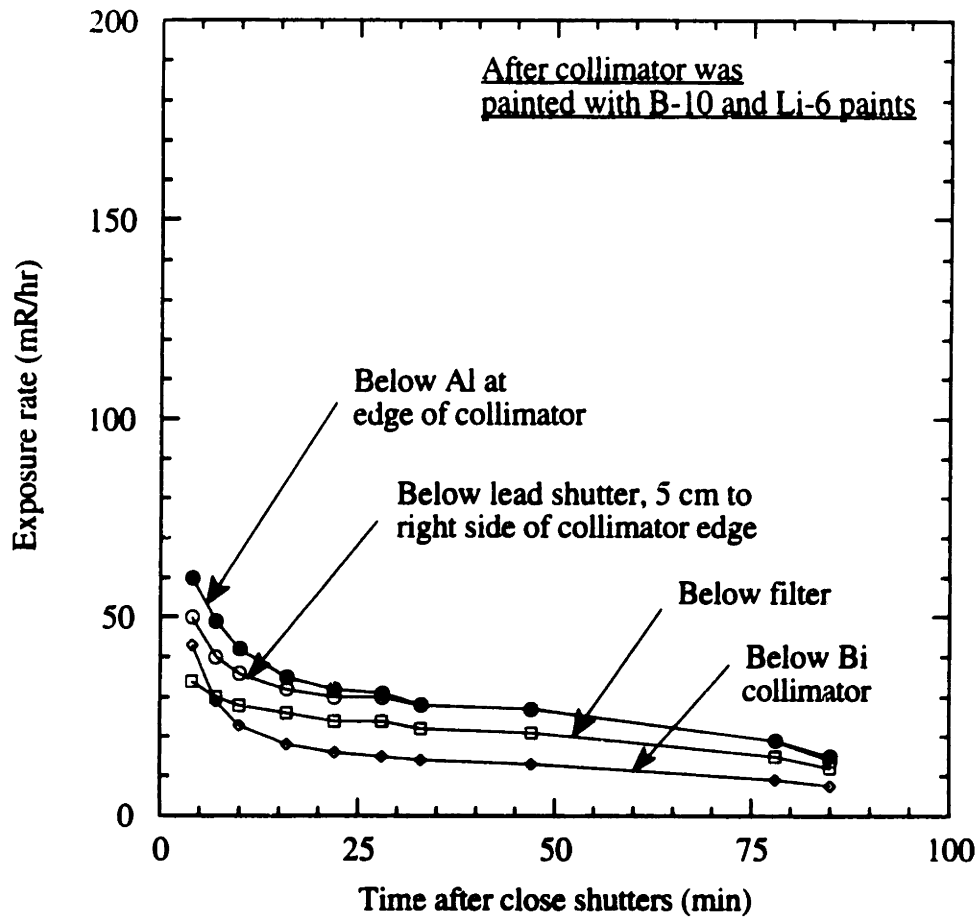

Figure 6.4. Exposure rates for the M62 beam after the collimator has been painted with the B-10 and Li-6 loaded paints. There was a 1.5 hour irradiation at 4.0 MW_n to build up activation products. The exposure rates were measured with all the shutters closed. Reactor power was reduced to 50 kW so that radiations from the core were much lower than those from the activation products. Comparing these results with those presented in figure 6.3 (before the collimator was painted), there is a factor of 3 reduction in the initial exposure rates below the bismuth collimator. At 40 minutes, exposure rates at the other areas are a factor of 2 lower than before.

Exposure rates are to be less than 50 mR/hr before medical and other personnel enter the medical room after an irradiation of a patient, except in an emergency.

6.3 DESIGN OF A NEW LEAD SHUTTER

The fast neutron dose rate in the medical room with all shutters closed is rather high. For example, in the beam line and just below the lead shutter, the fast neutron dose rates have been measured at 2-3 rem/hr for beams like M62 and M57 which have the same amount of fast neutron shielding. Photons and thermal neutrons also add to the dose, but are significantly lower (factor of 40) than the fast neutron dose. Refer to Chapter 5 for the results of some health physics surveys. Unless the reactor power is temporarily lowered, personnel will be exposed to these doses while setting up the patient for an irradiation.

6.3.1 Shielding calculations

The lead shutter is a 28 cm thick slab of lead. Some shielding calculations were done to see if replacing some of the lead in the top part of the shutter with a better fast neutron shielding material could reduce the fast neutron dose rate, and the total dose rate, significantly The goal was to design a shield that would be more effective in reducing the fast neutron dose without resulting in a much higher photon dose. Fast neutron and photon doses were calculated for a shutter composed of various amounts of polyethylene and lead. Polyethylene was chosen as the fast neutron shield since it has a large hydrogen atom density and is relatively inexpensive. The hydrogen density of some neutron shielding materials is provided in table 6.2. Similar shielding calculations were done for a polyethylene and depleted uranium shutter. The calculations were done for the M62 beam; however, they are equally applicable to the currently used M67 clinical beam since

Table 6.2. Densities and hydrogen densities of some neutron shielding materials.

Shielding material	Density (g/cm^3)	H atoms/cm^3 ($x10^{-22}$)
TiH_2 (pure)	3.78	9.12
Polyethylene	-	7.9
Paraffin	0.87-0.91	7.82-8.01
Aliphatic HC	0.77-0.80	6.6-7.14
Water	1.0	6.69
Masonite	1.3	4.7

Ref: CRC Handbook of Chemistry and Physics, 50th edition, Chemical Rubber Co., Cleveland, Ohio.

these two beams have about the same photon and fast neutron dose rates with all the shutters closed.

Polyethylene attenuates the fast neutron dose by scattering and thermalization. Thermalized neutrons can be absorbed in B-10 or Li-6. The attenuation in the fast neutron dose was calculated using an exponential model with an experimentally determined attenuation coefficient. The attenuation coefficient was determined by adding a 1" thick slab of polyethylene above the lead shutter and measuring the reduction in fast neutron dose rate with a Bonner sphere.

The attenuation of the photon dose was calculated using an exponential model and a buildup factor. An effective attenuation coefficient for lead was estimated from an experiment. Two and 4" of lead were placed between the bottom of the lead shutter and an air ionization chamber. There was a reduction in exposure with the additional shielding which was found to be equal to that expected for a monoenergetic gamma ray beam in the 3-4 MeV range. The attenuation coefficient for uranium was calculated by scaling the 3-4 MeV value for lead by the density ratio of uranium to lead.

The thickness of the shutter was kept constant at the current thickness of 28 cm. If 2 cm of polyethylene were added, for example, the fast neutron dose was lowered using the exponential model. Also, the photon dose was increased using the buildup factor - attenuation model since 2 cm of lead was removed.

The model assumes that the area of the polyethylene is at least 60 cm x 60 cm square; that is, that the polyethylene shields all of the higher intensity part of the beam below the filters. No credit is given for photon attenuation in the polyethylene or for neutron attenuation in the lead. Finally, prompt gamma production in the polyethylene was not accounted for. The latter 2 assumptions could be accounted for by an approximate model at a later time. However, they might not be as severe as one might first expect. Prompt gamma production in the polyethylene is estimated to make less than a 10 mR/hr contribution to the gamma dose for realistic thicknesses of polyethylene and

lead (or depleted uranium) in the beam. Also, for the optimum amounts of polyethylene and lead (or depleted uranium) that are provided next, there is a greater thickness of lead (or depleted uranium) in the beam than polyethylene; therefore, not giving credit to photon attenuation in the polyethylene is an excellent assumption.

Figure 6.5 shows the photon buildup factors for lead and uranium. These buildup factors are for a plane monodirectional source and were extracted from the Radiological Health Handbook.[3] Figure 6.6 shows the doses calculated for various amounts of polyethylene and lead. Figure 6.7 shows the doses when depleted uranium is used.

With all shutters closed, the M62 beam had a photon dose rate of 61 mrem/hr and a fast neutron dose rate of 2606 mrem/hr. Adding polyethylene at the expense of lead changes these doses as shown in figure 6.6. The fast neutron dose drops slowly (HVL = 4.4 cm). The photon dose rises as more lead is removed. The minimum total dose, reached with 6-8 cm of polyethylene, is 1375 mrem/hr. Therefore, the total dose rate can only be cut in half relative to the existing shield where only lead is in the beam. The thermal neutron dose was ignored; it is very small (10-20 mrem/hr).

Uranium is a better photon shield than lead because of its higher density (lead, 11.3 g/cm^3; uranium, 19.1 g/cm^3). As shown in figure 6.7, the photon doses are smaller with depleted uranium, and a minimum total dose of 681 mrem/hr is predicted for 10 cm of polyethylene and 18 cm of uranium. The total dose rate, then, is reduced by almost a factor of 4. Production of fission products in the depleted uranium shield is not an issue; the average thermal flux in the shield will be only of the order 1 E4 to 1 E5 n/cm^2-sec.

A new product offered commercially (Reactor Experiments, Inc., Sunnyvale, Ca.) is a mixture of tungsten and polyethylene. The tungsten slows neutrons by inelastic scattering ($\sigma_{inel} \approx$ 2-3 barns) and also is a good photon shield. As an alternative to the commercially available product, which is very expensive, powdered tungsten can be purchased and mixed with melted paraffin. This shield would work as well and be much cheaper.

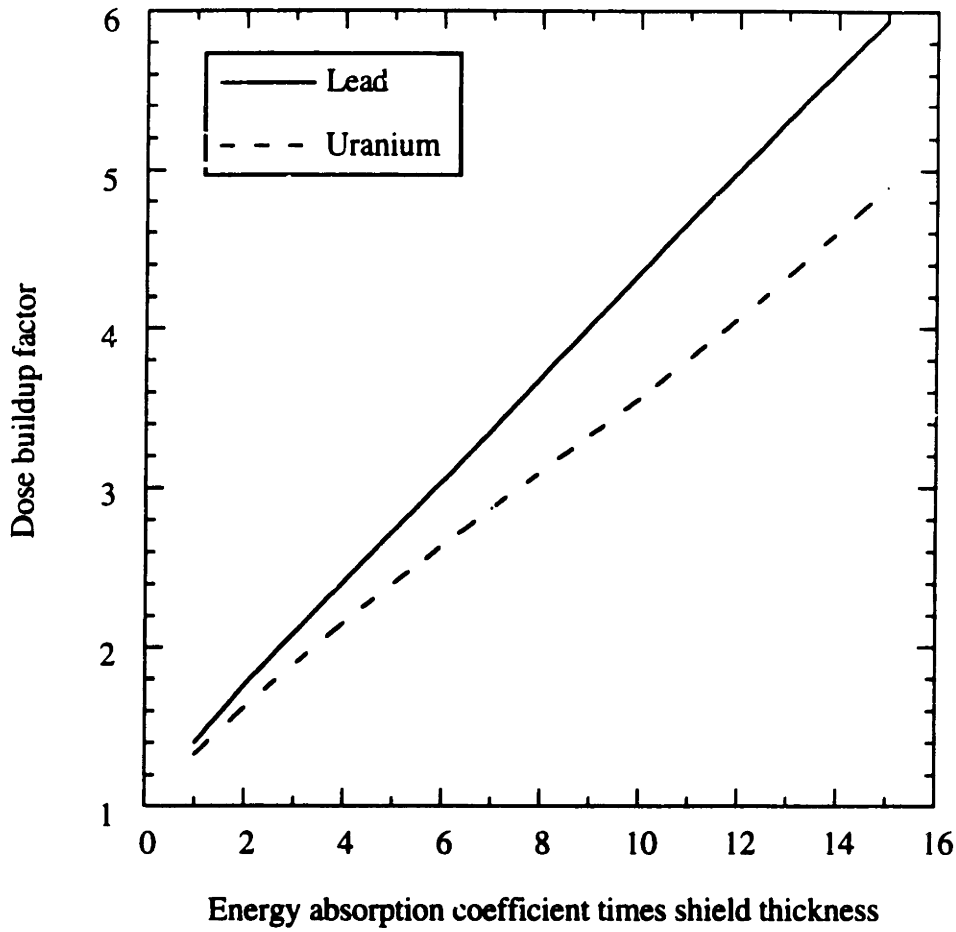

Figure 6.5. Dose buildup factors for lead and uranium.[3] These factors are for a plane monodirectional source.

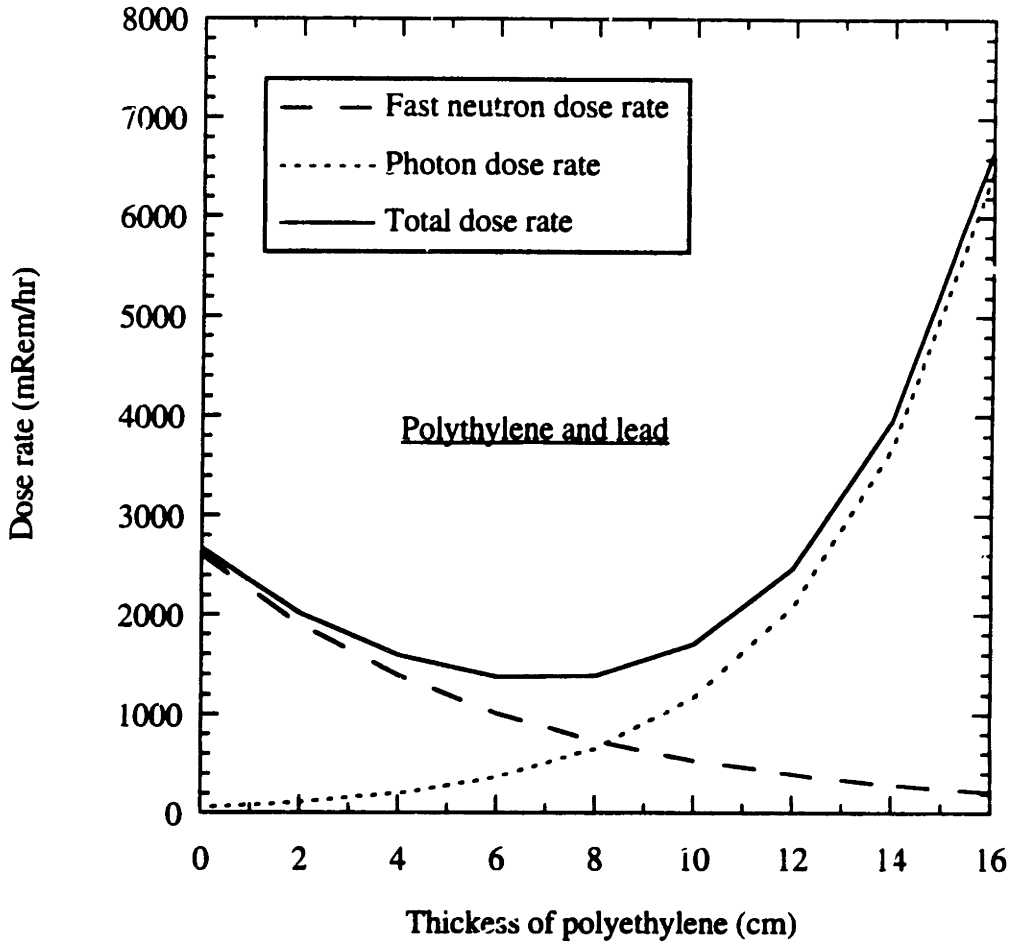

Figure 6.6. Predicted dose rates in a shield made with lead and polyethylene. The total dose rate is the sum of the photon and fast neutron dose rates. The thickness of the shutter was kept constant at 28 cm. Adding polyethylene results in a lower fast neutron dose, but removing an equivalent thickness of lead results in a higher photon dose. The minimum total dose rate is 1370 mrem/hr, about half the 2670 mrem/hr dose rate with the current configuration (no added polyethylene).

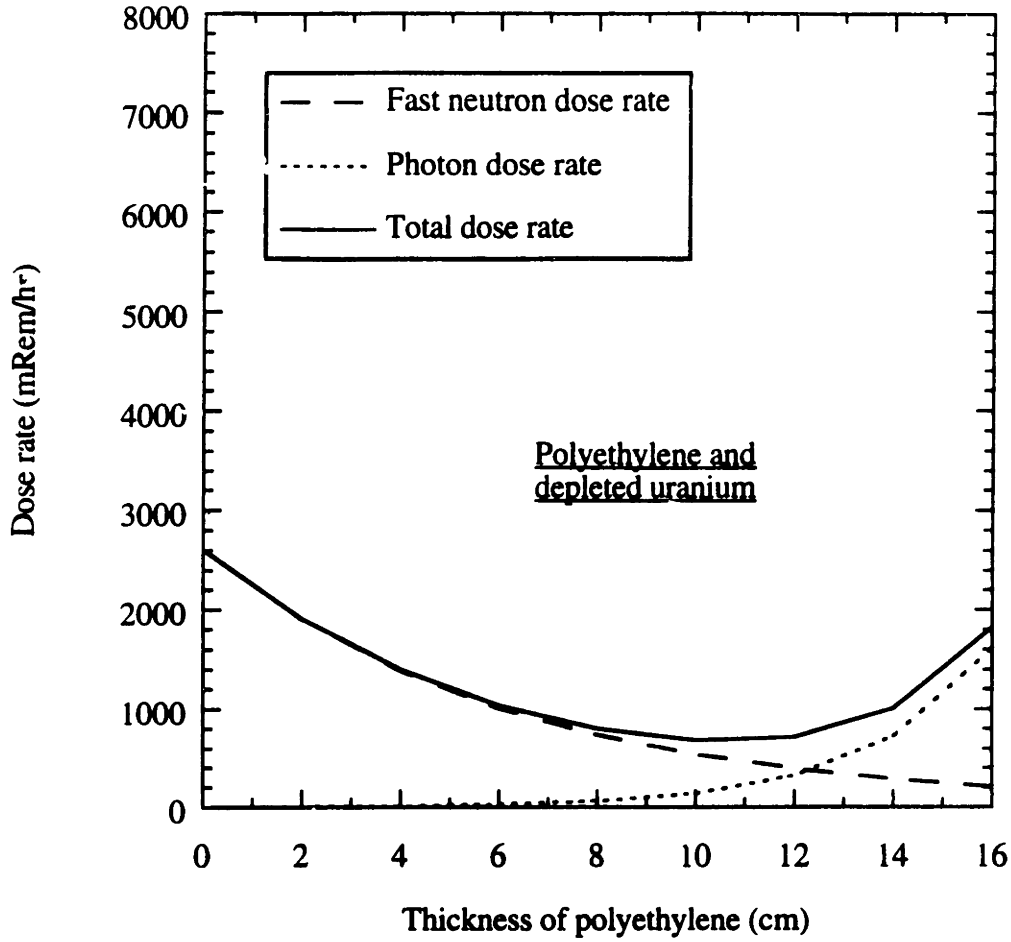

Figure 6.7. Predicted dose rates in a shield made with depleted uranium and polyethylene. The total dose rate is the sum of the photon and fast neutron dose rates. The thickness of the shutter was kept constant at 28 cm. Adding depleted uranium results in a lower fast neutron dose, but removing an equivalent thickness of lead results in a higher photon dose. The minimum total dose rate is 680 mrem/hr. This is 3.9 times lower than the 2670 mrem/hr dose rate with the current configuration (no added polyethylene). No consideration has been given to gamma rays from fission product buildup. These decay gammas are not significant.

No further analysis was done to estimate the performance of a tungsten - polyethylene shield. However, as several hundred pounds of tungsten might be used in the new shutter design, theoretical and experimental analyses were done to estimate how activated the tungsten shield would become and to determine if such activation would increase the exposure rates in the medical room. Using the depleted uranium - polyethylene shield data of figure 6.7, about 400 pounds of powdered tungsten mixed either homogeneously or in layers with a paraffin or polyethylene like material would seem promising as an effective neutron and photon shield. The shield would be roughly a cube 30 cm on a side. It would have a steel liner. The outside of the shield would be painted with a Li-6 or B_4C loaded paint to absorb thermal neutrons that could cause activation. B_4C would be added within the shield to capture thermal neutrons produced by thermalization of epicadmium neutrons.

Table 6.3 shows the expected activation products. It was assumed that the thermal flux within the shield would be small (less than 1 E4 n/cm^2-sec). Then, most of the activation would be caused by epicadmium neutrons that penetrate the cadmium surrounding the shield. Under these conditions, it would be expected that W-187 would be the most intense activation product; its precursor, W-186, has a high abundance and a large resonance integral, and W-187 has the shortest half-life.

Activation of tungsten was tested experimentally. A 10 gram tungsten sample (Alpha Products, -100 mesh, m3N8, Lot #033076, Danvers, Ma.) was irradiated a short time (5 minutes at 4.0 MWn) in a rabbit (1PH2) for neutron activation analysis and a long time (2 hours at 4.0 MW_n) in the M62 beam for radiation surveys. For the rabbit irradiation, the tungsten was placed in a polyethylene bag which was then heat sealed. This bag was placed in another heat sealed bag for double protection. Neutron activation analysis (Detector #4, a Ge(Li) detector, 5.48" source-to-detector distance, half-hour count) 40 minutes later showed about 10 peaks, all corresponding to W-187. No Ta-182 from the W-182(n,p) reaction was found was found in this half-hour count. Rhenium and

Table 6.3. Important tungsten isotopes and their activation products.

Isotope	Atomic abundance (%)	σ_{th} (b)	RI (b)	Radio-nuclide	Decay mode	$T_{1/2}$ (days)	$E\gamma$ (MeV)
W-180	0.13	7	-	W-181	EC	121	0.006
W-184	30.67	1.8	14	W-185	β^-	75.1	0.125
W-186	28.6	38	500	W-187	β^-	0.996	0.686, 0.480

hafnium can occur as impurities in tungsten samples; however, no rhenium and hafnium activation products were found.

The tungsten was then wrapped in a 0.040" layer of cadmium, which is black to thermal neutrons. It was positioned in the centerline of the collimator, 1.3 cm below the shutter. A 5.1 cm thick borated polyethylene slab with a 20 cm diameter hole was in position as a delimiter. The epicadmium flux in this position is comparable to that where the shield would actually be located. Thus, activation results in this position should be applicable to estimates of activation of tungsten in the actual shield.

The tungsten was irradiated with all the shutters open. The tungsten was surveyed with a GM tube 16 hours later. The reading through the window of the GM tube was 20 mR/hr on contact. Through the side of the tube (photons only) the reading was 8 mR/hr on contact. There was probably significant photon attenuation within the tungsten itself.

An experiment was done with one and two inch thick layers of lead to determine how effectively the activation gammas could be attenuated. The source to detector distance was constant. Exposure rates with no lead and with 1 and 2" of lead were 0.45, 0.015, and <0.01 mR/hr, respectively. The exposure rate, therefore, was reduced by a factor of 30 with one inch of lead.

These experimental data were scaled to a 10 hour continuous irradiation at 5 MW_n. With 2" of lead below the tungsten polyethylene shield, exposure rates from tungsten activation are expected to be about 1 mR/hr or less.

6.3.2 Shield design engineering

Perhaps the best way to design this would be to make a large shield plug, similar to the collimator. The plug could be bolted into the bottom of the lead shutter. In this type of design, the shielding configuration can be easily modified. Mechanical stresses in this design would be small, just coming from the weight of the shielding itself. Heat

generation and induced thermal stresses would be small. Radiation damage, even in polyethylene if used, would be small.

The lead should not activate appreciably. If depleted uranium is chosen, it would have to be protected from corrosion and air oxidation with a coat of paint or shellac. Activation and production of prompt gammas and fast neutrons from fission would have to be assessed. A Monte Carlo analysis of these effects would be helpful. Uranium can be fabricated much like steel, but the machining would probably have to be done with an outside machine shop. Polyethylene is strong enough for our purposes and can be machined easily. It's limited resistance to heat and radiation would not be a problem.

A step in the polyethylene might be needed to minimize neutron streaming. A similar step might be needed in the lead or uranium part of the shield to minimize photon streaming.

6.3.3 Additional work on shield design and engineering

Work on this shield design and engineering was continued by Carlos Flores. He started with the shield design just presented as well as several Monte Carlo results [4], and designed an improved shield. A report on his analysis is included in Appendix F of this thesis for completeness.

6.4 MEDICAL

Section 10CFR35 of the NRC's Code of Federal Regulations requires that a patient being treated by a NRC regulated device be under continuous visual supervision during the treatment. The medical room has a viewing window through which the patient can be viewed at a distance of about 4 meters. To see the other side of the patient, a closed circuit TV camera and monitor were installed. The camera is mounted on the back

wall of the medical room. It will be pointed so that the patient's face is visible on the monitor outside the medical room. The camera has been tested with the beam on; the TV image was clear and no radiation damage was seen. A spare TV camera is available. The spare camera is a CCD type camera, however, and is sensitive to radiation damage. When the beam is on, streaks and flashes of white areas are seen on the TV monitor. The patient can still be seen; however, some of the radiation damage is permanent and the life of the camera under such radiation conditions is estimated to be 50 hours.

In addition to the camera and monitor, two large convex mirrors were purchased. One mirror is mounted on the back wall so the back side of the patient can be seen. The other mirror is mounted on the left side wall. With the camera and mirrors, the patient can be viewed from all directions.

An intercom has been installed so the patient and physician can talk to one another during the treatment. Also, a stereo system has been installed; music could help relax and comfort some patients who must stay in a fixed position for about an hour during each treatment.

The medical room is equipped with a heavy shielded door that is opened and closed with a motor. Hand operated winches have been added to both sides of the door so that it can be opened manually in the event of an electrical power failure. (The reactor has a backup power supply system which engages when outside power is lost.) A new control panel to operate the various shutters has been designed and installed. The control panel has buttons to scram the reactor, to open and close the beam shutters, and to open and close the shielding door.

A gurney was obtained. Also on hand are: sheets, pillows, lab coats, portable ECG monitor, elastic bandages, Band Aids, labeled polyethylene and Teflon vials for the blood and tissue samples, gloves, and pipettes. For positioning the patient: safety belts, Velcro strips, arm slings, inclinometer, foam cushions, a set of spacer bars to measure the distance between the patient and the delimiter, and Alpha cradle kits.

6.5 APPEARANCE OF THE MEDICAL ROOM

The appearance of the medical room has been improved. The walls and floor have been cleaned, and wallpaper was added to the ceiling. The lighting was improved with two spotlights. Also, two paintings were added. The spotlights and paintings are on the walls of the medical room far from the neutron beam; they have not become activated.

In the work area outside the medical room, the cabinets were cleaned and labeled. A new table was added. A clock was installed by the viewing window. Also, the lighting was improved by installing new panels.

6.6 SUMMARY

Many modifications were made to the medical room in preparation for clinical trials. A TV camera/monitor and an intercom system have been installed to more effectively see and talk with the patient. A new control panel for the beam shutters and a music system have been installed. The appearance of the room was improved by cleaning, and by adding additional lights and paintings. Neutron activation has been reduced by installing boral on the floor, by painting the lead shutter and the ceiling with a thermal neutron absorbing paint, and by painting the collimator itself. A GM tube was installed inside the medical room so personnel would know the exposure rates before entering the room. Outside the medical room, a new table and clock were added; lighting was also improved. Most of the medical supplies needed for the patient were purchased and are now on hand. Finally, an insert to the lead shutter was designed which would

reduce (by a factor of 2-4) the doses to personnel working inside the medical room or setting up the patient when the reactor is at power and the shutters are closed.

References

1. Chun-Shan Yam, *Design of Patient Positioning System, Body Phantom, and Patient Shielding for the Boron Neutron Capture Therapy Project at MITR-II*, (Master's Thesis, Massachusetts Institute of Technology, 1993).

2. Paul Menadier kindly purchased and installed the GM tube.

3. John C. Villforth, George R. Shultz, *Radiological health Handbook, Revised Edition*, (U. S. Department of Health, Education, and Welfare, Rockville, Md, 1970).

4. Monte Carlo shielding calculations done by Professor Yanch.

CHAPTER 7. BIODISTRIBUTION AND PHARMACOKINETICS OF BPA IN HUMANS

7.1 INTRODUCTION

L-p-boronophenylalanine (BPA) has been shown to have favorable toxicological and biodistribution properties in animals.[1-5] Our own group carried out a BPA biodistribution and pharmacokinetic study in a GL261 glioma bearing C57BL/6 mouse model.[1] Mice received oral doses of BPA ranging from 30-100 mg of B-10/kg body weight. Tumor uptake of BPA reaches a maximum 3 hours after BPA administration. The tumor-to-brain B-10 ratio was in the range 3:1 from 1 to 9 hours after BPA administration. The B-10 concentrations in tumor are about 25% of the administered amount. Tumor-to-blood B-10 ratios are 12:1 at 3 hours after BPA administration.

Our group also carried out a pharmacological toxicity study with 16 New Zealand white rabbits. This study was needed to obtain an Investigational New Drug (IND) amendment from the FDA to permit the administration of BPA to human subjects, at the pharmacological levels required for the phase-I study, together with neutron irradiation. (Another pharmacological toxicity study, with rats, had been completed by colleagues at BNL/Stonybrook.) Six rabbits received single oral doses of 5000 mg BPA/kg body weight; six rabbits received five daily oral doses of 1000 mg BPA/kg body weight. The four control rabbits received saline. Mice were sacrificed at 2.5 and 4.5 weeks after the first administration. No histomorphologic alterations were noted in the tissue samples. Spontaneous lesions were noted in both control and treated rabbits at essentially comparable incidences.

Others [2-5] have also shown that BPA has favorable toxicological and biodistribution properties. L-p-BPA presumably exploits the large neutral amino acid transport system.[2,3] Finally, Mishima [4] and Hatta [5] have shown selective uptake of BPA in melanoma. The reader is referred to these references for more details on the toxicological and biodistribution properties of BPA.

Subsequently, our group participated in an interinstitutional study with Brookhaven National Laboratory and Stonybrook Medical Center, NY, to determine the biodistribution and pharmacokinetics of BPA in humans. The study was headed by Dr. Allen Meek at Stonybrook Medical Center. This study, performed under an IND application to the FDA and submitted by Dr. Meek, was a necessary step in obtaining an amendment to the IND to use BPA for clinical treatment of patients by BNCT in a phase-I study. Phase-I studies involve dose escalation, evaluation of safety and maximum acceptable toxicity, and pharmacokinetics in human subjects, but involve no requirement or criteria for assessing anti-tumor activity.

Six patients, two with glioblastoma and four with melanoma, participated in the study at T-NEMC, which was carried out in 1991. The patient selection and clinical protocols can be found in reference 6. Patients were given oral doses of racemic BPA as an aqueous slurry with orange juice on the side. Afterwards, blood and urine samples were taken periodically; the B-10 concentrations of these samples were measured by prompt gamma neutron activation analysis (PGNAA) at the MITR-II reactor. Also, skin and tumor samples were taken; the B-10 concentrations of these samples were measured by high resolution alpha-track autoradiography.[7] It was the measurement of the blood and urine concentrations that was a part of this thesis. This chapter focuses on the method (PGNAA) used to analyze these samples and the measured B-10 concentrations.

The two glioblastoma patients were given 90 and 135 mg BPA/kg body weight, at 8 and 9.5 hours, respectively, before their scheduled I-125 implant surgery.[7] Blood and urine samples were taken periodically over the next 3 days. Patients had IV's installed

with heparin locks in place between coliections. Three cc blood samples were collected in heparinized vacutainers. Skin and tumor samples were taken during the implant surgery. The skin samples were 3 x 3 mm. Tumor samples were 1 cc cores from the central/necrotic, intermediate, and outer peritumoral regions. These samples were immediately frozen in acetone and dry ice; they were later analyzed by the high resolution alpha-track technique.[7]

The four melanoma patients were given 90, 135, 135, and 189 mg BPA/kg body weight, 6-12 hours before their scheduled cutaneous nodule biopsy.[7] Blood and urine samples were taken periodically over the next 3 days. Patients had IV's installed with heparin locks in place between collections. Three cc blood samples were collected in heparinized vacutainers.

7.2 PGNAA FOR ANALYSIS OF B-10 CONCENTRATIONS OF BLOOD AND URINE

7.2.1. Prompt gamma neutron activation analysis

The B-10 concentrations of the blood and urine samples were measured by a nuclear technique called prompt gamma neutron activation analysis. A simplified experimental setup is shown in figure 7.1. The B-10 containing sample is placed in a thermal neutron beam. The nuclear reaction used to detect boron by PGNAA is B-10(n,α)Li-7. The recoiling Li-7, initially in an excited state, decays with 94% abundant Doppler broadened 478 keV prompt gammas.[8,9] These prompt gammas can be detected by a High Purity Germanium Detector (HPGE) or a Ge(Li) detector. The count rate of the prompt gammas is a measure of the amount of B-10 in the sample. PGNAA has many advantages over conventional chemical methods of assaying: it is rapid, accurate, nondestructive (allowing for re-analysis), sensitive to the ppm level, generally

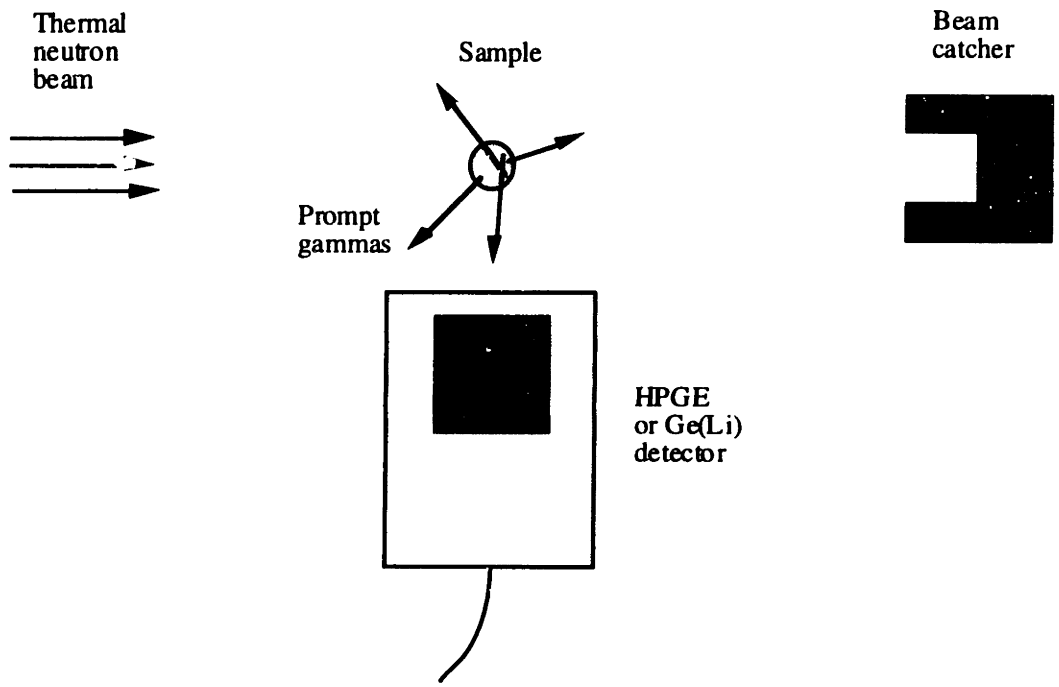

Figure 7.1. Basics of prompt gamma neutron activation analysis (PGNAA). A thermal neutron beam is extracted form the reactor. Radiative capture reactions occur in the sample that has been placed in the beam. Prompt gammas are detected by the HPGE or Ge(Li) detector. A calibration curve giving the count rate of a particular prompt gamma peak versus the amount of element in the sample can be made using standards. The beam catcher stops the neutrons and any photons.

independent of the chemical or physical matrix, and does not require chemical manipulations of the sample.[9]

A schematic of the actual system is shown in figure 7.2. Details of the system are given in reference 9. A beam from the 6SH4 tangential beam port of the MITR-II was first filtered of fast neutrons and photons with a 15 cm long sapphire crystal, and then Bragg diffracted off the basal plane (002) of two slightly misaligned pyrolytic graphite crystals. The beam energy is 0.06 ± 0.01 eV. The steel collimator had two rectangular inserts made of Li-6 carbonate in epoxy. The thermal neutron flux averaged over the beam cross section at the sample, as measured by a high transmission type of fission counter that sampled the entire beam, was 3.5×10^6 n/cm^2-sec at a reactor power of 5 MW. The HPGE detector (Canberra Model GC 3020, 30.4% efficient relative to a 3"x3" NaI crystal at 1332 keV) was 6.5 cm from the sample. The sample was surrounded by a four sided box which had thin Teflon walls that were filled with 0.5 cm of powdered Li-6 carbonate. This shield absorbed neutrons by the Li-6(n,α)H-3 reaction that would otherwise have scattered off the sample and produced radiative capture reactions that would have increased the background seen by the detector. Neutron absorption by Li-6 is unique in that the abundance of prompt gammas is negligible. The B-10 sensitivity of aqueous solutions was about 3 cps/μg, depending of the volume and geometry of the sample.

A sample spectrum for human blood is shown in figure 7.3. There are two peaks within the Doppler broadened B-10 peak - the 472 keV peak of sodium and the 478 keV peak of Li-6. The area of these peaks is subtracted from the total area to get the net B-10 area. To obtain this figure, a blood sample was irradiated for a long time so that the statistical counting error for these two peaks was small ($\pm$5%). A calibration curve of B-10 count rate versus the known B-10 concentration could be made for a fixed reactor power. However, a slightly different approach was used that is more accurate since it accounts for the number of neutrons incident on the sample and does not require a stable

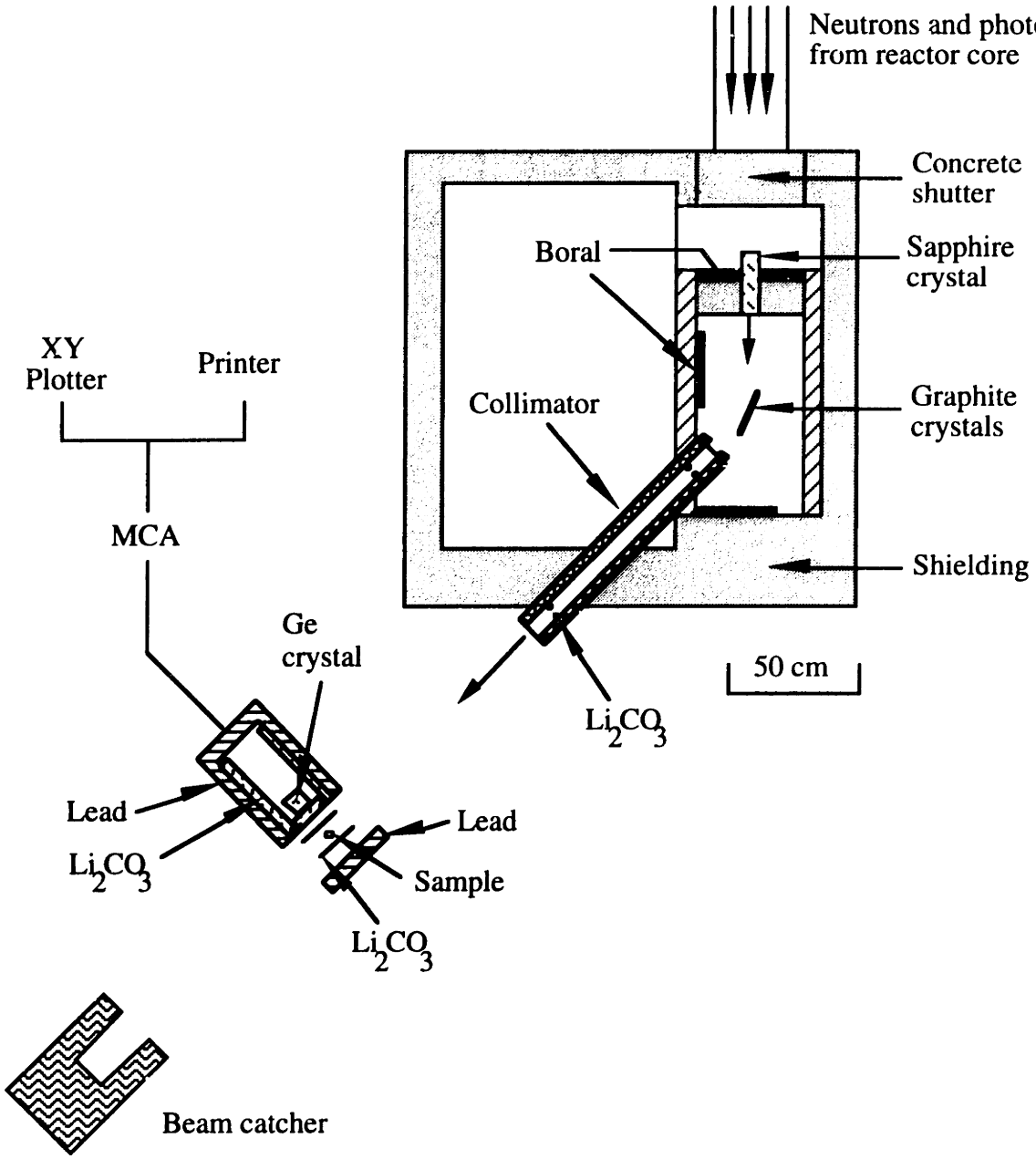

Figure 7.2. Schematic of the prompt gamma neutron activation analysis system at the 6SH4 beam port. The beam from a tangential port is first filtered with 15 cm long sapphire crystal and then Bragg diffracted off the (002) basal plane of two slightly misaligned pyrolytic graphite crystals. The steel collimator had two rectangular inserts of Li-6 carbonate in epoxy. The sample was surrounded by a four sided box which had thin Teflon walls that were filled with 0.5 cm of powdered Li-6 carbonate.

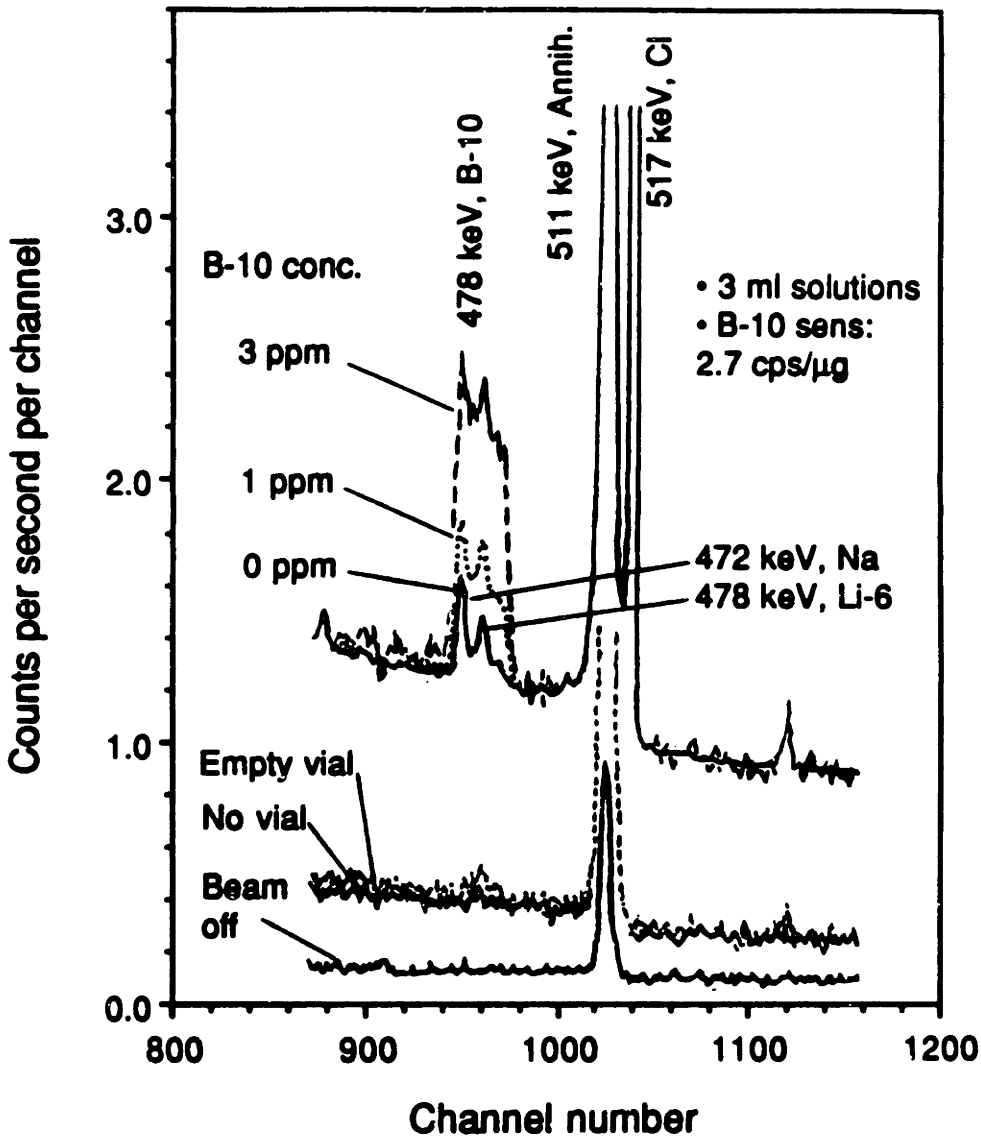

Figure 7.3. Sample spectrum for human blood. The B-10 peak is Doppler broadened. There are two peaks within the B-10 peak - the 472 keV peak of sodium and the 478 keV peak of Li-6. The area of these two peaks is subtracted from the total area to get the net B-10 area. This spectrum was obtained with a HPGE detector. The channel width is 0.56 keV. The H prompt gamma energy is 2223 keV and so is not seen in this part of the spectrum.

beam intensity. The B-10 count rate is normalized to the H capture prompt gamma rate. This eliminates any error in the B-10 count rate that could result from changes in experimental conditions, such as fluctuations in reactor power, or more importantly, positioning of the sample in the beam or changes in the sample - detector distance.

A sample calibration curve is shown in figure 7.4. The net B-10 counts/H counts ratio is plotted versus the known B-10 concentration. The net B-10 counts are the total counts in the Doppler broadened peak minus the contribution from the sodium and Li-6 peaks. The curve is linear ($R^2 = 0.999$). The offset, -0.02 ppm B-10, is negligible; there is little or no background source of B-10 with this system. If there is no B-10 in the sample, the net B-10 counts is zero, within statistical uncertainty. That is, the net B-10 counts is still equal to the total number of counts in the B-10 peak minus the counts due to background. Both the total counts in the B-10 peak and the background counts have an associated statistical uncertainty, and the difference between these counts also has an associated statistical uncertainty. If the difference between the total and background counts is comparable to or less than the uncertainty in the difference, the net B-10 counts is zero, within that statistical uncertainty.

Similar calibration curves to the one shown in figure 7.4 have been made for B-10 in distilled water and B-10 in urine.

7.2.2 Intercalibration of the MIT and BNL prompt gamma systems

The prompt gamma neutron activation analysis systems at MIT and Brookhaven National Laboratory (BNL) have been intercalibrated. As the B-10 levels of blood, urine, and tissue samples need to be determined accurately, the intercalibration was required by the FDA as part of the human BPA biodistribution study. The intercalibration was carried out by measuring ppm levels of B-10 in boric acid solutions.

The detection system included a HPGE detector (Canberra Model GC 3020, 30.4% efficient relative to a 3" x 3" NaI crystal at 1332 keV) , MCA (Canberra

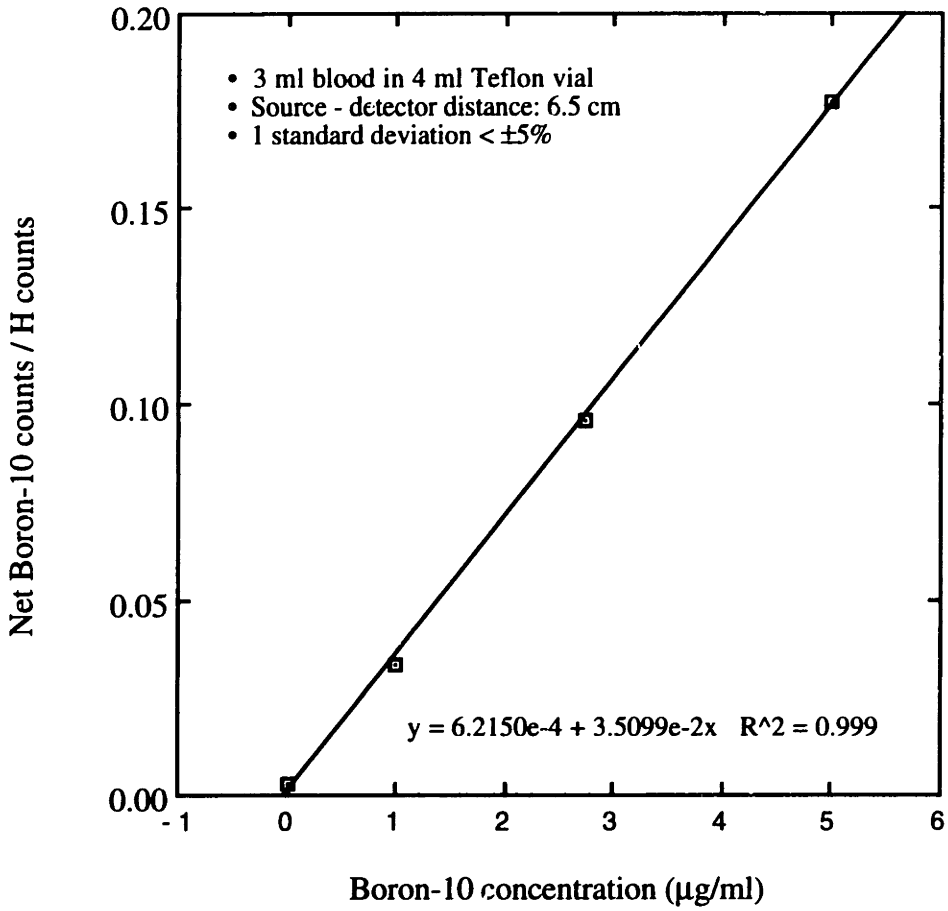

Figure 7.4. Sample calibration curve using the B-10/H ratio method. This calibration curve was prepared for the analysis of B-10 levels in blood in the range 0-5 ppm. The blood standards were made by adding boric acid crystals, with a known B-10 abundance, to human blood. The net B-10 counts was determined by subtracting the contribution of the Na and Li-6 peaks within the Doppler broadened B-10 peak. The curve is linear ($R^2 = 0.999$). The offset, -0.02 ppm B-10, is negligible. Blood samples from the patients were counted under identical conditions - same type of vials, source-to-detector distance, and shielding around the HPGE detector.

Series 85, Model 8505), and associated equipment (Canberra Model 3105 High Voltage Power Supply, Model 2022 Amplifier, and Model 8521 ADC/SCA).

Standard boric acid solutions with concentrations of 10, 20, 30, 40, and 50 ppm B-10 were freshly prepared from boric acid crystals (Fisher Scientific Co., Certified A.C.S. Grade, Certified B-10 abundance of 19.9%) and deionized water. Three ml of each solution were pipetted into 5 ml Teflon vials (Berghof/America). The standard solutions were run sequentially and for a sufficiently long time to obtain a statistical counting error of the B-10 to H prompt gamma count ratio of less than ± 1%. The calibration curve is shown in figure 7.5.

Three boric acid solutions, one prepared at MIT and two prepared at BNL, were independently analyzed on both systems. The concentrations of the solutions prepared at BNL were not known by the MIT team. These samples were run in the same manner as the samples used to obtain the calibration curve. Sample A was run for 18 minutes, which was sufficient to obtain a statistical counting error of the B-10 to H ratio of ± 1.0 %. Sample B had a very low B-10 concentration; time constraints limited this run to 18 minutes, which resulted in a statistical counting error of ± 13%.

The B-10 concentrations of BNL samples A and B were determined using the calibration curve and the measured B-10 / H ratios. This is shown in figure 7.6. The B-10 concentration of MIT sample 1 was determined in a similar manner. However, a slightly different experimental setup and associated calibration curve were used for this sample. Results are summarized in table 7.1.

The most important solution for the intercalibration was BNL sample A. This sample had a B-10 concentration in the range of interest for BNCT, was counted on both systems to within ± 1% statistical counting error, and its concentration was not known beforehand by the MIT team. The prepared concentration was 13.0 ppm. It was measured at 13.8 ± 0.14 ppm at MIT and 13.3 ± 0.13 ppm at BNL. These values are 6±0.06 and 2±0.02 % higher, respectively, than the prepared concentration.

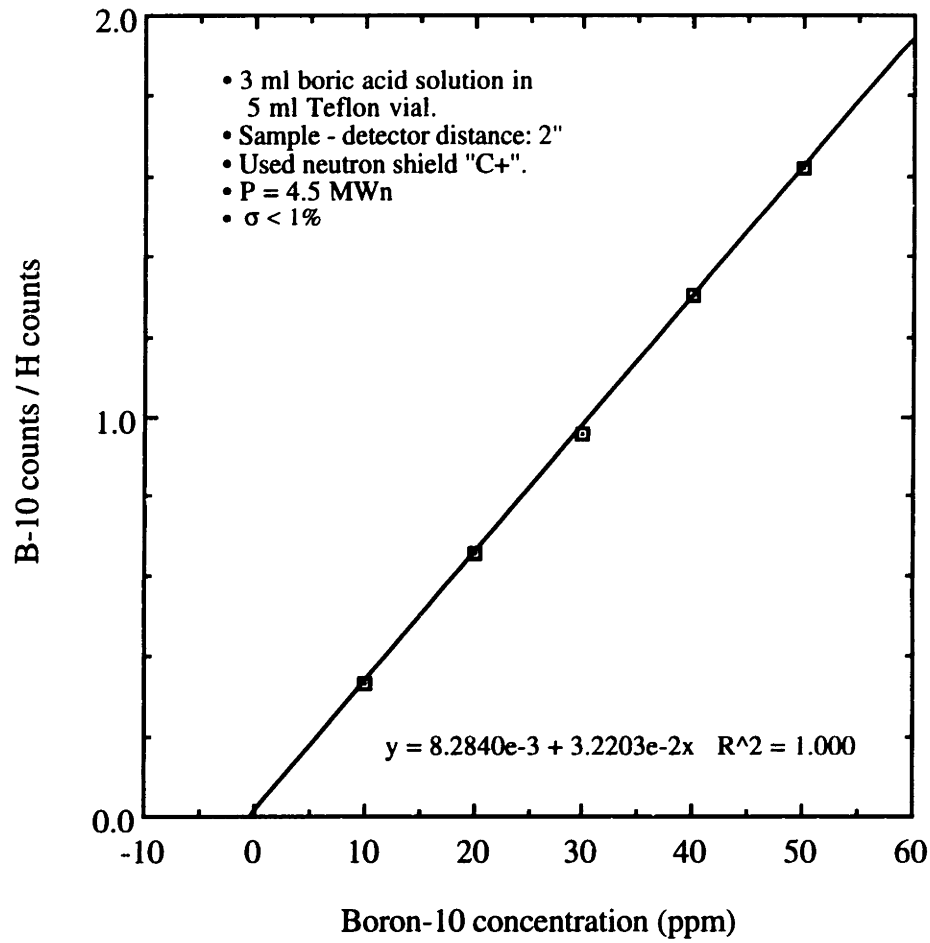

Figure 7.5. Boron-10 calibration curve for the boric acid solutions using the B-10/H ratio method. The curve is linear and the offset is negligible at -0.2 ppm B-10. Neutron shield "C+" specifies the use of two additional Li-6 carbonate shields, one around the sample and one in front of the detector. The Li-6 shields absorb thermal neutrons that have scattered off the sample; Li-6 absorbs neutrons without producing prompt gammas that would increase the background.

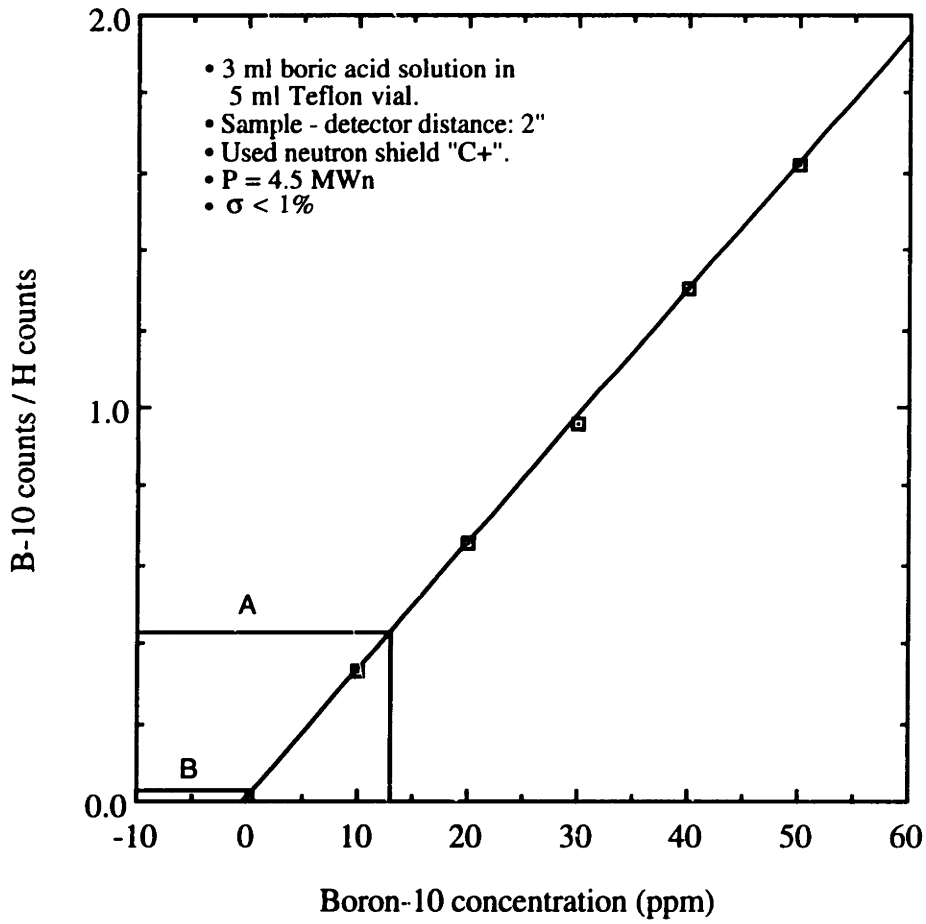

Figure 7.6. Results of assessing the B-10 concentrations in samples A and B from BNL.

Table 7.1. Summary of intercalibration data.

Sample	Prepared at:	Prepared concentration (ppm)	Measured concentration (ppm)	
			BNL*	MIT
1	MIT	10.0	9.4±0.28	9.6±0.43
A	BNL	13.0	13.3±0.13	13.8±0.14
B	BNL	0.8	0.45±0.045	0.67±0.087

* Measured by Peggy Micca.

Good agreement was also found with MIT sample 1, which was prepared at 10.0 ppm. It was measured at 9.6 ± 0.43 ppm at MIT and 9.4 ± 0.28 ppm at BNL.

The concentration of BNL sample B (0.8 ppm B-10) was several times lower than would normally be analyzed by either system for BNCT purposes. Such low boron solutions might need additional quality control procedures, such as determining the B-10 concentration of the vial. However, although this was not done and although the MIT value is based on an extrapolated part of the calibration curve, the MIT value of 0.67 ± 0.087 ppm agrees well with the prepared concentration. BNL's estimate agrees less well at 0.45 ± 0.045 ppm.

The MIT - BNL intercalibration was successful. Results from both laboratories agree within the overall accuracy of the method. A similar intercalibration using blood might also be useful. With blood, there is a prompt gamma peak due to sodium (σ_a = 0.53 barn) at 472 keV, which lies within the Doppler broadened B-10 peak. The peak due to sodium can be seen in figure 7.3. The area of the sodium peak must be subtracted from the total area within the B-10 peak to get the net B-10 counts. An intercalibration with blood at a low B-10 concentration (around 1 ppm B-10) would ensure that the interference due to the sodium peak is appropriately accounted for. An intercalibration with blood would also be more closely associated with the important use of the prompt gamma system, that is, the B-10 analysis of the patient's blood.

7.2.3 Inter-laboratory calibration of B-10 containing samples in a round robin

There was an additional inter-laboratory calibration of samples containing B-10. The intercalibration, involving seven BNCT groups, was directed by Professor Detlef Gabel of the University of Bremen. Each group analyzed samples of chicken liver loaded with various amounts of boron, from 1.8 - 184 ppm B-10. The chicken liver samples were analyzed by Dr. Richard Choi. His results and correspondence are provided in

Appendix G. Results agreed within ±6% of the prepared B-10 concentrations, except for the sample with the lowest concentration (1.8 ppm B-10) which had an error of 18%.

7.3 BLOOD AND URINE B-10 CONCENTRATIONS

Results are now presented for the six patients, two with glioblastoma and four with melanoma, who participated in the study at MIT/T-NEMC. The blood calibration curve is shown in figure 7.7. The blood concentrations for the patients are shown in figures 7.8-7.13. The 1σ error shown on the plots is that due to counting statistics only. There is an additional uncertainty of ±0.2 ppm B-10 for all data shown, which reflects an absolute uncertainty associated with the measurement of these blood samples. The urine calibration curve is shown in figure 7.14. The urine concentrations for the patients are shown in figures 7.15-7.20. The B-10 concentrations of the urine samples are much higher than those of the blood samples; therefore, the measurement error is smaller than the error due to counting statistics. The counting statistics error on the urine samples was ±4%.

A one-compartment oral absorption model, assuming first order absorption and first order elimination, was used to fit the blood data.[10] For this model, the equation for the concentration of B-10 in blood is:

$$y = \left(\frac{FD}{V}\right)\left(\frac{a}{a-b}\right)\left(e^{-at} - e^{-bt}\right) \qquad (7.1)$$

where

y = the B-10 concentration (ppm) in blood at time t,

F = the absorbed fraction of the absorbed dose,

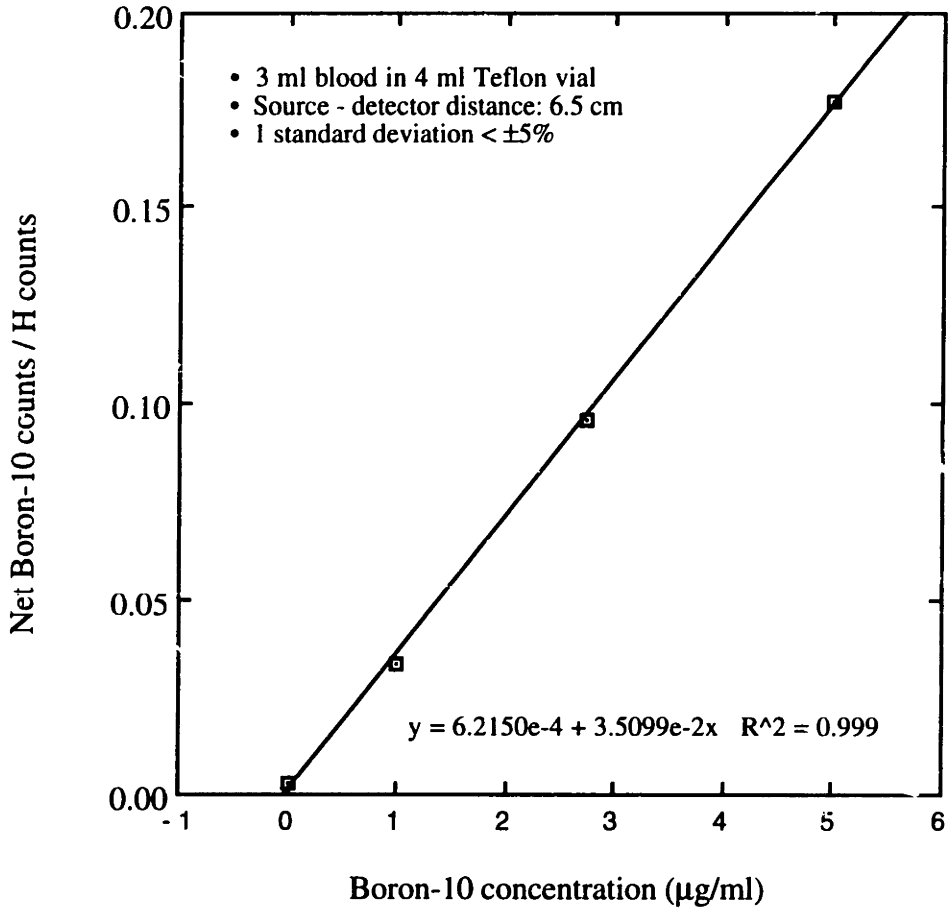

Figure 7.7. Boron-10 calibration curve for blood. The blood standards were made by adding boric acid crystals, with a known B-10 abundance, to human blood. The net B-10 counts was determined by subtracting the contribution of the Na and Li-6 peaks within the Doppler broadened B-10 peak. The offset, -0.02 ppm B-10, is negligible. Blood samples from the patients were counted under identical conditions - same type of vials, source-to-detector distance, and shielding around the HPGE detector. The error due to counting statistics alone is ±5%; an additional random error due to the method is ±0.2 ppm B-10.

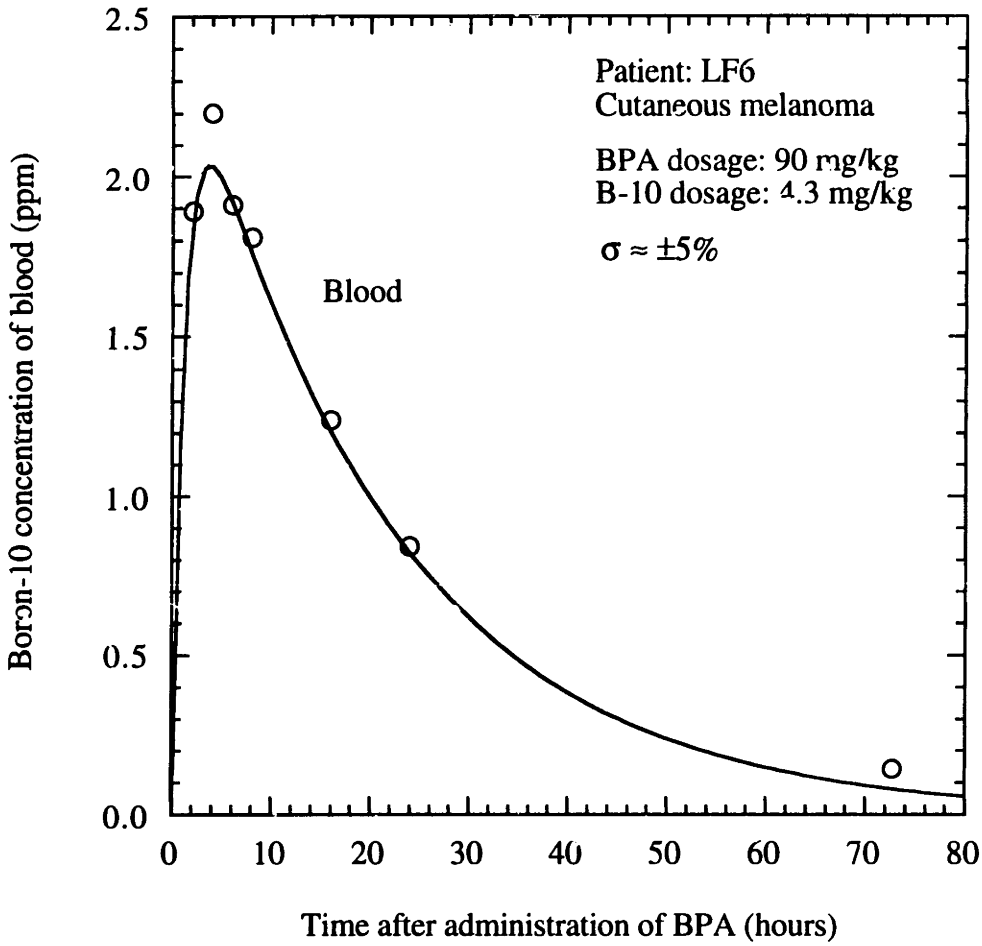

Figure 7.8. Boron-10 concentration of blood for patient LF6. Open circles: B-10 concentrations in blood samples as measured by PGNAA. The curve fit is based on a one-compartment oral absorption model, assuming first order absorption and first order elimination as discussed in the text. The error due to counting statistics alone is ±5%; an additional random error due to the method is ±0.2 ppm B-10.

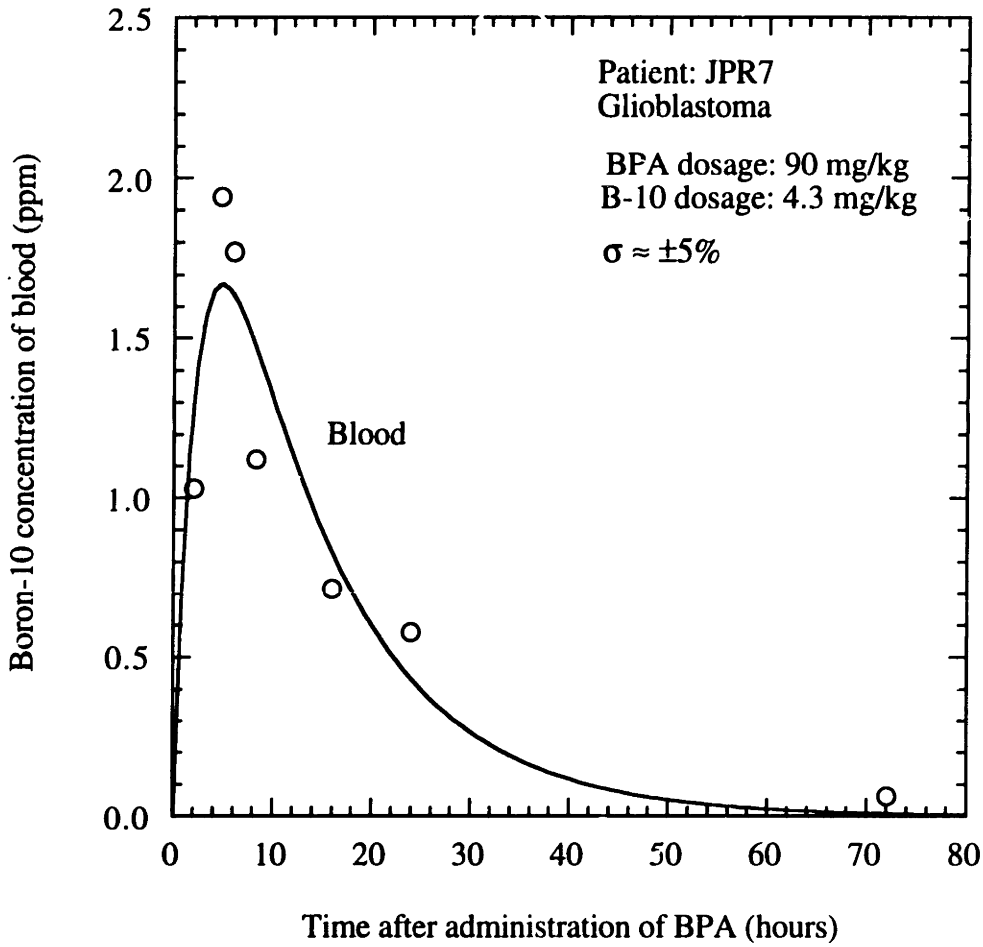

Figure 7.9. Boron-10 concentration of blood for patient JPR7. Open circles: B-10 concentrations in blood samples as measured by PGNAA. The curve fit is based on a one compartment oral absorption model, assuming first order absorption and first order elimination as discussed in the text. The error due to counting statistics alone is ±5%; an additional random error due to the method is ±0.2 ppm B-10.

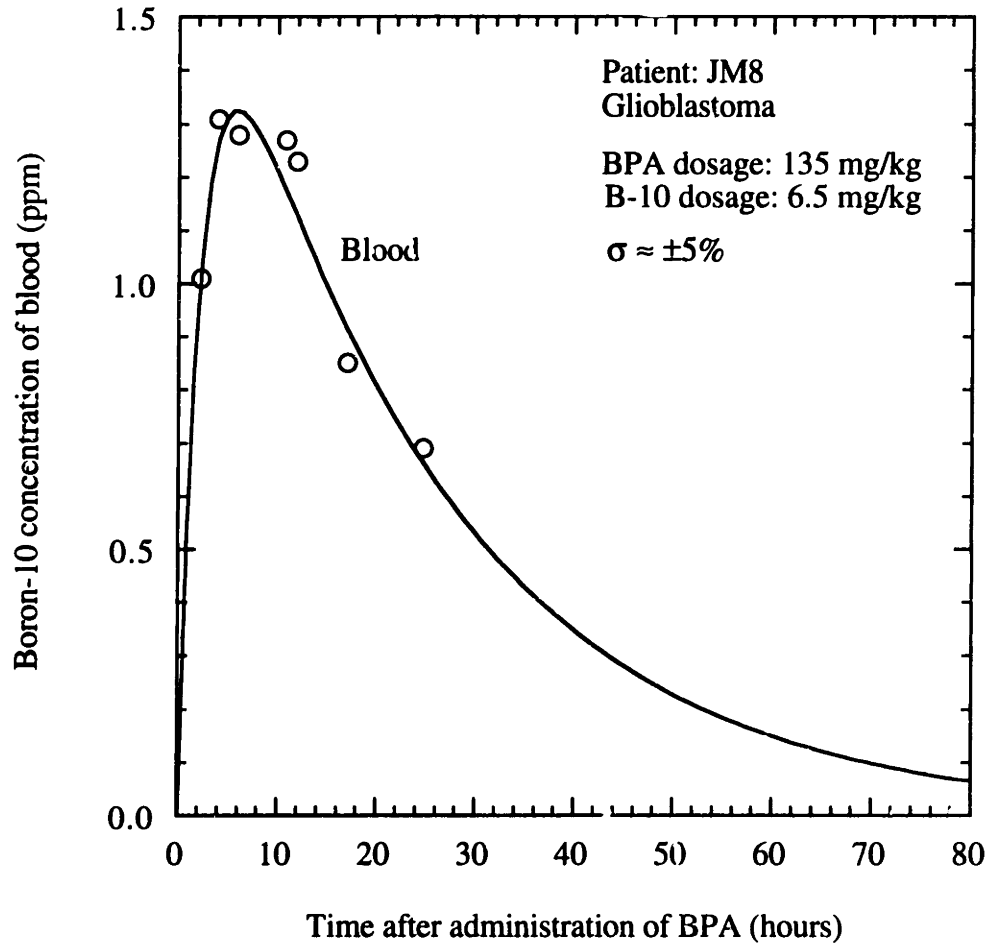

Figure 7.10. Boron-10 concentration of blood for patient JM8. Open circles: B-10 concentrations in blood samples as measured by PGNAA. The curve fit is based on a one-compartment oral absorption model, assuming first order absorption and first order elimination as discussed in the text. The error due to counting statistics alone is ±5%; an additional random error due to the method is ±0.2 ppm B-10.

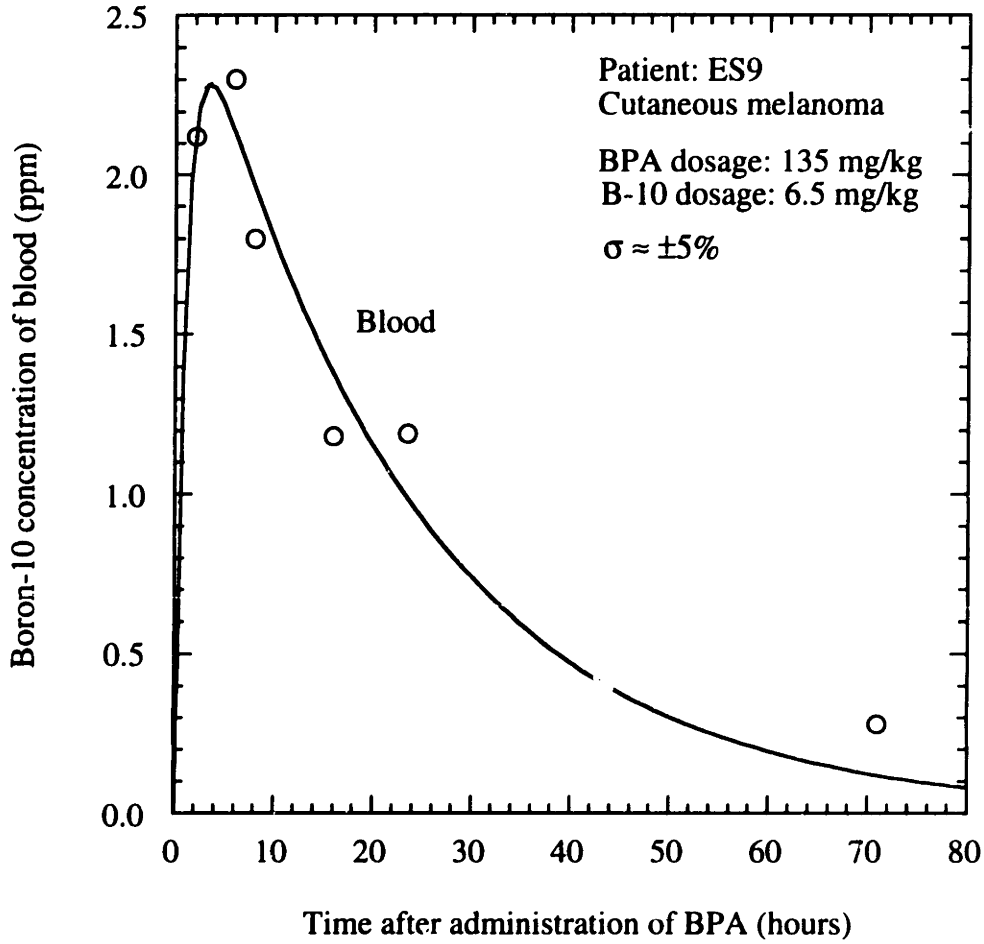

Figure 7.11. Boron-10 concentration of blood for patient ES9. Open circles: B-10 concentrations in blood samples as measured by PGNAA. The curve fit is based on a one-compartment oral absorption model, assuming first order absorption and first order elimination as discussed in the text. The error due to counting statistics alone is ±5%; an additional random error due to the method is ±0.2 ppm B-10.

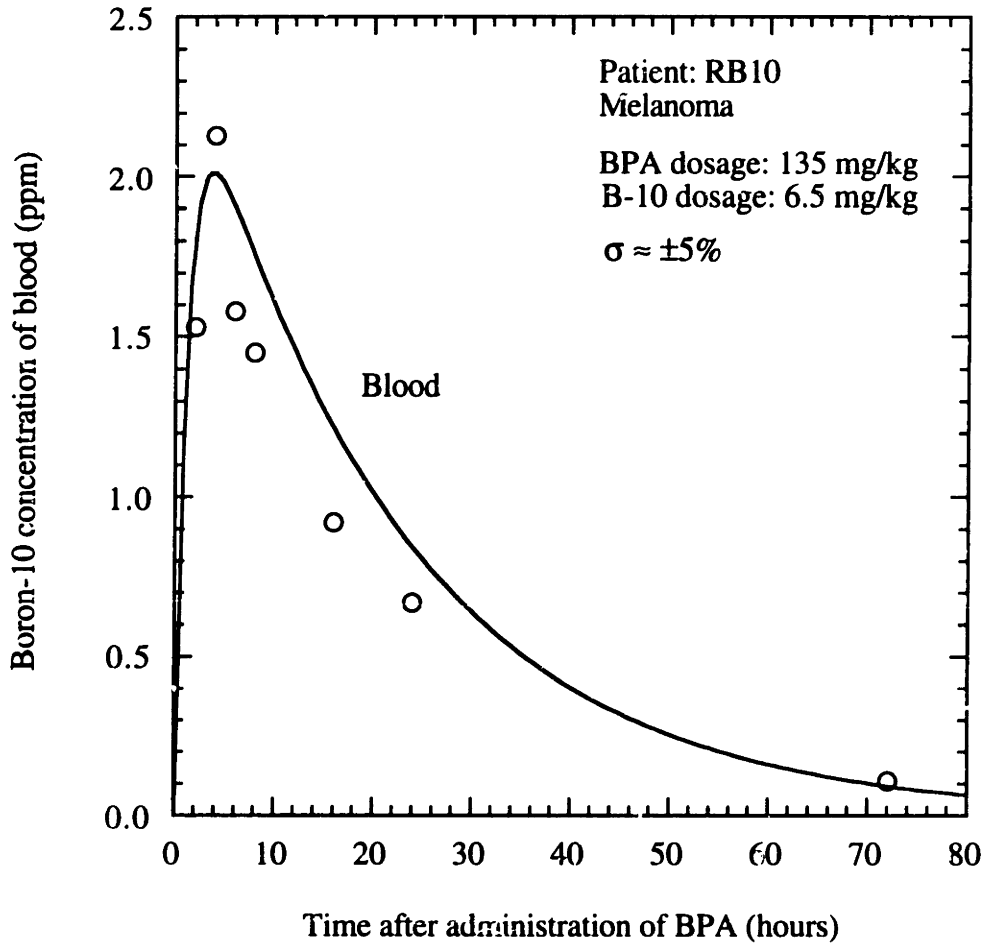

Figure 7.12. Boron-10 concentration of blood for patient RB10. Open circles: B-10 concentrations in blood samples as measured by PGNAA. The curve fit is based on a one-compartment oral absorption model, assuming first order absorption and first order elimination as discussed in the text. The error due to counting statistics alone is ±5%; an additional random error due to the method is ±0.2 ppm B-10.

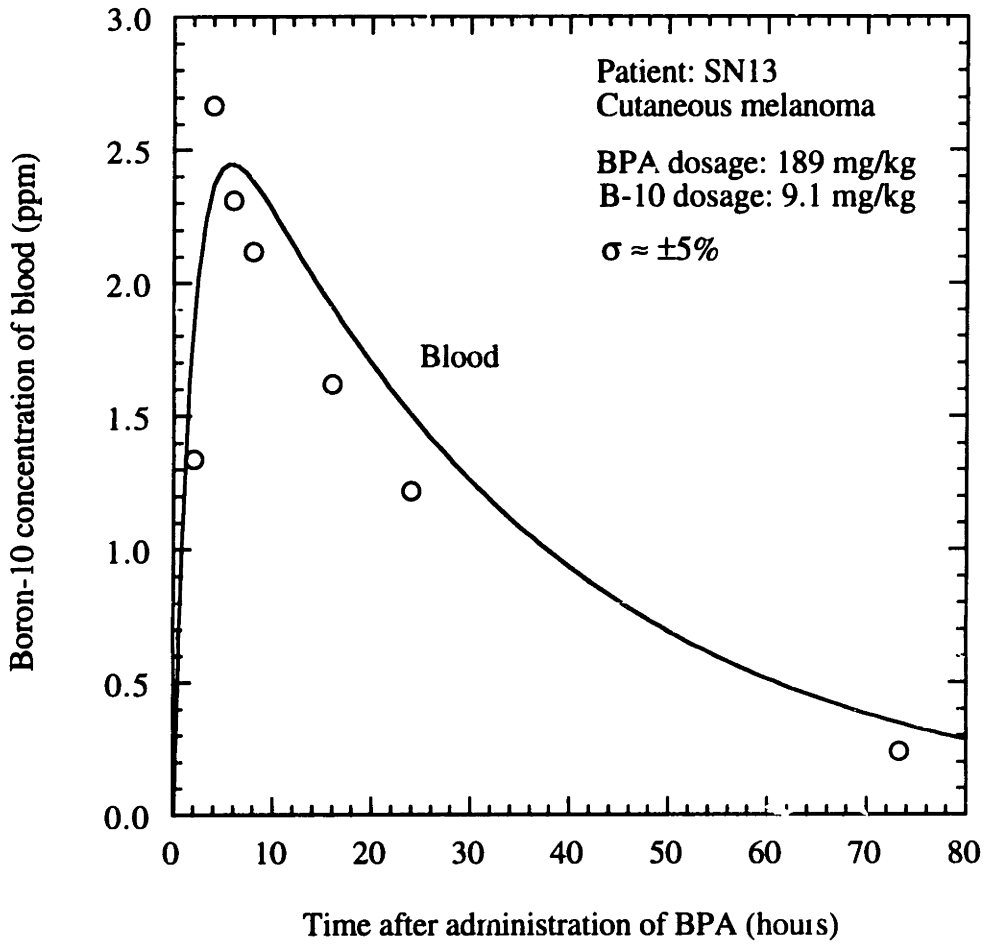

Figure 7.13. Boron-10 concentration of blood for patient SN13. Open circles: B-10 concentrations in blood samples as measured by PGNAA. The curve fit is based on a one-compartment oral absorption model, assuming first order absorption and first order elimination as discussed in the text. The error due to counting statistics alone is ±5%; an additional random error due to the method is ±0.2 ppm B-10.

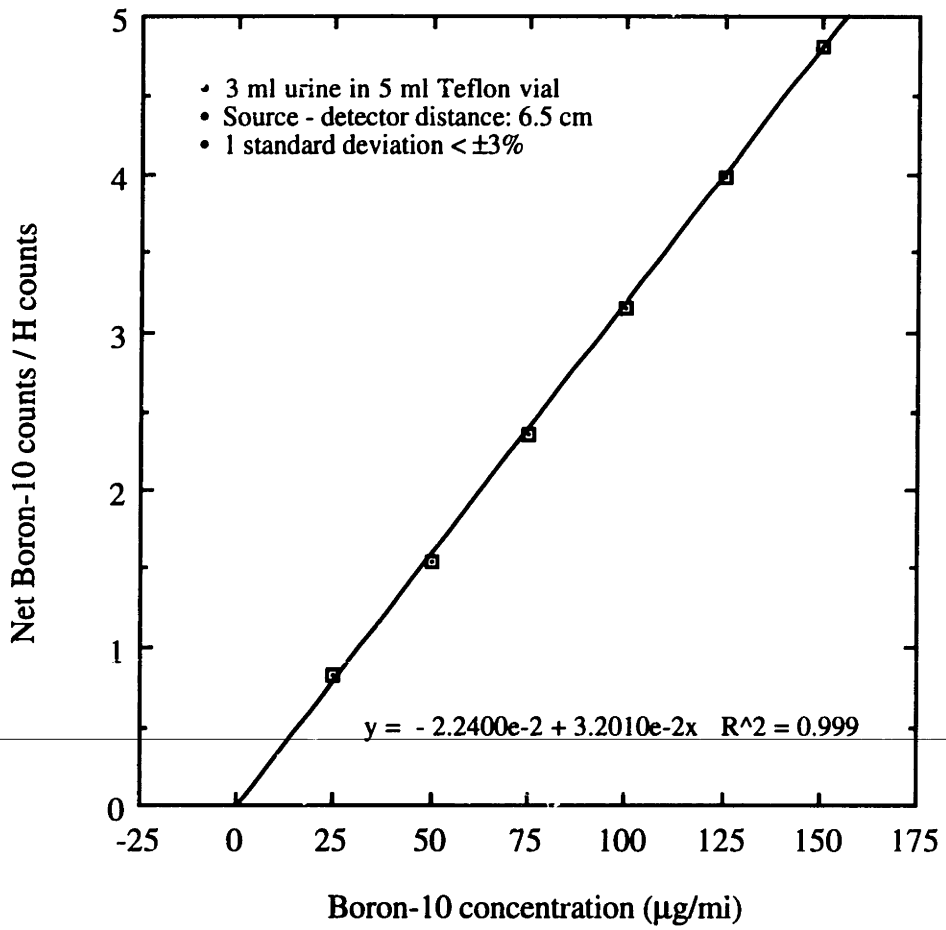

Figure 7.14. Boron-10 calibration curve for urine. The urine standards were made by adding boric acid crystals, with a known B-10 abundance, to urine. The net B-10 counts was determined by subtracting the contribution of the Na and Li-6 peaks within the Doppler broadened B-10 peak; this effect is less than 1% for the high B-10 concentrations measured here. The offset is negligible. Urine samples from the patients were counted under identical conditions - same type of vials, source-to-detector distance, and shielding around the HPGE detector.

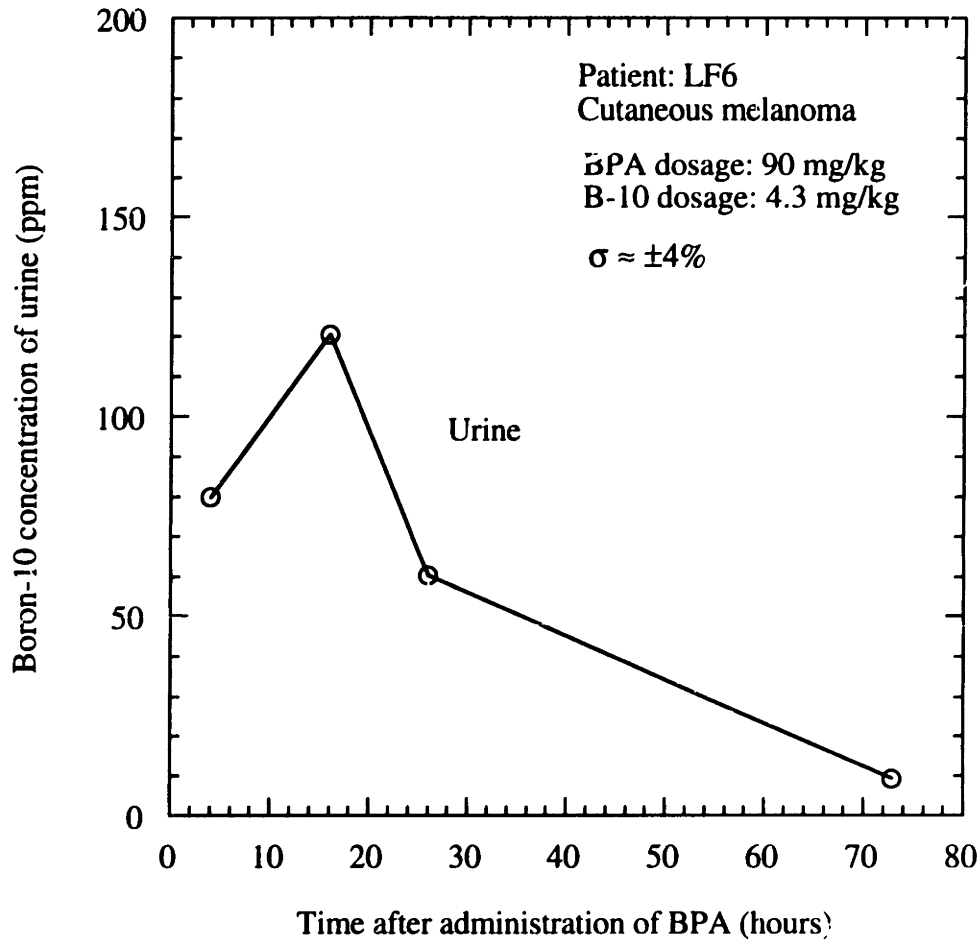

Figure 7.15. Boron-10 concentration of urine for patient LF6. Open circles: B-10 concentrations in urine samples as measured by PGNAA. The error due to counting statistics alone is ±4%; an additional random error due to the method is ±0.2 ppm B-10.

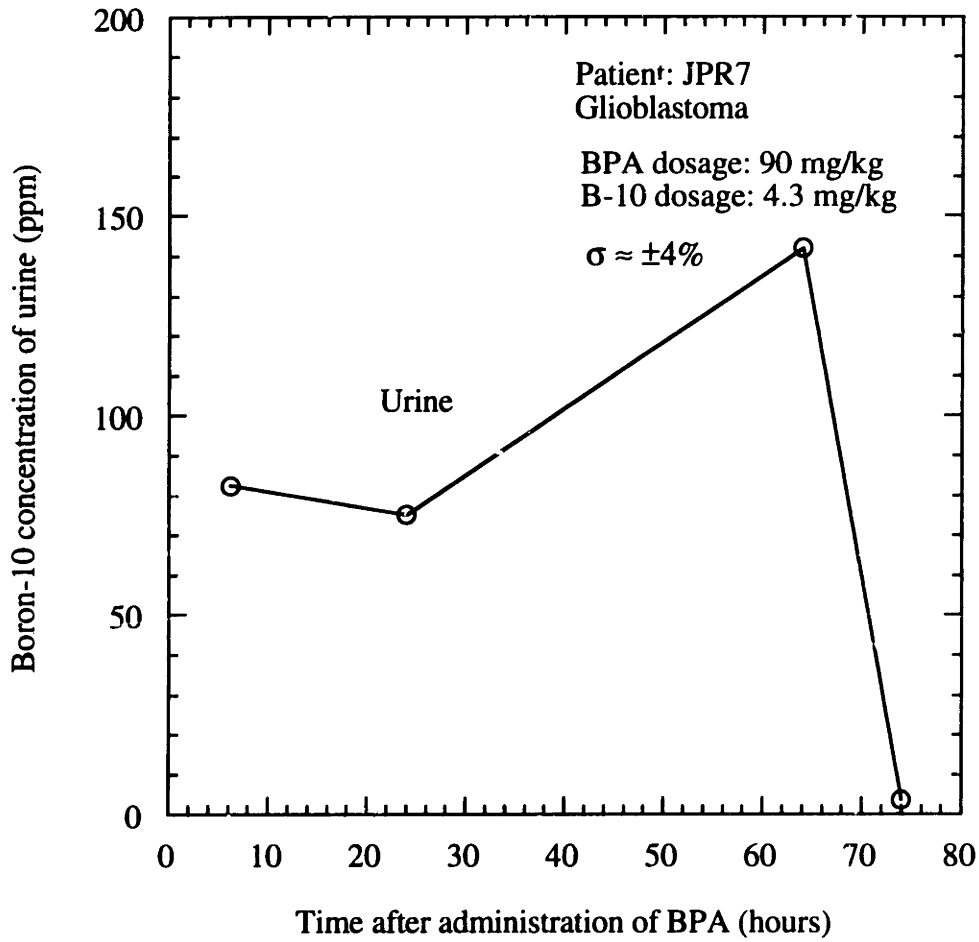

Figure 7.16. Boron-10 concentration of urine for patient JPR7. Open circles: B-10 concentrations in urine samples as measured by PGNAA. The error due to counting statistics alone is ±4%; an additional random error due to the method is ±0.2 ppm B-10.

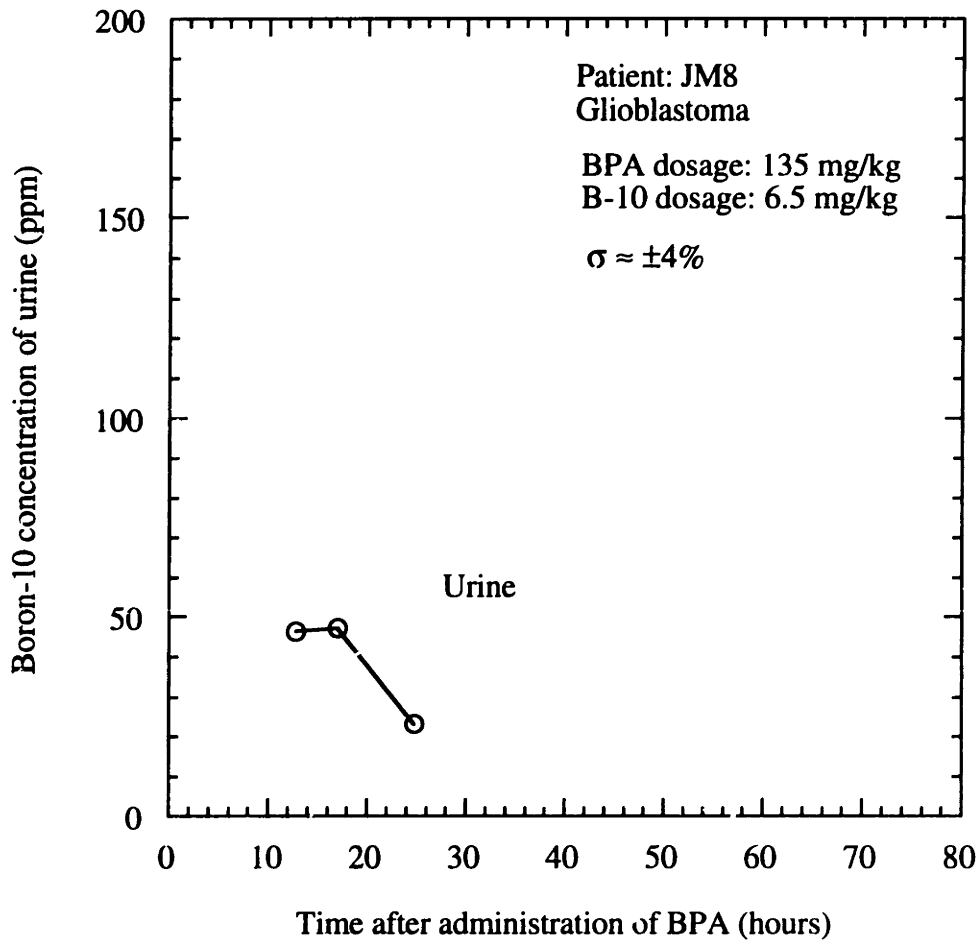

Figure 7.17. Boron-10 concentration of urine for patient JM8. Open circles: B-10 concentrations in urine samples as measured by PGNAA. The error due to counting statistics alone is ±4%; an additional random error due to the method is ±0.2 ppm B-10.

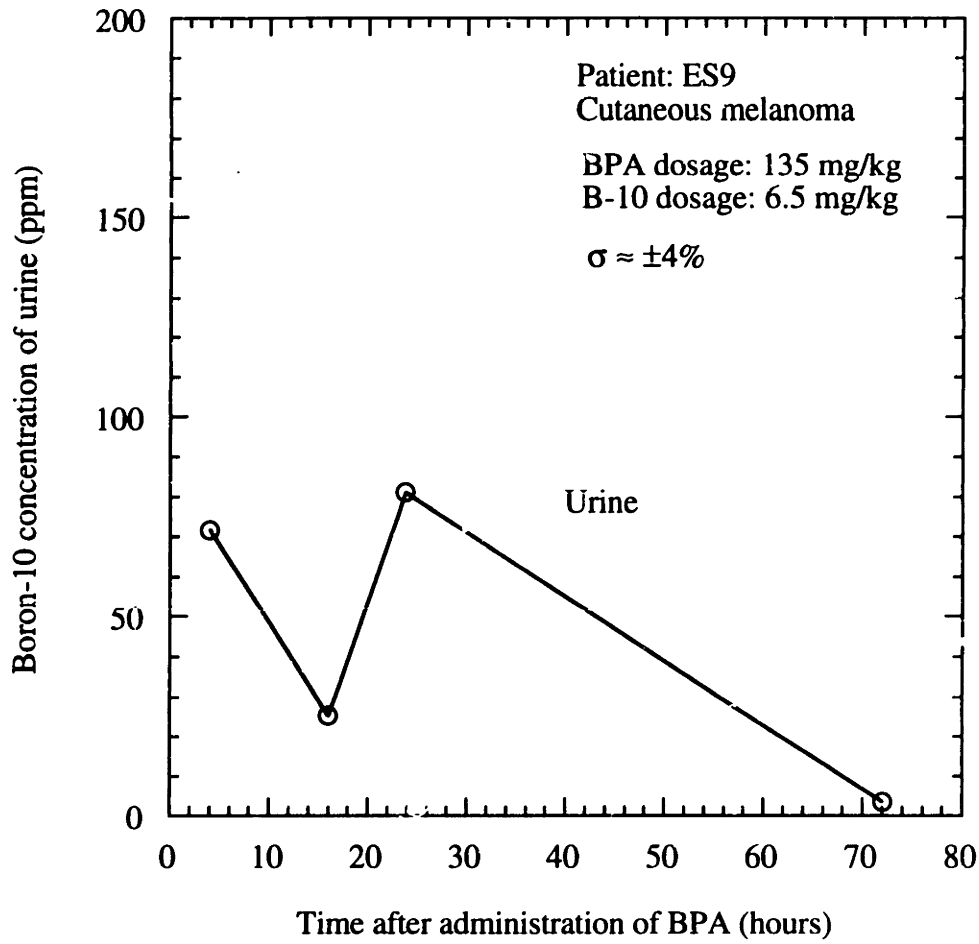

Figure 7.18. Boron-10 concentration of urine for patient ES9. Open circles: B-10 concentrations in urine samples as measured by PGNAA. The error due to counting statistics alone is ±4%; an additional random error due to the method is ±0.2 ppm B-10.

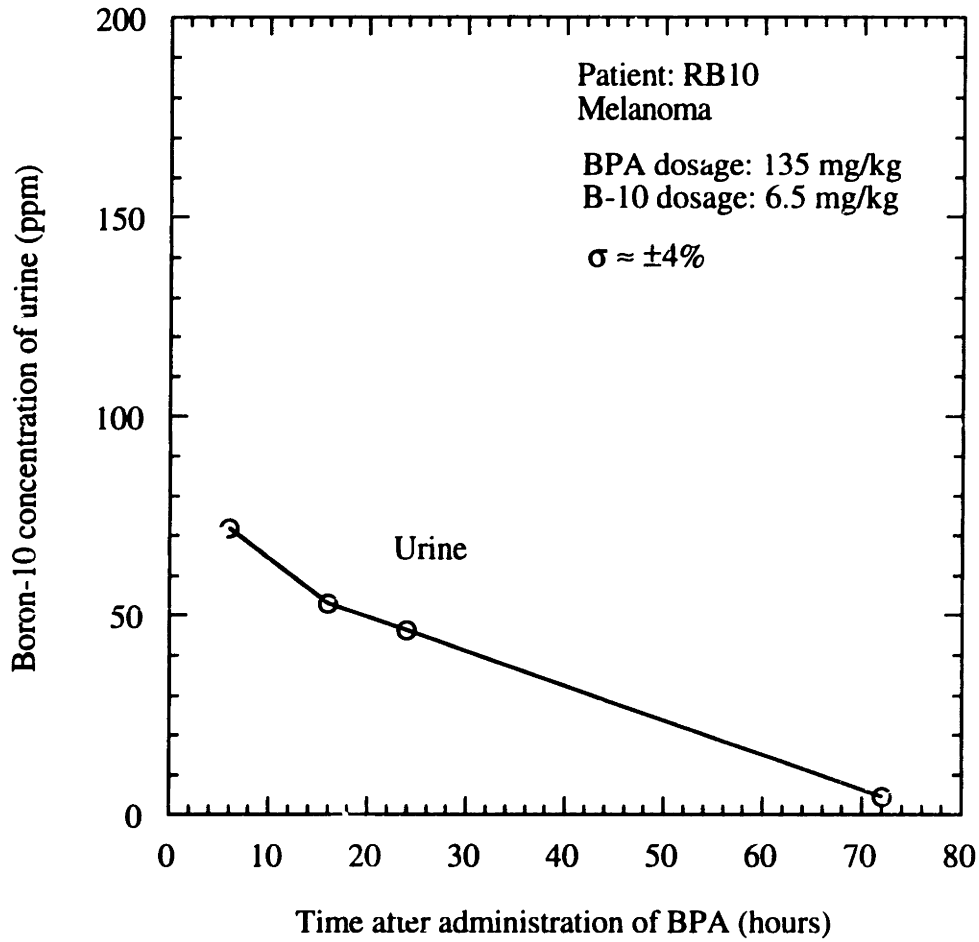

Figure 7.19. Boron-10 concentration of urine for patient RB10. Open circles: B-10 concentrations in urine samples as measured by PGNAA. The error due to counting statistics alone is ±4%; an additional random error due to the method is ±0.2 ppm B-10.

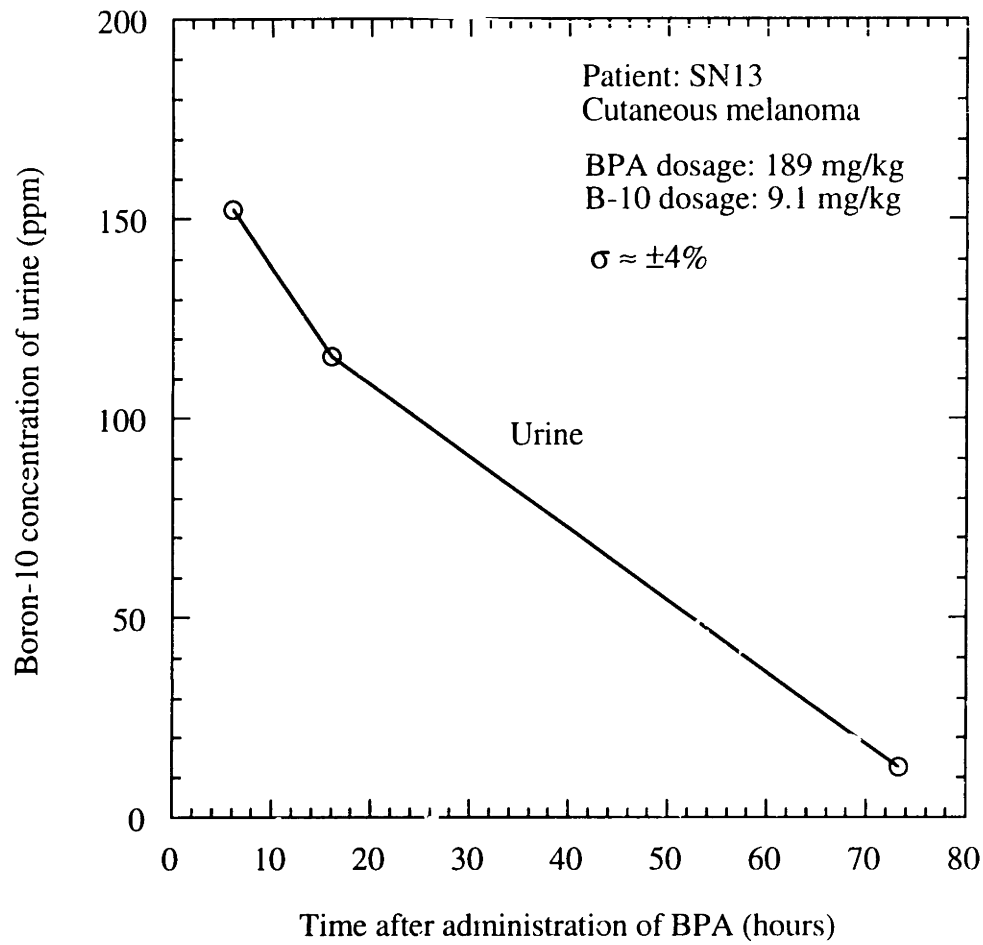

Figure 7.20. Boron-10 concentration of urine for patient SN13. Open circles: B-10 concentrations in urine samples as measured by PGNAA. The error due to counting statistics alone is ±4%; an additional random error due to the method is ±0.2 ppm B-10.

D = the administered dose (mg of B-10), assumed to be given orally in a single dose,

V = the total body water (kg), assumed to be 65% of the total body weight,

a = the first order rate constant for absorption (hr^{-1}),

b = the first order rate constant for elimination (hr^{-1}),

t = time after administration (hr).

The absorbed fraction is the fraction of the administered B-10 that gets into the single compartment. If all of the administered B-10 is absorbed from the gut, then F = 1. The two rate constants reflect how rapidly the B-10 is absorbed and excreted from the compartment. It will be shown that the B-10 concentration appears more rapidly in blood than it is excreted (b<a). The parameters (F, a, b) in equation 7.1 were fit to the measured blood concentrations by successive iterations of the curve fitting function.[10] These parameters are shown in table 7.2.

The pharmacokinetic parameters are highly variable. The absorbed fraction (F) varies by a factor of two; the absorption and elimination constants also vary by a factor of two. A test dose of BPA, therefore, will have to be given to each patient, and the absorbed fraction estimated from the results of a B-10 analysis of a blood sample. Then, the amount of BPA that needs to be administered to obtain a desired B-10 blood concentration will be known. The absorbed fraction, F, might depend on the administered amount of BPA. The variability in the absorption and elimination constants is less of a problem. Their variability will mainly affect the time interval needed between the administration of the BPA and the start of the neutron irradiation. Since the elimination constant is only about 0.04 hr^{-1}, the blood concentration will drop only 4% during an hour long irradiation. This assumes that the neutron irradiation will commence sometime after the peak occurs in the B-10 blood level.

Table 7.2. Pharmacokinetic data for the blood of the patients in this study.

Patient	Weight (kg)	V (kg)	D (mg B-10)	F (%)	a (hr^{-1})	b (hr^{-1})	$t_{1/2}$ absolute (hr)	$t_{1/2}$ elim (hr)
LF6	64.5	41.9	284.4	35.80	0.8113	0.0476	0.85	14.56
JPR7	91.0	59.2	401.3	36.60	0.421	0.0816	1.72	8.49
JM8	75.0	48.8	496.1	16.71	0.4430	0.0421	1.56	16.46
ES9	63.6	41.3	420.7	26.18	0.9237	0.0444	0.75	15.61
RB10	70.4	45.3	465.7	23.28	0.8075	0.0459	0.86	15.10
SN13	93.0	60.5	861.3	20.41	0.5299	0.0298	1.31	23.26

The B-10 concentrations in tumor and healthy tissue are shown in table 7.3.[7] Also shown is the B-10 concentration in blood at the time the biopsies were taken. For the two glioblastoma patients, patient JPR7 had a tumor B-10 concentration of 11.2±1.1 ppm, blood concentration of 1.5 ppm, and a tumor-to-blood ratio of 7.0. Patient JM8 had a tumor B-10 concentration of 5.1±0.2 ppm, blood concentration of 1.2 ppm, and a tumor-to-blood ratio of 4.2. The measurement errors associated with the tumor-to-blood ratios is estimated at ±10%. These tumor-to-blood ratios are greater than the 3:1 ratio thought needed for effective therapeutic treatment.

For the two melanoma patients ES9 and RB10, patient ES9 had a tumor B-10 concentration of 12.1 ppm, blood concentration of 2.2 ppm, and a tumor-to-blood ratio of 5.5. The tumor-to-normal tissue ratio was 20. Patient RB10 had a tumor B-10 concentrations of 10.5 and 11.5 ppm, blood concentration of 1.8 ppm, and an average tumor-to-blood ratio of 6.1. Again, the measurement error associated with these ratios is ±10%. These tumor-to-blood ratios are also greater than 3:1 ratio thought needed for effective therapeutic treatment.

Melanoma patients LF6 and SN13 did not have sufficiently high tumor-to-blood concentrations.

For orally administered BPA, then, uptake of B-10 in blood, tumor, and healthy tissue was found to be highly variable. Before treatment, therefore, each patient needs to undergo an uptake and biodistribution study with a test dose of BPA. B-10 concentrations need to be determined in tumor, healthy tissue, blood, and urine. Only if there is acceptable uptake of BPA, and acceptable tumor-to-blood and tumor-to-healthy tissue ratios would the patient be treated by BNCT. The uptake and biodistribution study using a test dose has been incorporated in the MIT/T-NEMC Clinical Protocol.

Table 7.3. Summary of BPA concentrations in tumor and normal tissue.

Patient	Tumor type	BPA dosage (mg/kg)	Time[a] (hours)	B-10 (ppm) Tumor tissue	B-10 (ppm) Normal tissue	B-10 (ppm) Blood[b] sample	Tumor/ blood ratio[d]	Tumor/ healthy tissue ratio[d]
LF6	Cutaneous melanoma	90	6	0.2	-	2.1	0.095	-
JPR7	Glioblastoma	90	8	10.1, 12.3	-	1.6	7.0	-
JM8	Glioblastoma	135	9.5	4.9, 5.3	-	1.2	4.2	-
ES9	Cutaneous melanoma	135	6	12.1	0.6	2.2	5.5	20.
RB10	Melanoma (axillary node biopsy)	135	6.5	10.5, 11.5	0.2[c], 0.1[c]	1.8	6.1	-
SN13	Cutaneous melanoma	189	7.5	3.0	0.8	2.3	1.3	3.8

a. Time between BPA administration and the taking of the biopsy.
b. At the time the biopsy was taken.
c. Concentration in necrotic tumor.
d. Estimated total measurement uncertainties for the tumor-to-blood and tumor-to-healthy tissue ratios is ±10%. Note that the variability in the B-10 concentration within the same tumor is 10-20%.

7.4 SUMMARY

Blood and urine samples from two glioblastoma and four melanoma patients who had been administered BPA orally were analyzed for B-10 concentration by PGNAA. This study was needed to obtain an IND amendment from the FDA to permit the administration of BPA to human subjects, at the pharmacological levels required for the phase-I study, together with neutron irradiation. Calibration curves were made for B-10 in urine and blood, and the prompt gamma system was intercalibrated with BNL and other laboratories. Blood and urine B-10 concentrations were presented for each patient. A one-compartment oral absorption model, assuming first order absorption and first order elimination, was used to fit the blood data. The absorbed fractions and the absorption and elimination rate constants were determined; parameters varied by a factor among the patients. When combined with tumor and healthy tissue B-10 concentrations determined by high resolution alpha-track autoradiography, tumor-to-blood ratios (ranging from 4.2 - 7.0) were favorable in four of the six patients, while tumor-to-healthy tissue ratios (3.8, 20) were favorable in both patients in which healthy tissue samples were taken. Because of the variability in uptake for orally administered BPA, an uptake and biodistribution study for each patient using a test dose of BPA has been incorporated in the MIT/T-NEMC Clinical Protocol.

In the next chapter, the thesis work is summarized, and conclusions and recommendations for future work are provided.

References

1. G. Solares, R. Zamenhof, S. Saris, D. Wazer, S. Kerley, M. Joyce, H. Madoc-Jones, L. Adelman, and O. Harling, "Biodistributions and Pharmacokinetics of p-Boronophenylalanine in C57BL/6 mice with GL261 Intracerebral Tumors, and Survival Following Neutron Capture Therapy," in *Progress in Neutron Capture Therapy for Cancer* (Barry J. Allen, Douglas E. Moore, Baiba V. Harrington, eds., Plenum Press, New York, 1992).

2. J. A. Coderre, J. D. Glass, R. G. Fairchild, et al, "Selective targeting of boronophenylalanine to melanoma in BALB/c mice for neutron capture therapy," Can. Res. **47**, 6377-6383 (1987).

3. J. A. Coderre, J. D. Glass, R. G. Fairchild, P. L. Micca, I. Fand, and D. D. Joel, "Selective delivery of boron by the melanin precursors analogue p-boronophenylalanine to tumors other then melanoma," Can. Res. **50**, 138-141 (1990).

4. S. Hatta, M. Tsuji, C. Handa, M. Ichihasi, and Y. Mishima, "Selective Affinity of ^{10}B-paraboronophenylalanine HCl to Malignant Melanoma," in *Boron Neutron Capture Therapy for Tumors* (H. Hatanaka, ed., Niigata, Japan, Nishimura Co., Ltd., 1986).

5. Y. Mishima, M. Ichihashi, M. Tsui, S. Hatta, M. Ueda, C. Honda, and T. Susuki, "Treatment of malignant melanoma by single thermal neutron capture therapy with melanoma-seeking ^{10}B compound," Lancet. **2**, 388-389 (1989).

6. A Clinical Trial of Boron Neutron Capture Therapy for Cutaneous and Subcutaneous Melanoma at the New England Medical Center and the MIT Research Reactor - Proposed Clinical Protocol, Nuclear Reactor Laboratory, MIT.

7. Guido Solares, *High Resolution Alpha Track Autoradiography and Biological Studies of Boron Neutron Capture Therapy*, (Ph.D. Thesis, Massachusetts Institute of Technology, 1991).

8. C. M. Lederer, Virginia Shirley, *Table of Isotopes,* 7th ed. (Lawrence Berkeley Laboratory, Wiley-Interscience Publication, John Wiley & Sons, Inc., N.Y., 1978).

9. R. Rogus, O.K. Harling, I. Olmez, and S. Wirdzek, "Boron-10 prompt gamma analysis using a diffracted neutron beam," in *Progress in Neutron Capture Therapy for Cancer,* (Barry Allen, Douglas Moore, Baiba Harrington, eds., Plenum Press, New York, 1992).

10. Oral absorption model curve fitting done by Dr. Allen Meek.

CHAPTER 8. CONCLUSIONS AND RECOMMENDATIONS FOR FUTURE WORK

8.1 SUMMARY AND CONCLUSIONS

The T-NEMC/MIT BNCT research program was initiated in 1988 and is now in its sixth year. In place are all the technical elements and all the necessary federal and institutional administrative approvals to initiate a phase-I clinical study of neutron capture therapy for the treatment of subcutaneous melanoma in the extremities. Most of the work in this thesis was dedicated towards developing the mixed field dosimetry needed to accurately measure the radiation doses within realistic phantoms, to design and dosimetrically characterize a "final" epithermal neutron beam that has sufficient quality and intensity to be used clinically, to develop and write a set of Procedures pursuant to MITR-II Technical Specification No. 6.5 which covers irradiations of patients in the medical room, to make modifications to the medical room in preparation for clinical trials, to improve a prompt gamma neutron activation analysis system for the measurement of low ppm B-10 levels in blood, urine, and tissue samples, to participate in two inter-laboratory calibrations with samples containing B-10, and finally to use the prompt gamma system to measure the B-10 levels in blood and urine samples from patients who volunteered in a human biodistribution study of the drug BPA.

A clinical protocol for the mixed field dosimetry has been developed and presented. The photon and fast neutron doses are measured with ionization chambers using the dual chamber technique. Buildup caps were designed and machined for these chambers. The electrometer and ionization chambers have been officially calibrated by the University of Wisconsin Accredited Dosimetry Calibration Laboratory. The thermal

neutron flux is measured with gold foils using the cadmium difference technique. The dosimetry protocol has been carefully reviewed by Professor Steven Goetsch of U.C.L.A., an expert on mixed field dosimetry. Dr. Goetsch also visited us for two days at the NRL to discuss the dosimetry protocol and to review the experimental method. Four sets of Procedures on the dosimetry were written; they were reviewed and approved pursuant to MITR Technical Specification No. 6.5.

Over 20 different epithermal neutron beams were designed, installed, and characterized in air and along a central axis in realistic phantoms. A new head phantom was made after an improved construction technique was developed. Some beams were characterized with more than one phantom, with different delimiters, or were characterized in off-axis positions as well as along the central axis. In two of these beams, the experimentally determined central and off-axis data were compared with dosimetry generated by MCNP. One of these beams, the M67 beam, was selected as the beam that would be used in the initial clinical trials.

The M67 clinical beam is moderated with D_2O, filtered with cadmium, aluminum, and sulfur, and has a final photon shield of bismuth. It has a 15 cm diameter delimiter made of lithiated paraffin, and whole body shields made of borated polyethylene to minimize the radiation doses to the patient outside the treatment area. Dosimetry has been provided assuming the tissue of interest is muscle or brain. For muscle kermas and the standard size ellipsoidal head phantom, the M67 clinical beam has an AR of 2.1, ADDR of 7.7 RBE cGy/min, and an AD of 6.6 cm. For brain kermas and the standard size ellipsoidal head phantom, the clinical beam has an AR of 2.4, ADDR of 7.4 RBE cGy/min, and an AD of 6.6 cm. For these advantage parameters, the B-10 concentrations were assumed to be 30 ppm in tumor tissue and 7.5 ppm in healthy tissue. The clinical beam has good skin sparing; the total tumor dose at the surface is about 1/2 its maximum value at 2 cm. The thermal flux drops off rapidly at the surface. The fast neutron dose falls off with a half-value of 3 cm.

Centerline and off-axis dosimetry has been provided for the clinical beam. These experimental results were compared with those generated by MCNP. Normalization factors were applied to the MCNP generated dose components to fit the experimental results in a least squares sense. The normalization factors for the B-10 and thermal neutron doses were 0.87; when this factor is multiplied by the MCNP generated B-10 and thermal neutron doses, the shapes and intensities of the MCNP and experimentally derived doses agree throughout the central axis of the phantom within the known uncertainties. The normalization factor for the fast neutron dose was 1.10; when this factor is multiplied by the MCNP generated fast neutron dose, the MCNP generated fast neutron dose is significantly higher in the top 1 cm of the phantom, and slightly lower throughout the remaining central axis of the phantom but within the known uncertainties . For the photon dose, a normalization factor of 1.8 was applied to the MCNP generated structural component of the photon dose. When added to the MCNP generated phantom induced photon dose, the MCNP and experimentally derived doses agree along the central axis of the phantom within the known uncertainties.

Whole body doses have been estimated. They are relatively high at 50-60 RBE cGy for a unilateral irradiation that delivers 2000 RBE cGy peak dose to healthy tissue in the treatment zone. Whole body doses will be determined for each patient and will depend on the part of the body that is treated and the orientation of the patient relative to the beam. Some aspects of in-vivo dosimetry were addressed. Cadmium covers for activation foils cannot be used in the treatment area since prompt gammas create a locally high photon dose. An alternative cover using Li-6 carbonate has been designed and tested. Health physics related doses, including the doses that will be received while setting up the patient, during the irradiation of the patient, and during a potential medical emergency with the patient, have been investigated and documented.

Many modifications were made to the medical room in preparation for clinical trials. A closed circuit TV system, mirrors, and an intercom were installed to better see

and talk with the patient, as required by Section 10CFR35 of the NRC's Code of Federal Regulations. Hand operated winches were installed so that the shielding door of the medical room can be opened in the event that electrical power is lost. To reduce activation, boral sheets were obtained and installed on the floor. The lead shutter and ceiling, surgical couch, and collimator were painted with a thermal neutron absorbing (borated) paint. A GM tube was installed inside the medical room pursuant to MITR Technical Specification No. 6.5. Finally, a shield plug that could be inserted into the lead shutter was designed that would reduce the doses to experimenters working with the beam and to personnel setting up the patient. The dose rates could be reduced by a factor of 2 to 4, depending on the chosen design.

A prompt gamma neutron activation analysis system has been improved and set up for the analysis of ppm levels of B-10 in blood, urine, and tissue samples. The system is unique in that it uses a Bragg diffracted neutron beam. The background from the Compton continuum in this system is low; also, there is little or no background source of B-10. The B-10 sensitivity was 3 cps/μg for 3-5 ml samples of blood, urine, or tissue. As required by the FDA as part of the human BPA biodistribution study, this prompt gamma system was successfully intercalibrated with the prompt gamma system at Brookhaven National Laboratory. It was also intercalibrated with an inter-laboratory round robin.

As part of an interinstitutional study to determine the biodistribution and pharmacokinetics of BPA in humans, about 70 blood and urine samples from 6 cancer patients were analyzed for B-10. This work, performed under an IND application to the FDA, was needed to obtain an amendment to the IND to use BPA for clinical treatment of patients by BNCT in the phase-I clinical study. Calibration curves were made for blood and urine. The blood data were fit to a one compartment oral absorption model. Tumor-to-healthy tissue and tumor-to-blood ratios were also determined. For orally administered BPA, uptake of B-10 in blood, tumor, and healthy tissue was found to be

highly variable. Tumor-to-blood B-10 ratios varied from 7-1 to 0.1-1, due to high variability in tumor uptake. Tumor-to-healthy tissue B-10 ratios were 20-1 in one patient and 3.7-1 in another (both melanoma patients). Before treatment, each patient needs to undergo an uptake and biodistribution study with a test dose of BPA. Only if there is acceptable uptake of BPA, and acceptable tumor-to-blood and tumor-to-healthy tissue ratios may the patient be treated by BNCT. The uptake and biodistribution study for each patient using a test dose of BPA has been incorporated into the NEMC/MIT Clinical Protocol.

8.2 RECOMMENDATIONS FOR FURTHER WORK

All technical elements and necessary federal and institutional administrative approvals to initiate a phase-I clinical study of neutron capture therapy for the treatment of subcutaneous melanoma in the extremities are in place. There are only three recommendations for further work.

1. To better estimate and to reduce the patient's whole body dose.

The whole body doses for an assumed BNCT treatment of the mid-thigh have been estimated (Chapter 5). They are relatively high at 50-60 RBE cGy for a unilateral irradiation that delivers 2000 RBE cGy peak dose to healthy tissue in the treatment zone; they have been estimated from some in-phantom measurements and from in-air measurements taken along the lead shutter. Whole body doses have not been estimated for treatments of other parts of the body, or for different orientations of the patient's body relative to the beam. It's recommended that some dosimetric information be obtained at various places around the main beam for the all-shutters-open condition. This would allow a better estimate of the patient's whole body dose. Improved shielding of the

patient to reduce the whole body dose is also recommended. This could be done by trying to orient the patient's body down and away from the main beam, and by adding shielding between the patient and the beam. Estimating the B-10 concentrations in the patient's abdominal organs would also be useful; only then can the B-10 dose in this area be estimated. Perhaps a rough estimate of the B-10 concentration could be obtained by in-vivo PGNAA using a collimated, epithermal neutron beam or a neutron guide tube.

2. To reduce the beam-off dose rates in the medical room.

The dose rates in the medical room with the beam off are quite high; at 5 MW_n the dose rates are 2000-3000 mrem/hr near the beam exit in the ceiling. Most of the dose in this area is from fast neutrons. This dose rate needs to be substantially reduced. An insert for the lead shutter has been designed that would reduce the dose by a factor of 2-4, depending on the design (Chapter 6). A dose reduction factor of 100 would be desirable, but is not easily achievable. A rail system such that additional shielding could be temporarily slid into place might work to reduce the dose rates in those working situations where the additional shielding would not be in the way.

Also, the dose rates towards the back wall of the medical room can also become quite high, up to 2000 mrem/hr. Most of this dose is from photons. Adding 2" of lead over most of the area, and 4" towards the back wall would be helpful. There is potent streaming at the back wall; the 1" gap between the shielding on the ceiling and the back wall should be filled in with lead.

3. To periodically review the Procedures and Surveillance Schedule.

Procedures are now in place to ensure safe delivery of the prescribed radiation dose. It's recommended that after several patients have been treated, the Procedures and Surveillance Schedule be reviewed. The goal would be to modify the Procedures and

Surveillance Schedule such that the prescribed radiation dose is delivered with improved safety and accuracy, and with less manpower.

APPENDIX A OUTSIDE REVIEW OF CLINICAL DOSIMETRY

The dosimetry protocol (Chapter 3) has been thoroughly reviewed by Professor Steven Goetsch, of U.C.L.A., an expert on mixed field dosimetry. Dr. Goetsch also visited the MITR-II medical beam facility and reviewed our experimental method. His comments on the protocol and experimental technique are provided in this appendix.

Important recommendations by Dr. Goetsch included:

1. To seal the carbon graphite to preclude diffusion of air through the graphite thimble.
2. To calibrate the ionization chambers at an Accredited Calibration Laboratory with either Cs-137 or Co-60 (buildup caps needed for the Co-60 calibrations).
3. To set up a Quality Control and Quality Assurance program.
4. To build and set up a calibration jig at the Cs-137 source to periodically check the calibrations of the ionization chambers.
5. To cross calibrate the K-617 and K-616 electrometers.
6. To keep log books of the periodic calibration checks.
7. To adhere to the written protocols.

These recommendations have been followed. The carbon graphite chamber was sealed (and tested to ensure that the sealing did not change the calibration), and the chambers were calibrated using Co-60 and buildup caps. The QA/QC program is a part of our Procedures, some of which are provided in Appendix D. The calibration jig was made and tested, and the electrometers were cross calibrated. Procedures have been

written for the periodic calibration checks and the electrometer cross calibration. Log books are kept in the form of filed Procedures.

DEPARTMENT OF RADIATION ...
UCLA SCHOOL OF MEDICINE
200 UCLA MEDICAL PLAZA SUITE ...
LOS ANGELES, CALIFORNIA ...

February 4, 1993

Professor Otto K. Harling
Director, Nuclear Reactor Laboratory
Professor of Nuclear Engineering
Massachusetts Institute of Technology

Dear Professor Harling:

Thank you for offering me this opportunity to review your protocol in Boron Neutron Capture Therapy. I believe it is an exciting avenue of research that offers hope for intractable primary brain cancers.

I believe your protocol is generally well-written, thorough and carefully researched. The two-ion chamber detector measurements are strikingly similar to those I made as part of my doctoral thesis in Paul DeLuca's Gas Target Neutron Source group, with Herb Attix as my advisor. I regret that he is at this time unable to give you the benefit of his inestimable wisdom and experience in this area.

I am enclosing my overall evaluation and specific comments. My compliments to Ronald Rogus for his extreme attention to detail, even extending to punctuation and spelling. There are virtually no typographical errors in the entire manuscript. Having reviewed numerous papers for technical journals, I find this is a rarity.

Please call me at 310-825-6319 if you have any questions regarding my evaluation or if you require further assistance. I hope to visit Boston some time in the next 12 months and hope I will be able to visit your facility.

Steven J. Goetsch, Ph.D.
Associate Clinical Professor

Review of MIT Protocol for Mixed Field Dosimetry for Boron Neutron Capture Therapy at the MITR-II Research Reactor

Steven J. Goetsch, Ph.D.
UCLA Medical Center
Dept. of Radiation Oncology

February 4, 1992

I. General Evaluation

This protocol is thorough, well written and technically sound. The paired dosimeter technique for mixed neutron-gamma dosimetry was first originated in England in 1944 (Bretscher and French, classified reports, de-classified in 1957). Attix utilized this technique to evaluate the fast neutron and gamma radiation absorbed doses in the near field of the Middle Atlantic Neutron Therapy Association (MANTA) cyclotron at the Naval Research Laboratory in 1977. It was later utilized to evaluate the dose in air and at depths along the central axis as well as off-axis in a water phantom at the Gas Target Neutron Source (GTNS) at the University of Wisconsin (Goetsch, thesis 1983). This is a valid technique for neutron-gamma dose separation for neutrons above about 1 MeV.

The thermal and epithermal neutron beam dose measurements rely on bare and cadmium-covered gold activation foils. This is also a standard technique and is recommended by the American Association of Physicists in Medicine in their Report No. 19, "Neutron Measurements around High Energy X-ray Radiotherapy Machines" (Nath et al, 1986).

Calculation of each of these dose rates enables the MIT Nuclear Reactor Laboratory staff to estimate patient doses for boron neutron capture therapy in the field of the MITR-II epithermal beam. Limitations of these measurements are properly described. It is assumed in this protocol that the calculated and measured dose sensitivities for neutrons and gamma radiation of the ionization chambers employed here are unchanged at various depths in the phantom, even though the spectral composition of the beam is known to change. This assumption is generally made in this type of dosimetry, however. It is also difficult to make simultaneous measurements with two or more ionization chambers in an identical portion of the mixed neutron-gamma beam. Therefore, one has to make sequential measurements and assume that the beam is time invariant. If the beam is known to change temporally, then some

correction for this behavior is best. The power history correction procedure described in the protocol is an attempt to account for this behavior. Lastly, the dosimetry must be performed in advance of treatment of the patient. Other monitors must be used to analyze the radiation field while the patient is being treated and the dosimetry phantom has been removed from the beam. It is assumed that the intensity and spectrum of the beam does not change between the dosimetry measurement and the actual patient treatment. Mock irradiations are a standard way of testing the validity of this assumption and certainly should be performed as a regular part of a Quality Control/Quality Assurance protocol once the clinical trials are underway.

II. Specific Comments

A. Photon and Fast Neutron Doses

The Far West ionization chambers described in the protocol are standard chambers that have a wide range of applicability at neutron therapy and dosimetry centers throughout the world. It is useful to employ flowing gases which match or at least mimic the composition of the dosimeter material. A tissue equivalent gas has been available for some time from Matheson Gas Company and is used in this protocol. Alternatively, a gas which more closely resembles the atomic composition of A150 "tissue equivalent plastic" was proposed by Attix and Awschalom (1982) and has been experimentally tested (DeLuca 1982).

It is extremely important to note that graphite ionization chambers are notoriously treacherous when filled with flowing carbon dioxide. This problem was described by Attix *et al* in 1980, who noted a 15 to 20% deficiency in ionization (compared to expected values) produced in graphite chambers filled with flowing carbon dioxide. The explanation was published by Pearson *et al* in 1980 who explained the phenomenon on the basis of the natural porosity of graphite. The chamber may backfill with air, even though a stable flow rate of filling gas is assured. Since the density of carbon dioxide is more than 50% greater than air, even though the stopping power and mean energy per ion pair are quite comparable, a substantial

...ney in ionization is produced when air diffuses into the chamber. Increasing the flow rate to compensate for this effect can lead to over-pressurization, causing a surplus of ionization. This phenomenon has caused problems for numerous neutron dosimetry groups around the world and lead to substantial errors by some groups participating in the International Neutron Dosimetry Intercomparison (INDI, ICRU 27) at Brookhaven Laboratory in 1978. Difficulty in ascertaining that the graphite ion chamber was properly filled with carbon dioxide lead this reviewer to use static air in place of carbon dioxide in fast neutron dosimetry measurements (Goetsch, thesis, 1983). The MIT reactor staff may wish to assess this problem after consulting Pearson's paper (copy enclosed).

Racetrack timing is often employed for ionization measurements in the field of radiation sources which can not conveniently be switched on and off (Attix, 1986). The Keithley 616 electrometer lends itself well to such application since it can be electronically ungrounded by a timing pulse and the display can be frozen by a second pulse. This method was used in paired ion chamber work at the GTNS facility (Goetsch, 1983) and subsequently used by Goetsch *et al* in the field of high dose-rate remote afterloading iridium-192 sources (1991). In the later work a Fluke Model 8840A digital voltmeter was electronically started and stopped while reading accumulated charge on a Keithley Model 602 electrometer. Either of these methods offers a precision of approximately plus-or-minus one clock pulse (60 Hz). Design of the electronic device which made this timing possible is available from Dr. David Pearson at the University of Wisconsin.

Saturation of the ionization chambers during these measurements should be checked at least once during initial calibration of this facility. This may be checked by simple measurement at full and half voltage (see Attix, 1986). If the correction is substantial, it should be measured each time and appropriate correction applied.

The equations for dosimeter response follow the notation of Attix (1986). The ratio B/A is referred to as the "neutron sensitivity factor" in the protocol, but is more properly called the "neutron to gamma sensitivity ratio". The presumed gamma ray spectrum on

page 19 is quite reasonable. It would be extremely difficult to analyze the photon spectrum in the presence of the neutron field, so the assumptions provided as to the source and energy of the gamma radiation is justified. NOTE: A sentence fragment: "The calibration irradiation facilities had ..." was found at the bottom of page 17.

A value of $(B/A)_{TE}$ of 0.92 is obtained for the spectrum of neutron energies expected to be found in this beam. This value is reasonable in light of the somewhat unknown nature of the neutron spectrum as a function of depth in the phantom. The calculated value of $(B/A)_{CG}$ 0.0437, from a previous study, suffers from a similar uncertainty. One way to assess the validity of these assumptions is to perform a Monte Carlo analysis of the neutron-photon spectrum in the phantom. Many codes are available for such work and one or more are probably available at MIT. These codes require a reasonably precise knowledge of the input spectrum, which could be the calculated or measured reactor spectrum at the epithermal neutron beam port used for this work. Transport calculations are cumbersome and time-consuming, but they do allow a comparison of theoretical calculations with measured results. Without some point of comparison, one is left no independent means of assessing the reliability of the dose separation. This might be the subject of future thesis work.

Calibration of the Far West ionization chambers to obtain photon response is not quite optimal. The protocol authors have elected to use ionization chambers with walls that are not quite thick enough (approximately $0.5 g/cm^2$) to be in charged particle equilibrium for cobalt-60 gamma radiation, although that is the source that was used for calibration. (Far West can construct these chambers with cobalt-60 equilibrium thickness walls.) Since the wall thickness is stated as 2.51mm ($0.28 g/cm^2$) for the A-150 plastic chamber and 1.65mm (0.31 to 0.38 g/cm^2) for the graphite chamber, these ionization chambers could be calibrated with gamma radiation from a large cesium-137 radiation source. This reviewer was formerly director of the University of Wisconsin Accredited Dosimetry Calibration Laboratory where calibration of ionization chambers with a certificate directly traceable to National Institute of Standards and Technology primary national standards was offered. These calibrations were offered for x-radiation in the range of 60 to

250 kVcp, cesium-137, iridium-192 and cobalt-60. The response for a given chamber typically varied by about 1% between cobalt-60 and cesium-137. It is never appropriate to calibrate an ionization chamber with photon radiation if the walls are not thick enough to provide full equilibrium for that energy. It might be wise, and legally prudent, to have the ionization chambers used for this work calibrated by one of the five Accredited Dosimetry Calibration Laboratories for photon response at cesium-137. In the medical field it is important to always strive for the highest attainable standard and to demonstrate good-faith effort in having done so. Calibration at an ADCL would provide traceability to primary national standards laboratories, as is legally required for conventional radiation therapy facilities in the United States.

There is some "hysteresis" in these measurements. According to the protocol, the neutron and photon output change as a function of time. The power history correction factor f_{hist} has been introduced to correct for this effect. It is stated that fast neutron dose was underestimated by a factor of two when this was not taken into account. However, under steady-state conditions, the final ionization currents were found to be within 1% of the initial readings over a period of five hours. Clearly, it is important when human patients are being treated that the dose rate be known during treatment. If is not possible to hold the output constant, then the dose rates for neutron and gamma radiation must be measured before and after the treatment, and interpolated during the treatment itself.

A second factor, f_{RP}, was introduced to account for variations in overall reactor power. It is stated that ionization current measured in phantom may not scale linearly with this factor. A beam monitor is now being installed. It is not clear whether this monitor will intercept the beam at the reactor port prior to the phantom or skull of the patient. Linear accelerators used in conventional photon therapy are equipped with two such redundant transmission ionization "monitor" chambers. The entire beam is transmitted through these chambers and treatment is prescribed in terms of "monitor units" as measured by these devices. This accounts for temporal variations of the output of the accelerator. Perhaps this "beam monitor" will serve this same function and therefore permit these variations to be automatically accounted for. Absent such a device, every effort should be made to

stabilize the beam and assure that it closely resembles the spectrum at time of last calibration.

B. Thermal Neutron Dose

The dose to the normal brain from neutron capture reactions in nitrogen-14 is calculated. The calculation is straight-forward and seems quite reasonable. The dose rate from this reaction amounts to about 10% of the dose rate due to gamma radiation and 16% of that for fast neutrons. The dose rate to tumor with a 1 ppm concentration of boron-10 is calculated as 6cGy/min, or about equal to the sum of the above doses. Hopefully, to maintain a therapeutic advantage with respect to normal brain tissue, the tumor concentration will be at least 1ppm or greater. Presumably some measurements will be made of the levels of boron concentration attained in tumors of patients to be treated, as well as concentrations in circulating blood and normal brain tissue. This would permit calculation of dose to the tumor as well as dose to surrounding normal brain, which is the dose limiting factor.

The thermal neutron dose was determined from gold foil experiments. Again, if the relative neutron-photon ratio changes due to xenon buildup in the reactor or for other reasons, then the thermal flux may change somewhat. It is critical that the reactor flux be kept the same as is was at the time of measurement with gold activation foils. This measurement may need to be repeated periodically. Experience at the Gas Target Neutron Source indicated that aluminum activation foils agreed extremely well with paired ionization chambers and could be used as point dosimeters in animal irradiations.

C. Epithermal Neutron Flux

Epithermal neutron flux measurements rely on cadmium covered gold foils and are evaluated in the same calibrated system. It is prudent that the Ge(Li) and HPGE detectors are calibrated with a source set traceable to NIST primary standards. Cadmium-covered gold foils are also a well-tested method of neutron flux evaluation. Calculations appear to yield reasonable results.

D. Effects Not Accounted For and Error Analysis

Lack of neutron and photon spectral measurements in phantom have already been discussed. The assumption that the neutron and photon sensitivity of the ionization chambers does not change with changing neutron and photon spectra is common in all neutron dosimetry facilities. A Monte Carlo calculational model of this epithermal neutron irradiation port might help to alleviate some of these uncertainties and help to validate some of the above assumptions.

Error analysis indicates the overall error to be +/-7.4%. The International Atomic Energy Authority has recommended that overall uncertainty in delivered dose to a tumor be no greater than +/-5%. Due to the experimental nature of this project and the absence of a means of comparison with a direct primary national standard, this level of uncertainty should be acceptable to clinicians.

III. Conclusions

This document elaborates the protocol by which the epithermal neutron port at the MIT Research Reactor will be calibrated for use in boron capture clinical trials. The protocol is thorough, well-researched and scientifically valid. I would recommend that the ionization chambers employed be calibrated by an Accredited Dosimetry Calibration Laboratory, so that the doses administered may be more closely related to NIST primary standards. Fast neutron dosimetry groups in the United States and abroad have inter-compared their dosimetry and set up working standards committees. I would urge the MIT Reactor Laboratory staff to seek such links with other groups preparing for boron neutron capture therapy trials as well as the existing treatment center in Japan.

It is not clear whether a separate protocol will be written describing th Quality Control and Quality Assurance program that such a clinical tri requires. I do not know how often these dosimetry measurements will b made (monthly, daily) or how precisely these measurements will be related t the treatment of an individual patient. State and federal regulations for conventional radiation therapy facilities require daily, monthly and annual

spot checks and calibrations. ... some monitoring be employed in ... while the treatment is progressing? Will the treatment be terminated after a pre-determined reading is obtained? Will any attempt be made to analyze the concentration of boron in the tumor prior to treatment so that the known dose rate from boron capture may be calculated for this particular patient? Is there a separate treatment planning system to plan treatments for individual patients, taking into account the three-dimensional nature of the tumor as revealed by surgery or imaging studies? I can not comment on these issues.

Boron neutron capture therapy offers the promise of successful treatment for patients with primary brain neoplasms, especially glioblastoma multiforme. These patients have a uniformly grim prognosis. Little progress has been made in extending the survival of glioblastoma patients in the past 20 years. It is hoped that boron capture therapy, gene technology or immunotherapy can offer some hope to these victims.

References

AAPM Report No. 19, Neutron Measurements Around High Energy X-ray Radiotherapy Machines, AAPM, New York, NY, 1986.

Attix, F.H., Theus, R.B., Shapiro, R., Surratt, R.E., Nash, A.E. and Gorbics, S.G., "Neutron Beam Dosimetry at the NRL Cyclotron", Phys. Med. Biol. **16**, 497, 1973.

Attix, F.H., August, L.S., Shapiro, P. and Theus, R.B., "Scattered Radiation from a Neutron Collimator", NBS SP456 and Med. Phys., **4**, 118, 1977.

Attix, F.H., Pearson, D.W., DeLuca, P.M., Jr. and Goetsch, S.J., "Comparison of the Bragg-Gray theory corollaries to fast-neutron cavity ionization measurements at 14.8 MeV", Health Physics, **38**, 623-633, 1980.

Awschalom, M., Rosenberg, I., Ten Haken, R.K., Pearson, D.W., Attix, F.H., and DeLuca, P.M., Jr., "Characteristics of A-150 plastic-equivalent gas in A-150 plastic ionization chambers for *p*(66)Be(49) neutrons", Med Phys **9**, (6), 884-887, 1982.

Attix, F.H., Introduction to Radiological Physics and Dosimetry, John Wiley and Sons, New York, 1986.

Bretscher, E. and French, A.P., "The Measurement of Neutron Flux in the Presence of Gamma Rays", Cavendish Laboratories, UK Report BR517, 1944.

Bretscher E. and French, A.P., "Neutron Flux Measurements (D + D and C + D neutrons)", Cavendish Laboratories, UK Report BR386, 1944.

DeLuca, P.M., Jr., Attix, F.H., Pearson, D.W., Schell, M.C., and Awschalom, M., "Application of A-150 plastic-equivalent gas in A-150 plastic ionization chambers for Co-60 γ rays and 14.8 MeV neutrons", Med Phys **9**, (3), 378-384, 1982.

Goetsch, S., "Neutron/Gamma Dose Separation by the Multiple Ion Chamber Method", Ph.D. thesis, May, 1983, University of Wisconsin Madison, published by University Microfilms, Ann Arbor, MI.

Goetsch, S., Attix, F.H., Pearson, D.W. and Thomadsen, B.R., "Calibration of ^{192}Ir high-dose-rate afterloading systems", Med Phys **18**, (3), 462-467, 1991.

International Commission on Radiation Units and Measurement, "An International Neutron Dosimetry Intercomparison", Report No. 27, 1978.

Pearson, D., Attix, F., DeLuca, P., Goetsch, S. and Torti, R., "Ionization Error due to Porosity in Graphite Ionization Chambers", Phys. Med. Biol., **25**, No. 2., p. 333-338, 1980.

Ionisation error due to porosity in graphite ionisation chambers

D W Pearson, F H Attix, P M DeLuca Jr, S J Goetsch and R P Tom
Medical Physics Division, University of Wisconsin, Madison, Wisconsin 53706, USA

Received 5 June 1979, in final form 14 August 1979

1. Introduction

In an earlier progress report (Attix *et al* 1978), and in a 'work-in-progress' session at the 1978 annual meeting of the American Association of Physicists in Medicine, the authors of this paper described some ionisation chamber measurements which indicated systematic anomalous behaviour by graphite chambers. The cause was unknown at that time, hence the preliminary report was essentially phenomenological, concluding with the suggestion that the porosity of the graphite might be an important factor. That has turned out to be the case, and this note is intended to update the previous report and solve the apparent mystery. Inasmuch as none of this work has appeared in the open literature before, some review of the earlier finding will be included here.

2. Theoretical background

It has been pointed out in another paper (Attix *et al* 1980) that the comparison of Bragg–Gray (BG) cavity theory with experimental results is facilitated by recognition of the existence of two corollaries to that theory, the first of which can be stated as follows:

'To the extent that the BG theory is satisfied, the ratio of ionisations in two gases x and y sequentially contained in the same cavity chamber and identically irradiated will be given approximately by:

$$\frac{Q_x}{Q_y} = \frac{\overline{(S/\rho)}_x}{\overline{(S/\rho)}_y} \frac{\overline{W}_y}{\overline{W}_x} \frac{\rho_x}{\rho_y} \tag{1}$$

where $\overline{(S/\rho)}$ is the mass stopping power of the gas in each case, evaluated at the mean energy of the charged-particle spectrum crossing the cavity, $\overline{W}$ is the mean energy spent by these particles per ion pair produced, and ρ is the gas density.'

It is interesting to notice that this equation is explicitly independent of the chamber wall material, although some minor degree of wall influence might be implicit in either the stopping power or $\overline{W}$ terms if the charged-particle spectrum were strongly wall-dependent. This is certainly not the case for media with low values of Z in which γ-rays interact only by the Compton effect. Thus one would expect this BG corollary to apply, for example, to ion chambers of tissue-equivalent (TE) plastic, graphite, magnesium and aluminium for ^{60}Co γ-rays, provided that the usual BG requirements for the cavity were satisfied (i.e., that it does not perturb charged particles incident upon it, and that direct γ-ray interactions with the gas inside are negligible).

0031-9155/80/020333+06$01.00

3. Review of earlier findings

Briefly stated, the observed anomaly in the behaviour of graphite cavity chambers was a 15–20% deficiency in the amount of ionisation produced by penetrating photon or electron beams when Ar or CO_2 was flowed through, as compared with that expected from BG theory considerations. The gas flow rate was typically 5 ml min^{-1}, as used by EG&G, Inc. in the γ-ray calibrations of their chambers. Tissue-equivalent gas showed only a slight (~4%) ionisation deficiency, while air behaved normally in the graphite chamber. By contrast, under the same conditions, ion chambers of comparable size but having walls of TE plastic, Mg, or Al responded normally for all of the above gases

Table 1. Q_x/Q_{air} ratios, theoretical vs experimental.

Gas x	Q_x/Q_{air}[a]	Experimental (Q_x/Q_{air}) for various chambers			
		TE plastic[b]	Mg[c]	Al[d]	Graphite[e]
Air	1·00	1·00	1·00	1·00	1·00
Ar	1·43	1·45	1·45	1·46	1·16
CO_2	1·57	1·56	1·55	1·53	1·32
TE	1·17	1·17	1·18	1·17	1·12
He[f]	0·171	—	0·205 (0·185)[g]	—	0·700 (0·160)[g]

[a] Calculated with equation (1), using data from table 2.
[b] Model IC-17 chamber, 0·94 cm^3, type A-150 plastic, 0·57 g cm^{-2} wall thickness, from EG&G, Inc., Goleta, CA.
[c] EG&G model IC-17M, 2·40 cm^3, Mg wall 0·53 g cm^{-2} thick.
[d] 'Homemade' cylindrical chamber, 15 cm^3, Al wall ~0·5 g cm^{-2} thick. Flow rate = 20 ml min^{-1}.
[e] EG&G model IC-17G, 2·45 cm^3, graphite wall 0·53 g cm^{-2} thick.
[f] Helium data were not yet available, hence were not included by Attix *et al* (1978). Also, table 1 in that reference was erroneously labelled as containing ratios of ionisations *per unit mass*; actually they were ratios of (Q_x/Q_{air}), as above.
[g] Helium data in parentheses were obtained with the ion chamber enclosed in a condom and with a gas flow rate = 200 ml min^{-1}. Corresponding data without parentheses were obtained with a flow rate of ~30 ml min^{-1}, and no condom. Applied potentials were limited to ±100 V to avoid gas multiplication. Only ^{60}Co γ-rays were used for He measurements.

These results are summarised in the first four lines of table 1, where theoretical versus experimental values of (Q_x/Q_{air}) are shown for the various gases x flowed through the chambers. Provenance and dimensions of the chambers are listed in the footnotes to that table. The results shown were obtained with ^{60}Co γ-rays, at 95 cm from a Picker radiotherapy unit yielding = $1{\cdot}88 \times 10^{-2}$ C kg^{-1} min^{-1} (73 R min^{-1}), with the 10 cm × 10 cm beam incident perpendicular to the chamber axis. Ionisation was measured with applied potentials of ±100, ±300, and ±500 V (except in the case of He), revealing only minor (~1%) recombination losses which were eliminated by the usual $1/Q$ against $1/V$ extrapolation technique. Substitution of an 18 MeV electron beam from a Clinac 18 accelerator in place of γ-radiation made no significant difference in the experimental results.

Clearly table 1 shows that for Ar, CO_2 and TE gas the experimental (Q_x/Q_{air}) ratios agree reasonably well with each other and with theory, being independent of chamber wall material as expected, except for the graphite chamber results in the last column. (The case of helium will be discussed later.)

A number of parameters were varied to discover the cause of anomalous behaviour by the graphite chambers, some of which were discussed by Attix *et al* (1978). Most of

Table 2. Data on theoretical Q_w/Q_{air} ratios used in table 1.

Gas	S/ρ[a]	$\overline{W}$[b]	ρ[c]
Air	1.081	33.7	1.196
Ar	1.676	26.2	1.651
CO_2	1.087	32.9	1.829
TE[d]	1.382	29.2 (41.5)	1.057
He	1.268	29.7	0.1652

[a] Units of MeV cm^2 g^{-1}. Taken from the collision stopping power tables of Berger and Seltzer (1964) for an electron energy of 0.3 MeV, which is roughly the mean value of the equilibrium spectrum of secondary electrons from ^{60}Co γ-rays.

[b] Units of eV per ion pair. Myers (1968), Smith *et al* (1975). The parenthetical figure for He is applicable only to ultrapure gas; impurities reduce $\overline{W}_{He}$ to about 29.7 (see Myers).

[c] Units of $g\,l^{-1}$ at 760 Torr, 22 °C.

[d] Composition as specified by manufacturer (Matheson Co.): 32.4% CO_2, 3.2% N_2, and 64.4% CH_4 by partial pressure.

this work was later found to be irrelevant when the true cause was identified. One early finding was in fact misleading, namely that the anomalous behaviour persisted when the graphite chamber was enclosed in a stainless steel tank containing the gas in question. This observation was found upon repetition of the experiment to be irreproducible, and definitely incorrect, leading to the conclusion that graphite is too porous to be used with a different gas flowing through the cavity from that surrounding the chamber. As will be seen in the next section, the anomaly is primarily due to air flowing in through the porous graphite wall, thus diluting and contaminating the cavity gas.

4. Flow-rate studies

The cylindrical Al ion chamber used to obtain the results shown in table 1 had a 15 cm^3 volume and replaceable walls of either graphite or aluminium, with the same Al collecting electrode used in both cases. The gas-filling port and the vent hole were both fixed in the stem end plate, which was the same for either wall. Thus the effects (if any) of overpressuring and of air diffusion back through the vent could be observed and evaluated. Figure 1 shows the results of varying the CO_2 flow rate for both the aluminium and graphite walls. The response ratio (Q_{CO_2}/Q_{air}) with the aluminium wall 'saturates' at nearly the NO predicted value for gas flow rates greater than about six volumes (90 ml) per minute, indicating that air diffusing back through the vent hole is only significant at lower flow rates. The flatness of the curve above ~100 ml min^{-1} indicates that no overpressuring occurs for flow rates at least up to twenty volumes (300 ml) per minute.

The same chamber with a graphite wall, but having the same filling port and vent hole, shows a much more gradual approach to flow-rate saturation with CO_2, showing ≈20% ionization deficiency at 20 ml min^{-1}, and about 3% even with a flow rate of 20 chamber volumes per minute. If the chamber is then covered with a condom so that the graphite wall is surrounded by an atmosphere of CO_2, but the gas is still vented to

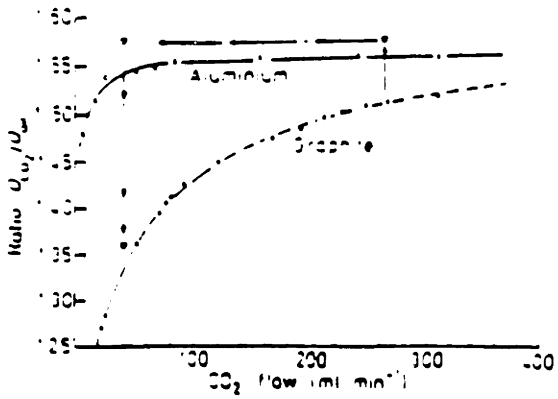

Figure 1. (Q_{CO_2}/Q_{air}) plotted against CO_2 flow rate for 15 cm^3 cylindrical ion chamber with 0.5 g cm^{-2} Al or graphite walls. ×—× aluminium wall, ratio of ionisation in flowing CO_2 to ionisation in static air, as a function of CO_2 flow rate. The data were taken with both increasing and decreasing flow rates. ○- - -○ same data for graphite wall. ▽—▽ same data for graphite wall, showing the effect of covering the graphite wall with a vented condom. Arrows show the time sequence: Covering the chambers at a high flow rate, reducing the flow rate with no reduction in ionisation current, and then removing the condom at low flow rate giving a rapid return to the anomalously low ionisation. The sequence is reversible, requiring a few minutes at the low flow rate for complete flushing of the chamber.

prevent pressure build-up in the chamber, a flow rate of about three volumes per minute is sufficient to maintain the full ionisation response. The ionisation ratio then agrees within about one per cent with that of the Al chamber at high flow rates of CO_2. Removal of the condom restores the anomalous response within a minute, as indicated by the arrows in figure 1, revealing the rapidity with which air diffuses in through a graphite wall of about 3 mm thickness. Similar results were observed for the EG&G graphite chamber described in footnote 'e' of table 1.

Helium presents the most severe test of diffusion barriers because it is monatomic and relatively small in atomic mass and size. As shown in table 1, the expected ionisation in helium is only about one sixth of that in air for the same gas volume, unlike the other gases for which (Q_x/Q_{air}) exceeds unity. Helium in this situation is a poor dielectric. The chambers show gas multiplication effects for voltages over 100 V. Therefore ±20, ±40, and ±100 V were used in the $1/Q$ against $1/V$ extrapolation, to correct for minor ionic recombination losses.

Figure 2 shows the results of flowing He gas in the EG&G graphite and Mg chambers. The response of the magnesium chamber nearly saturates at a helium flow rate above ten volumes per minute, giving an ionisation ratio of about 0·20 relative to air. However, covering the chamber with a condom and using a flow greater than 100 volumes per minute further lowers the ionisation ratio to ≈0·185, approaching reasonable agreement with the so calculated value of 0·171. The fact that the condom thus reduced the ionisation for the non-porous magnesium chamber indicates that some air diffusion in through the vent hole was occuring without the condom. The presence of the rubber barrier provides (at high flow rates) a helium atmosphere in the region outside the vent hole, thus eliminating the backflow of air.

The EG&G graphite chamber shows a very gradual decrease in the ionisation ratio as a function of helium flow rate. Saturation of the response was not observed for flow rates of at least up to 200 volumes per minute. Covered with a condom, the chamber shows an ionisation ratio of 0·175 which could be maintained at a flow rate of only 20 volumes per minute.

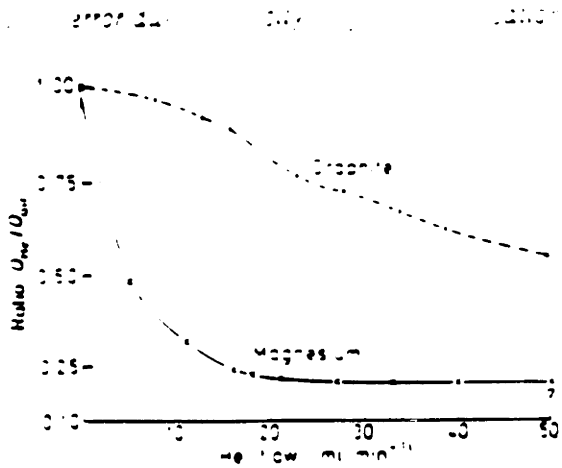

Figure 2. (Q_{He}/Q_{air}) plotted against He flow rate for EG&G graphite and magnesium chambers. ● ratio of ionisation in flowing He to ionisation in static air for graphite chamber. ▽ ratio of ionisation for condom-covered graphite chamber. × ratio of ionisation in flowing He to ionisation in static air for magnesium chamber.

It is clear from comparing the case of He with that of Ar, CO_2, or TE that the effect of air diffusing in and diluting the gas is to make (Q_g/Q_{air}) assume a value closer to unity, since the gas mixture thereby becomes more air-like.

5. Conclusions

The results of these experiments lead us to conclude that the anomalous ionisation yield for gases other than air in graphite chambers is due essentially to the diffusion of air through the graphite walls, thus contaminating and diluting the other gases. The air flows inward because its partial pressure is greater outside the wall than inside, which would occur even if the total pressure inside exceeded that outside. The simple expedient of covering the chamber with a condom eliminates this effect. However, in the future, graphite chambers should always be constructed with a gas-impervious barrier such as a plastic or Al shell, properly vented to prevent backflow of air through the exit port.

Our measurements also suggest that flow-gas overpressuring of these chambers apparently does not occur for flow rates up to at least 20 volumes per minute. The desire to avoid this effect has led to the typical use of very low flow rates (~2 vol min^{-1}) which cause a greater error because of gas dilution than would occur at higher flow rates, as shown by the figures.

We suggest that all measurements made with bare-walled graphite ion chambers containing gases other than the ambient gas (usually air) are likely to be significantly in error. Also suspect are measurements with a covered graphite chamber, in water phantoms for example, which are interpreted on the basis of a γ-ray calibration of the uncovered chamber with the same gas flow. This latter procedure, using CO_2 gas, has been commonly employed in n–γ mixed field dosimetry for many years, and has no doubt handicapped progress in that difficult field. The more recent replacement of the graphite–CO_2 chamber by Mg–Ar offers not only lower neutron sensitivity, but eliminates the porosity problem as well. However, this replacement would not be satisfactory in the presence of low-energy γ-rays which would excite photoelectric effects in Mg and Ar.

...k was supported by the US Department of Energy Contract No. EY-76-S-02-1105.

The authors thank J J Broerse for drawing our attention to a communication by Maier and Burger (1978) disclosing similar findings, of which we were previously unaware.

References

Attix F H, Pearson D W, Goetsch S J, DeLuca P M Jr and Tarr R P 1978 *Wisconsin Medical Physics Report* No. WMP-101, Section No. COO-1105-259

—— 1980 Comparison of the Bragg–Gray theory corollaries to fast-neutron cavity ionization measurements at 14.8 MeV *Health Phys.* in press

Berger M J and Seltzer S M 1964 *Tables of Energy Losses and Ranges of Electrons and Positrons*, NASA Report No. SP-3012.

Maier E and Burger G 1978 in *Proc. 3rd Symp. on Neutron Dosimetry in Biology and Medicine*, EUR 5848 (Luxembourg: CEC) p 165

Myers I T 1968 *Radiation Dosimetry*, 2nd ed vol I ch 7 ed F H Attix and W C Roesch (New York: Academic Press)

Smith A R *et al* 1975 *Med. Phys.* 2 195

NIVERSITY OF CALIFORNIA, LOS ANGELES

UCL

BERKELEY • DAVIS • IRVINE • LOS ANGELES • RIVERSIDE • SAN DIEGO • SAN FRANCISCO

SANTA BARBARA •

DEPARTMENT OF RADIATION ONCOLOGY
UCLA SCHOOL OF MEDICINE
200 UCLA MEDICAL PLAZA, SUITE B265
LOS ANGELES, CALIFORNIA 90024-6951

March 12, 1993

Professor Otto K. Harling
Director, Nuclear Reactor Laboratory
Professor of Nuclear Engineering
Massachusetts Institute of Technology

Dear Professor Harling:

I am writing to give you my comments and observations regarding the ionization chamber measurements in which I participated while a guest at your laboratory this week. My general observation is that your present protocol and practice are quite good. My suggestions will make incremental improvements in a program which is already well thought out.

I spoke with Paul DeLuca yesterday. I gave him a synopsis of my visit to MIT. He told me that Herb Attix seems to be improving slowly from day to day. He tries to read technical journals and can speak and move, but only laboriously. He will probably be in University Hospital in Madison for several more weeks and then decisions will have to be made about further rehabilitation. At least the news is encouraging.

Once again I would like to thank you for inviting me to visit your outstanding facility. I truly enjoyed the hospital your provided as well as the staff at New England Medical Center. My wife was thrilled with the "onesies" for our son David. We will send you a picture when he finally makes his appearance, on or about April 11. I seem to have left just in time: I understand a blizzard is coming. We are having summer weather here. I would be pleased to continue our association in any way possible and hope to visit Boston again in the future.

Steven J. Goetsch, Ph.D.
Associate Clinical Professor

You may wish to acquire a Keithley Model 261 Picoampere Source to do calibration checks on your electrometers. John L. Fluke also makes such instruments.

I discussed with Ron Rogus the sensitivity of A150 Tissue Equivalent plastic chambers to humidity. The nylon component (Zytel) of such chambers swells in response to humidity, increasing the sensitive volume. The effect is usually noticeable in very humid summer conditions and manifests itself by high leakage (greater than $5 * 10^{-14}$A) and by an instability in readings. Many consecutive readings may continue to monotonically increase. There is little that can be done under such conditions. If the relative humidity is controlled, then you may not have a problem. It may be wise to store the chamber with desiccant. This will help to keep it dry in between uses, but will not help once it is removed from storage.

Phantom Measurements

During the measurements in which I participated, we did not attempt to assess ionization collection efficiency, but this is something which should be assessed at infrequent intervals. The dose rates which you obtain for fast neutrons result in relatively low ionization currents, so the ion collection efficiency should be nearly unity.

The new Keithley 617 electrometer which you have now offers the capability of either self-timed readings of 60 seconds or more, or can be interfaced directly with the IBM computer program written by Dr. Solares. I think that is certainly preferable to timing by observation against a stopwatch. The dose rate is low enough that this does not introduce very large errors, but the electronically timed methods offer much higher precision.

I did not review all of your protocols and submissions to various licensing authorities in detail, but I understand that the elliptical head phantom or the leg phantom, as appropriate, will be used on the day before any human patient is to be treated. Once clinical trials begin, you may have patients every week. If not, I would recommend that a protocol be established for periodic measurements even in the absence of patients. A single point measurement, such as the one we made on the central axis with the TE plastic chamber and the graphite chamber at 2cm depth would be a good check on your overall calibration. Additionally, I understand that you have agreed to do a full characterization of the entire phantom

Comments on MIT BNCT Calibration Protocol

Cesium-137 Calibration Verification

Now that your Far West ionization chambers have been calibrated by an Accredited Dosimetry Calibration Laboratory, the cesium-137 gamma radiation source can be used to provide a good constancy check. Ron Rogus is working on a design for a calibration jig to hold the ionization chamber at a fixed location on the central axis of the beam. The jig should be rigidly affixed to the source housing, and should be at an optimal distance of 20 to 30cm. This will minimize errors due to positioning, while providing and acceptable signal to noise ratio. The chambers should be used with either of your Keithley electrometers.

I suggest that the Keithley 616/6169 electrometer and ion chamber interface now be cross-calibrated with the Keithley 617 electrometer that was sent to the University of Wisconsin calibration lab. The graphite ion chamber would be a good chamber to use: simply obtain consecutive readings (perhaps 300 seconds) at an optimal distance from the cesium-137 source, and then, without touching the chamber, connect it to the Keithley 616 electrometer. A simple ratio of charges collected will enable you to deduce the electrometer scale correction factor for this electrometer. If anything ever happens to the calibrated electrometer, you can then check your readings against the "in-house" calibrated electrometer.

Part of the protocol should also be a check of the bias supply on the electrometer before it is used. The Keithley 617 has a bias battery which may last several years, but can go bad. The 6169 ion chamber interface also has a battery. A good digital multimeter with about a 10 M-ohm impedance will give good results. The lo lead of the probe should be placed against the grounded part of the triax connector and the other lead should be carefully inserted to touch the middle (brass) portion of the triax connector. Each battery should supply about 300 volts.

I would recommend that a calibration log book be maintained for the ionization chambers and electrometers. Copies of the calibration certificates and readings for all calibration checks should be included in the lab book. This provides a history of the calibration of your ionization chambers and electrometers.

including cross-check with the thermal and epithermal beam monitors and the gold foils every 6 months. I believe that periodic checks at one point will help you spot any potential changes in the beam quality early on.

I believe that all essential components of an excellent calibration protocol are now in place. You have ionization chambers and electrometers that have a calibration directly traceable to national standards. All that is required now is diligent adherence to your written protocols.

APPENDIX B CALIBRATION REPORTS FOR THE IONIZATION CHAMBERS AND ELECTROMETER

Calibration reports are provided for the carbon graphite and tissue equivalent ionization chambers that were used in the experimental dosimetry. A calibration report is also provided for a magnesium ionization chamber; this chamber was not used in this study, but was a backup for the carbon graphite chamber.

Two calibration reports are provided for the K-617 electrometer. In the second calibration (April 5, 1993), a smaller standard capacitor was used to better calibrate the electrometer in the range around 1E-12 amperes, which is typical of the currents collected during the actual chamber measurements. The electrometer calibration factor (1.001 nC/"nC") obtained during this calibration was applied to the electrometer-chamber measurements.

Report No. ION1753

University of Wisconsin - Madison
Department of Medical Physics
Accredited Dosimetry Calibration Laboratory

1530 Medical Sciences Center, 1300 University Ave., Madison, WI 53706
Office: (608) 262-6320 Fax: (608) 262-5012

Report of Calibration

for

Ionization Chamber

Submitted by:

Ronald Rogus
Nuclear Reactor Laboratory
Massachusetts Institute of Technology
138 Albany St.
Cambridge, MA 02139

Ion Chamber:

Far West
Model IC-18G
S/N 132-CG

Date Received: 25/FEB/93 **Calibration Completed:** 26/FEB/93

Form Revised 26/FEB/91

University of Wisconsin - Madison
Department of Medical Physics
Accredited Dosimetry Calibration Laboratory

Cobalt-60 Measurement Data

Calibration Date: February 26, 1993 Report Date: March 1, 1993

Ionization Chamber

Far West
Model IC-18G

Serial Number : 132-CG
Nominal Volume : 0.1 cm^3
Type : Cylindrical
Build-up cap : 1.4 mm Plexiglass

Electrometer used in Calibration

UW-ADCL Keithley Model 602
Fluke Model 8840A Digital Multimeter

Serial Number : 171736
Range : 10^{-8} Coulomb
Feedback : Fast

IRRADIATION CONDITIONS

Field Size : 10 x 10 cm^2
Pre-Irradiation Leakage : +2.2 x 10^{-14} A
Chamber Orientation : Random
Polarizing Voltage : -250 V
Charge Collected : Negative

Source-Chamber Distance : 95 cm
Source-Collimator Distance : 61 cm

(Central electrode grounded, shell hot)
Calibration Classification : I

Beam Quality	NIST Nomenclature	Symbol	Output Rate	Calibration Factor (At 22°C and 760 mm Hg)
Co-60	Exposure	N_x	31.5 R/min.	2.128 x 10^{10} R / C
Co-60	Air Kerma	N_K	0.28 Gy/min.	1.871 x 10^8 Gy / C

Comments: The chamber was found to be open to atmospheric communication. The ratio of charge collected at full (250V) voltage to that collected at half (125V) voltage was 1.000, which corresponds to an A_{ion} of 1.000. Please refer to the Appendix for a description of reported calibration factors.

Recorded in data book: UW ADCL CO-02 Pages: 461-465

Calibrated by: Carol Gifford, B.S.
Physicist, Accredited Dosimetry
Calibration Laboratory

Reviewed by: P.M. DeLuca, Jr., Ph.D.
Chairman,
UW-ADCL Advisory Committee

Report No. IQN175

University of Wisconsin - Madison
Department of Medical Physics
Accredited Dosimetry Calibration Laboratory

1530 Medical Sciences Center, 1300 University Ave., Madison, WI 53706
Office: (608) 262-6320 Fax: (608) 262-5012

Report of Calibration

for

Ionization Chamber

Submitted by:

Ronald Rogus
Nuclear Reactor Laboratory
Massachusetts Institute of Technology
138 Albany St.
Cambridge, MA 02139

Ion Chamber:

Far West
Model IC-18
S/N 131-TG

Date Received: 25/FEB/93 Calibration Completed: 26/FEB/93

Form Revised 26/FEB/91

Report No. IQN1752

University of Wisconsin - Madison
Department of Medical Physics
Accredited Dosimetry Calibration Laboratory

Cobalt-60 Measurement Data

Calibration Date: February 26, 1993

Report Date: March 1, 1993

Ionization Chamber

Far West
Model IC-18

Serial Number : 131-TG
Nominal Volume : 0.1 cm^3
Type : Cylindrical
Build-up cap : 1.8 mm Plexiglass

Electrometer used in Calibration

UW-ADCL Keithley Model 602
Fluke Model 8840A Digital Multimeter

Serial Number : 171736
Range : 10^{-8} Coulomb
Feedback : Fast

IRRADIATION CONDITIONS

Field Size : 10 x 10 cm^2
Pre-Irradiation Leakage : +1.4 x 10^{-14} A
Chamber Orientation : Random
Polarizing Voltage : -250 V
Charge Collected : Negative

Source-Chamber Distance : 95 cm
Source-Collimator Distance : 61 cm

(Central electrode grounded, shell hot)
Calibration Classification : I

Beam Quality	NIST Nomenclature	Symbol	Output Rate	Calibration Factor (At 22°C and 760 mm Hg)
Co-60	Exposure	N_x	31.5 R/min.	2.538 x 10^{10} R / C
Co-60	Air Kerma	N_K	0.28 Gy/min.	2.231 x 10^8 Gy / C

Comments: The chamber was found to be open to atmospheric communication. The ratio of charge collected at full (250V) voltage to that collected at half (125V) voltage was 1.000, which corresponds to an A_{ion} of 1.000. Please refer to the Appendix for a description of reported calibration factors.

Recorded in data book: UW ADCL CO-02 Pages: 461-465

Calibrated by: Carol Gifford, B.S.
Physicist, Accredited Dosimetry
Calibration Laboratory

Reviewed by: P.M. DeLuca, Jr., Ph.D.
Chairman,
UW-ADCL Advisory Committee

Report No. IQN1754

University of Wisconsin - Madison
Department of Medical Physics
Accredited Dosimetry Calibration Laboratory

1530 Medical Sciences Center, 1300 University Ave., Madison, WI 53706
Office: (608) 262-6320 Fax: (608) 262-5012

Report of Calibration

for

Ionization Chamber

Submitted by:

Ronald Rogus
Nuclear Reactor Laboratory
Massachusetts Institute of Technology
138 Albany St.
Cambridge, MA 02139

Ion Chamber:

Far West
Model IC-18
S/N 670-TMW

Date Received: 25/FEB/93 Calibration Completed: 26/FEB/93

Form Revised 26/FEB/91

University of Wisconsin - Madison
Department of Medical Physics
Accredited Dosimetry Calibration Laboratory

Cobalt-60 Measurement Data

Calibration Date: February 26, 1993 Report Date: March 1, 1993

Ionization Chamber

Far West
Model IC-18

Serial Number : 670-TMW
Nominal Volume : 0.1 cm^3
Type : Cylindrical
Build-up cap : 3.35 mm Plexiglass

Electrometer used in Calibration

UW-ADCL Keithley Model 602
Fluke Model 8840A Digital Multimeter

Serial Number : 171736
Range : 10^{-8} Coulomb
Feedback : Fast

IRRADIATION CONDITIONS

Field Size : 10 x 10 cm^2
Pre-Irradiation Leakage : +1.1 x 10^{-14} A
Chamber Orientation : Random
Polarizing Voltage : -250 V
Charge Collected : Negative

Source-Chamber Distance : 95 cm
Source-Collimator Distance : 61 cm

(Central electrode grounded, shell hot)
Calibration Classification : I

Beam Quality	NIST Nomenclature	Symbol	Output Rate	Calibration Factor (At 22°C and 760 mm Hg)
Co-60	Exposure	N_x	31.5 R/min.	2.177 x 10^{10} R / C
Co-60	Air Kerma	N_K	0.28 Gy/min.	1.914 x 10^8 Gy / C

Comments: The chamber was found to be open to atmospheric communication. The ratio of charge collected at full (250V) voltage to that collected at half (125V) voltage was 1.000, which corresponds to an A_{ion} of 1.000. Please refer to the Appendix for a description of reported calibration factors.

Recorded in data book: UW ADCL CO-02 Pages: 461-465

Calibrated by: Carol Gifford, B.S.
Physicist, Accredited Dosimetry
Calibration Laboratory

Reviewed by: P.M. DeLuca, Jr., Ph.D.
Chairman,
UW-ADCL Advisory Committee

Report No. EM[illegible]

University of Wisconsin - Madison
Department of Medical Physics
Accredited Dosimetry Calibration Laboratory

1530 Medical Sciences Center, 1300 University Ave., Madison, WI 53706
Office: (608) 262-6320 Fax: (608) 262-5012

Report of Calibration

for

Electrometer

Submitted by:

Ronald Rogus
Nuclear Reactor Laboratory
Massachusetts Institute of Technology
138 Albany St.
Cambridge, MA 02139

Electrometer:

Keithley Instruments Inc.
Model 617
S/N 524188

Date Received: 05/APR/93 Calibration Completed: 05/APR/93

Form Revised 01/AUG/91

Report No. [illegible]

University of Wisconsin - Madison
Department of Medical Physics
Accredited Dosimetry Calibration Laboratory

Electrometer Measurement Data

Calibration Date: February 26, 1993

Report Date: February 26, 1993

Electrometer

Keithley Instruments, Inc.
Model Number: 617
Serial Number : 524188

Electrometer Settings

Function	:	Coulomb
Ranges	:	Auto
Current Suppress	:	Off
Volt/Ohm Guard	:	Off
Zero Correct	:	On

Calibrated Capacitors
Standard set of four Polystyrene Capacitors
Model PS-6S
A: 0.001 µF, B: 0.01 µF, C: 0.10 µF, D: 1.00 µF
Capacitor used in calibration: B

Potentiometer
Leeds and Northrup, Model 7552
Serial Number: 313373

Charge Calibration Factor

Scale	Leakage	Zero-Drift	Calibration Factor
Coulomb	$+2.4 \times 10^{-14}$ A	-2.3×10^{-14} A	0.998 nC / 'nC'

Comments: The electrometer was found to be linear within +/- 0.044 % over the full range of the scale. Please refer to the Appendix for a description of reported calibration factors.

Recorded in data book: UW ADCL EM-04 Page: 278

L A DeWerd

Calibrated by: L.A. DeWerd, Ph.D.
Director, Accredited Dosimetry
Calibration Laboratory

Reviewed by: P.M. DeLuca, Jr., Ph.D.
Chairman,
UW-ADCL Advisory Committee

University of Wisconsin - Madison
Department of Medical Physics
Accredited Dosimetry Calibration Laboratory

Electrometer Measurement Data

Calibration Date: April 5, 1993

Report Date: April 5, 1993

Electrometer

Keithley Instruments, Inc.
Model Number: 617
Serial Number : 524188

Electrometer Settings

Function	:	Coulomb
Ranges	:	Auto
Current Suppress	:	Off
Volt/Ohm Guard	:	Off
Zero Correct	:	On

Calibrated Capacitors
Standard set of four Polystyrene Capacitors
Model PS-6S
A: 0.001 µF, B: 0.01 µF, C: 0.10 µF, D: 1.00 µF
Capacitor used in calibration: A

Potentiometer
Leeds and Northrup, Model 7552
Serial Number: 313373

Charge Calibration Factor

Scale	Leakage	Zero-Drift	Calibration Factor
Coul (E-10)	$+2.4 \times 10^{-14}$ A	-2.3×10^{-14} A	1.001 nC / 'nC'

Comments: The electrometer was found to be linear within +/- 0.04% over the full range of the scale. Please refer to the Appendix for a description of reported calibration factors.

Recorded in data book: UW ADCL EM-05 Page: 58

L A DeWerd

Calibrated by: L.A. DeWerd, Ph.D.
Director, Accredited Dosimetry
Calibration Laboratory

Reviewed by: P.M. DeLuca, Jr., Ph.D.
Chairman,
UW-ADCL Advisory Committee

APPENDIX

DESCRIPTION OF REPORTED UW-ADCL CALIBRATION FACTORS

University of Wisconsin - Madison
Department of Medical Physics
Accredited Dosimetry Calibration Laboratory

Proper function and reliability of the radiation measuring devices described in this document are dependent upon handling and use. Therefore, the duration of responsibility of the University of Wisconsin, Department of Medical Physics, Accredited Dosimetry Calibration Laboratory (ADCL) and its employees for the calibration results extends only to the time the instruments leave the premises of the University of Wisconsin. It is recommended that the instrument user establish an appropriate technique of monitoring the constancy of the instrument response before and after its submission to the ADCL and on a regular basis thereafter. In addition, it is the express responsibility of the instrument user to assure (by personal communication if necessary), that interpretation of the information in this document is consistent with the interpretation intended by the ADCL.

Reported Calibration Factors for Ionization Chambers

The **air kerma calibration factor**, N_K, for an ionization chamber is the quotient of the X- or gamma-ray air kerma K_{air} (in gray) at the location of the center of the chamber (in the theoretical absence of the chamber), to the corresponding charge collected from the chamber (in coulomb), corrected to the density of air at 1 ATM (760 Torr, or 101.3 kPa) and 22°C. The **exposure calibration factor**, N_x, is the quotient of exposure (in roentgen) to the charge (in coulomb). Both N_K and N_x are given in this report, and are based on the same calibration measurements. N_x is the factor occurring in Equation 5 of the TG-21 protocol of the AAPM (Medical Physics, **10**, 741, 1983), from which the quantity N_{gas} can be calculated for the chamber by the method described in that protocol and an accompanying communication (Medical Physics, **13**, 755, 1986).

N_K is related to N_x as follows:

$$N_K = N_x \frac{k \left(\frac{\overline{W}}{e}\right)_{air}}{(1-g)} \qquad \text{where:} \qquad k = 2.58 \times 10^{-4} \left[\frac{C/kg}{R}\right]$$

$$\left(\frac{\overline{W}}{e}\right)_{air} = 33.97 \left[\frac{J}{C}\right]$$

The factor g in the above equation is the fractional energy lost to bremsstrahlung, having the value 0.0032 for ^{60}Co gamma rays, 0.0016 for ^{137}Cs gamma rays, and zero for photons below 300 KeV.

Thus:

$$N_K \left[\frac{Gy}{C}\right] = (8.79 \times 10^{-3})\, N_x \left[\frac{R}{C}\right] \qquad \text{For } {}^{60}\text{Co},$$

$$N_K \left[\frac{Gy}{C}\right] = (8.78 \times 10^{-3})\, N_x \left[\frac{R}{C}\right] \qquad \text{For } {}^{137}\text{Cs, and}$$

$$N_K \left[\frac{Gy}{C}\right] = (8.76 \times 10^{-3})\, N_x \left[\frac{R}{C}\right] \qquad \text{For photons below 300 KeV.}$$

If the chamber was open to the atmosphere, the currents were normalized to 1 ATM (760 Torr, or 101.3 kPa) at 22°C. Use of the chamber at other pressures and temperatures requires correction of the ion currents to these conditions. The correction factor F may be computed from the following expression:

$$F = \frac{273.15 + T}{295.15} \times \frac{760}{P},$$

where for the ambient conditions T is the temperature in °C and P is the pressure expressed in Torr, (mm Hg at 0°C) or pascal/133.289. No corrections are made in this report for air humidity, which has a nearly constant effect between 20% and 80% relative humidity (Niatel, 1969). Thus, the chamber should be used *without* a humidity correction when operated within this range of relative humidities.

During the calibration, the exposure at the calibration position was measured by a cavity ionization chamber and an electrometer, both with calibrations directly traceable to the National Institute of Standards and Technology (NIST) primary standards. The ionization chamber was centered in the beam with the stem perpendicular to the beam direction, except for end-window chambers, which are calibrated with the window normal to the beam direction. The source-chamber distance given in the *Measurement Data* sheet is the distance from the source to the geometrical center of the active volume of the chamber, or to the inner proximal surface of a parallel plate chamber. The source-collimator distance is the distance from the source to the extreme end of the collimator. Chamber stem effect was not investigated. The calibration field size is given by the distance across the field from one 50% intensity line to the other (in air) measured at the calibration distance. The calibration factor applies only to the field size stated.

The ion collection efficiency (A_{ion} in the TG-21 protocol) is calculated from a method described by Attix (Medical Physics, **11**, 714, 1984) and is given by:

$$A_{ion} = \frac{4}{3} - \left(\frac{1}{3} \times \frac{Q_1}{Q_2}\right)$$

where Q_1 and Q_2 are the charge readings measured at nominal (300 V) and half (150 V) potential, respectively.

Reported Calibration Factors for Electrometers

Calibration of electrometers is performed using a set of calibrated capacitors and a calibrated potentiometer. A precisely known voltage is introduced onto one side of the capacitor and the electrometer to be calibrated is connected to the other side. The charge introduced onto the capacitor is given by the product of the voltage and capacitance. The electrometer reads this charge, and a calibration factor is computed from the ratio of that charge to the charge indicated on the electrometer. (Calibration of String Electrometers is performed using an alternate procedure and is addressed within the String Electrometer report). The electrometer calibration factor (E.C.F.) is reported in units of coulomb / reading (C / rdg) for electrometers with exposure or charge readout units, or nC / "nC" if the electrometer readout is in units of nano-coulomb. If the electrometer has an external output, the calibration factor can be given in coulomb / volt = farad. Please note that if a digital multi-meter (DMM) is supplied as a readout device for the electrometer to be calibrated, the electrometer and DMM will be calibrated as a system, and the calibration factor is only valid for the electrometer and DMM together. In either case, the corrected charge in coulomb is obtained by multiplying the instrument reading by the E.C.F.

Electrometer leakage is obtained by measuring the leakage current *after* a half-scale charge injection on the feedback capacitor. Zero Drift is obtained by measuring the leakage current *prior* to any charge injection on the feedback capacitor. The electrometer scale linearity is specified as a percent of the full scale, and is based on charge readings taken at 20% and 80% of full scale.

Use of Reported Calibration Factors

The factors for ionization chambers and electrometers provided in the UW-ADCL report can be used to calculate the exposure or air kerma of the output device (uncorrected for temperature and pressure) in the following manner:

Exposure-

$$X\ [R] = N_X\ [R/C]\ \text{x}\ \text{E.C.F.}\ [C/rdg]\ \text{x}\ \text{Electrometer Reading}\ [rdg]$$

Air Kerma-

$$K_{air}\ [Gy] = N_K\ [Gy/C]\ \text{x}\ \text{E.C.F.}\ [C/rdg]\ \text{x}\ \text{Electrometer Reading}\ [rdg]$$

For ion chambers that cannot be calibrated independently of their electrometers, a "system" calibration factor is reported which has units of *R/rdg*. This factor can also be used to calculate the exposure and air kerma, but does not provide enough information to determine N_{gas}. The Victoreen R-meter is an example of one such instrument, and will not be discussed in this appendix. Further information is given in the specific "system" reports.

Reported Calibration Accuracy

The accuracy of the air-kerma or exposure calibration factors for reference and field class instruments is reflected below in the UW-Radiation Calibration Lab classification scheme. Classes I, II and III apply to ADCL (AAPM accredited services), Class IV applies to general diagnostic X-ray calibrations, and Class V applies to radiation safety survey instrument calibrations.

CLASS	Cobalt - 60	Cesium - 137	X-Rays
I	+/- 0.5 %	+/- 0.5 %	+/- 1.0 %
II	+/- 0.5 %	+/- 0.5 %	+/- 2.0 %
III	+/- 1.0 %	+/- 1.0 %	+/- 2.0 %
IV	N/A	N/A	+/- 5.0 %
V	+/- 10 %	+/- 10 %	+/- 10 %

The calibration class stated in the UW-ADCL calibration report reflects the deviation from the NIST standard calibration. The reported calibration factors for ionization chambers are given to four digits to prevent rounding errors up to 0.5% when the first digit is unity.

Notice

Please note that calibration factors in this report are consistent with a change in the NIST value of exposure rate implemented January 1, 1986. These factors should be *less than* factors reported prior to that date by 1.1% for ^{60}Co, 0.8% for ^{137}Cs, and 0.2% for X-ray beam qualities.

Form Revised 20/MAR/91

APPENDIX C SAFETY REVIEWS FOR BEAM MODIFICATIONS INCLUDING DRAWINGS OF COMPONENTS, AND SULFUR FILTER TEMPERATURE DATA

Two safety reviews are included - one for the installation of the new horsecollar, stovepipe, and other beam components; the other for the extension of the stovepipe and for adding additional shot to the cone region of the filter.

Sulfur temperature data for a long irradiation of the sulfur can is included at the end.

Item: Medical Room Horsecollar and Filter Removal/Installation

Submitted by R. Rogus Date 04/25/91

Q/A number if required M-88-4

Does the item change or contradict the

Technical Specifications? ____ Yes* X No

SAR? ____ Yes* X No

* Attach explanation

Description of Change (Attach extra pages if necessary):

See attached sheets.

Safety Evaluation (Attach extra pages if necessary):

See attached sheets.

Summary of Review:

a) Does the proposal:	Yes	No
i) involve an unreviewed safety question (10CFR50.59(a)(2))	___	X
ii) decrease scope of requalification program (10CFR50.54(i-1))	___	X
iii) decrease effectiveness of security plan (10CFR50.54(p))	___	X
iv) decrease effectiveness of emergency plan (10CFR50.54(q))	___	X

b) Reviewer's Comments:

Recommend Approval ✓ Yes ____ No RRPQ [signature] Date 5/6/91

Reviewer [signature] Date 05/06/91

Reviewer [signature] Date 05-06-91

Approved [signature] Date 5-6-91
(Director of Reactor Operations)

10CFR50.59 & 50.54(p and q) changes logged for reporting to NRC, Date ____

Copy to Director for Operations
Copies circulated to and initialled by all Licensed Personnel
Original to Safety Review File

Unreviewed Safety Question (URSQ) Determination for SR#-0-91-7

This safety review does NOT involve an URSQ. The basis for that conclusion is documented below as required by 10 CFR 50.59(b).

(a) The change does not meet any of the three criteria that define an URSQ. This is shown below:

- No increase in probability of occurrence or consequences of any accident or malfunction of equipment important to safety previously evaluated in the safety analysis report (SAR) will occur because this change does not increase the severity of any accident analyzed in the SAR. This structural change to an existing experimental facility will not require the removal or inhibit any existing permanent reactor shielding.

- No new type of accident is created.

- No margin of safety is reduced because the proposed change does not alter or contradict any of the bases for the technical specifications.

Safety Review #-0-91-7

Description of Change

The Phase I configuration to be installed is shown in Figure 1. The current M-055 configuration is shown in Figure 2 for comparison. The new horsecollar has an outer region of lead, a lead insert, and an inner bismuth insert. Drawings of the new horsecollar are provided in Appendix A. These inserts can be removed at a later time to provide for an even larger diameter beam (Phase II). The Phase I bismuth insert has a 23-cm diameter hole, which is slightly larger than the old hole. A 1/8" boral plate sits on top of the horsecollar; this will reduce activation of antimony in the lead. Results of a neutron activation analysis of the lead are provided in Appendix B. The casing of the new horsecollar is aluminum-6061. The outer dimensions of the new horsecollar are the same as those of the old one. The new horsecollar should therefore fit into the outer plug.

The new stove pipe is made of aluminum-6061 and has a 23-cm OD, which is also slightly larger than the old stove pipe. The new filters will also be slightly larger. The stove pipe is 61 cm high. Drawings of the stove pipe are provided in Appendix C. The stove pipe can be pushed up high enough to allow the aluminum shot to drop out. Only aluminum shot (99.99% purity) will be used. No lithiated-aluminum or bismuth shot will be used.

Experience with the old configuration has shown that the shot, stove pipe, cadmium sheets, and aluminum structure in the filter region are safe. Likewise, the sulfur and bismuth in the collimator region (in the lead shutter) are safe. However, the old sulfur can ruptured at the weld joining the top plate to the tube. This can had been filled completely with sulfur. It is thought that a portion of the sulfur reached the melting point; the lower density of the liquid phase resulted in an expansion of the sulfur and a sufficiently high pressure inside the can caused failure. The new sulfur can, therefore, was designed with several safety features that will insure against rupture.

Description of Sulfur Filter Can

Drawings of the sulfur filter are provided in Appendix D. Chemical properties of sulfur are provided in Appendix E. The can has 3 safety features. First, an aluminum tube

runs through the can in which a thermocouple will be inserted. Several experiments will be done initially to make sure that the sulfur temperature is reasonable. Second, 3 aluminum bars have been welded to the top plate and positioned in the hottest part of the sulfur. The additional heat removal will keep this region of sulfur cooler. Third, an air gap has been left in the can. The sulfur can has been pressure tested to 10 psi. The can will be sealed with a lead-coated Inconel C-ring.

Radiological Issues

Radiological issues have been discussed extensively with MIT RRPO. These issues have been incorporated into the removal and installation procedure (Appendix F). The major concern is the high exposure rates (20 R/hr) expected when the lead shutter and outer shield are removed. However, this high exposure field will be limited to 2 feet in diameter near the ceiling and 6 feet in diameter near the floor (Appendix G). Scattered radiations will result in high radiation levels throughout the room. Provisions have been made to maintain doses in accordance with ALARA.

Safety Evaluation

The Reactor Operations Staff, after independent review concurs with the findings of the experimenter that the proposed change does not involve an unreviewed safety question. It is further noted that no permanent change is made in shielding and that the materials used in the filter's construction are compatible. Relative to the materials, the sulfur is a potential issue, but its container will be leak-tight and a record of the hydrostatic test of that container will be filed in Q/A #M-88-4. The major concern is therefore one of personnel safety during the installation. To that end, meetings were held with Reactor Operations, Maintenance, Radiation Protection, and the Machine Shop Personnel on 04/19/91 and 04/26/91 to review the procedure. Also, MIT RRPO held a separate meeting on 05/03/91. Finally, the Supervisor of Reactor Maintenance and the MIT RRPO Officer inspected all equipment, tools, and components on the evening of 05/03/91 following the reactor shutdown.

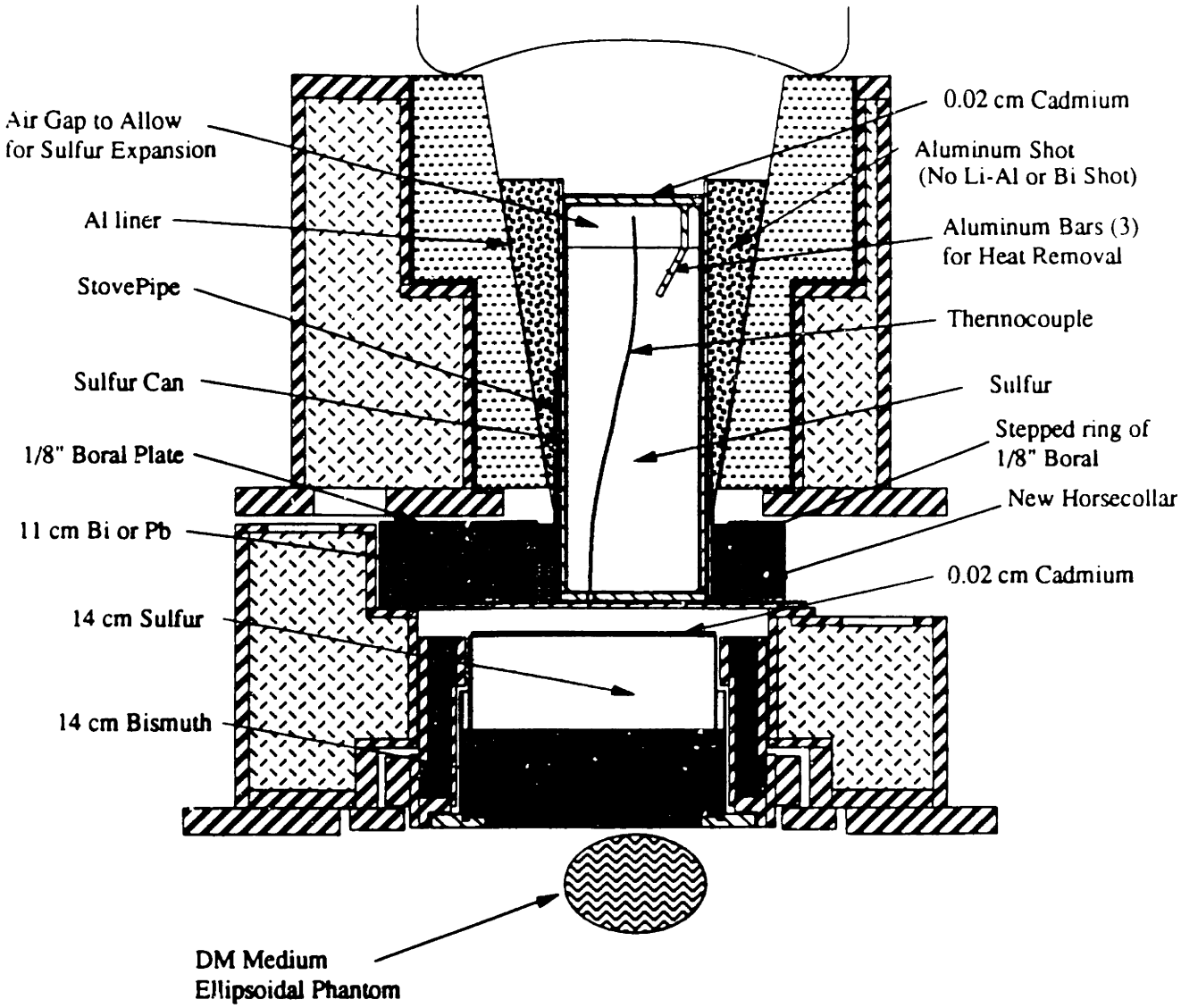

Phase 1 Configuration
Beam R10

Boral	Lead	Aluminum shot
Graphite	Bismuth	Water
Heavy Concrete	Aluminum	Polyethylene
Steel	Sulfur	

Scale: 1/10

Figure 1: New Phase I Configuration.

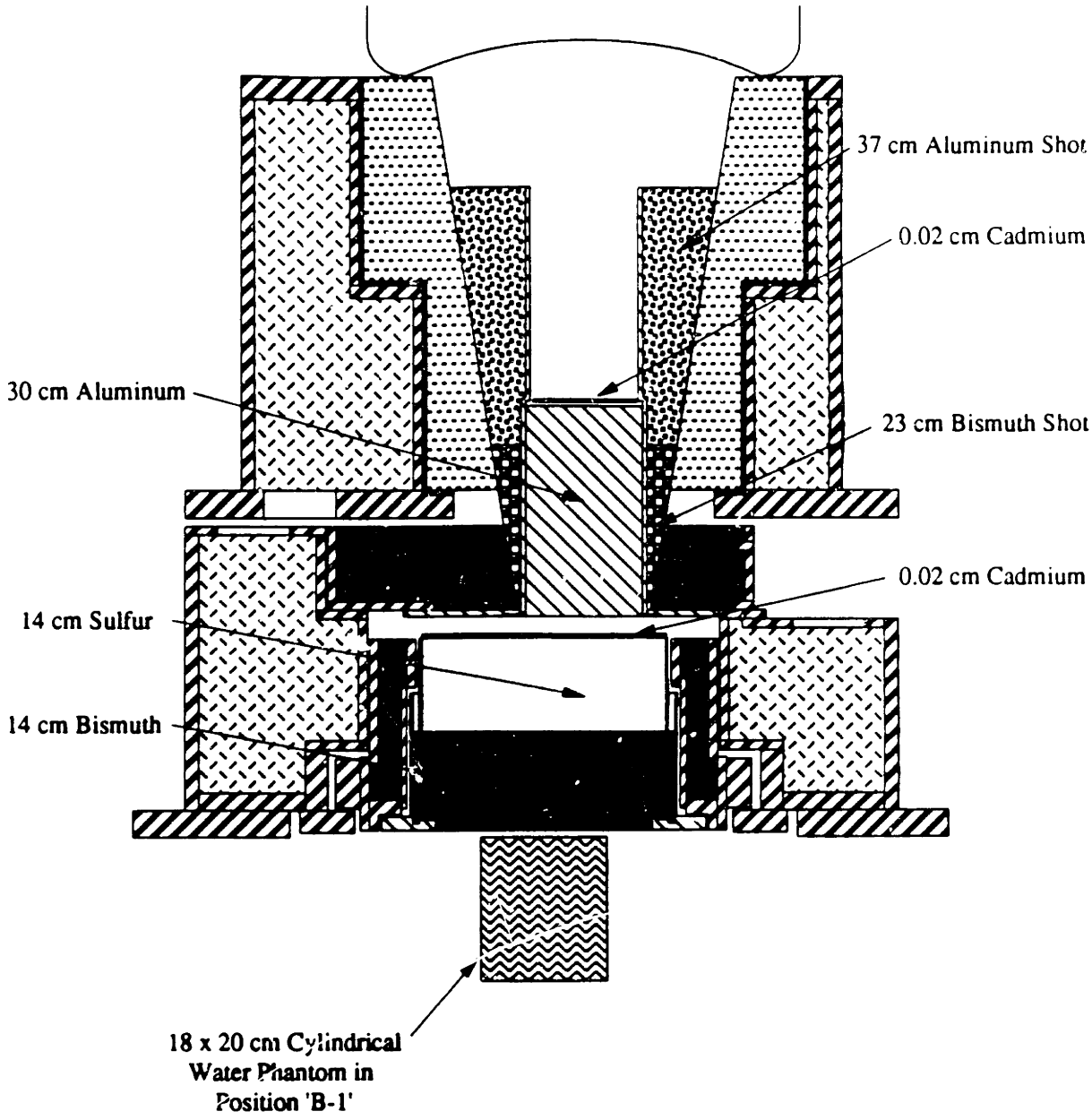

M-055 Configuration

Boral	Lead	Al/Li Shot (1300 ppm)
Graphite	Bismuth	Bismuth Shot
Heavy Concrete	Aluminum	Water
Steel	Sulfur	Polyethylene

Scale: 1/10

Figure 2: M-055 Configuration for Comparison with New Phase I Configuration.

Appendix A:

Drawings of the New Horsecollar.

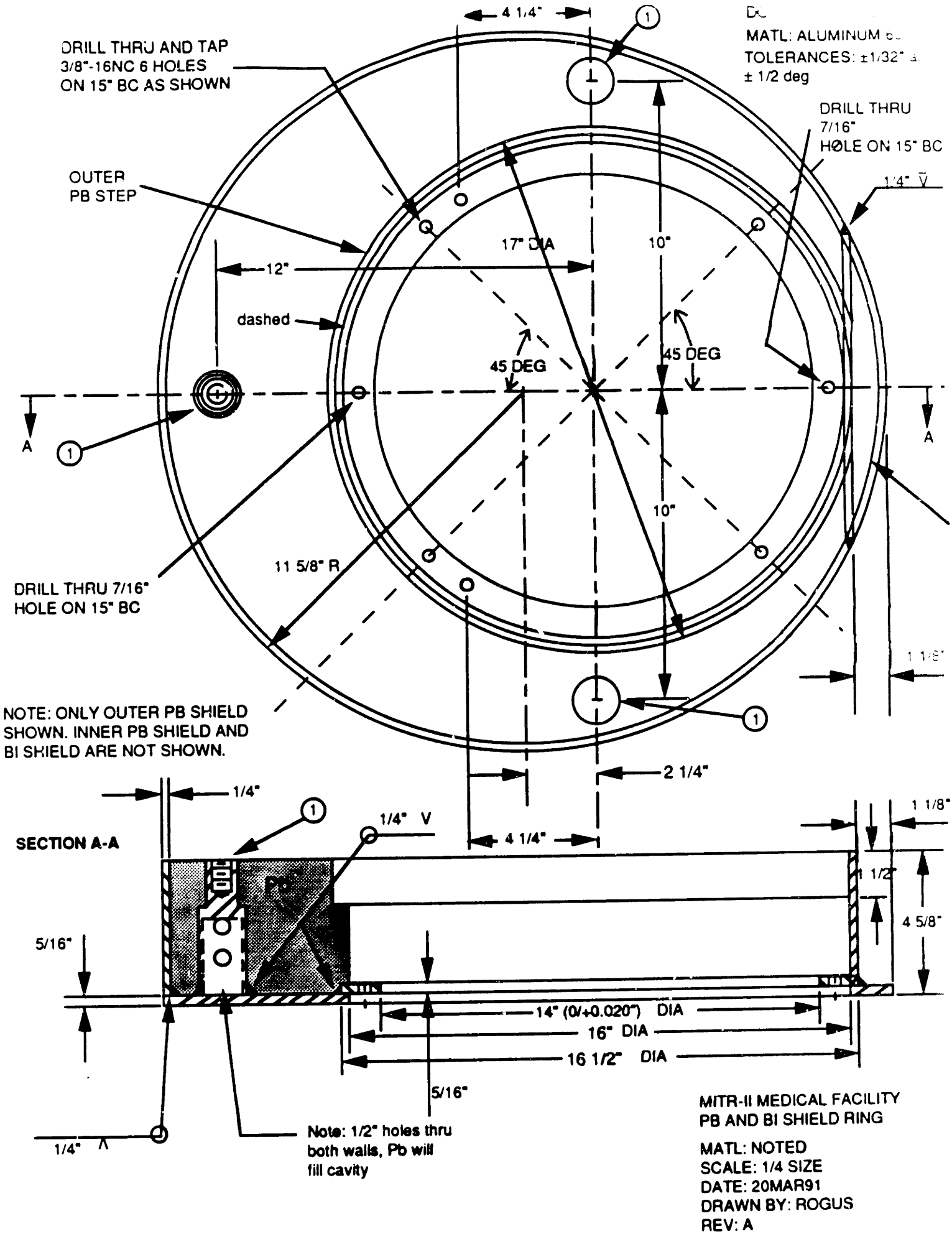
4 1/4"
DRILL THRU AND TAP
3/8"-16NC 6 HOLES
ON 15" BC AS SHOWN
MATL: ALUMINUM
TOLERANCES: ±1/32"
± 1/2 deg
DRILL THRU
7/16"
HOLE ON 15" BC
OUTER
PB STEP
1/4" V
17" DIA
10"
12"
dashed
45 DEG
45 DEG
A
A
10"
11 5/8" R
DRILL THRU 7/16"
HOLE ON 15" BC
1 1/8"
NOTE: ONLY OUTER PB SHIELD
SHOWN. INNER PB SHIELD AND
BI SHIELD ARE NOT SHOWN.
2 1/4"
1/4"
SECTION A-A
1/4" V
4 1/4"
1 1/8"
1 1/2"
4 5/8"
5/16"
14" (0/+0.020") DIA
16" DIA
16 1/2" DIA
5/16"
1/4"
Note: 1/2" holes thru
both walls, Pb will
fill cavity
MITR-II MEDICAL FACILITY
PB AND BI SHIELD RING
MATL: NOTED
SCALE: 1/4 SIZE
DATE: 20MAR91
DRAWN BY: ROGUS
REV: A

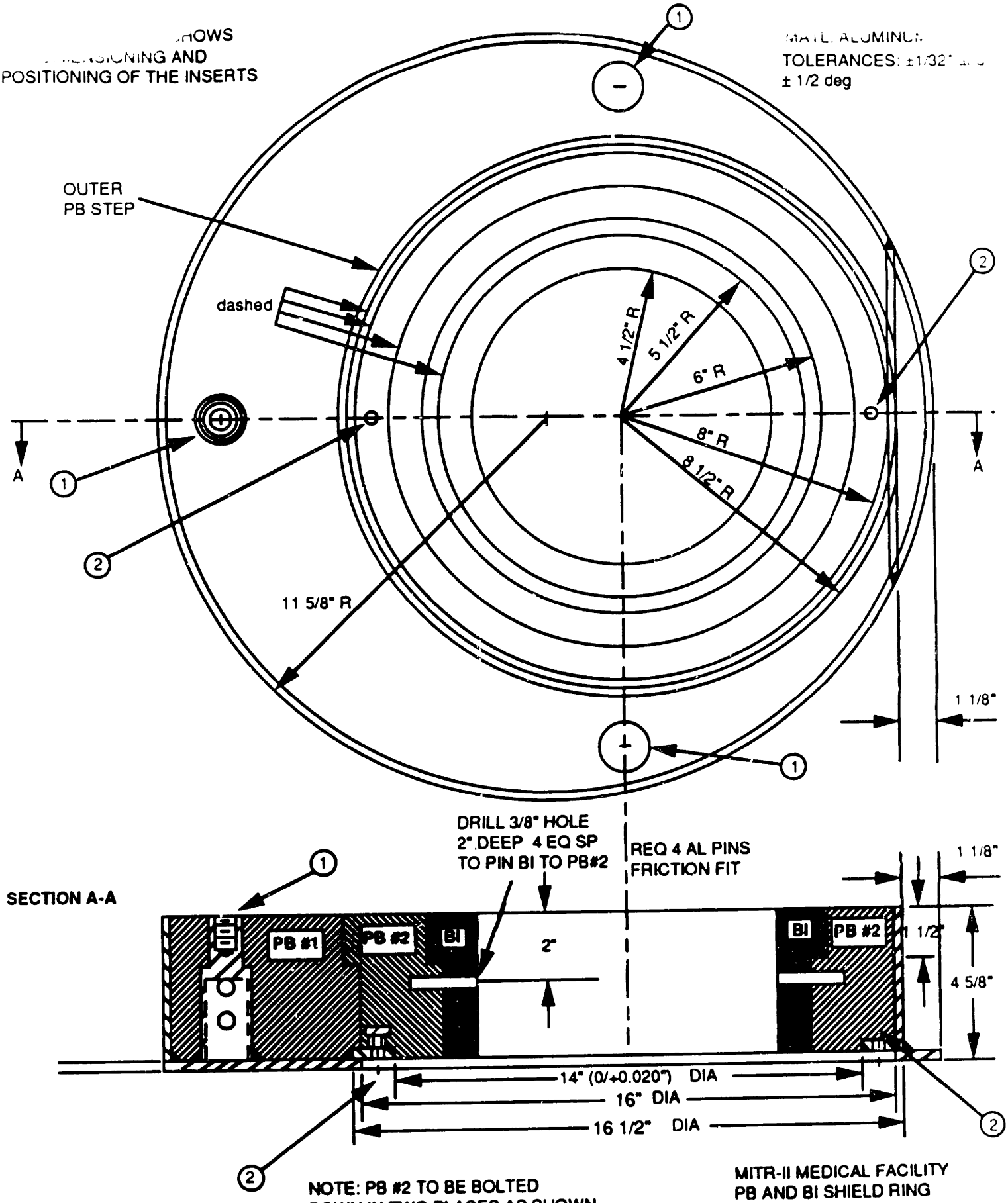

NOTE: PB #2 TO BE BOLTED
DOWN IN TWO PLACES AS SHOWN.

NOTE: PB AND BI PIECES TO BE MACHINED
SO THE GAP SPACE IS LESS THAN 1/32".

MITR-II MEDICAL FACILITY
PB AND BI SHIELD RING

MATL: NOTED
SCALE: 1/4 SIZE
DATE: 20MAR91
DRAWN BY: ROGUS
REV: A

MATL: AL 6061

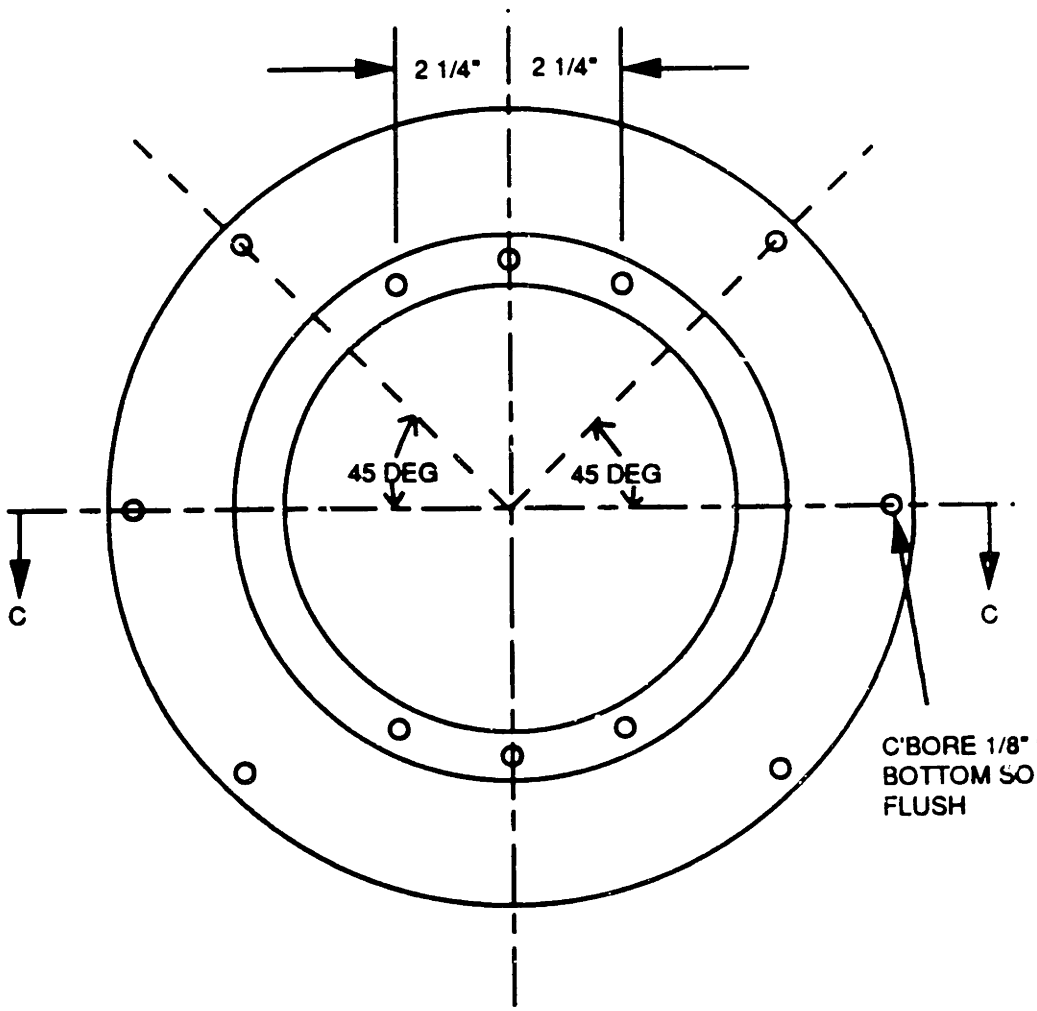

SECTION CC

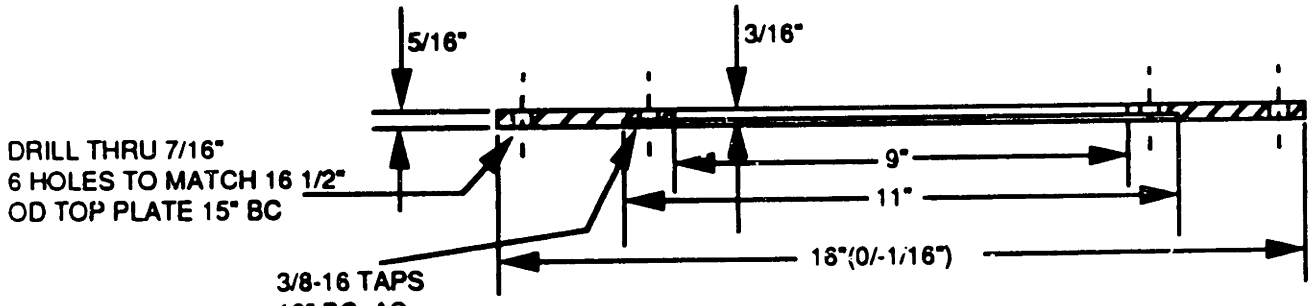

MITR-II MEDICAL FACILITY
PB AND BI SHIELD RING

MATL: NOTED
SCALE: 1/4 SIZE
DATE: 20MAR91
DRAWN BY: ROGUS
REV: A

DETAIL 1

MATL: AL 6061

3 REQ'D

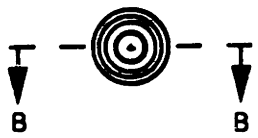

SECTION BB

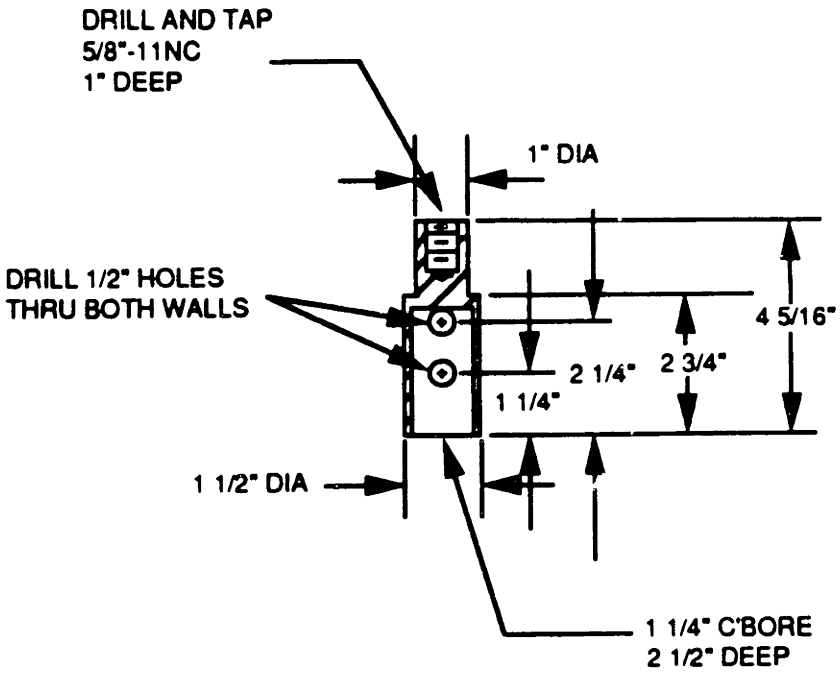

DETAIL 2

1/2 SIZE

MATL: AL 6061
OR STEEL

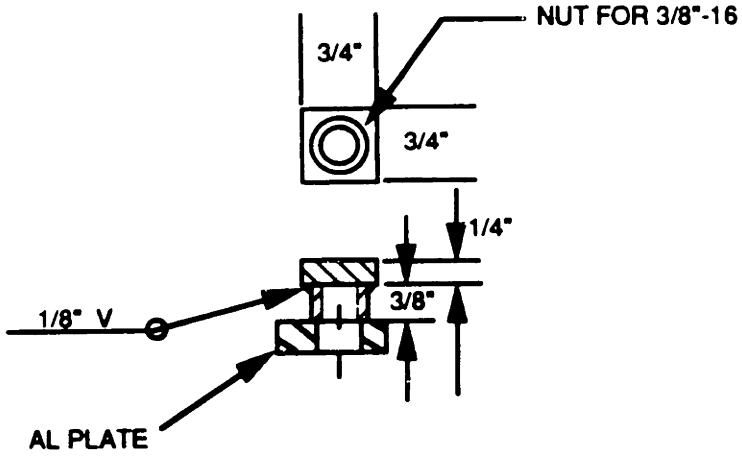

DETAIL OF PINS

AL 6061
REQ 4

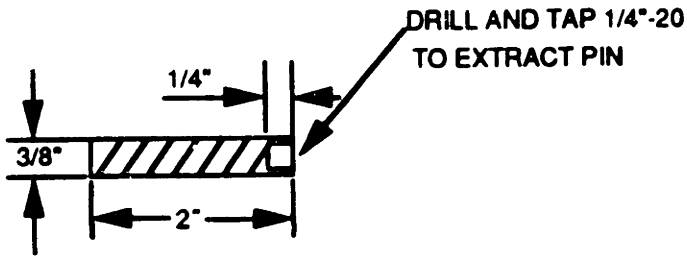

Appendix B:

Neutron Activation Analysis of Lead.

To: Professor Otto Harling
From: Ronald Rogus RR
Date: 7April91
Re: NAA of lead for the horse collar

The lead that will be used in the new horse collar has been analyzed by NAA. We were mostly interested in identifying activation products that could lead to a radiological concern during the potential conversion to the Phase II design. Another concern was the build-up of activation products that could create a photon source nearer the patient.

Lead samples were obtained from two local smelters. Samples were taken from the same batch of lead that would be used in the horse collar. Samples (1"x1"x1/2") were irradiated in the M55 beam, just below the collimator, for 2 hours. Samples were irradiated both bare and covered with a 1/2" boral plate.

The important activation products were:

RN	$T_{1/2}$	Decay Mode
Sb-122	2.75 days	β^- to stable isotope
Sb-124	60.9 days	"
In-116m	54 mins	"

Just after irradiation, the major source was Sb-122. The lead samples had different levels of antimony activation:

Sample	Sb-122 (counts/wt) norm	$/pound
Cambridge Smelting	22.4	0.75
Somerville Smelting		
gen purpose Pb	100.	0.70
corroding Pb	17.0	0.75

The Somerville corroding lead had the least activation and cost about the same as the other samples. Covering the lead with a boral plate reduced the activation in all samples by a factor of 2.4. The bare, Somerville general purpose

sample just after irradiation gave a net exposure of 1.3 mR/hr (β^- and γ on contact) and 0.3 mR/hr (β^- on contact). Exposure rates were determined with a calibrated GM tube. Exposure data is available for the other samples, but the above table can be used for scaling.

Before installing Phase II, the Sb-122 and In-116m would be allowed to decay to negligible levels. The remaining activation product would be Sb-124. A rough scaling was made of activation levels, time, flux, and mass for the boral covered lead horse collar. It is estimated that the exposure rate (β^- and γ) on contact would be only 10 mR/hr for the Somerville corroding sample. An upper bound would be 100 mR/hr. These exposure rates would be only a minor radiological concern. Also, this level of activation would not increase the patient's photon dose.

It is recommended that the Somerville corroding lead be used for the horse collar. As it turns out, the horse collar is being made only several blocks from Somerville Smelting.

Appendix C:

Drawings of the Stove Pipe.

Stove Pipe

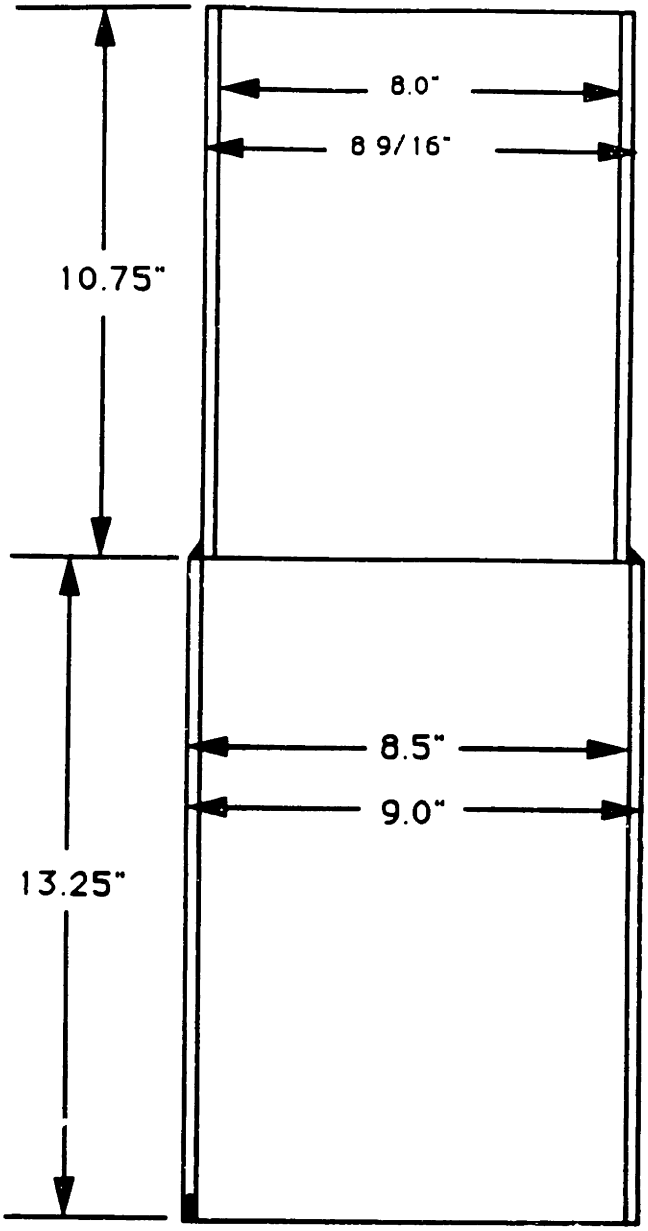

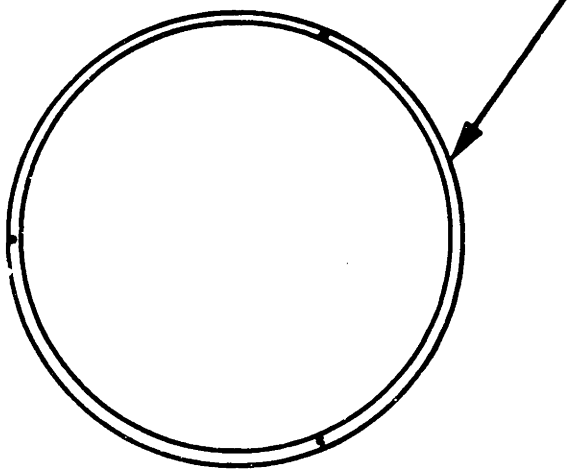

3 EqSp 10-24 tap holes
8 3/4" BC, 1/2" deep,
to match filter support
ring

Scale: 1/4 size

All matls 6061 Aluminum
Tolerance limits ± 0.010"

Sulfur Can Inside Stove Pipe

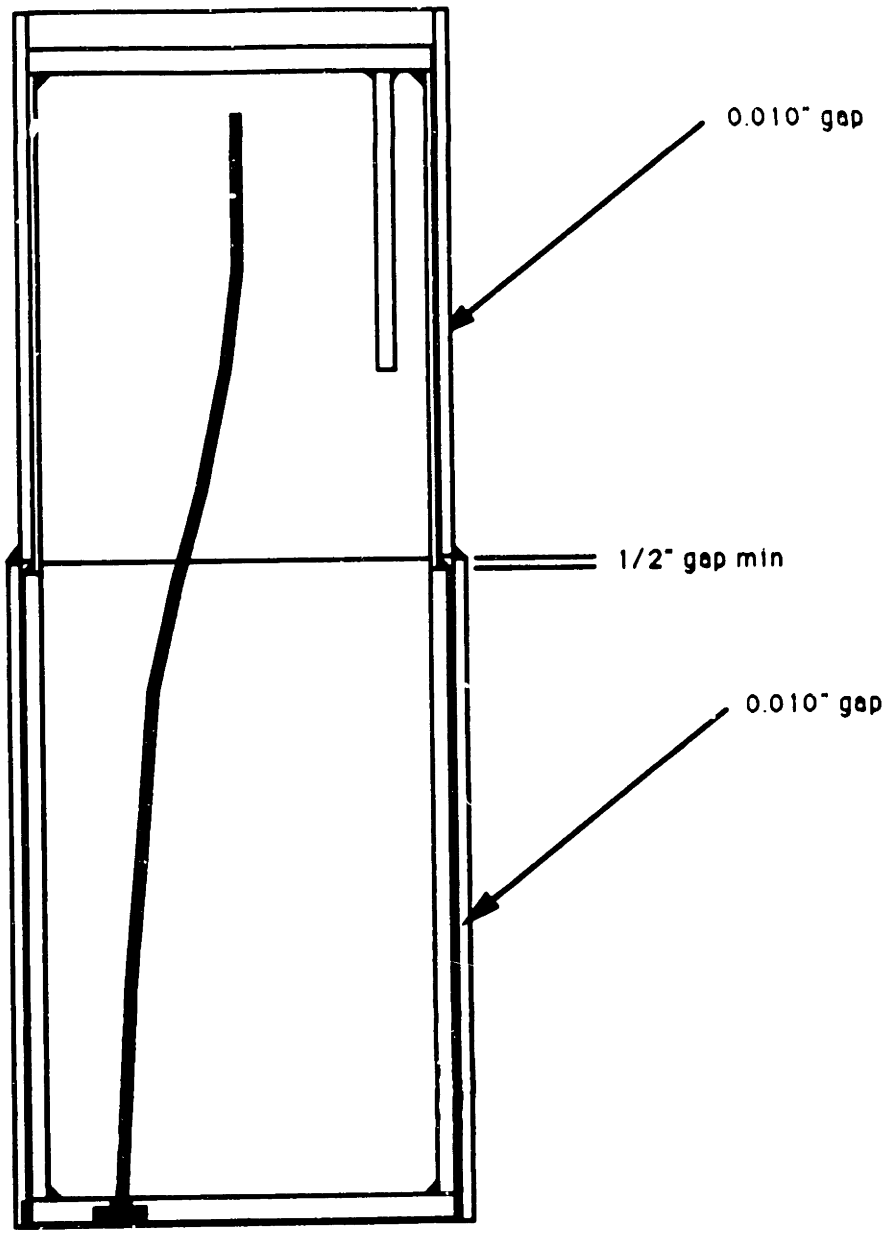

Appendix D:

Drawings of the Sulfur Filter.

Sulfur Can

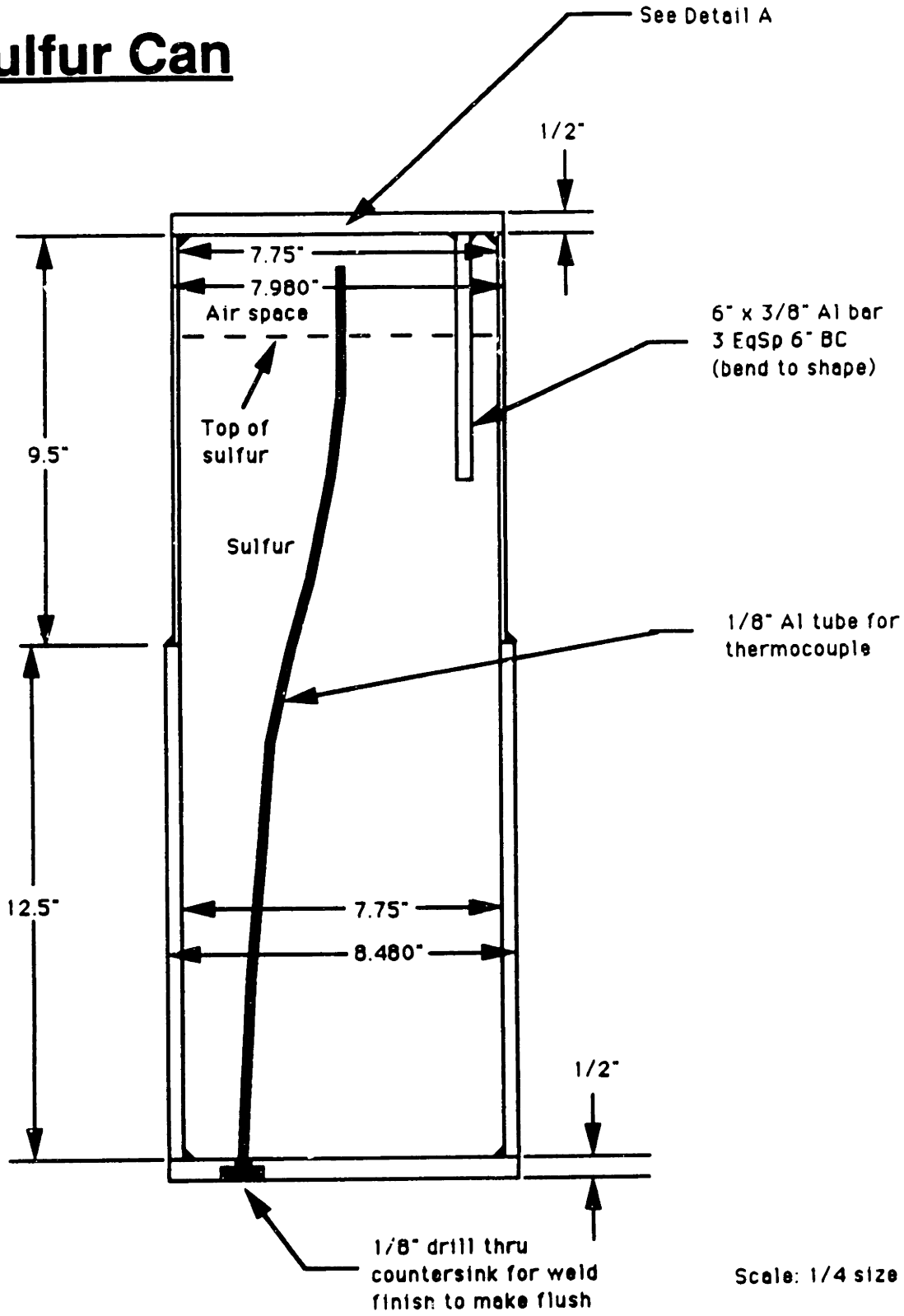

Scale: 1/4 size

All metls 6061 Aluminum
Tolerance limits ± 0.010"

Lid of Sulfur Can - Detail A

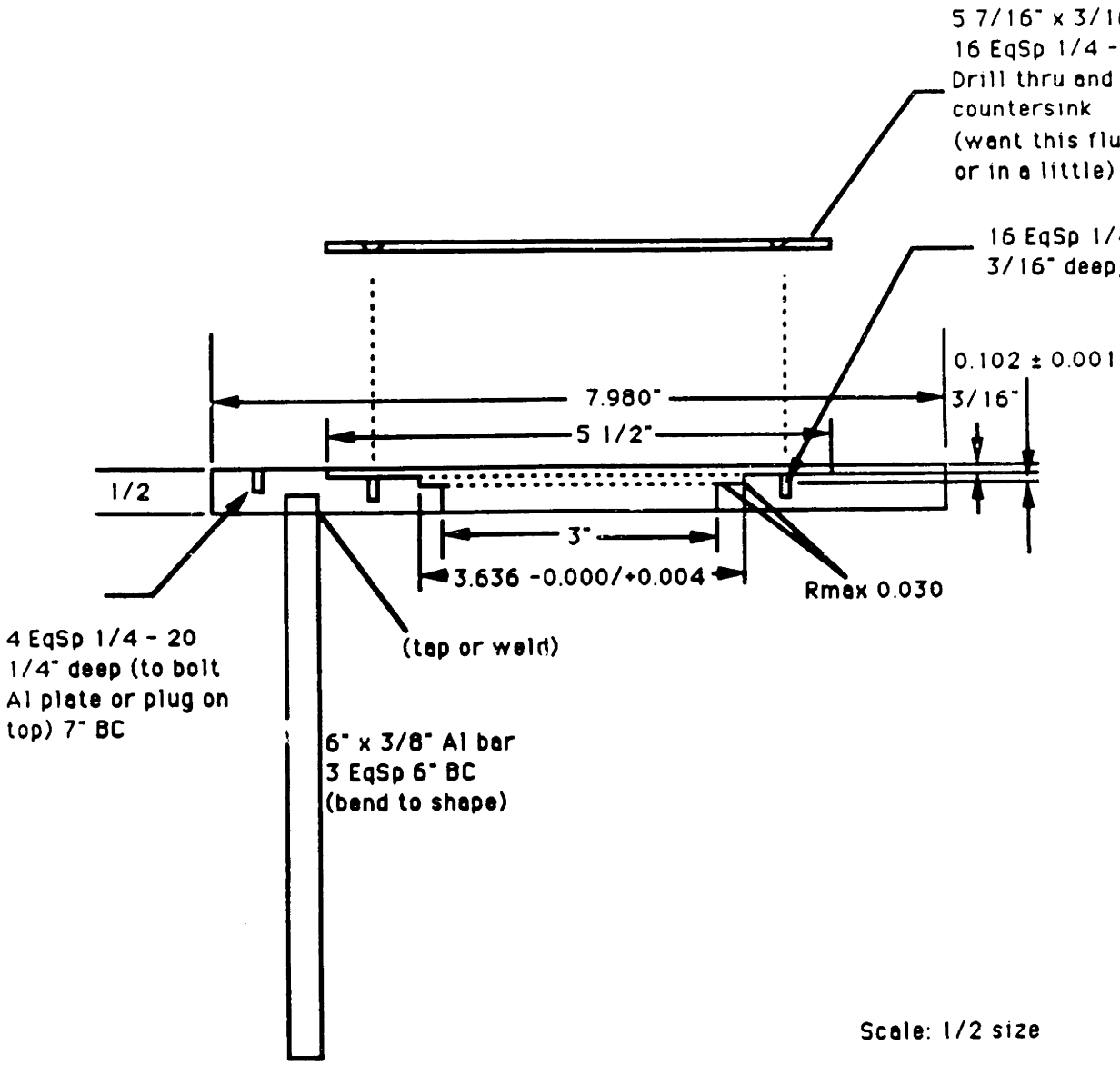

Scale: 1/2 size

All matls 6061 Al
Tol limits ± 0.010"

Internal pressure metal C ring
OD 3.628" with 0.002" Pb plate

Note: Changed all 8-32 to 1/4 - 20

Appendix E:

Chemical Properties of Sulfur.

Dangerous Properties of Industrial Materials

Fifth Edition

N. IRVING SAX

SULFUR. Syns: *brimstone, flowers of sulfur, sulfur flour.* Rhombic yellow crystals or yellow powder. S_8, mw: 256.48, mp: 119°, bp: 444.6°, flash p: 405°F (CC), d: 2.07; d(liquid): 1.803; autoign. temp.: 450°F, vap. press: 1 mm @ 183.8°.

THR = Very LOW. See nuisance dusts. A fungicide. Chronic inhal can cause irr of mu mem.

Radiation Hazard: For permissible levels, see Section 5A, Table 5A.5. Artificial isotope ^{35}S, $T_{\frac{1}{2}}$ = 88d, decays to stable ^{35}Cl via β's of 0.17 MeV.

Fire Hazard: Slight, when exposed to heat or flame, or by chemical reaction with oxidizers.

Spont Heating: No.

Explosion Hazard: In the form of dust, when exposed to flame. Can react violently with halogens, carbides, halogenates, halogenites, zinc, uranium, tin, sodium, lithium, nickel, palladium, phosphorus, potassium, indium, calcium, boron, aluminum, (aluminum + niobium pentoxide), ammonia, ammonium nitrate, ammonium perchlorate, BrF_5, BrF_3, (Ca + VO + H_2O), $Ca(OCl)_2$, Ca_3P_2, Cs_3N, charcoal, (Cu + chlorates), ClO_2, ClO, ClF_3, CrO_3, $Cr(OCl)_2$, hydrocarbons, IF_5, IO_3, PbO_2, $Hg(NO_3)_2$, HgO, Hg_2O, NO_2, P_2O_3, (KNO_3 + As_2S_3), K_3N, $KMnO_4$, $AgNO_3$, Ag_2O, NaH, ($NaNO_3$ + charcoal), (Na + SnL_4), SCl_2, Tl_2O_3. [*19*]

Disaster Hazard: Dangerous; when heated it burns and emits highly toxic fumes of SO_x. Can react with oxidizing materials.

To Fight Fire: Water or special mixtures of dry chemical.

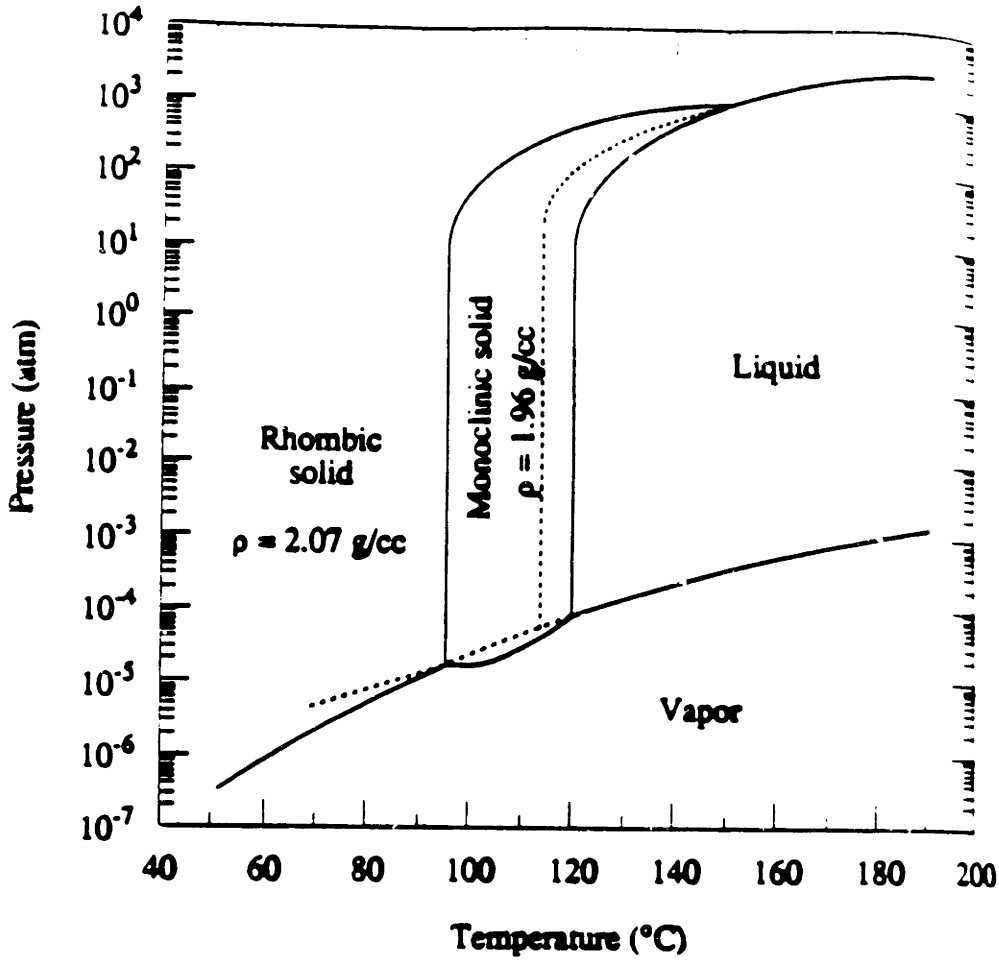

Phase diagram for sulfur. The dashed lines represent metastable transition lines for sulfur. The solid lines represent stable transition lines.[4]

Appendix F:

Procedure for Removal and Installation.

Procedure for Medical Room Horsecollar and Filter Removal/Installation

Initial Conditions

_____ Work schedule coordinated with Operations and RRPO.

_____ Reactor shutdown at least 48 hours.

_____ All equipment, tools, and materials at the ready.

_____ Transporter fully charged and at the medical area. (maximum load of transporter is 5000 pounds.)

_____ Big Joe with new battery, fully charged, at the medical area.

_____ D_2O and H_2O shutters full.

_____ Personnel performing evolution in continuous communication with the Control Room.

_____ Use buddy system at all times.

_____ RRPO to provide monitoring as needed during the procedure.

Preparation of Medical Room

_____ Remove tables and unnecessary items from the medical room. RRPO to survey all items removed from the medical room for contamination or induced activity.

_____ Wrap remaining items in plastic to protect them from contamination.

_____ Station a large fire extinguisher outside the medical room.

_____ RRPO to survey the medical room.

Removal of Stove Pipe, Aluminum Shot, and Liner

_____ Use remote handling tools whenever possible.

_____ Remove the collimator.

_____ Notify Control Room that the medical door will be bypassed.

_____ Bypass medical room door and open lead shutter.

_____ Close and tag CV-77 (compressed air supply to pneumatic cylinders).

_____ RRPO establish local beam port ventilation.

_____ RRPO establish step-off pad area.

_____ RRPO set-up and test air sampling rig.

_____ RRPO to provide hoods, boots, and respirators.

_____ Personnel performing installation to don full protective clothing and respiratory protection.

_____ The aluminum plug in the stove pipe will be kept in place for the time being.

_____ Secure a tent around bottom of stove pipe.

_____ Unbolt stove pipe from flange. Push aluminum plug up until it hits the step in the stove pipe and then push up another inch or until the aluminum shot starts pouring out. Support Al plug and stove pipe with push rod.

_____ Collect shot in shielded barrel.

_____ Lower aluminum plug and stove pipe.

_____ Remove sulfur from bottom of H_2O shutter. This will be done by brushing and by sucking with a vacuum hose that penetrates the tent.

_____ Remove liner. Practice this procedure beforehand in mock-up.

_____ Remove tent. Survey floor and air for contamination.

_____ RRPO to survey for contamination.

_____ Open CV-77 and clear tag.

Removal of Medical Room Lead Shutter

_____ All ceiling interference removed.

_____ Disconnect lead shutter from operating shaft.

_____ Rolling masonite shield will have already been removed.

_____ Plug air filter in medical room exhaust and attach a sucker hose for venting the shutter area.

_____ Remove 8 bolts from the outer plug ring and install 4 angle clips (2 bolts for each clip).

_____ Hang 4 chain falls and shackles to clips.

_____ Secure chain falls to eye bolts in spacing frame and elevate to the shutter. Secure to frame. Cribbing may be used if needed.

_____ Remove bolts from shutter rails. Drop rails and place them on spacing frame.

_____ Carefully lower shutter on chain falls. Maintain level.

_____ RRPO to monitor radiation levels and check for contamination.

_____ Remove chain falls and shutter rails from medical room.

_____ Wheel shutter to one side of the medical room. (Note: Lift frame has casters. The shutter will not be removed from the medical room.)

Removal of Medical Shutter Outer Plug

_____ Lead shutter removed. All ceiling interference removed.

_____ RRPO to monitor radiation levels and check for contamination.

_____ Position transporter and lifting frame under shield plug.

_____ Remove bolts securing shield to reactor structure.

_____ Carefully lower shield plug with transporter.

_____ Raise temporary lead shield to block the direct beam.

_____ Lift old bismuth collar and set it on the floor.

_____ Lift new horsecollar and position it on top of outer plug.

Installation of Shield Plug, Lead Shutter, and New Filter

_____ Remove temporary lead shield.

_____ Raise outer plug and bolt.

_____ Install lead shutter.

_____ Install new aluminum liner. Practice this procedure beforehand in mock-up.

_____ Insert stove pipe and bolt to bottom of horsecollar.

_____ Blow aluminum shot into place.

_____ Install the sulfur filter can.

Recovery from Installation

_____ Tools and equipment removed from the medical room in accordance with the proper radiation protection procedures.

_____ Perform contamination survey and establish area free for normal entry.

_____ Perform radiation surveys upon resumption of reactor operation but prior to permitting general access to the medical room.

Appendix G:

Sketch of the Expected Radiation Field After Removal of the Lead Shutter and Outer Shield.

Dose Rate (R/h) versus Distance (feet) from Lead Shutter on Centerline with all Filters Removed, Lead Shutter Opened, and Bismuth Plug Removed.

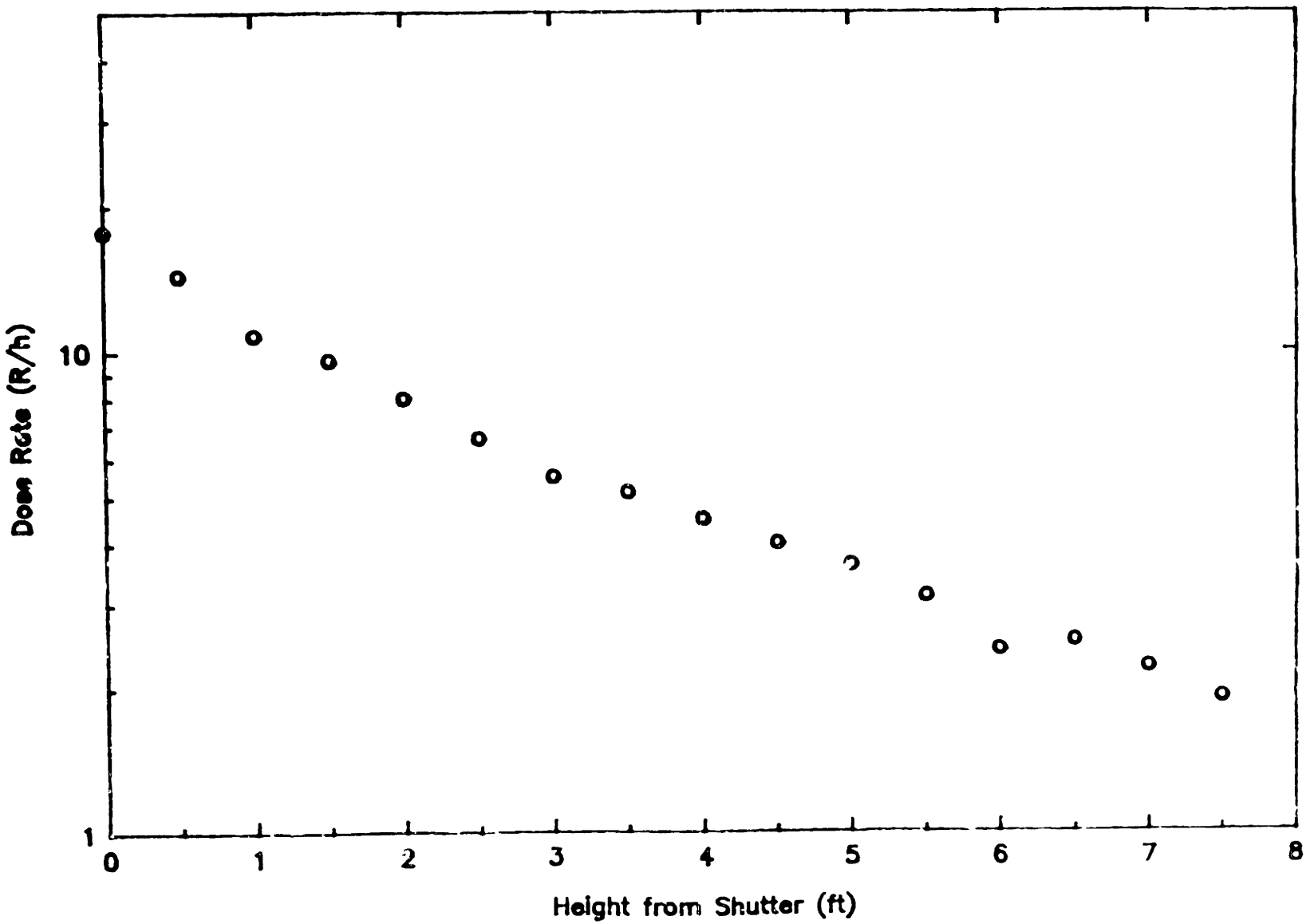

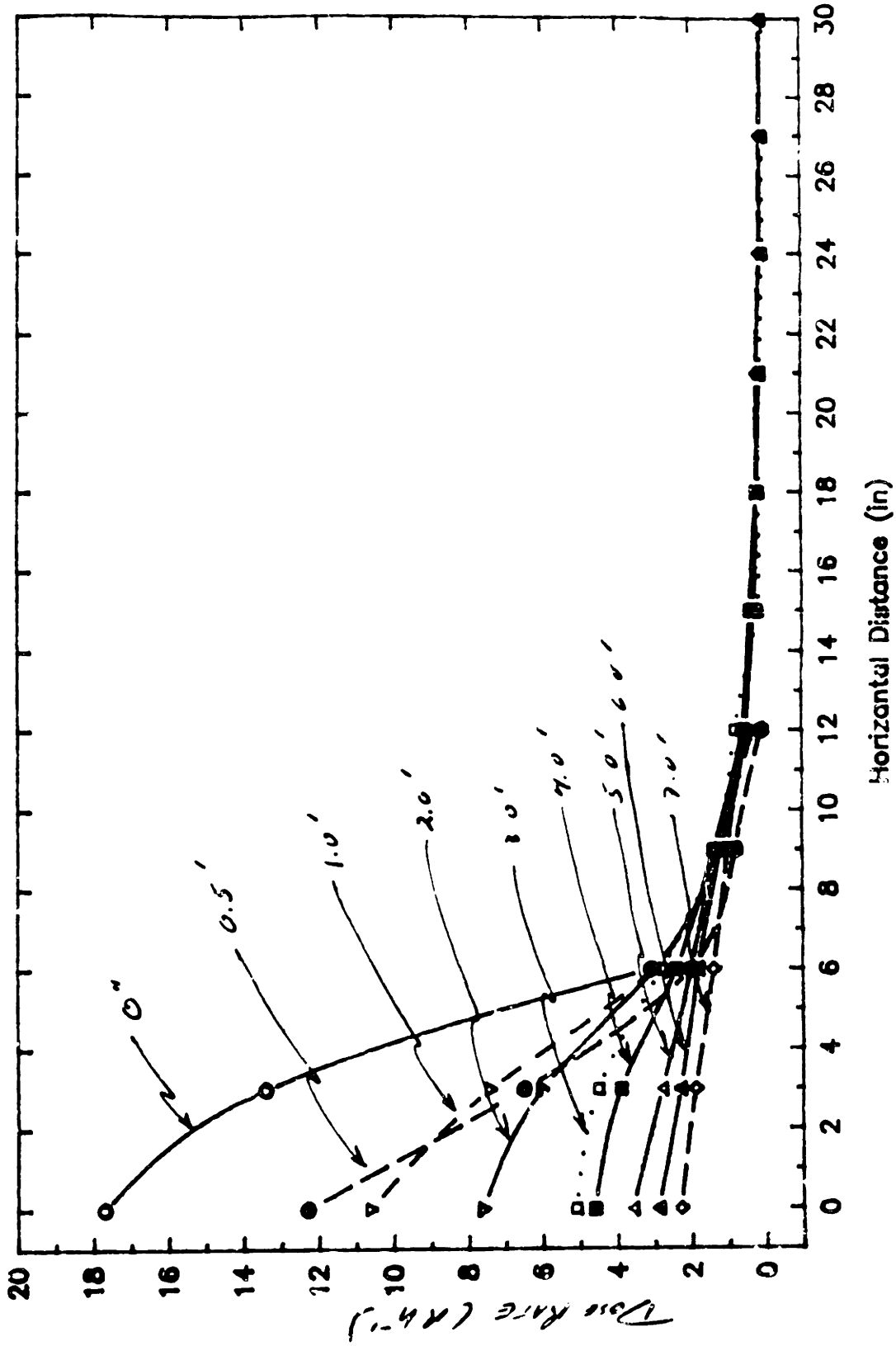
0"
0.5'
1.0'
2.0'
3.0'
4.0'
5.0'
6.0'
7.0'
Horizontal Distance (in)
0
2
4
6
8
10
12
14
16
18
20
22
24
26
28
30
20
18
16
14
12
10
8
6
4
2
0

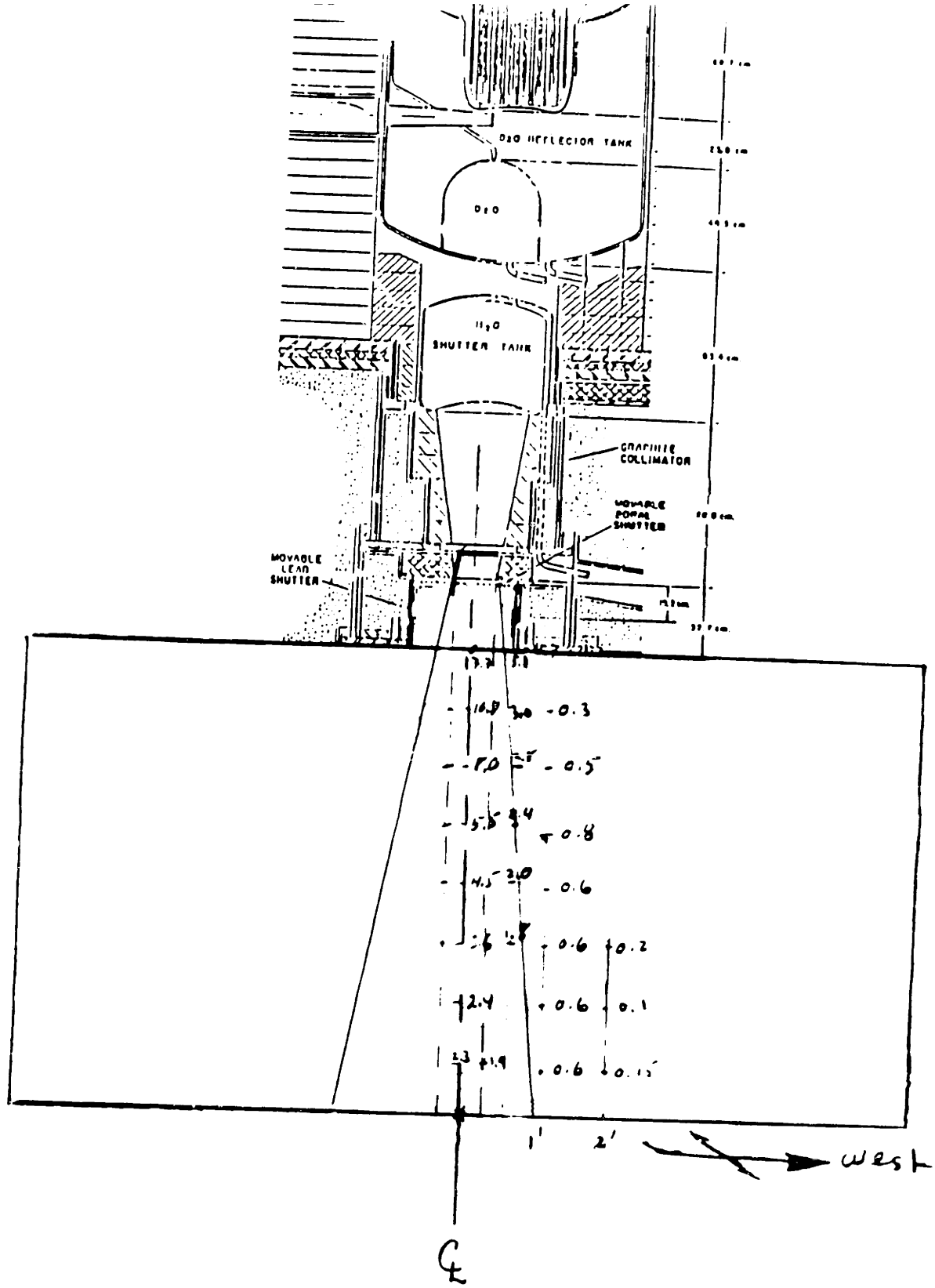
D2O REFLECTOR TANK
D2O
H2O SHUTTER TANK
GRAPHITE COLLIMATOR
MOVABLE POWER SHUTTER
MOVABLE LEAD SHUTTER
-0.3
-0.5
-0.8
-0.6
-0.6
-0.2
-0.6
-0.1
-0.6
-0.1
1'
2'
west
℄

3/8" ≈ 1

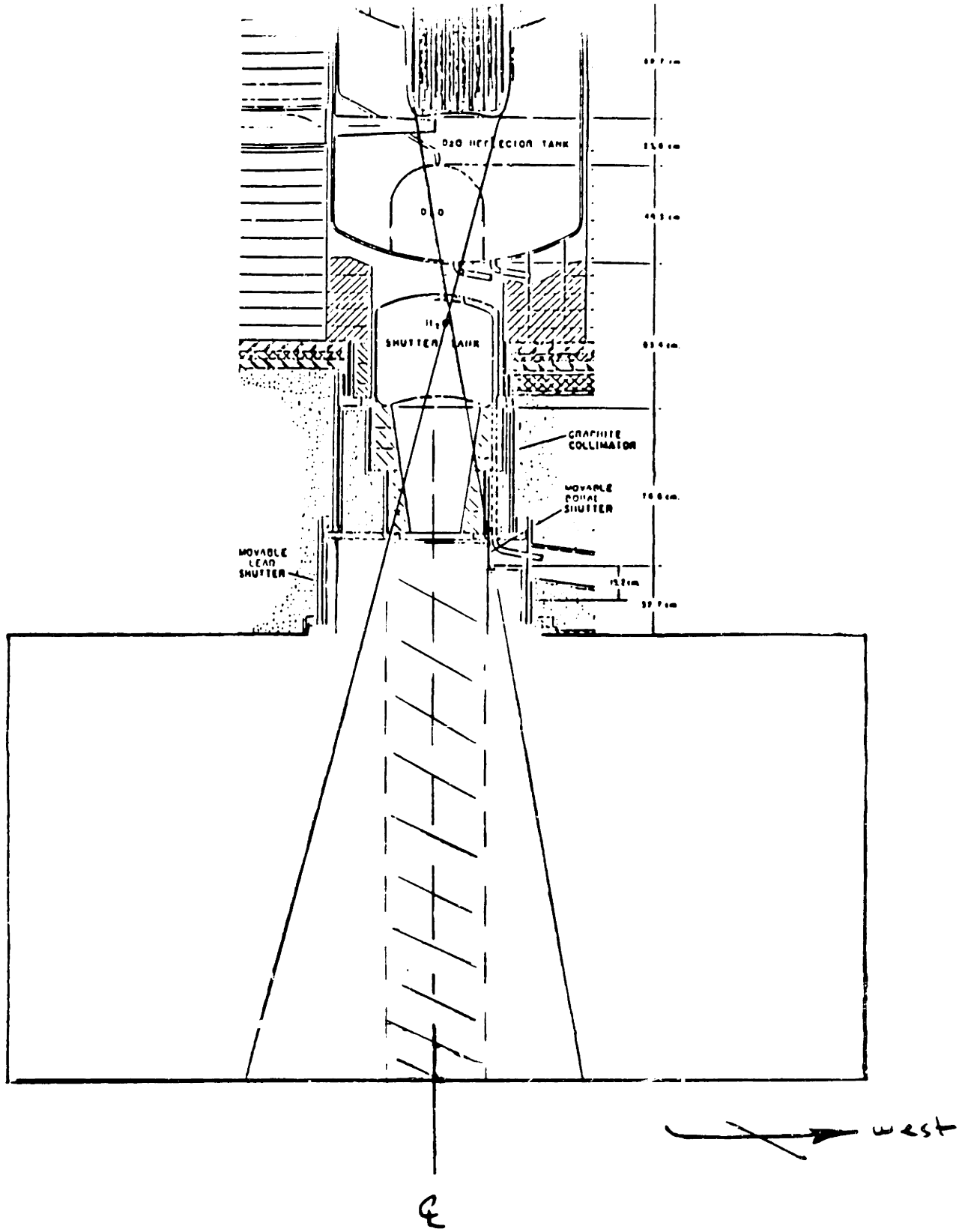
SHUTTER GAIN
GRAPHITE COLLIMATOR
MOVABLE BORAL SHUTTER
MOVABLE LEAD SHUTTER
west
℄

Item: Medical Room Stovepipe Modification and Shot Addition

Submitted by R. Rogus Date 02/28/92

Q/A number if required M-88-4

Does the item change or contradict the

Technical Specifications? ____ Yes* X No

SAR? ____ Yes* X No

* Attach explanation

Description of Change (Attach extra pages if necessary):

See attached sheet.

Safety Evaluation (Attach extra pages if necessary):

See attached sheet.

Summary of Review:

a) Does the proposal:	Yes	No
i) involve an unreviewed safety question (10CFR50.59(a)(2))	___	X
ii) decrease scope of requalification program (10CFR50.54(i-1))	___	X
iii) decrease effectiveness of security plan (10CFR50.54(p))	___	X
iv) decrease effectiveness of emergency plan (10CFR50.54(q))	___	X

b) Reviewer's Comments:

Recommend Approval // Yes ____ No RRPO [signature] Date 3/2/92

Reviewer [signature] Date 03/02/92

Reviewer [signature] Date 3/2/92

Approved [signature] Date 3-2-92
(Director of Reactor Operations)

10CFR50.59 & 50.54(p and q) changes logged for reporting to NRC, Date ____

Copy to Director for Operations
Copies circulated to and initialled by all Licensed Personnel
Original to Safety Review File

Unreviewed Safety Question (URSQ) Determination for SR#-0-92-4

This safety review does NOT involve an URSQ. The basis for that conclusion is documented below as required by 10 CFR 50.59(b).

(a) The change does not meet any of the three criteria that define an URSQ. This is shown below:

- No increase in probability of occurrence or consequences of any accident or malfunction of equipment important to safety previously evaluated in the safety analysis report (SAR) will occur because this change does not increase the severity of any accident analyzed in the SAR. This structural change to an existing experimental facility will not require the removal or inhibit any existing permanent reactor shielding.

- No new type of accidents are created.

- No margin of safety is reduced because the proposed change does not alter or contradict any of the bases for the technical specifications.

Safety Review #-0-92-4

Medical Room Stovepipe Modification and Shot Addition

Reference: SR#-0-91-7, "Medical Room Horsecollar and Filter Removal/Installation"

Description of Change

The stovepipe will be extended with a 4.75" long aluminum spacer tube. The spacer will be positioned below the stovepipe and then the spacer and stovepipe lifted with the transporter. Three threaded rods will be run along this spacer tube to secure the original stovepipe. Shot (aluminum and cadmium-plated aluminum) will be air-lifted over the top of the stovepipe to bring the shot level up to the level of the stovepipe. Drawings of the current beam (Figure 1), the proposed beam (Figure 2), and the spacer (Figure 3) are attached. A procedure for accomplishing this change is also attached (Appendix A).

The spacer is made of aluminum-6061 and has an OD and ID that are close to that of the stovepipe. Three grooves have been milled into the sides of the spacer to allow space for the threaded rods. These rods will be threaded into the bottom of the stovepipe. Nuts will secure them to the retainer plate that is bolted into the horsecollar.

The aluminum shot is the same 2-5 shot (disc shaped, 1/2" diameter, 1/5" thick) that is currently used. The purity is 99.99%. In addition to this pure aluminum shot, some cadmium-plated aluminum shot will also be used. About a two-inch layer of the cadmium-plated shot will be used at the top of the shot column. The base material for the cadmium-plated shot is the usual 2-5 shot. This shot was first flashed with nickel at 50 millionths of an inch and then cadmium-plated at 0.0005 inch.

Experience with the shot, stovepipe, cadmium sheets, and aluminum structure in the filter region in the Phase I beams has shown no structural or other adverse effects. The proposed beam is similar to the Phase I beam except for the two-inch layer of cadmium-plated shot. Cadmium is being used as a thermal neutron absorber. The radiative capture reactions will produce gammas that will locally increase the gamma heating. As a result, melting of the cadmium is a concern. The melting point of cadmium is 321 °C.

Temperatures in this region have been measured by Choi, Rogus, and Lau. Choi measured the temperature at the surface of the graphite in a region just below the water shutter (Figure 4). The equilibrium temperature was 40 °C and was reached after several days at full reactor power. Then, with the water and D_2O shutters open, the temperature increased to 47 °C in one hour (average of 7 °C/hr). Choi also measured the temperature on top of the original sulfur filter can (Figure 5). The starting temperature was 30 °C, and the temperature increased to 60 °C in 105 minutes (average of 17 °C/hr). He estimated that it might take ten hours to reach the melting point of sulfur, 113 °C, if the heating trend continued.

Rogus measured the temperature inside of and near the top of the Phase I sulfur filter can. Two experiments were done. In the first (Figure 6), the starting temperature was 28 °C, and the temperature increased to 73 °C in 205 minutes (average of 13 °C/hr). In the second experiment (Figure 7), the graphite and sulfur were initially at the end of the week steady-state temperature. The starting temperature was 37 °C, and the temperature increased to 69 °C in six hours (average of 6 °C/hr). In this latter irradiation, the temperature rose more slowly than in the first.

Lau measured the temperature distribution in the 3GV2 vertical thimble. A simplified view of the thimble is shown in Figure 8. The measured temperature profiles are shown in Figure 9. At the bottom region of graphite, the temperature is about 120 °C. The temperature appears to continue dropping with distance from the core.

In all these measurements the temperature showed some degree of saturation effect. That is, the rate of temperature increase slowed down with time.

From the above data, it is concluded that the temperature of the graphite surrounding the aluminum shot will be at most 120 °C with both the D_2O and H_2O shutters open. Also, the temperature of the sulfur filter will not be allowed to rise above 90 °C. Given that heat transfer through the shot itself is good, it is concluded that the shot will remain cool, well below the melting temperature of cadmium.

It should also be noted that in a previous design a sheet of cadmium was in contact with an aluminum plate that rested at the top of the old stovepipe. There was no apparent heating problem.

Radiological Issues of Installing the Modification

Radiological issues have been discussed with the MITR Radiation Protection Officer and are addressed in the installation procedure (Appendix A). The major concern is the high exposure rates just below the stovepipe where six bolts must be removed and three threaded rods inserted. Air-lifting the aluminum shot has been done safely before.

Safety Evaluation

The Reactor Operations Staff, after independent review concurs with the findings of the experimenter that the proposed change does not involve an unreviewed safety question. It is further noted that no permanent change is made in shielding for the reactor and that the materials used in the filter's construction are compatible. The temperature data are from several independent sources, each of whom is known to be a careful experimenter. Accordingly, it is also agreed that melting of the cadmium is not an issue. The major concern is therefore one of personnel safety during the installation. To that end, meetings were held with Reactor Operations, Maintenance, and Radiation Protection on 02/27/92 to review the procedure. Also, MIT RRPO held a separate meeting on 02/28/92.

Appendix A:

Procedure for Installation

Procedure for Installation of the Stovepipe Spacer and Shot

Initial Conditions

____ Installation schedule coordinated with Operations and RRPO.
____ Reactor shutdown at least 48 hours.
____ All equipment, tools, and materials at the ready.
____ Transporter fully charged and at the medical area.
____ Little Big Joe fully charged and at the medical area.
____ D_2O and H_2O shutters full.

Precautions

____ Keep D_2O and H_2O shutters full.
____ Keep control room operator informed of progress or problems.
____ Use buddy system at all times.
____ RRPO to provide monitoring as needed during the procedure.

Preparation of medical room

____ Remove tables and unnecessary items from the medical room. (Note: RRPO to survey all items removed from the medical room for contamination or induced activity.)
____ Wrap remaining items in plastic to protect them from additional contamination.
____ RRPO to survey the medical room.

Installation

____ Drop the collimator and remove from medical room.
____ RRPO to establish local beam port ventilation.
____ RRPO to establish step-off pad area.
____ RRPO to set up and test air sampling rig.
____ RRPO to provide hoods, boots, respirators, and any other protective gear.
____ Notify Control Room that the medical room door will be bypassed.
____ Bypass medical room door and open lead and boral shutters.
____ Disable operation of lead and boral shutters.

____ Use remote handling tools whenever possible.
____ Drop sulfur filter and replace with aluminum filter.
____ Personnel performing installation don full protective clothing and respiratory protection.
____ Position transporter underneath the filter with the lowering unit in place.
____ Undo the three screws in the retaining ring that thread into the stovepipe.
____ Undo the three bolts in the retaining ring that thread into the horsecollar.
____ Lower the retaining ring.
____ Screw the three aluminum-threaded rods into the stovepipe. Adjust so the flats face inwards.
____ Position the spacer tube and retainer ring. Use nuts to secure retainer and spacer to existing stovepipe.
____ Secure a tent around bottom of spacer.
____ Raise transporter bed slowly. Raise stovepipe and spacer using a flat bar to span both surfaces
____ Remove tent from bottom of spacer.
____ Bolt retainer ring to the horsecollar.
____ Drop aluminum filter.
____ Re-install tent.
____ Blow aluminum shot into place. Bring level to 2" below top of stovepipe. Top off with the cadmium-plated shot.
____ Install sulfur filter with 7 cm aluminum on top. Insert thermocouple into sulfur filter.
____ Remove tent.
____ Enable lead and boral shutters. Close shutters.
____ Re-install the collimator.
____ Survey floor and air for contamination.

Recovery from Installation

____ Tools and equipment removed from medical room in accordance with the proper radiation protection procedures.
____ Perform contamination survey and establish area free for normal entry.
____ Perform radiation surveys upon resumption of reactor operation but prior to permitting general access to the medical room.

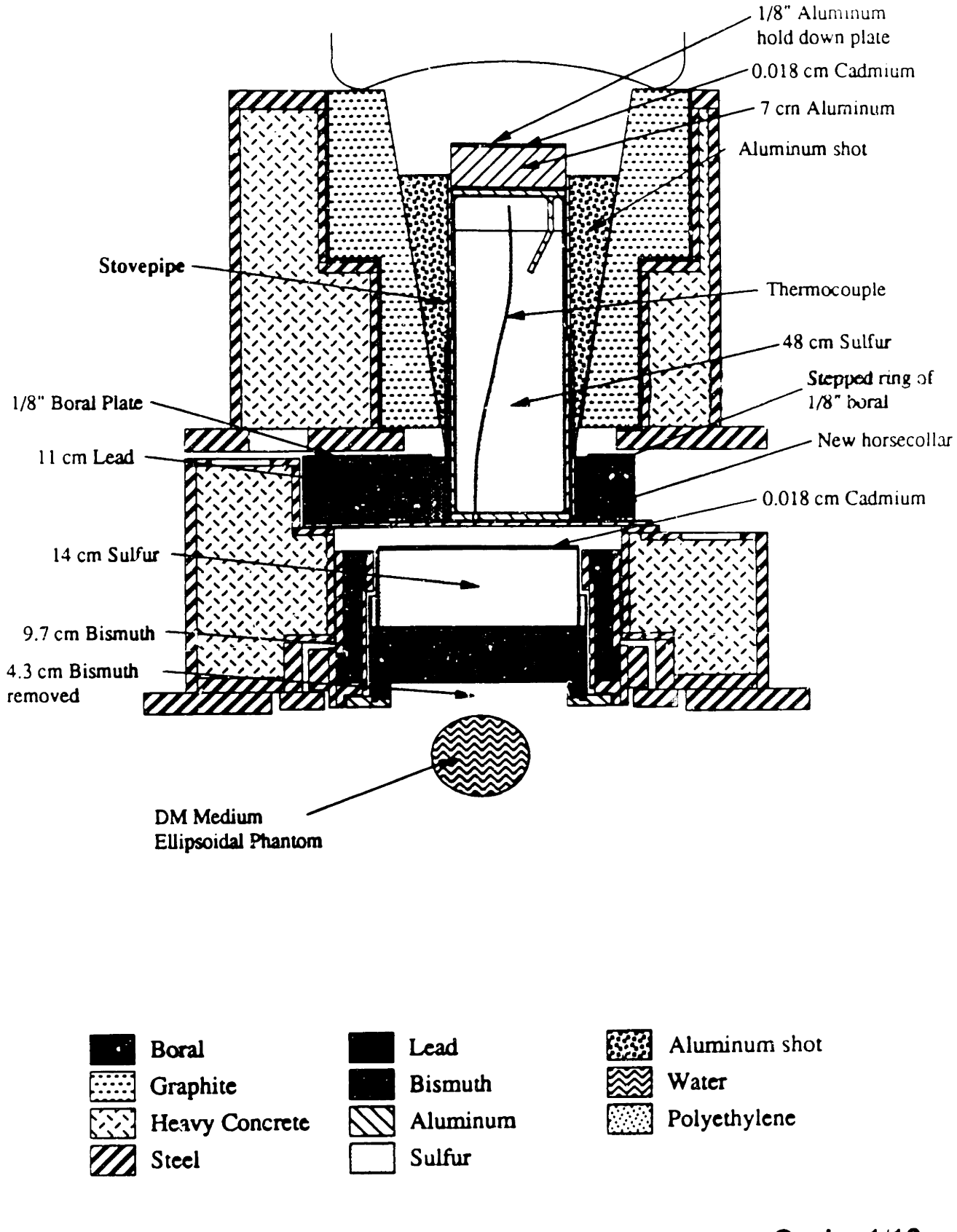

Figure 1. Current phase I configuration (beam M61) for comparison with proposed Phase II configuration.

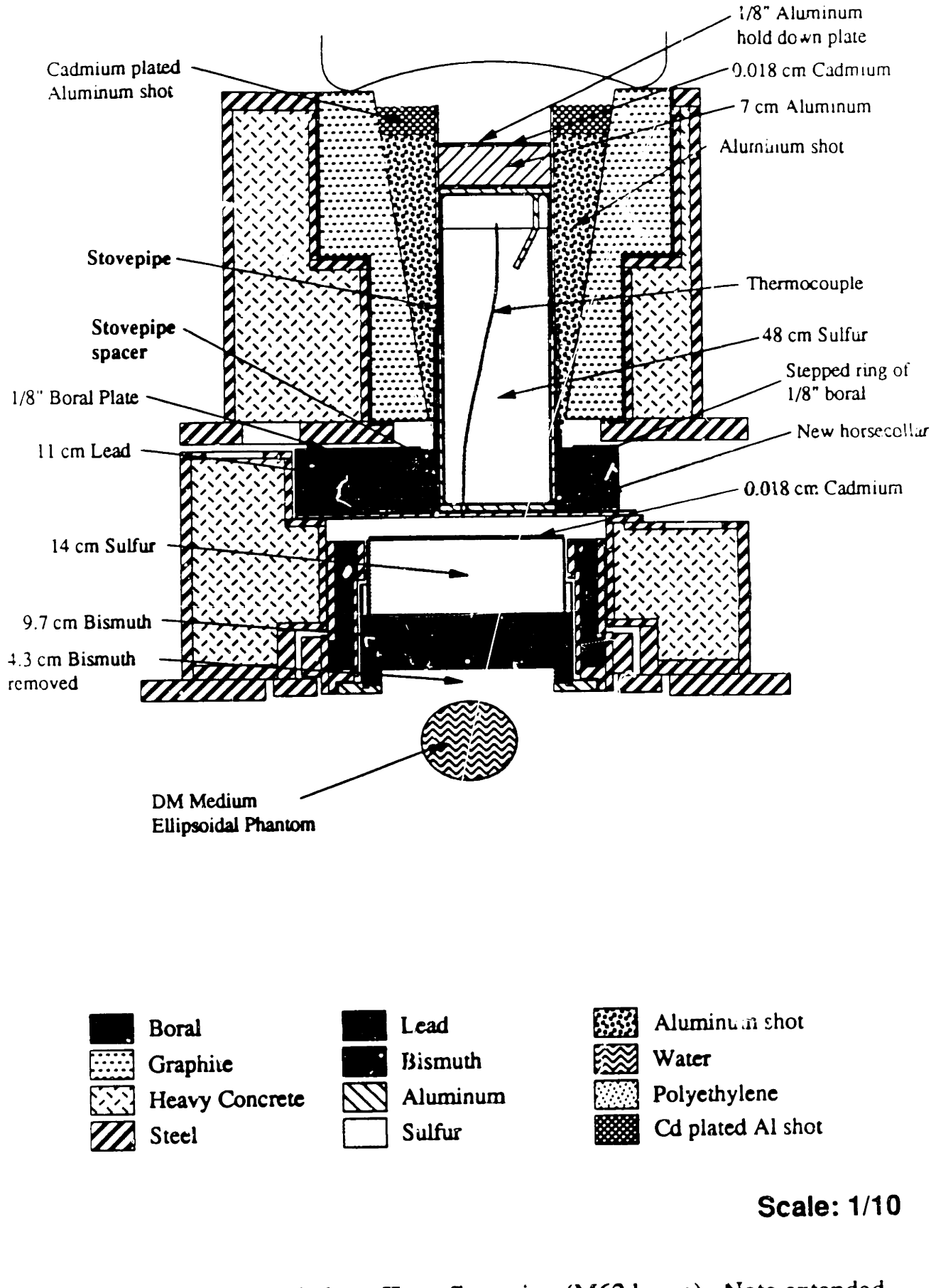

Figure 2. Proposed phase II configuration (M62 beam). Note extended stovepipe and additional shot.

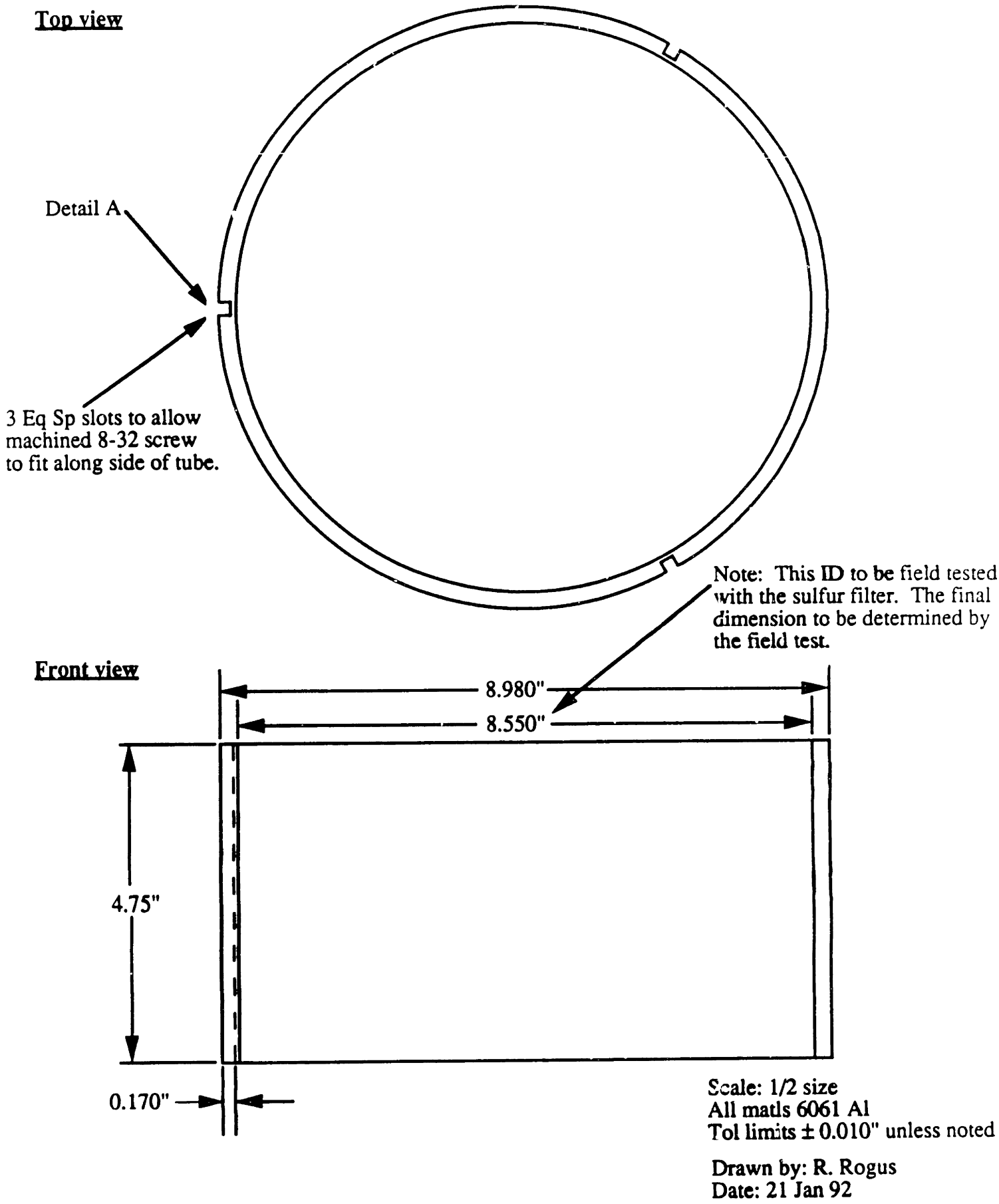

Figure 3. Drawing of spacer tube that will extend the stovepipe.

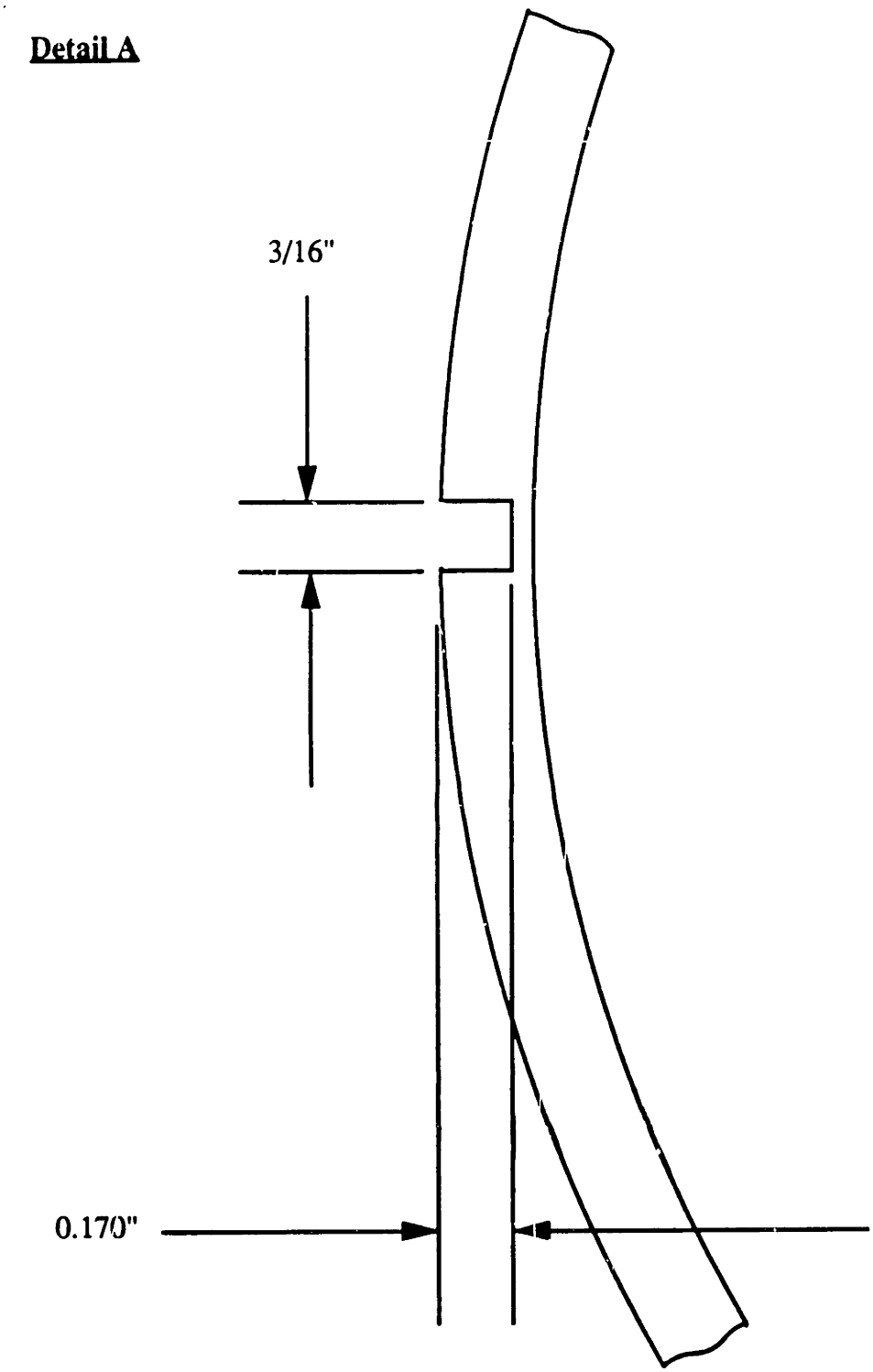

Note: Use 3/16" diameter end mill.

Detail A of Figure 3

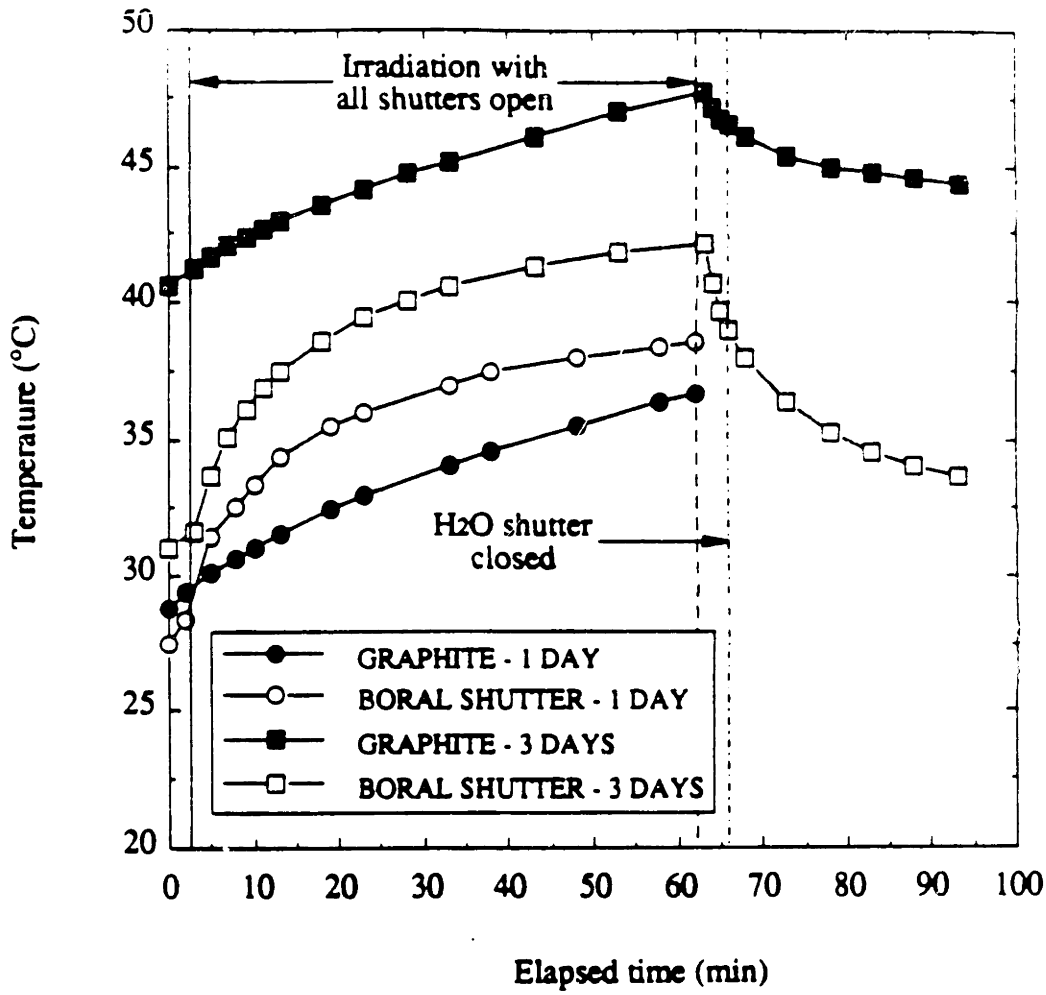

Figure 4. Temperature increase in the boral shutter and the graphite collimator as a function of medical shutter opening at first day and third day after reactor startup. (Source: Choi.)

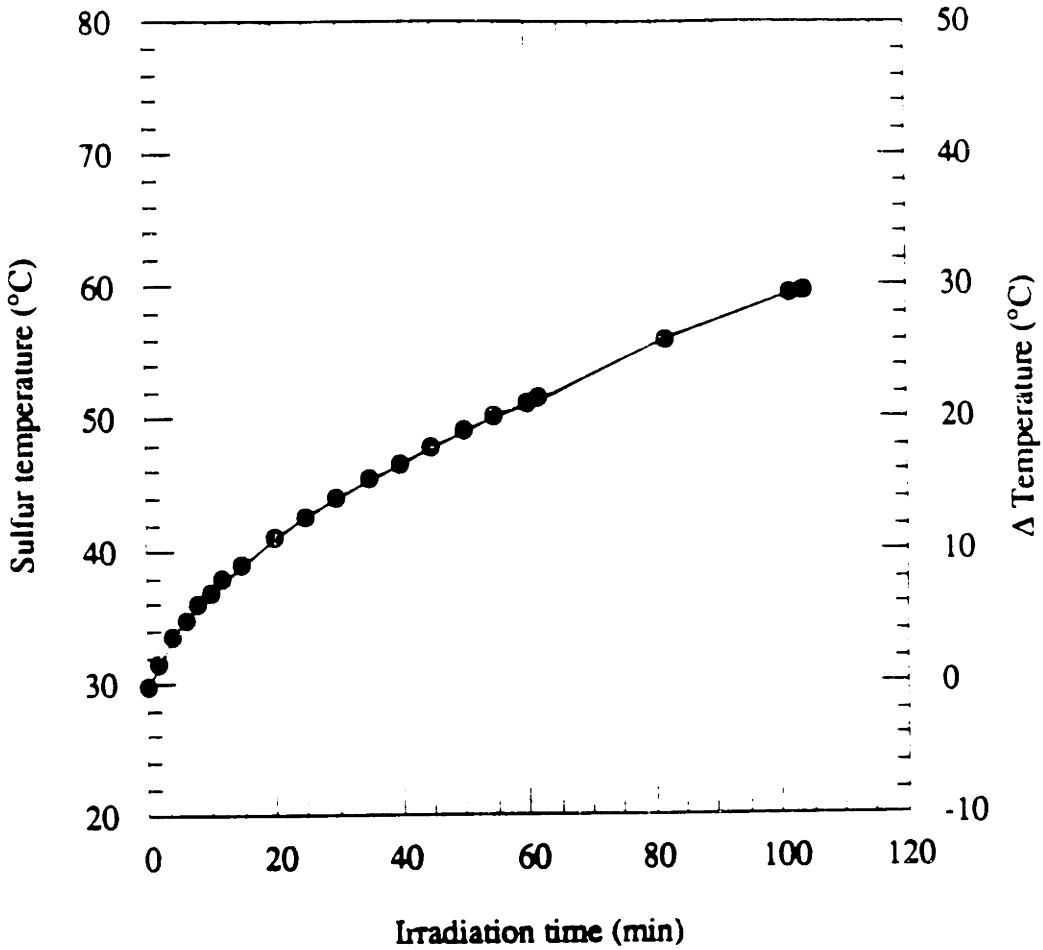

Figure 5. Temperature increase in the sulfur filter as a function of irradiation time. Reactor power at 4.5 MW. (Source: Choi.)

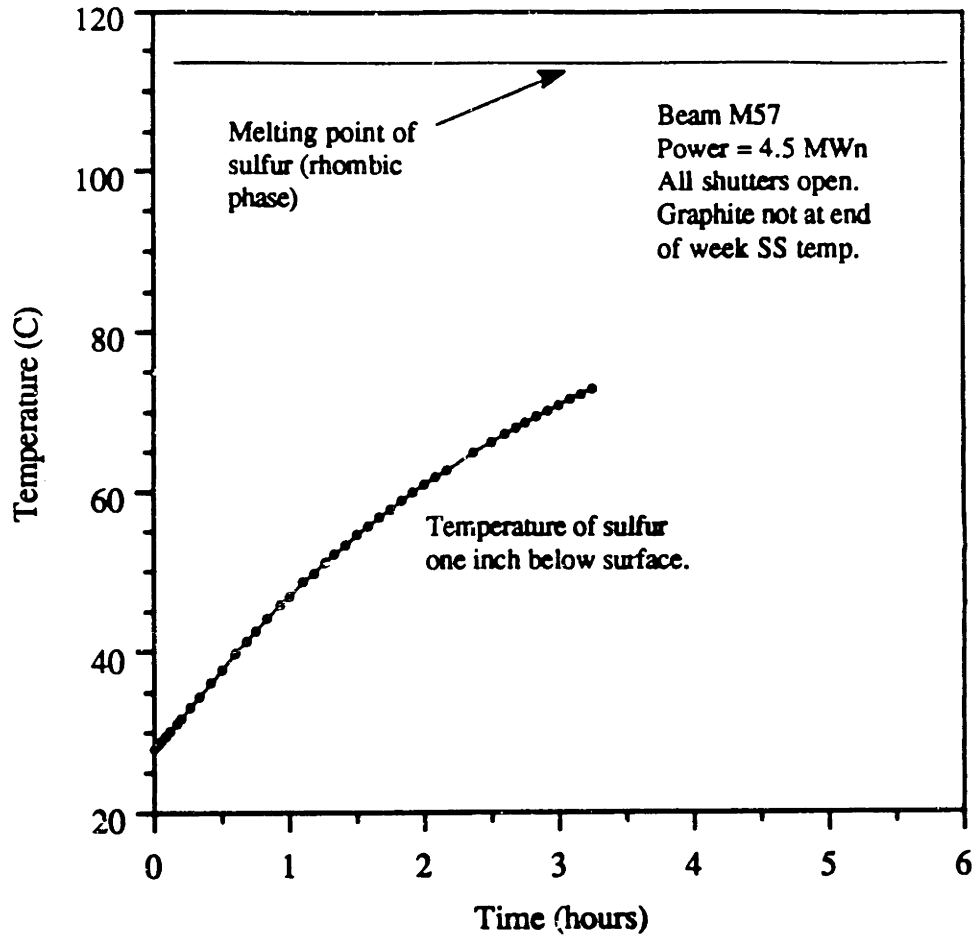

Figure 6. The sulfur temperature was measured on the axis of the can about one inch below the top surface of the sulfur. This region is expected to have the highest temperature. These results are for the first long irradiation of the Phase I sulfur filter. (Source: Rogus)

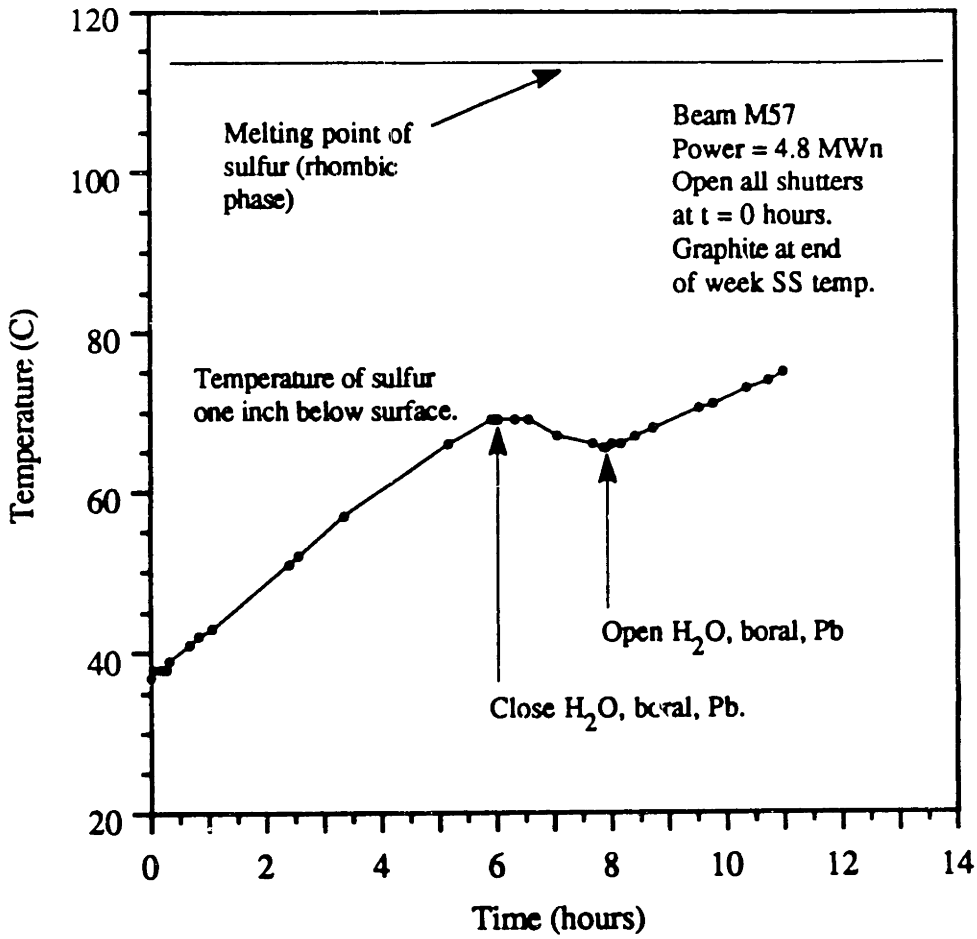

Figure 7. The sulfur temperature was measured on the axis of the can about one inch below the top surface of the sulfur. This region is expected to have the highest temperature. These results are for the second long irradiation of the Phase I sulfur filter. In this irradiation, the temperature rose more slowly than in the first irradiation. (Source: Rogus)

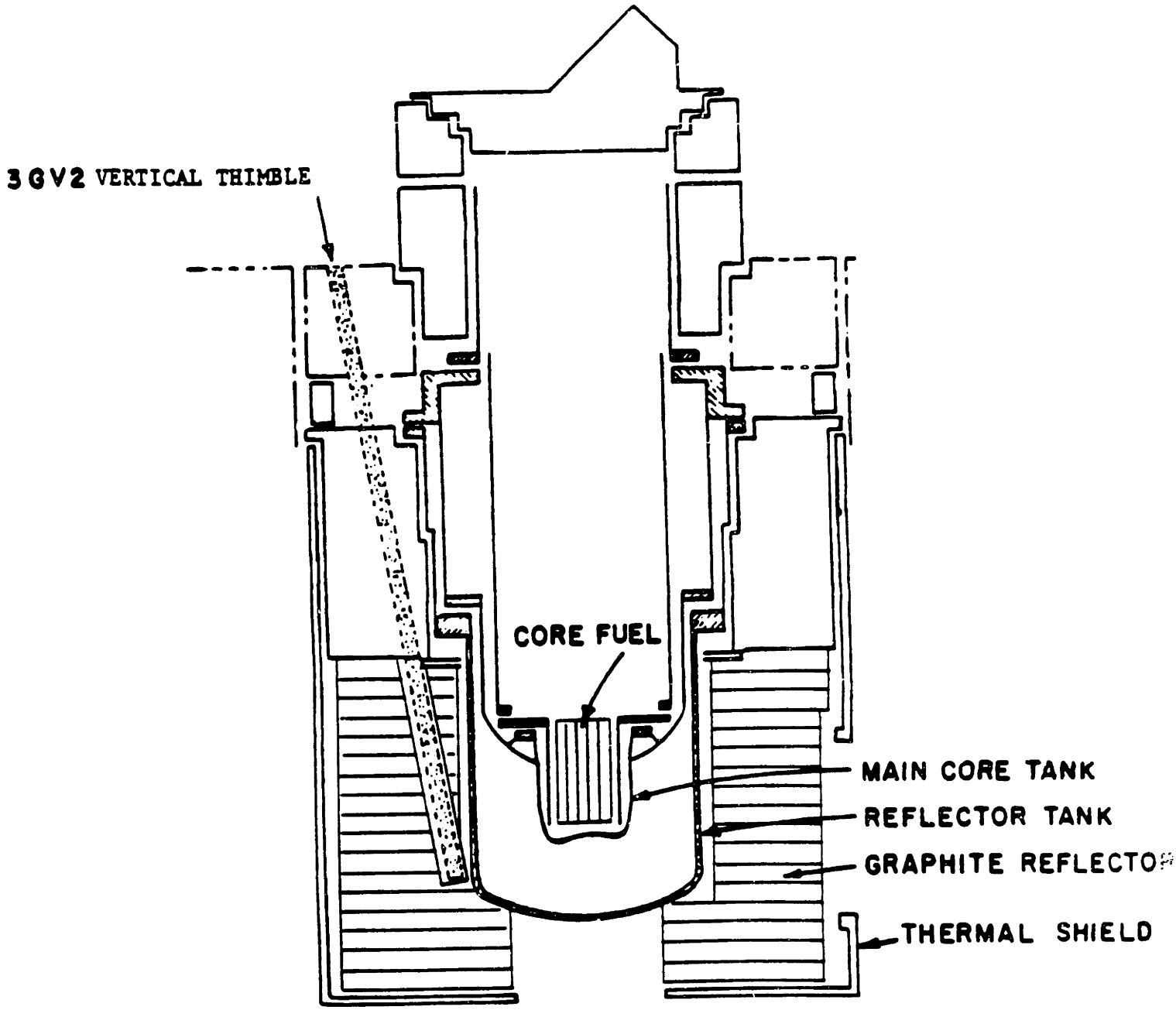

Figure 8. Simplified view of MITR-II.
(Source: Lau "Measurement of Wigner Stored Energy and Combustibility of the MIT Research Reactor Graphite Reflector.")

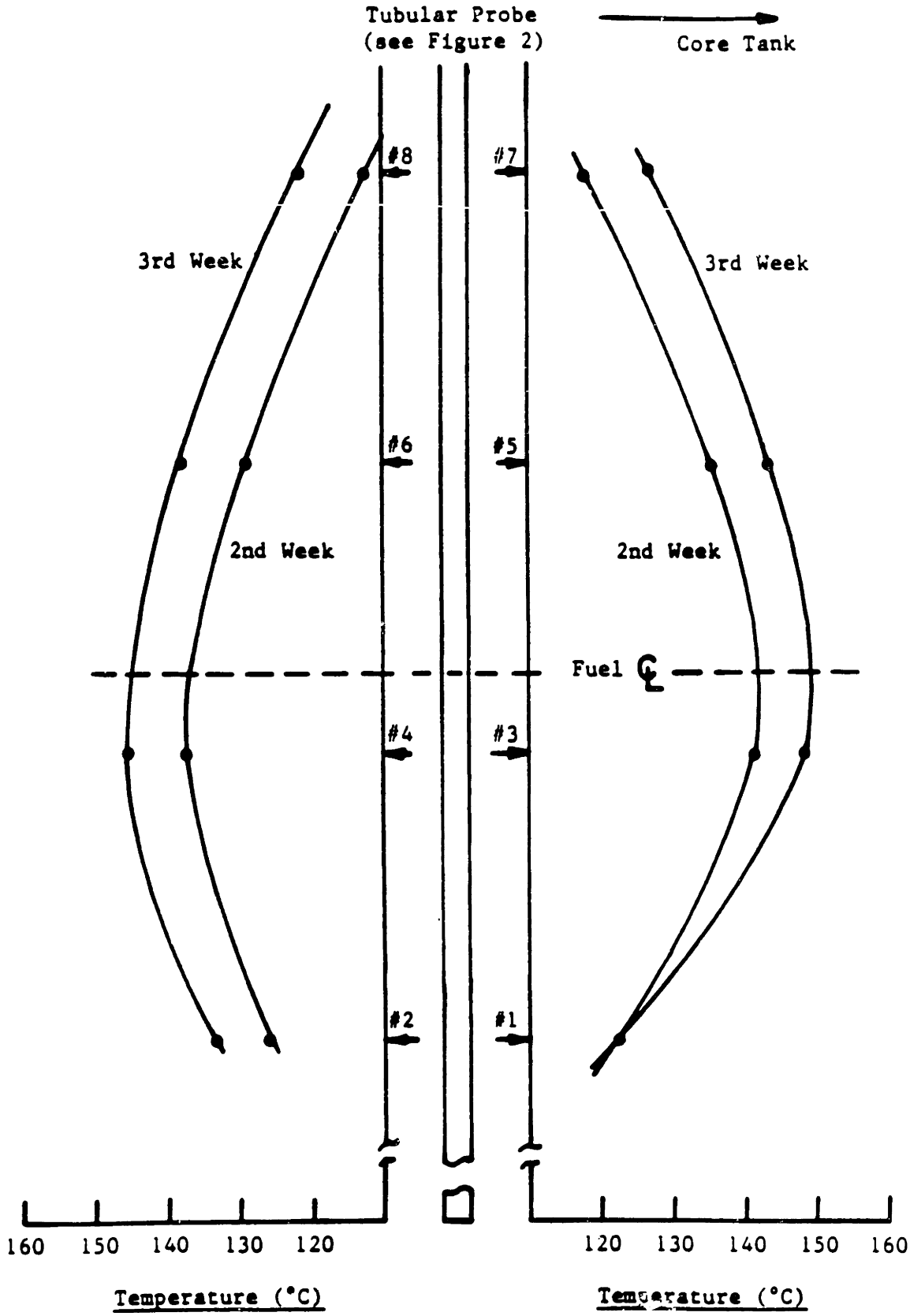

Figure 9. Vertical temperature profile for the 3GV2 thimble. (Source: Lau "Measurement of Wigner Stored Energy and Combustibility of the MIT Research Reactor Graphite Reflector.")

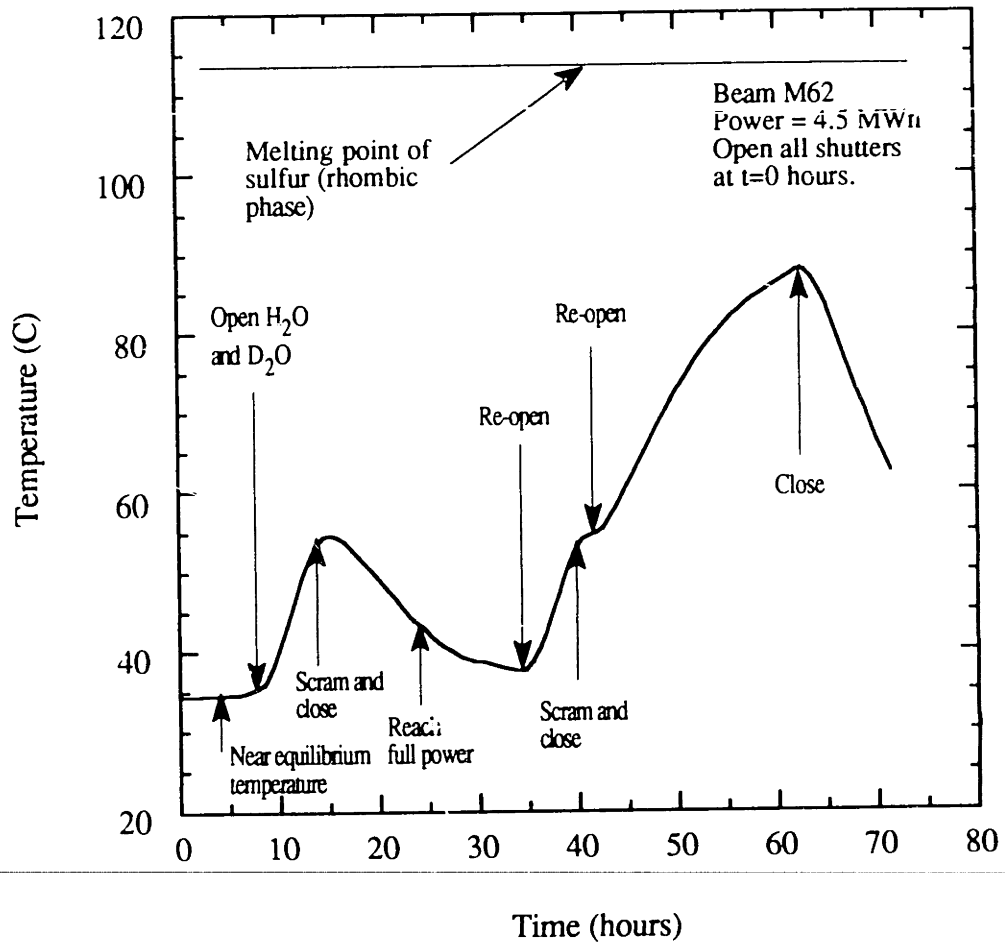

Figure C.1 These results are for the third long irradiation of the sulfur filter. The thermocouple was positioned on the central axis of the can, about 1" below the surface of the sulfur. During the third opening, it's clear that the temperature is not rising linearly, but is starting to bend over. The rate of reaching saturation, however, is less than a $(1 - e^{-\alpha t})$ dependence, where α is an effective time constant and t is the time.

APPENDIX D PROCEDURES RELATED TO BEAM DOSIMETRY

Six Procedures related to dosimetry were written pursuant to MITR Technical Specification No. 6.5. They are:

1. PM 3.14.2.2B Calibration Check of the Medical Therapy Facility Beam via Foil Activation
2. PM 3.14.2.2C Calibration Check of the Medical Therapy Facility Beam via the Dual Ion Chamber Technique
3. PM 3.14.2.4 Characterization of the Medical Therapy Beam
4. PM 3.14.2.5 Cross-Calibration of Electrometers
5. PM 3.14.2.6 Calibration and Stability Check of Ionization Chambers and Electrometers
6. PM 3.14.2.7 Determination of High Purity or Ge(Li) Detector Efficiency

Another Procedure, PM 3.14.1.8, Surveillance Schedule for Medical Therapy Facility Procedures, is also included here as it establishes a schedule for the performance of the above Procedures. Some Procedures may be modified in the future. PM 3.14.2.2 (A, B, or C) may be combined with PM 3.14.2.1, which is a functional check procedure of the medical therapy facility beam monitors. This will save time. Also, the surveillance schedule for some procedures will be changed. PM 3.14.2.4 will be done annually, not semi-annually.

These Procedures are discussed briefly here.

1. PM 3.14.2.2B Calibration Check of the Medical Therapy Facility Beam via Foil Activation

This Procedure ensures that the beam has not changed in significant way by measuring the thermal and epithermal fluxes in phantom and comparing them with those obtained during the most recent characterization.

2. PM 3.14.2.2C Calibration Check of the Medical Therapy Facility Beam via the Dual Ion Chamber Technique

This Procedure ensures that the beam has not changed in significant way by measuring the photon and fast neutron doses in phantom and comparing them with those obtained during the most recent characterization.

3. PM 3.14.2.4 Characterization of the Medical Therapy Beam

This Procedure provides a standard method to determine the dose-depth profiles in phantom and in air. The results of the characterization also serve as a reference for subsequent calibration checks of the beam and for the beam monitor functional checks.

4. PM 3.14.2.5 Cross-Calibration of Electrometers

This Procedure provides a standard method for calibrating a field electrometer against the AAPM Calibrated electrometer.

5. PM 3.14.2.6 Calibration and Stability Check of Ionization Chambers and Electrometers

This Procedure provides a standard method for checking the calibration and stability of both the ionization chambers and the electrometers. The exposure rate at a fixed distance from a Cs-137 source is measured. Agreement with the previously measured exposure rate ensures that the calibration of the ionization chambers and

electrometers has not changed. An independent, simple method to rapidly check the calibration of the electrometers was also developed.

6. PM 3.14.2.7 Determination of High Purity or Ge(Li) Detector Efficiency

This Procedure provides a standard method for determining the efficiency of a HPGE or Ge(Li) detector that is used to count the gold foils.

7. PM 3.14.1.8 Surveillance Schedule for Medical Therapy Facility Procedures

This Procedure establishes a schedule for the performance of Procedures required to implement MITR Technical Specification No. 6.5 and its associated Quality Management Program.

PM 3.14.2.2B Calibration Check of the Medical Therapy Beam via Foil Activation

Purpose:

The purpose of this calibration check is to ensure that the beam has not changed in a significant way (e.g., energy spectrum or intensity) from the beam that was characterized.

Background:

A beam calibration check can be accomplished via any one of the following: foil activation; use of a fission chamber; use of an ion chamber; or an equivalent process. The procedure for checking beam intensity and spectrum via the determination of thermal and epithermal fluxes from gold foil activation analysis is given here. Additional information on the procedure as applied to the MIT Research Reactor's Medical Therapy Room Beam is given by Rogus [1].

Acceptance Criteria:

The thermal and epithermal fluxes are, upon normalization to a common reactor power, consistent (± 10%) with the values measured during the most recent beam characterization.

Prerequisites:

1. Reactor operating at a power level in excess of 1 MW.

2. Beam delimiter and whole body shields are installed. These shields should be in the same position (± 2 mm side-to-side, ± 2 mm front-to-back, and ± 2 mm up-and-down) as that used in the most recent characterization of the beam.

3. A standard phantom is available. This phantom is a right circular cylinder that is made of polyethylene and which is 18 cm in diameter and 20 cm long. This phantom is cut into ten layers so as to allow foils to be positioned at various depths. (Note: Other phantoms with equivalent capability for positioning the foils may be used provided that there is a measured correlation between them and the standard phantom.)

4. Standard radiological procedures for use of the medical therapy facility are to be observed.

Procedure:

_____ 1. Weigh two gold foils (5-10 mg, ~0.002" thick) on a calibrated balance (Mettler AT 201 or equivalent) that has an absolute accuracy and repeatability of less than 1%. Place a small piece of pressure-sensitive polyester film tape on the top and bottom of each foil, pinch the sticky sides together, and then trim the tape. The foils can be marked with a number written with a permanent marker on the tape. Note: Gold foils that have been previously irradiated may be used provided that the residual activity is less than 0.3 % of the initial amount. This corresponds to a decay interval of three weeks.) Record foils #s and weight:

#_____/_____ mg; #_____/_____ mg.

_____ 2. Place one of the gold foils in the phantom at a depth of 2 cm. Designate this foil as the 'bare' foil. Weight of foil: _____ mg.

_____ 3. Position the phantom so that it is under the centerline of the bismuth collimator (its centerline when the lead shutter is open) using the fiduciary marks on the bottom of the delimiter. The top of the phantom should be immediately below the bottom of the delimiter.

_____ 4. Commence the foil irradiation using the following sequence for opening of the D_2O shutter and the shutters that control beam delivery:

a) Record time and date: _____ _____.
Time Date

b) Record reactor power level:

Ch. 7 _____ μa ; Ch. 9 _____ μa ; Nominal Power _____ MW

c) Clear the medical therapy facility room of personnel and close the shield door.

d) Open the D_2O shutter. (This usually requires three minutes.)

e) Depress the open button for the H_2O shutter and observe that it is draining. Wait forty seconds and then open the lead and boral shutters. The 'irradiation start time' is the moment when the lead shutter indicates open.

f) Record irradiation start time: _____ _____.
Time Date

g) Record readings of reactor power indicators once all shutters are open:

Ch. 7 _____ μa ; Ch. 9 _____ μa

_____ 5. Irradiate the foil for approximately sixty minutes. (Note: Shorter irradiations are acceptable. The consideration is that a long irradiation minimizes both the effect of the shutter cycle times and the required counting time.)

_____ 6. Monitor reactor power channels No. 7 and 9 during the irradiation. The drift should be less than 1 %.

_____ 7. Terminate the foil irradiation using the following sequence for closing the D_2O shutter and the shutters that control beam delivery:

a) Specify time at which irradiation is to be terminated:

_____ _____.
Time Date

b) Ten seconds prior to the specified termination time, depress the close button for the H_2O shutter.

c) Close the lead and boral shutters at the official termination time and then close the D_2O shutter.

d) Record time at which the lead shutter was closed:

_____ _____.
Time Date

_____ 8. Enter the medical therapy room facility, survey, and remove the bare foil from the phantom.

_____ 9. Fold a 0.020 inch thick, half-inch diameter cadmium disc in half and use it to cover the second gold foil. This is the 'covered' foil. Weight of foil: _____ mg.

_____ 10. Place the covered foil in the phantom at a depth of 2 cm. Use one of the phantom slices that has a counterbore on the centerline. The cadmium should fit into the counterbore so that the phantom slice above it is flush with the slice below it.

_____ 11. Position the phantom so that it is under the centerline of the bismuth collimator (its centerline when the lead shutter is open) using the fiduciary marks on the bottom of the delimiter. The top of the phantom should be immediately below the bottom of the delimiter.

_____ 12. Commence the foil irradiation using the following sequence for opening of the D_2O shutter and the shutters that control beam delivery:

a) Record time and date: _____ _____.
Time Date

b) Record reactor power level:

Ch. 7 _____ μa ; Ch. 9 _____ μa ; Nominal Power _____ MW

c) Clear the medical therapy facility room of personnel and close the shield door.

d) Open the D_2O shutter. (This usually requires three minutes.)

e) Depress the open button for the H_2O shutter and observe that it is draining. Wait forty seconds and then open the lead and boral shutters. The 'irradiation start time' is the moment when the lead shutter indicates open.

f) Record irradiation start time: _____ _____.
Time Date

g) Record readings of reactor power indicators once all shutters are open:

Ch. 7 _____ μa ; Ch. 9 _____ μa

_____ 13. Irradiate the foil for approximately sixty minutes. (Note: Shorter irradiations are acceptable. The consideration is that a long irradiation minimizes both the effect of the shutter cycle time and the required counting time.)

_____ 14. Monitor reactor power channels No. 7 and 9 during the irradiation. The drift should be less than 1 %.

_____ 15. Terminate the foil irradiation using the following sequence for closing the D_2O shutter and the shutters that control beam delivery.

a) Specify time at which irradiation is to be terminated:

_____ _____.
Time Date

b) Ten seconds prior to the specified termination time, depress the close button for the H_2O shutter.

c) Close the lead and boral shutters at the official termination time and then close the D_2O shutter.

d) Record time at which the lead shutter was closed:

_____ _____.
Time Date

_____ 16. Enter the medical therapy room facility, survey, and remove the covered foil from the phantom.

_____ 17. Obtain the efficiency of the detector (a high purity Ge, Ge(Li), or equivalent) that is to be used for counting the foils from the most recent calibration of the detector (PM 3.14.2.7). Record the following:

Detector Type: _____, Serial No.: _____

Distance between detector face and source: _____ inches

Efficiency at 411 keV where the source was counted: _____

_____ 18. Remove the cadmium cover from the covered foil.

_____ 19. Count the foils. Details are again given in [1] with the principal considerations summarized here.

a) Place the one bare and the one covered foil in specially-prepared cardboard holders (similar to 35 mm projector slides). Then place each sequentially in the counting position that was used for the standard source and count.

b) For each foil record the following:

		Bare	Covered
(i)	Position relative to detector:	_____	_____
(ii)	Time count started:	_____	_____
(iii)	Counting time (live time):	_____	_____
(iv)	Net area under the Au-198: Peak @ 411 keV	_____	_____

_____ 20. Calculate the thermal and epithermal neutron fluxes using the procedure summarized in Appendix A to this procedure.

Thermal Flux: _____ neutrons/cm^2-s.

Epithermal Flux: _____ neutrons/cm^2-s.

_____ 21. Normalize the thermal and epithermal fluxes calculated in step (20) above to the neutronic power that existed during the most recent beam characterization. To do this, use the ratio of the channel #7 readings that exist with all shutters closed. Fluxes normalized for comparison with those obtained during beam characterization:

a) Thermal Flux: _____ neutrons/cm^2-s.

b) Epithermal Flux: _____ neutrons/cm^2-s.

_____ 22. Normalize the fluxes to 5 MWt by using channel #7 data obtained under conditions of thermal equilibrium. Fluxes normalized to 5 MWt:

a) Thermal Flux: _____ neutrons/cm^2-s.

b) Epithermal Flux: _____ neutrons/cm^2-s.

_____ 23. Obtain flux data from the most recent beam characterization and compare the values from step (21) above to these values:

a) Thermal Flux from Characterization: _____ neutrons/cm^2-s.

b) Epithermal Flux from Characterization: _____ neutrons/cm^2-s.

c) Deviation in Thermal Flux: _____ %

d) Deviation in Epithermal Flux: _____ %

_____ 24. Record the following:

Beam Designation: _____

Date Installed: _____

_____ 25. Secure medical room facility and equipment or continue with other scheduled procedures as appropriate.

The acceptance criteria is a deviation of less than 10% in flux.

Acceptance Criteria Met: Yes ☐ No ☐

Check performed by: _____ _____
NCT Research Scientist Date

Check verified by: _____ _____
NCT Research Scientist Date

Results reviewed by: _____ _____
NRL Director Date

Reference:

1. Rogus, R., "Protocol for Mixed-Field Dosimetry of Epithermal Neutron Beams for Boron Neutron Capture Therapy at the MITR-II Research Reactor," MITNRL-054, October 1992.

Appendix A

Calculation of Thermal and Epithermal Neutron Fluxes

The method for calculating the thermal and epithermal fluxes for the MITR Medical Therapy Room Beam is described in detail by Rogus [1]. A summary is given here. The equation numbers used here correspond to those in Reference One and are therefore not consecutive.

The saturated activity for an infinitely-long irradiation and the 2200 m/s flux are given by the relations:

$$A_{sat} = \frac{\lambda C}{\varepsilon\left(1 - e^{-\lambda t_o}\right)\left(e^{-\lambda t_1} - e^{-\lambda t_2}\right)} \tag{36}$$

$$\phi_{2200} = \frac{MW}{A_v \sigma_{2200}}\left[\left(\frac{A_{sat}}{m_b}\right) - F_{Cd}\left(\frac{A_{sat}}{m_c}\right)\right] \tag{37}$$

where A_{sat} is the saturated activity (disintegrations/s);

λ is the decay constant (s^{-1} in the numerator and inverse days in the denominator);

C is the net counts under the 411 keV Au-198 peak (total counts minus background counts);

ε is the overall counting efficiency, which accounts for self-absorption (ε_a), detector efficiency (ε_d), and abundance of the detected radiation (ε_r) with all efficiencies given as numbers, not percents;

t_o is the irradiation time (days);

t_1 is the count start time (days);

t_2 is the count end time (days);

ϕ_{2200} is the 2200 m/s absorption cross-section for gold-197 (cm^2/atom);

m_b is the bare foil mass (mg);

m_c is the covered foil mass (mg); and

F_{cd} is the cadmium correction factor.

All times are referenced to the start of the irradiation which is considered zero. Upon substitution of known constants, the following are obtained:

Specific Saturated Activity of the Bare Foil:

$$\left(\frac{A_{sat}}{m}\right) = \frac{2.975\,E\text{-}6 \times (C/m_b)}{0.989 \times 0.955 \times \varepsilon_d \times \left(1-e^{-0.257t_0}\right)\left(e^{-0.257t_2}\right)}$$

where t_o, t_1, and t_2 are in days.

Specific Activity of the Covered Foil:

$$\left(\frac{A_{sat}}{m}\right) = \frac{2.97\,E\text{-}6 \times (C/m_c)}{0.989 \times 0.955 \times \varepsilon_d \times \left(1-e^{-0.257t_0}\right)\left(e^{-0.257t_1} - e^{-0.257t_2}\right)}$$

where t_o, t_1, and t_2 are in days.

Neutron Flux at 2200 m/s:

$$\phi_{2200} = \left[\frac{196.7 \times 1000}{6.02\,E\text{+}23 \times 98.8E\text{-}24}\right]\left[\left(\frac{A_{sat}}{m}\right)_b - 1.02\left(\frac{A_{sat}}{m}\right)_c\right]$$

where the factor of 1000 in the numerator of the last equation is to convert grams to milligrams. Also, it has been assumed that the correction for self-absorption of 411 keV photons in the gold foil is 0.989, that the 411 keV photon abundance is 0.955, and that the cadmium correction factor is 1.02. The latter quantity is a function of foil thickness.

Epithermal Neutron Flux:

The epithermal neutron flux can now be found. It is given by the relation:

$$\phi_{epi} = \frac{10.1(F_{cd})(A_{sat}/m)_c(MW)}{(Au)(RI)(F_{res})} \qquad (50)$$

where ϕ_{epi} is the epithermal neutron flux (n/cm^2-s);

RI is the resonance integral for an ideal, infinitely dilute gold foil (cm^2); and

F_{res} is the resonance self-shielding factor.

Upon substitution of known constants, the following is obtained:

$$\phi_{epi} = \frac{10.1 \times 1.02\,(A_{sat}/m)_c \times 196.97 \times 1000}{6.02E\text{+}23 + 1560E\text{-}24 \times 0.28}$$

where the resonance integral is taken as 1560 barns, and the resonance self-shielding factor is 0.28.

PM 3.14.2.2C Calibration Check of the Medical Therapy Beam via the Dual Ion Chamber Technique

Purpose:

The purpose of this calibration check is to ensure that the beam has not changed in a significant way (e.g., energy spectrum or intensity) from the beam that was characterized.

Background:

A beam calibration check can be accomplished via any one of the following: foil activation; use of a fission chamber; use of an ion chamber; or an equivalent process. The procedure for checking beam intensity and spectrum via the determination of the photon and fast neutron dose rates via the dual ion chamber technique is given here. Additional information on the procedure as applied to the MIT Research Reactor's Medical Therapy Room Beam is given by Rogus [1].

Acceptance Criteria:

The photon and fast neutron dose rates are, upon normalization to a common reactor power, consistent (± 10%) with the values measured during the most recent beam characterization.

Prerequisites:

1. Reactor operating at a power level in excess of 1 MW.

2. Beam delimiter and whole body shields are installed. These shields should be in the same position (± 2 mm side-to-side, ± 2 mm front-to-back, and ± 2 mm up-and-down) as that used for previous characterizations of the beam.

3. A standard phantom is available. This phantom is a right circular cylinder that is made of polyethylene and which is 18 cm in diameter and 20 cm long. This phantom is cut into ten layers so as to allow foils to be positioned at various depths. This phantom is also used for the calibration checks and beam monitor functional checks. Other phantoms may be used provided that there is consistency with these checks. These include the Wax-130 leg phantom and the paraffin half-body phantom.

4. Instruments required for the measurements of the beam's fast neutron and photon components are available including:

   a) Tissue-equivalent chamber (Far West IC-18),

   b) Graphite-wall ionization chamber (Far West IC-18G),

   c) Two electrometers (Keithley 616 or 617).

The tissue-equivalent and graphite-wall chambers as well as one of the electrometers shall have been calibrated by a Secondary Calibration Laboratory within the last two years. The electrometer for which this is done is designated here as the 'calibrated' instrument (Keithley 617) while the other is referred to as the 'field' instrument (Keithley 616). The latter is calibrated against the former using PM 3.14.2.5, "Cross-Calibration of Electrometers." The 'field' instrument is the one used for the characterization. Each electrometer can be calibrated by itself or the electrometer and each chamber can be calibrated as an electrometer-chamber pair.

5. Low-noise signal cables, a high voltage power supply (Canberra HV Supply #2816A or equivalent), high-voltage cables, and a stop watch with an accuracy and resolution of 0.1 s. (Caution: The signal cables should be handled gently. In particular, they should not be bent to radii of less than 30 cm.)

6. Standard radiological procedures for use of the medical therapy facility are to be observed.

Quality Assurance:

1. Record the following for the instruments that are used to measure the beam's fast neutron and photon components:

Instrument	Serial #	Calibration Date	Secondary Lab
a) Tissue-Equivalent	_____	_____	_____
b) Graphite-Wall	_____	_____	_____
c) Keithley 617	_____	_____	_____
d) Keithley 616	_____	_____	PM 3.14.2.5

2. Verify that the following were done during the instrument calibrations:

   a) Tissue-equivalent chamber was flushed with a methane-based tissue-equivalent gas at 5 cc/minute;

   b) Graphite-wall chamber was flushed with CO_2 at 5 cc/minute.

Verified: _____ _____
NCT Research Scientist Date

Note: If flows of 5 cc/minute were not used, then corrections to the calibrations may be necessary. In that case, record the flow rates that were actually used on the attached data sheet.

Procedure:

_____ 1. Energize the field electrometer and adjust the high voltage or the HV power supply to + 250 V. Check the HV cable to be certain that the chamber would be at 250 ± 10 V. The background current, with the voltage applied to the chambers but with no radiation field, should be less than 5E-15 Amperes.

_____ 2. Allow the field electrometer to warm up for one hour.

_____ 3. Purge the CO_2 line for 20 minutes at ~100 cc/minutes. (CAUTION: The next step is to connect the graphite-wall chamber to the electrometer. When doing so, the electrometer should be in the zero position and the high voltage should be off.)

_____ 4. Connect the graphite-wall ionization chamber to the CO_2 line, snap on the Lucite tube, and insert it into the phantom at the 1 cm position for the head phantom or the 0 cm position for the other phantoms.

_____ 5. Position the phantom in the beam so that the area in which the measurement will be made is under the center line of the bismuth collimator (its center line when the lead shutter is open) using the fiduciary marks on the bottom of the delimiter. The top of the phantom should be immediately below the bottom of the delimiter.

_____ 6. Reduce the CO_2 flow rate to 5 cc/minute. (Note: Higher flow rates, up to 20 cc/minute are acceptable provided that a correction factor is applied to the chamber current.) Record the CO_2 flow rate on the attached data sheet or enter it on the appropriate spreadsheet.

_____ 7. Measure the temperature of the CO_2 flush gas with a thermometer and the barometric pressure with the barometer in the reactor control room Record data on the attached sheet or enter it on the appropriate sheadsheet.

_____ 8. Commence the measurement using the sequence given below. Information may either be recorded on the attached data sheet or, as an alternative, a spreadsheet may be used to perform and record these calculations. If used, these shall be signed, dated, and reviewed by two NCT Research Scientists.

a) Record time and date on the attached data sheet.

b) Record reactor power level on the attached data sheet.

c) Clear medical therapy room of personnel and close the shield door.

d) Open the D_2O shutter and then the H_2O, lead, and boral shutters. Wait until all shutters indicate full open.

e) Measure the current using racetrack timing. Collect charge for about one minute and then record the charge and time interval. Repeat twice and average the results of the three measurements. The three measurements should be within about 1% of the average. If not, several additional readings should be taken to ensure the system is at steady-state. Record data on the attached sheet.

f) Close all shutters, enter the medical therapy room facility, and survey.

_____ 9. Purge the tissue-equivalent gas line for 20 minutes at 100 cc/minute. (CAUTION: The next step is to disconnect the graphite-wall chamber and to connect the tissue-equivalent chamber to the electrometer. When doing so, the electrometer should be in the zero position and the high voltage should be off.)

_____ 10. Connect the tissue-equivalent ionization chamber to the tissue-equivalent gas line, snap on the Lucite tube, and insert it into the phantom. For convenience, the measurement should be taken at the 1 cm position for the head phantom and at the 0 cm position for the other phantoms.

_____ 11. Position the phantom in the beam so that the area in which the measurement will be made is under the center line of the bismuth collimator (its center line when the lead shutter is open) using the fiduciary marks on the bottom of the delimiter. The top of the phantom should be immediately below the bottom of the delimiter.

_____ 12. Reduce the tissue-equivalent gas flow rate to 5 cc/minute. (Note: Higher flow rates, up to 20 cc/minute are acceptable provided that a correction factor is applied to the chamber current.) Record the tissue-equivalent gas flow rate on the attached data sheet or enter it on the appropriate spreadsheet.

_____ 13. Measure the temperature of the tissue-equivalent gas with a thermometer and the barometric pressure with the barometer in the reactor control room Record data on the attached sheet or enter it on the appropriate spreadsheet.

_____ 14. Commence the measurement using the sequence given below. Information may either be recorded on the attached data sheets or, as an alternative, a spreadsheet may be used to perform and record these calculations. If used, these shall be signed, dated, and reviewed by two NCT Research Scientists.

a) Record time and date on the attached data sheet.

b) Record reactor power level on the attached data sheet.

c) Clear medical therapy room of personnel and close the shield door.

d) Open the D_2O shutter and then the H_2O, lead, and boral shutters. Wait until all shutters indicate full open.

e) Measure the current using racetrack timing. Collect charge for about one minute and then record the charge and time interval. Repeat twice and average the results of the three measurements. The three measurements should be within about 1% of the average. If not, several additional readings should be taken to ensure the system is at steady-state. Record data on the attached sheet.

f) Close all shutters, enter the medical therapy room facility, and survey.

_____ 15. Secure medical room facility and equipment or continue with other scheduled procedures as appropriate.

_____ 16. Record the MIT Research Reactor's power history for the seven days prior to the above measurements using the attached form or enter the information on the appropriate spreadsheet.

_____ 17. Calculate the photon and fast neutron dose rates using the procedure described in Appendix B of PM 3.14.2.4, "Characterization of the Medical Therapy Beam," and record results on the attached data sheet. As an alternative, a spreadsheet may be used to perform and record these calculations. If used, these shall be signed, dated, and reviewed by two NCT Research Scientists.

_____ 18. Record the measured and corrected currents for each chamber:

a) Graphite Chamber Current:

Measured: _____

Corrected: _____

b) Tissue Chamber Current:

Measured: _____

Corrected: _____

_____ 19. Perform a calibration check of the medical therapy facility beam by computing the photon and fast neutron dose rates, normalizing them to the neutronic power that existed during the most recent beam characterization, and computing the deviation between these dose rates and those measured during that characterization.

Quantity	Dose Rates (cGy/minute)			Deviation
	Measured	Normalized	Reference	
Photon/Brain				
Fast Neutron/ Brain				
Photon/Muscle				
Fast Neutron/ Muscle				

Acceptance Criteria (deviation <10%) met: Yes ☐ No ☐

Check performed by: _____ _____
NCT Research Scientist Date

Check verified by: _____ _____
NCT Research Scientist Date

Results reviewed by: _____ _____
NRL Director Date

Reference:

1. Rogus, R., "Protocol for Mixed-Field Dosimetry of Epithermal Neutron Beams for Boron Neutron Capture Therapy at the MITR-II Research Reactor," MITNRL-054, October 1992.

Record of Reactor Power History

Date	Time	Ch. 7 (μa)	Ch. 9 (μa)	Nominal Power

Data obtained by: _____ NCT Research Scientist _____ Date

Data verified correct: _____ Senior Reactor Operator _____ Date

Graphite-Wall Ionization Chamber Measurement

Beam Designation: _____ Date Installed: _____

Phantom Type: _____

Chamber Type: _____ ; Serial #: _____

CO_2 gas flow: _____ cc/minute

Temperature: _____ C; Barometric pressure: _____

CO_2 gas flow when chamber was calibrated: _____ cc/minute

Date and Time: _____ _____
Date Time

Reactor Power: Ch. 7 _____ μa; Ch. 9 _____ μa; Nominal Power _____ MW

Phantom Position	Measurement #	Collection Time	Charge	Deviation
1 cm	1			
	2			
	3			
	Average	N/A		0.0%

Tissue-Equivalent Ionization Chamber Measurement

Chamber Type: _____ ; Serial #: _____

Tissue-equivalent gas flow: _____ cc/minute

Temperature : _____ C; Barometric pressure: _____

Tissue-equivalent gas flow when chamber was calibrated: _____ cc/minute

Date and Time: _____ _____
Date Time

Reactor Power: Ch. 7 _____ μa; Ch. 9 _____ μa; Nominal Power _____ MW

Phantom Position	Measurement #	Collection Time	Charge	Deviation
1 cm	1			
	2			
	3			
	Average	N/A		0.0%

Certified by: _____ _____
NCT Research Scientist Date

Date reviewed by: _____ _____
NCT Research Scientist Date

PM 3.14.2.4 Characterization of the Medical Therapy Beam

Purpose:

The purpose of this characterization procedure is to determine the dose-versus-depth profile of the MITR medical therapy beam on a central axis from the surface of a phantom to a depth at least equivalent to the total thickness of the body part that is to be treated. Fast neutron, thermal neutron, and gamma ray components are determined. The results of the characterization serve as the reference for subsequent calibration checks of the beam and for beam monitor functional checks.

Background:

The thermal neutron flux, epithermal neutron flux, photon dose rate, and fast neutron dose rate are measured along the central axis of a phantom that approximates the part of the body that will be treated. A unilateral irradiation is assumed. Fluxes and doses are typically measured at depths of 0, 1, 2, 3, 4, 5, 6, 8, and 10 cm and then every 2 cm until the bottom of the phantom is reached. However, a coarser grid may be used in regions where the shape of the dose-depth profile has previously been shown to be monotonic. The thermal and epithermal neutron fluxes are measured using bare and cadmium-covered gold foils. The photon and fast neutron dose rates are measured using calibrated, paired graphite-wall and tissue-equivalent ionization chambers. A general reference on the methods used is Attix [1]. The application of these methods to the MITR medical therapy beam is given by Rogus [2].

Acceptance Criteria:

Beam parameters are, upon review of the characterization results by the Director of the MIT Nuclear Reactor Laboratory and by the program's Certified Medical Physicist, judged to be adequate for the conduct of human therapy.

Prerequisites:

1. Reactor operating at a power level in excess of 1 MW. (Caution: It is important that reactor operating conditions be maintained constant during beam characterization. Therefore, it is suggested that this procedure only be done when the reactor has been at constant power for at least forty-eight hours.)

2. Beam delimiter and whole body shields are installed. These shields should be in the same position (± 2 mm side-to-side, ± 2 mm front-to-back, and ± 2 mm up-and-down) as that used for previous characterizations of the beam.

3. A standard phantom is available. This phantom is a right circular cylinder that is made of polyethylene and which is 18 cm in diameter and 20 cm long. This phantom is cut into ten layers so as to allow foils to be positioned at various depths. This phantom is also used for the calibration checks and beam monitor functional checks. Other phantoms may be used provided that there is consistency with these checks. These include the Wax-130 leg phantom and the paraffin half-body phantom.

4. Instruments required for the measurements of the beam's fast neutron and photon components are available including:

a) Tissue-equivalent chamber (Far West IC-18),

b) Graphite-wall ionization chamber (Far West IC-18G),

c) Two electrometers (Keithley 616 or 617).

The tissue-equivalent and graphite-wall chambers as well as one of the electrometers shall have been calibrated by a Secondary Calibration Laboratory within the last two years. The electrometer for which this is done is designated here as the 'calibrated' instrument (Keithley 617) while the other is referred to as the 'field' instrument (Keithley 616). The latter is calibrated against the former using PM 3.14.2.5, "Cross-Calibration of Electrometers." The 'field' instrument is the one used for the characterization. Each electrometer can be calibrated by itself or the electrometer and each chamber can be calibrated as an electrometer-chamber pair.

5. Low-noise signal cables, a high voltage power supply (Canberra HV Supply #2816A or equivalent), high-voltage cables, and a stop watch with an accuracy and resolution of 0.1 s. (Caution: The signal cables should be handled gently. In particular, they should not be bent to radii of less than 30 cm.)

6. Standard radiological procedures for use of the medical therapy facility are to be observed.

Quality Assurance:

1. Record the following for the instruments that are used to measure the beam's fast neutron and photon components:

Instrument	Serial #	Calibration Date	Secondary Lab
a) Tissue-Equivalent	_____	_____	_____
b) Graphite-Wall	_____	_____	_____
c) Keithley 617	_____	_____	_____
d) Keithley 616	_____	_____	PM 3.14.2.5

2. Verify that the following were done during the instrument calibrations:

a) Tissue-equivalent chamber was flushed with a methane-based tissue-equivalent gas at 5 cc/minute;

b) Graphite-wall chamber was flushed with CO_2 at 5 cc/minute.

Verified. _____ _____
NCT Research Scientist Date

Note: If flows of 5 cc/minute were not used, then corrections to the calibrations may be necessary. In that case, record the flow rates that were actually used on the attached data sheet.

3. Use PM 3.14.2.6, "Calibration and Stability Check of Ionization Chambers and Electrometers," to test the electrometer-chamber pairs for stability and to verify their calibration. Append completed procedure to this document.

Stability Check Satisfactory: _____ _____
NCT Research Scientist Date

Measurement of Thermal and Epithermal Neutron Fluxes

_____ 1. Weigh twenty-six gold foils (5-10 mg, ~0.002" thick) on a calibrated balance (Mettler AT 201 or equivalent) that has an absolute accuracy and repeatability of less than 1%. Place a small piece of pressure-sensitive polyester film tape on the top and bottom of each foil, pinch the sticky sides together, and then trim the tape. The foils can be marked with a number written with a permanent marker on the tape. Note: Gold foils that have been previously irradiated may be used provided that the residual activity is less than 0.3 % of the initial amount. This corresponds to a decay interval of three weeks.)

_____ 2. Place the needed number of foils in the phantom at depths of 0, 1, 2, 3, 4, 5, 6, 8, and 10 cm and then every 2 cm until the bottom of the phantom is reached. The uppermost foil (0 cm) can be secured directly on the top of the phantom. Designate these foils as 'bare'. Record foil weights on the attached data sheet or enter them on a spreadsheet. If the latter is used, it shall be signed, dated, and reviewed by two NCT Research Scientists.

_____ 3. Position the phantom so that it is under the centerline of the bismuth collimator (its centerline when the lead shutter is open) using the fiduciary marks on the bottom of the delimiter. The top of the phantom should be immediately below the bottom of the delimiter.

_____ 4. Commence the foil irradiations using the following sequence for opening of the D_2O shutter and the shutters that control beam delivery:

a) Record time and date: _____ _____.
Time Date

b) Record reactor power level:
Ch. 7 _____ μa ; Ch. 9 _____ μa ; Nominal Power _____ MW

c) Clear the medical therapy facility room of personnel and close the shield door.

d) Open the D_2O shutter. (This usually requires three minutes.)

e) Depress the open button for the H_2O shutter and observe that it is draining. Wait forty seconds and then open the lead and boral shutters. The 'irradiation start time' is the moment when the lead shutter indicates open.

f) Record irradiation start time: _____ _____.
Time Date

g) Record readings of reactor power indicators once all shutters are open:

Ch. 7 _____ μa ; Ch. 9 _____ μa

_____ 5. Irradiate the foils for approximately sixty minutes. (Note: Shorter irradiations are acceptable. The consideration is that a long irradiation minimizes both the effect of the shutter cycle times and the required counting time.)

_____ 6. Monitor reactor power channels No. 7 and 9 during the irradiation. The drift should be less than 1 %.

_____ 7. Terminate the foil irradiations using the following sequence for closing the D_2O shutter and the shutters that control beam delivery:

a) Specify time at which irradiation is to be terminated:

_____ _____.
Time Date

b) Ten seconds prior to the specified termination time, depress the close button for the H_2O shutter.

c) Close the lead and boral shutters at the official termination time and then close the D_2O shutter.

d) Record time at which the lead shutter was closed:

_____ _____.
Time Date

_____ 8. Enter the medical therapy room facility, survey, and remove the bare foils from the phantom.

_____ 9. Fold 0.020 inch thick, half-inch diameter cadmium discs in half and use them to cover the other gold foils. These are the 'covered' foils. Record the foil weights on the attached data sheet.

_____ 10. Use polyester film tape to position the covered foils along one of the thin plastic rods that are available for each phantom. The foils should be at depths of 0, 2, 4, 6, 8, and 10 cm and then every 2 cm until the bottom of the phantom is reached. The uppermost foil (0 cm) can be secured directly on the top of the phantom.

_____ 11. Position the phantom so that it is under the centerline of the bismuth collimator (its centerline when the lead shutter is open) using the fiduciary marks on the bottom of the delimiter. The top of the phantom should be immediately below the bottom of the delimiter.

_____ 12. Commence the foil irradiations using the following sequence for opening of the D_2O shutter and the shutters that control beam delivery:

a) Record time and date: _____ _____.
Time Date

b) Record reactor power level:
Ch. 7 _____ μa ; Ch. 9 _____ μa ; Nominal Power _____ MW

c) Clear the medical therapy facility room of personnel and close the shield door.

d) Open the D_2O shutter. (This usually requires three minutes.)

e) Depress the open button for the H_2O shutter and observe that it is draining. Wait forty seconds and then open the lead and boral shutters. The 'irradiation start time' is the moment when the lead shutter indicates open.

f) Record irradiation start time: _____ _____.
Time Date

g) Record readings of reactor power indicators once all shutters are open:
Ch. 7 _____ μa ; Ch. 9 _____ μa

_____ 13. Irradiate the foils for approximately sixty minutes. (Note: Shorter irradiations are acceptable. The consideration is that a long irradiation minimizes both the effect of the shutter cycle time and the required counting time.)

_____ 14. Monitor reactor power channels No. 7 and 9 during the irradiation. The drift should be less than 1 %.

_____ 15. Terminate the foil irradiations using the following sequence for closing the D_2O shutter and the shutters that control beam delivery.

a) Specify time at which irradiation is to be terminated:

_____ _____.
Time Date

b) Ten seconds prior to the specified termination time, depress the close button for the H_2O shutter.

c) Close the lead and boral shutters at the official termination time and then close the D_2O shutter.

d) Record time at which the lead shutter was closed:

_____ _____.
Time Date

_____ 16. Enter the medical therapy room facility, survey, and remove the covered foils from the phantom.

_____ 17. Use PM 3.14.2.7, "Determination of High Purity Ge or Ge(Li) Detector Efficiency," to determine the efficiency of the detector (a high purity Ge, Ge(Li), or equivalent) that is to be used for counting the foils. Record the following:

Detector Type: _____, Serial No.: _____

Distance between detector face and source: _____ inches

Efficiency at 411 keV where the source was counted: _____

_____ 18. Remove the cadmium discs from the covered foils.

_____ 19. Count the foils. Details are again given in [2] with the principal considerations summarized here.

a) In order to accelerate the counting process, position the foils close to or on top of the detector surface. In order to ensure accuracy, each foil that is counted should be positioned so that it is within ± 2 mm of the original foil. Cardboard holders similar to 35 mm projector slides are available and should be used to position the foils. Obtain the detection efficiency at this in-close position from PM 3.14.2.7. Record the following:

Efficiency at 411 keV where the gold foils are counted: _____

b) For each foil, record the relevant data on the attached sheet.

_____ 20. Calculate the thermal and epithermal neutron fluxes using the method summarized in Appendix A to this procedure. Record calculations on the attached sheet. As an alternative, a spreadsheet may be used to perform and record these calculations. If used, these shall be signed, dated, and reviewed by two NCT Research Scientists.

_____ 21. Normalize the fluxes calculated in step (20) to 5 MWt. Record calculations on the attached sheet. As an alternative, a spreadsheet may be used to perform and record these calculations. If used, these shall be signed, dated, and reviewed by two NCT Research Scientists.

_____ 22. Secure any equipment not required for the subsequent portions of this procedure.

Functional and Calibration Check of Medical Therapy Facility Beam Monitors

_____ 1. Perform PM 3.14.2.1, "Functional Check of Medical Therapy Facility Beam Monitors," and PM 3.14.2.2A, "Calibration Check of the Medical Therapy Beam via Chamber Measurements." Append a copy of the results to this procedure.

Measurement of the Photon and Fast Neutron Dose Rates

_____ 1. Energize the field electrometer and adjust the high voltage or the HV power supply to + 250 V. Check the HV cable to be certain that the chamber would be at 250 ± 10 V. The background current, with the voltage applied to the chambers but with no radiation field, should be less than 5E-15 Amperes.

_____ 2. Allow the field electrometer to warm up for one hour.

_____ 3. Purge the CO_2 line for 20 minutes at ~100 cc/minutes. (CAUTION: The next step is to connect the graphite-wall chamber to the electrometer. When doing so, the electrometer should be in the zero position and the high voltage should be off.)

_____ 4. Connect the graphite-wall ionization chamber to the CO_2 line, snap on the Lucite tube, and insert it into the phantom. For convenience, measurements should be initiated at the 1 cm position for the head phantom and at the 0 cm position for the other phantoms.

_____ 5. Position the phantom in the beam so that the area in which the measurement will be made is under the center line of the bismuth collimator (its center line when the lead shutter is open) using the fiduciary marks on the bottom of the delimiter. The top of the phantom should be immediately below the bottom of the delimiter.

_____ 6. Reduce the CO_2 flow rate to 5 cc/minute. (Note: Higher flow rates, up to 20 cc/minute are acceptable provided that a correction factor is applied to the chamber current.) Record the CO_2 flow rate on the attached data sheet or enter it on the appropriate spreadsheet.

_____ 7. Measure the temperature of the CO_2 flush gas with a thermometer and the barometric pressure with the barometer in the reactor control room Record data on the attached sheet or enter it on the appropriate sheadsheet.

_____ 8. Commence the measurements using the sequence given below. Information may either be recorded on the attached data sheet or, as an alternative, a spreadsheet may be used to perform and record these calculations. If used, these shall be signed, dated, and reviewed by two NCT Research Scientists.

a) Record time and date on the attached data sheet.

b) Record reactor power level on the attached data sheet.

c) Clear medical therapy room of personnel and close the shield door.

d) Open the D_2O shutter and then the H_2O, lead, and boral shutters. Wait until all shutters indicate full open.

e) Measure the current using racetrack timing. Collect charge for about one minute and then record the charge and time interval. Repeat twice and average the results of the three measurements. The three measurements should be within about 1% of the average. If not, several additional readings should be taken to ensure the system is at steady-state. Record data on the attached sheet.

f) Close all shutters, enter the medical therapy room facility, survey, and reposition the chamber for the next measurement.

g) Repeat steps (c) - (f) above with measurements taken at 0, 1, 2, 3, 4, 5, 6, 8, and 10 cm and then every 2 cm until the bottom of the phantom is reached. For the head phantom, data for the 0 cm position is obtained by placing the chamber on the top surface of the phantom. During the other head-phantom measurements, it is important that the head phantom be completely filled with water. When using the leg or half-body phantoms, the void above the chamber should be filled with a Wax-130 or paraffin insert.

h) Upon completion of the measurement at the bottom of the phantom, repeat the measurement for the top of the phantom. Compare this result to the one obtained at the outset of the measurements series. The two should agree within 1%.

_____ 9. Purge the tissue-equivalent gas line for 20 minutes at 100 cc/minute. (CAUTION: The next step is to disconnect the graphite-wall chamber and to connect the tissue-equivalent chamber to the electrometer. When doing so, the electrometer should be in the zero position and the high voltage should be off.)

_____ 10. Connect the tissue-equivalent ionization chamber to the tissue-equivalent gas line, snap on the Lucite tube, and insert it into the phantom. For convenience, measurements should be initiated at the 1 cm position for the head phantom and at the 0 cm position for the other phantoms.

_____ 11. Position the phantom in the beam so that the area in which the measurement will be made is under the center line of the bismuth collimator (its center line when the lead shutter is open) using the fiduciary marks on the bottom of the delimiter. The top of the phantom should be immediately below the bottom of the delimiter.

_____ 12. Reduce the tissue-equivalent gas flow rate to 5 cc/minute. (Note: Higher flow rates, up to 20 cc/minute are acceptable provided that a correction factor is applied to the chamber current.) Record the tissue-equivalent gas flow rate on the attached data sheet or enter it on the appropriate spreadsheet.

_____ 13. Measure the temperature of the tissue-equivalent gas with a thermometer and the barometric pressure with the barometer in the reactor control room Record data on the attached sheet or enter it on the appropriate spreadsheet.

_____ 14. Commence the measurements using the sequence given below. Information may either be recorded on the attached data sheets or, as an alternative, a spreadsheet may be used to perform and record these calculations. If used, these shall be signed, dated, and reviewed by two NCT Research Scientists.

a) Record time and date on the attached data sheet.

b) Record reactor power level on the attached data sheet.

c) Clear medical therapy room of personnel and close the shield door.

d) Open the D_2O shutter and then the H_2O, lead, and boral shutters. Wait until all shutters indicate full open.

e) Measure the current using racetrack timing. Collect charge for about one minute and then record the charge and time interval. Repeat twice and average the results of the three measurements. The three measurements should be within about 1% of the average. If not, several additional readings should be taken to ensure the system is at steady-state. Record data on the attached sheet.

f) Close all shutters, enter the medical therapy room facility, survey, and reposition the chamber for the next measurement.

g) Repeat steps (c) - (f) above with measurements taken at 0, 1, 2, 3, 4, 5, 6, 8, and 10 cm and then every 2 cm until the bottom of the phantom is reached. For the head phantom, data for the 0 cm position is obtained by placing the chamber on the top surface of the phantom. During the other head-phantom measurements, it is important that the head phantom be completely filled with water. When using the leg or half-body phantoms, the void above the chamber should be filled with a Wax-130 or paraffin insert.

h) Upon completion of the measurement at the bottom of the phantom, repeat the measurement for the top of the phantom. Compare this result to the one obtained at the outset of the measurements series. The two should agree within 1%.

_____ 15. Record the MIT Research Reactor's power history for the seven days prior to the above measurements using the attached form or enter the information on the appropriate spreadsheet.

_____ 16. Calculate the photon and fast neutron dose rates using the procedure described in Appendix B and record results on the attached data sheet. As an alternative, a spreadsheet may be used to perform and record these calculations. If used, these shall be signed, dated, and reviewed by two NCT Research Scientists.

_____ 17. Review the RBE factors and record the values to be used.

Component	RBE	Source*
B-10	_____	_____
N-14	_____	_____
Fast Neutron	_____	_____
Photon	_____	_____

* If RBE values are unchanged from previous characterization, indicate 'N/A.'

_____ 18. Calculate the nitrogen-14, boron-10, and RBE-weighted dose rates (including the dose rate in healthy tissue and tumor) using the procedure given in Appendix C. (Note: Concentrations of 7.5 ppm boron in healthy tissue and 30 ppm boron in tumor are assumed.) Record the results on the attached data sheet. As an alternative, a spreadsheet may be used to perform and record these calculations. If used, these shall be signed, dated, and reviewed by two NCT Research Scientists.

_____ 19. Plot the data obtained from steps (16) and (17) above as dose-depth distribution curves. These curves are to include the 30 ppm B-10, N-14, photon, fast neutron, healthy tissue, and tumor dose rates. The plots should be signed and dated by both the NCT Research Scientist who prepared them and the NCT Research Scientist who reviewed them.

_____ 20. Secure any equipment not required for the subsequent portions of this procedure.

Calibration of Medical Therapy Facility Beam Monitors

_____ 1. Boot-up the beam monitor data acquisition program's computer system.

_____ 2. Use PM 3.14.3.4., "Beam Monitor System Setpoints," to verify the settings of all beam monitor system parameters (gains, discriminator setpoints, etc.).

_____ 3. Initiate the beam monitor data acquisition program.

_____ 4. Record the reactor power level (Ch. 7, Ch. 9, and nominal) on the attached data sheet or enter this information on the appropriate spreadsheet.

_____ 5. Take five one-minute counts for each monitor. Record data on the attached sheet and compute the average for each monitor. As an alternative, a spreadsheet may be used to perform and record these calculations. If used, these shall be signed, dated, and reviewed by two NCT Research Scientists.

_____ 6. Normalize the average counts for each monitor to 5 MWt. (Note: Channel No. 7 should be used for this purpose unless otherwise indicated by a Senior Member of the Operations Staff.) Describe method used for normalization: _____

_____

_____

_____ 7. Use the dose-depth plot obtained from step (18) of the third part of this procedure to determine the dose rate to healthy tissue: _____ RBE-cGy/minute at 1 cm on the beam's central axis in a head phantom with 7.5 ppm boron assumed in healthy tissue and 30 ppm boron assumed in tumor.

_____ 8. Calibrate the output of each beam monitor in terms of the dose rate delivered to healthy tissue. The resulting calibration factor will have units of 'cps per RBE-cGy/minute.' Record the results on the attached data sheet. As an alternative, a spreadsheet may be used to perform and record these calculations. If used, these shall be signed, dated, and reviewed by two NCT Research Scientists.

_____ 9. Secure the medical room facility and equipment or continue with other scheduled procedures as appropriate.

_____ 10. Provide results of this characterization and beam monitor calibration to the Director of the MIT Nuclear Reactor Laboratory and to the Program's Certified Medical Physicist.

Characterization performed by: _____ _____
NCT Research Scientist Date

Characterization reviewed by: _____ _____
NCT Research Scientist Date

Beam judged adequate for the conduct of human therapy: Yes ☐ No ☐

_____ _____
Certified Medical Physicist Date

_____ _____
NRL Director Date

References

1. Attix. F.H., Introduction to Radiological Physics and Radiation Dosimetry," John-Wiley & Sons, New York, 1986.

2. Rogus, R., "Protocol for Mixed Field Dosimetry of Epithermal Neutrons for Boron Neutron Capture Therapy at the MITR-II Research Reactor," MITNRL-054, October 1992.

Record of Foil Weights

Bare Foils		Covered Foils	
#	Weight (mg)	#	Weight (mg)
1	_____	14	_____
2	_____	15	_____
3	_____	16	_____
4	_____	17	_____
5	_____	18	_____
6	_____	19	_____
7	_____	20	_____
8	_____	21	_____
9	_____	22	_____
10	_____	23	_____
11	_____	24	_____
12	_____	25	_____
13	_____	26	_____

Balance Type: _____ Serial No.: _____ Calibration Date: _____

Foils weighed by: _____ _____
NCT Research Scientist Date

Weights spot-checked by: _____ _____
NCT Research Scientist Date

Record of Foil Counts

Foil #	Position Relative to Detector	Time Count Started	Counting Time(s)	Area Under 411 keV peak
1				
2				
3				
4				
5				
6				
7				
8				
9				
10				
11				
12				
13				
14				
15				
16				
17				
18				
19				
20				
21				
22				
23				
24				
25				
26				

Counts taken by: _____ NCT Research Scientist _____ Date

Data reviewed by: _____ NCT Research Scientist _____ Date

Record of Thermal and Epithermal Neutron Fluxes

Reactor Power: Ch. 7 _____ μa ; Ch. 9 _____ μa ; Nominal Power: _____ MW

Beam Designation: _____ Date Installed: _____

Phantom Position (cm)	Nominal Power		Normalized to 5 MWt	
	Thermal Flux	Epithermal Flux	Thermal Flux	Epithermal Flux
0				
1				
2				
3				
4				
5				
6				
8				
10				
12				
14				
16				
18				

Calculations performed by: _____ NCT Research Scientist _____ Date

Calculations reviewed by: _____ NCT Research Scientist _____ Date

Graphite-Wall Ionization Chamber Measurements (Continued)

Phantom Position	Measurement #	Collection Time	Charge	Deviation
5 cm	1			
	2			
	3			
	Average	N/A		0.0%
6 cm	1			
	2			
	3			
	Average	N/A		0.0%
8 cm	1			
	2			
	3			
	Average	N/A		0.0%
10 cm	1			
	2			
	3			
	Average	N/A		0.0%
12 cm	1			
	2			
	3			
	Average	N/A		0.0%
14 cm	1			
	2			
	3			
	Average	N/A		0.0%
16 cm	1			
	2			
	3			
	Average	N/A		0.0%

Graphite-Wall Ionization Chamber Measurements (Continued)

Phantom Position	Measurement #	Collection Time	Charge	Deviation
0 cm	1			
	2			
	3			
	Average	N/A		0.0%

1. For each phantom position, the deviation of each of its three measurements from the average is less than 1%.

2. The average value of the charge collected for the 0-cm measurement at the end of the measurement series is within 1% of that obtained for the 0-cm measurement at the start of the measurement series.

Certified by: _____ _____
NCT Research Scientist Date

Date reviewed by: _____ _____
NCT Research Scientist Date

Tissue-Equivalent Ionization Chamber Measurements (Continued)

Phantom Position	Measurement #	Collection Time	Charge	Deviation
5 cm	1			
	2			
	3			
	Average	N/A		0.0%
6 cm	1			
	2			
	3			
	Average	N/A		0.0%
8 cm	1			
	2			
	3			
	Average	N/A		0.0%
10 cm	1			
	2			
	3			
	Average	N/A		0.0%
12 cm	1			
	2			
	3			
	Average	N/A		0.0%
14 cm	1			
	2			
	3			
	Average	N/A		0.0%
16 cm	1			
	2			
	3			
	Average	N/A		0.0%

Tissue-Equivalent Ionization Chamber Measurements (Continued)

Phantom Position	Measurement #	Collection Time	Charge	Deviation
0 cm	1			
	2			
	3			
	Average	N/A		0.0%

1. For each phantom position, the deviation of each of its three measurements from the average is less than 1%.

2. The average value of the charge collected for the 0-cm measurement at the end of the measurement series is within 1% of that obtained for the 0-cm measurement at the start of the measurement series.

Certified by: _____ _____
NCT Research Scientist Date

Data reviewed by: _____ _____
NCT Research Scientist Date

Record of Reactor Power History

Date	Time	Ch. 7 (μa)	Ch. 9 (μa)	Nominal Power

Data obtained by: _____ NCT Research Scientist _____ Date

Data verified correct: _____ Senior Reactor Operator _____ Date

Calculation of Photon and Fast Neutron Dose Rates: Beam No. _____

Phantom Position	Graphite Chamber		Tissue Chamber		Brain Dose Rates (cGy/minute)		Muscle Dose Rates (cGy/minute)	
(cm)	Measured	Corrected	Measured	Corrected	Photon	Fast Neutron	Photon	Fast Neutron
0								
1								
2								
3								
4								
5								
6								
8								
10								
12								
14								
16								

Calculation performed by: _____ NCT Research Scientist _____ Date

Calculation reviewed by: _____ NCT Research Scientist _____ Date

Calculation of N-14, B-10, and RBE-Weighted Dose Rates

Phantom Position (cm)	N-14 Dose Rate (cGy/minute)		B-10 Dose Rate (cGy/minute)	
	Muscle	Brain	Healthy	Tumor
0				
1				
2				
3				
4				
5				
6				
8				
10				
12				
14				
16				

Calculation performed by: _____ _____
NCT Research Scientist Date

Calculation reviewed by: _____ _____
NCT Research Scientist Date

Calculation of N-14, B-10, and RBE-Weighted Dose Rates (Continued)

RBE-Weighted Dose Rates

Phantom Position (cm)	30 ppm B-10	7.5 ppm B-10	N-14	Fast Neutron	Photon	Healthy Tissue	Tumor
0							
1							
2							
3							
4							
5							
6							
8							
10							
12							
14							
16							

Calculation performed by: _____ NCT Research Scientist _____ Date

Calculation reviewed by: _____ NCT Research Scientist _____ Date

Data Sheet for Beam Monitor Calibration

Beam Designation: _____ Date Installed: _____

Date and Time: _____ _____
Date Time

Reactor Power: Ch. 7 _____ μa ; Ch. 9 _____ μa ; Nominal Power: _____ MW

Beam Monitor Counts (cps)

Count #	Epithermal #1	Epithermal #2	Thermal #1	Thermal #2	Gamma
1					
2					
3					
4					
5					
Average					
5 MWt Normalized					

Data Sheet for Beam Monitor Calibration (Continued)

Calibration Factor for Dose

Monitor	Dose Rate to Healthy Tissue (RBE-cGy/minute)	Normalized Count Rate (cps)	Calibration Factor (cps)/(RBE-cGy/minute)
Epithermal #1	_____	_____	_____
Epithermal #2	_____	_____	_____
Thermal #1	_____	_____	_____
Thermal #2	_____	_____	_____
Gamma	_____	_____	_____

CAUTION: The above correlation factors are for dose to healthy tissue at 1 cm on the beam's central axis in a head phantom with 7.5 ppm boron assumed in healthy tissue and 30 ppm boron assumed in tumor.

Data certified by: _____ _____
NCT Research Scientist Date

Data reviewed by: _____ _____
NCT Research Scientist Date

Appendix A

Calculation of Thermal and Epithermal Neutron Fluxes

The method for calculating the thermal and epithermal fluxes for the MITR Medical Therapy Room Beam is described in detail by Rogus [2]. A summary is given here. The equation numbers used here correspond to those in Reference Two and are therefore not consecutive.

The saturated activity for an infinitely-long irradiation and the 2200 m/s flux are given by the relations:

$$A_{sat} = \frac{\lambda C}{\varepsilon\left(1-e^{-\lambda t_o}\right)\left(e^{-\lambda t_1}-e^{-\lambda t_2}\right)} \tag{36}$$

$$\phi_{2200} = \frac{MW}{A_v \sigma_{2200}}\left[\left(\frac{A_{sat}}{m_b}\right) - F_{Cd}\left(\frac{A_{sat}}{m_c}\right)\right] \tag{37}$$

where A_{sat} is the saturated activity (disintegrations/s);

λ is the decay constant (s^{-1} in the numerator and inverse days in the denominator);

C is the net counts under the 411 keV Au-198 peak (total counts minus background counts);

ε is the overall counting efficiency, which accounts for self-absorption (ε_a), detector efficiency (ε_d), and abundance of the detected radiation (ε_r) with all efficiencies given as numbers, not percents;

t_o is the irradiation time (days);

t_1 is the count start time (days);

t_2 is the count end time (days);

ϕ_{2200} is the 2200 m/s absorption cross-section for gold-197 (cm^2/atom);

m_b is the bare foil mass (mg);

m_c is the covered foil mass (mg); and

F_{cd} is the cadmium correction factor.

All times are referenced to the start of the irradiation which is considered zero. Upon substitution of known constants, the following are obtained:

Specific Saturated Activity of the Bare Foil:

$$\left(\frac{A_{sat}}{m}\right) = \frac{2.975\,E\text{-}6 \times (C/m_b)}{0.989 \times 0.955 \times \varepsilon_d \times \left(1-e^{-0.257t_0}\right)\left(e^{-0.257t_2}\right)}$$

where t_0, t_1, and t_2 are in days.

Specific Activity of the Covered Foil:

$$\left(\frac{A_{sat}}{m}\right) = \frac{2.97\,E\text{-}6 \times (C/m_c)}{0.989 \times 0.955 \times \varepsilon_d \times \left(1-e^{-0.257t_0}\right)\left(e^{-0.257t_1} - e^{-0.257t_2}\right)}$$

where t_0, t_1, and t_2 are in days.

Neutron Flux at 2200 m/s:

$$\phi_{2200} = \left[\frac{196.7 \times 1000}{6.02\,E\text{+}23 \times 98.8E\text{-}24}\right]\left[\left(\frac{A_{sat}}{m}\right)_b - 1.02\left(\frac{A_{sat}}{m}\right)_c\right]$$

where the factor of 1000 in the numerator of the last equation is to convert grams to milligrams. Also, it has been assumed that the correction for self-absorption of 411 keV photons in the gold foil is 0.989, that the 411 keV photon abundance is 0.955, and that the cadmium correction factor is 1.02. The latter quantity is a function of foil thickness.

Epithermal Neutron Flux:

The epithermal neutron flux can now be found. It is given by the relation:

$$\phi_{epi} = \frac{10.1(F_{cd})(A_{sat}/m)_c(MW)}{(Au)(RI)(F_{res})} \qquad (50)$$

where ϕ_{epi} is the epithermal neutron flux (n/cm^2-s);

RI is the resonance integral for an ideal, infinitely dilute gold foil (cm^2); and

F_{res} is the resonance self-shielding factor.

Upon substitution of known constants, the following is obtained:

$$\phi_{epi} = \frac{10.1 \times 1.02\,(A_{sat}/m)_c \times 196.97 \times 1000}{6.02E\text{+}23 + 1560E\text{-}24 \times 0.28}$$

where the resonance integral is taken as 1560 barns, and the resonance self-shielding factor is 0.28.

Appendix B

Calculation of Photon and Fast Neutron Dose Rates

The method for calculating the photon and fast neutron dose rates for the MITR Medical Therapy Room Beam is described in detail by Rogus [2]. A summary is given here. The equation numbers used here correspond to those in Reference Two and are therefore not consecutive.

The first step is to correct the currents measured with the electrometer for the gas flow rate, reactor power history, gas temperature, and gas pressure. This is done using the relation:

$$I_c = (f_H / f_f)(f_{TP})I_m - (f_t)(\phi_5)/(f_{RP}) \qquad (19)$$

where I_c is the corrected current [Coulombs/minute],

f_H is the correction factor for the reactor's power history,

f_f is the correction factor for the gas flow rate,

f_{TP} is the correction factor for the gas temperature and pressure,

I_m is the measured current [Coulombs/minute],

f_t is the thermal response correction factor [cpm/(n/cm^2-s)],

ϕ_5 is the 5 MW 2200 m/s flux in the sensitive volume of the chamber [n/cm^2-s], and

f_{RP} is the scale factor for the reactor power.

The quantity f_H is determined from the reactor's power history [2]. It is unity if the reactor is at steady-state during the measurements. That is, the reactor should have been at constant power for a sufficiently long time prior to the initiation of measurements so that thermal equilibrium has been attained. The quantity f_f is unity if the gas flow rates used during the measurements were those employed during the chamber calibrations. If this was not the case, refer to Reference Two for tabulated corrections. The quantity f_{TP} is given by the relation:

$$f_{TP} = \left(\frac{T+273}{22+273}\right)\left(\frac{29.92}{P}\right)$$

where T and P are respectively the temperature (C) and pressure (inches Hg) of the purge gas in the sensitive volume of the chamber. The thermal response correction factor f_t, which has units of [(counts/minute)/(n/cm^2-s)] and has a magnitude of 1.5E-20 for the graphite-wall chamber and 4.77E-20 for the tissue-equivalent chamber. Finally, the quantity f_{RP} is scale factor for the reactor power and is given by:

$$f_{RP} = 5.0 / n_p$$

where n_p is the reactor power (MW) that equates to the reading on MITR Channel No. 7 during the characterization. The correction for relative humidity is less than 0.3% and is therefore omitted.

It is assumed that f_H and f_f are unity, then upon substituting known values, equation (19) becomes:

For the graphite-wall (carbon-graphite) chamber:

$$I_{CG} = \left(\frac{T+273}{293}\right)\left(\frac{29.92}{P}\right)I_m - (1.50E-20)(\phi_5)(5.0/n_p)$$

For the tissue-equivalent chamber:

$$I_{TE} = \left(\frac{T+273}{293}\right)\left(\frac{29.92}{P}\right)I_m - (4.77E-20)(\phi_5)(5.0/n_p)$$

Once these corrected currents are available, the photon and fast neutron dose rates can be calculated from the relations:

$$\dot{D}_\gamma = \frac{B_{TE}\dot{Q}_{CG} - B_{CG}\dot{Q}_{TE}}{B_{TE}A_{CG} - B_{CG}A_{TE}} \quad (3)$$

$$\dot{D}_n = \frac{A_{TE}\dot{Q}_{CG} - A_{CG}\dot{Q}_{TE}}{A_{TE}B_{CG} - A_{CG}B_{TE}} \quad (4)$$

where $\dot{D}_\gamma$ is the photon dose rate (cGy/minute),

$\dot{D}_n$ is the fast neutron dose rate (cGy/minute),

$\dot{Q}_{CG}$ is the corrected current of the graphite-wall (carbon-graphite) ionization chamber due to the mixed field (Coulombs/minute), and

$\dot{Q}_{TE}$ is the corrected current of the tissue-equivalent ionization chamber due to the mixed field (Coulombs/minute).

The parameters in equations (3) and (4) that are designated by the letters A and B describe the photon and neutron sensitivities of the chambers [2]. The $\dot{Q}$ values equal to the I values calculated above for each chamber. Upon substitution of known quantities into equations (3) and (4), the dose rates to brain and muscle can be determined. These are given below by equations (13) and (14) respectively. As an aid to the prospective user, units are also shown in these equations.

Brain:

Photon Dose Rate:

$$\dot{D}_\gamma = \frac{4.29E-11\,\frac{C}{cGy}\,I_{CG}\,\frac{C}{min} - 3.33E-12\,\frac{C}{cGy}\,I_{TE}\,\frac{C}{min}}{4.29E-11\,\frac{C}{cGy}\,7.62E-11\,\frac{C}{cGy} - 3.33E-12\,\frac{C}{cGy}\,4.67E-11\,\frac{C}{cGy}} \quad (13a)$$

or

$$\dot{D}_\gamma = \frac{4.29E-11\,\frac{C}{cGy}\,I_{CG}\,\frac{C}{min} - 3.33E-12\,\frac{C}{cGy}\,I_{TE}\,\frac{C}{min}}{3.114E-21\,\frac{C^2}{cGy^2}} \quad (13b)$$

Fast Neutron Dose Rate:

$$\dot{D}_n = \frac{4.67E-11\,\frac{C}{cGy}\,I_{CG}\,\frac{C}{min} - 7.62E-11\,\frac{C}{cGy}\,I_{TE}\,\frac{C}{min}}{4.67E-11\,\frac{C}{cGy}\,3.33E-12\,\frac{C}{cGy} - 7.62E-11\,\frac{C}{cGy}\,4.29E-11\,\frac{C}{cGy}} \quad (14a)$$

or

$$\dot{D}_n = \frac{4.67E-11\,\frac{C}{cGy}\,I_{CG}\,\frac{C}{min} - 7.62E-11\,\frac{C}{cGy}\,I_{TE}\,\frac{C}{min}}{-3.114E-11\,\frac{C^2}{cGy^2}} \quad (14b)$$

Muscle:

Photon Dose Rate:

$$\dot{D}_\gamma = \frac{4.43E-11\,\frac{C}{cGy}\,I_{CG}\,\frac{C}{min} - 3.33E-12\,\frac{C}{cGy}\,I_{TE}\,\frac{C}{min}}{4.43E-11\,\frac{C}{cGy}\,7.62E-11\,\frac{C}{cGy} - 3.33E-12\,\frac{C}{cGy}\,4.67E-11\,\frac{C}{cGy}} \quad (15a)$$

or

$$\dot{D}_\gamma = \frac{4.43E-11\,\frac{C}{cGy}\,I_{CG}\,\frac{C}{min} - 3.33E-12\,\frac{C}{cGy}\,I_{TE}\,\frac{C}{min}}{3.221E-21\,\frac{C^2}{cGy^2}} \quad (15b)$$

Fast Neutron Dose Rate:

$$\dot{D}_n = \frac{4.67E-11\frac{C}{cGy}I_{CG}\frac{C}{min} - 7.62E-11\frac{C}{cGy}I_{TE}\frac{C}{min}}{4.67E-11\frac{C}{cGy}3.33E-12\frac{C}{cGy} - 7.62E-11\frac{C}{cGy}4.43E-11\frac{C}{cGy}} \quad (16a)$$

or

$$\dot{D}_n = \frac{4.67E-11\frac{C}{cGy}I_{CG}\frac{C}{min} - 7.62E-11\frac{C}{cGy}I_{TE}\frac{C}{min}}{-3.221E-11\frac{C^2}{cGy^2}} \quad (16b)$$

The photon and fast neutron doses calculated here are to be normalized to a reactor power of 5 MW. This should be done using the Channel 7 value with all shutters closed. The latest calibration of Channel 7 to reactor thermal power at the end of the week should be used.

Appendix C

Calculation of N-14, B-10, and RBE-Weighted Dose Rates

A. N-14 Dose Rate

For brain: $\dot{D} = 1.401E-11\ cGy\,cm^2/n \times \phi_{2200}\ n/cm^2\text{-}s \times 60\ s/min$

For muscle: $\dot{D} = 2.724E-11\ cGy\,cm^2/n \times \phi_{2200}\ n/cm^2\text{-}s \times 60\ s/min$

B. B-10 Dose Rate in Healthy tissue @ 7.5 ppm B-10

$\dot{D} = 8.66E-12\ cGy\,cm^2/n\text{-}ppm \times 7.5\ ppm \times \phi_{2200}\ n/cm^2\text{-}s \times 60\ s/min$

C. B-10 Dose Rate in Tumor Tissue @ 30 ppm B-10

$\dot{D} = 8.66E-12\ cGy\,cm^2/n\text{-}ppm \times 30\ ppm \times \phi_{2200}\ n/cm^2\text{-}s \times 60\ s/min$

D. RBE - Weighted Dose Rates

The relations given below are predicated on the following RBE values: 4.0 for B-10; 2.3 for N-14, 2.3 for fast neutrons; and 0.5 for photons. These values should be reviewed at every characterization of the MITR Medical Therapy Facility Beam.

a) RBE 30 ppm B-10 dose rate = $4.0 \times D_{B\text{-}10,\ 30\ ppm}$
RBE 7.5 ppm B-10 dose rate = $4.0 \times D_{B\text{-}10,\ 7.5\ ppm}$
RBE N-14 dose rate = $2.3 \times D_{N\text{-}14}$ (muscle or brain)
RBE fast neutron dose rate = $2.3 \times D_{fn}$
RBE photon dose rate = $0.5 \times D_{\gamma}$

b) RBE healthy tissue dose rate
$= 4.0 \times D_{B\text{-}10,\ 7.5\ ppm} + 2.3 \times D_{N\text{-}14} + 2.3 \times D_{fn} + 0.5 \times D_{\gamma}$
Use muscle N-14 dose to calculate the muscle tissue dose and use brain N-14 dose to calculate the brain dose.

c) RBE tumor tissue dose rate
$= 4.0 \times D_{B\text{-}10,\ 30\ ppm} + 2.3 \times D_{N\text{-}14} + 2.3 \times D_{fn} + 0.5 \times D_{\gamma}$
Use muscle N-14 dose to calculate the muscle tissue dose and use brain N-14 dose to calculate the brain dose.

PM 3.14.2.5 Cross-Calibration of Electrometers

Purpose:

This procedure provides a standard method for calibrating electrometers against an electrometer that has been calibrated at a secondary calibration laboratory.

Acceptance Criteria:

Two Coulomb scales (E-10 C and E-09 C) of the field electrometer are calibrated to within ± 2 % against the unit that was sent to the secondary calibration laboratory.

Background:

Provision No. 14(c) and Definition (5) of MITR Technical Specification No. 6.5 establish a requirement that "the beam monitors be calibrated at two-year intervals against instruments that measure dose including a tissue-equivalent chamber and a graphite or magnesium wall ionization chamber (or the equivalent to any of these three) that have in turn been calibrated by a secondary calibration laboratory." As part of this requirement, one of the facility's electrometers is included in the instruments sent to the secondary calibration laboratory. This procedure provides a means for calibrating the facility's other electrometers (if any) against the one calibrated at the secondary laboratory.

Prerequisites:

1. The following are available:

   a) Graphite-wall ionization chamber (Far West IC-18G),

   b) Two or more electrometers (Keithley 616 or 617).

2. The graphite-wall chamber as well as one of the electrometers shall have been calibrated by a Secondary Calibration Laboratory within the last two years. The electrometer for which this is done is designated here as the 'calibrated' instrument while the other is referred to as the 'field' instrument. The latter is calibrated against the former. Each electrometer can be calibrated by itself or the electrometer and each chamber can be calibrated as an electrometer-chamber pair.

3. Low-noise signal cables, a high voltage power supply (Canberra HV Supply #2816A or equivalent), high-voltage cables, a calibration jig, and a stop watch with an accuracy and resolution of 0.1 s. (Caution: The signal cables should be handled gently. In particular, they should not be bent to radii of less than 30 cm.)

4. Standard radiological procedures are to be observed.

5. 5 Ci Cs-137 source.

6. A thermometer and a means of monitoring barometric pressure.

7. The area in which the calibration is to be performed is to be secured and posted as a 'High Radiation' area.

Procedure:

The Keithley 617 is the unit sent to the secondary calibration laboratory. The Keithley 616 is the field instrument. The calibration method is to measure the same current with both electrometers and then to assign an electrometer calibration factor to the field instrument (K-616). The graphite-wall chamber is exposed to about a 1 R/min field from the Cs-137 source. Charge is collected using the K-617 electrometer. The results of four measurements, each about 1 minute long, are averaged. The K-616 electrometer is then used similarly to measure the same current. The above currents are compared.

_____ 1. Record the following information:

Instrument	Serial #	Calibration Date	Secondary Lab
K - 616 electrometer	_____	N/A	N/A
K - 617 electrometer	_____	_____	_____
Graphite-wall Chamber	_____	_____	_____

_____ 2. Describe the signal cable: _____

_____

_____ 3. Energize both electrometers and adjust the high voltage or the HV power supply to + 250 V. Check the HV cables to be certain that the chambers would be at 250 ± 10 V. The background currents, with the voltage applied to the chambers but with no radiation field, should be less than 1E-14 Amperes.

_____ 4. Allow both electrometers to warm up for two hours.

_____ 5. Attach the calibration jig to the Cs-137 source and plug in the Cs-source warning lights.

_____ 6. Monitor ambient temperature and pressure using the thermometer and the control room barometer. Correction to the calibration will be required if variations in temperature and pressure that occur during the actual calibration affect the currents by more than 0.2%.

_____ 7. Set the K-617 electrometer to the Coulomb mode and for autoranging. Check that the Volt/Ohm Guard is Off.

_____ 8. Position the graphite-wall ionization chamber in the calibration jig (the position closer to the source) and connect it to the electrometer that was sent the secondary calibration laboratory. This should be the K-617. (Note: The K-617 is autoranging. A particular scale need not be specified.)

_____ 9. Allow the system to stabilize for ten minutes.

_____ 10. Perform the following with the unit sent to the secondary calibration laboratory (K-617):

____ a) Disable the zero-check.

____ b) Collect charge for about one minute.

____ c) Record the collected charge: _____ Coulombs and the collection time: _____ minutes.

____ d) Compute the current: _____ Coulomb/minute.

____ e) Repeat steps (a) - (d) and record the collected charge: _____ Coulombs and the collection time: _____ minutes.

____ f) Compute the current: _____ Coulombs/minute.

____ g) Average the currents obtained in Steps (d) and (f) above: _____ Coulombs/minute. This is the background current of the K-617 unit.

_____ 11. Verify that the background current for the electrometer is less than ± 6E-13 Coulombs/minute. If not, notify the Director of the MIT Nuclear Reactor Laboratory and the program's Certified Medical Physicist.

_____ 12. Lift the depleted uranium shield to irradiate the chamber. (Note: The chamber is open to the air; no flushing gas is needed.) Four measurements should be taken and the results recorded on the attached data sheet.

_____ 13. Check the repeatability of the measurements obtained in step (12) above. If the repeatability is not within 1%, then the electrometer, chamber, or system as a whole (including cables) is not stable. Suspend the procedure until the cause is identified and rectified.

_____ 14. Lower the depleted uranium shield to shut off the beam.

_____ 15. Remove the signal cable from the electrometer that was sent to the secondary calibration laboratory and attach it to the field electrometer. This should be the K-616.

_____ 16. Set the K-616 electrometer to the E-10 C range. Select the triax mode for the cable and the fast mode for the collection time.

_____ 17. Allow the system to stabilize for ten minutes.

_____ 18. Perform the following for the field unit (the K-616).

____ a) Disable the zero-check.

____ b) Collect charge for about one minute.

____ c) Record the collected charge: _____ Coulombs and the collection time: _____ minutes.

____ d) Compute the current: _____ Coulomb/minute.

____ e) Repeat steps (a) - (d) and record the collected charge: _____ Coulombs and the collection time: _____ minutes.

____ f) Compute the current: _____ Coulombs/minute.

____ g) Average the currents obtained in Steps (d) and (f) above: _____ Coulombs/minute. This is the background current of the K-616 unit on the E-10 C scale.

_____ 19. Verify that the background current for the electrometer is less than ± 6E-13 Coulombs/minute. If not, notify the Director of the MIT Nuclear Reactor Laboratory and the program's Certified Medical Physicist.

_____ 20. Lift the depleted uranium shield to irradiate the chamber. (Note: The chamber is open to the air; no flushing gas is needed.) Four measurements should be taken and the results recorded on the attached data sheet.

_____ 21. Check the repeatability of the measurements obtained in step (20) above. If the repeatability is not within 1%, then the electrometer, chamber, or system as a whole (including cables) is not stable. Suspend the procedure until the cause is identified and rectified.

_____ 22. Lower the depleted uranium shield to shut off the beam.

_____ 23. Set the K-616 electrometer to the E-09 C range. Select the triax mode for the cable and the fast mode for the collection time.

_____ 24. Allow the system to stabilize for ten minutes.

_____ 25. Perform the following for the field unit:

____ a) Disable the zero-check.

____ b) Collect charge for about one minute.

____ c) Record the collected charge: _____ Coulombs and the collection time: _____ minutes.

____ d) Compute the current: _____ Coulomb/minute.

____ e) Repeat steps (a) - (d) and record the collected charge: _____ Coulombs and the collection time: _____ minutes.

____ f) Compute the current: _____ Coulombs/minute.

____ g) Average the currents obtained in Steps (d) and (f) above: _____ Coulombs/minute. This is the background current of the K-616 unit on the E-09 C scale.

_____ 26. Verify that the background current for the electrometer is less than ± 6E-13 Coulombs/minute. If not, notify the Director of the MIT Nuclear Reactor Laboratory and the program's Certified Medical Physicist.

_____ 27. Lift the depleted uranium shield to irradiate the chamber. (Note: The chamber is open to the air; no flushing gas is needed.) Four measurements should be taken and the results recorded on the attached data sheet.

_____ 28. Check the repeatability of the measurements obtained in step (27) above. If the repeatability is not within 1%, then the electrometer, chamber, or system as a whole (including cables) is not stable. Suspend the procedure until the cause is identified and rectified.

_____ 29. Lower the depleted uranium shield to shut off the beam.

_____ 30. Average the currents for each electrometer and record on the data sheet.

_____ 31. Obtain the 'electronic calibration factor' or ECF for the electrometer that was calibrated at the secondary calibration laboratory:

$$(ECF)_{K\text{-}617} = \text{\_\_\_\_\_}$$

(Note: In 1993, this factor was 1.001.)

_____ 32. Calculate the ECFs for the two scales of the field instrument from the relation:

$$(ECF)_{K-616} = \frac{(ECF)_{K-617}\ (\text{Avg. Current of } K-617)}{(\text{Avg. Current of } K-616)}$$

$(ECF)_{K-616}$ for E-10 C scale: _____

$(ECF)_{K-616}$ for E-09 C scale: _____

_____ 33. Deenergize and store all equipment.

The acceptance criteria is that the field instrument's two Coulomb scales (E-10 and E-09) are calibrated to within ± 2% of the electrometer that was sent to the secondary calibration laboratory.

Acceptance Criteria Met: Yes ☐ No ☐

Calibration performed by: _____ _____
NCT Research Scientist Date

Calibration checked by: _____ _____
NCT Research Scientist Date

Results reviewed by: _____ _____
NRL Director Date

Data Table for Electrometer Cross-Calibration

Electrometer	Charge collected (C)	Collection time (min)	Average current (C/min)
K-617	1. _____	_____	
	2. _____	_____	
	3. _____	_____	
	4. _____	_____	_____
K-616 E-10 C scale	1. _____	_____	
	2. _____	_____	
	3. _____	_____	
	4. _____	_____	_____
K-616 E-09 C scale	1. _____	_____	
	2. _____	_____	
	3. _____	_____	
	4. _____	_____	_____

Certified by: _____ _____
NCT Research Scientist Date

Data reviewed by: _____ _____
NCT Research Scientist Date

PM 3.14.2.6 Calibration and Stability Check of Ionization Chambers and Electrometers

Purpose:

This procedure provides a standard method for checking the calibration and stability of both the ionization chambers and the electrometers. The method is a relative, not an absolute, calibration and is intended to detect trends.

Acceptance Criteria:

Exposure rates measured with the Cs-137 check source are within ± 3% of those obtained during the most recent calibration of the instruments in question at a secondary calibration laboratory.

Prerequisites:

1. The following are available:
   a) Tissue-equivalent chamber (Far West IC-18),
   b) Graphite-wall ionization chamber (Far West IC-18G),
   c) Magnesium-wall ionization chamber (Far West IC-18 #670-TMW),
   d) An electrometer (Keithley 616 or 617). Only one electrometer is required. Either may be used.
2. The three chambers and the Keithley 617 shall have been calibrated by a Secondary Calibration Laboratory within the last two years. The Keithley 616 shall have been calibrated against the Keithley 617 within the last two years.
3. Low-noise signal cables, a high voltage power supply (Canberra HV Supply #2816A or equivalent), high-voltage cables, a calibration jig, a digital voltmeter, and a stop watch with an accuracy and resolution of 0.1 s. (Caution: The signal cables should be handled gently. In particular, they should not be bent to radii of less than 30 cm.)
4. Standard radiological procedures are to be observed.
5. 5 Ci Cs-137 source.
6. A thermometer and a means of monitoring barometric pressure.
7. The area in which the calibration is to be performed is to be secured and posted as a "High Radiation' area.

Procedure:

_____ 1. Record the following information:

Instrument	Serial #	Calibration Date	Secondary Lab
Tissue-equivalent Chamber	_____	_____	_____
Graphite-Wall Chamber	_____	_____	_____
Magnesium-Wall Chamber	_____	_____	_____
K - 616 electrometer	_____	_____	PM 3.14.2.5
K - 617 electrometer	_____	_____	_____

_____ 2. Describe the signal cable: _____

_____

_____ 3. Energize the electrometer and adjust the high voltage or the HV power supply to + 250 V. Use the digital voltmeter to verify that the voltage applied to the cable is + 250 V ± 10 V. The background current, with the voltage applied to the chamber but with no radiation field, should be less than 1E-14 Amperes.

_____ 4. Allow the electrometer to warm up for one hour.

_____ 5. Attach the calibration jig to the Cs-137 source and plug in the Cs-source warning lights.

_____ 6. Set the K-617 electrometer to the Coulomb mode and for autoranging. Check that the Volt/Ohm Guard is Off.

_____ 7. Attach any one of the ionization chambers to the electrometer and position one of the chambers in the calibration jig. Record the position number (one or two) on the attached data sheet. The chamber should now be at +250 V.

_____ 8. Allow the chamber-electrometer pair to stabilize for several minutes.

_____ 9. Depress the electrometer's 'zero correct' button so as to zero the unit.

_____ 10. Perform the following:

____ a) Disable the zero-check.

____ b) Collect charge for about one minute.

____ c) Record the collected charge: _____ Coulombs and the collection time: _____ minutes.

____ d) Compute the current: _____ Coulomb/minute.

____ e) Repeat steps (a) - (d) and record the collected charge: _____ Coulombs and the collection time: _____ minutes.

____ f) Compute the current: _____ Coulombs/minute.

____ g) Average the currents obtained in steps (d) and (f) above: _____ Coulombs/minute. This is the background current of the electrometer.

_____ 11. Verify that the background current for the electrometer is less than ± 6E-13 Coulombs/minute. If not, notify the Director of the MIT Nuclear Reactor Laboratory and the program's Certified Medical Physicist.

_____ 12. Lift the depleted uranium shield to irradiate the chamber. (Note: The chamber is open to the air; no flushing gas is needed.) Four measurements should be taken and the results recorded on the attached data sheet. Also record ambient temperature and pressure.

_____ 13. Check the repeatability of the measurements obtained in step (15) above. If the repeatability is not within 1%, then the electrometer, chamber, or system as a whole (including cables) is not stable. Suspend the procedure until the cause is identified and rectified.

_____ 14. Lower the depleted uranium shield to shut off the beam.

_____ 15. Compute the average of each of the four measurements and record it on the attached data sheet.

_____ 16. Repeat steps (7) - (14) for each of the three ionization chambers.

_____ 17. Obtain the Co-60 calibration factors in air at 22 °C and 29.92 inches of Hg from the most recent calibration of the three ionization chambers by a secondary calibration laboratory. Record these below:

Tissue-equivalent: _____ Roentgen/Coulomb

Graphite-wall: _____ Roentgen/Coulomb

Magnesium-wall: _____ Roentgen/Coulomb

Date of Calibration: _____ _____; Laboratory _____

_____ 18. Calculate and record the measured exposure rates for each chamber. Use the following equation:

$$\dot{X} = N_x \dot{Q} \frac{T + 273°}{22° + 273°} \frac{29.92}{P} (ECP)$$

where $\dot{X}$ is the exposure rate (Roertgen/minutes),

N_x is the Co-60 exposure calibration factor in air at 22 °C and 29.92 inches of Hg,

$\dot{Q}$ is the chamber current (Coulomb/minute),

T is the temperature of gas in sensitive volume of chamber (°C), and

P is the pressure of gas in sensitive volume of chamber (inches of Hg).

ECP is the electrometer calibration factor for the particular electrometer and scale.

_____ 19. Obtain the expected exposure rate from the most recent reference calibration of the Cs-137 source: _____ Roentgen/Coulomb on _____. (Note: This would normally be the exposure rate obtained following the most recent calibration of the chambers by a secondary calibration laboratory.)

_____ 20. Calculate and record the expected exposure rate. Use the following equation:

$$\dot{X} = \dot{X}_o e^{-\frac{0.6935}{t_{1/2}}}$$

where $\dot{X}$ is the expected exposure rate (Roentgen/Coulomb),

$\dot{X}_o$ is the exposure rate measured at the time of the most recent reference calibration (Roentgen/Coulomb),

t is the time elapsed since the reference calibration (years), and

$t_{1/2}$ is the half-life of Cs-137 (30.17 years).

_____ 21. Calculate the percent difference between the measured and expected exposure rates and record on the attached data sheet.

_____ 22. Deenergize and store all equipment.

The acceptance criteria is that the measured and expected exposure rates agree within ± 2%.

Acceptance Criteria Met: Yes ☐ No ☐

Calibration performed by: _____ _____
NCT Research Scientist Date

Calibration checked by: _____ _____
NCT Research Scientist Date

Results reviewed by: _____ _____
NRL Director Date

Data Sheet for Ionization Chamber Calibration and Stability Check

Position number (1 or 2)	Ionization chamber	Measured Charge (C)	Measured Time (s)	Average Current (C/min)	Pressure (inches Hg)	Temperature (°C)	Measured Exposure Rate (R/min)	Error (Meas-Exp)/Exp (%)
_____	Chamber	1. _____	_____					
		2. _____	_____					
Time _____		3. _____	_____					
		4. _____	_____	_____	_____	_____	_____	_____
_____	Tissue	1. _____	_____					
		2. _____	_____					
Time _____		3. _____	_____					
		4. _____	_____	_____	_____	_____	_____	_____
_____	Graphite	1. _____	_____					
		2. _____	_____					
Time _____		3. _____	_____					
		4. _____	_____	_____	_____	_____	_____	_____
_____	Magnesium	1. _____	_____					
		2. _____	_____					
Time _____		3. _____	_____					
		4. _____	_____	_____	_____	_____	_____	_____

Expected Exposure Rate (R/min): _____

Certified by: _____ NCT Research Scientist _____ Date

Data reviewed by: _____ NCT Research Scientist _____ Date

PM 3.14.2.7 Determination of High Purity Ge or Ge(Li) Detector Efficiency

Purpose:

This procedure provides a standard method for determining the counting efficiency of high purity Ge or Ge(Li) detectors.

Acceptance Criteria:

The absolute efficiency at 411 keV (Au-198) is determined to within ± 2%.

Prerequisites:

1. The following are available:

   a) Diode detector.

   b) NIST Standard Mixed Radionuclide Source (SRM 4275C-45) or an equivalent made as a thin deposit of small area (< 0.125" diameter).

   c) Data sheet for the source in which photon energies and disintegration rates are listed. (Note: A data sheet for SNM 4275C-45 is attached.)

   d) Sources for use in energy calibrating the detector.

   e) Plexiglass holder that is used to position the standard source and foils at a fixed distance from the detector.

   f) A gold foil (5-10 mg, -0.002" thick). The foil should have been irradiated to a fluence of about $3.6 \cdot 10^{13}$ neutrons/cm^2.

Procedure:

_____ 1. Record detector type and serial number.

Type: _____ ; Serial #: _____ .

_____ 2. Energy calibrate the detector using Cs-137, Co-60, Na-22 or other appropriate radionuclides such as those corresponding to the gamma-ray emitters of the SRM source. If possible, the energy peaks of the nuclides chosen should bracket the energy peaks of the nuclide(s) to be measured. Record the following:

   a) Nuclide(s) to be measured: _____ , _____ .

   Energy Peaks: _____ , _____ , _____ , _____ (keV).

b) Nuclide(s) for calibration: _____ , _____ .

Energy Peaks: _____ , _____ , _____ , _____ (keV).

The energy calibration procedure is itself largely automated. The user need only identify the peaks of the source nuclides.

_____ 3. Position the standard source four-six inches from the detector. This distance is selected so as to minimize summing errors. Record the distance from the face of the detector to the source: _____ inches.

_____ 4. Count the standard source until the peaks that will be used to determine efficiency have a counting error of about ± 1% (one standard deviation). This will require approximately one hour. For each peak, complete Part A of the attached data table and determine the count rate, which is the net area divided by the counting (live) time. As an alternative, a spreadsheet may be used to perform and record these calculations. If used, these shall be signed, dated, and reviewed by two NCT Research Scientists.

_____ 5. Complete Part B of the attached data table. As an alternative, a spreadsheet may be used to perform and record these calculations. If used, these shall be signed, dated, and reviewed by two NCT Research Scientists.

_____ 6. Determine the detector efficiency at the distance recorded in step (3) above for the 411 keV peak by plotting the 'log of detector efficiency' versus 'log of photon energy' for several peaks between 250 and 700 keV. A straight line, least squares fit should be used and the efficiency at 411 keV determined by linear interpolation. A sample efficiency plot is attached. Sign and date the efficiency plot and append it to this procedure.

Efficiency at 411 keV at _____ inches: _____ (%)

_____ 7. Determine the 411 keV efficiency for the gold foil placed directly on top of the detector. (Note: In order to ensure accuracy when other foils are subsequently counted in this position, it is necessary that each be positioned within ± 2 mm of the foil used here for the calibration. Cardboard holders similar to 35 mm projector slides are available and should be used to position this and subsequent foils.) The detection efficiency at this in-close position is determined by counting a gold foil at the 4-6" distance and then counting the same foil at the close distance. This gives a ratio of count rates which, when multiplied by the efficiency at the 4-6" distance, gives the efficiency at the in-close distance. Foils should be counted at each position until a statistical counting error of less than ± 1% is obtained. A small correction accounting for decay of the Au-198 during the time that elapses between these measurements should be applied. It is best, however, to calculate the saturated activity per unit mass of the foil with the foil at both

positions. The ratio of the efficiencies is equal to the ratio of the calculated saturated activities per unit mass. In this way, the decay correction is accounted for automatically. Record the following:

a) Count rate with foil at 4-6 inches: _____ (cps) ± _____ %

b) Count rate with foil on top of detector: _____ (cps) ± _____ %

c) Ratio of count rates (near/far): _____ ± _____ %

_____ 8. Compute the detector efficiency at 411 keV for the foil on top of the detector by multiplying the count rate rate ratio from step (7(c)) above by the efficiency determined in step (6) above. Detector efficiency at 411 keV for foil on top of the detector: _____ %

_____ 9. Deenergize and store all equipment.

The acceptance criteria is that the absolute efficiency at 411 keV is determined to within ± 2%.

Acceptance Criteria Met: Yes ☐ No ☐

Calibration performed by: _____ NCT Research Scientist _____ Date

Calibration checked by: _____ NCT Research Scientist _____ Date

Results reviewed by: _____ NRL Director _____ Date

Data Table for Calculation of Ge/Ge(Li) Detector Efficiency

Detector Type: _____ Serial No.: _____ Date: _____

Part A

	Peak (keV)	Net Area (counts)	Live Time(s)	Count Rate (cps)
1.				
2.				
3.				
4.				
5.				

Part B

	Peak (keV)	Reference Disintegration Rate (dps)	Current Disintegration Rate (dps)	Measured Count Rate (cps)	Efficiency (%)
1.					
2.					
3.					
4.					
5.					

Notes: (1) Obtain reference disintegration rate from the data sheet supplied with the source.

(2) Obtain current disintegration rate by correcting the reference disintegration rate for decay from the time of the source's manufacture to the present. Use the half-lives provided on the data sheet that was supplied with the source.

(3) The efficiency is a measured count rate divided by the current disintegration rate, expressed as a percent.

Date Certified by: _____ NCT Research Scientist _____ Date

Data Reviewed by: _____ NCT Research Scientist _____ Date

National Institute of Standards & Technology

Certificate

Standard Reference Material 4275C
Radioactivity Standard

MIXED-RADIONUCLIDE POINT-SOURCE STANDARD
for the
EFFICIENCY CALIBRATION OF GERMANIUM-SPECTROMETER SYSTEMS

Antimony-125-Tellurium-125m
Europium-154
Europium-155

Source identification	SRM 4275C-45
Source description	Point source on polyester tape (1)*
Reference time	1200 EST September 1, 1988

This standard is intended for use in measuring the full-energy-peak efficiencies of spectrometry systems for x and gamma rays from 27 to 1596 keV, provided that the responses to radiations approximately 5 keV apart can be resolved. Emission rates are specified at 18 energies for photon radiations from a mixture of antimony-125-tellurium-125m, europium-154, and europium-155. Uncertainties are estimated and combined at a level corresponding to a standard deviation of the mean, with the intent that the user can propagate this uncertainty along with the other uncertainties in the spectrometer calibration. For a more conservative overall uncertainty corresponding to that given on other NIST radioactivity certificates, multiply the combined uncertainty by three.

Table 1 gives the energies, emission rates, and uncertainties for selected radiations. A footnote indicates how emission rates will change with time. If there are any changes in measured emission rates that would correspond to an emission rate 0.5 percent different from that calculated from Table 1, or in measured half lives that would cause a corresponding difference after five years, notification will be sent to purchasers of the standard.

Table 2 lists the estimates of component uncertainties which have been added in quadrature to give the combined uncertainty in each emission rate.

Notes on the use of this standard are appended. One of the tables in the supplemental notes gives relative emission rates for radiations close in energy to the certified radiations; for spectrometry systems of poorer resolution, it may be necessary to use a combined emission rate for some multiple peaks.

This Standard Reference Material was prepared in the Center for Radiation Research, Ionizing Radiation Division, Radioactivity Group, Dale D. Hoppes, Group Leader.

Gaithersburg, MD 20899
September, 1988

Stanley D. Rasberry, Chief
Office of Standard Reference Materials

*Notes on page 4

SR#-0-93-5

MAY 28 1993

TABLE 1

X-Ray and Gamma-Ray Energies, Emission Rates [2,3], and Uncertainties for Standard Reference Material 4275C-45

Radionuclide	Photon Energy (keV)	Emission Rate ($\times s^{-1}$) or (γs^{-1}) 1200 EST September 1, 1988	Total Estimated Uncertainty (%)*
^{125}Sb-^{125m}Te	Kα, 27.4	4.704×10^4	1.3
^{154}Eu-^{155}Eu	Kα, 42.8	2.775×10^4	1.3
^{155}Eu	86.5	1.062×10^4	0.9
^{155}Eu	105.3	7.396×10^3	1.3
^{154}Eu	123.1	4.321×10^4	0.8
^{125}Sb	176.3	5.162×10^3	0.6
^{154}Eu	247.7	7.325×10^3	0.6
^{125}Sb	427.9	2.244×10^4	0.8
^{125}Sb	463.4	7.888×10^3	0.7
^{154}Eu	591.8	5.242×10^3	0.6
^{125}Sb	600.6	1.333×10^4	0.7
^{125}Sb	635.9	8.518×10^3	0.6
^{154}Eu	723.3	2.127×10^4	0.6
^{154}Eu	873.2	1.291×10^4	0.7
^{154}Eu	996.3	1.105×10^4	0.9
^{154}Eu	1004.7	1.917×10^4	0.7
^{154}Eu	1274.5	3.694×10^4	0.5
^{154}Eu	1596.4	1.878×10^3	0.7

* Estimated total uncertainties have the significance of one standard deviation of the mean. Components of these estimates are given in Table 2.

TABLE 2

Estimates of the Component Uncertainties for
Photon-Emission-Rate Values for SRM 4275C

TYPICAL UNCERTAINTY COMPONENTS (%)

Photon Energy (keV)	Number of Determi-nations	Std. Dev. of the Mean	Effici-ency	Peak Analysis	Pile-up Compen-sation	Geometry	Other*	Combined Uncer-tainty**
27.4	6	0.3	1.0	0.7	0.3	0.1	0.3	1.3
42.8	12	0.05	1.0	0.7	0.1	0.1	0.3	1.3
86.5	12	0.06	0.70	0.5	0.1	0.1	0.3	0.9
105.3	12	0.06	1.2	0.5	0.1	0.1	0.4	1.3
123.1	6	0.08	0.6	0.4	0.1	0.08	0.4	0.8
176.3	6	0.09	0.5	0.2	0.2	0.1	0.4	0.6
247.7	6	0.04	0.5	0.3	0.1	0.08	0.4	0.6
427.9	6	0.23	0.7	0.2	0.2	0.08	0.4	0.8
463.4	7	0.22	0.58	0.2	0.2	0.08	0.4	0.7
591.8	6	0.12	0.45	0.3	0.1	0.08	0.4	0.6
600.6	7	0.20	0.42	0.4	0.2	0.08	0.4	0.7
635.9	6	0.19	0.42	0.2	0.2	0.08	0.4	0.6
723.3	6	0.05	0.54	0.2	0.1	0.08	0.4	0.6
873.2	5	0.12	0.63	0.3	0.1	0.08	0.4	0.7
996.3	5	0.11	0.54	0.75	0.1	0.08	0.4	0.9
1004.7	5	0.06	0.54	0.4	0.1	0.08	0.4	0.7
1274.5	5	0.06	0.45	0.1	0.1	0.08	0.4	0.5
1596.4	6	0.43	0.40	0.1	0.2	0.15	0.4	0.7

* Includes contributions for the half lives for the Te x ray, for the decay schemes for the Gd x ray, and for gravimetric factors in the source preparation.

**Components of the uncertainty have been added in quadrature. This is the uncertainty for a typical detector, and some of the values are slightly greater than those given in the last column in Table 1.

NOTES

1) Sample consists of a dried deposit of the radionuclides between two layers of polyester type 0.006-cm thick which are mounted on an aluminum annulus (3.8-cm inside diameter and 5.4-cm outside diameter).

2) These values are based on gamma-ray spectrometry measurements made at the National Institute of Standards and Technology, which are described in the reference: B.M. Coursey, D.D. Hoppes, and F.J. Schima, "Determination of the Photon Emission Rates of the NBS Long-Lived Mixed-Radionuclide Standard", Nuclear Instruments and Methods 193, 1 (1982).

3) Emission rates at later times can be calculated using the following evaluated half-life values and decay constants:

	Half Life	Decay Constant
^{125}Sb	1008 ± 2 days	6.876×10^{-4} days^{-1}
^{154}Eu	3141 ± 12 days	2.207×10^{-4} days^{-1}
^{155}Eu	1738 ± 4 days	3.986×10^{-4} days^{-1}

4) For the 42.8-keV Gd K_α x rays, the emission rate N_t is given by

$$N_t = N_o \times (0.6724\, e^{-2.207 \times 10^{-4}\, t} + 0.3276\, e^{-3.986 \times 10^{-4}\, t}),$$

where N_o is the emission rate given in Table 1, and t is the time in days from 1200 EST September 1, 1988.

For further information contact Dr. F.J. Schima (301) 975-5537 or Dr. D.D. Hoppes (301) 975-5532.

SRM 4275C

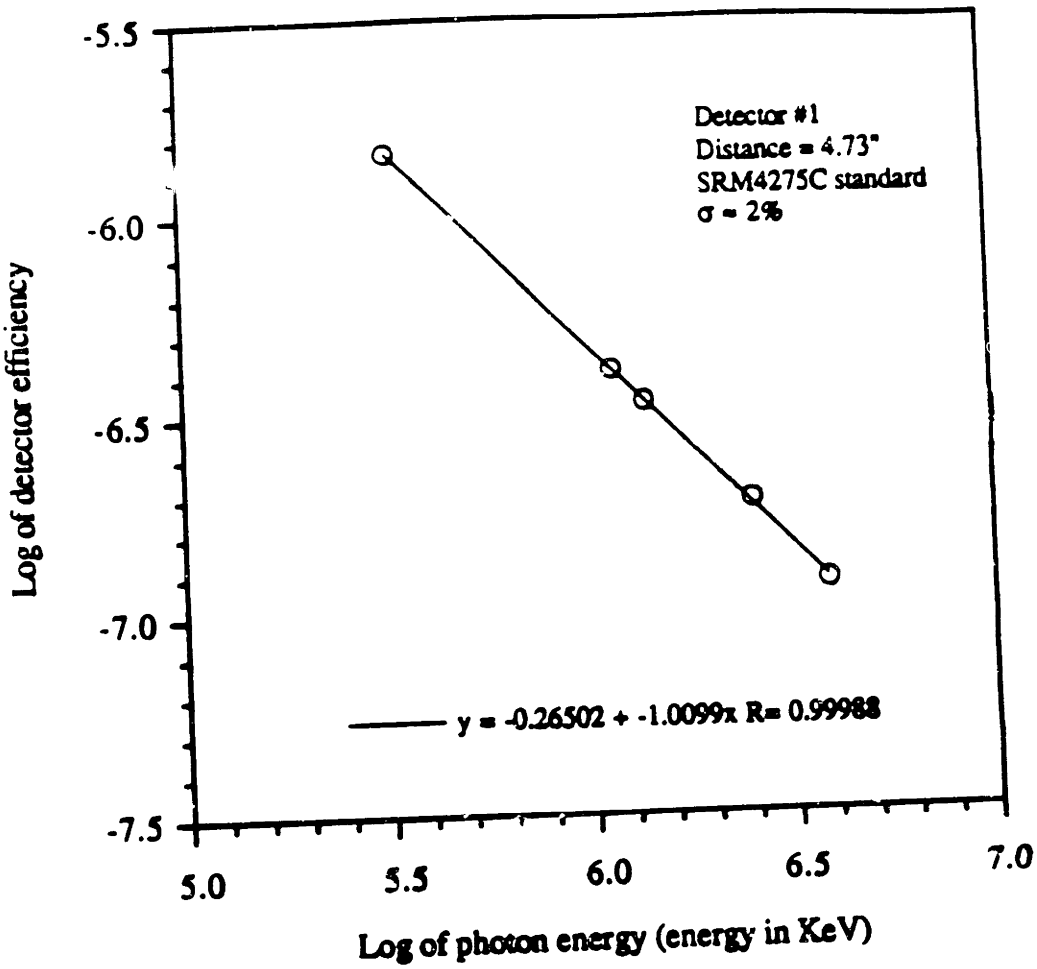

This is a typical efficiency-energy plot. Detector #1 is a Ge(Li) detector.

PM 3.14.1.8 Surveillance Schedule for Medical Therapy Facility Procedures

Purpose:

This procedure establishes a schedule for the performance of procedures required to implement MITR Technical Specification No. 6.5 and its associated Quality Management Program. Surveillances listed in this procedure are only required if human therapy is planned for the interval of the surveillance. However, in the event of a hiatus in the scheduled performance of any given surveillance, that surveillance shall be performed prior to the initiation of human therapy during the interval in question.

Acceptance Criterion:

Procedures are performed at the specified frequency subject to the following:

a) A maximum allowable extension not to exceed 25% of the specified surveillance interval, unless otherwise stated in this procedure;

b) A total maximum combined interval time for any three consecutive surveillance intervals not to exceed 3.25 times the specified surveillance interval.

Surveillance Schedule

#	Title	Frequency	Months
3.14.1.1	Test of Requirements Listed in MITR Technical Specification No. 6.5	Monthly	All
3.14.1 2	Calibration of Medical Therapy Facility Radiation Monitor	Quarterly	Mar, June, Sept., Dec.
3.14.1.3	Source Check and Alarm Operability Test of Medical Therapy Facility Radiation Monitor	Therapy only*	--
3.14.1.4	Test of Patient Positioning System	Annual	Jan.
3.14.1.5	Verification of Neutron Beam Geometric Center	Preop Only**	
3.14.1.6	Sensitivity Test of the Medical Therapy Room Beam Monitors	Preop Only**	
3.14.1.7	Activation Test of Patient Positioning System	Preop Only**	
3.14.1.8	Surveillance Schedule for Medical Therapy Facility Procedures	N/A	N/A
3.14.2.1	Functional Check of the Medical Therapy Facility Beam Monitors	Weekly	--
3.14.2.2	Calibration Check of Medical Therapy Facility Beam	Weekly***	--
3.14.2.3	Beam Monitor Plateau and Discriminator Setpoint Tests	Semi-Annual	Jan., July
3.14.2.4	Characterization of the Medical Therapy Facility Beam	Semi-Annual	Jan., July
3.14.2.5	Cross-Calibration of Electrometers	Biennial	Jan.
3.14.2.6	Calibration and Stability Check of Ionization Chambers and Electrometers	Semi-Annual	Jan., July
3.14.2.7	Determination of High Purity Ge or Ge(Li) Detector Efficiency	Semi-Annual	Jan., July
3.14.3.1	General Preparations for Use of the Medical Therapy Facility Beam for Human Therapy	Therapy only*	

#	Title	Frequency	Months
3.14.3.2	Use of Prompt-Gamma Facility for Boron Assay	Therapy only*	
3.14.3.3	Conduct of Human Therapy Using the Medical Therapy Facility Beam	Therapy only*	
3.14.3.4	Beam Monitor System Setpoints	Therapy only*	
3.14.5.1	Non-Licensed Medical Personnel Qualification Program for Use of the MITR Medical Therapy Facility	As Required	N/A
3.14.5.2	Test of Emergency Evacuation of a Patient from the Medical Therapy Facility Room	Therapy only*	

* A walk-through of these procedures shall be conducted prior to a patient therapy if there has been no patient therapy for the past twelve months.

** Also required following any design modification.

*** Performance of PM 3.14.2.2A or PM 3.14.2.2B or PM 3.14.2.2C satisfies the requirement. In addition, either PM 3.14.2.2B or PM 3.14.2.2C is to be done quarterly.

APPENDIX E MINUTES OF PATIENT TRIAL RUNS

For the first patient irradiation to run smoothly, practice runs were carried out. These usually involved personnel from the NRL Headquarters, Reactor Operations, Radiological Protection Office, clinicians and medical physicists from T-NEMC, and students working on the project. Minutes of the first five practice runs are provided here. Minutes for the later runs are on file in the Operations office.

NUCLEAR REACTOR LABORATORY
AN INTERDEPARTMENTAL CENTER OF
MASSACHUSETTS INSTITUTE OF TECHNOLOGY

O K HARLING
Director

138 Albany Street Cambridge Mass 02139-4296
Telefax No (617) 253-7300
Telex No 92-1473-MIT-CAM
Tel No (617)

J A BERNARD JR
Director of Reactor Operations

To: BNCT Group

From: Ronald Rogus

Re: Trial run of patient positioning and needed improvements

Date: November 10, 1992

Today, several of us participated in a trial run of the patient positioning system. This system now consists of the hydraulic lift, recently constructed platform, and surgical couch. The surgical couch is equipped with new cushions, and has straps that are used to secure the patient. A procedure to raise, position, and lower the patient has been written.

The "patient" was positioned on the couch and raised to the level of the delimiter. The treatment area was the mid-thigh, which was positioned with a plumb bob. Afterwards, the patient was lowered to the floor.

This trial run went well, no major glitches. About 30 minutes will be needed to raise and position an actual patient. Several minutes will be needed to lower the patient, although this could be reduced to about 1 minute in an emergency.

Following are comments and suggested improvements.

1. The treatment area must be firmly secured to the bed of the couch. The straps used in this trial run were ineffective; the α-cradle method will be used instead. The cradle will be secured to the bed of the couch.

2. Care must be used during the last 3 cm of lifting the patient. In this run, several strokes of the foot pedal forced the patient's kneecap against the bottom plate of the delimiter with a compressive load of about 50 pounds. To remove the load, the patient must be compressed further as the foot pedal must be pushed to the floor and held there to relieve the hydraulic pressure. Pushing down on the foot pedal resulted in a momentary load on the kneecap of about 150 pounds. Padding the bottom of the delimiter might be useful.

3. Better straps to secure the patient will be used. The new straps will be wider with a quick release buckle (like a seat belt). An alternative, or perhaps complement, to the straps would be a side rail that could be raised to secure and support the patient.

4. The pumping station will be soundproofed. The panels rattle when the foot pump is used. The rotary handle is quieter and can lift the patient at a reasonable speed.

5. The delimiter and whole body shields will be secured to the lead or concrete shielding.

6. A method to lower the patient rapidly, in 30 seconds, will be developed.

7. An intercom will be installed.

8. A method will be developed so the patient can be repositioned in the same place for each fraction.

9. The EKG and blood gasses will be monitored during the irradiation. There is adequate room for this cabling to run through the duct in the shielding of the medical room. The instrumentation will be outside the room.

10. There is room for additional whole body shielding. The thickness and composition of this shielding will depend on the size of the patient and the area being irradiated. A layered approach seems best.

11. The boral on the floor, as well as areas around the beam monitor detectors, might have to be adequately grounded.

12. Many of the live wires will be housed in electrical conduit.

13. A small TV will be mounted on the ceiling for the patient's use. A VCR or cable will be needed.

14. Sharp edges on the platform and other items will be removed.

15. The cracks between the boral plates will be filled.

16. A new ceiling will be installed. The lead shielding will be painted.

17. The room lighting is OK as is.

18. Pictures will be added to the medical room.

19. Cleaning of the bedding, Li-6 blankets, and other items that the patient will be in contact with will be done in accordance with T-NEMC procedures. Additional bedding and a "pillow case" for the Li-6 blanket will be obtained.

20. The couch, platform, and hydraulic lift will be tested for activation.

21. Clothing that will be worn by the patient will be tested for activation. Bedding also.

NUCLEAR REACTOR LABORATORY
AN INTERDEPARTMENTAL CENTER OF
MASSACHUSETTS INSTITUTE OF TECHNOLOGY

D. K. HARLING
Director

138 Albany Street, Cambridge, Mass. 02139-4296
Telefax No. 617-253-7300
Telex No. 92-1473-MIT-CAM
Tel. No. (617)

J. A. BERNARD, JR.
Director of Radiation Safety

To: BNCT Group

From: Ronald Rogus

Re: Working meeting on current status of the medical room and list of things to be done

Attendees: R. Zamenhof, G. Solares, P. Menadier, S. Yam, R. Rogus

Date: December 21, 1992

Today, several of us met for 3 hours in the medical room to review the recent modifications and renovations of the medical room and to plan future work. A new video camera has been installed; it has been tested with the beam on and works well. A convex circular mirror has also been installed and works well. A new, longer alpha cradle has been built and tested. An activation analysis was done last week; there are no activation problems. Also, the exposure rates were measured in the medical room, near the door, during and after an irradiation. This experiment has provided health physics data important to those entering the room just after an irradiation.

Following are comments and suggested improvements.

1. The treatment area could be more accurately positioned if the digital level was held directly on the alpha cradle instead of being mounted on the base of the surgical couch. The patient will be CT'ed with the cradle and the cradle will be made in an appropriate geometry.

2. A small monitor will be purchased and mounted in the medical room so the camera can be quickly aimed at the patient. Otherwise, you have to talk with a person outside the room who is looking at the outside monitor.

3. Regarding a Tech Spec item, the results of last weeks exposure rate experiment indicate that we have to set the "background" level as that which is expected after an irradiation. Then, a multiple of this background level can be used as the set point to trigger an audible and light alarm when the door is opened.

4. An audible and bright light alarm indicators should be mounted near the motor driven door. See item 3.

5. A sign will be posted near the relief valve of the surgical couch. It will indicate what the valve is and which direction will release the pressure.

6. New steps will be made that are longer than the current ones.

7. Foam padding will be added to the bottom of the half-moon to prevent people or patients from hitting their heads.

8. The safety cord on the motor driven door will be repaired.

9. A circle will be drawn on the bottom of the delimiter to indicate the size and position of the aperture.

10. Secure CO2 and TE tanks. Clamp to wall.

11. PM will need about 2 weeks to work on the panel. He plans to do much of the work the last week in January.

12. The UV lights should be removed.

13. A line could be put on the floor to indicate a area of higher radiation doses outside the medical room while the beam is on.

14. The EKG will be tested with an EKG tester while the beam is on.

15. A hole will be cut in the side of the cradle to allow a person to see better while positioning the patient.

16. A sign will be put inside the medical room describing where the buttons are to open the motorized door.

17. A sticker will be put inside the medical room designating that the room is an FDA investigational device.

NUCLEAR REACTOR LABORATORY
AN INTERDEPARTMENTAL CENTER OF
MASSACHUSETTS INSTITUTE OF TECHNOLOGY

O K HARLING
Director

138 Albany Street, Cambridge, Mass. 02139-4296
Telefax No. 617) 253-7300
Telex No. 92-1473-MIT-CAM
Tel. No. (617) 253-5720

J. A. BERNARD, JR.
Director of Reactor Operations

To: BNCT Group and BNCT QA File
From: Ronald Rogus
Re: Walkthrough of patient irradiation
Date: March 2, 1993
Attendees: Otto Harling, Jacquelyn Yanch, John Bernard, Guido Solares, Ronald Rogus, Eddy Lau, Sam Yam, Gopika Yasuda, Paul Menadier, Fred McWilliams, Marcia Austin, Todd Date, John DiCiaccio

On March 1, 1993 several members of the NRL BNCT Group, along with people from Reactor Operations and RRPO, participated in a trial run of a patient irradiation. The recently written procedure (PM 3.14.3.3) on the conduct of human therapy using the medical therapy beam was followed. Comments and changes to the procedure were made along the way. The mock patient, Sam Yam, was positioned in the beam. An emergency evacuation of the patient (PM 3.14.3.4) was practiced.

A revised conduct procedure reflecting the changes and comments will be written. A list was made of 25 items that need to be addressed. Four more trial runs have been scheduled to be held during the next two weeks.

NUCLEAR REACTOR LABORATORY
AN INTERDEPARTMENTAL CENTER OF
MASSACHUSETTS INSTITUTE OF TECHNOLOGY

O. K. HARLING
Director

138 Albany Street, Cambridge, Mass. 02139-4296
Telefax No. 617 253-7300
Telex No. 92-1473-MIT CAM
Tel. No. 617

J. A. BERNARD, JR.
Director of Reactor Operations

To: BNCT Group and BNCT QA File
From: Ronald Rogus RR
Re: Fourth walkthrough of patient irradiation
Date: March 7, 1993
Attendees: Otto Harling, John Bernard, Guido Solares, Ronald Rogus, Eddy Lau, Sam Yam, Paul Menadier, Fred McWilliams, Mark Feldmeier

On March 5, 1993 several members of the NRL BNCT Group, along with people from Reactor Operations and RRPO, participated in the fourth trial run of a patient irradiation. The list of 30 tasks that came out of the previous walkthrough had been completed. Procedure PM 3.14.3.3 on the conduct of human therapy using the medical therapy beam was followed. Comments and changes to the procedure were made along the way. A mock patient was positioned in the beam.

A revised conduct procedure reflecting the changes and comments will be written. Several tasks need to be addressed. Three more trial runs have been scheduled to be held during the next two weeks.

NUCLEAR REACTOR LABORATORY
AN INTERDEPARTMENTAL CENTER OF
MASSACHUSETTS INSTITUTE OF TECHNOLOGY

O. K. HARLING
Director

138 Albany Street Cambridge Mass 02139-4296
Telefax No 617 253-7300
Telex No 92-1473-MIT CAM
Tel No 617

J. A. BERNARD JR
Director of Reactor Operations

To: BNCT Group and BNCT QA File
From: Ronald Rogus
Re: Fifth walkthrough of patient irradiation
Date: March 10, 1993
Attendees: Otto Harling, Robert Zamenhof, John Bernard, Tom DiPetrillo, Guido Solares, Ronald Rogus, Eddy Lau, Sam Yam, Paul Menadier, Fred McWilliams, Mark Feldmeier

On March 8, 1993 several members of the NRL/T-NEMC BNCT Group, along with people from Reactor Operations and RRPO, participated in the fifth trial run of a patient irradiation. Procedure PM 3.14.3.3 on the conduct of human therapy using the medical therapy beam was followed. People were assigned roles, such as nurse, clinician and so on, and performed what would be their responsibilities during an actual patient irradiation. Comments and changes to the procedure were made along the way. A mock patient was positioned in the beam.

With experience from the previous trial runs and walkthroughs, and improvements to the medical room, this walkthrough went more smoothly, and more quickly, than previous walkthroughs.

A revised conduct procedure reflecting the changes and comments will be written. Several tasks need to be addressed. Two more trial runs have been scheduled to be held next week.

APPENDIX F CARLOS FLORES' REPORT ON SHIELD INSERT FOR THE LEAD SHUTTER

22.901

A Special Problem Report
for 6 credit units

MITR-II Medical Beam Shutter Modification and Engineering Design

Submitted by:

Carlos D. Flores
MIT
27 August, 1993

Table Of Contents

1.0 Introduction:

1.1. Background:

At the M.I.T. Nuclear Reactor Laboratory, a program is underway to investigate a medical procedure known as Boron Neutron-Capture Therapy (BNCT). This program requires the use of a neutron beam provided by the MIT Nuclear Reactor. A beam collimator and filter is located just below the reactor which produces an effective epithermal neutron beam for the medical room below. Currently, this beam is attenuated by light and heavy water shielding. There is also a lead shutter in the ceiling of the medical room which has the function of effectively 'shutting off' the neutron beam. As the situation exists, however, the fast neutron dose rate as the beam enters the medical room, even with the shutter closed, is still rather high. In the beam line and just below the lead shutter the fast neutron dose rates have been measured at 3-7 rem/h depending on beam configuration (with the reactor at full power)[1]. Photons and thermal neutrons also add to the dose rates below the shutter but to a much lesser degree. If the power level of the reactor were not dropped during patient preparation, BNCT personnel would be exposed to these dose rates for extended periods of time while preparing a patient for irradiation. It is the objective of this special project report to propose an engineering solution to this problem which would result in a lower dose rate during patient setup while the reactor is at full power.

The current shutter, which is to be modified, consists of 23.174 cm of lead which is contained in a steel support structure. This steel structure provides an added 4.5 cm of shielding at the bottom of the shutter. There also exists a borated-poly delimiter (2 inches thick) just below the lead shutter with a 20 cm diameter hole. Experimental measurements performed by Ronald Rogus (See Appendix I) show that the shutter allows an approximate fast neutron dose rate of 2600 mrem/h and a photon dose rate of 61 mrem/h with beam configuration M62, all shutters closed, and the power of the reactor at 5 MW.[2] The delimiter attenuates the fast neutron beam to 1000 mrem/h at the center of the above collimator.

From the experimental data presented in Rogus's measurements it is evident that neutron scattering plays a significant role in the shielding problem, and that the beam is no longer (if it ever was) a mono-directional, well defined source. This is seen in two ways: 1) the maximum point for thermal neutron dose rate is 50 cm away from where the center of the beam is expected to be, and 2) there is attenuation by a factor of 2 at the center of the delimiter hole where a mono-directional beam should not be attenuated. For this reason, it is recommended that MCNP calculations be done in addition to the following study to benchmark the results.

---

[1] "Memo on Pb shutter design - photon and fast neutron attenuation", From Ronald Rogus to Professors Harling and Yanch, 4 May, 1992.

[2] "Memo on Health Physics Measurements with a borated-poly delimiter", From Ronald Rogus to Professors Harling and Yanch, 20 July, 1992. (Fast neutron measurements were made using a Rem-Ball just below the shutter with and without the presence of the delimiter. There was no specific quality factor used in determining these dose rates because the detector was calibrated from a known source.)

1.2 Shutter Modification History:

Re-design of the current lead shutter initially took the path of modifying the shielding material within the shutter structure.[3] From the data presented in Appendix I, it is clear that the major concern for modifying the shielding material is the attenuation of the fast-neutron dose rate. For this reason, a material with a high hydrogen density, such as polyethylene, was chosen for initial modification calculations. The initial design concept was that of a layer of polyethylene over a bottom layer of lead. This design was again modified by changing the lead to depleted uranium. Simple hand calculations were done by Ronald Rogus assuming an exponential attenuation of neutrons as the polyethylene layer increased and an exponential attenuation of the photons as the metal (lead or depleted uranium) layer increased. Build-up factors were accounted for in the lead and depleted uranium, but the major assumption made was that no photon attenuation occurred in the polyethylene and no neutron attenuation occurred in the metal.

For these initial calculations, the attenuation coefficients for both fast neutrons and photons were experimentally determined. For neutrons this was done by adding a 1" slab of polyethylene above the lead shutter and measuring the reduction in fast neutron dose rate with a Bonner sphere.[4] Scattering of the neutrons was not directly accounted for in the calculations, but, due to the experimental determination of this number, it is partially taken into account.

The attenuation coefficient for photon dose was determined experimentally for lead using an exponential model and a build-up factor. The linear attenuation coefficient was found to be equal to that of a 3-4 MeV mono-energetic photon beam, and the attenuation coefficient for uranium was determined by taking the experimentally determined value for lead and multiplying by the density ratio of uranium to lead.[5]

2.0. Initial Dose Rate Calculations:

2.1 Dose Rate Attenuation Equations:

The forms of the equations used in Rogus's hand calculations for dose rates below the modified shutter are as follows:

Fast Neutron Dose Rate

$$\text{Dose Rate} = (nC)(e^{-\Sigma T_{poly}})$$

Where: nC is the initial fast neutron dose rate above the shutter,
Tpoly is the thickness of the polyethylene, and
Σ is the macroscopic cross-section used for the attenuation of fast neutrons.

(The values used for the cross-sections of various elements are tabulated in the MathCAD calculations

---

3 "Memo on Pb shutter design", R. Rogus.
4 "Memo on Pb shutter design", R. Rogus.
5 "Memo on Pb shutter design", R. Rogus.

in Appendix II. Rogus's experimentally determined value for polyethylene was 0.15535/cm.)

There was no specific quality factor used for the experimentally determined fast neutron dose rates. The detector was calibrated with the use of a known source.

Photon Dose Rate

$$\text{Dose Rate} = (\gamma C)(B_M)(e^{-\mu T})$$

Where: γC is the initial photon dose rate above the shutter,
T is the thickness of the metal,
μ is the linear attenuation coefficient of the metal and,
B_M is the build-up factor of the respective metal.

(The values used for attenuation coefficients of the various shielding materials can be seen in runs 1, 2, and 4 of Appendix II. B_M was extracted from the Radiological Health Handbook for Rogus's calculations and for subsequent MathCAD calculations was approximated using the Taylor formula.)

The configuration of the shielding for Ron Rogus's initial calculations is as follows:

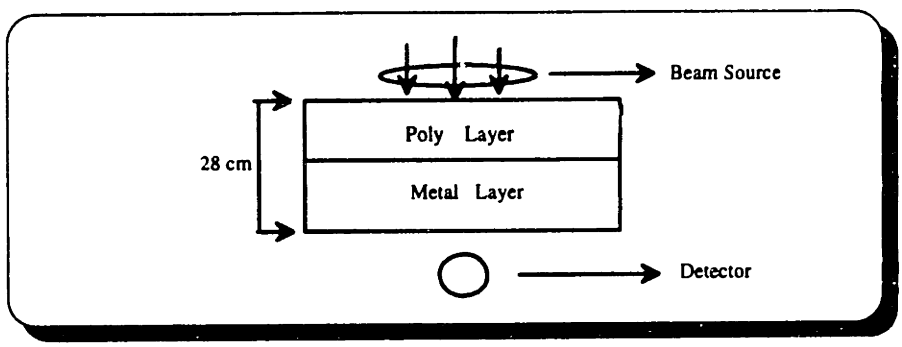

Figure 2.1: Conceptual drawing of Rogus' attenuation calculations.

The resulting graphs of dose rate for the first two modifications are as follows:

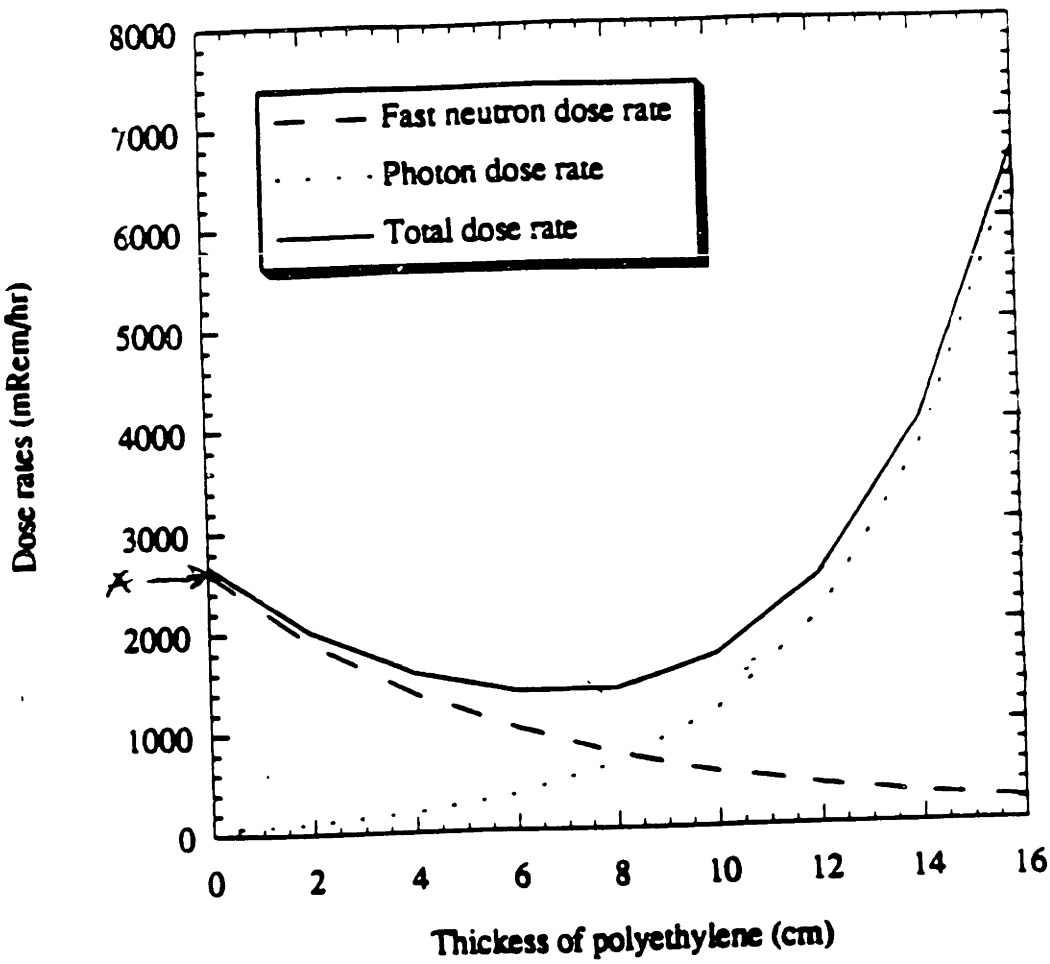

Calculated dose rates using a layer of Poly and a layer of Lead
(Note that these calculations were extrapolated from the present condition of all Lead and no Poly. This corresponds to the R.R's measured photon dose rate of 61mrem/h and fast neutron dose rate of 2606 mrem/h as presented in his memo (i.e. the dose rates of the un-modified shutter correspond to where the thickness of polyethylene is zero.)

5

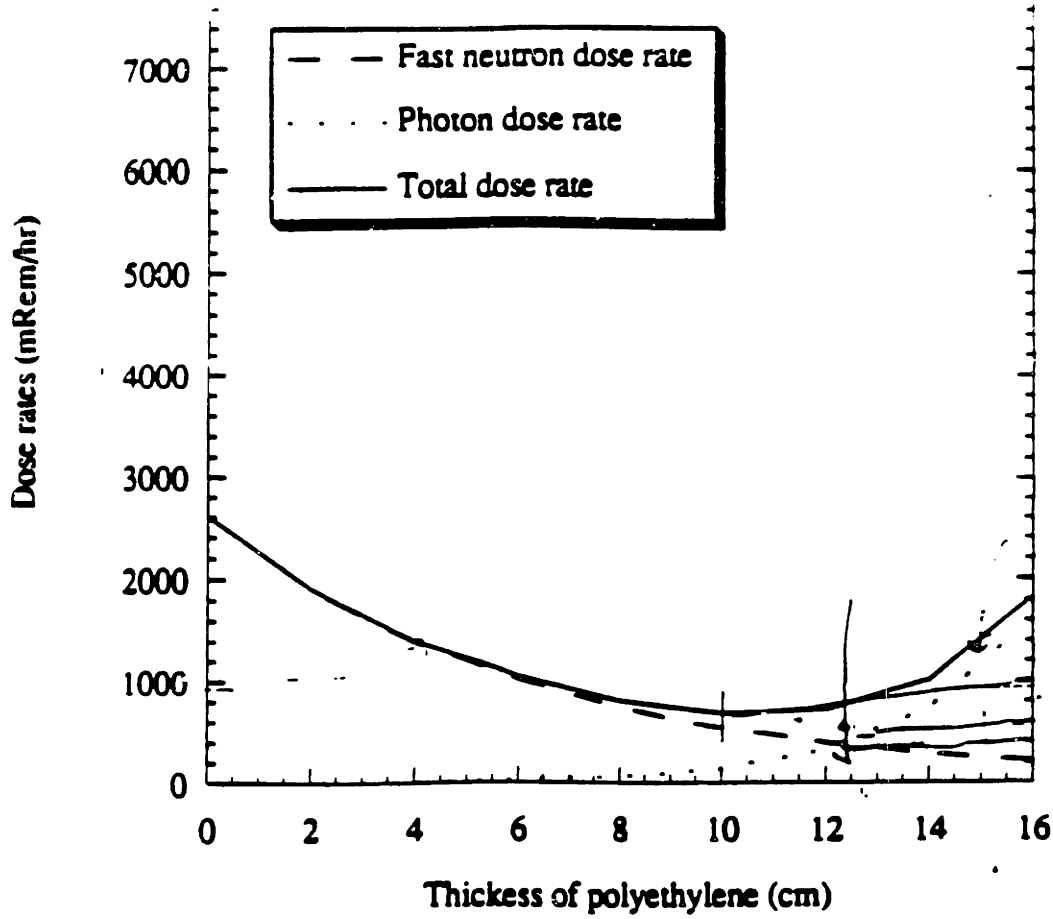

Calculated dose rates using a layer of Poly and a layer of Uranium
(Note that the only difference between this figure and the previous is the photon attenuation which differs due to the increase in the photon attenuation factor. This difference was made by multiplying the attenuation factor of lead by the ratio of the densities of uranium to lead.)

Further notes of importance pertaining to the above graphs are as follows:

1) The total thickness of the shielding layers was assumed to be 28 cm. The TOTAL thickness is fixed, but the thickness of the polyethylene and the metal vary. (Note that the actual shield thickness is not 28 cm, but for a rough calculation it provides approximate results. For exact thickness see the engineering design of the shutter in Appendix III. The thickness of the modified section is 23.175 cm and the thickness of the bottom steel plate is 4.5 cm.)
2) It should also be noted that the dose rates for a lead shutter with no polyethylene were measured with all shutters closed and the M62 beam. The result was a dose rate of 61 mrem/h photon and 2606 mrem/h fast neutron which was used in the above graphs. All other calculations and experimental measurements, however, show this photon dose rate to be 230 mrem/h. For this reason, and to give conservative estimates of the shielding required, a photon dose rate of 230 mrem/h will be used subsequently.

The results of Rogus's calculations justified further research into the modification of the shutter. Some suggestions made were the use of tungsten, borated-poly, or a combination of tungsten/boron/poly as a suitable shielding material to replace the existing lead.

2.2 Monte-Carlo Calculations:

In the previous calculations, prompt gamma production was not accounted for which might make a difference in the final results and engineering design. This and the difficulty of calculating reasonable neutron dose rates analytically, led to the use of the MCNP (Monte-Carlo) code to estimate the results of shielding modifications.

A Monte-Carlo simulation was run by Professor J. Yanch comparing the use of lead with uranium and tungsten in a metal/poly layered configuration. This simulation also accounted for the induced photon dose. In this run the shield thickness was fixed at 27.4cm, but the configuration was similar to the one used for Rogus's initial calculations. The results are as follows:

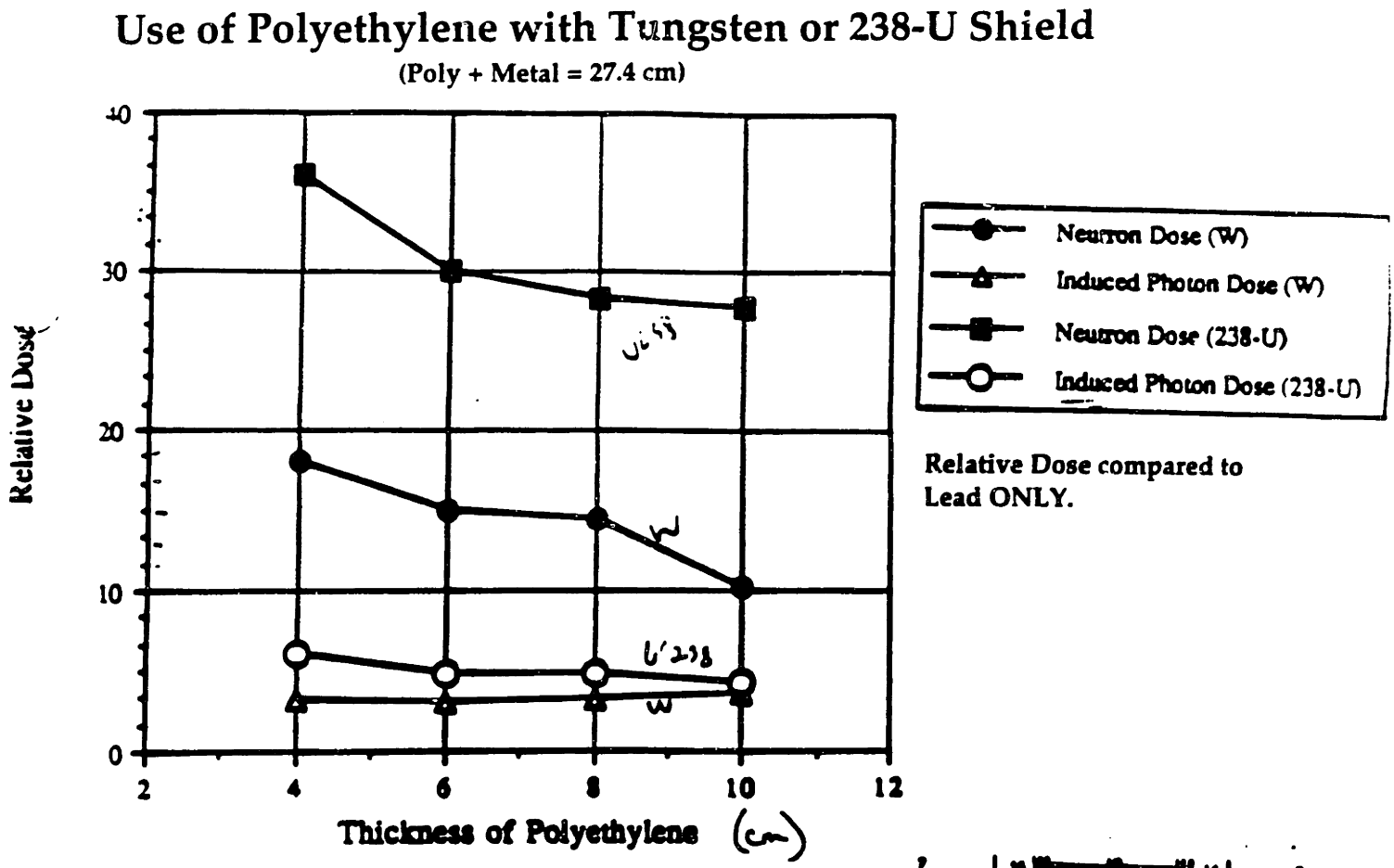

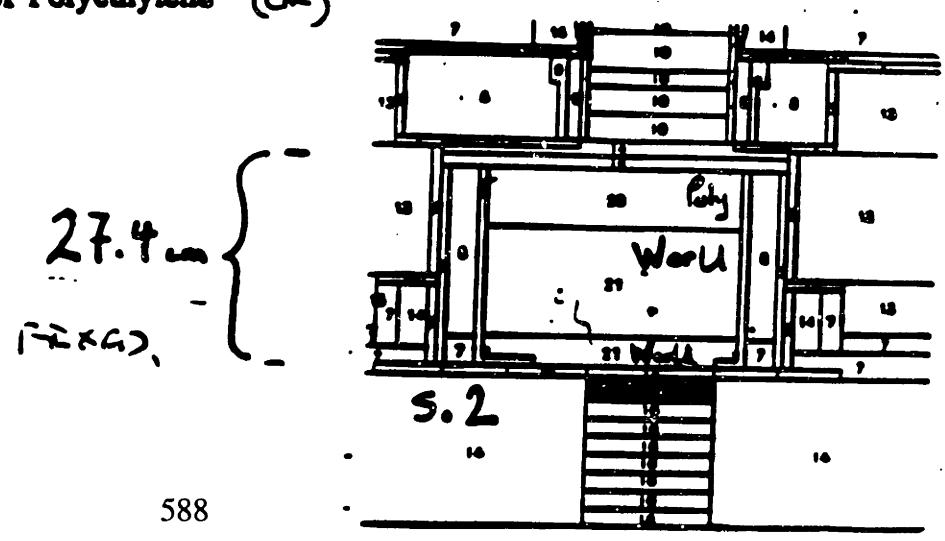

Based on the above information, tungsten is the best choice of the metal shield materials. It attenuates neutrons better, has a lower induced photon dose, and there is no fission problem associated with its use as a neutron shield.

3.0 Further Analysis:

3.1. Dose rate analysis at the top of the shutter:

With the use of MathCAD, other simple calculations were done to determine the optimal shielding configuration. The first calculation was to determine the macroscopic attenuation cross-section of polyethylene for fast neutrons. Rogus determined this cross-section experimentally, and knowing that he used an exponential attenuation equation form, the value was readily obtained by fitting an appropriate curve to his data. Linear attenuation coefficients for 4 MeV photons in tungsten and uranium were obtained from the literature available. With this information, and knowing the dose rates at the bottom of the solid lead shutter (2600 mrem/h for fast neutrons and 230 mrem/h for the photon dose rate as seen in Appendix I), the dose rates at the top of the shutter were easily calculated using the exponential equations. (See Appendix II, Run 1.) (It should be noted that secondary activation of the shielding material and self-shielding effects are not accounted for in the following calculations.)

The macroscopic cross-section for fast neutrons on polyethylene that was used in these calculations was determined by averaging Rogus's experimentally determined value (0.15535/cm) with the value calculated from the barn book[6] for the 1 MeV microscopic cross-section of hydrogen. This was done because both numbers are considered to be good and were weighted equally. Using the density of hydrogen in polyethylene as 7.8×10^{22}atoms/cc[7], the 1 MeV microscopic cross-section value was calculated as 0.3276/cm and the resulting average is 0.24/cm.

3.2. Comparison of uranium and tungsten:

The next calculation compared the poly-uranium layered shield to the poly-tungsten layered shield. (See Appendix II, Run 2.) The fast neutron dose rates for the poly-uranium layered shielding were recalculated as Rogus had done, and because the relative fast neutron dose rates were calculated in the Monte-Carlo simulation, these numbers were used to obtain a number for fast neutron dose rates coming through a poly-tungsten layered shield.

After initial estimates of the amount of solid tungsten required for the above configuration at optimal shielding levels, it was ruled out due to its high cost and unavailability of such quantities. The cost of the tungsten alone would be exorbitant, and powdered tungsten could have at most 60% of the density of solid tungsten. The effect of using powdered tungsten in the poly-tungsten layered shield configuration is seen in Appendix II, Run 3. Because of the loss in

---

[6] Neutron Cross Sections, Hughes-Harvey.

[7] This number was obtained from data sheets provided by Reactor Experiments Inc. concerning their polyethylene product.

shielding capability of this form, the concept of a homogenous shield was postulated. This shield design would be a mixture of polyethylene, tungsten, and boron. (The boron is to stop the production of induced photons by absorbing thermal neutrons.) Also, for the purpose of these calculations, paraffin and polyethylene are interchangeable. They both have similar hydrogen densities and attenuation coefficients for both photons and fast neutrons[8], and for the remainder of the calculations these substances will be used interchangeably.

3.3. Tungsten activation:

Activation of the tungsten in the shield was also evaluated by simple activation calculations of the tungsten using a microscopic cross-section for W-186 of 38.38 barns. To get more help with this problem Reactor Experiments, Inc., which produces a product known as Tungsten-Poly, was contacted. Their product is polyethylene with a 59% by volume additive of tungsten. The problem of activation was discussed with a technician at the factory, and it was determined that this problem is greatly diminished by the self shielding of the tungsten. Also, it was determined that for the shutter design, any addition of boron to the mixture would make the problem negligible. For further investigation, a series of MathCAD calculations were performed. One of these was the idea of using a layer of paraffin-boron mixture on top of a tungsten layer as the shield structure. Again, this had the problem that powdered tungsten did not have the attenuation factor necessary to stop the photons when it was in a layer by itself. The next idea tried was to use a poly/boron layer on top and a poly/tungsten layer below. Again, the photon dose alone went well above 2 Rem/h.

An addition to the MathCAD calculations was the calculation of the macroscopic absorption cross-section for boron and the macroscopic activation cross-section for tungsten. For a safe margin, the boron macroscopic cross-section was calculated to be 10 times greater than the tungsten cross section in order to adequately account for the secondary photons that might be produced. It should be noted that run 4 used the natural abundance of ^{10}B in boron (19.9%). Also, the cross section used for tungsten was the activation cross section for W-186 (38.38 barns). This cross-section was chosen for two reasons: 1) the technician at Reactor Experiments, Inc. stated that if any secondary activation problem occurred in their tungsten-poly product it was due to W-187, and 2) according to the radionuclide chart, the other activation products have gamma energies which are quite low and would be stopped by self-shielding.

Further hand calculations on this point were done after the optimal shield mixture was determined (see the following section on optimal shield mixture) to confirm that activation of tungsten would not be a problem. It was seen that with boron in the mixture, the thermal neutrons created from fast neutron scattering would be absorbed immediately by the boron. Therefore, no thermal neutron or secondary activation problem is expected at the bottom of the shutter.

---

[8] Data obtained from the Reactor Handbook, 2nd Ed., Volume I, Materials.

3.4. Optimal shield mixture:

The next series of MathCAD calculations were to determine the effectiveness of a shielding mixture. In this series of calculations, the mixture was first set to 60%W/40%poly **by volume** and a sheet of solid tungsten was added below this. This was done to see if there was an optimum shielding level for a mixture and metal layered shield. Bismuth was also substituted for the tungsten metal layer, but after several runs, it was seen that the optimum level was with all mixture, and no metal layer below.

A solve block was then added to the MathCAD program. This was done in order to vary the percent weights of tungsten, polyethylene, and boron in the mixture in order to reach an optimum level in total dose rate (i.e. to reach a minimum dose rate due to fast neutrons plus photons.) The results are seen in Appendix II, run 4, and they show that a 55.4%W-3.3%B-41.3%Poly **by volume** mixture would be optimum.

Several other variations of the above calculations were done, all confirming the best choice to be a homogenous shield layer of paraffin, tungsten, and boron. It is recommended, however, that MCNP calculations be done that vary the percentage composition of the shielding material, and that these calculations be used to determine the final composition of the homogenous shield structure.

3.5. Other calculations:

Yet another MathCAD calculation made was to determine the dose rates with 0.5 cm of boron carbide at the bottom to allow for a thermal capture layer. (See Appendix II, Run 5.) The thermal neutron dose rate, however, should not be too great a problem due to the boron in the mixture which will capture most thermal neutrons in the upper layers of the shield. The results of run 5, however, should be similar to those if a 0.5 cm layer of lead was added in place of the boron-carbide. The reason for this option is to attenuate induced photons from tungsten activation.

One last effort for a more economical modification was evaluated using MathCAD. This was to replace a portion of the lead at the top of the shutter with paraffin or borated polyethylene. The graphs at the end of Appendix II (run 6) show the results, but as can be seen, the attenuation of dose rates is not significant.

One last note is that the use of paraffin in the engineering design might be limited by the heat in the area of the shutter. Two incidents due to high heat that occurred previously were the explosion of a sulfur can in the beam path, and the melting of paraffin at a position above the shutter. A simple hand calculation of the heating problem quickly dismisses it, however. The total dose rate at the top of the shutter was calculated as being approximately 4000 Rad/h. Assuming that this was deposited in the first 5 cm of the 50 cm radius area of modification the calculations would be as follows:

$$3.14(50\ cm)^2(5\ cm) = 39250\ cm^3$$
$$39250\ cm^3\ (12g/cm^3)\ (4000\ Rad/h)\ (100\ erg/g) = 188.4 \times 10^9\ ergs/h$$
$$188.4 \times 10^9\ ergs/h\ (1h/3600s)\ (1J/10^7 ergs) = 5.2\ W$$

5.2 Watts distributed over this volume would not be enough to melt the mixture.

4.0 Engineering Design:

The engineering design of the existing shutter with the modified area can be seen in Appendix III. The hatched area on the design drawings is the section of the shutter to be modified. This volume was chosen by looking at the dose rate information given in Appendix I. From this information it was decided that the effective attenuation should occur for 50 cm on either side of the center of the beam. The best design to achieve this goal would be a cylinder with a 50 cm radius and a height of 23.175 cm; the thickness of the current lead shielding. This cylinder will not fit within the steel support structure, however, and thus engineering practicality calls for further modification. (See Figures 1.1-1.4 in Appendix III) From an engineering standpoint it seems practical to reduce the area of modification (looking from the top-view) to only the area to the right of the left-side steel structure-support plate and to the left of the beam port. (See Figures 2.1-2.4) Not only will this cut down on the cost of materials, but it will make any modification to the existing shutter much easier; one will notice the 'arc' on the left side of the initial modification concept has been deleted. This reduced-volume modification is the basis for the following calculations.

The total volume of the modified area is 4,272 cubic inches. With the above calculated optimal shield mix (the mix calculated in run 4) which has an effective density of 11.145 g/cc this would require the use of 748.3 kg tungsten, 26.6 kg paraffin, and 5.5 kg of boron. With an average price of $10 to $15 dollars per pound for powdered tungsten, one would expect to have to pay $20,000 for the tungsten alone. High purity tungsten is required in order to avoid the problems resulting from impurity activation; one of the common impurities being tantalum which has a very high activation cross section. Also, 1g of enriched boron was listed at $109 per gram in the Aesar catalog At these prices (even with a 50% discount on bulk purchases of enriched boron), the new shield material would cost at least one million dollars. With natural abundance boron, the cost of the shield material (boron + paraffin + tungsten) would be approximately $25,000. This assumes a cost for boron of $400 per kg which is a 20% discount on what is listed in the Aesar catalog.

In another effort to reduce cost, Cambridge Street Metal Company was also called for their prices on tungsten and boron. Rogus had previously purchased bismuth needles from this company for a very low price. They, however, sell neither boron nor tungsten.

4.1 Modification Versus New Shutter:

After discussion with experienced machinists at the MIT Nuclear Reactor Laboratory, the consensus was that the best way to modify the existing shutter would be to remove the section of lead mechanically. Three options that arose were:

1) A network of holes could be drilled in the form of the modified area. Melting is not a viable option because radioactive antimony would be released into the atmosphere, but machining is possible in the hot-shop because conservative estimates of the activity of the lead shutter are on the order of 10 mrem/h on the surface. Once the network of holes is drilled the lead sections can be lifted out. It should be noted that the lead could be removed in several sections. This only depends on how the network of holes is drilled.
2) The second option is to bore out the area that needs to be modified. This would cause many more chips, but a ventilation system would be required for either procedure.
3) The third option is to build an entirely new shutter. The shutter is a simple design and the actual welding according to Ramsay Welding and Fabricatuion could be done in a day. Also, the current guides that the shutter rides on could be taken off the old shutter and put on the new one thus reducing machining costs. This option still has one drawback, and that is disposal of the old shutter. This question is possibly answered by what might have been a fourth option on how to get the lead out of the shutter. This option was to send the shutter to Oak Ridge to have them melt out the lead and make lead bricks of it. After discussing this option with the MIT RPO, it was ruled out as a way to remove the lead for modification. No specific function such as melting out the lead and returning the empty shutter could be performed by Oak Ridge, but the entire shutter could be sent to be treated as waste.

The machining for removing the lead in the area that needs to be modified would take at least two to three days at $500 per day for machining alone. This estimate assumes that the above mechanical methods will work on the first try, and does not include the fact that the shutter weighs 3.5 tons and would be very cumbersome to work with. This is made even more cumbersome by the fact that it is slightly activated.

After weighing the various financial options, it seems that the least expensive option would be to modify the existing shutter. A rough estimate of the cost of a new shutter (including materials and labor) given by Ramsay Welding and Fabrication was $2500. There is also the cost of refilling the new shutter with lead. At $0.50 per pound of lead, and 3500 lbs of lead required to fill the new shutter (this means filling everything to the right of the beam port and everything to the left of the left-side steel structure support-plate), the total cost of new lead (including labor) would be approximately $1900. Mechanically removing the lead would incur only $2500 for machining if it took one man week to remove the lead. This option also reduces the problem of waste lead. It should be noted, however, that although this option appears to cost less financially, the consensus of the engineers and machinists working at the M.I.T. Nuclear Reactor Laboratory whose vast experience in such matters far outweighs my own was to build a completely new shutter. Their decisions were based mostly on the belief that the removal of the lead from the shutter would be much more difficult than initially expected.

4.2 Modification Techniques:

If modification of the lead shutter were to occur, it could take place in the hot-shop. Although the shutter is much too heavy to place on any workbench, it could be set upon a series of 6x6's laid on the floor of the shop. Removal of the lead could start by trying to pull out

sections of the lead as mentioned in the first option for modification. Blocks of lead that are connected to the steel shutter structure only at the bottom could be made by drilling networks of holes in a grid format. Eyebolts could be screwed into the individual sections of the lead and each section could be lifted out. If this proves not to work well, boring out of the lead could proceed by taking out 0.25 to 0.5 inches each time around starting from the center.

The shielding mixture composed of 95.9% tungsten, 3.4% paraffin, and 0.7% boron **by weight** will be poured in the following fashion. To keep the mixture as homogenous as possible, several individual pours into the shutter structure will be made. The area of the modified zone from the top view is 7687cm^2. With this in mind, 15,500cm^3 of the mixture (approximately 1/12 of the total modified volume) will be measured out and melted. This will be done by melting the hydrogenated paraffin and adding the appropriate percentages of boron powder and tungsten powder. After pouring this in one should obtain a layer approximately 2 cm thick. This process should be repeated approximately a dozen times to fill the entire modified area.

5.0 Conclusion and Summary:

In conclusion, modification of the shutter is possible, but it will be extremely expensive. For $25,000 for materials only, the shutter can be modified to reduce the total dose rates by approximately 2 Rem/h. If three people work for only 30 minutes near the beam in the med room, this would correspond to a 3 manRem reduction in dose.

It is recommended that a new shutter be made and filled with lead excluding the designated areas to be modified as seen in Figures 2.1-2.4. The partially lead-filled shutter can then be completed at the MIT Nuclear Reactor Laboratory by adding the modified shield material as described in section 4.2 of this report. The modified shield material would be as follows:

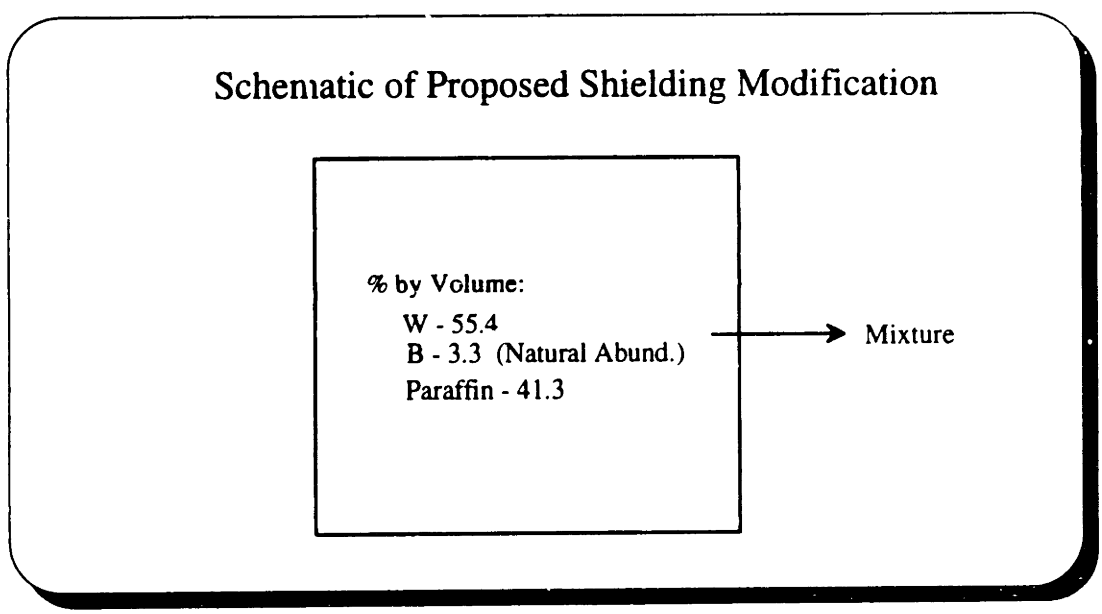

Figure 5.1: Schematic of proposed shield material and configuration.

Also, due to the self-shielding of tungsten, the calculated levels of boron in the mixture could be lowered. It is recommended that for any shielding choice, a prototype be made and installed in the filter system to benchmark the calculations. Also, because the new shielding material is so expensive, this prototype could be remelted and added to the final mixture if the new design is adopted.

APPENDIX I

Rogus' Dose Rate Data

1 A BORATED POLY DELIMITER

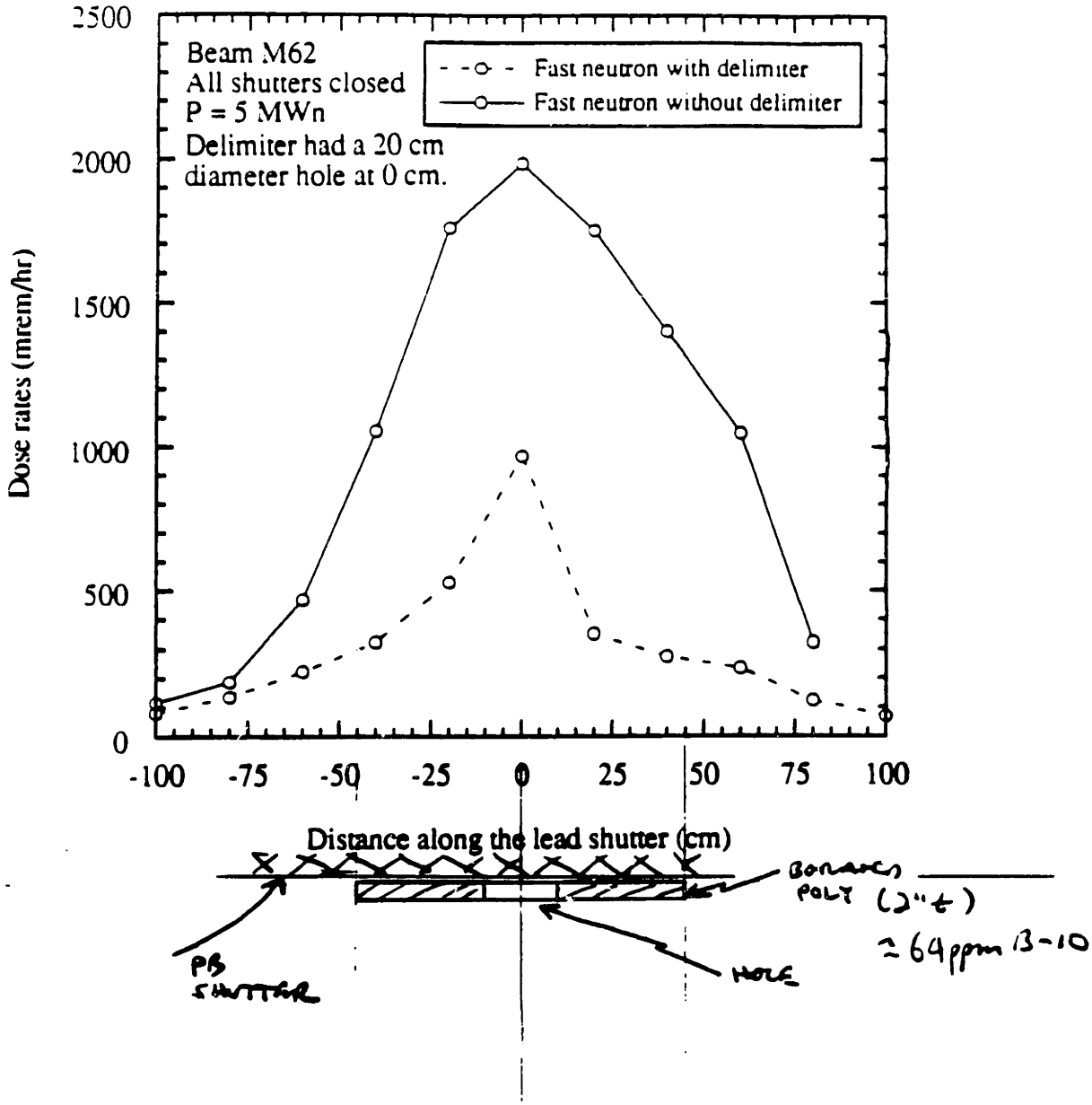

NOTE ON QUALITY FACTOR FOR NEUTRON DOSE RATE CAN BE SEEN IN FOOTNOTE #2

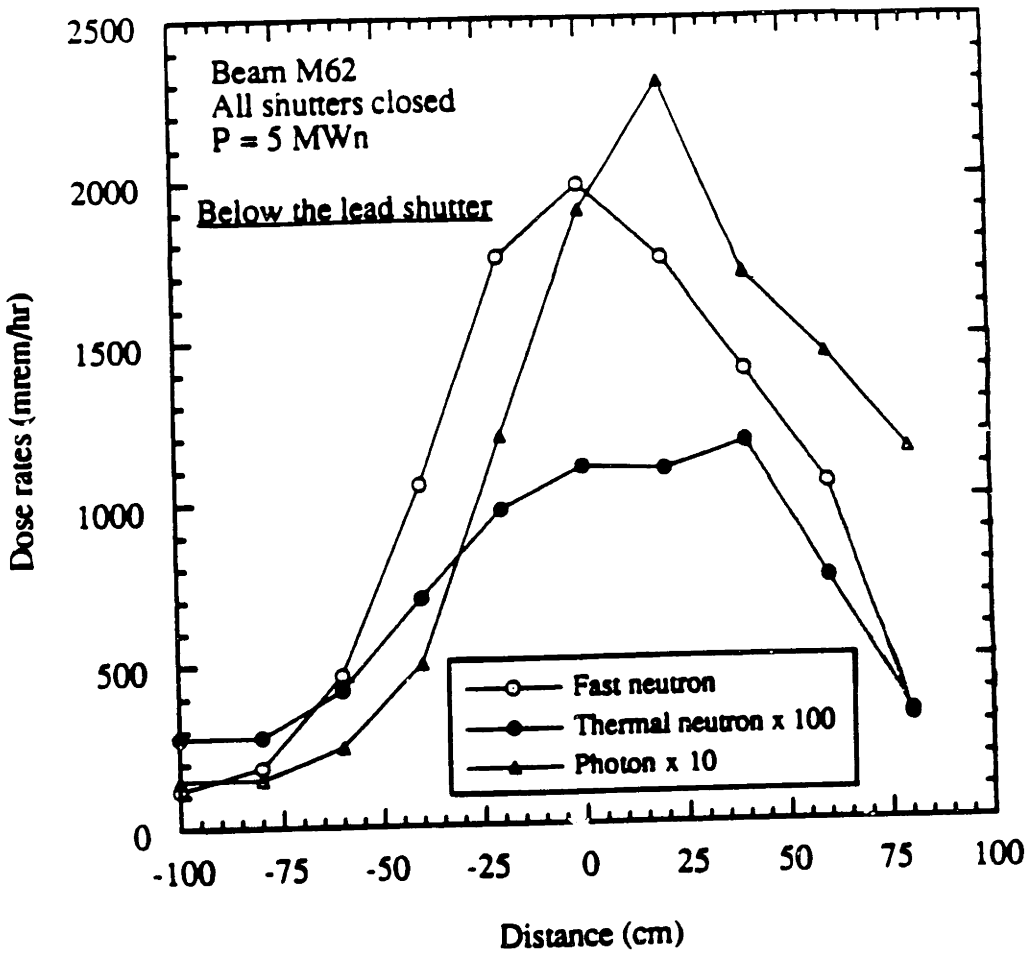
Beam M62
All shutters closed
P = 5 MWn
Below the lead shutter
Fast neutron
Thermal neutron x 100
Photon x 10
Dose rates (mrem/hr)
Distance (cm)
2500
2000
1500
1000
500
0
-100
-75
-50
-25
0
25
50
75
100

no definite

APPENDIX II

Dose Rate Calculations

...calculation ... estimate ... source dose rate just above the ... shutter.

NOTE: The symbyol, := , means "is defined as."

$k := 1..4$

$T_{Poly_k} := 0$ Polyethylene thickness (cm)

$T_{M_k} := 23.175$ Thickness of Lead (cm)

The following initial doses (at the top of the lead shutter) were chosen so as to obtain the desired results for dose rates at the bottom of the lead shutter.

$\gamma C := 4.135 \cdot 10^6$ Initial Photon Dose Rate (mrem/h)

$nC := 83100$ Initial Fast Neutron Dose Rate (mrem/h)

ALL ATTENUATION FACTORS CHOSEN FOR 4 MeV PHOTONS.

$\mu_{Pb} := 0.469$ Obtained from, The Photon Shielding Manual, by Anthony Foderhard

$\mu_{Fe} := .26$ (Units of 1/cm)

Macroscopic cross-sections used for fast neutron attenuation. These valuse were obtained from Table 51.8 in Tipton's Reactor Handbook on Materials. All values are the Removal Cross-Sections for 8 MeV neutrons. (Units of 1/cm)

$\sigma_{Pb} := 0.1168$ Note that the 1MeV Total cross sections for these numbers were initially used, but found to be too high when compared to experimental values obtained by R.Rogus. These values were much closer.

$\sigma_{Fe} := 0.1684$

Build-up factor coefficients for the Taylor form build-up factor calculations. Obtained from Appendix B of The Photon Shielding Manual by Anthony Foderard.

LEAD		IRON	
$A1P := 3.897$	$A2P := 1 - A1P$	$A1F := 9.624$	$A2F := 1 - A1F$
$\alpha 1P := -.08468$	$\alpha 2P := -.02383$	$\alpha 1F := -.04698$	$\alpha 2F := .00175$

Build-up factor calculations

$$B_{Pb_k} := A1P \cdot \exp\left[-\alpha 1P \cdot \left(\mu_{Pb} \cdot T_{M_k}\right)\right] + A2P \cdot \exp\left[-\alpha 2P \cdot \left(\mu_{Pb} \cdot T_{M_k}\right)\right]$$

$$B_{Fe} := A1F \cdot \exp(-\alpha 1F \cdot (\mu_{Fe} \cdot 4.5)) + A2F \cdot \exp(-\alpha 2F \cdot (\mu_{Fe} \cdot 4.5))$$

Dose Rate Calculations (mrem/h) for both fast neutron (fn) and gamma doses:

$D_{Pb\gamma_k} := \gamma C \cdot B_{Pb_k} \cdot \exp\left(-\mu_{Pb} \cdot T_{M_k}\right)$ $D_{Pbfn_k} := nC \cdot \exp\left(-\sigma_{Pb} \cdot T_{M_k}\right)$ Attenuation in lead

$D_{T\gamma_k} := D_{Pb\gamma_k} \cdot B_{Fe} \cdot \exp(-\mu_{Fe} \cdot 4.5)$ $D_{Tfn_k} := D_{Pbfn_k} \cdot \exp(-\sigma_{Fe} \cdot 4.5)$ Attenuation in bottom steel plate

Dose Rate Values at the bottom of the lead shutter.

$D_{T\gamma_k}$

230.011
230.011
230.011
230.011

D_{Tfn_k}

$2.6 \cdot 10^3$
$2.6 \cdot 10^3$
$2.6 \cdot 10^3$
$2.6 \cdot 10^3$

These values were desired to match experimental measurements made by R. Rogus. The initial doses above were varied until these numbers were obtained.

$k := 1..4$

NOTE: The symbyol, := , means "is defined as."

Constants:

$\sigma_{Poly} := .24$ "Attenuation Coefficient" (Σ_{tot}) for fast neutron attenuation. (Units of 1/cm)
Calculated from RR's Dose Rate Graph for depleted Uranium shielding.

$\mu_U := 0.812$
$\mu_W := 0.768$
$\mu_{Fe} := .26$
Attenuation Coefficients for photons on Uranium and Tungsten. (Units of 1/cm)
Obtained from, The Photon Shielding Manual, by Anthony Foderhard
(*The photon energy chosen was **4 MeV** to account for photons from* ^{16}N)

$\gamma C := 4.135 \cdot 10^6$
$nC := 83100$
Initial Dose Rates of fast neutrons and photons (mrem/h)

$T_{Poly_k} := 2 + 2 \cdot k$
$T_{M_k} := 23.175 - T_{Poly_k}$
Calculations of the Poly and Metal layer shield thicknesses. (cm)

Build-up factor coefficients:

Uranium		Tungsten	
$A1U := .975$	$A2U := 1 - A1U$	$A1W := 1.273$	$A2W := 1 - A1W$
$\alpha 1U := -.15866$	$\alpha 2U := .21101$	$\alpha 1W := -.17257$	$\alpha 2W := -.12178$

Iron

$A1F := 5.867$ $A2F := 1 - A1F$
$\alpha 1F := -.06150$ $\alpha 2F := .00186$

Build-up Factor Calculations

$$B_{U_k} := A1U \cdot \exp\left[-\alpha 1U \cdot \left(\mu_U \cdot T_{M_k}\right)\right] + A2U \cdot \exp\left[-\alpha 2U \cdot \left(\mu_U \cdot T_{M_k}\right)\right]$$

$$B_{W_k} := A1W \cdot \exp\left[-\alpha 1W \cdot \left(\mu_W \cdot T_{M_k}\right)\right] + A2W \cdot \exp\left[-\alpha 2W \cdot \left(\mu_W \cdot T_{M_k}\right)\right]$$

$$B_{Fe} := A1F \cdot \exp(-\alpha 1F \cdot (\mu_{Fe} \cdot 4.5)) + A2F \cdot \exp(-\alpha 2F \cdot (\mu_{Fe} \cdot 4.5))$$

$C_k :=$

.5092
.5
.5
.3704

This value is the conversion factor that was determined from the Monte-Carlo simulation done by JY. The relative values in JY's graph are used to convert the calculated fast neutron dose-rate from RR's graph to a fast neutron dose rate for Tungsten shielding.

Rate Calculations:

$$Ufn_k := nC \cdot \exp\left(-\sigma_{Poly} \cdot T_{Poly_k}\right) \cdot \exp\left(-.173 \cdot T_{M_k}\right) \cdot \exp(-.168 \cdot 4.5)$$

$$D_{U\gamma_k} := B_{U_k} \cdot \exp\left(-\mu_U \cdot T_{M_k}\right) \cdot \gamma C$$

Dose rate for fast neutron and photons using depleted Uranium and Poly as shielding. (mREM/h)

$$D_{Wfn_k} := D_{Ufn_k} \cdot C_k$$

$$D_{W\gamma_k} := B_{W_k} \cdot \exp\left(-\mu_W \cdot T_{M_k}\right) \cdot \gamma C$$

Dose rate for fast neutron and photons using Tungsten and Poly as shielding. (mREM/h)

$$D_{TU\gamma_k} := D_{U\gamma_k} \cdot B_{Fe} \cdot \exp(-\mu_{Fe} \cdot 4.5)$$

$$D_{TW\gamma_k} := D_{W\gamma_k} \cdot B_{Fe} \cdot \exp(-\mu_{Fe} \cdot 4.5)$$

Accounting for bottom sheet of steel

$$D_{WT_k} := D_{TW\gamma_k} + D_{Wfn_k}$$

$$D_{UT_k} := D_{TU\gamma_k} + D_{Ufn_k}$$

TOTAL DOSE RATES: (mREM/h)

The total dose rates are defined as those dose rates consisting of the gamma + fast neutron doses. This does not include seconday gammas.

Total Dose Rates using either Tungsten/Poly or Uranium/Poly Layers

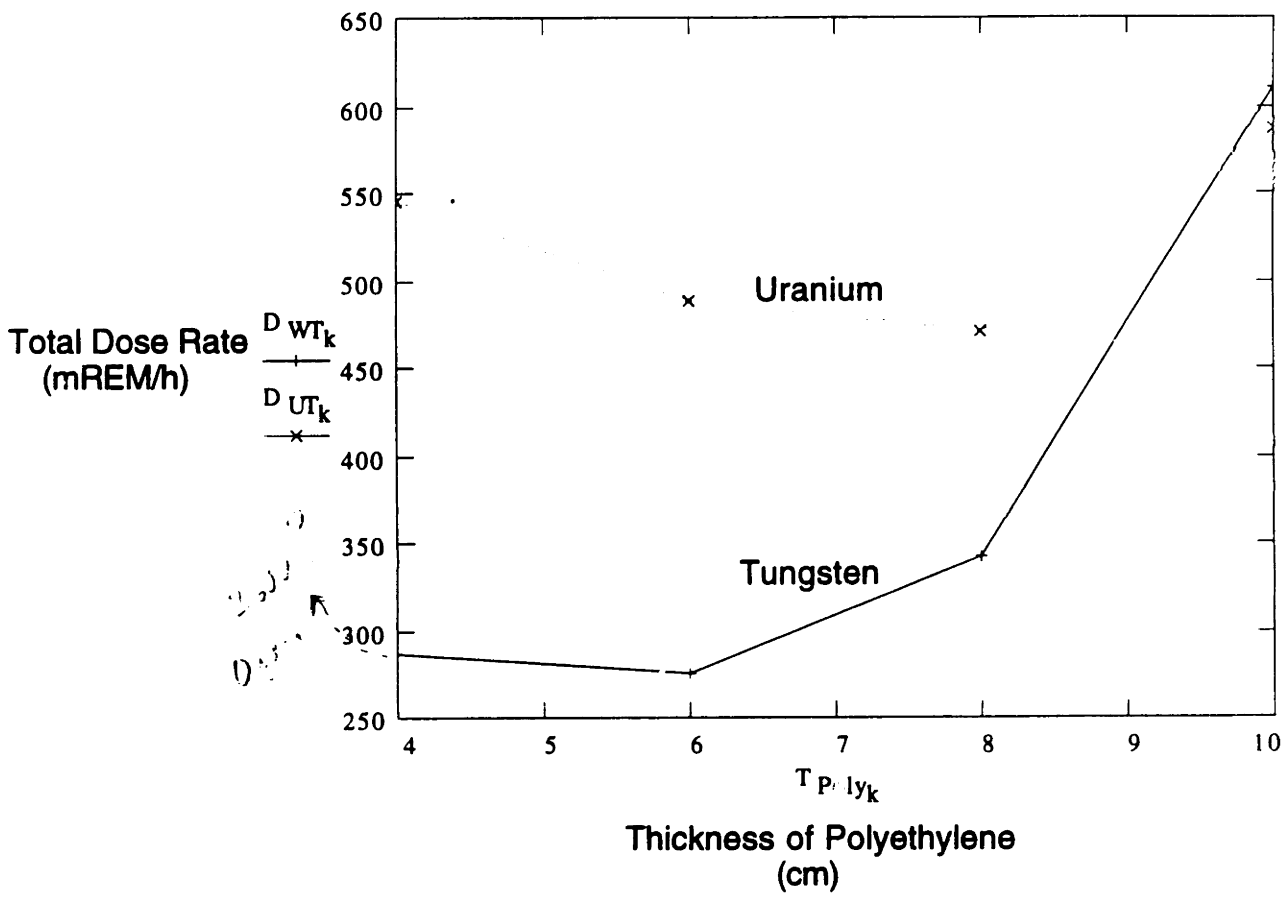

CDF 22 Aug, 1993: Layers of shield material with powdered tungsten used.

$k := 1..4$

NOTE: The symbyol, := , means "is defined as."

Constants:

$\sigma_{Poly} := .24$ "Attenuation Coefficient" (Σ_{tot}) for fast neutron attenuation. (Units of 1/cm) Calculated from RR's Dose Rate Graph for depleted Uranium shielding.

$\mu_U := 0.812$ Attenuation Coefficients for photons on Uranium and Tungsten. (Units of 1/cm)

$\mu_W := 0.6 \cdot 0.768$ Obtained from, The Photon Shielding Manual, by Anthony Foderhard

$\mu_{Fe} := .26$ (*The photon energy chosen was **4 MeV** to account for photons from* ^{16}N)

The attenuation for tungsten is multiplied by 0.6 to account for powder density.

$\gamma C := 4.135 \cdot 10^6$ Initial Dose Rates of fast neutrons and photons (mrem/h)

$nC := 83100$

$T_{Poly_k} := 2 + 2 \cdot k$

$T_{M_k} := 23.175 - T_{Poly_k}$

Calculations of the Poly and Metal layer shield thicknesses. (cm)

Build-up factor coefficients:

Uranium

$A1U := .975$ $A2U := 1 - A1U$

$\alpha 1U := -.15866$ $\alpha 2U := .21101$

Tungsten

$A1W := 1.273$ $A2W := 1 - A1W$

$\alpha 1W := -.17257$ $\alpha 2W := -.12178$

Iron

$A1F := 5.867$ $A2F := 1 - A1F$

$\alpha 1F := -.06150$ $\alpha 2F := .00186$

Build-up Factor Calculations

$$B_{U_k} := A1U \cdot \exp\left[-\alpha 1U \cdot \left(\mu_U T_{M_k}\right)\right] + A2U \cdot \exp\left[-\alpha 2U \cdot \left(\mu_U T_{M_k}\right)\right]$$

$$B_{W_k} := A1W \cdot \exp\left[-\alpha 1W \cdot \left(\mu_W T_{M_k}\right)\right] + A2W \cdot \exp\left[-\alpha 2W \cdot \left(\mu_W T_{M_k}\right)\right]$$

$$B_{Fe} := A1F \cdot \exp(-\alpha 1F \cdot (\mu_{Fe} \cdot 4.5)) + A2F \cdot \exp(-\alpha 2F \cdot (\mu_{Fe} \cdot 4.5))$$

$C_k :=$

.5092
.5
.5
.3704

This value is the conversion factor that was determined from the Monte-Carlo simulation done by JY. The relative values in JY's graph are used to convert the calculated fast neutron dose-rate from RR's graph to a fast neutron dose rate for Tungsten shielding.

Dose Rate Calculations:

$$D_{Ufn_k} := nC \cdot \exp\left(-\sigma_{Poly} \cdot T_{Poly_k}\right) \cdot \exp\left(-.173 \cdot T_{M_k}\right) \cdot \exp(-.168 \cdot 4.5)$$

$$D_{U\gamma_k} := B_{U_k} \cdot \exp\left(-\mu_U \cdot T_{M_k}\right) \cdot \gamma C$$

Dose rate for fast neutron and photons using depleted Uranium and Poly as shielding. (mREM/h)

$$D_{Wfn_k} := D_{Ufn_k} \cdot C_k$$

$$D_{W\gamma_k} := B_{W_k} \cdot \exp\left(-\mu_W \cdot T_{M_k}\right) \cdot \gamma C$$

Dose rate for fast neutron and photons using Tungsten and Poly as shielding. (mREM/h)

$$D_{TU\gamma_k} := D_{U\gamma_k} \cdot B_{Fe} \cdot \exp(-\mu_{Fe} \cdot 4.5)$$

$$D_{TW\gamma_k} := D_{W\gamma_k} \cdot B_{Fe} \cdot \exp(-\mu_{Fe} \cdot 4.5)$$

Accounting for bottom sheet of steel

$$D_{WT_k} := D_{TW\gamma_k} + D_{Wfn_k}$$

$$D_{UT_k} := D_{TU\gamma_k} + D_{Ufn_k}$$

TOTAL DOSE RATES: (mREM/h)

Total Dose Rates using either Tungsten(Powder)/Poly or Uranium/Poly Layers

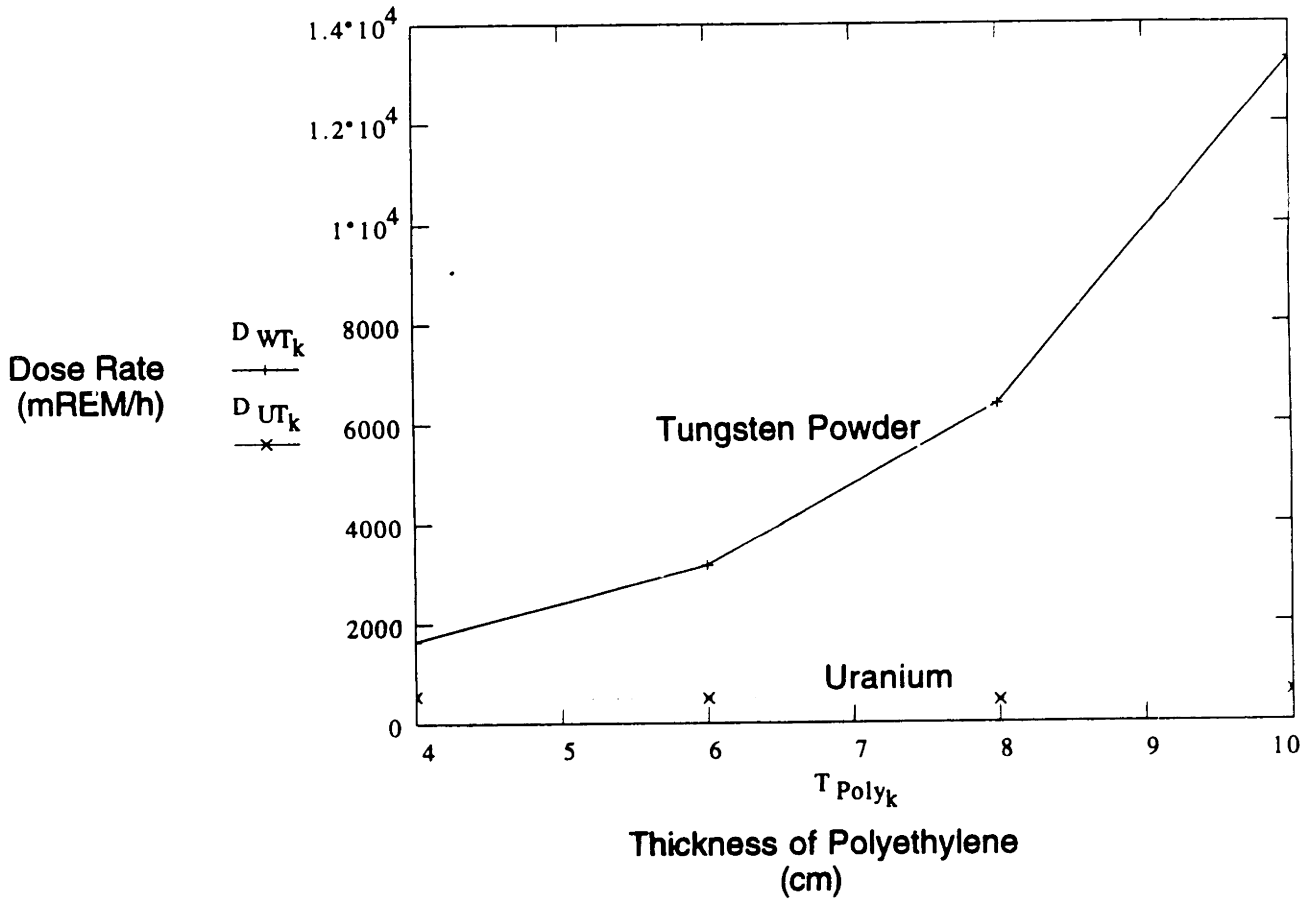

...ov, 1993: Optimal Poly/Tungsten/Boron Mixture

...ould be noted that the **GOAL** of these calculations is to determine the shield mixture that results in the maximum attenuation of the TOTAL dose (i.e. gamma + fast neutron dose) while at the same time keeping the tungsten activation to a minimum. For this latter reason boron is added to the mixture and cross-section calculations are done at the end of this run.

NOTE: The symbyol, := , means "is defined as."

$k := 0..100$ Define the size of the one-dimensional array:

Constants:

Define Constants:

% of Components by Weight

$W\%_W := 0.9589$ $W\%_{Poly} := 0.0341$ $W\%_B := 0.007$

Density of soild materials when not a part of the mixture (g/cc).

$\delta_W := 19.3$ $\delta_{Poly} := .92$ $\delta_B := 2.35$

CALCULATED CONSTANTS:

Initial guesses of % of Components by Volume (a:W,b:Poly,c:Boron)

$a := 0.59$ $b := 0.41$ $c := 0.05$

$d := 11.8$ Initial guess of Total Density of Mixture (g/cc)

---

given

$$a = W\%_W \cdot \frac{d}{\delta_W}$$

$$b = W\%_{Poly} \cdot \frac{d}{\delta_{Poly}}$$

$$c = W\%_B \cdot \frac{d}{\delta_B}$$

SOLVE BLOCK

$c + b + a = 1$ (solves for volume percentages and density of mixture)

$d = \delta_W \cdot a + \delta_{Poly} \cdot b + \delta_B \cdot c$

$$\begin{bmatrix} V\%_W \\ V\%_{Poly} \\ V\%_B \\ \delta_{MIX} \end{bmatrix} := \text{Find}(a, b, c, d)$$

Calculated volume percentages of the components of the mixture.

$V\%_W = 0.554$ $V\%_{Poly} = 0.413$ $V\%_B = 0.033$

Densities of individual Mixture Components

$\delta_{WMIX} := W\%_W \cdot \delta_{MIX}$ Density of tungsten in the mixture (g/cc)

$\delta_{PolyMIX} := W\%_{Poly} \cdot \delta_{MIX}$ Density of poly in the mixture (g/cc)

$\delta_{BMIX} := W\%_B \cdot \delta_{MIX}$ Density ofboron in the mixture (g/cc)

Poly and Paraffin are interchengable. From the Reactor Handbook, 2nd Ed., Volume ... values for paraffin and poly are 0.109/cm and 0.111/cm respectively. The value RR exp... determined was 0.15535 for poly. Using the barn book value of 4.2 b for the total cross section of H at 1 MeV, and using Reactor Experiments value of 7.8 x 10^{22} H atoms/cc a value of 0.3276/cm was calculated. These latter two values were averaged to result in the value of 0.24/cm for the macroscopic cross-section of poly and paraffin.

$\delta_{WMIX} = 10.687$

$\delta_{PolyMIX} = 0.38$

$\delta_{BMIX} = 0.078$

$\delta_{MIX} = 11.145$ This final density is that of the total mixture (g/cc)

Neutron Attenuation Constants: (The attenuation coefficients have units of 1/cm)

$\sigma_{Poly} := .24$ "Attenuation Coefficient" (Σ) for fast neutron attenuation. This term was calculated 1)from the barn book by using the microscopic cross section for 1MeV neutrons in H {0.3276/cm}, and 2) from RR's Dose Rate Graph for depleted Uranium shielding {0.15535} according to the exponential attenuation eqn. These numbers were averaged to come up with the shown term.

$\sigma_B := 0.127$
$\sigma_{Bi} := 0.0985$
$\sigma_{Fe} := 0.168$
$\sigma_W := 0.198$

Total macroscopic cross sections for effective removal of 8 MeV neutrons. These values were originally obtained by calculating their values from the 1MeV microscopic cross-sections in the barn book. These numbers were found to be too high, however, when Tipton's Reactor Handbook of Materials was referenced. In lieu of the previous numbers, the shown set was obtained from Table 51.8 of Tipton's. They are the values for the removal cross sections for 8 MeV neutrons.

The effective macroscopic cross section for removal of fast neutrons in the mixture is calculated as follows:

$$\sigma_{MIX} := \sigma_{Poly} \cdot \frac{\delta_{PolyMIX}}{\delta_{Poly}} + \sigma_W \cdot \frac{\delta_{WMIX}}{\delta_W} + \sigma_B \cdot \frac{\delta_{BMIX}}{\delta_B} \quad \text{(units of 1/cm)}$$

Gamma Attenuation Constants: (The attenuation coefficients have units of 1/cm)

$\mu_B := 0.0658$
$\mu_W := 0.768$
$\mu_{Fe} := .26$
$\mu_{Bi} := .4263$

Total Linear Attenuation Coefficients for photons.
Obtained from, The Photon Shielding Manual, by Anthony Foderhard
(*The photon energy chosen was 4 MeV to account for photons from* ^{16}N)

This term is the effective linear attenuation coefficient for the Poly mixture. The first term accounts for the Tungsten and the second term accounts for the Poly. This second term is the linear attenuation coefficient for 4MeV Gammas in paraffin and was found in Tipton's. It is estimated to be the same for poly. The third term accounts for the boron in the mixture.

$$\mu_{MIX} := \mu_W \cdot \frac{\delta_{WMIX}}{\delta_W} + 0.0322 + \mu_B \cdot \frac{\delta_{BMIX}}{\delta_B} \quad \text{(units of 1/cm)}$$

$$\mu_{WMIX} := \mu_W \cdot \frac{\delta_{WMIX}}{\delta_W}$$ This term is used for calculating the build-up factor due to Tungsten in the Tungsten/Poly mixture. It is a ratio of the densities multiplied by the attenuation factor of solid Tungsten

.is:

$\gamma := 4.135 \cdot 10^{0}$ These terms are the Dose Rates that were calculated as doses just before the shield. (mRem/h)

$nC := 83100$

Calculations of the Mixture (T_{MIX}) and Metal (T_M) thicknesses.

$T_{MIX_k} := k \cdot .23175$ $\qquad$ $T_{M_k} := 23.175 - T_{MIX_k}$

The 'Metal' used in this run is a layer of solid Bismuth at the bottom of the shield. This layer is laying directly upon the bottom steel plate of the shutter.

Build-up Factor Calculations: These were calculated using the Taylor Form from The Photon Shielding Manual, by Anthony Foderhard.

NOTE:The Build-Up for BORON is Ignored in this Run

Build-up Factor Coefficients

Iron

$A1F := 9.624$ $\qquad$ $A2F := 1 - A1F$

$\alpha 1F := -.04698$ $\qquad$ $\alpha 2F := .00175$

Tungsten

$A1W := 5.52$ $\qquad$ $A2W := 1 - A1W$

$\alpha 1W := -.08857$ $\qquad$ $\alpha 2W := -.0457$

Lead

$A1P := 3.897$ $\qquad$ $A2P := 1 - A1P$

$\alpha 1P := -.08468$ $\qquad$ $\alpha 2P := -.02383$

Build-up for Bismuth (The coefficents for lead are used)

$$B_{Bi_k} := A1P \cdot \exp\left[-\alpha 1P \cdot \left(\mu_{Bi} \cdot T_{M_k}\right)\right] + A2P \cdot \exp\left[-\alpha 2P \cdot \left(\mu_{Bi} \cdot T_{M_k}\right)\right]$$

Build-up for Tungsten

$$B_{W_k} := A1W \cdot \exp\left[-\alpha 1W \cdot \left(\mu_{W} \cdot T_{M_k}\right)\right] + A2W \cdot \exp\left[-\alpha 2W \cdot \left(\mu_{W} \cdot T_{M_k}\right)\right]$$

Buillld-up for Iron

$B_{Fe} := A1F \cdot \exp(-\alpha 1F \cdot (\mu_{Fe} \cdot 4.5)) + A2F \cdot \exp(-\alpha 2F \cdot (\mu_{Fe} \cdot 4.5))$ The thickness of the bottom steel plate is 4.5 cm.

Build-up for the Tung/Poly Mixture

$$B_{MIX_k} := A1W \cdot \exp\left[-\alpha 1W \cdot \left(\mu_{WMIX} \cdot T_{MIX_k}\right)\right] + A2W \cdot \exp\left[-\alpha 2W \cdot \left(\mu_{WMIX} \cdot T_{MIX_k}\right)\right]$$

DOSE RATE CALCULATIIONS (All dose rates are in **mREM/h**):

Total Gamma Dose Rate

$$TD_{\gamma_k} := \gamma C \cdot B_{MIX_k} \cdot \exp\left(-\mu_{MIX} \cdot T_{MIX_k}\right) \cdot B_{Fe} \cdot \exp(-\mu_{Fe} \cdot 4.5) \cdot B_{Bi_k} \cdot \exp\left(-\mu_{Bi} \cdot T_{M_k}\right)$$

Total Fast Neutron Dose Rate

$$TD_{fn_k} := nC \cdot \exp\left(-\sigma_{MIX} \cdot T_{MIX_k}\right) \cdot \exp(-\sigma_{Fe} \cdot 4.5) \cdot \exp\left(-\sigma_{Bi} \cdot T_{M_k}\right)$$

Total Combined Dose Rate

$$TD_k := TD_{\gamma_k} + TD_{fn_k}$$

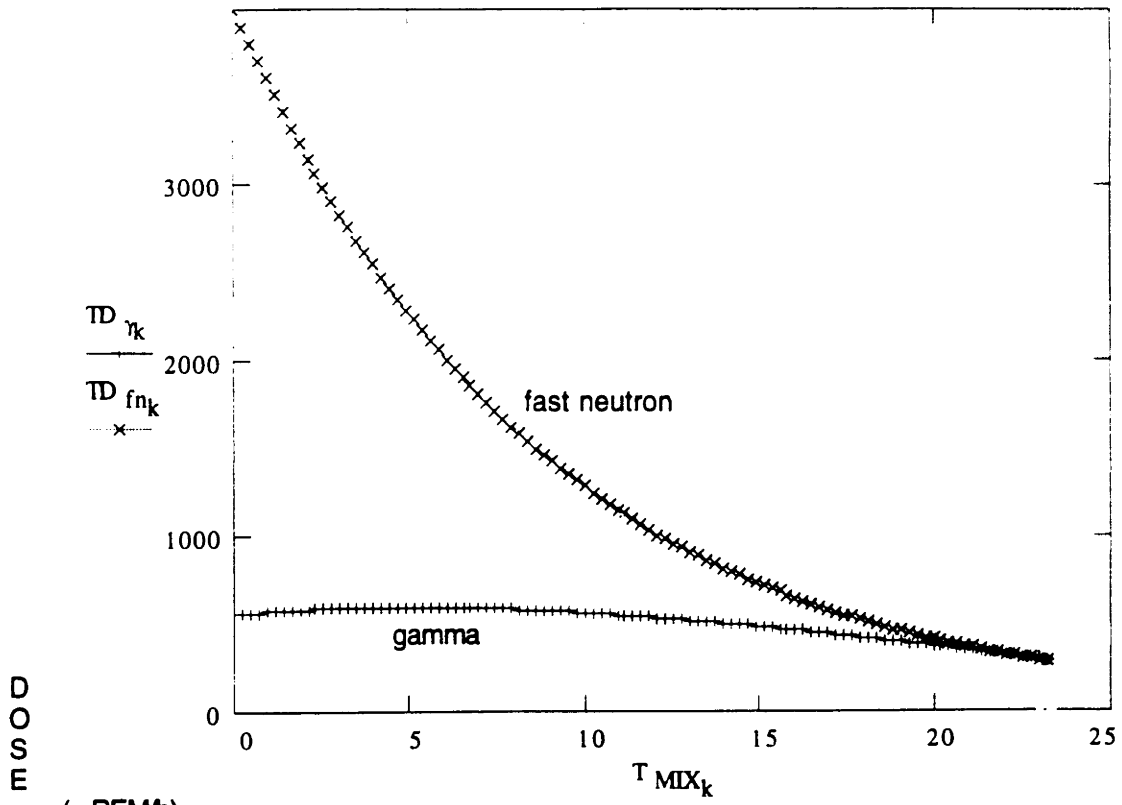

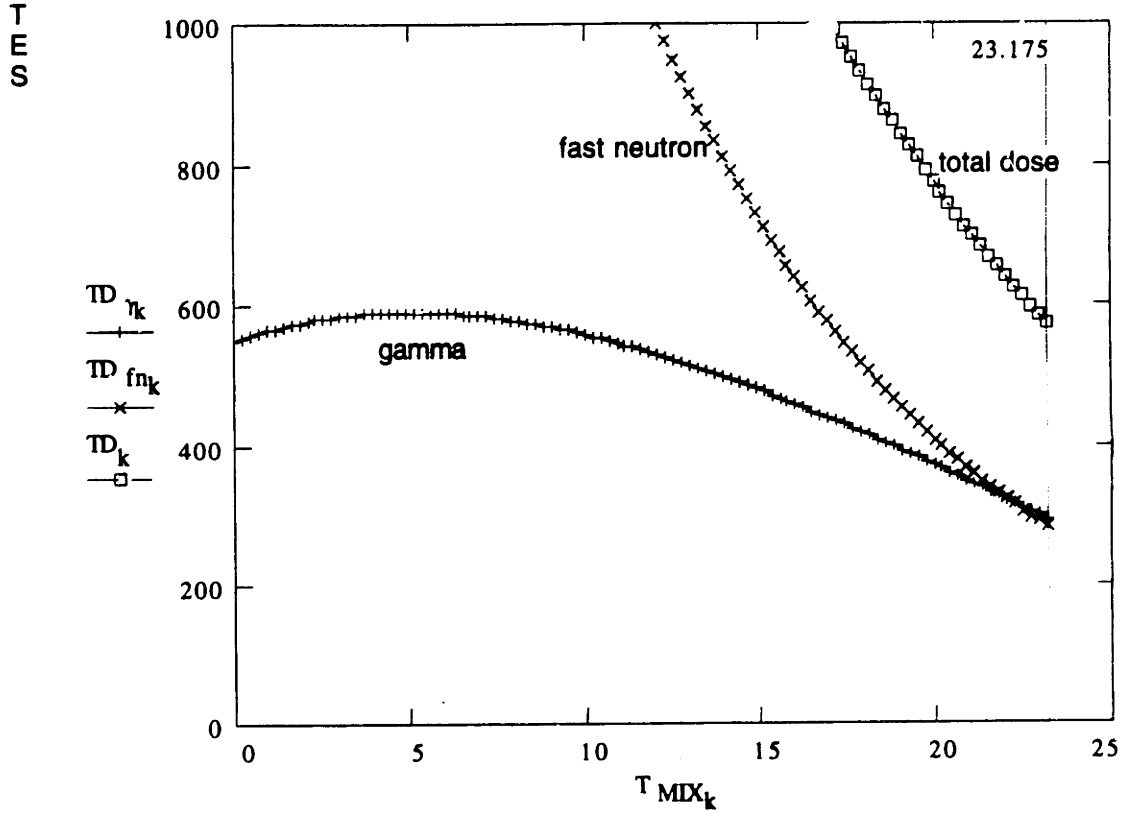

TD_{100} = 570.403 This is the dose rate at the bottom of the shutter. (mrem/h)

...LATIONS:
...ne the necessary amount of boron to stop secondary gammas)

NOTE: The following calculations use the densities calculated in the above dose rate calculations which were determined for **maximum attenuation of the Total Dose.**

σ activation numbers are found in Tipton's Handbook.

$\sigma_{Wact} := 38 \cdot 10^{-24}$ (cm^2) Activation/Absorbtion Cross-Sections for W-187/B-10

$\sigma_{Babs} := 3838 \cdot 10^{-24}$ (cm^2)

$N_{Bsolid} := 1.31 \cdot 10^{23} \left(\frac{atoms}{cc}\right)$

$N_{Wsolid} := 6.336 \cdot 10^{22} \left(\frac{atoms}{cc}\right)$

Natural abundance of Boron-10

$AB10 := 0.199$

$N_{WMIX} := \frac{\delta_{WMIX} \cdot 6.02 \cdot 10^{23}}{183.85}$ Atoms of tungsten/cc of mixture

$N_{BMIX} := \frac{\delta_{BMIX} \cdot 6.02 \cdot 10^{23}}{10.811}$ Atoms of boron/cc of mixture

The following two calculations compare the macroscopic cross-section of B-10 to the activation cross section of tungsten. Note that the cross-section of tungsten is multiplied by 10 in order to build in a safety margin. If these two calculated numbers are approximately equal, there should be negligible activation of the tungsten.

$\sigma_{Babs} \cdot AB10 \cdot N_{BMIX} = 3.318$ $\qquad 10 \cdot \sigma_{Wact} \cdot N_{WMIX} \cdot 0.286 = 3.803$

RU[illegible] November, 1993: The following graphs use the same mixture [illegible], but, the shield is composed entirely of the mixture excluding the bottom 0.5 cm which is a layer of B_4C. The points on the graphs show the dose rates just below the shutter. (mrem/h)

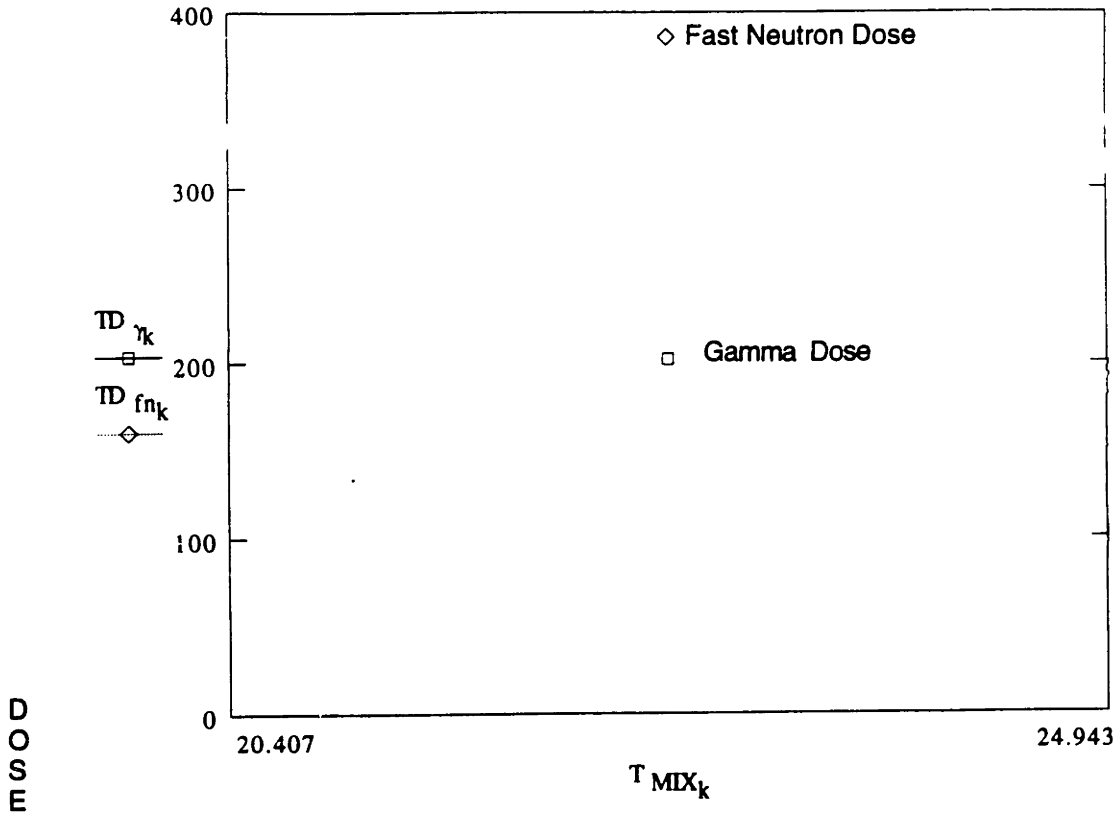

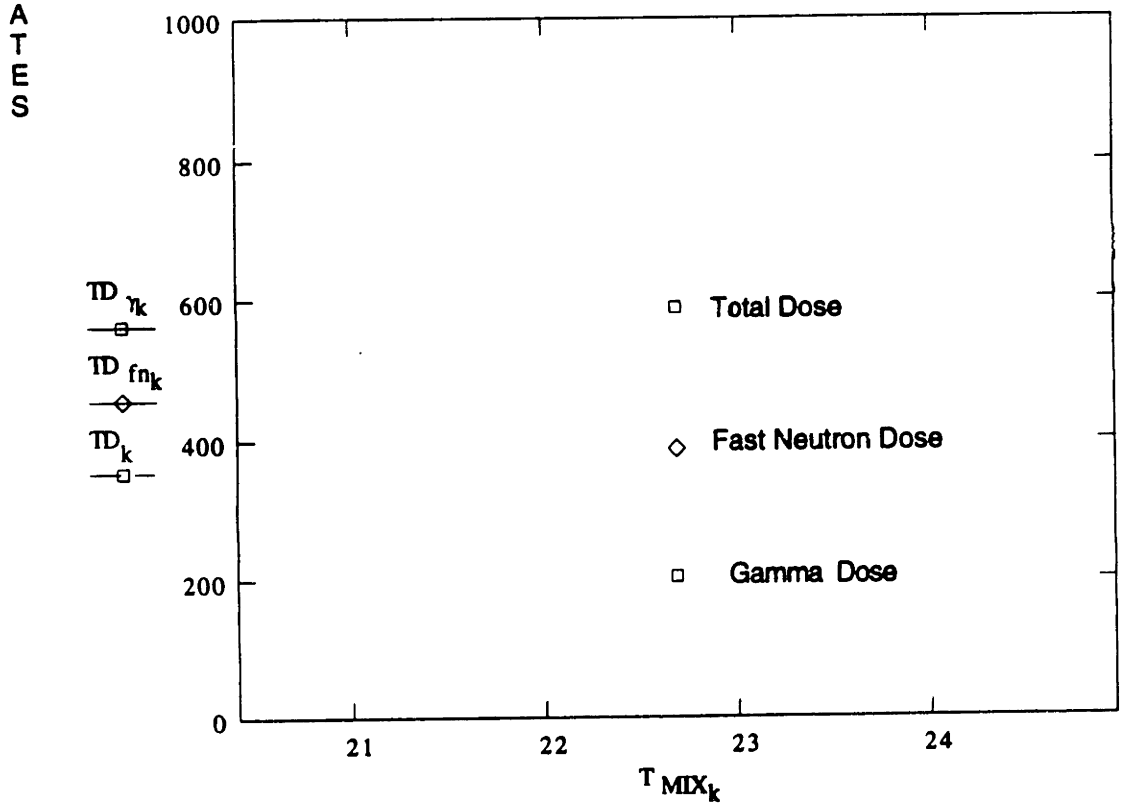

THICKNESS OF TUNGSTEN/POLY/BORON MIXTURE (cm)

TD_{100} = 587.048 This is the TOTAL dose rate at the bottom of the shutter. (mrem/h)

2: 01 November, 1993: A polyethylene layer on top of a lead layer.

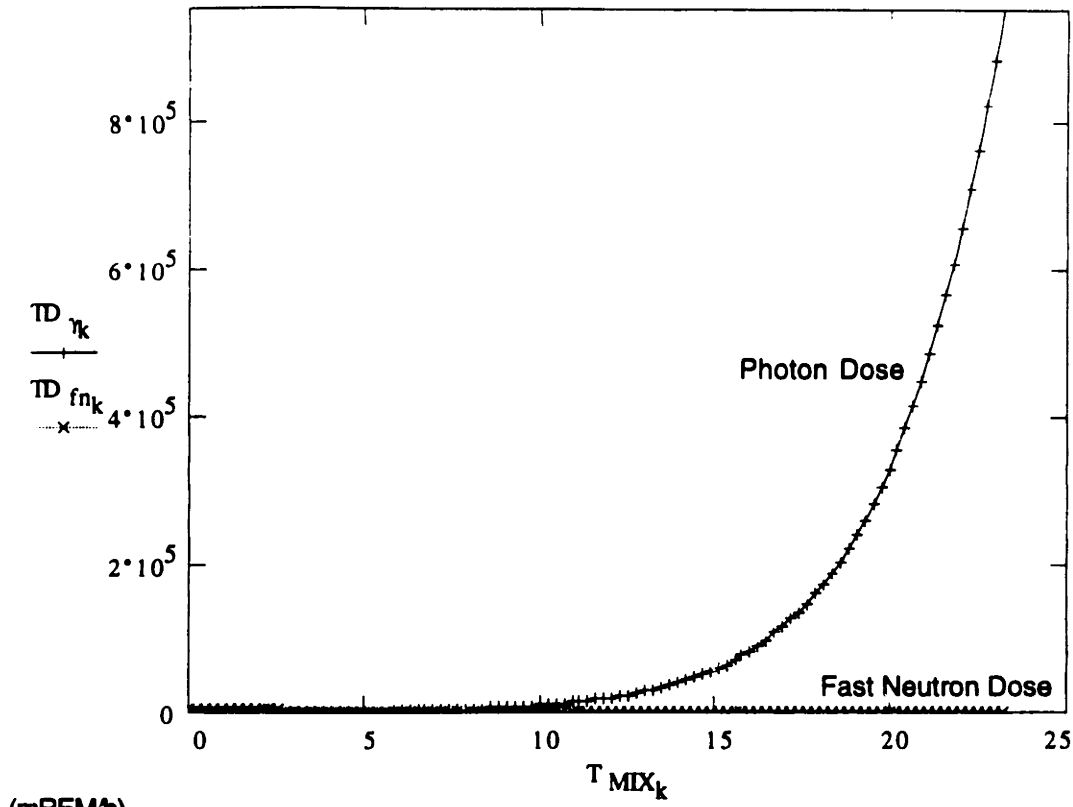

DOSE RATES (mREM/h)

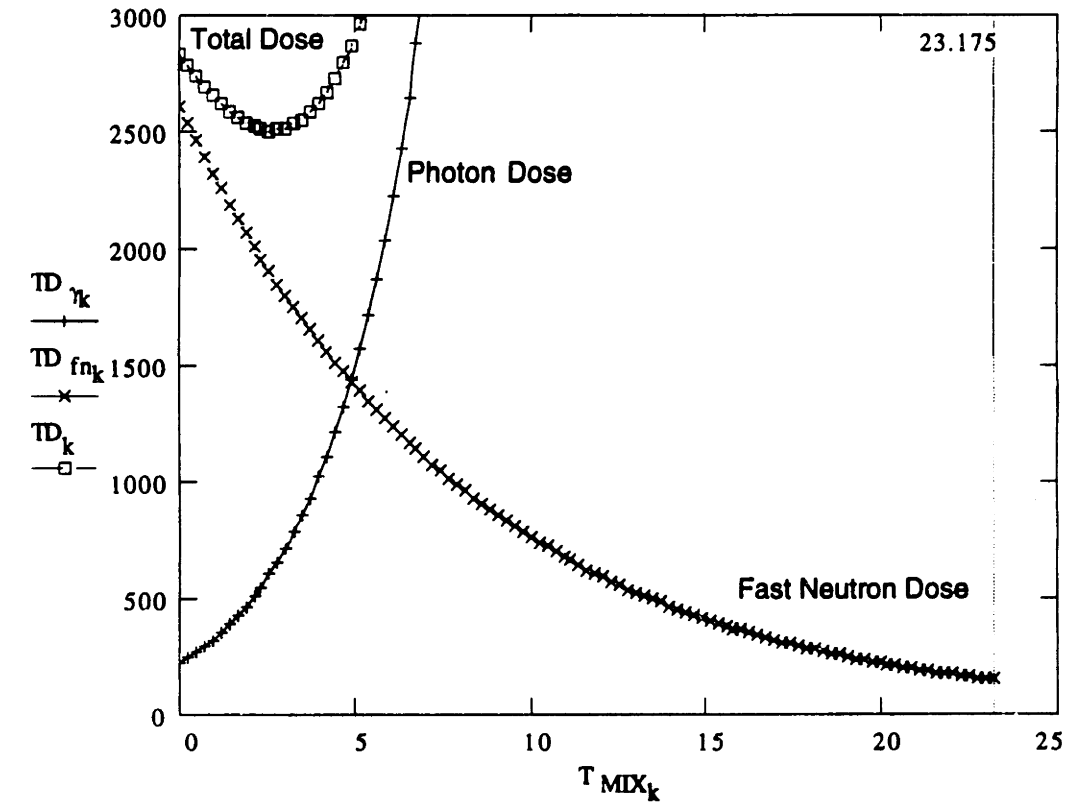

THICKNESS OF POLY LAYER ON TOP OF LEAD
Lead + Poly = 23.175 cm
(cm)

$TD_{11} = 2.506 \cdot 10^3$ This is the minimum total dose rate (gamma + fast neutron)at the bottom of the shutter. (mrem/h)

APPENDIX III

Engineering Design Drawings

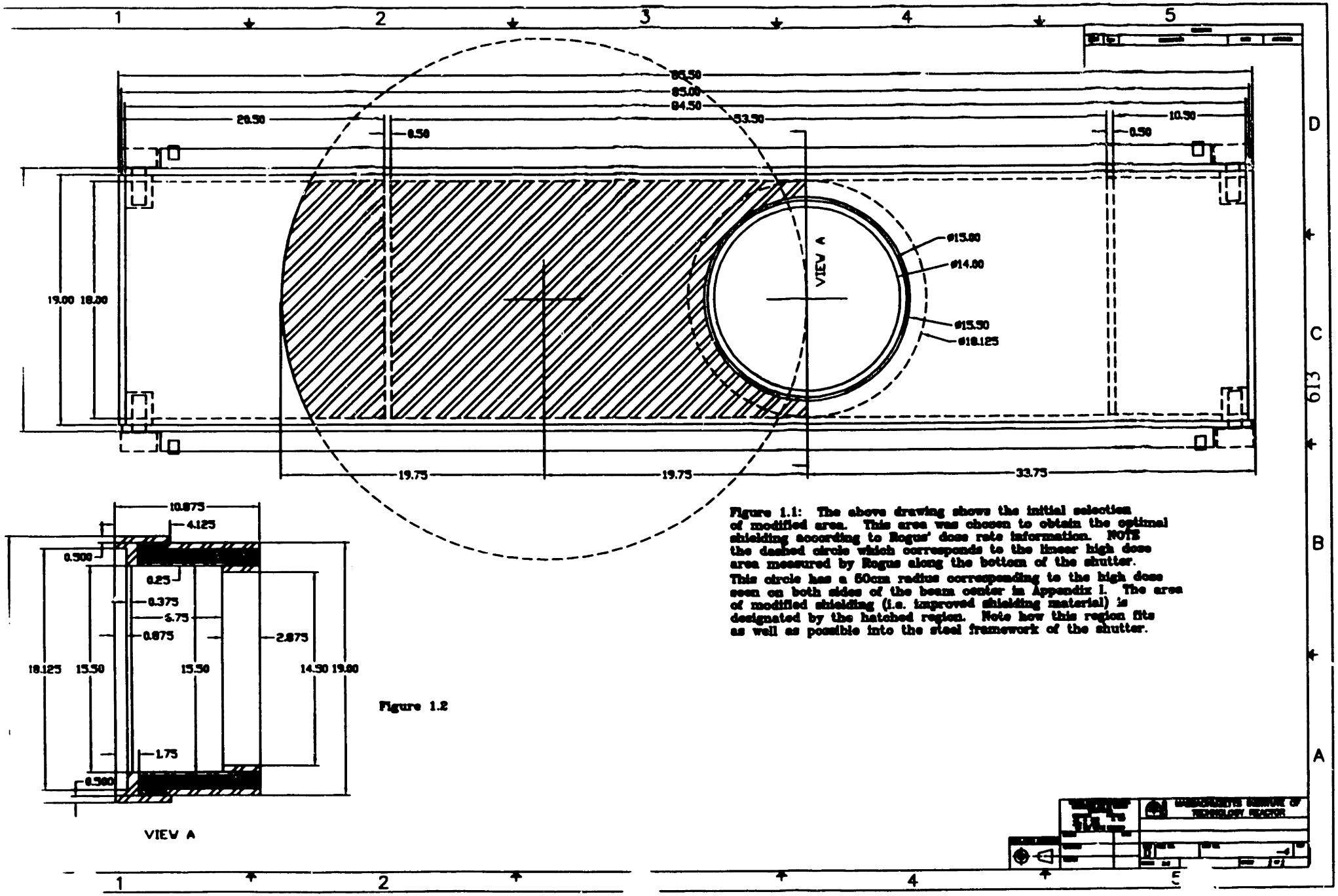

Figure 1.1: The above drawing shows the initial selection of modified area. This area was chosen to obtain the optimal shielding according to Rogue' dose rate information. NOTE the dashed circle which corresponds to the linear high dose area measured by Rogue along the bottom of the shutter. This circle has a 50cm radius corresponding to the high dose seen on both sides of the beam center in Appendix I. The area of modified shielding (i.e. improved shielding material) is designated by the hatched region. Note how this region fits as well as possible into the steel framework of the shutter.

Figure 1.2

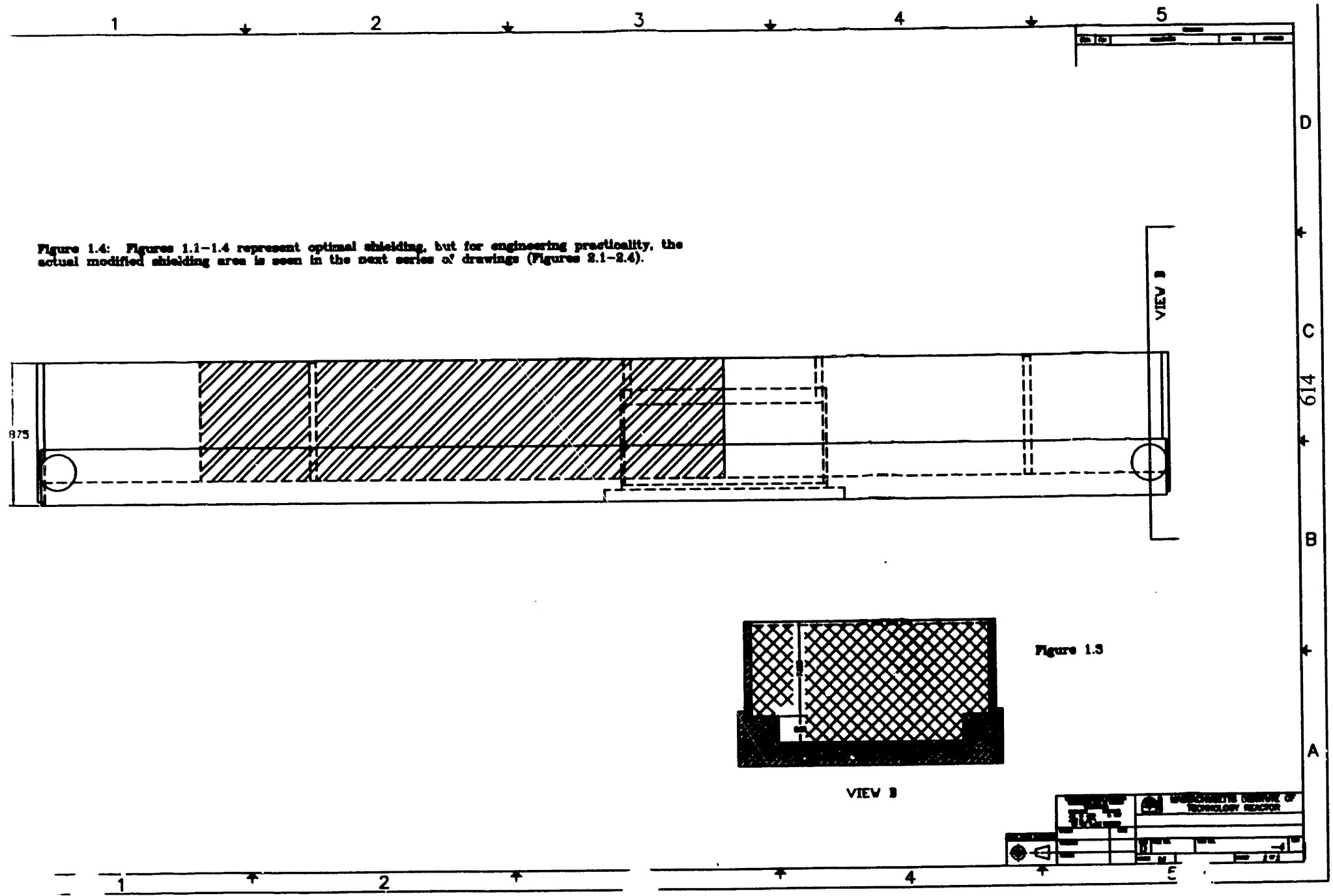

Figure 1.4: Figures 1.1–1.4 represent optimal shielding, but for engineering practicality, the actual modified shielding area is seen in the next series of drawings (Figures 2.1–2.4).

Figure 1.3

Figure 2.1: TOP VIEW of the proposed modified shutter.
The hatched area in the below drawing is the section to contain the new shield material.

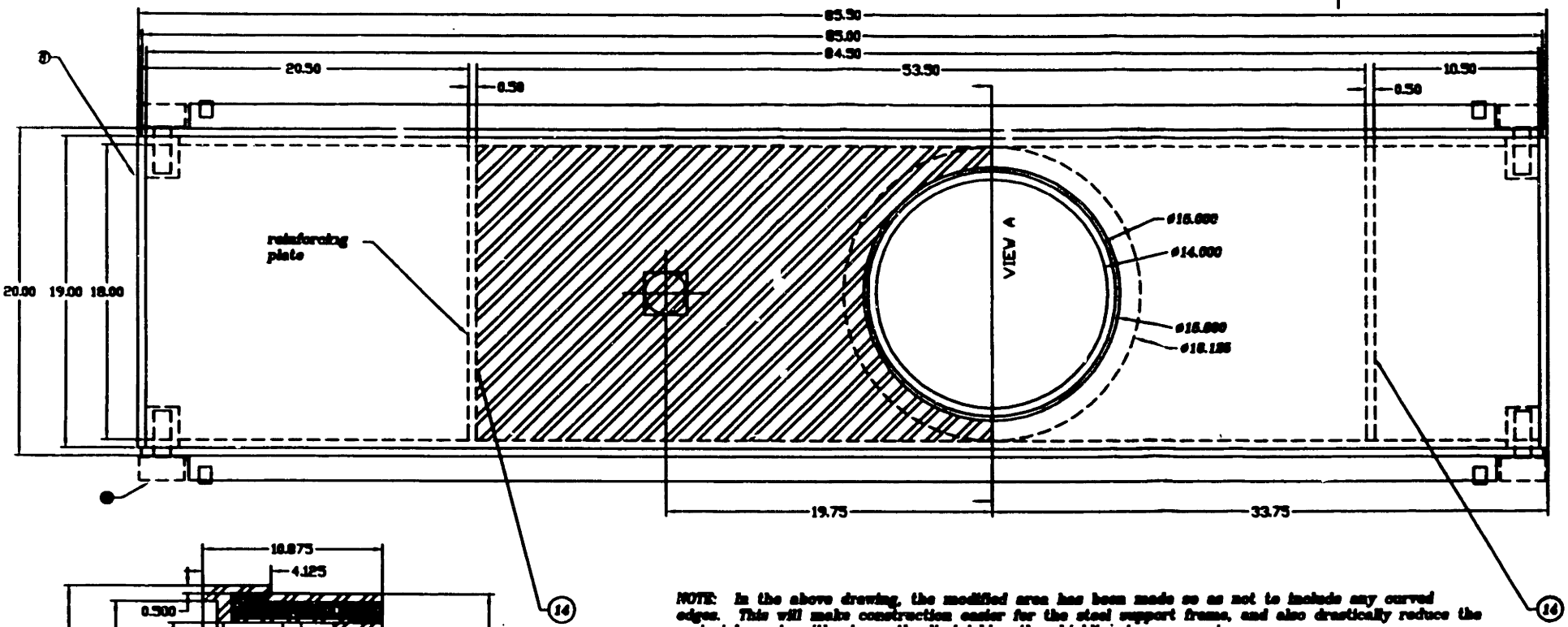

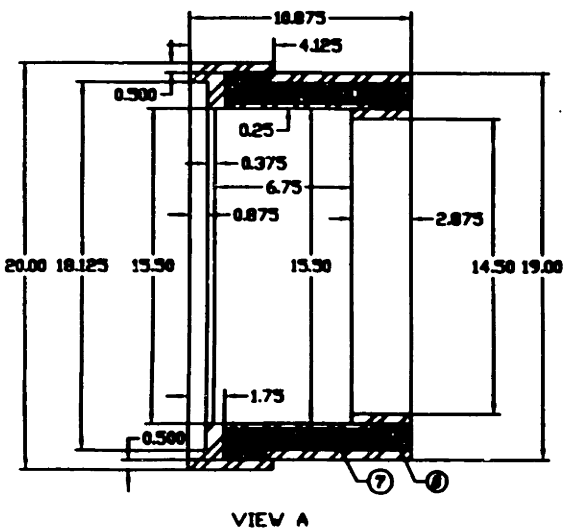

Figure 2.2

NOTE: In the above drawing, the modified area has been made so as not to include any curved edges. This will make construction easier for the steel support frame, and also drastically reduce the materials costs without greatly diminishing the shielding improvement.

Figure 2.3

Figure 2.4

APPENDIX IV

Referenced Memos

To: Professors Harling and Yanch

From: Ronald Rogus

Re: Tungsten activation

Date: July 19, 1992

As several hundred pounds of tungsten might be used in the new shutter design, theoretical and experimental analyses were done to estimate how activated the tungsten shield would become and to determine if such activation would increase the exposure rates in the medical room. At this point in the design stage, about 400 pounds of powdered tungsten mixed either homogeneously or in layers with a paraffin or polyethylene like material looks promising as an effective neutron and photon shield. The shield would be roughly a cube 30 cm on a side. It would have a steel liner. The shield would be wrapped with cadmium to remove thermal neutrons. B_4C would be added within the shield to capture thermal neutrons produced by thermalization of epicadmium neutrons.

Table 1 shows the expected activation products. It was assumed that the thermal flux within the shield would be small. Then, most of the activation would be caused by epicadmium neutrons that penetrate the cadmium surrounding the shield. Under these conditions, it would be expected that W-187 would be the most intense activation product; Its precursor, W-186, has a high abundance and a large resonance integral, and W-187 has the shortest half-life.

Activation of tungsten was tested experimentally. A 10 gram tungsten sample (Alpha Products, -100 mesh, m3N8, Lot #033076, Danvers, Ma.) was irradiated a short

Table 1. Tungsten isotopes and their activation products.

Isotope	Atomic abundance (%)	σ_{th}	RI	Radio-nuclide	Decay	$T_{1/2}$ (days)	E_γ (MeV)
W-180	0.13	7	-	W-181	EC	121	0.006
W-184	30.67	1.8	14	W-185	β^-	75.1	0.125
W-186	28.6	38	500	W-187	β^-	0.996	0.686, 0.480

time (5 minutes) for neutron activation analysis and a long time (2 hours) for radiation surveys. Before irradiation, the tungsten was placed in a polyethylene bag which was then heat sealed. This bag was placed in another heat sealed bag for double protection. The tungsten was then wrapped in a 0.040" layer of cadmium, which is black to thermal neutrons.

The tungsten was positioned in the centerline of the collimator, 1.3 cm below the shutter. A 5.1 cm thick borated polyethylene slab with a 20 cm diameter hole was in position as a delimiter. The epicadmium flux in this position is probably comparable to that where the shield would actually be located. Thus, activation results in this position should be applicable to estimates of activation of tungsten in the actual shield.

The tungsten was irradiated with all the shutters open. The tungsten was first irradiated for 5 minutes at 4.0 MWn. Neutron activation analysis (Detector #4, 5.48" distance, half-hour count) 40 minutes later showed about 10 peaks, all corresponding to W-187. In an earlier phone call with Professor Simonson, he recommended searching for Ta-182, which results from (n,p) reactions on W-182. No Ta-182 was found was found in this half-hour count. He also recommended searching for activation products of rhenium and hafnium, which could be impurities in the tungsten sample. No rhenium and hafnium activation products were found.

The tungsten was then irradiated for 2 hours at 4.0 MWn. The position was the same as before. The tungsten was surveyed with a GM tube 16 hours later. The reading through the window of the GM tube was 20 mR/hr on contact. Through the side of the tube (photons only) the reading was 8 mR/hr on contact. There was probably significant photon attenuation within the tungsten itself.

An attenuation experiment was done with one and two inch thick layers of lead. The source to detector distance was constant. Exposure rates with no lead and with 1 and 2" of lead were 0.45, 0.015, and <0.01 mR/hr, respectively. The exposure rate, therefore, was reduced by a factor of 30 with one inch of lead.

These experimental data were scaled to a 10 hour continuous irradiation at 5 MWn. With 2" of lead below the tungsten polyethylene shield, exposure rates from tungsten activation are expected to be about 1 mR/hr or less.

To: Professors Harling and Yanch

From: Ronald Rogus

Re: Pb shutter design - photon and fast neutron attenuation analysis

Date: May 4, 1992

Introduction

The fast neutron dose rate in the medical room with all shutters closed is rather high. In the beam line and just below the lead shutter, the fast neutron dose rates have been measured at 3-7 rem/hr, depending on the beam configuration. Photons and thermal neutrons also add to the dose, but at lower levels. People will be exposed to these doses while setting up the patient for an irradiation.

In this task, some shielding calculations were done to see if replacing some of the lead in the top part of the lead shutter with a better fast neutron shielding material could reduce the total dose rates significantly. Fast neutron and photon doses were calculated for a shutter composed of various amounts of polyethylene and lead. Polyethylene was chosen as the fast neutron shield since it has a large H atom density and is relatively inexpensive. Similar calculations were done for a polyethylene and depleted uranium shutter.

Method

Polyethylene attenuates the fast neutron dose by scattering and thermalization. The attenuation in the fast neutron dose was calculated using an exponential model with an experimentally determined attenuation coefficient. The attenuation coefficient was

determined by adding a 1" thick slab of polyethylene above the lead shutter and measuring the reduction in fast neutron dose rate with a Bonner sphere.

The attenuation of photon dose was calculated using an exponential model and a buildup factor. An effective attenuation coefficient for lead was estimated from an experiment. It was found to be roughly equal to that for a monoenergetic beam in the 3-4 MeV range. The attenuation coefficient for uranium was calculated by scaling the 3 MeV value for lead by the density ratio of uranium to lead.

The thickness of the shutter was kept constant at 28 cm. If 2 cm of polyethylene was added, for example, the fast neutron dose was lowered using the exponential model. Also, the photon dose was increased using the buildup factor - attenuation model since 2 cm of lead was removed.

The model assumes that the area of the polyethylene is at least 2 feet by 2 feet square. As well, no credit is given for photon attenuation in the polyethylene or for neutron attenuation in the lead. And finally, prompt gamma production in the polyethylene was not accounted for. The latter 2 assumptions will have to accounted for by an approximate model at a later time. However, they might not be as severe as one might first expect. Prompt gamma production in the polyethylene might not make a major contribution to the gamma dose for realistic thicknesses of polyethylene and lead in the beam. Also, the photon attenuation in the polyethylene might well be small relative to the attenuation if the lead.

Results

Figure 1 shows the photon buildup factors for lead and uranium. These buildup factors are for a plane monodirectional source and were extracted from the Radiological Health Handbook. Figure 2 shows the doses calculated for various amounts of polyethylene and lead. Figure 3 shows the doses when depleted uranium is used.

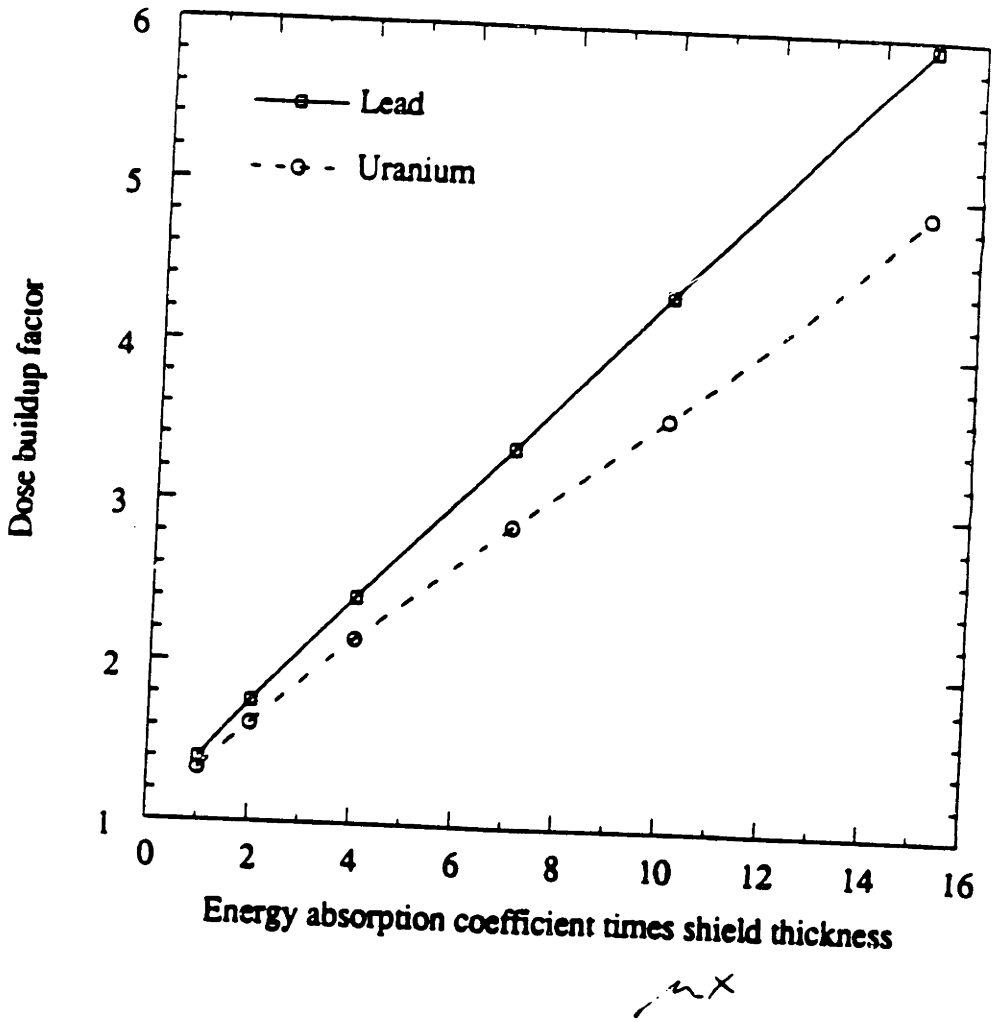
Lead
Uranium
Dose buildup factor
Energy absorption coefficient times shield thickness
μx
6
5
4
3
2
1
0
2
4
6
8
10
12
14
16

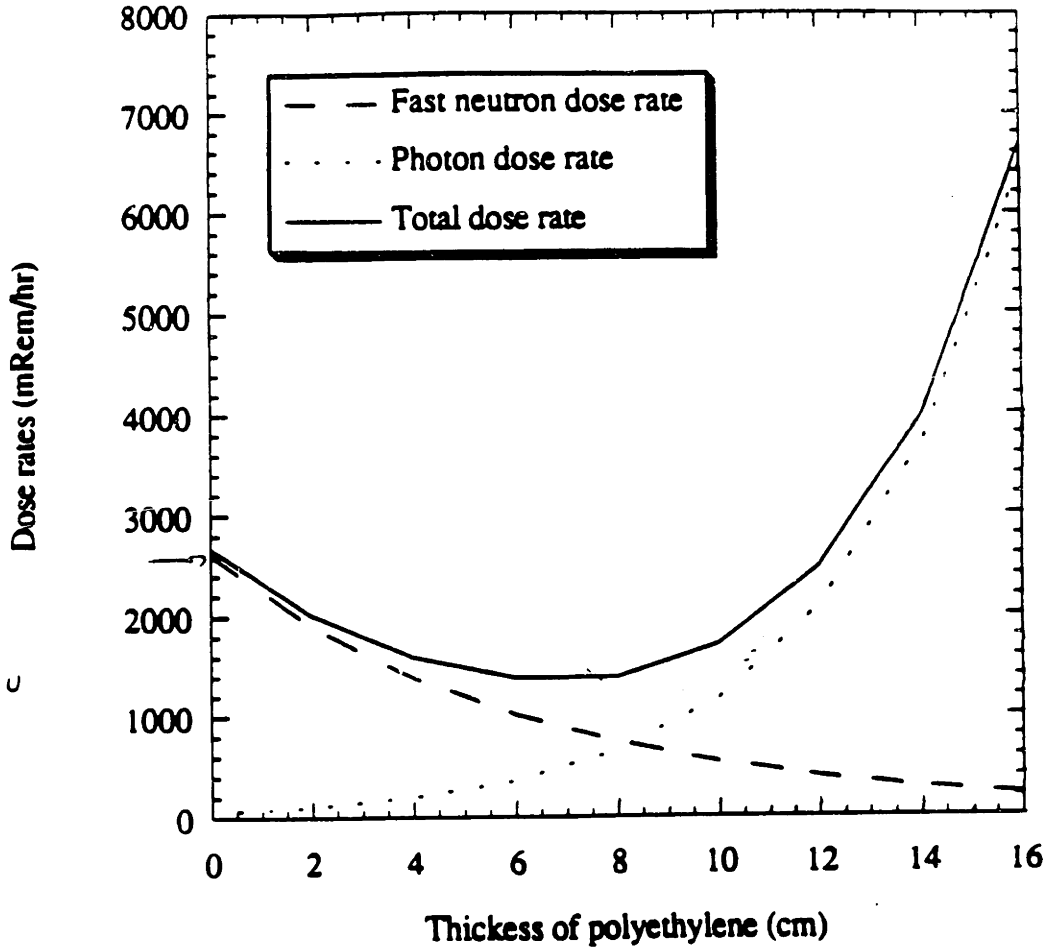
8000
7000
6000
5000
4000
3000
2000
1000
0
Dose rates (mRem/hr)
— — Fast neutron dose rate
. . . . Photon dose rate
——— Total dose rate
0
2
4
6
8
10
12
14
16
Thickess of polyethylene (cm)

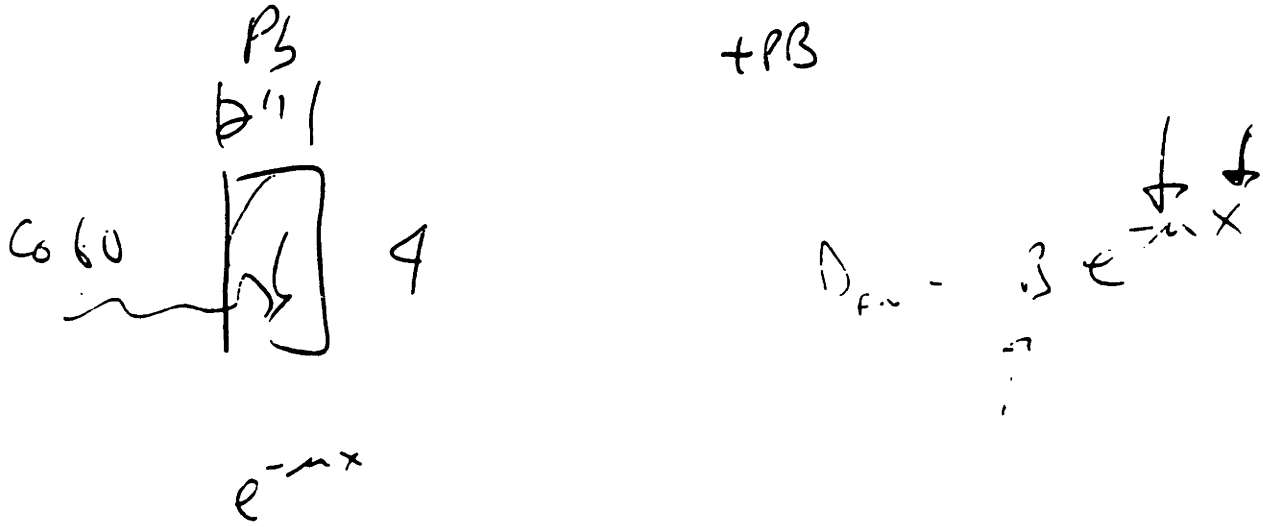
Pb
Cu
Co 60
+Pb

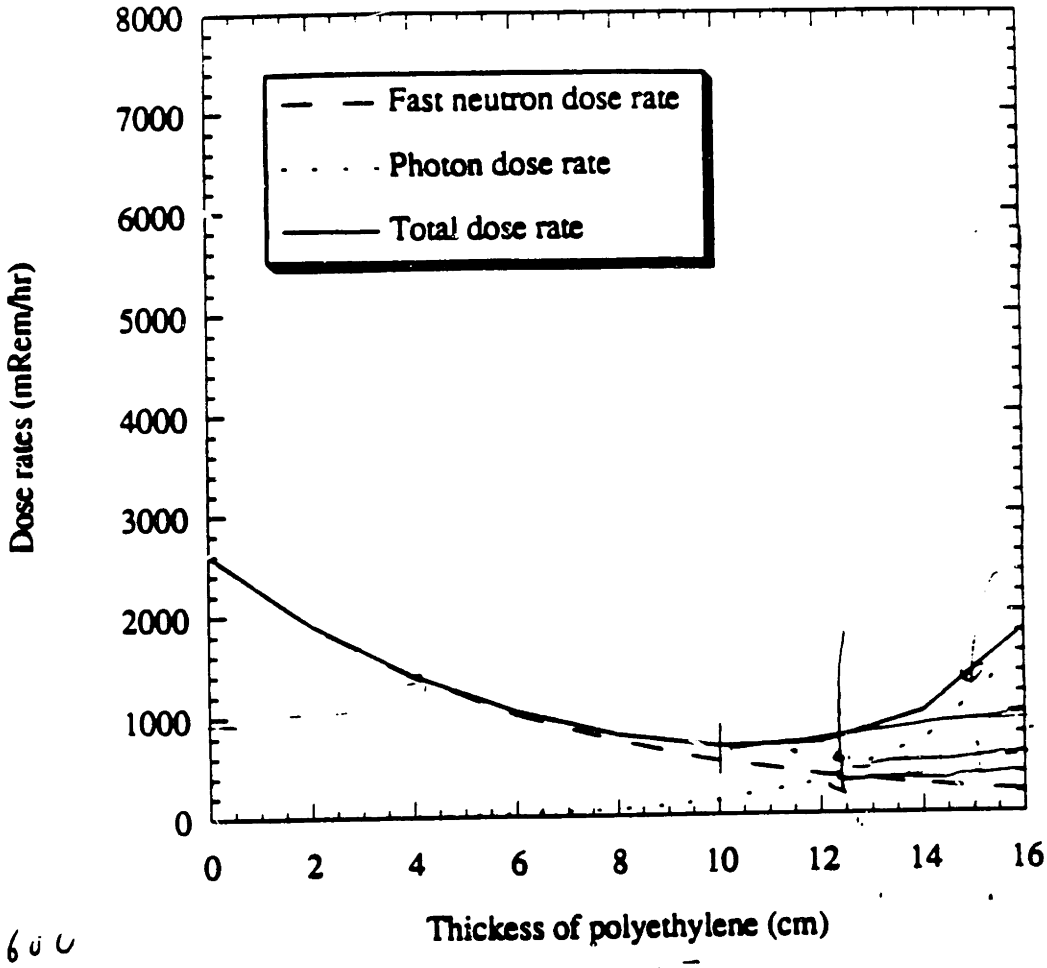

2600

8°00 7.400 (hr)

+ DEPLETION

$Dose = 2600 e^{-2x}$

Discussion

With all shutters closed, the M62 beam had a photon dose rate of 61 mrem/hr and a fast neutron dose rate of 2606 mrem/hr. Adding polyethylene at the expense of lead changes these doses as shown in Figure 2. The fast neutron dose drops slowly (HVL = 4.4 cm). The photon dose rises as more lead is removed. The minimum total dose, reached with 6-8 cm of polyethylene, is 1375 mrem/hr. Therefore, the total dose rate can only be cut in half. (Doses from thermal neutrons are ignored in this report. However, they are small.)

Uranium is a better photon shield than lead. As shown in Figure 3, the photon doses are smaller and a minimum total dose of 681 mrem/hr is predicted for 10 cm of polyethylene and 18 cm of uranium. The total dose rate, then, is reduced by almost a factor of 4.

Additional comments

JY and OH have recommended looking at deuterated polyethylene. Using deuterium would reduce the prompt gamma production. However, prompt gamma production in the polyethylene might not make a significant contribution to the photon dose. Deuterated polyethylene is expensive and would not be expected to thermalize the beam as rapidly as regular hydrogenated polyethylene. A borated or lithiated hydrogenous polyethylene might be cheaper and work better.

Compounds such as TiH2 and ZrH2 were considered briefly. TiH2 has a slightly higher number of H atoms per cm3 than polyethylene (at least in the pure, crystalline form). However, as I understand it, we would have to buy TiH2 as a powder and have it

formed with powder met tech. For a 10 cm thick slab, the TiH2 would cost $11,000. Powder met technology is also expensive. JY and OH have also recommended looking at TiD2 and ZrD2. However, I haven't found much information on these materials yet.

A new product offered commercially is a mixture of tungsten and polyethylene. The tungsten slows neutrons by inelastic scattering (2-3 barns) and also is a good photon shield. Attenuation curves have been requested from this manufacturer.

Are there any advantages to using a homogeneous shield? That is, would a mixture of lead and polyethylene work better than having polyethylene on top and lead on the bottom.

Monte Carlo help is needed. Values for prompt gamma generation in the polyethylene are needed. Also, Monte Carlo runs could help assess the accuracy of the attenuation model.

Comments on shield design engineering

Perhaps the best way to design this would be to make a large shield plug, similar to the collimator. The plug could be bolted into the bottom of the lead shutter. This would give us the flexibility to change the shielding configuration. Mechanical stresses would be small, just coming from the weight of the shielding itself. Heat generation and induced thermal stresses will probably be small. Radiation damage, even in polyethylene if used, will probably be small.

The lead should not activate appreciably. We would have to run a NAA as we did with the horsecollar. If depleted uranium is chosen, it would have to be protected from corrosion and air oxidation. It is mildly radioactive so some additional shielding would be needed beneath it. Activation and production of prompt gammas and fast neutrons from fission would have to be assessed. Monte Carlo work would be helpful here. While uranium can be fabricated like steel, I'm not sure how much machining we can do here. Polyethylene is strong enough for our purposes and we can machine it easily. It's limited resistance to heat and radiation should not be a problem.

A step in the polyethylene might be needed to minimize neutron streaming. A similar step might be needed in the lead or uranium part of the shield to minimize photon streaming.

APPENDIX G RICHARD CHOI'S B-10 ANALYSIS OF CHICKEN LIVERS IN ROUND ROBIN

NUCLEAR REACTOR LABORATORY

AN INTERDEPARTMENTAL CENTER OF
MASSACHUSETTS INSTITUTE OF TECHNOLOGY

O K HARLING
Director

138 Albany Street, Cambridge Mass 02139
Telefax No (617)253-7300
Telex No. 92-1473-MIT-CAM
Tel. No (617) 253-4201

J A BERNARD JR
Director of Reactor Operations

July 8, 1991

Professor Detlef Gabel
Department of Chemistry
University of Bremen
Box 33 04 40
D-2800 Bremen 33
Federal Republic of Germany

Dear Detlef:

The chicken liver samples which you provided for a "round robin" have recently been analyzed for ^{10}B using our prompt gamma facility. The results from Dr. Richard Choi's measurements are enclosed. We use the 0.5 MeV annihilation gamma rays from the hydrogen in the sample to accurately determine or normalize for the neutrons incident upon the sample vial.

Fresh chicken liver standards with known concentrations of ^{10}B were used to determine the calibration curve. The samples we received from you were deteriorated to some extent as evidenced by the odor. If some of the water evaporated from your samples, an error is possible in the prompt gamma since we determine (μg B-10/gm sample) and evaporation of water could affect this.

Please send me all the results you have obtained in this "round robin."

Sincerely,

Otto Harling
Director, Nuclear Reactor Laboratory
Professor of Nuclear Engineering

OKH:DKE

Enclosure

Dr. Gabel's chicken liver standard analysis

We received 6 vials of chicken liver marked 1, 3, 5, 20, 30, and 100. They were in very bad condition with signs of leakage and spoilage. Small samples from each vial was analyzed for B-10 concentration using the 6SH4 Prompt-gamma beam at MITR-II. The resulting ratio of B-10 peak (478 keV) to H peak (2.2 MeV) was then compared to that of a fresh chicken liver standard made by Choi. The following table summarizes the result.

Vial #	^{10}B/H Ratio	^{10}B Conc.†	Remarks
1	0.07	1.5*	*Determined by comparing the B/H ratio to Choi's standard from a plot. Not calculated.
3	0.16	4.3*	*Determined by comparing the B/H ratio to Choi's standard from a plot. Not calculated.
5	0.31	9.2	Very little sample in the vial. It could have been dehydrated.
20	1.2	37	
30	1.9	58	
100	6.0	180	Very thick (much thicker than other samples).

† Calculated based on Choi's chicken liver standards.
(^{10}B/H area ratio = 0.033/ppm ^{10}B)

With the exception of vials #1 and 3 (which were consistent with each other), Dr. Gabel's standards were internally consistent with the markings on the vials (vial #100 was approximately 5 times as conc. as vial #20, which in turn was 4 times as conc. as vial #5, etc.) If we assume that the markings on the vials are meant to correspond to the actual concentrations of boron; then, the discrepancy with the calculated concentrations in the table seem to indicate a systematic problem with either uniform dehydration of the samples or incorrect boron-liver mixtures.

EUROPEAN COLLABORATION
ON
BORON NEUTRON CAPTURE THERAPY

The Project Leader
Prof. Dr. Detlef Gabel

Prof. Dr. Otto Harling
Mass. Inst. of Technology
Nuclear Reactor Laboratory
138 Albany Street
Cambridge, MA 02139
USA

JUL 29

Department of Chemistry
University of Bremen
Box 33 04 40
D-2800 Bremen 33
FR Germany
Tel. (0421) 218-2200
218-3128
218-2119
Fax (0421) 218-2871
Telex 245811 UNIBR D

19 July 1991

Dear Otto,

Please find enclosed the present status of the cross-calibration for boron determination. As I understand from Bob Zamenhof, tissues are analyzed by him with the Lexan/Ixan technique. would thinke these data to be of very great value when and if it is demonstrated that these data are consistent with the standards.

Best wishes,

Detlef Gabel

Cross-calibration of boron determination

Boron enrichment (MS) 92 %

Center								
Sample	200.00	60.00	40.00	10.00	5.00	2.00		
Boron-10	184.00	55.20	36.80	9.20	4.60	1.84		
Petten	201.10	62.80	39.70	9.99	4.99	2.07	ICP	
30/10/90	1.54	1.46	0.23	0.04	0.06	0.02	1.04	± SD
%of nomin	100.55	104.67	99.25	99.90	99.80	103.50	101.28 % of actual	
Lausanne	243.00	72.60	44.40	10.80	6.10	2.60	ICP	
01/03/91	3.40	1.74	1.32	0.29	0.13	0.24	3.47	± SD
%of nomin	121.50	121.00	111.00	108.00	122.00	130.00	118.92 % of actual	
	240.00	69.60	52.10	11.70	6.10	2.00	ICP	
	3.80	1.40	1.60	0.30	0.55	0.13	4.12	± SD
%of nomin	120.00	116.00	130.25	117.00	122.00	100.00	117.54 % of actual	
BNL	184.80	57.00	36.60	8.90	4.30	1.80	PGS	
23/04/91	6.30	2.70	1.20	0.50	0.30	0.30	6.78	± SD
%of nomin	100.43	103.26	99.46	96.74	93.48	97.83	98.53 % of actual	
Bremen	136.86	52.60	27.99	7.83	4.12	0.35	QNCR	
DH 23/04/	10.06	3.07	1.09	0.97	2.03	0.05	15.50	± SD
%of nomin	74.38	95.29	76.06	85.11	89.57	19.02	73.24 % of actual	
Lund	350.00	92.00	39.00	10.00	8.00	6.00	QNCR	
20/06/91	30.00	16.00	3.30	0.10	1.10	0.70	10.14	
%of nomin	190.22	166.67	105.98	108.70	173.91	326.09	178.59 % of actual	
INEL								
MIT/Tufts	180.00	58.00	37.00	9.20	4.30	1.50	PGS	
08/07/91								
	97.83	105.07	100.54	100.00	93.48	81.52	96.41 % of actual	